Measurement of the double polarization observables G and E in neutral and positive pion photoproduction off the proton

Dissertation zur Erlangung des
Doktorgrades (Dr. rer. nat.)
der
Mathematisch-Naturwissenschaftlichen Fakultät
der
Rheinischen Friedrich-Wilhelms-Universität Bonn

vorgelegt von
Karsten Philipp Spieker
aus
Bielefeld

Bonn, November 2019

Angefertigt mit Genehmigung der Mathematisch-Naturwissenschaftlichen Fakultät der Rheinischen Friedrich-Wilhelms-Universität Bonn

1. Gutachter: Prof. Dr. Reinhard Beck
2. Gutachter: Prof. Dr. Michael Ostrick

Tag der Promotion: 18.12.2019
Erscheinungsjahr: 2020

Abstract

The nucleons, as one of the most fundamental building blocks of visible matter, are built up of quarks and gluons. However, the interactions and dynamics inside the nucleons, which are mediated by the strong force and described by Quantum Chromodynamics (QCD), are still a major challenge to modern physics. In the mass region of the excited states of the nucleons, known as resonances, perturbative calculations are not feasible in QCD, and thus phenomenological approaches and numerical methods are essential for the description of the strong interaction. From the experimental side, complementary probes are available to study the excitation spectrum of the nucleon and different sensitivities to unique observables provide stringent tests of the available theoretical approaches. In the past, most resonances have been found in pion-nucleon scattering experiments. However, the meson photoproduction reactions gained more attention during the last decades since several resonances might only weakly couple to the pion-induced reactions. Although over the years a lot of experimental effort from several collaborations at various accelerator facilities was conducted, discrepancies between theoretical models and experimental results are still present, e.g., regarding the number of resonances. From the experimental point of view, the short lifetimes of the resonances are a possible explanation for these discrepancies. They lead to many broad and overlapping resonances that even contribute selectively to distinct decay channels. The measurement of the total unpolarized cross sections alone is not able to identify all resonances since they are only sensitive to the dominant contributing resonances. For the identification of all resonances and their properties, an unambiguous Partial Wave Analysis (PWA) solution needs to be obtained. This requires precise knowledge of several well-chosen single and double polarization observables in different decay channels. Therefore, current experiments measure these polarization observables that are sensitive to weakly contributing resonances. They can be accessed by either polarizing the initial state, by measuring the polarization of the recoiling nucleon in the final state, or even both.

One experiment, which can measure polarization observables through the meson photoproduction process, is the Crystal Ball experiment within the A2 collaboration. It is located at the electron accelerator MAMI in Mainz, Germany. The G/E measurements made use of elliptically polarized photons that have a linearly and circularly polarized component at the same time. They are produced by the interaction of a longitudinally polarized electron beam with a diamond radiator. In combination with a longitudinally polarized butanol target, the elliptically polarized photons are used to obtain for the first time the double polarization observables G and E simultaneously in one experimental

run. Whereas for the determination of E the circular polarization component is needed, the linear polarization component of the photon beam allows to access G with the same experiment.

The double polarization observable G was determined for the reactions $\vec{\gamma}\vec{p} \to p\pi^0$ and $\vec{\gamma}\vec{p} \to n\pi^+$ in a beam photon energy range from 230 MeV to 840 MeV ($W = 1145\,\text{MeV} - 1569\,\text{MeV}$) with a full angular coverage. In addition, the double polarization observable E was extracted in the same beam photon energy range for the $\vec{\gamma}\vec{p} \to n\pi^+$ reaction. Background contamination could be effectively reduced and the desired reaction channels were clearly identified. Asymmetries in the selected azimuthal angular distribution of the final state meson were used to extract the double polarization observable G. For the extraction, two methods were used, namely a χ^2-fit to the binned event yield asymmetries and an unbinned maximum likelihood fit. The double polarization observable E was determined via the carbon subtraction method.

The results for the double polarization observable G in both analyzed channels provide the first precise measurement in the first resonance region and parts of the second resonance region. Furthermore, the new A2 data in the $p\pi^0$ channel close the gap between the region of the $\Delta(1232)3/2^+(P_{33})$ resonance and the already existing data in the second resonance region. Both data sets are in good agreement with each other in the overlapping region. Furthermore, the high sensitivity of the double polarization observable G to weakly contributing resonances in combination with the new precise data reveal even contributions of partial waves with angular momentum up to $l = 4$ (G-waves) in the first resonance region. In the future, the measurement of both channels will allow an isospin separation of the partial waves and might help, in particular, to improve the uncertainties of the partial wave P_{11} to which the Roper resonance $N(1440)1/2^+(P_{11})$ couples.
For the double polarization observable E in the $n\pi^+$ channel, a very good agreement between the measurements with elliptically and circularly polarized photons was observed. Therefore, the results of this work give experimental evidence that an elliptically polarized photon beam can be used to extract the double polarization observable E. In comparison to the existing data, the new A2 data provide additional points in the backward direction of the charged pion and for beam photon energies below 350 MeV. In the overlapping regions, the data sets agree very well with each other.
Overall, the results of the polarization observables still show notable differences to recent PWA models. Therefore, the new data will help to further constraint the different models.

Table of contents

Chapter 1

Introduction

Already the Greek scientists and philosophers tried to understand the fundamental building blocks of matter. Over 2500 years ago, Demokrit was the first person who assumed that matter is built up of small and inseparable units, which he finally called the "atom" (old greek for atomos = inseparable). Nowadays, we know that the atom is separable and that it is formed by a nucleus built up of protons and neutrons, along with negatively charged electrons surrounding the nucleus.
Until the year 1933, the proton and therefore also the atom were assumed to be the most fundamental building blocks of matter and therefore to behave as point-like particles. This picture changed after Stern and Gerlach measured the magnetic moment of the proton in 1933 which differed from the theoretical prediction for a point-like spin 1/2 particle [1]. Followed in the late 1950s, R. Hofstadter and colleagues performed an experiment where electrons were scattered on a proton [2]. The resulting measured cross section disagreed with the scattering of an electron on a point-like particle. Thus, by the introduction and determination of the electric form factor, the root-mean-square charge radius of the proton was deduced. Through the measurement of this extension of the proton, the final proof of an inner structure of the proton was given. However, although over the last 50 years, the spectroscopy of the proton revealed the inner structure of it in terms of quarks and gluons, the interactions and dynamics inside the proton are still a major challenge of modern physics.
Therefore, the purpose of this thesis is to contribute to a better understanding of the dynamics between the quarks and gluons inside the proton, by performing measurements of so-called polarization observables.
This chapter aims to give a good overview of the necessary theoretical background for this thesis.

1.1 The Standard Model of Particle Physics

The Standard Model of Particle Physics (SM) belongs to the most successful physical theories of all time. It is capable of describing a wide range of observed phenomena via twelve elementary fermion fields and the three fundamental interactions among them, namely the strong, electromagnetic, and weak interaction. The interactions between particles are described by the exchange of vector gauge

bosons with spin 1, where the form of the interaction is determined by local gauge principles. The Higgs mechanism and its associated scalar Higgs boson with spin 0 are the final important parts of the Standard Model since the Higgs mechanism is the solution to the problem that the vector gauge bosons of the weak interaction have to acquire mass without breaking the local gauge symmetry of the Standard Model [3]. Moreover, it gives the fundamental fermions their masses.
The twelve elementary fermions have spin 1/2 and are grouped into two groups of six particles each, called leptons and quarks, with each having their antiparticle. They are arranged in three generations in which the particles have similar physical quantities. An overview of the elementary particles and their properties can be found in Tab. 1.1 [4].

Table 1.1: Overview of the different elementary particles in the SM and some of their properties. The weak isospin (T) corresponds to a conserved quantum number of the weak interaction. In the table, the third component of the weak isospin for left-handed fermions is given.

	1. Generation	2. Generation	3. Generation	Electric charge	Weak isospin
leptons	$\begin{pmatrix} e \\ \nu_e \end{pmatrix}$	$\begin{pmatrix} \mu \\ \nu_\mu \end{pmatrix}$	$\begin{pmatrix} \tau \\ \nu_\tau \end{pmatrix}$	$\begin{pmatrix} -1 \\ 0 \end{pmatrix}$	$\begin{pmatrix} 1/2 \\ -1/2 \end{pmatrix}$
quarks	$\begin{pmatrix} u \\ d \end{pmatrix}$	$\begin{pmatrix} c \\ s \end{pmatrix}$	$\begin{pmatrix} t \\ b \end{pmatrix}$	$\begin{pmatrix} 2/3 \\ -1/3 \end{pmatrix}$	$\begin{pmatrix} 1/2 \\ -1/2 \end{pmatrix}$

The three main interactions differ in their strength, range, and interaction with the particle properties. An overview is presented in Tab. 1.2 [4].

Table 1.2: Overview of the properties of the different interactions in the SM.

Interaction	Mediator	Acts on	Relative strength	Range
strong	gluon (g)	color charge	1	≈ 1 fm
electromagnetic	photon (γ)	electric charge	10^{-2}	∞
weak	$W^{\pm}$ Z^0	weak isospin weak isospin electric charge	10^{-15}	< 1 fm

The underlying framework of quantum field theory for the strong interaction is called quantum chromodynamics (QCD). In this theory, the strong force is mediated by gluons which are acting via the so-called color charge on quarks and themselves. Every quark carries one of three possible color charges (red (r), green (g), and blue (b)), whereas their anti-particles likewise carry the anti-color charge. Gluons can have eight independent color states, which are combinations of a color and an anti-color, e.g., $r\bar{g}$. By that, the color charge can be conserved at a quark-gluon reaction vertex. Furthermore, this property of the gluons allows them to directly interact with each other, which leads

to two major aspects of QCD.

The first property is the effect of asymptotic freedom, and it is connected to the large energy dependence of the strong coupling constant $\alpha_S(Q^2)$. Thereby, the coupling constant is a quantity of the strength of the interaction of a gluon with itself or a quark at the QCD vertex. It depends on the momentum transfer Q^2 at the vertex. In the case of the coupling constant $\alpha_{EM}(Q^2)$ of the electromagnetic interaction, the particle-antiparticle pairs coming out of the vacuum shield the color charge, reducing its value for decreasing energies. This effect is known as the screening effect of the effective charge in QED. However, since gluons carry a color charge and thus can self-interact, virtual gluon pairs are possible in QCD, which smear the color charge and lead to an anti-screening effect. This effect acts with an opposite sign from that of quarks and dominates over the screening effect from quark-antiquark loops (cf. Fig. 1.1). As a result, the running coupling constant of the strong interaction tends to decrease with small distances (equivalent to high energies) whereas the coupling constant of the electromagnetic interaction $\alpha_{EM}(Q^2)$ increases (cf. Fig. 1.2). This effect is known

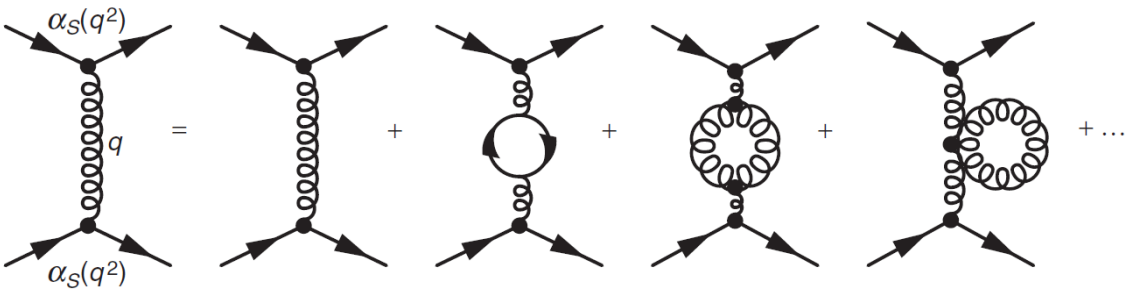

Fig. 1.1: Feynman loop diagrams for the strong running coupling constant. Some loop diagrams, which are responsible for the running coupling constant of the strong interaction, are presented. Thereby, q^2 is the momentum transfer at the vertex. The third diagram shows the production of quark-antiquark pairs (straight lines) in the vacuum, which are responsible for the screening effect of the color charge. The remaining diagrams present loop diagrams for the self-interaction of gluons (curly lines), leading to the anti-screening of the color charge (figure taken from [3]).

as asymptotic freedom since quarks behave asymptotically like quasi-free particles with increasing energy. Due to the small coupling constant in this range, perturbative quantum chromodynamics, can be applied to describe the strong interaction.

The opposite effect appears at larger distances and thus smaller energies where the coupling between the quarks becomes very large. As a result, despite many experimental attempts to detect isolated quarks and gluons, they have never been detected. The phenomenon is explained by the hypothesis of color confinement. Its main message is that colored objects, like the quarks and gluons, are always confined to color-singlet states. To produce a color singlet-state, they have to be bound in systems of several quarks, named hadrons. These hadrons are realized most simply in either three quarks (baryons) or a quark-antiquark pair (mesons) [5]. In fact, even more complex structures, known as exotic states are possible, e.g., $qqqq\bar{q}$ systems in the baryon sector. These objects are called pentaquarks. The LHCb collaboration has published the observation of two charmed pentaquark

states with a minimum quark content $c\bar{c}uud$ at invariant masses close to 4.4 GeV [6]. In the meson sector, due to the self-coupling of gluons, mesons made of bound gluons (glueballs) and $q\bar{q}$ with an excited gluon (hybrids) may exist. In addition, color singlet states are possible by a multiquark system consisting of $q\bar{q}q\bar{q}$. Thereby, a distinguishment between a compact diquark-antidiquark system, called tetraquarks, and a "molecular" bound state of two mesons is made. These molecular states have also been predicted in the baryon sector [7]. A separation of these quark configurations inside the hadrons always leads to the formation of new hadrons. This phenomenon is known as hadronization and thus free quarks and gluons can not be observed.

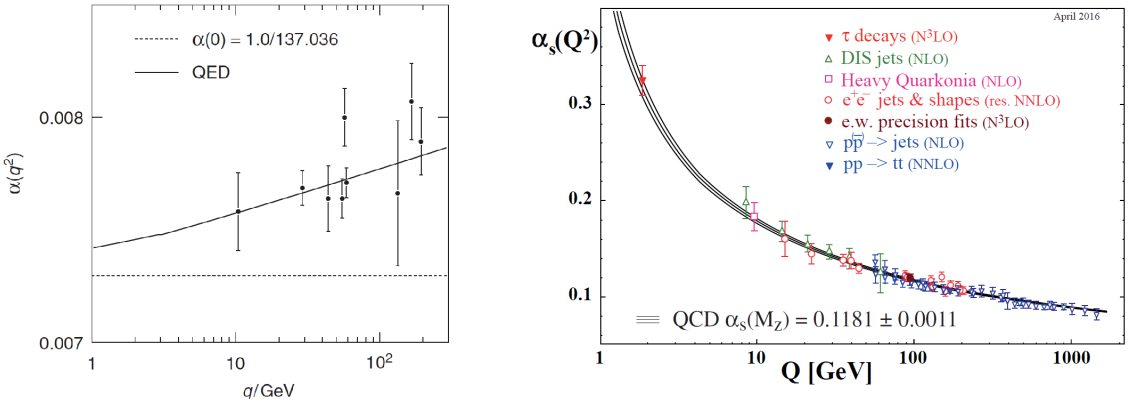

Fig. 1.2: Coupling constants of the electromagnetic and strong interaction. On the left side, the measured coupling constant of the electromagnetic interaction is shown as a function of the energy scale q. The data are obtained from $e^+e^- \to f\bar{f}$ data with the OPAL experiment at LEP [3]. The dotted line shows the limit of $\alpha_{em} \approx 1/137$ at $q^2 = 0$. The right side presents the analogous picture of the strong running couling constant $\alpha_S(Q^2)$. Thereby, the running coupling of QCD (solid line) is plotted together with recent data. Note that Q^2 = -q^2 holds where q^2 is the momentum transfer as shown in Fig. 1.1. The energy scale q is equal to $Q = |q|$ (figure left taken from [3], right from [7]).

1.2 Bound states in QCD (Hadrons)

All hadrons have in common that their total wave function is a product of the spin and flavor components, the color content, and the spatial wave function and is given by [3]:

$$\Psi_{total} = \chi_{spin}\phi_{flavor}\xi_{color}\eta_{spatial}. \tag{1.1}$$

For the simplest composition of baryons (qqq) and mesons ($q\bar{q}$), the flavor component of the total wave function can be constructed using the assumption of a SU(3)$_f$ flavor symmetry of the three lightest quarks (up (u), down (d) and strange (s)).

Using the fundamental SU(3) representation for quarks and the conjugate representation for the antiquarks, the flavor wave function of a meson consisting of a $q\bar{q}$ decomposes into an octet and a singlet,

$$3 \otimes \bar{3} = 8 \oplus 1. \tag{1.2}$$

As these mesons are built up of two fermions with spin 1/2, the individual spins can either be aligned to each other (triplet state with total spin $S = 1$) or not (singlet state with $S = 0$). Therefore, each flavor state has two possible spin configurations. The parity of a meson is given by:

$$P(q\bar{q}) = P(q)P(\bar{q}) \times (-1)^L = (+1)(-1)(-1)^L = (-1)^{L+1} \tag{1.3}$$

with $P(q)$ and $P(\bar{q})$ being the intrinsic parities of the quark and likewise the antiquark. Thus, together with the convention J^P, the lightest mesons with an orbital angular momentum of $L = 0$ can be grouped into a 0^- pseudoscalar meson multiplet and a 1^- vector meson multiplet. They are plotted in Fig. 1.3.

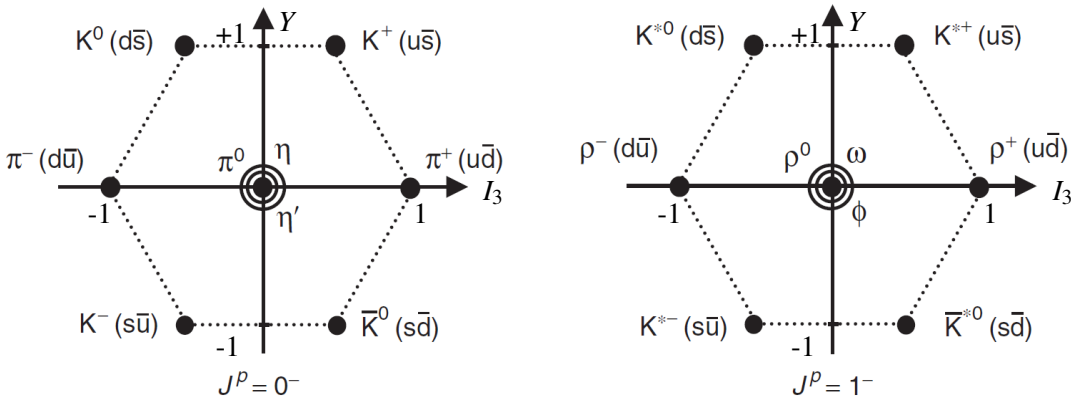

Fig. 1.3: The meson nonets of the ground state. On the left side, the pseudoscalar nonet with $J^P = 0^-$ is shown whereas on the right side the vector meson nonet with $J^P = 1^-$. On the y-axis of both plots, one finds the hypercharge Y, which is the sum of the strangeness S and the baryon number B, and on the x-axis one has the third component of the strong isospin I_3 (figure modified from [3]).

The flavor wave function of the baryons can be constructed in a similar way and is given by:

$$3 \otimes 3 \otimes 3 = 10_S \oplus 8_{MS} \oplus 8_{MA} \oplus 1_A. \tag{1.4}$$

Thereby, S stands for symmetric, A for antisymmetric and M for mixed flavor states, i.e. mixed-symmetric (MS) and mixed-antisymmetric (MA). As baryons are made of quarks which are fermions and thus have to fulfill the Pauli-principle, the overall wave function of the baryon needs to be antisymmetric under the interchange of any two of the three quarks. Since the bound systems always need to be color-neutral, the color wave function needs to be antisymmetric. Furthermore, the spatial wave function is symmetric for the ground state baryons. As a consequence, the product of the spin and flavor function has to be symmetric. This can be achieved either by a symmetric spin 3/2 wave function in combination with the symmetric decuplet or the mixed symmetric flavor octet with the mixed symmetric spin state with a total spin of 1/2. The corresponding multiplets in form of the $1/2^+$

octet, which includes the proton (p) and neutron (n), and the 3/2 $^+$ decuplet, including the Δ, are depicted in Fig. 1.4.

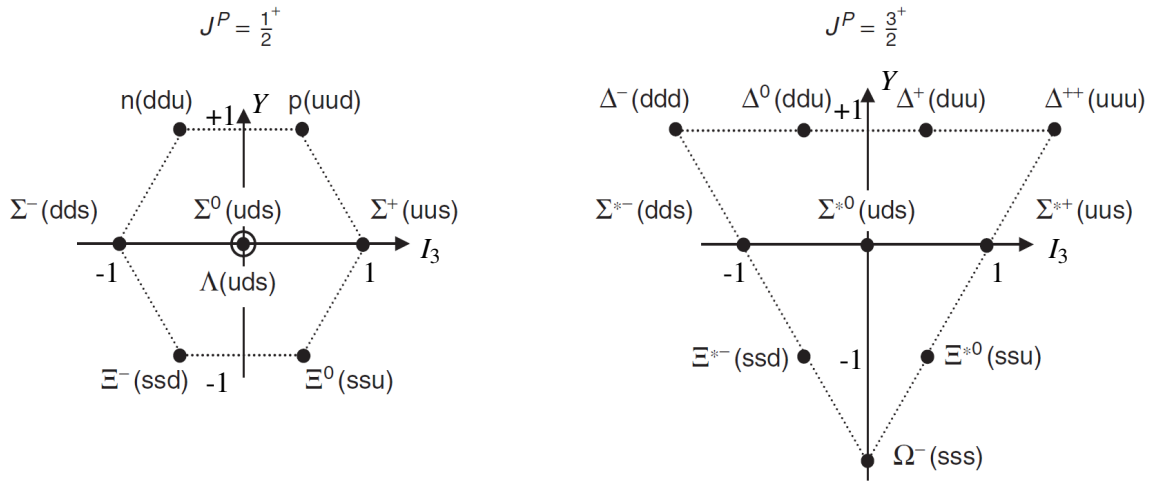

Fig. 1.4: The baryon multiplets of the ground state. On the left side, the octet with $J^P = 1/2^+$ is shown whereas on the right side the decuplet with $J^P = 3/2^+$ can be seen. Both of them are plotted as a function of the hypercharge Y, which is the sum of the strangeness S and the baryon number B, and the third component of the strong isospin I_3 (figure modified from [3]).

As the SU(3) flavor symmetry of the up-, down- and strange-quarks is not exact, the masses of the baryons and mesons inside their corresponding multiplets are not the same. Moreover, the mass increases with the number of strange-quark inside the hadrons as the mass of the strange quark ($m_s \approx 95\,\text{MeV}$) is greater than of the up- ($m_u \approx 2.2\,\text{MeV}$) and down-quark ($m_d \approx 4.7\,\text{MeV}$). As an example, the mass of the lightest baryon, the proton, is in the order of 938 MeV whereas the mass of the Ξ in the same multiplet with two strange quarks is already in the order of 1320 MeV [7]. The mass difference between the octet and decuplet states can be assigned to the chromomagnetic spin-spin interactions of the involved quarks [3]. As an example, the mass of the Δ^+ with the same quark content as the proton but with a total spin of $S = 3/2$ is about 300 MeV heavier than the proton. It is noteworthy that the Δ states with a mass of about 1232 MeV were the first-ever observed resonances which were seen in πN scattering experiments performed by Fermi and collaborators in 1952 [8].
Notably, the up- and down quark and even the strange quark have extremely small masses in comparison to the baryon masses. In fact, the sum of the quark masses inside the proton contributes with only about 1% to the total mass. The remainder can be attributed to the energy associated with the internal color gluon field which produces a sea of virtual quarks and gluons. A final problem, related to the masses of the baryons, is that the energy scale of their masses is in the region where the strong coupling constant is large, making perturbation calculations of QCD impossible. Thus, phenomenological approaches in the form of the constituent quark model or even numerical methods like lattice calculations are essential to model the strong interaction and to describe the dynamics between the quarks and gluons. These will be briefly introduced, with respect to the nucleon excitation spectrum, in the next section.

Constituent Quark Models

The constituent quark models assume that the baryons are built up of three constituent quarks with the same particle properties as the valence quarks but a mass of about one third of the baryon mass, i.e. the up- and down constituent quark mass is roughly 350 MeV, whereas the one of the strange quark is 500 MeV [9]. The high mass arises from the valence quarks, introduced in the previous section, which are surrounded by a cloud of quark-antiquark pairs (called sea-quarks) and gluons. Following the requirements of the color confinement, these constituent quarks need to be bound inside the baryons via a potential. Thereby, the potential depends on the considered quark model. Over the years, many different approaches for the potential have been developed [9], starting from a simple non-relativistic harmonic-oscillator potential [10] to relativistic models like the Bonn model [11].
The Bonn model respects the color confinement through a potential which increases proportionally to the average distance between the quarks. A spin-flavor dependent interaction, based on instanton induced interactions, can describe most of the spin-dependent splittings in the baryon excitation spectrum [12].
The obtained excitation spectra, including the prediction of the Bonn model and the experimentally measured resonances, are depicted in Fig. 1.5 for the N^*-states with the strong isospin $I = 1/2$ and for the Δ^*-states with strong isospin $I = 3/2$. The nomenclature of a resonance state is given by their isospin, the resonance mass M, the total angular momentum and parity $J^{P_{res}}_{res}$, and finally the partial wave $(l)_{2I2J}$. Thereby, as the resonance notation is defined for resonances that decay via the strong interaction into a meson and a nucleon, the term l in the partial wave expression is the orbital angular momentum between the meson and nucleon in the final state. Instead of using $l = 0,1,2,3,4,5\ldots$, the notation from atomic spectroscopy is used, namely $l = S,P,D,F,G\ldots$. Altogether, this means that a resonance is described by $(N/\Delta)(M)J^{P_{res}}_{res}((l)_{2I2J})$, i.e. the Δ-resonance of the decuplet is given in this notation by $\Delta(1232)3/2^+(P_{33})$. Due to this notation, the baryon excitation spectra are categorized in terms of total angular momentum J and parity P. The predictions are indicated by the blue lines, whereas the red line presents the corresponding experimental measurements with their uncertainties indicated by the boxes. Finally, their PDG rating, taken from [13], is included by the number of stars above the state[1]. In the low mass resonance region with masses below 1.8 GeV, the predictions are mostly compatible with the experimental measurements. Only some discrepancies are seen, e.g., in the N^* section, the predicted resonance position of the $N(1535)1/2^-(S_{11})$ is 51 MeV smaller than the measured one. Opposite behavior is given for the $N(1680)5/2^+(F_{15})$, where the predicted position is even 81 MeV larger. Similarities are also present in the Δ^* section, i.e. the $\Delta(1700)3/2^-(D_{33})$ is predicted 109 MeV lower than the measured one. Nevertheless, the overall pattern and number of resonances agree in the low mass region. This situation changes dramatically above 2 GeV, as more resonances are predicated than have been measured. This problem is typically denoted in literature as the missing resonance problem [10]. One of the two major explanations for these discrepancies is a wrong assumption on the number of degrees of freedom in the theoretical models. The constituent

[1] A high number of stars means that the state is well established and seen by several experiments.

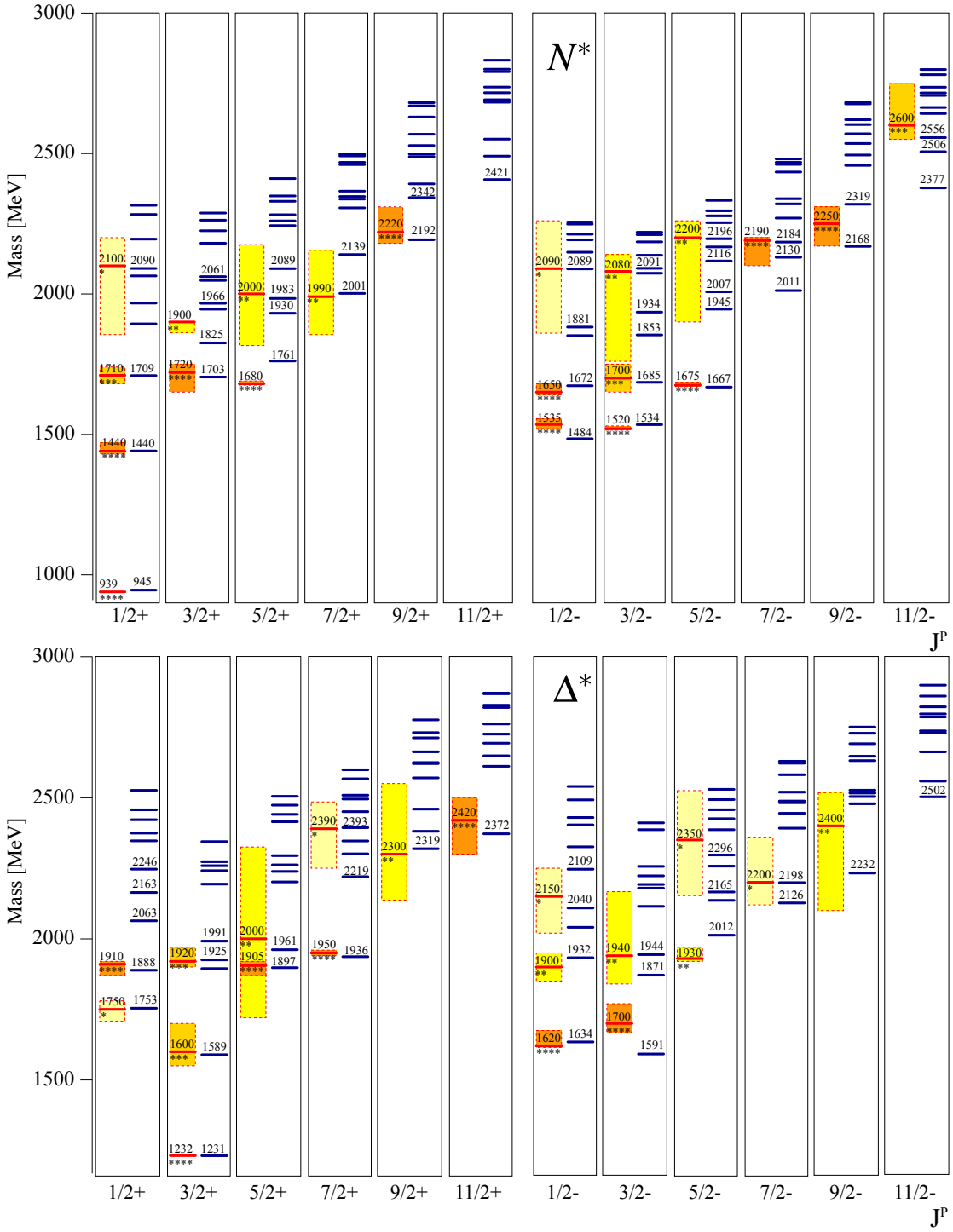

Fig. 1.5: Excitation spectrum obtained with the Bonn model. The excitation spectrum predicted by the Bonn model (blue line) is compared to the experimental measurements (red lines) and their uncertainties (boxes). The PDG rating of the excited states, taken from [13], is included by the number of stars above the state. The upper row presents the results for the resonance states with isospin $I = 1/2$ whereas the lower one the resonances with isospin $I = 3/2$ (figure taken from [14]).

quarks might be in a quark-diquark system rather than a three quark system and thus one degree of freedom would be frozen. However, recent experimental results do not support this diquark model [15] and lattice QCD calculation, as will be shown in the next section, neither. Finally, it is noteworthy that most of the observed resonance states have been measured in πN-scattering experiments. Thus, from the experimental side, a possible explanation of the missing resonance problem is that the high lying resonances might have a small coupling to the pion induced reaction.

Lattice QCD

Another theoretical prediction for the excitation spectrum can be determined via lattice gauge theories. Thereby, lattice QCD defines the Lagrangian of the strong interaction on a space-time which has been discretized into a lattice with a lattice spacing a and length L [16]. To extract the excitation spectrum, the lattice spacing a needs to be minimized whereas the simulated volume of the lattice needs to go to infinity. As these calculations need a high amount of computing power, calculations are performed for different lattice spacing a with increasing length L and nonphysical masses for the quarks. Finally, the lattice QCD results can be used as a starting point for an extrapolation into the continuum limit ($a \to 0$). In this limit, the Lorentz-invariance of the Lagrangian, which was broken by the lattice structure, is recovered and together with the extrapolation of the assumed unphysical mass of the pion ($m_{\pi^0} = 396\,\text{MeV}$) to the physical mass of about 135 MeV, the excitation spectrum can be obtained [16]. Fig. 1.6 shows the predicted excitation spectrum for the nonphysical quark masses with a mass of $m_{\pi^0} = 396\,\text{MeV}$. Although the resonance positions of the constituent quark models and the

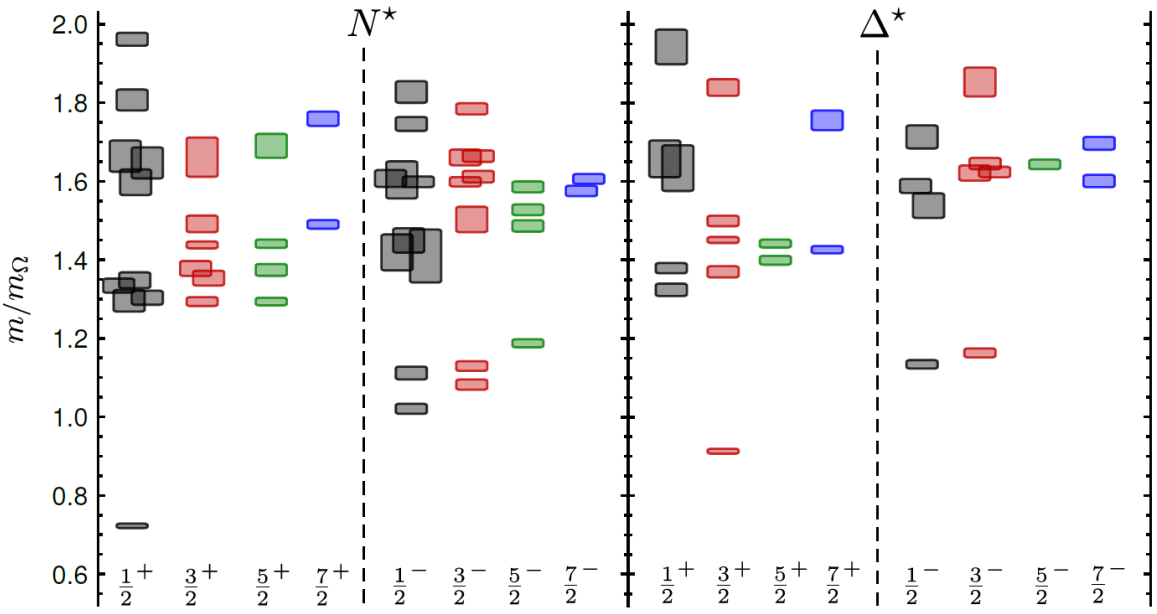

Fig. 1.6: Excitation spectrum obtained from lattice QCD calculations. The resonance states are shown as a function of their mass divided by the Ω^- mass and their total angular momentum and parity configuration J^P. Note that the calculations were performed with the nonphysical pion mass of $m_{\pi^0} = 396\,\text{MeV}$ (figure taken from [16]).

lattice calculation do not agree[2], the number of resonance states matches quite well. Most importantly, the lattice QCD calculation has the missing resonance problems as well, which is a strong hint that the diquark-model can be ruled out as a possible explanation. Nevertheless, the statement should be treated with caution since, in addition to the nonphysical pion mass, the resonances can not decay within these calculations.

1.3 Experimental Access to the Nucleon Excitation Spectra

In the past, most of the observed resonance states in the nucleon excitation spectra have been obtained from πN-scattering experiments. However, it is mandatory to use complementary probes to provide experimental information for the theoretical models. Thus, during the last decades, the photoproduction of pseudoscalar mesons off the nucleon gained more attention. This section will present the basic concepts of the photoproduction of pseudoscalar mesons, the importance of the measurement of so-called polarization observables and will finally outline different partial wave analyses, which use the polarization observables as input to determine contributing resonances in a desired reaction channel.

1.3.1 Pseudoscalar Meson Photoproduction

To get a better understanding of the major challenges of photoproduction experiments and of baryon spectroscopy overall, Fig. 1.7 shows the total photoabsorption cross section off the proton as a function of the beam photon energy E_γ and the center of mass energy W[3], along with several single- and double-meson final states. In addition, all listed four-star N^* and Δ^* resonances in the PDG are indicated by the dashed vertical lines [7].
The inspection of the cross sections directly shows that the number of peaks, which indicates a possible resonance behavior, does not at all agree with the number of included dashed vertical lines for the established resonances. This can be attributed to the fact that the nucleon resonance states decay via the strong interaction with a typical lifetime in the order of 1×10^{-24} s [7]. As a consequence of Heisenberg's uncertainty principle, the decay width is typically in the order of 100 MeV and thus several resonances overlap in the cross sections. Other remarkable observations are the different structures in the cross section of individual final states compared to the total photoproduction cross section. This can be explained by the contribution of different resonances and their coupling strength to explicit final states. Thus, to obtain a maximal amount of information on each contributing resonance in a given final state, polarization observables are measured via the process of pseudoscalar meson photoproduction. The basic formalism will be presented in the following section.

[2] This is expected due to the assumption of nonphysical quark masses.

[3] Photoproduction experiments are fixed-target experiments. Thus, the corresponding center of mass energy W, which corresponds to the resonance invariant mass, is given by $W = \sqrt{2E_\gamma m_p + m_p^2}$ where E_γ is the incoming beam photon energy and m_p the rest mass of the target proton at rest.

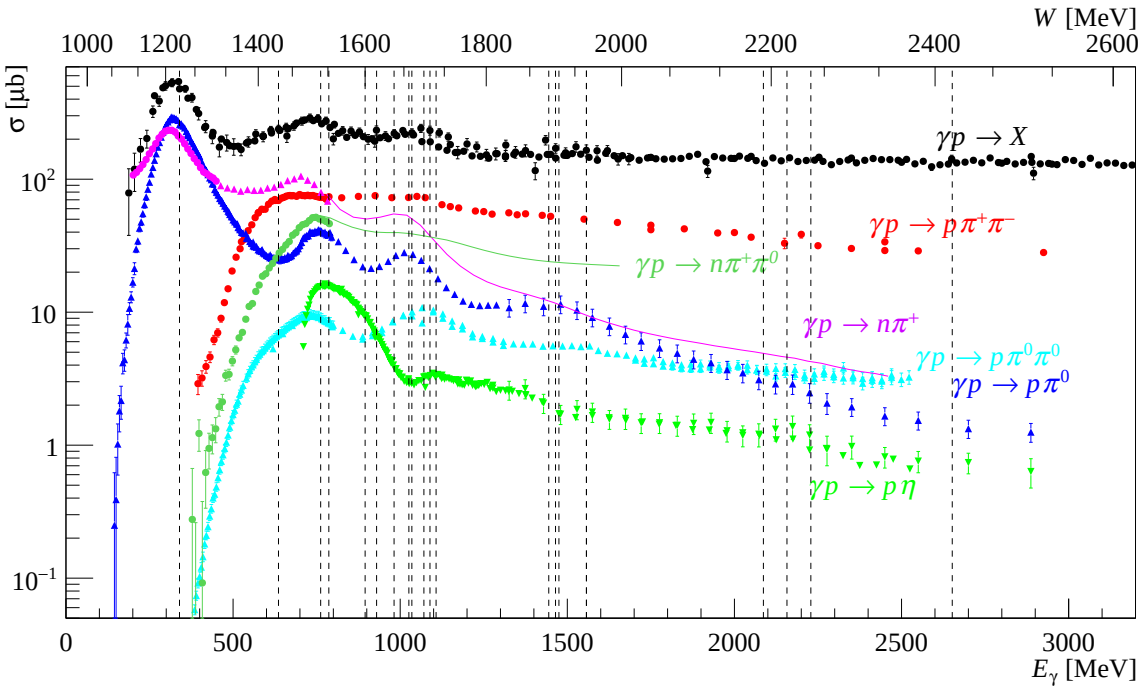

Fig. 1.7: Photoproduction cross sections off the proton. The total photoproduction cross section off the proton [7] is presented together with the cross sections for the production of several single- and multimeson final states as a function of the incoming beam photon energy E_γ and center of mass energy W. Data for the reaction $\gamma p \to p\pi^0$ are taken from [17, 18], for $\gamma p \to n\pi^+$ from [19, 20], for $\gamma p \to p\eta$ from [21, 22, 23], for $\gamma p \to p\pi^+\pi^-$ from [24, 25, 26], for $\gamma p \to p\pi^0\pi^0$ from [27, 28, 18], and for $\gamma p \to n\pi^+\pi^0$ from [29]. For the higher energies in the $\gamma p \to n\pi^+$ reaction the SAID-CM12 solution (solid line) was included [30] and for the $\gamma p \to n\pi^+\pi^0$ the $\pi\pi$ MAID was selected [31]. In addition, all listed four star N^* and Δ^* resonances in the PDG are indicated by the dashed vertical lines [7].

Formalism of Pseudoscalar Meson Photoproduction

Following the principles of scattering theory, the transition of an initial state $|\, i \,\rangle$ to the final state $|\, f \,\rangle$ can be described by a scattering matrix S, which includes the unit matrix $\mathbb{1}$ to account for the non-interaction term and a transition matrix T which contains all information on the scattering process [3]. The probability P_{fi} for an initial state $|\, i \,\rangle$ to scatter into the final state $|\, f \,\rangle$ is connected to these matrices via:

$$P_{fi} = P(|\, i \,\rangle \to |\, f \,\rangle) = |\langle f|S|\, i\rangle|^2 = \left|S_{fi}\right|^2 \quad \text{with} \quad S = \mathbb{1} + iT. \tag{1.5}$$

For the photoproduction process of a pseudoscalar meson M on a nucleon N, the reaction, including the corresponding four momenta p_i, can be written as:

$$\gamma(p_\gamma)N(p_N) \to N'(p_{N'})M(p_M). \tag{1.6}$$

The matrix element S_{fi} and thus as well the transition matrix T_{fi} take the shape:

$$S_{fi} = \delta_{fi} + \frac{1}{(2\pi)^2}\delta^4(p_{N'} + p_M - p_N - p_\gamma)\sqrt{\frac{m_N^2}{4E_{N'}E_M E_N E_\gamma}} \cdot i\mathscr{M}_{fi} \tag{1.7}$$

where m_N is the nucleon mass, p_i the four momenta of the corresponding particle i and E_i their energy [32]. Whereas the first two factors in the second term in Eq. (1.7) are responsible for the phase space and energy- and momentum-conservation, the matrix element $\mathscr{M}_{fi}$ contains all information on the scattering process. An overview of the dominant tree-level diagrams in the scattering process is presented in Fig. 1.8. It is built up of the non-resonant background terms, including the s- and

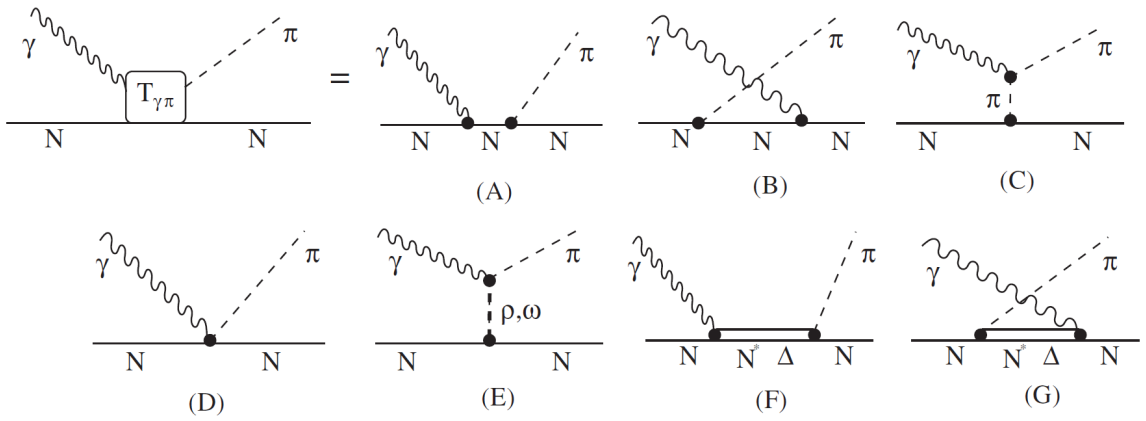

Fig. 1.8: Feynman diagrams for the photoproduction of pions from free nucleons. Shown are the Feynman diagrams which contribute to the scattering process. It includes the s- and u-channel Born terms ((A) and (B)), the pion pole term (C), the Kroll-Ruderman contact term (D), and the vector-meson exchange (D). Whereas these are all non-resonant contributions, the resonant s- and u-channel process with a resonance N^* or Δ in the intermediate state are presented in the diagrams (F) and (G) (figure taken from [33]).

u-channel Born terms, where a nucleon is exchanged in the intermediate state (diagrams (A) and (B)), the pion-pole term in diagram (C), the Kroll-Ruderman contact term in diagram (D), and the vector-meson exchanges in diagram (E). The resonant terms are given by the resonant s- and u-channel process, with a resonance $N*$ or Δ^* in the intermediate state (diagrams (F) and (G)). Within this thesis, the pseudoscalar mesons in the final state are the neutral pion (π^0) and the charged pion (π^+) of the reactions $\vec{\gamma}\vec{p} \to p\pi^0$ and $\vec{\gamma}\vec{p} \to n\pi^+$ [4]. It is noteworthy that the pion-pole term and the Kroll-Ruderman contact term can not contribute in the final states where only neutral mesons are involved, because photons can only couple to charged particles (cf. Tab. 1.2). Thus, only the s- and u-channel Born terms need to be considered as non-resonant terms to the resonance excitations in the photoproduction of neutral pions. The situation is different for charged pions in the final state where the contribution of both these terms to the overall photoproduction is significant. In particular, the Kroll-Ruderman contact term plays a very important role near the threshold production but also contributes together

[4] $\vec{\gamma}$ and $\vec{p}$ denote a polarized photon and target-nucleon, respectively

with the pion-pole term at higher beam photon energies [34].
The matrix $\mathscr{M}$ is related to the photoproduction matrix $\mathscr{F}$, which is evaluated in the center of mass system. Depending on the basis used for the quantization of the involved spins, the matrix can be parameterized from the theoretical point of view by different amplitudes, i.e. helicity amplitudes, transversity amplitudes or the CGLN-amplitudes. The latter will be discussed in further detail here whereas information about the other systems of amplitudes can be found in [35].
To describe the photoproduction matrix $\mathscr{F}$ and thus the matrix $\mathscr{M}$, four complex CGLN-amplitudes are introduced. In the basis of Pauli spinors χ for the initial and final nucleon, the relation between both matrices is given by [36]:

$$\mathscr{M} = \frac{4\pi W}{m_N} \left| \left\langle \chi(N') \left| \mathscr{F} \right| \chi(N) \right\rangle \right|^2 \tag{1.8}$$

with the center-of-mass energy

$$W = \sqrt{s} = \sqrt{(p_\gamma + p_N)^2}. \tag{1.9}$$

The photoproduction matrix $\mathscr{F}$ is a 2×2 matrix and can be expressed by the four complex Goldberger-Low-Nambu (CGLN)-amplitudes F [36] via:

$$\mathscr{F} = i(\vec{\sigma}\cdot\vec{\varepsilon})F_1 + \frac{(\vec{\sigma}\cdot\vec{q})(\vec{\sigma}\cdot(\vec{k}\times\vec{\varepsilon}))}{qk}F_2 + i\frac{(\vec{\sigma}\cdot\vec{k})(\vec{q}\cdot\vec{\varepsilon})}{qk}F_3 + i\frac{(\vec{\sigma}\cdot\vec{q})(\vec{q}\cdot\vec{\varepsilon})}{q^2}F_4 \tag{1.10}$$

with $\vec{\sigma}$ being the Pauli spin operators, $\vec{\varepsilon}$ the photon polarization vector, and $\vec{k}$ and $\vec{q}$ the three momenta of the initial state photon and the final state meson, respectively. The amplitudes are functions of the center of mass energy W and the polar angle θ of the outgoing meson in the center of mass system. The conservation of angular momentum allows the decomposition of the F_i into partial waves with a well-defined angular momentum. Hereby, the eigenstates are represented by Legendre polynomials $P_k(\cos\theta)$ and their derivatives, whereas the complex expansion coefficients are given by electric $E_{l\pm}(W)$ and magnetic $M_{l\pm}(W)$ multipoles with l being the relative orbital momentum of the final state meson M to the recoil nucleon. The multipole-expansion of the CGLN-amplitudes reads [36]:

$$\begin{aligned}
F_1(W,\theta) &= \sum_{l=0}^{\infty} \left[lM_{l+}(W) + E_{l+}(W) \right] P_{l+1}^{'}(\cos\theta) + \left[(l+1)M_{l-}(W) + E_{l-}(W) \right] P_{l-1}^{'}(\cos\theta), \\
F_2(W,\theta) &= \sum_{l=0}^{\infty} \left[(l+1)M_{l+}(W) + lM_{l-}(W) \right] P_{l}^{'}(\cos\theta), \\
F_3(W,\theta) &= \sum_{l=0}^{\infty} \left[E_{l+}(W) - M_{l+}(W) \right] P_{l+1}^{''}(\cos\theta) + \left[E_{l-}(W) + M_{l-}(W) \right] P_{l-1}^{''}(\cos\theta), \\
F_4(W,\theta) &= \sum_{l=0}^{\infty} \left[M_{l+}(W) - E_{l+}(W) - M_{l-}(W) - E_{l-}(W) \right] P_{l}^{''}(\cos\theta).
\end{aligned} \tag{1.11}$$

The term $\pm$ indicates whether the spin of the final state nucleon $S_{N'}$ is added to or subtracted from l to obtain the total angular momentum J_{res} of the intermediate resonance state with a parity P_{res}. Thereby,

the intrinsic parity of the nucleon is $P_N = P_{N'} = +1$ and of the meson $P_M = -1$ (cf. Sec. 1.2), which leads to the following constraints for the intermediate state:

$$\begin{aligned} |l - 1/2| = |l - S_{N'}| \leq & J_{res} \leq |l + S_{N'}| = |l + 1/2|, \\ & P_{res} = P_{N'} P_M (-1)^l = (-1)^{l+1}. \end{aligned} \tag{1.12}$$

To produce the intermediate resonance state with total angular momentum J_{res}, the orbital angular momentum L_γ of the initial state photon interacts with the nucleon with spin S_N, leading to an intermediate resonance state with

$$\begin{aligned} |L_\gamma - 1/2| = |L_\gamma - S_N| \leq & J_{res} \leq |L_\gamma + S_N| = |L_\gamma + 1/2|, \\ & P_{res} = P_N P_\gamma = P_\gamma. \end{aligned} \tag{1.13}$$

As parity P and angular momentum J need to be respected in the initial and final state, the following conditions need to be fulfilled in the intermediate resonance state as well:

$$\begin{aligned} P_\gamma = P_{res} &= (-1)^{l+1}, \\ |L_\gamma \pm 1/2| = J_{res} &= |l \pm 1/2|. \end{aligned} \tag{1.14}$$

The parity of the photons, initialized by electric radiation, is given by $P_\gamma = (-1)^{L_\gamma}$ and the corresponding multipole is the electric photon multipole EL_γ. The parity of the initialization via magnetic radiation is $P_\gamma = (-1)^{L_\gamma + 1}$ with the magnetic photon multipole ML_γ. Finally, the strong isospin I of the final state mesons, i.e. $I_\pi = 1$ in case of a pion, and the nucleon $I_{N'} = 1/2$ need to be respected. As the intermediate resonance state decays via the strong interaction and strong isospin is conserved, the intermediate resonance states need to have an isospin of either $I = 1/2$, corresponding to N^* resonances, or $I = 3/2$, corresponding Δ^* resonances. With these information and the initial state and final state properties, the intermediate resonance state can be characterized as shown in Tab. 1.3 for $L_\gamma = 1$ and $L_\gamma = 2$. Different resonances can couple to a defined partial wave, i.e. the $\Delta(1232)3/2^+(P_{33})$ resonance can be excited by the E_{1+} or M_{1+} photoproduction multipoles. In addition, the photoproduction multipoles consist always of a partial wave which is attributed to the isospin $I = 1/2$ component and one to the isospin $I = 3/2$. To get access to only one of these components, an isospin separation needs to be performed.

The isospin of the initial state photon has an isoscalar component with $I_\gamma = 0$ and an isovector component with $I_\gamma = 1$. By that, the isovector component can couple with the isospin of the initial state nucleon to a resonance state with either isospin $I = 1/2$ (N^*) or $I = 3/2$ (Δ^*). On the other hand, the isoscalar component can only contribute to the N^* resonances.

Table 1.3: Connection between multipoles and their corresponding partial waves. For $L_\gamma = 1$ and $L_\gamma = 2$, the corresponding photon- and photoproduction multipoles and their partial waves are shown. The partial waves are separated by the total isospin I of the intermediate resonance states and their connection to the quantum numbers of the initial state (IS), the intermediate resonance state (RES), and the final state (FS).

Photon multipole	IS		RES	FS		Photoprod. multipole	Partial waves $(l)_{2I2J}$	
EL_γ/ML_γ	$L_\gamma^{P_\gamma}$	$S_N^{P_N}$	$J_{res}^{P_{res}}$	$S_{N'}^{P_{N'}}$	l^{P_M}	$E_{l\pm}/M_{l\pm}$	$I=1/2$	$I=3/2$
$E1$	1^-	$1/2^+$	$1/2^-$	$1/2^+$	0^-	E_{0+}	S_{11}	S_{31}
			$3/2^-$	$1/2^+$	2^-	E_{2-}	D_{13}	D_{33}
$M1$	1^+	$1/2^+$	$1/2^+$	$1/2^+$	1^+	M_{1-}	P_{11}	P_{31}
			$3/2^+$	$1/2^+$	1^+	M_{1+}	P_{13}	P_{33}
$E2$	2^+	$1/2^+$	$3/2^+$	$1/2^+$	1^+	E_{1+}	P_{13}	P_{33}
			$5/2^+$	$1/2^+$	3^+	E_{3-}	F_{15}	F_{35}
$M2$	2^-	$1/2^+$	$3/2^-$	$1/2^+$	2^-	M_{2-}	D_{13}	D_{33}
			$5/2^-$	$1/2^+$	2^-	M_{2+}	D_{15}	D_{35}

Respecting charge conservation, the four possible πN final states, can be expressed by three isospin dependent multipoles $\mathcal{M}_{l\pm}^{i}$ [5] via [37]:

$$\mathcal{M}_{l\pm}^{(\gamma p\to n\pi^+)} = \sqrt{2}\cdot\left(\mathcal{M}_{l\pm}^{0} + \frac{1}{3}\mathcal{M}_{l\pm}^{1/2} - \frac{1}{3}\mathcal{M}_{l\pm}^{3/2}\right), \tag{1.15}$$

$$\mathcal{M}_{l\pm}^{(\gamma n\to p\pi^-)} = \sqrt{2}\cdot\left(\mathcal{M}_{l\pm}^{0} - \frac{1}{3}\mathcal{M}_{l\pm}^{1/2} + \frac{1}{3}\mathcal{M}_{l\pm}^{3/2}\right), \tag{1.16}$$

$$\mathcal{M}_{l\pm}^{(\gamma p\to p\pi^0)} = \mathcal{M}_{l\pm}^{0} + \frac{1}{3}\mathcal{M}_{l\pm}^{1/2} + \frac{2}{3}\mathcal{M}_{l\pm}^{3/2}, \tag{1.17}$$

$$\mathcal{M}_{l\pm}^{(\gamma n\to n\pi^0)} = -\mathcal{M}_{l\pm}^{0} + \frac{1}{3}\mathcal{M}_{l\pm}^{1/2} + \frac{2}{3}\mathcal{M}_{l\pm}^{3/2}. \tag{1.18}$$

The three different isospin dependent multipoles are thereby defined by their indices via [38]:

- The index $i = 0$ corresponds to an isoscalar transition amplitude with $I_\gamma = 0$. Initial and final state have isospin $I = 1/2$.
- The index $i = 1/2$ corresponds to an isovector transition amplitude with $I_\gamma = 1$. Initial and final state have isospin $I = 1/2$ ($\Delta I = 0$).
- The index $i = 3/2$ corresponds to an isovector transition amplitude with $I_\gamma = 1$. Initial state has isospin $I = 1/2$, final state has isospin $I = 3/2$ ($\Delta I = 1$).

To measure either the multipole contribution of the N^*- or the Δ^*-states, the channel-dependent linear combination of the isospin dependent multipoles need to be combined in such a way that only one contribution remains. This is achieved by measuring the same quantities for two of these channels.

[5] Based on Eq. (1.8), they contain all information on the individual photoproduction multipoles, mentioned in Tab. 1.3.

An example is the separation of the M_{1+} multipole in the region of the $\Delta(1232)3/2^+(P_{33})$ resonance region by the measurement of the reactions $\vec{\gamma}\vec{p} \to p\pi^0$ and $\vec{\gamma}\vec{p} \to n\pi^+$. Using the Eq. (1.15) and Eq. (1.17), the multipole $M_{1+}^{3/2}$ can be expressed in the following way [37]:

$$M_{1+}^{3/2} = M_{1+}^{(\gamma p \to p\pi^0)} - \frac{1}{\sqrt{2}} \cdot M_{1+}^{(\gamma p \to n\pi^+)}. \tag{1.19}$$

Similarly, a different linear combination can give access to the N^*-star resonances which couple to the M_{1+}^0 and $M_{1+}^{1/2}$ multipoles. The main advantage of this decomposition is that one can get access to weakly contributing resonances in a multipole. An impressive example is given in reference [39]. The authors quote that the M_{3-} multipole in the particle representation (cf. Eq. (1.17)) is dominated by the $N(1680)3/2^+(F_{15})$ with isospin $I = 1/2$ and that the resonance $\Delta(1905)5/2^+(F_{35})$ with isospin $I = 3/2$ is hardly seen. This changes dramatically in the isospin basis where clear evidence for this state is seen. Fig. 1.9 presents the multipole as a function of the center of mass energy W and for the particle representation on the left and in the center, and the isospin separation on the right. Note that the shown multipoles are obtained by different partial wave analyses which will be explained later within this chapter. However, as a first step, polarization observables are introduced which are used as input for the different partial wave analyses.

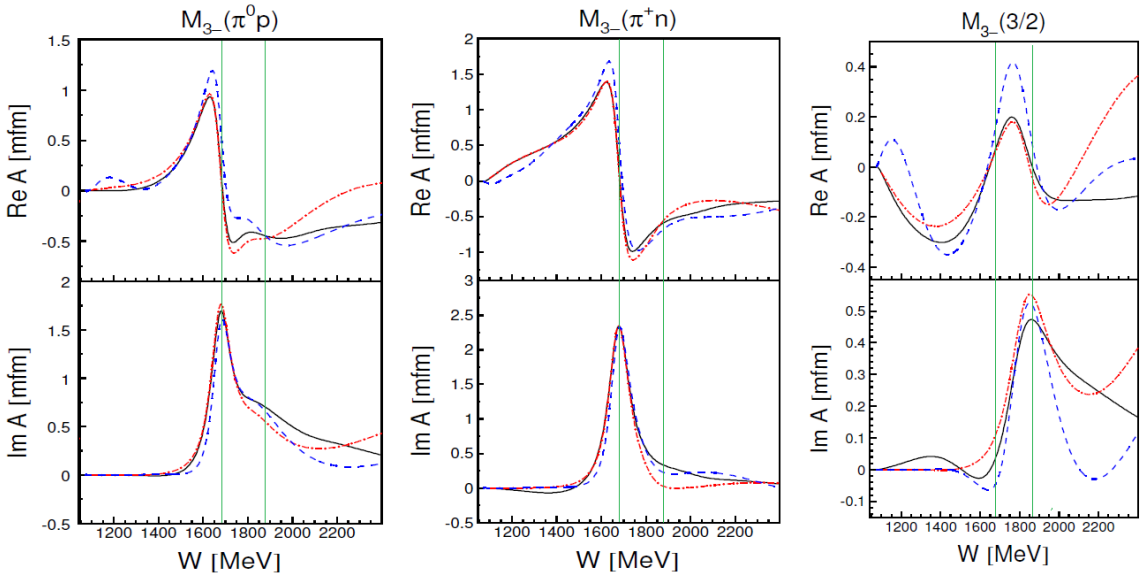

Fig. 1.9: The M_{3-} multipole for different representations and PWA solutions. Shown are the three representations of the multipole M_{3-} for three PWA solutions (black solid line: BnGa-2014-02, blue dashed: JüBo-2016-01, red dashed-dotted: SAID) [39]. The first two columns represent the particle basis whereas the last one shows the isospin basis with $I = 3/2$. Clear evidence for the $\Delta(1905)5/2^+(F_{35})$ with isospin $I = 3/2$ is present, which is not seen so pronounced in the other two representations. The extracted Breit-Wigner resonance positions from the BnGa solutions are included by the green lines. The figure demonstrates the importance of the isospin separation through the measurement of both pion photoproduction processes off the proton (figure modified from [39]).

1.3.2 Measurement of Polarization Observables

To obtain information about the contributing resonances in a given final state, the scattering amplitudes need to be known precisely. This can be achieved by determining the four complex CGLN amplitudes, including their absolute values, their three relative phases, and one overall global phase. Experimentally this can be accomplished by the measurement of cross sections and so-called polarization observables. Polarization observables can be accessed by either polarizing the initial state, measuring the polarization in the final state, or even both. In this way, 16 polarization observables are accessible which are summarized in Tab. 1.4.

Table 1.4: Overview of the polarization observables in the pseudoscalar meson photoprodction reactions. Shown are all 16 possible polarization observables. (x,y,z) is the cartesian coordinate system of the initial state in the CM system, whereas (x',y',z') indicates the system of the final state. The coordinate systems are depicted in Fig. 1.10 (table modified from [40]).

		Target			**Recoil**			**Target+Recoil**			
		-	-	-	x'	y'	z'	x'	x'	z'	z'
$\mathbf{p}_\gamma$		x	y	z	-	-	-	x	z	x	z
unpolarized	σ	-	T	-	-	P	-	T_x	$-L_{x'}$	$T_{z'}$	$-L_{z'}$
linearly polarized	Σ	H	$-P$	$-G$	$O_{x'}$	$-T$	$O_{z'}$	-	-	-	-
circularly polarized	-	F	-	$-E$	$-C_{x'}$	-	$-C_{z'}$	-	-	-	-

For a unique extraction of the CGLN-amplitudes, Chiang and Tabakin suggest for the photoproduction of pseudoscalar mesons the measurement of eight of these observables, known as the complete experiment. The latter compromises the measurement of the unpolarized cross section, all single polarization observables and four well-chosen double polarization observables [41].
Following this proposal, the double polarization observable G and E are determined in this thesis by using elliptically polarized photons in combination with a longitudinally polarized target. Thereby, the elliptically polarized photons have a linearly polarized component and a circularly polarized component. With this spin configuration, the unpolarized differential cross section is modified to[6]:

$$\frac{d\sigma}{d\Omega}(W,\theta,\varphi) = \left.\frac{d\sigma}{d\Omega}\right|_0 (W,\theta) \cdot \Big(1 - p_L \Sigma \cos 2\varphi + p_L p_Z G \sin 2\varphi - p_C p_Z E\Big) \tag{1.20}$$

with $\left.\frac{d\sigma}{d\Omega}\right|_0 (W,\theta)$ being the unpolarized differential cross section, p_L (p_C) the linear (circular) polarization degree of the beam photons, and p_Z the polarization degree of the longitudinally polarized target. φ is the angle between the linear polarization plane and the reaction plane. The definition of the angle is shown in Fig. 1.10 where the coordinate system in the initial and final state for the center of mass system is depicted.
The importance of the polarization observables can be directly seen in the CGLN-amplitude representation of the unpolarized cross section and both profile functions of the polarization observables,

[6]The modification of the polarized differential cross section due to the contribution of the remaining polarization observables, listed in Tab. 1.4, is presented in detail in [42].

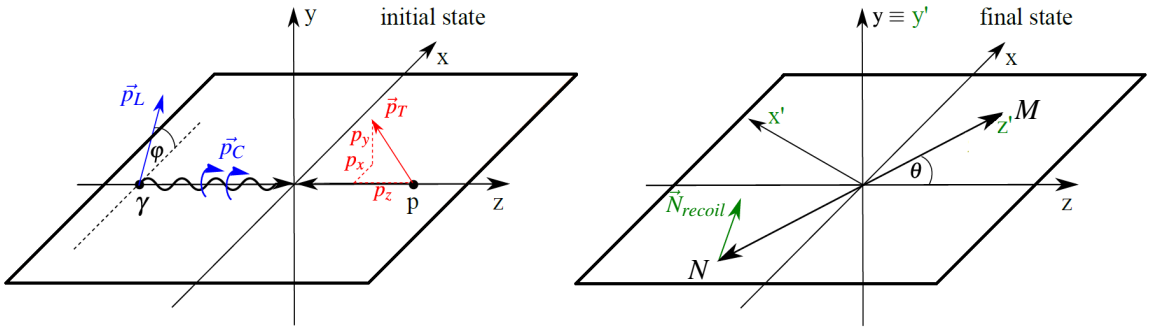

Fig. 1.10: Coordinate systems for the definition of the polarization observables . Shown are the coordinate systems in the center of mass system for the initial state on the left and for the final state on the right. The reaction plane in x-z direction is defined by the final state meson M and the nucleon N as both have to fly back-to-back. The linear polarization plane of the linearly polarized photons is tilted by an angle φ relative to this reaction plane. The target spin vector $\vec{p_T}$ can either be polarized in z-direction, corresponding to a longitudinally polarized target (p_Z), or in x- or y-direction, corresponding to a transversely polarized target (p_X and p_Y). For the measurement of recoil polarization observables, the coordinate system needs to be rotated by the angle θ which results in the (x',y',z') system. Thereby, θ is the angle of the meson M with respect to the reaction plane (figure modified from [14]).

which are the product of the polarization observable and the unpolarized cross section (cf. Eqs (1.21)-(1.23)).

$$\left.\frac{d\sigma}{d\Omega}\right|_0 (W,\theta,\varphi) = \mathrm{Re}\Big\{|F_1|^2+|F_2|^2+\frac{1}{2}\sin^2\theta\left(|F_3|^2+|F_4|^2\right) + \sin^2\theta(F_2^*F_3+F_1^*F_4+\cos\theta F_3^*F_4)-2\cos\theta F_1^*F_2\Big\}\rho, \tag{1.21}$$

$$\check{E}(W,\theta) = E\cdot\left.\frac{d\sigma}{d\Omega}\right|_0 = \mathrm{Re}\Big\{|F_1|^2+|F_2|^2-2\cos\theta F_1^*F_2+\sin^2\theta(F_2^*F_3+F_1^*F_4)\Big\}\rho, \tag{1.22}$$

$$\check{G}(W,\theta) = G\cdot\left.\frac{d\sigma}{d\Omega}\right|_0 = \sin^2\theta\,\mathrm{Im}\Big\{F_2^*F_3+F_1^*F_4\Big\}\rho, \tag{1.23}$$

with ρ being the phase space factor. Whereas the unpolarized cross section and the profile function $\check{E}$ have the square of the amplitudes included, the profile function $\check{G}$ only contains interference terms. As will be shown now, this is the reason why the double polarization observable G is perfectly suited to study weakly contributing resonances in a given final state. Moreover, as mentioned before, the measurement of the observable for the neutral and charged pion photoproduction reaction off the proton at the same time allows for an isospin decomposition of the multipoles.

Since polarization observables can be described by the CGLN amplitudes and these can be decomposed into partial waves (cf. Eq. (1.11)), it is obviously meaningful to expand the results of the polarization observables in a similar way. The profile functions therefore can be expressed in a truncated PWA

decomposition[7] by [43]:

$$\check{\mathrm{G}}\,(W,\cos\theta) = \rho \sum_{k=2}^{2\mathrm{L}_{\max}} (a_{\mathrm{L}_{\max}})_k^{\check{\mathrm{G}}}\,(W)\,P_k^2\,(\cos\theta)\,, \tag{1.24}$$

$$\check{\mathrm{E}}\,(W,\cos\theta) = \rho \sum_{k=0}^{2\mathrm{L}_{\max}} (a_{\mathrm{L}_{\max}})_k^{\check{\mathrm{E}}}\,(W)\,P_k^0\,(\cos\theta)\,. \tag{1.25}$$

Here, ρ is the phase space factor, $(a_{\mathrm{L}_{\max}})_k^{\check{\Omega}}$ are the energy-dependent real expansion coefficients of the observable $\check{\Omega}$ truncated at a defined $\mathrm{L}_{\max}$, and $P_k^m\,(\cos\theta)$ are the angular-dependent associated Legendre polynomials [44]. The information about the contributing multipoles is included in the expansion coefficients, as these are bilinear Hermitean forms of the multipoles, which are defined via Hermitean matrices $C_k^{\check{\Omega}}$ and the multipole vector $|\mathscr{M}_{\mathrm{L}_{\max}}\,(W)\rangle$:

$$(a_{\mathrm{L}_{\max}})_k^{\check{\Omega}}\,(W) = \langle \mathscr{M}_{\mathrm{L}_{\max}}\,(W)|\,\mathscr{C}_k^{\check{\Omega}}\,|\mathscr{M}_{\mathrm{L}_{\max}}\,(W)\rangle\,. \tag{1.26}$$

The dimension of the matrices $\mathscr{C}_k^{\check{\Omega}}$ is given by the number of multipoles which contribute up to a certain truncation and is given by $4\mathrm{L}_{\max} \times 4\mathrm{L}_{\max}$. The multipole vector $|\mathscr{M}_{\mathrm{L}_{\max}}\,(W)\rangle$ has $4\mathrm{L}_{\max}$ entries and contains the multipoles in the form of:

$$|\mathscr{M}_{\mathrm{L}_{\max}}\,(W)\rangle = (E_{0+},E_{1+},M_{1+},M_{1-},E_{2+},E_{2-},M_{2+},M_{2-},\cdots,E_{\mathrm{L}_{\max}+},E_{\mathrm{L}_{\max}-},M_{\mathrm{L}_{\max}+},M_{\mathrm{L}_{\max}-})^T. \tag{1.27}$$

The multipoles and their corresponding partial waves are listed in Tab. 1.5. As the terms for the expansion coefficients are quite large, it is meaningful to introduce a short-notation where the contributing partial waves are presented only for their corresponding l_M, i.e. an interference between the partial wave S_{11} and the P_{11} is contained in the $\langle S,P\rangle$ term, whereas an interference between P_{11} and P_{33} is contained in $\langle P,P\rangle$. The first coefficient $(a_1)_2^{\check{\mathrm{G}}}$ for the double polarization observable G, which is truncated at $\mathrm{L}_{\max} = 1$, is depicted in Eq. (1.28) and the first coefficient $(a_1)_0^{\check{\mathrm{E}}}$ for E in Eq. (1.29).

$$\begin{aligned}(\mathrm{a}_1)_2^{\check{\mathrm{G}}} &= \begin{pmatrix} E_{0+}^* & E_{1+}^* & M_{1+}^* & M_{1-}^* \end{pmatrix} \begin{pmatrix} 0 & 0 & 0 & 0 \\ 0 & 0 & i & i/2 \\ 0 & -i & 0 & -i/2 \\ 0 & -i/2 & i/2 & 0 \end{pmatrix} \begin{pmatrix} E_{0+} \\ E_{1+} \\ M_{1+} \\ M_{1-} \end{pmatrix} \\ &= \mathrm{Im}\big\{M_{1-}^* \cdot (E_{1+} - M_{1+}) - 2E_{1+}^* M_{1+}\big\} = \langle P,P\rangle\,.\end{aligned} \tag{1.28}$$

[7] The infinite multipole expansion is only considered up to a finite angular momentum quantum number $\mathrm{L}_{\max}$. The procedure will be called $\mathrm{L}_{\max}$-fit procedure in the following.

Table 1.5: Overview of photoproduction multipoles and their corresponding partial waves. For different truncation orders L_{max}, the corresponding multipoles and their partial waves are shown. Thereby, l_M is the relative orbital momentum of the final state meson M to the recoil nucleon, J the total angular momentum of the resonance state, P its parity, and I its isospin.

L_{max}	l_M	Multipoles		J^P	Partial waves $(l_M)_{2I2J}$	
		$E_{l_M\pm}$	$M_{l_M\pm}$		$I=1/2$	$I=3/2$
1	0	E_{0+}	-	$1/2^-$	S_{11}	S_{31}
	1	-	M_{1-}	$1/2^+$	P_{11}	P_{31}
	1	E_{1+}	M_{1+}	$3/2^+$	P_{13}	P_{33}
2	2	E_{2-}	M_{2-}	$3/2^-$	D_{13}	D_{33}
	2	E_{2+}	M_{2+}	$5/2^-$	D_{15}	D_{35}
3	3	E_{3-}	M_{3-}	$5/2^+$	F_{15}	F_{35}
	3	E_{3+}	M_{3+}	$7/2^+$	F_{17}	F_{37}
4	4	E_{4-}	M_{4-}	$7/2^-$	G_{17}	G_{37}
	4	E_{4+}	M_{4+}	$9/2^-$	G_{19}	G_{39}

$$(a_1)_0^{\check{E}} = \left(E_{0+}^* \; E_{1+}^* \; M_{1+}^* \; M_{1-}^*\right) \begin{pmatrix} 1 & 0 & 0 & 0 \\ 0 & 3 & 3 & 0 \\ 0 & 3 & -1 & 0 \\ 0 & 0 & 0 & 1 \end{pmatrix} \begin{pmatrix} E_{0+} \\ E_{1+} \\ M_{1+} \\ M_{1-} \end{pmatrix} \tag{1.29}$$
$$= |E_{0+}|^2 + 3|E_{1+}|^2 + 3E_{1+}^* M_{1+} + 3M_{1+}^* E_{1+} - |M_{1+}|^2 + |M_{1-}|^2 = \langle S,S\rangle + \langle P,P\rangle \,.$$

From the inspection of the interference terms in Eq. (1.28), it becomes clear that the observable G, in the region where $L_{max} = 1$ is valid, is only sensitive to P-waves. Another remarkable fact is that the observable G is completely described by interference terms of different multipoles and thus can help to study small contributing multipoles which interfere with a strong multipole (cf. Eq. (1.23)). The interference of the dominant multipole M_{1+} with the rather small M_{1-} in the profile function $\check{G}$ is perfectly suited to study the Roper resonance $N(1440)1/2^+(P_{11})$. In case of contributions of D-waves and thus $L_{max} = 2$, two additional expansion coefficients need to be considered in case of each observable. Furthermore, additional interference terms in the first coefficient need to be respected which leads to:

$$\begin{aligned} (a_2)_2^{\check{G}} &= \langle P,P\rangle + \langle S,D\rangle + \langle D,D\rangle \,, \\ (a_2)_3^{\check{G}} &= \langle P,D\rangle \,, \\ (a_2)_4^{\check{G}} &= \langle D,D\rangle \,. \end{aligned} \tag{1.30}$$

All interference terms for the individual multipoles can be found in [45] up to $L_{max} = 3$. As an example, Fig. 1.11 shows the expansion coefficient $(a_3)_2^{\check{G}}$ for the $p\pi^0$ analysis which has been determined within

this thesis. More details are given in Sec. 9.2. The L_{max}-fit has been performed for a truncation order of $L_{max} = 3$. The result for the fitted coefficient is presented together with the individual interference terms of the multipole solution of the BnGa-2016 PWA (see next section) up to $L_{max} = 4$ [46].

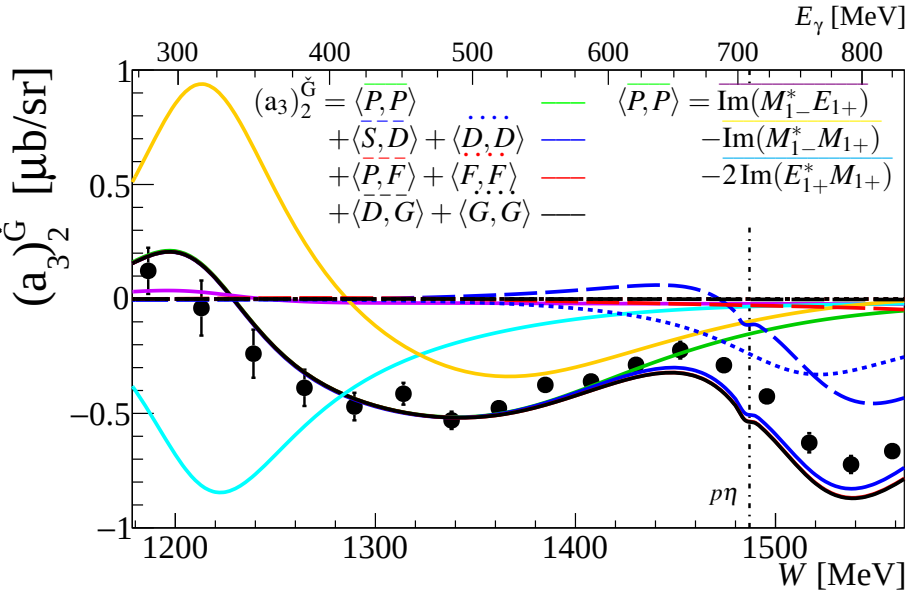

Fig. 1.11: Contributing interference terms for the $\langle \mathbf{P},\mathbf{P}\rangle$ block in the fit coefficient $(\mathbf{a_3})^{\check{\mathbf{G}}}_{\mathbf{2}}$ for the $p\pi^0$ channel. The individual interference terms obtained with the BnGa multipoles together with the extracted expansion coefficient can be used to further study the contributing resonances. The expansion coefficient is compared to continuous curves which have been determined from the multipole solutions of the BnGa-2016 PWA solution [46]. The reconstruction of the expansion coefficient from the BnGa-2016 model have been truncated at different L_{max}. Hereby, the green solid curve corresponds to $L_{max} = 1$, the blue solid curve to $L_{max} = 2$, the red solid curve to $L_{max} = 3$, and the black solid curve to $L_{max} = 4$. On the right panel, the contributing partial wave interference terms are given for the different L_{max} values. Thereby, $L_{max} = 1$ only contains the contribution of S-and P-waves, $L_{max} = 2$ additionally D-waves, $L_{max} = 3$ additionally F-waves, and $L_{max} = 4$ additionally G-waves. The individual interference terms are included as well and are indicated by their color and dashed or dotted curves. In addition, the different interference terms for the $\langle P,P\rangle$ block are plotted to show the sensitivity to the Roper resonance which couples to the M_{1-} multipole. The dashed-dotted line marks the photoproduction threshold of the $p\eta$ channel. More details can be found in Sec. 9.2.

Inspecting Eq. (1.29), the first coefficient for E contains interference terms between different multipoles but also the absolute square of multipoles. Thus, in case one multipole dominates in a certain energy range, the absolute square of this multipole has also the strongest contribution to the expansion coefficient and thus no sensitivity to the interference terms with small contributing multipoles is present. Especially at beam photon energies below 600 MeV ($W = 1400$ MeV), the $|M_{1+}|^2$ term, to which the $\Delta(1232)3/2^+(P_{33})$ resonance belongs, is huge. Thus, at low energies and in the region where $L_{max} = 1$ is valid, no high sensitivity to the $N(1440)1/2^+(P_{11})$ is expected in the first coefficient. However, as can be seen in Eq. (1.31), expansion coefficients with an odd number for k are only

sensitive to interference terms and thus can be sensitive to small contributing resonances.

$$
\begin{aligned}
(\mathrm{a}_1)_0^{\check{\mathrm{E}}} &= \langle S,S\rangle + \langle P,P\rangle\,,\\
(\mathrm{a}_1)_1^{\check{\mathrm{E}}} &= \langle S,P\rangle\,,\\
(\mathrm{a}_1)_2^{\check{\mathrm{E}}} &= \langle P,P\rangle\,.
\end{aligned}
\tag{1.31}
$$

Therefore, the measurement of both double polarization observables G and E might help to further constrain the resonance properties. Moreover, they can be used as input for the energy-dependent partial wave analyses (PWA), performed by different groups worldwide. The different PWAs are the topic of the following section.

1.4 Model Dependent Partial Wave Analyses

Using the results of the measurement of the polarization observables as input, partial wave analyses (PWAs) are used to extract multipoles and thus resonance properties. They are even capable of providing predictions for polarization observables. By performing sensitivity studies of certain resonances to polarization observables, the PWAs can help to decide which observables should be measured in the future.

For this thesis, the most relevant models are the SAID, BnGa, MAID, and JüBo PWAs. All models have in common that their amplitudes are analytic functions of the invariant mass and that two-body unitarity is at least approximately fulfilled. In addition, all models are able to allow for coupled channel effects [39]. The biggest difference comes from the parametrization of the scattering amplitude in Eq. (1.5), which includes the description of the resonant and the non-resonant terms. Moreover, different amounts of experimental data are used for the models.

One way to paramaterize the amplitude is the K-matrix approach, which constructs the transition matrix T and thus the scattering amplitude. They are connected by:

$$T = K \cdot (\mathbb{1} - iK)^{-1}. \tag{1.32}$$

The K-matrix elements can be written as a sum of all poles together with non-resonant background terms. A resonance is thereby a pole in the complex energy plane of the T-matrix with a mass corresponding to the real part of the pole position E_0 and a width corresponding to the imaginary part via $-2Im(E_0)$ [47]. However, one should stress that in the most general case, there is no direct one-to-one correspondence between K-matrix poles and T-matrix poles. The main advantage of this approach is that it can handle several overlapping resonances and even superpositions of resonances with non-resonant background terms. A Breit-Wigner parametrization is only applicable in case of a well-isolated resonance. This is nearly given for the $\Delta(1232)3/2^+(P_{33})$ resonance in the M_{1+} multipole as can be seen in Fig. 1.12 on the left side where the mass and width can be extracted from the real and imaginary parts, respectively. At that point, a comparison with the E_{0+} multipole in the

middle of Fig. 1.12 and the M_{3-} multipole in Fig. 1.9 makes sense. It can be seen that the structure is much more complex and thus a Breit-Wigner parametrization becomes questionable.

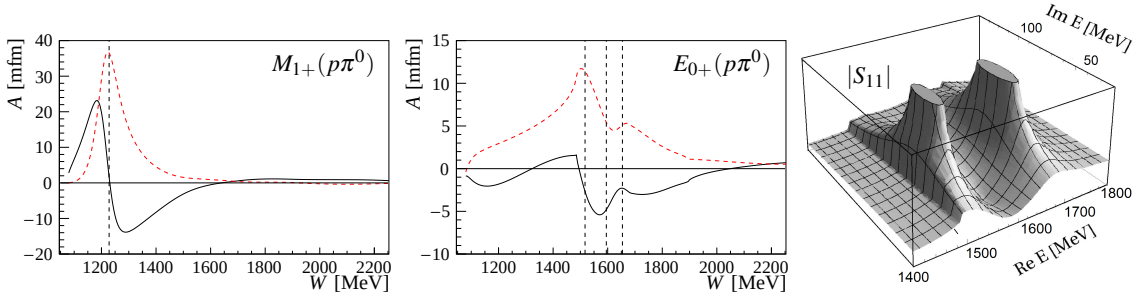

Fig. 1.12: The parametrization of a resonance state. On the left side, the real (solid black line) and imaginary part (dashed red line) of the particle representation multipole $M_{1+}(p\pi^0)$ of the reaction $\gamma p \to p\pi^0$ is presented for the BnGa-2016 PWA solution [46]. For the Breit-Wigner paramterization, the zero-crossing in the real part defines the mass of the resonance state (dashed vertical line) and the imaginary part is used to determine its width. In the middle, the similar plot is shown for the $E_{0+}(p\pi^0)$ multipole where the three resonances $N(1535)1/2^-(S_{11})$, $\Delta(1620)1/2^-(S_{31})$, and $N(1650)1/2^-(S_{11})$ are overlapping and interfere with each other. Since Breit-Wigner distributions are not feasible anymore, a much better approach is the parametrization via the complex energy plane of the T-matrix as shown on the right side for the JüBo meson exchange approach. The modulus |T| for the S_{11} partial wave in $\pi N \to \pi N$ is plotted as a function of the complex scattering energy E. The $N(1535)1/2^-(S_{11})$ and $N(1650)1/2^-(S_{11})$ resonances are clearly seen as an enhancement (figure right modified from [48]).

The Scattering Analysis Interactive Dial-in (**SAID**) model is based on the Chew-Mandelstam K-matrix approach [30] with the most recent solution being the SAID-CM12 solution. Resonances, expect the $\Delta(1232)3/2^+(P_{33})$ resonance, are dynamically generated by the parametrization of the K-matrix with energy-dependent polynomials up to the fifth order. The masses, widths and hadronic couplings are obtained from fits to data for pion-induced reactions. The photocouplings of the resonances are finally determined by fitting to photoproduction data. Thus, new resonances can not be extracted with photoproduction data within this approach.

The situation is different for the Bonn Gatchina PWA (**BnGa**) which is a multi-channel PWA relying on a dispersion-relation Ansatz which is based on the N/D technique. It is the most phenomenological model of the four approaches as the resonances are included by hand. Within the analysis of the newest data, the BnGa group added above 2.2 GeV resonances as relativistic multi-channel Breit-Wigner amplitudes [39]. To account for non-resonant contributions, amplitudes are included which represent the t- and u-channel exchanges. As mentioned before, the BnGa group performs a multi-channel analysis which fits simultaneously a large data base. It utilizes the SAID WI08 energy-dependent amplitude solution together with pion-, photon-induced reactions, and even 3-body final states. A list of all reactions is given in [39]. The recent solution is the BnGa-2016 [46].

The Mainz Isobar Model (**MAID**) is based on a T-matrix approach in which resonances are parameterized as multi-channel Breit-Wigner amplitudes [49]. Thereby, mass, width and coupling strength of the 13 four-star resonances below $W = 2\,\text{GeV}$ are taken from the PDG [7] as start parameters for the PWA. The non-resonant terms are modeled by Born terms which are described by an

energy-dependent mixing of pseudovector-pseudoscalar πNN couplings and t-channel vector meson exchanges [39]. The MAID-2007 solution is the oldest of all models and only includes data on photo- and electroproduction of pions up to the year 2002.
The final partial wave analysis mentioned here, namely the Jülich-Bonn model (**JüBo**), is a dynamical coupled-channel approach and strictly speaking no partial wave analysis [39]. The scattering potential of pion-induced reactions is constructed from an effective Lagrangian, which is iterated in a Lippmann-Schwinger equation [50][8]. Resonances can be included by hand in the pole-part of the scattering potential. In addition, generated resonances can occur via the interaction of t-and u-channel terms which are included in a non-pole potential to allow for non-resonant contributions as well. An example of a dynamically generated resonance in this approach is the Roper resonance $N(1440)1/2^+(P_{11})$. All resonances are obtained by studying the poles in the complex energy plane of the scattering matrix. The formalism of the photoproduction processes is realized by a parametrization of the kernel of the photoproduction multipole amplitude by energy-dependent polynomials. The JüBo approach uses the same data base as the BnGa group and determines the resonance parameters using the SAID WI08 energy-dependent amplitude solution together with pion- and photon-induced data. The latest version is the JüBo-2017 solution [50].

1.5 Current Data Base

The current data situation up to a beam photon energy of 1.5 GeV for the $p\pi^0$ and $n\pi^+$ final states are shown in Fig. 1.13 and Fig. 1.14. The data are presented by points in the kinematic variable $\cos\theta$, which is the polar angle of the meson in the center of mass system, and the beam photon energy E_γ .

The $p\pi^0$ channel is by far the best-measured photoproduction process. Apart from the differential cross section (e.g., [51, 52, 53, 54]), the beam asymmetry Σ has the biggest data base. It consists of data from the A2 collaboration shown in green [55, 56, 57], GRAAL collaboration in magenta [53], CBELSA/TAPS in red [58], CLAS in blue [54], LEPS in yellow [59] and all data before the year 2005 in gray. The polarization observables T, P and H have been measured in one experiment by the CBELSA/TAPS collaboration [60, 61], whereas an experiment from the A2 collaboration determined the obserables T and F [62]. The polarization observable E consists of a data set from the CBELSA/TAPS collaboration [63] and new unpublished data from the A2 collaboration [14].
For the polarization observable G, which will be extracted within this thesis, a data base below 600 MeV is nearly not present as only a few data points are available. Above 600 MeV, data exist from the CBELSA/TAPS collaboration [64, 45] which have an overlapping energy region with the A2 experiment. The covered energy range for the observable G within this thesis is indicated by the blue area.

[8] The equation ensures automatically two-body unitarity and analyticity.

For the $n\pi^+$ channel, the data base, compared to the one of the $p\pi^0$ channel, compromises much less measurements. Although the differential cross section is well measured, only a few other polarization observables have been investigated since the year 2000. All data before the year 2000 are marked by the gray symbols. The beam asymmetry Σ was measured above 600 MeV with good statistics and angular coverage by the GRAAL collaboration (points shown in magenta) [65, 66] and above 1100 MeV by the CLAS collaboration (points in blue) [54]. Below 600 MeV, data are also available from the LEPS collaboration (yellow points) [59] and the A2 collaboration (green points) [67, 57]. The biggest data base is available for the double polarization observable E, which has been measured by the CLAS collaboration in blue [68]. With an energy starting already at 350 MeV, these data overlap with the new A2 data which are indicated by the blue area. Besides the arguments which have been mentioned in the previous section, the importance of the double polarization observable G can be seen directly in the small number of available data points in the analyzed energy region. Additionally to the old data with poor statistics and bad angular coverage before the year 2000 [69, 70], the most recent measurements come from the A2/GDH collaboration with only one energy bin and six points in the angular coverage as indicated by the green points [67].

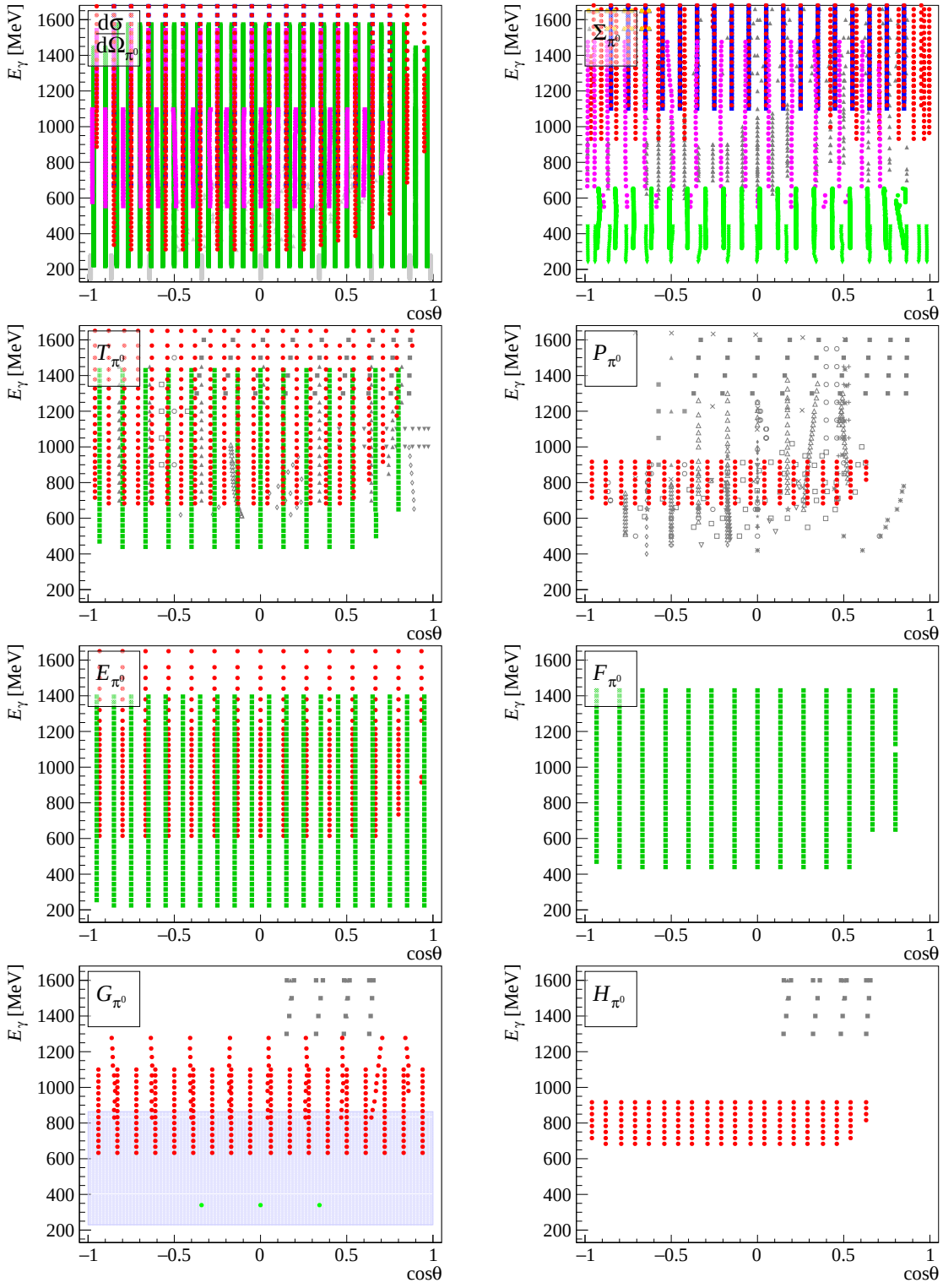

Fig. 1.13: Data base of the polarization observables for $\vec{\gamma}\vec{p}\to p\pi^0$. Shown are the experimental data points up to E_γ =1.5 GeV for the unpolarized cross section $\frac{d\sigma}{d\Omega}$, the three single polarization observables (Σ,T,P), and four double polarization observables (E,F,G,H). The full data base can be accessed in [71], whereas a list of all citations is given in Tab. 5 in reference [72]. The gray points indicate all data before the year 2005. Data from the CBELSA/TAPS collaboration are presented in red [17, 73, 58, 51, 63, 61, 64, 14] from the A2 collaboration in green [52, 62, 57, 55, 56], from the CLAS collaboration in blue [74, 54], from the GRAAL collaboration in magenta [53] and from the LEPS collaboration in yellow [59]. The blue area in the double polarization observable G marks the covered kinematic range by the new A2 data which are determined within this thesis.

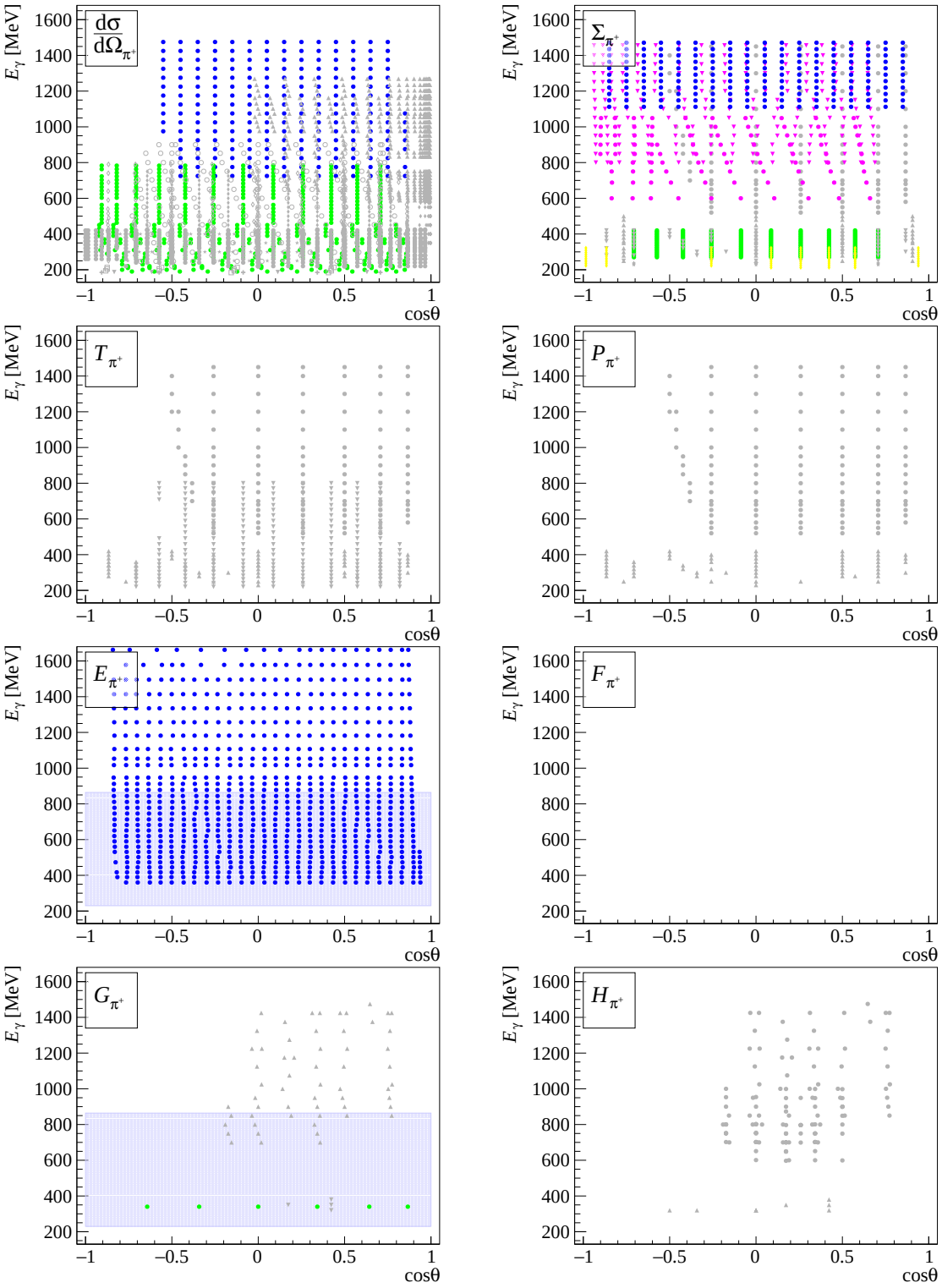

Fig. 1.14: Data base of the polarization observables for $\vec{\gamma}\vec{p}\to n\pi^+$. Shown are the experimental data points up to E_γ =1.5 GeV for the unpolarized cross section $\frac{d\sigma}{d\Omega}$, the three single polarization observables (Σ,T,P), and four double polarization observables (E,F,G,H). The full data base can be accessed in [71], whereas a list of all citations is given in Tab. 5 in reference [72]. The gray points indicate all data before the year 2000. Data from the A2 collaboration are presented in green [67, 75, 57], from the CLAS collaboration in blue [54, 68], from the GRAAL collaboration in magenta [65, 66] and from the LEGS collaboration in yellow [76]. The blue area in the double polarization observable G and E marks the covered kinematic range by the new A2 data which are determined within this thesis.

1.6 Aim of this Work

Within this thesis, the double polarization observable G will be extracted in the beam photon energy range from 230 MeV to 864 MeV. The measurement in the neutral pion photoproduction off the proton closes the gap from the $\Delta(1232)3/2^+(P_{33})$ region towards the already published CBELSA/TAPS data [64]. Together with the charged pion channel, an isospin separation of the contributing resonances is possible in a later analysis. Of special interest is the investigation of the M_{1-} multipole to which the Roper resonance $N(1440)1/2^+(P_{11})$ couples. It is mainly accessible in this observables due to its interference structure of the contributing multipoles. Besides that, the observable G is perfectly suited to study weakly contributing resonances in the region of the dominant $\Delta(1232)3/2^+(P_{33})$ resonance. Together with the measurement of the double polarization observable E, an experimental proof can be made that the measurements with elliptically polarized photons on a longitudinally polarized target are capable of determining the double polarization observables G (linearly polarized component) and E (circularly polarized component) at the same time within one experiment. Thus, within this PhD work, the double polarization observable E for the reaction $\vec{\gamma}\vec{p} \to n\pi^+$ will be determined in the beam photon energy range from 230 MeV to 864 MeV. The corresponding $p\pi^0$ and the $p\eta$ channel were part of the PhD work from F. Afzal [14].

The thesis is structured as follows. After an introduction to the experimental setup in Chapter 2, Chapter 3 concentrates on the experimental production of photons, including linearly, circularly and elliptically polarized photons which are needed to measure the double polarization observables G and E. Chapter 4 gives an overview of the data acquisition and software needed to analyze the data. Chapter 5 presents the methods to reconstruct the raw data into physical quantities which will then be calibrated in Chapter 6. Chapter 7 continues with the selection process of the $p\pi^0$ and $n\pi^+$ final state. The selected data are then used to extract the polarization observables in Chapter 8 and the final results will be discussed in Chapter 9.

Chapter 2

Experimental Setup

The A2 experiment, located at the electron accelerator MAMI in Mainz, is perfectly suited to fulfill the requirements for the measurement of polarization observables in photoproduction induced reactions. Thus in this chapter, an overview of the experimental setup is presented. After an introduction to the electron accelerator MAMI (**MA**inzer **MI**crotron), the equipment for the production and tagging of linearly polarized photons via coherent bremsstrahlung and of circularly polarized photons via helicity transfer is described. These photons are guided towards two different targets including the longitudinally polarized butanol target. Together, they form the requirements for the measurement of the polarization observables G and E for the analysis of this work. Since the polarization observables are analyzed for different final states, the decay particles have to be detected. Thus, the last two sections in this chapter will present the main components of the A2 experiment for the detection of neutral and charged particles. An overview of the experimental setup is illustrated in Fig.2.1.

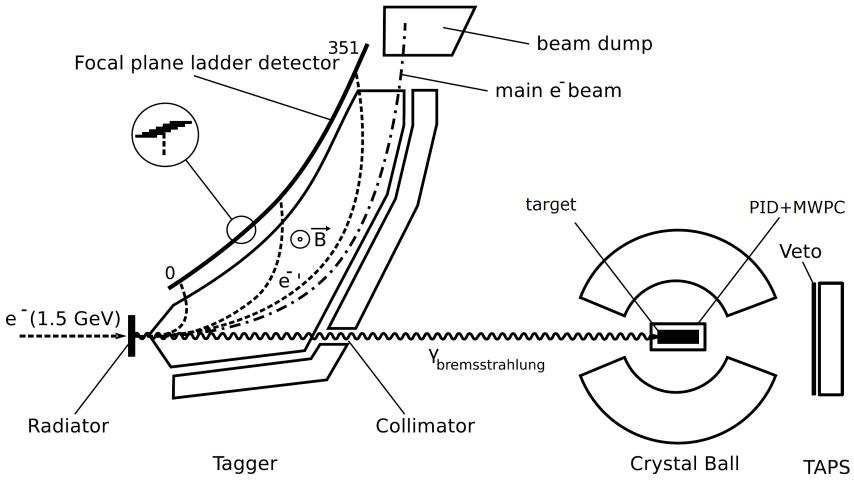

Fig. 2.1: Overview of the A2 experiment. A schematic overview of the setup is shown including the three main components of the A2 setup, namely the Tagger, the Crystal Ball, and the TAPS system (figure modified from [77]).

2.1 MAMI Electron Accelerator Facility

The MAMI electron accelerator facility is a continuous wave accelerator which is located at the University of Mainz. It is a four-stage accelerator consisting of three Race Track Microtrons (RTM) and a Double-Sided Harmonic Microtron (HDSM), which together can accelerate electrons up to an energy of 1602 MeV. An overview of the facility is shown in Fig. 2.2.

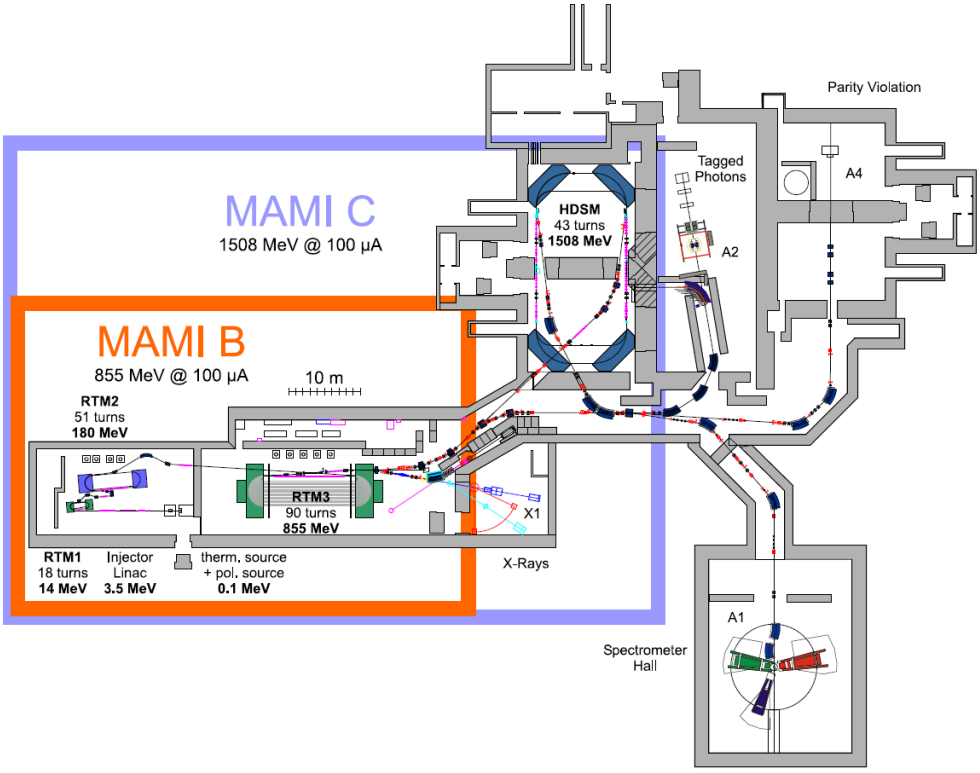

Fig. 2.2: Overview of the MAMI facility. Shown is the MAMI hall consisting of the three accelerating RTMs (MAMI B) and the HDSM (MAMI C). In addition, the four experimental halls X1, A1, A2, and A4 are shown (figure taken from [78]).

2.1.1 Electron Sources

For the acceleration, two electron sources are available. A thermal source is used for the unpolarized electrons and emits them with a maximum current of 100 µA. Polarized electrons with a polarization degree up to 80% and a current up to 20 µA can be produced via photoelectron emission of a GaAsP crystal (III-V semiconductor). A pulsed Ti:Sapphire laser provides linearly polarized photons, which are converted via a quarter-wave plate into circularly polarized photons. These photons are irradiated on the GaAsP crystal resulting in linearly polarized electrons [79]. To eliminate systematic effects due to instrumental asymmetries in the experiment, the helicity of the electron beam polarization is

flipped with a frequency of 1 Hz between parallel and anti-parallel. This is reached by using a Pockels cell as the quarter-wave plate where a flip in the voltage polarity causes a change in the optical axis of the used material and thus a helicity flip of the photons and electrons [80]. The degree of polarization is determined afterward with a Mott polarimeter.

2.1.2 The Four-Stage Acceleration

The electrons from the polarized source with an energy of 611 keV are injected into the injector linear accelerator (LINAC), where they are accelerated nearly to the speed of light with an energy of 3.97 MeV [81]. Afterwards, the first Race Track Microtron (RTM1) accelerates them to 14.86 MeV. A schematic overview of the Race Track Microtron is shown in Fig. 2.3.

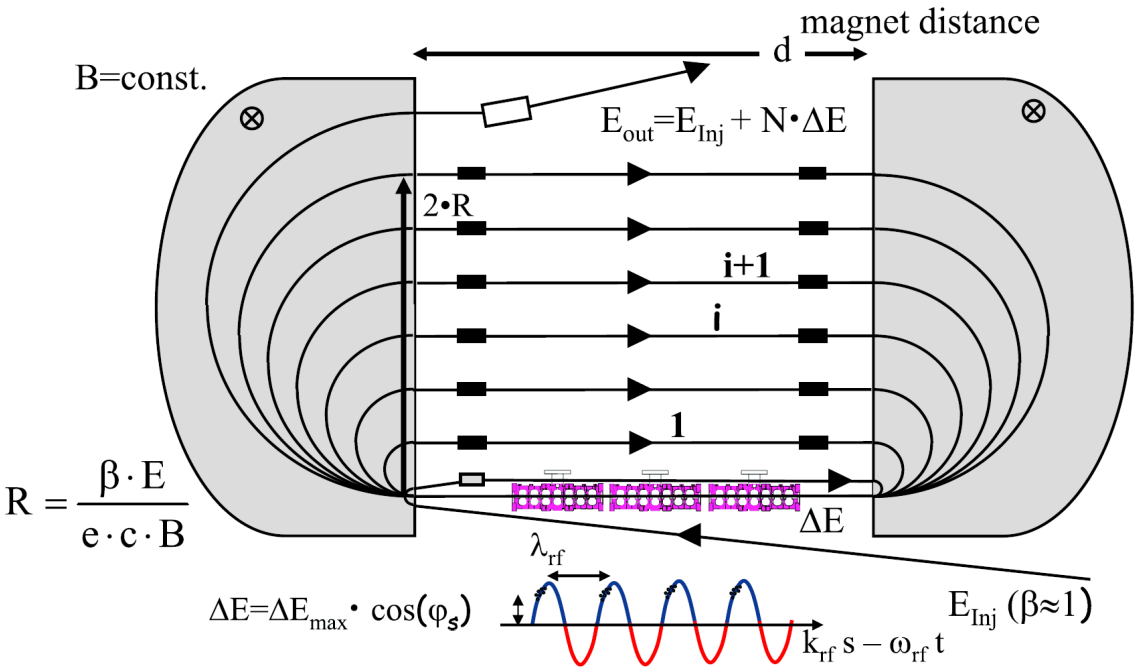

Fig. 2.3: Schematic overview of a Race Track Microtron (RTM). The lines indicate the passing of the electron through the two dipole magnets (figure taken from [82]).

The RTM consists of a LINAC with radio-frequency cavities with a wavelength of λ_{rf} in combination with two dipole magnets with an uniform magnetic field B. The magnets serve to deflect the electrons by 180° so that the electrons can pass the acceleration of the LINAC many times. In the case of RTM1, the number of circulations is 18. Since in each circulation the electrons gain a defined additional energy ΔE, the radius of the beam in the magnetic fields increases (see Fig 2.3). Thus, to ensure that the electrons are accelerated coherently in phase in the LINAC, two conditions have to be fulfilled. The first one is the static coherence-condition for the path length L_1 of the first complete circulation.

It is given by:

$$L_1 = k \cdot \lambda_{rf} = \frac{2\pi(E_{inj} + \Delta E)}{ecB} + 2d \tag{2.1}$$

and demands that the first path length L_1 must be an integer multiple of the rf-wavelength λ_{rf} [83]. It can be adjusted either by the injected energy E_{inj}, the distance d of the dipoles, or their magnet field strength B. Since a huge distance d between the magnets would result in a large beam emittance and a huge magnetic field in inhomogeneities in the field, the condition is fulfilled by the injected energy E_{inj} of 3.97 MeV of the injector LINAC. The second condition is the dynamic resonance-condition and requires a connection between the path length from one circulation L_i to the next one L_{i+1}:

$$L_{i+1} - L_i = 2\pi\Delta R = k \cdot \lambda_{rf} \ . \tag{2.2}$$

It is fulfilled by setting the energy gain ΔE per turn to:

$$\Delta E = \frac{ecB}{2\pi} \cdot k \cdot \lambda_{rf} \ . \tag{2.3}$$

Each RTM of the MAMI facility is adjusted in such a way that these conditions are fulfilled. Together with the technique of longitudinal phase focusing and quadrupole magnets which focus the electrons perpendicular to their momentum [84], a very good energy resolution and low divergences in the beam are achieved [83] [82]. All three RTMs together can accelerate the electrons up to an energy of 883 MeV. For further acceleration, another RTM is not feasible since the bending radius of the electrons in the magnets strongly depends on the injected energy and the applied magnetic field. Furthermore, due to the saturation of ferromagnetic materials, the maximum possible magnetic field is about 1.5 T and RTM3's magnetic field is already 1.29 T. Another problem is the dimension of the magnets. Since the magnets weight increase with the third power of the output energy, the magnets would require a mass of more than 3000 t per dipole if the output energy of RTM3 would be doubled [78]. Consequently, another solution was required by using a Harmonic Double-Sided Microtron (HDSM). A schematic overview of the HDSM is shown in Fig. 2.4. Instead of using two heavy dipole magnets that bend the electron beam by 180°, four lighter dipole magnets are implemented which each bend the beam by only 90°. By that, the electrons can also pass the two LINACs. To avoid defocusing effects and to reach a stable beam, one of the LINACs is driven at the fundamental frequency (2.45 GHz) and the other one at the first harmonic frequency (4.9 GHz). Finally, an energy of up to 1602 MeV with an uncertainty of only 10 keV can be extracted and guided towards the A2 experimental hall [78].

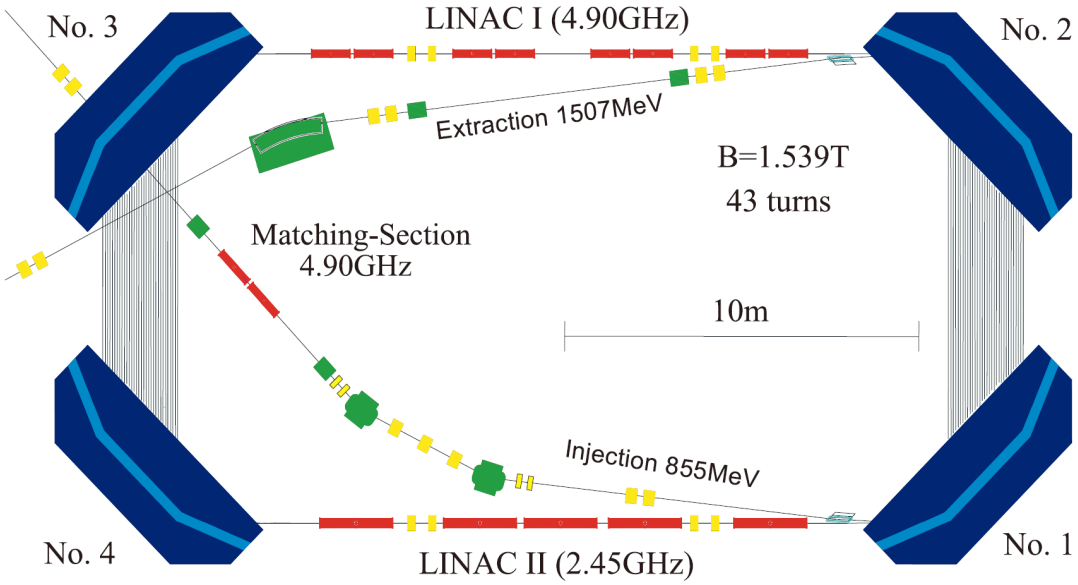

Fig. 2.4: Overview of the Harmonic Double Sided Microtron (HDSM). Shown is the HDSM with the two linacs LINAC I and LINAC II and the four dipole magnets (figure taken from [78]).

2.1.3 Summary

The MAMI electron accelerator facility provides a continuous wave electron beam with a final energy of 1602 MeV and an energy spread of only 110 keV. The electrons can either be unpolarized with a maximum current of 100 µA or longitudinally polarized with a polarization degree up to 80% and a maximum current of 20 µA. An overview of the main properties of MAMI is shown in Tab. 2.1.

Table 2.1: Overview of the main properties of the MAMI electron accelerator facility [82].

	Unit	Injector	RTM1	RTM2	RTM3	HDSM
Injection Energy	[MeV]	0.611	3.97	14.8	180	855
Extraction Energy	[MeV]	3.97	14.86	180	855	16002
Energy Gain / Turn	[MeV]	3.5	0.599	3.24	7.50	6.58-13.66
Number of Circulations		-	18	51	90	43
Energy Spread (1σ)	[keV]	1.2	1.2	2.8	13	110
Norm. Emittance Hor. (1σ)	$[\pi \cdot 10^{-6}]$	0.05	0.07	0.25	13	27
Norm. Emittance Bert. (1σ)	$[\pi \cdot 10^{-6}]$	0.04	0.07	0.13	0.84	1.2

2.2 Photon Beam

2.2.1 Goniometer

The A2 experiment makes use of a five-axis goniometer, which allows the goniometer to rotate in the azimuthal, horizontal, and vertical direction at the same time. It is located in a vacuum chamber in the beamline directly in front of the Glasgow Tagged Photon Spectrometer.

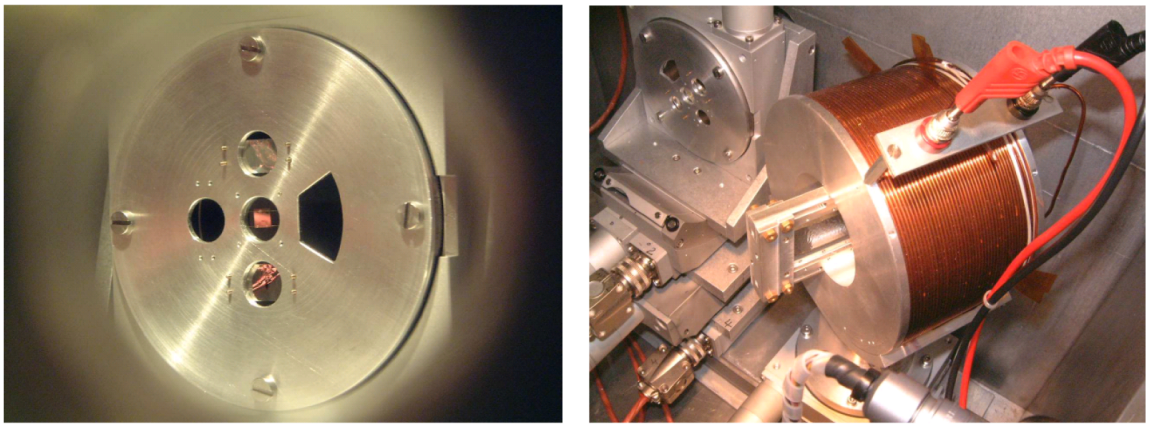

Fig. 2.5: The A2 goniometer. On the left side, the radiator wheel is shown with the diamond crystal located in the center of the wheel. On the right side, the Møller radiator and its magnetic coil is depicted (figure taken from [85]).

The radiator wheel is shown in Fig. 2.5 on the left side. It is equipped with different radiators for the production of bremsstrahlung photons (see Chap. 3). For this thesis, the two most important radiators are the diamond crystal and the Møller radiator. The diamond crystal, which is used for the production of linearly polarized photons (see Sec. 3.2), is located in the center of the goniometer and can be orientated with the five-axis goniometer to any position with respect to the electron beam. The Møller radiator with its magnetic coil is shown in Fig. 2.5 on the right side. The purpose of the radiator is to produce circularly polarized photons and to measure the polarization degree of the incoming electron beam (see Sec. 3.3).

2.2.2 Glasgow Tagged Photon Spectrometer

The Glasgow Tagged Photon Spectrometer serves to determine the energy of the produced bremsstrahlung photons and is located behind the radiators (see Sec. 5.1). A schematic overview of the spectrometer is shown in Fig. 2.6.

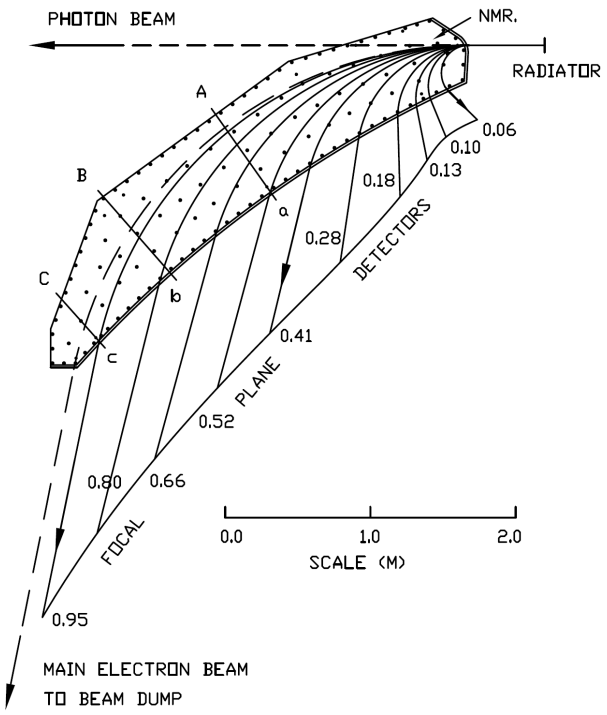

Fig. 2.6: Schematic overview of the Glasgow Tagged Photon Spectrometer. The schematic overview of the Glasgow Tagged Photon Spectrometer depicts the dipole magnet and the bending of the deflected electrons and their detection in the focal plane detector (figure taken from [86]).

The tagger consists of a large dipole magnet with a magnetic field strength of about 1.9 T at a current of 440 A. Therefore, the main electron beam that does not interact with the radiator is deflected by an angle of 79° and is guided into the beam dump. An additional Faraday cup serves to monitor the beam current. Decelerated electrons with an energy in the range of 5-93% of the incoming electron beam energy are deflected to lower angles according to their momentum. They are detected by the focal plane detector, which is instrumented with 353 plastic scintillators. Each scintillator has a length of 80 mm, a thickness of 2 mm, and a varying width of 9 mm to 32 mm. Therefore, the decreasing width along the focal plane detector ensures that the detected energy range of each element stays roughly constant. All elements are overlapping by slightly more than 50% with its neighboring element resulting in 352 possible coincidental signals with an energy resolution of about 4 MeV [86]. The corresponding energy for each overlapping channel can be estimated by a calibration procedure which will be explained in Sec. 6.1.1. The readout of each element is performed via photomultipliers (PMTs), which are shielded from the dipole magnetic field via Mu-metal. To ensure a long lifetime of the PMTs, the maximum count rate of an element is limited to 10 MHz. Since the bremsstrahlung process follows a $\frac{1}{E_\gamma}$ distribution, a high rate of low energetic electrons is expected. Therefore, it is possible to turn off several sections of the tagger to reach an optimal rate for the desired experiment.

2.2.3 Collimator

After the bremsstrahlung photons are produced in the radiator and the deflected electrons are detected in the focal plane detector, the photon beam passes through a lead collimator with a 2 mm diameter after a distance of 2.45 m. With that, the beam spot diameter is smaller than the target material diameter to which the photon beam is guided after an additional distance of about 11 m. Furthermore, the effect of collimation of the photon beam plays an important role in the achievable polarization degree of the photons. A detailed explanation will be given in Sec. 3.2.4.

2.2.4 Pb-Glass Detector

For the analysis, a good knowledge of the number of photons which pass the collimator is mandatory. Therefore, a Pb-glass detector with the dimensions $20 \times 20 \times 20$ cm^3 can be placed 5 m downstream from the goniometer. In dedicated runs, named tagging efficiency runs, the Pb-glass detector is placed inside the beamline and allows for comparison of the incoming electron flux in the tagger to the photon flux on the target. At low beam currents and a rate of about 10 kHz in the Pb-glass detector, photons which pass the target and enter the Pb-glass detector have a nearly 100% efficiency of converting into an electron-positron pair [87]. By requiring a time coincidence of these detected particles and a signal in a tagger channel, an electron hit in the tagger can be marked as photon tagged. The tagging efficiency of a channel can afterward be determined via:

$$\varepsilon_{\text{tagg}}(\text{ch}) = \frac{\text{N}_{\text{tagged},\gamma}(\text{ch})}{N_{e^-}(\text{ch})}, \tag{2.4}$$

where $N_{e^-}(\text{ch})$ is the overall number of detected electrons in a tagger channel and the number with a corresponding time coincidence with the Pb-glass detector is given by $N_{\text{tagged},\gamma}(\text{ch})$.

2.3 Targets

The collimated photon beam is guided towards different targets, which are located in the center of the Crystal Ball detector. For this thesis, two targets were available. The polarized butanol target provides the required polarized protons for the measurement of the double polarization observables. An additional carbon target is used for reactions on unpolarized protons and serves to study the carbon and oxygen contribution inside the butanol target.

2.3.1 Polarized Target

For the measurement of the double polarization observables G and E, reactions on polarized protons are required. For the alignment of the proton spins in the desired direction, a target material with a high amount of unbound protons needs to be operated at low temperatures in combination with a strong magnetic field. The most obvious target choice would be a liquid hydrogen target (LH_2). However, at very low temperatures, the two proton nuclear spins are aligned anti-parallel to each other, which

results in a vanishing total spin. Consequently, the protons inside liquid hydrogen can not be polarized. In addition, one of the severe problems of the alignment of the proton spin is its high mass, i.e. a 2.5 T magnet at a temperature of 1 K results only in a proton polarization degree of about 0.255%. At similar conditions, electrons can reach a polarization degree of 93.3% due to its low mass compared to the proton mass [88]. Based on this knowledge, the principle of dynamic nuclear polarization (DNP) is used. It has the aim to transfer the electron polarization to the proton polarization [89]. To do so, the A2 experiment utilizes a butanol target (C_4H_9OH). The non-existing spin of the carbon and oxygen in combination with the high amount of polarizable protons of the hydrogen allows for polarizing a large amount of protons inside the target without any background polarization. The butanol target is doped with the paramagnetic radical TEMPO ($C_9H_{18}NO$) with a ratio of 10^{-4} [84]. The electrons of the radical can be polarized to nearly 100% by applying a magnetic field of about 2.5 T in combination with a rather low temperature of about 300 mK. Afterward, the achieved polarization of the electrons can be transferred to the protons of the hydrogen atoms inside the butanol target. The transfer of the polarization is realized by irradiating the target with a defined microwave frequency. The frequency is selected in such a way that hyperfine transitions are stimulated and cause simultaneous spin-flips of the electron and proton[1]. By that, the polarization will be transferred to the proton and an alignment of the spin with respect to the magnetic field direction is possible. To ensure a high proton polarization degree over a long period, the relaxation time must be maximized. This is achieved by the frozen-spin method where small pellets of the doped butanol are kept at a temperature of about only 25 mK by a ^{3}He/^{4}He refrigerator system (see Fig. 2.7). More details about the principles of the refrigerator can be found in [91]. Due to the achieved low temperature, the holding magnetic field of 2.5 T can be exchanged by a superconducting internal holding coil of only 0.65 T. A schematic overview of the cryostat including the refrigerator system and the target is depicted in Fig. 2.7. The target can reach a polarization of up to 85% and measurement periods of up to approximately one week in the frozen spin mode [90]. The target polarization is measured with a Nuclear Magnetic Resonance (NMR) coil with only a few windings which is attached to the target material basket [92]. It is a serial resonance circuit and frequency is scanned over the Larmor frequency of the proton. During the scan, the interaction between the spins of the target and the NMR coil causes a change in the inductance of the coil and thus its impedance. By measuring the resulting NMR signal in thermal equilibrium and frozen spin mode at the end of a beamtime period, the polarization degree of the protons can be determined. The individual polarization degrees of a production run in a beamtime can be extrapolated between these points. The resulting polarization values of the individual beamtimes will be presented in Sec. 8.2.2.

[1] For a magnetic field of 2.5 T, the frequency is 70 GHz and is given by the difference in the Larmor frequencies of the proton and electron [90].

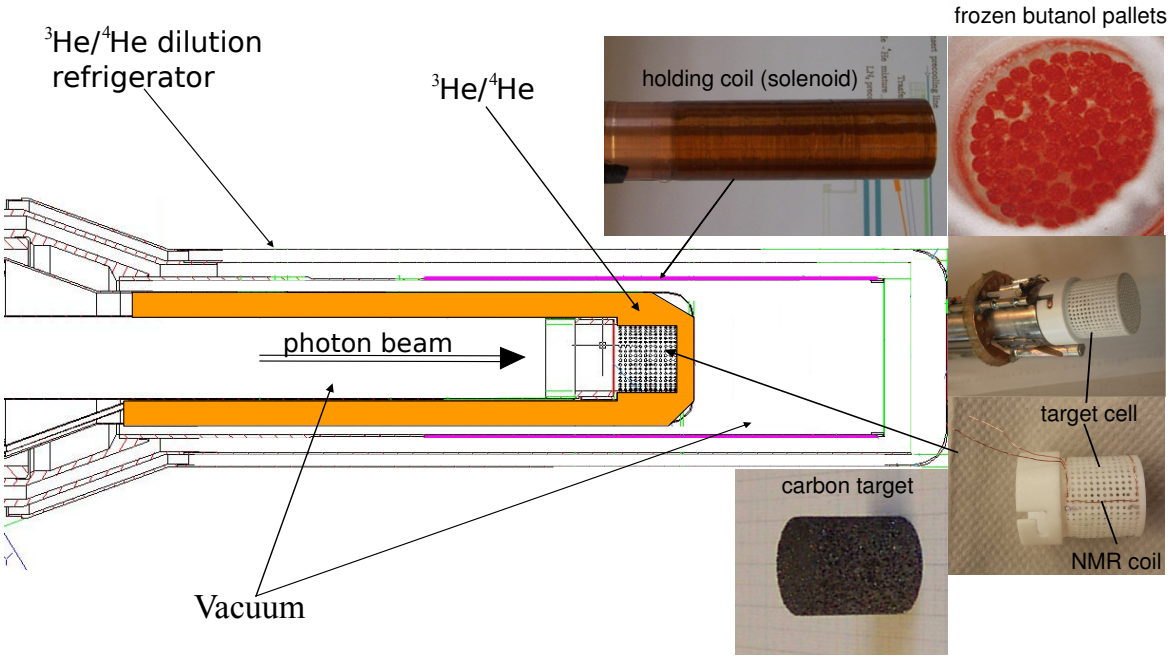

Fig. 2.7: Geometry of the front end of the polarized target cryostat. Shown is a schematic view of the cryostat, including the ^{3}He/^{4}He refrigerator system and the target basket which is filled with frozen butanol pallets. In addition, the NMR coil, the internal holding coil, and the carbon target can be seen (figure taken from [14]).

2.3.2 Carbon Foam Target

The carbon target is used to determine the background contribution of the carbon and oxygen inside the butanol target. Since the photoproduction cross section for carbon and oxygen behave in a similar way [93], the oxygen distribution can be described by the carbon distribution. Since the butanol target is used in the frozen spin mode, the helium mixture, which cools the target down to 2.5 mK, has to be taken into account as well. Hence, the carbon density and length is selected in such a way that its areal density is kept equal to the unpolarizable components of the butanol target plus the contribution of the helium mixture [14]. In addition, the same experimental conditions are achieved by placing the carbon target inside the same cryostat as the butanol target. With that, background coming from the cryostat windows or shells can also be subtracted.

2.4 Crystal Ball Setup

2.4.1 Crystal Ball (CB)

The Crystal Ball detector is the main electromagnetic calorimeter of the A2 experiment and surrounds the target, the PID, and the two MWPCs. A schematic overview has been presented in Fig. 2.1. Its main geometry is an icosahedron, which consists of 20 triangles. Each triangle is split into four

smaller equilateral triangles in which nine NaI(Tl) crystals are mounted in the form of a truncated triangular pyramid (see Fig. 2.8).

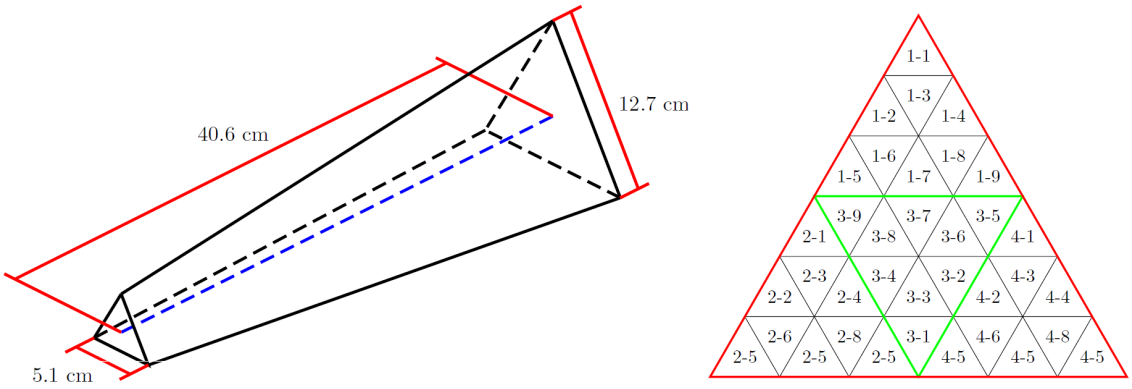

Fig. 2.8: The geometry and arrangement of the CB crystals. On the left side, the geometry of the CB crystals is shown and on the right side, its arrangement in one of the 20 main triangles (figure taken from [80]).

While a whole icosahedron is built up of 720 crystals, the CB only consists of 672 crystals. This is because the CB surrounds not only the target but also the beamline. An entry and exit point for the beam must be available, referred to as the tunnel region. Therefore, 48 crystals in the forward and backward directions are taken out, which results in a total of 672 crystals. These crystals are installed into two hemispheres and the upper one can be lifted for maintenance work. As a result of the two hemispheres, an inactive region of 2 mm $\times$ 1.5 mm steel plates in combination with a 5 mm air gap is present. Based on the fact that the crystals are very hygroscopic, both hemispheres are air-evacuated to ensure that the crystals are protected from dust and moisture. The crystals have a length of 40.6 cm, which corresponds to 15.7 radiation lengths. The front edge length of the pyramids is 5.1 cm, whereas the back length is 12.7 cm (see Fig. 2.8 on the left). Each crystal is wrapped in reflector paper and aluminized Mylar. With that, the crystals are optically isolated. The readout of the crystals is performed at the outside of the hemispheres by SRC L50 B01 photomultipliers. The produced scintillating light in the crystals is optically guided towards the PMTs via a glass window and a 5 cm air gap. The four-momentum of a particle is then reconstructed based on its reconstructed electromagnetic shower in the crystals. For further details about the reconstruction, see Sec. 5.2. The polar angular coverage of the CB is 21° to 158° with nearly full coverage in the azimuthal direction except for a small section between the two separated hemispheres.

2.4.2 Particle Identification Detector (PID)

The PID is in the form of a barrel and is located between the target and the two MWPCs. It consists of 24 EJ204 plastic scintillators with each scintillator covering 15° in azimuthal direction. Consequently, charged particles can be detected over the full azimuthal angular range. In contrast to the CB, the

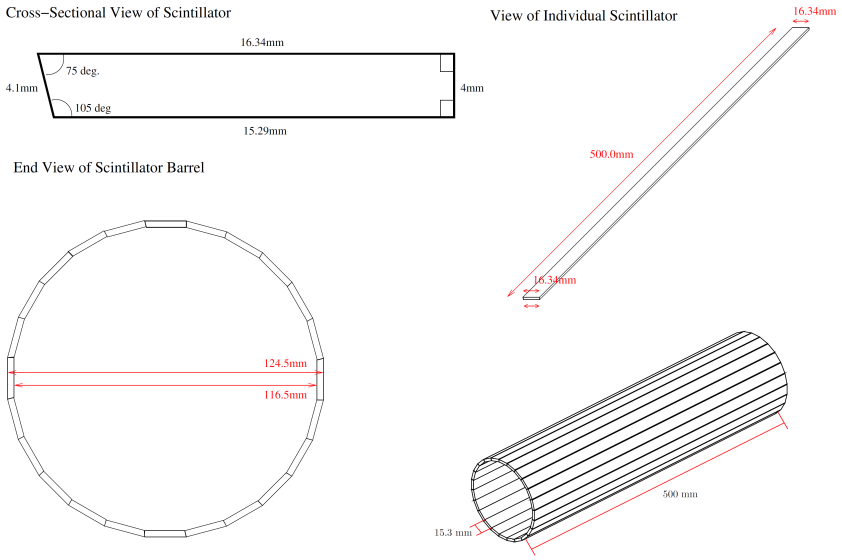

Fig. 2.9: The geometry of the PID plastic scintillators. The different geometries of the PID are shown (figure taken from [80]).

PID provides no polar angular information. Still, the length of the PID is selected in such a way that its polar angular coverage matches the one of the CB. Thus, by requiring an azimuthal angular correlation with the CB, a track in the CB can be marked as charged by detecting a signal in the corresponding PID element. Most importantly, different charged particles, i.e. electrons, charged pions, and protons, deposit a different amount of energy in the scintillators. Therefore, by plotting the deposited energy in the PID as a function of the deposited energy of the particle in the CB, a selection of distinct charged particles becomes possible. A detailed explanation of this reconstruction and selection will be described in Sec. 5.2.4 and Sec. 7.9.1. The geometry of each element is shown in Fig. 2.9 in which the cross-sectional view of the scintillator and its base parameters are depicted. It can be seen that the elements have a trapezoidal form to minimize the gaps between each other which results in a full azimuthal angular coverage. For optical isolation between the individual scintillators, each of them is wrapped in aluminum and the entire detector is isolated via a black Tedlar layer. The readout of the crystals is performed via light guides and PMTs (Hamamatsu H3164-10), which are located in the upstream direction. The purpose is to minimize the material between the target and the main calorimeters and thus, the amount of background produced in forward direction.

2.4.3 Multi-Wire Proportional Chambers (MWPCs)

Two MWPCs are installed between the PID and the CB for the tracking of charged particles. The exact reconstruction of these will be discussed in detail in Sec. 5.2.3. Each MWPC has an anode consisting of gold-coated wolfram wires with a diameter of 20 µm and a spacing of 2 mm. The wires are aligned parallel to the beam axis. They are surrounded by an inner and outer layer of aluminum cathode strips with a width of 4 mm and thickness of 0.1 µm. The strips, each having a distance of 0.5 mm to

its neighbor, are glued on a cylinder with Kapton foil and are mounted in the shape of a helix with an angle of 45° with respect to the beam axis. Most importantly, the inner and outer strips have a reversed direction of rotation. Due to that, each strip crosses each other twice, which is important for the reconstruction of a charged track. The MWPCs are filled with a gas-mixture of 65.5% argon, 28% ethane, 0.5% freon (CF4), and 6% alcohol. Between the wires and strips, a typical high voltage of 2.5 kV is applied. Thus, a charged particle ionizes the gas, and the ionized electrons/holes drift to the anodes/cathodes, which results in a changing voltage and a signal to readout. A schematic picture of the MWPC and the parameter details of each MWPC is shown in Fig. 2.10.

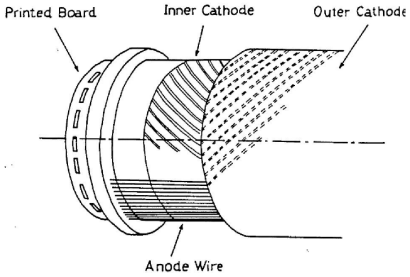

	Inner chamber	Outer chamber
No. of wires	232	296
No. of internal strips	69	89
No. of external strips	77	97
Wire layer radius, mm	74	94.5
Internal strip layer radius, mm	70	90.5
External strip layer radius, mm	78	98.5
Length, mm	570	
Angle beetween wires end strips, °	44.23	

Fig. 2.10: The geometry of the MWPC and its main parameters. On the left side, the geometry of a MWPC is shown and on the right side the corresponding main parameters are listed (figure taken from [94]).

2.5 TAPS Setup

2.5.1 Čerenkov Detector

The photon beam in combination with the target induces not only the desired photoproduction reactions but also undesirable electromagnetic backgrounds such as pair production and Compton scattering. This electromagnetic background is roughly five orders of magnitude larger than the photoproduction events [95]. Since the high energetically photon beam boosts the produced electrons and positrons in the forward direction, a gas threshold Čerenkov detector can be placed between the CB system and the TAPS. Its task is to reject the huge amount of electromagnetic background. To do so, it is filled with a gas mixture of the radiator gas C_4F_8 with a refractive index of n = 1.0013. With that, electrons with an energy above 10 MeV produce Čerenkov light, which is focused via a concave mirror on photomultipliers. Charged pions need an energy of at least 2.7 GeV and thus, do not produce any light in this experiment [96]. As will be shown in Sec. 4.2, the signal of the Čerenkov detector is used on the first level trigger of the data acquisition as a Veto signal and allows to reduce the amount of electromagnetic background in the forward direction. The dimensions of the detector are selected in such a way that the detector covers the same polar angular range as the TAPS and the full azimuthal polar range.

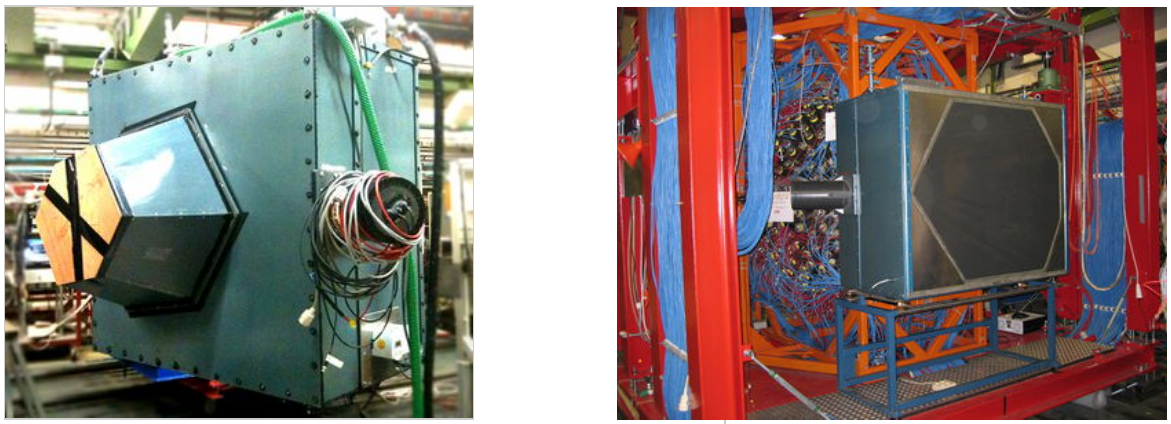

Fig. 2.11: Front and back view of the Čerenkov detector. On the left side, the front view of the detector is shown and the right side shows the back view (figure taken from [95]).

2.5.2 Two Arm Photon Spectrometer (TAPS)

The TAPS is an electromagnetic calorimeter and serves to detect the final state products in the forward direction. The detector covers the full azimuthal angular range and the polar angular range from 1° to 20°. For the case that the Čerenkov detector is installed, the TAPS has to be moved backward by about 32 cm, resulting in a decreasing polar angular coverage of only up to 17.5°. The detector consists of 366 BaF_2 and 72 $PbWO_4$ crystals, which are arranged in six logical sectors and eleven rings (see Fig. 2.12 on the left side).
The 366 BaF_2 crystals have the form of a hexagonal polyhedron with a length of 22.5 mm (see Fig.2.12 on the right top side). The length of the crystal in combination with a 2.5 cm long cylindrical end cap corresponds to 12 radiation lengths. Note that the BaF_2 crystals are very fast inorganic scintillators with a fast component of 0.9 ns for a scintillating wavelength of 220 nm and a slow component of 650 ns for a scintillation wavelength of 300 nm. The first provides, in combination with PMTs as a readout, a very good time resolution of about 0.6 ns and the latter one a good energy resolution. The existence of a short and fast component paired with a signal integration over a short and long time interval allows determining two different energy depositions, namely the long gate and short gate component. This components together can be used to identify particles via the Pulse-Shape Analysis technique, which will be explained in Sec. 6.1.4. To ensure good optical isolation, the crystals are wrapped in eight layers of 38 µm thick reflecting Teflon foil and one layer of 15 µm aluminum [77]. As readout, PMTs of the type Hamamatsu R2059-01 are installed at the end caps of the crystals. In the high forward direction, the crystals are exposed to a very high rate, mainly due to atomic Compton scattering [80]. Therefore, instead of BaF_2 in the inner two rings, 72 $PbWO_4$ crystals are installed. $PbWO_4$ has a higher density than BaF_2 and thus less space is required for these crystals. Instead of installing one BaF_2 crystal, four $PbWO_4$ crystals are used and the rate in each element is reduced by a factor of four (see Fig. 2.12 on the middle right side). In addition, $PbWO_4$ crystals have a shorter decay time than BaF_2 and thus, optimize the conditions of high rate stability. The individual crystals

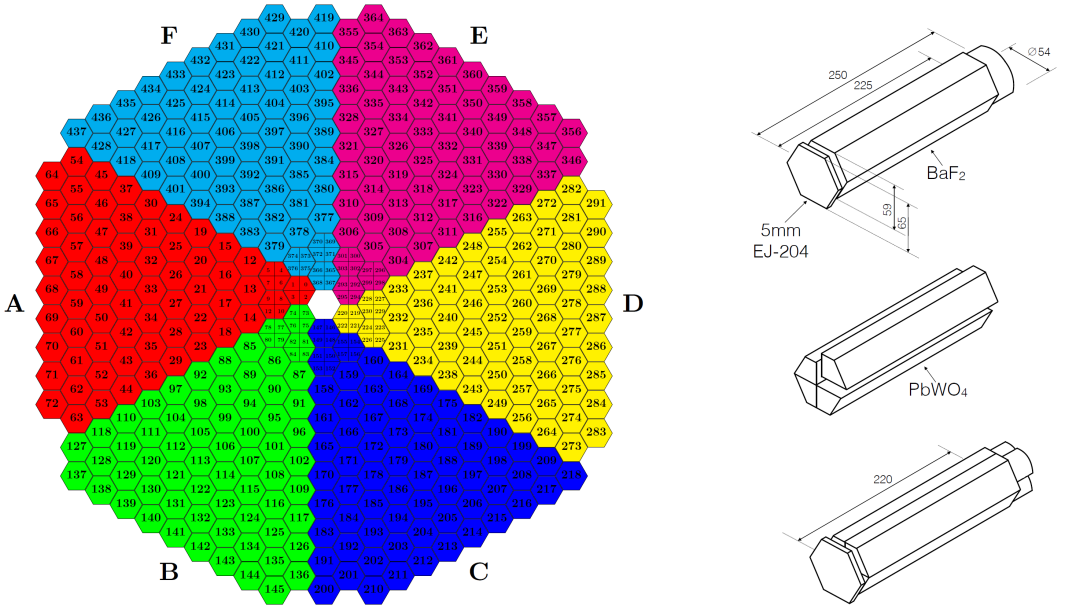

Fig. 2.12: The arrangement of the TAPS crystals and their dimensions. On the left side, the arrangement of the 438 TAPS crystals is shown. On the right side, the individual elements are depicted. In the upper row, the dimensions of a BaF_2 crystal are illustrated together with the EJ-204 plastic scintillators whereas in the middle, the decomposition of one BaF_2 into four $PbWO_4$. The lower row shows the dimension of one $PbWO_4$ crystal (figure modified from [97]).

are 20 cm long which corresponds to 22.5 radiation lengths. The optical isolation is achieved by wrapping each crystal in 70 µm reflector foil VME2000 and an additional layer of 20 µm aluminum foil. The readout is performed by a PMT of the type Photonics XP 1911 [77].

2.5.3 TAPS Veto Wall

To also identify charged particles in the TAPS acceptance region, the Veto Wall is mounted in front of the TAPS. In front of each BaF_2 crystal and a group of four $PbWO_4$ crystals, a hexagonally formed EJ-204 plastic scintillator with a thickness of 5 mm is installed. They are individually read out by a BCF-92 wavelength shifting fiber coupled to PMTs of the type Hamamatsu H6568. The deposited energy in these plastic scintillators can afterward be connected to the deposited energy in the corresponding TAPS crystals. Similar to the PID scintillators, electrons, charged pions, and protons deposit a different amount of energy in the plastic scintillators and thus a separation between these particles is possible. For further information, see Sec. 6.1.5 and Sec. 7.9.1.

Chapter 3

Production of Photons

The purpose of this thesis is to measure polarization observables via photoproduction induced reactions. Therefore, the electron beam coming from MAMI is guided towards different radiators (see Sec. 2.2.1). In the electromagnetic field of an atomic nucleus of the radiator material, electrons are deflected and decelerated. To ensure energy conservation, the lost kinetic energy of the decelerated electrons are radiated off by a photon. This process is called bremsstrahlung. The leading order Feynman diagrams are shown in Fig. 3.1.

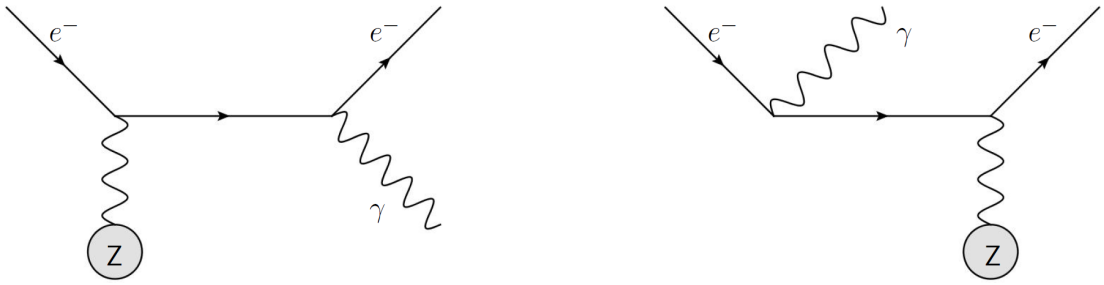

Fig. 3.1: Leading order Feynman diagrams for the Bremsstrahlung process. The two leading order Feynman diagrams for the bremsstrahlung process $e^- + N \rightarrow e^- + N + \gamma$ on an atomic nucleus with the atomic number Z are shown (figure taken from [45]).

The bremsstrahlung process has to fulfill several kinematic constraints which will be discussed in Sec. 3.1. In general, bremsstrahlung photons are not polarized. However, for the measurement of polarization observables, certain configurations of the incoming electron beam in combination with a radiator can produce linearly, circularly, or elliptically polarized photons. The different kinds of polarization will be discussed in the following sections as well.

3.1 Kinematics

The reaction and kinematics for the bremsstrahlung process is as following:

$$\begin{aligned} E_e &= E_{e'} + T + K, \\ p_e &= p_{e'} + q + k, \end{aligned} \tag{3.1}$$

where E_e and p_e are the energy and momentum of the incoming electron, $E_{e'}$ and $p_{e'}$ are of the outgoing electron, K and k are of the emitted photon, and T and q are of the recoiling participating nucleus, respectively [40]. Since the nucleus is heavy compared to the electron, it's momentum after the collision is negligibly small and its kinetic energy T can be neglected in the following calculations. Under this assumption, kinematic constraints can be derived in first-order approximation for the recoil momentum q of the participating nucleus using Eq. (3.2) [98]. Due to rotational symmetry of the bremsstrahlung process around the axis of the incoming electron momentum p_e, the recoil momentum is split into a momentum part, which is longitudinal (q_l), and one transverse (q_t) to the electron momentum. The calculation will show that most of the recoil momentum is carried in the transverse direction with respect to the incoming momentum p_e and that the longitudinal component is comparably small. Using Eqs. (3.2) and the angles defined in Fig. 3.2, the split momenta are given by:

$$q_l = p_e - p_{e'}\cos\Theta_e - k\cos\Theta_k, \tag{3.2}$$

$$q_t^2 = p_{e'}\Theta_e^2 + k^2\Theta_k^e 2 + 2pk\Theta_e\Theta_k\cos\Psi, \tag{3.3}$$

where Θ_e and Θ_k are the emission angles of the electron and photon with respect to the incoming electron direction and Ψ is the azimuthal angle between the planes (p_e,k) and (p_e,$p_{e'}$). The minimum

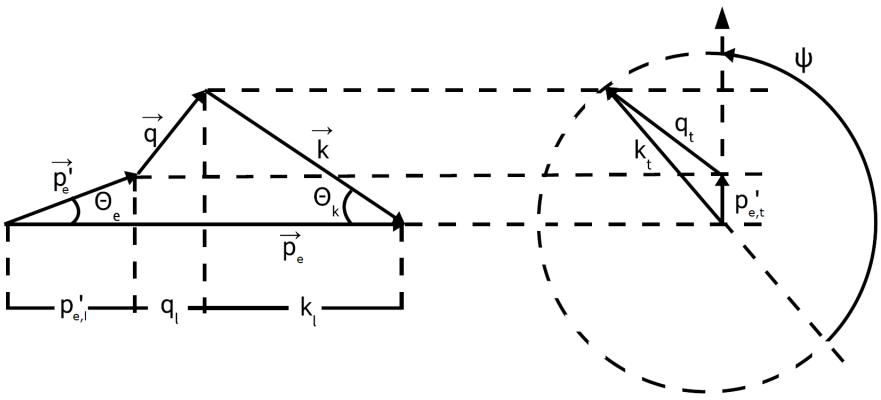

Fig. 3.2: Momentum relation for the bremsstrahlung process. Shown are the momentum relations parallel (left side) and perpendicular (right side) with respect to the incoming electron momentum p_e. It is important to note that this is not to scale, and in reality $q \ll p_e, p_{e'}, k$ and $\Theta_e, \Theta_l \ll 1$ (figure modified from [99]).

longitudinal momentum q_l^{min} is obtained if the electron and photon are both emitted in forward direction ($\Theta_e = \Theta_k = q_t = 0$) and is given by:

$$x = \frac{E_e}{k}, \;\; q_l^{min} = \delta(x) = \frac{1}{2E_0}\frac{x}{1-x}, \tag{3.4}$$

where x is the relative photon energy. An approximated upper limit can be estimated by using the characteristic angle of the emitted bremsstrahlung photon as the upper limit for the polar angle of the emitted photons. Therefore, the characteristic angle Θ_c is the polar angle of a cone around the beam axis in which half of all produced photons are emitted and is given by:

$$\Theta_c = \frac{m_e c^2}{E_e}. \tag{3.5}$$

Since emission angles larger than Θ_c are rare, this condition is a good approximation for the upper limit of the longitudinal momentum q_l^{max} which is given by:

$$q_l^{max} = 2\delta(x). \tag{3.6}$$

The maximum transverse momentum is obtained for the case that Ψ is zero. This yields to:

$$q_t^{max} = 2x. \tag{3.7}$$

Finally, the following approximated constraints have been found for the recoil momentum of the nucleus:

$$\begin{aligned} \delta(x) &\leq q_l \leq 2\delta(x), \\ 0 &\leq q_t \leq 2x. \end{aligned} \tag{3.8}$$

As mentioned before, the constraints in Eq. (3.8) already give a good approximation on the allowed momentum region. However, for the minimum longitudinal momentum q_l given by Eq. (3.4), the calculation assumed a vanishing transversal momentum q_t which is only valid if the momentum transfer q is relatively small. An exact calculation, described in detail in [98], gives the final constraints:

$$\delta(x) + \frac{(q_t^{max})^2}{2E_e} \leq q_l \leq \frac{\delta(x)}{x}, \tag{3.9}$$

$$0 \leq q_t \leq 1 \tag{3.10}$$

with the maximum transversal component

$$q_t^{max} = \sqrt{2E_e(q_l - \delta(x))}. \tag{3.11}$$

These conditions are known as the "pancake" constraints as depicted in Fig. 3.3. The allowed kinematic regions are indicated by the gray box for the approximated and for the exact constraints by the dashed area. Clearly visible is that the allowed momentum transfer is dominated by the transversal component, as already mentioned in the introduction.

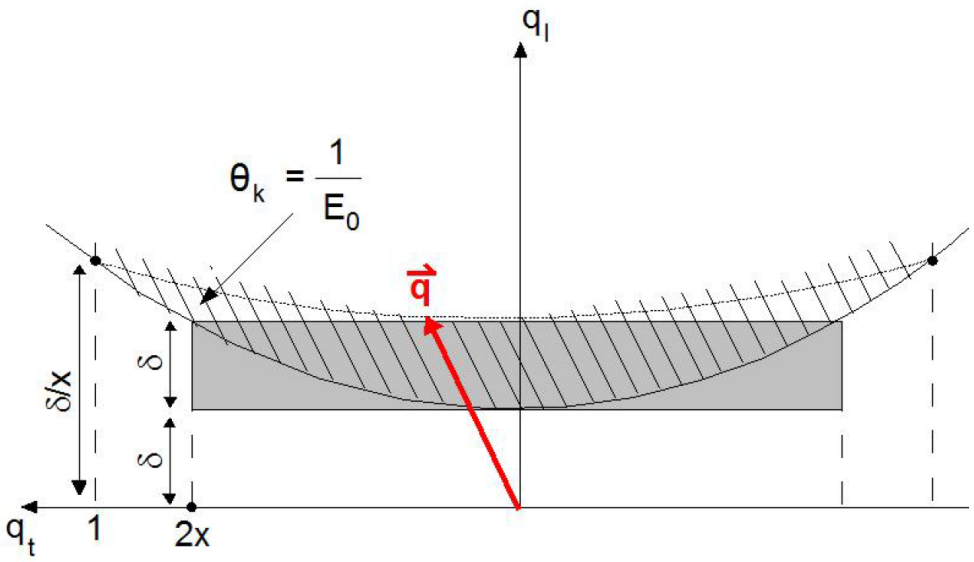

Fig. 3.3: "Pancake" region for the allowed recoil momentum q to the nucleus. Shown are the allowed regions for the recoil momentum q. Thereby, the gray box shows the approximated limits, following Eq. (3.8), and the dashed area the exact limits, follwing Eq. (3.10) (figure taken from [45]).

3.2 Linearly Polarized Photons

Bremsstrahlung photons can be produced incoherently or coherently. The incoherent bremsstrahlung is not polarized, whereas the coherent is. Thus, after a short summary of the main features of incoherent bremsstrahlung, this section will explain the production of linearly polarized photons via coherent bremsstrahlung.

3.2.1 Incoherent Bremsstrahlung

Incoherent bremsstrahlung takes place if electrons are irradiated on an amorphous radiator. An amorphous radiator does not have lattice structures and thus does not construct any further constraints on the recoil momentum q of the nucleus. Therefore, in the incoherent bremsstrahlung process, single atoms can absorb any allowed momentum in the "pancake" region. As a result, no preferred plane between the incoming electron and outgoing photon momentum is present and no preferred orientation of the electric field vector of the photon and consequently no linear polarization of the photon. The energy distribution of incoherent bremsstrahlung can be derived by the three times Bethe-Heitler

differential cross section. After integration, the bremsstrahlung photons energy distribution is in good approximation proportional to the inverse of the photon energy K. Thus, the amount of produced photons is decreasing with increasing photon energy.

3.2.2 Coherent Bremsstrahlung

By replacing the amorphous radiator with a crystalline radiator with a defined lattice structure, additional kinematic constraints on the recoil momentum q of the nucleus exist, which finally leads to a preferred plane and an orientation of the electric field vector. The lattice structure of a crystal is given by the reciprocal lattice vector $\vec{g}$ and is defined as:

$$\vec{g} = \sum_{i=1}^{3} \vec{b_i} \cdot h_i, \tag{3.12}$$

where $\vec{b_i}$ are the basis vectors and h_i are the Miller indices of the reciprocal lattice. Therefore, the lattice can be described as a function of the Miller indices $[h_1, h_2, h_3]$. For the production of linearly polarized photons, the Laue condition must be fulfilled, namely that the recoil momentum q must be a multiple of the lattice vector $\vec{g}$. In that case, a defined recoil momentum q is selected and the produced photons can interfere constructively, resulting in coherent bremsstrahlung and an orientation of the electric field vector of the photons. Studies have shown that the maximum polarization degree of the photons is achieved by the lattices [0,2,2] and [0,2,$\bar{2}$] [100]. To select these lattices for the production of the coherent bremsstrahlung, the crystal must be aligned relative to the incoming electron momentum. For this purpose, three angles are defined as depicted in Fig. 3.4 on the left. Thereby, ϕ is the angle between the [022] lattice and the lab horizontal, c the angle between the electron momentum and the [02$\bar{2}$] lattice and i the angle between the electron momentum and the orthogonal planes [100]. The angle c serves to control the position of the coherent peak, which is the position of highest polarization. It occurs at the relative photon energy x where the lattice vector leaves the allowed longitudinal momentum region of the pancake. Using Eq. (3.4), the corresponding fractional energy is given by:

$$x_d = \frac{2E_e\delta(x)}{1+2E_e\delta(x)}. \tag{3.13}$$

The coherent peak appears as a sharp discontinuity at $x = x_d$ in the enhancement distribution as it is depicted in Fig. 3.4 on the right. After the coherent peak position has been adjusted, the angle i can be used to adjust the lattice contributions. Thereby, c is selected in such a way that the lattices [022] and [02$\bar{2}$] fall in the allowed momentum regions and higher lattices are rejected so that interference with them can be avoided. Finally, to also avoid systematic effects due to detector inefficiencies, the ϕ angle is selected in such a way that the polarization plane is once parallel to the lab horizontal and once perpendicular. Thereby, it is sufficient to adjust the ϕ parallel to the lab horizontal. The perpendicular setting is reached by swapping the values for c and i. In the following section, the basic

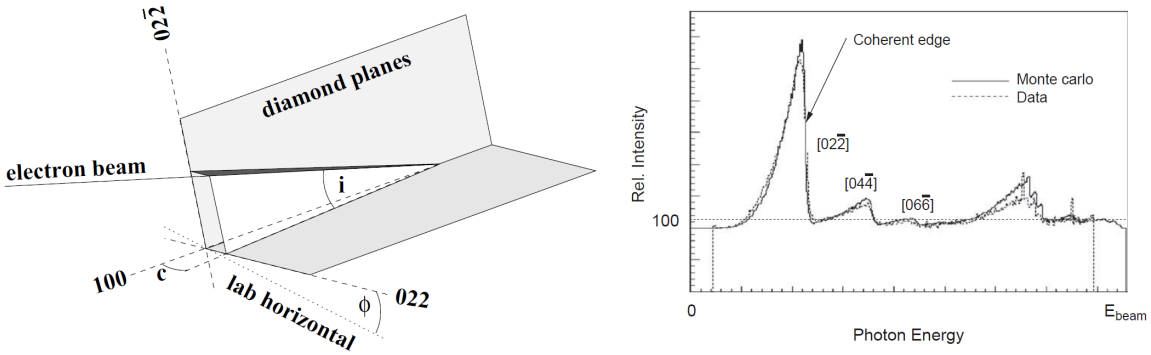

Fig. 3.4: Angles for the alignment of the crystal and the resulting coherent bremsstrahlung enhancement. On the right side, the resulting energy dependent enhancement for coherent bremsstrahlung is shown together with their corresponding lattices. The spectrum is adjusted with the angles *i,c*,and ϕ as defined on the left side. Note that the enhancement is normalized with an incoherent reference spectrum to 100 in a region where no contribution is present from incoherent bremsstrahlung (figure modified from [100]).

principles of the adjustment of the angles are given which is performed with the Stonehenge technique developed by Ken Livingston [100].

3.2.3 Stonehenge Technique for the Crystal Alignment

As mentioned above, the crystal has to be aligned in such a way that a desired lattice lies in the allowed momentum range. To do so, the A2 experiment makes use of a five-axis goniometer which, in addition to allowing movement in the vertical and horizontal directions (x,y), allows the radiator to be rotated about the azimuthal, horizontal and vertical axes (roll, pitch, yaw). The horizontal and vertical scanning is reached by varying an angular radius Θ_r of a cone around the crystal axis via:

$$\begin{aligned} \Theta_h &= S_h + \Theta_r \cos\phi_r, \\ \Theta_v &= S_v + \Theta_r \sin\phi_r, \end{aligned} \tag{3.14}$$

where ϕ_r is varied from 0 to 360° and S_v and S_h are the origin of the scan with respect to the origin of the goniometer axes. In small steps, the values of Θ_h and Θ_v are changed and for each setting the distribution in Fig. 3.4 is recorded and saved. Afterward, the distribution is plotted as a function of the variables Θ_h and Θ_v. The photon energy increases radially outwards from 0 MeV at the inner circle to the maximum energy of 1488 MeV at the outer circle. The intensity of the distribution is indicated by the color scheme where red corresponds to a high intensity. The resulting plot is shown in Fig. 3.5 and is referred to as a Stonehenge plot. On the left side, the Stonehenge plot is shown for a polarization plane orientated at +45° and a scan started from $S_v = S_h = 0$. Four clear enhancements are visible which originate from the [022] and [02$\bar{2}$] lattice. Due to the symmetry of the lattice, these four points need to construct two orthogonal lines where the intersection points determine the position of the

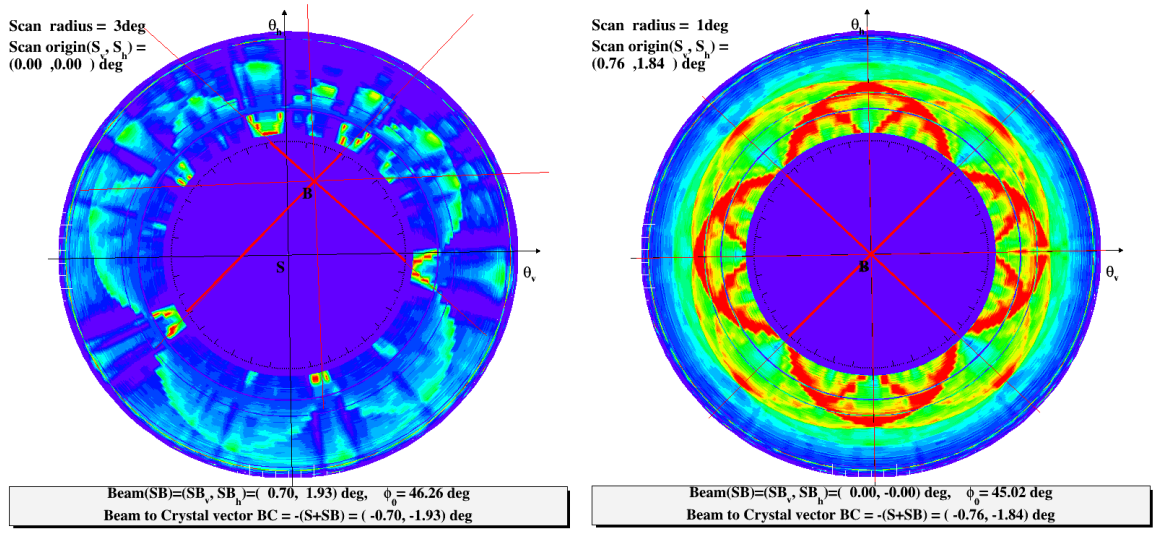

Fig. 3.5: Angles for the alignment of the crystal and the resulting energy-dependent photon distribution. On the right side, the resulting energy-dependent photon distribution for coherent bremsstrahlung is shown which is adjusted with the angles *i* and as defined on the left side (figure taken from [101]).

electron beam B relative to the center of the scan S. As a further cross-check, additional lines with a respective angle of 45° are drawn which correspond to the [044] and [04$\bar{4}$] lattice and also indicate a small enhancement. Adjusting the scan origins S_v and S_h to the calculated beam position results in the final Stonehenge plot shown on the right side of Fig. 3.5. With this plot and an additional scan with a known rotated angle ϕ_s of the crystal, the necessary offsets are determined so that finally the crystal can be aligned as desired. A detailed explanation is given in [100].

3.2.4 Collimation

As mentioned earlier, the collimation of the photon beam is used to increase the degree of linear polarization. This effect can be explained by the fact that the emission angular distribution of incoherently and coherently produced photons differ. Whereas the incoherent distribution is independent of the photon energy and only depends on the incoming electron energy (cf. Eq. 3.5), the angular distribution of the emitted photon highly depends on the photon energy. As shown in reference [98], the emission angle of the bremsstrahlung photons becomes more forward-directed towards the coherent edge position. Consequently, a collimation of the photon beam allows for accepting the forward-directed coherent distribution and simultaneously rejecting the incoherent distribution at similar photon energies. At the same time, low energetic photons in the coherent peak will be rejected and thus narrow the coherent peak. As a result, the ratio between coherent to incoherent distribution can be increased and also the degree of linear polarization. The effect of the collimation can be seen in Fig. 3.6 where the enhancement is shown once before the collimation and once afterward. Since the

intensity of the enhancement is related to the degree of linear polarization, this figure nicely illustrates the effect of the collimation.

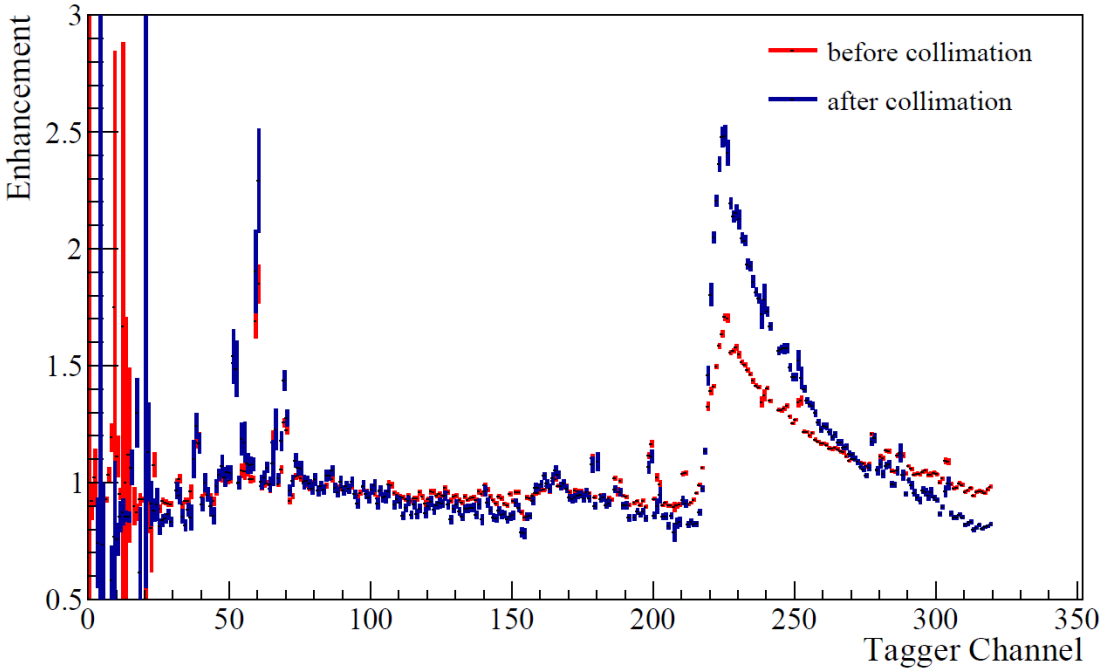

Fig. 3.6: Enhancement spectrum before and after collimation. Shown are the enhancement before the collimation (red) and after the collimation (blue). It is clearly visible that the collimation increases the intensity of the enhancement and that the coherent edge is narrower compared to the uncollimated one. Note that the enhancement is plotted as a function of the tagger channel. A high tagger channel corresponds to low photon energies and vice versa (figure taken from [102]).

3.2.5 Determination of the Polarization Degree

As previously mentioned, the photons are polarized if they are produced coherently. In fact, bremsstrahlung photons produced on a crystal also have an incoherent distribution which originates from thermal vibrations of the crystal lattices. For the calculation of the polarization degree, an enhancement plot is constructed which is the bremsstrahlung spectrum of the crystalline normalized with the spectrum of the amorphous radiator. The amorphous radiator serves to describe the incoherent distribution in the coherent bremsstrahlung spectrum and thus a normalization is required in the region where no enhancement from coherent bremsstrahlung is present. Since the photon beam is passing a collimator, the enhancement and the determination of the linear polarization degree should only be considered for the photons which pass the collimator. Therefore, the enhancement is produced by taking daily tagging efficiency runs (see Sec. 2.2.4). The enhancement is afterward fit with a complex phenomenological function and from its parameters, the degree of linear polarization can be extracted. The function is based on the formalism of coherent bremsstrahlung production and includes additional smearing parameters that takes experimental aspects such as beam divergence

and multiple scattering into account [103]. A typical enhancement fit with the phenomenological function is depicted in Fig. 3.7 on the left and the resulting linear polarization on the right. Once an

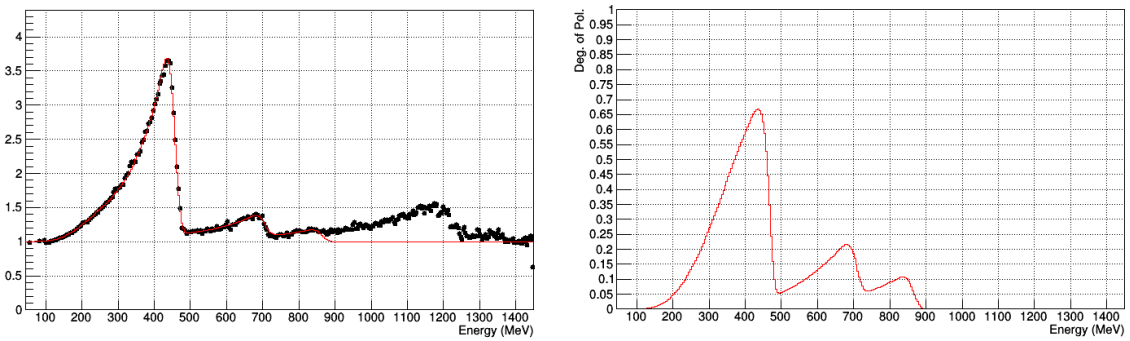

Fig. 3.7: Enhancement spectrum with the fitted function and the resulting polarization degree. On the left side, the enhancement as a function of the beam photon energy for a typical tagging efficiency run is shown. The distribution is fitted with the function (red line) which has been mentioned in the text above. The resulting polarization degree of the photons as a function of the beam photon energy is shown on the right side (figure modified from [104]).

enhancement fit is available, the polarization degree can be determined for any coherent edge position. Thus, the extracted fit parameters for the enhancement are used for the active determination of the degree of linear polarization. Active determination means that after 10,000 events in a production run, new polarization degrees are determined. The necessity of this procedure is justified by the fact that small shifts in the crystal radiator position or drifting of the electron beam cause a change in the crystal lattices orientation and the position of the coherent edge as well. Therefore, the coherent edge position is estimated after 10,000 events are accumulated. From the determined edge position, new polarization degrees are determined. A detailed study of the stability of the coherent edge position and its determination was a part of the systematic error studies of the polarization observables in Sec. 8.2.1.1.

3.3 Circularly Polarized Photons

For the production of circularly polarized photons, the MAMI accelerator provides a longitudinally polarized electron beam with a polarization degree p_e, which interacts with a radiator. With that, the helicity of the electron is transferred to the emitted bremsstrahlung photon resulting in circularly polarized photons with a polarization degree p_c. Since the helicity of the electron beam polarization is flipped with a frequency of 1 Hz (see Sec. 2.1.1), the polarized photons are produced with positive and negative helicity. The degree of polarization is calculated by QED and is given by:

$$p_c = p_e \cdot \frac{4E_\gamma E_e - E_\gamma^2}{4E_e^2 - 4E_\gamma E_e + 3E_\gamma^2}, \tag{3.15}$$

where E_γ is the energy of the produced photon and E_e is the incoming electron energy. The resulting photon polarization degree as a function of the photon energy is shown in Fig. 3.8 on the left side. Important to note is that the maximum polarization degree of the photons is limited by the maximum polarization degree of the electrons and is reached at the maximum photon energy.

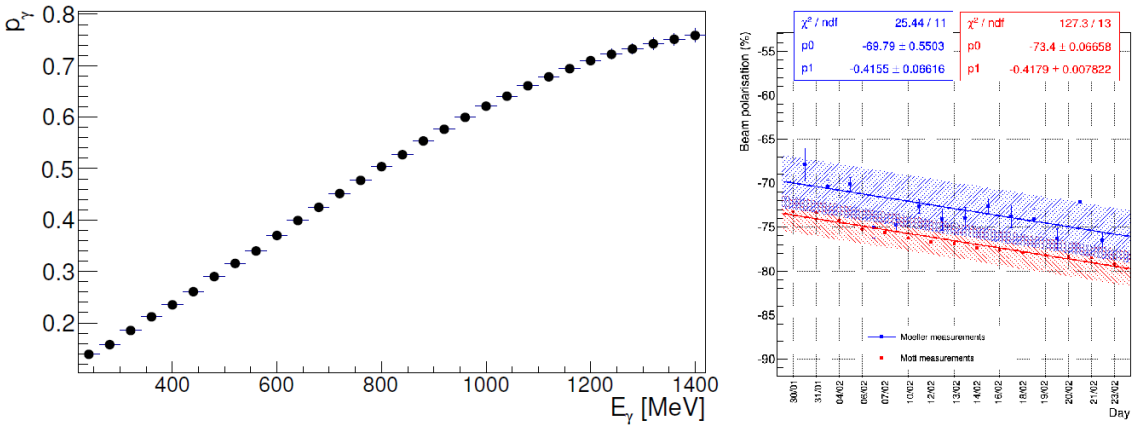

Fig. 3.8: Degree of polarization of the produced photons and the incoming electron beam. On the left side, the polarization degree of the photons as a function of the photon energy is shown, following Eq. 3.15. On the right side, the extracted degree of polarization of the electron beam is shown for the two independent polarimeters. Thereby, the blue points indicate the measured polarization degree extracted from the Møller polarimeter whereas the red points from the Mott. The systematic errors are given by the shaded areas (figure on the right taken from [105]).

Two independent measurements are performed for the calculation of the photon polarization degree since the polarization degree of the electrons is mandatory. On the accelerator side, a Mott polarimeter is located directly behind the injector LINAC. Electrons in a gold target interact via spin-orbit coupling with the longitudinally polarized electrons from MAMI resulting in an asymmetry in backscattering. From the asymmetry, the polarization degree of the electrons can be extracted. More details about the Mainz Mott polarimeter can be found in [106]. In addition, the A2 experiment has a Møller polarimeter, which is located at the goniometer and thus directly at the position of the photon production. It consists of a 10 µm thick foil of Vacoflux surrounded by a magnetic coil. The magnetic coil serves to polarize the electrons inside the Vacoflux. These polarized electrons with a known polarization degree interact with the incoming electron beam via the Møller-scattering process, which depends on the spin orientation of the electron beam. By measuring the spin asymmetry again of this process, the polarization degree of the incoming electron beam can be determined. For further details about the Møller-polarimeter, see [107] and [84]. For all beamtimes, the consistency between both methods has been checked by S. Costanza of the A2 collaboration [105]. The result for the November 2013 beamtime is depicted in Fig. 3.8 on the right. It is visible that both methods are in good agreement within their systematic uncertainties with polarization degree of about 70%. Since the statistical uncertainty of the Mott measurement is smaller than that of the Møller measurement,

the polarization values of the Mott measurements are used to calculate the photon polarization using Eq. (3.15).

3.4 Elliptically Polarized Photons

Elliptically polarized photons are photons which have a linearly and circularly polarized component at the same time. They are produced by combining a longitudinally polarized electron beam with a crystalline radiator. The circularly polarized photons occur due to the helicity transfer from the electrons to the photons as described in Sec. 3.3. The linearly polarized photons are produced by the reciprocal lattice constraints by the crystalline radiator (see Sec. 3.2). Within the G/E measurements, the elliptically polarized photons are used to extract the double polarization observables E and G. Whereas E requires the circularly polarization component, G needs the linear polarization component. By comparing the results with recent data, an experimental study of elliptically polarized photons becomes possible. Here, it is important to check if both polarizations influence each other. An analysis of F. Afzal showed that within the statistical precision a very good agreement between results for the double polarization observable E with elliptically polarized photons and only circularly polarized photons is achieved [14] in the $p\pi^0$ channel. This thesis will present similar results for the $n\pi^+$ channel. The obtained results for the double polarization observable G within this thesis do also not show any evidence that the linearly polarized component of the elliptically polarized photons disagrees with the directly produced linearly polarized photons.

Chapter 4

Data Acquisition and Software

The analog signals from the PMTs of the individual detector elements are collected by the data acquisition system (DAQ), which stores all recorded information into digital files. Time to digital converters (TCDs) are used for time information, analog to digital converters (ADCs) for energy information and scalers as counters. The different possible readouts are discussed in this chapter. For the later analysis, only events with a defined pattern are of interest and thus, before the information are saved, the collected signals have to pass a trigger system. Finally, an overview of the acquired data for this measurements is presented and the software which is used to store and analyze them.

4.1 Read Out

4.1.1 Glasgow Tagged Photon Spectrometer

After the analog signal of a focal plane detector element exceeds a preset discriminator threshold, a logical signal is sent to a CATCH[1] multi-hit TDC. As the name indicates, the module allows recording the time of multiple hits in an event. More details about CATCH TDCs can be found in [108]. Moreover, a signal is led to a FASTBUS scaler unit. This unit counts the number of detected hits in each element. Since the energy information of the detected particle is determined via a geometric-based calibration (see Sec. 6.1.1), the detector has no ADC readout.

4.1.2 CB

The analog signals of the 672 NaI(Tl) crystals are first sorted to 42 Uppsala fan out modules with each module connecting 16 channels. Afterward, each fan-out module splits the signal into three separate branches.
The first one is the Energy Sum trigger branch in which the 16 individual analog signals are added up to one analog signal. In the next step, the resulting analog signal of each fan-out module is added up to a single analog signal, which represents an overall sum of the deposited energy in the CB. This

[1] COMPASS Accumulate, Transfer and Control Hardware

signal finally runs through two discriminators, each having their own defined threshold. One of them has an adjustable threshold and is used to set up the ESum trigger (see Sec. 4.2). The other one has a threshold of only a few MeV to achieve a better timing for the main trigger. Only if both thresholds have been crossed, a logical signal is generated, which can be used as a first-level trigger.
The second branch from the individual 42 fan-out modules is the Timing/Multiplicity trigger branch. The Multiplicity trigger allows for triggering on a rough lower limit on the number of detected particles in the final state. To do so, the 16 analog signals are fed into a dual-threshold discriminator. A low discriminator threshold of about 3 MeV is used to suppress electronic noise. If this threshold is passed, the individual signals of the channels are sent to CATCH TDCs for the time information. The other discriminator, which is used for triggering, is set to a threshold of about 20 MeV for each analog signal. The 16 resulting logical signals of one fan out module are fed into a 16 channel OR. Since the CB readout electronics are built up of 42 fan-out modules, this results finally in 42 possible logical signals. If these individual signals again exceed the threshold, the multiplicity is increased by one so that in total a multiplicity of 42 in total is possible in the CB. Note again that this trigger is just an approximation for the number of detected particles. For instance, if two particles are detected within one fan out module, the multiplicity is increased only by one instead of two. On the other hand, a high energetically particle can spread its energy over two or more fan out modules and thus cause a higher multiplicity than one [77]. Nevertheless, the multiplicity trigger can be used as a second level trigger and will be discussed in Sec. 4.2.
The final branch of the fan-out modules is the Energy branch. In this branch, the individual analog signals are delayed by about 300 ns and fed into sampling ADCs where the signals are integrated. The signal is then proportional to the deposited energy in the crystals. For more information about sADCs see reference [109].

4.1.3 PID and MWPCs

Both the PID and the MWPC are not included in the trigger and thus its readout is simple. The energy information from the PID is provided by traditional ADCs, whereas the MWPC strips energy information, similar to CB, is given by sampling ADCs. The time information for both are read out by CATCH TDCs.

4.1.4 Čerenkov

The Čerenkov PMT signal is split into three parts [95]. The first one, after passing a discriminator, is used to obtain the time information via a CATCH TDC. The second one is delayed by 20 ns, amplified and fed into a traditional ADC for the energy information. The last one is used for vetoing in the trigger system and will be discussed in Sec. 4.2.

4.1.5 TAPS

TAPS is read out by customized VME[2] modules. For the BaF_2 crystals, one board has four readout channels [110]. Each channel is equipped with a constant fraction discriminator (CFD), two leading edge discriminators (LED1 & LED2), four charge to amplitude converters (QADCs), and one time to digital converter (TAC). As a first step, the CFD is set to a threshold of about 3 MeV to reject electronic noise. Its logical output signal serves to start the integration gate of the fast scintillation component of the QADCs and the TAC for the time information. The four QADCs, responsible for the energy information, integrate the signal over different time periods and gains. As already mentioned in Sec. 2.5.2, only two of the four QADCs have been used, the "short gate" ADC and the "long gate" ADC. The first one only integrates the fast component of the scintillating light and the latter one the whole signal. In addition, two LEDs are available for triggering (see Sec. 4.2). The LED1 threshold of each element is used to set a trigger on the condition that TAPS has seen any particle. Therefore, the six logical sectors of TAPS can contribute as well to the multiplicity of the CB, which results in a total of 48 possible logical signals for the multiplicity. The LED2 thresholds can be used for an additional multiplicity trigger for TAPS.

4.2 Trigger

The A2 trigger consists of a two-level decision trigger with the possible conditions presented in Tab. 4.1. By combining different trigger conditions, desired reactions can be prefiltered during the data recording. The two important triggers for the *G/E* beamtime will be discussed in detail in the following section.

Table 4.1: Overview of the main trigger possibilities and their aims in the A2 experiment.

Trigger	Task
CBEsum (low/high)	minimum energy deposited overall in the CB
TAPS LED1 or BaF_2	at least one crystal per logical sector above LED1 threshold
TAPS LED2 M2+ BaF_2	at least two TAPS sector with a crystal above the LED2 threshold
TAPS Ped. Pulser	read out of pedestals for TAPS calibration
M(X)+	at least *X* logical multiplicity signals
Čerenkov	signal from Čerenkov

4.2.1 CB Energy Sum

In the first level trigger, a trigger condition on the CBEsum low trigger was set. The threshold of about 30 MeV was selected so that a trigger signal is started if the energy sum is above the noise level. In the second level trigger, the CBEsum high ensured that the overall deposited energy is above

[2] Versa Module Eurocard

a certain higher value. This value is selected in such a way that the beamtimes are sensitive to the desired reactions, namely $\gamma p \to p\pi^0/p2\pi^0/p\eta/n\pi^+$. Whereas the first beamtime in November 2013 had a very open ESum high trigger (>40 MeV), the other beamtimes had a higher threshold so that a higher sensitivity to the $\eta \to 2\gamma$ and $2\pi^0 \to 4\gamma$ final states could be achieved[3]. An upper limit of 120 MeV has been chosen so that low energetic mesons in the $\Delta(1232)3/2^+(P_{33})$ resonance region which are decaying in the CB can be analyzed as well. For the analysis of the double polarization observables, it is mandatory to detect the particles over the entire polar angular range. However, the CBEsum trigger alone is mostly only sensitive to events where both photons are detected in the CB. If one of the photons is detected in the TAPS, the other low energetic photon in the CB would not activate the CBEsum trigger. An additional problem of the CBEsum trigger is the fact that this trigger is not very sensitive to the $n\pi^+$ final state. Consequently, for the first time in the A2 experiment, an additional TAPS trigger is applied, referred to as the TAPS Anti C trigger. A logical OR between both of these triggers finally defines the trigger for the *G/E* beamtimes.

4.2.2 TAPS Anti C

In addition to the CBEsum trigger, an additional TAPS LED1 or BaF_2 trigger was activated in the first level, which allows to detect particles in the TAPS with at least one crystal per sector having an energy above the LED1 threshold. The threshold has been selected in such a way that the trigger is selective on charged pions in the TAPS. As mentioned in Sec. 2.5.1, a huge amount of electromagnetic background is produced in the forward direction which would trigger the TAPS LED1 or BaF_2 trigger and cause a ratio of roughly 1:10 between the CBEsum and TAPS trigger [111]. As a result, the TAPS trigger had to be extended by an additional trigger signal from the Čerenkov detector. The final TAPS Anti C is an AND condition between the TAPS LED1 or BaF_2 trigger and the Čerenkov trigger. By varying the individual LED thresholds, the ratio between the TAPS Anti C and the CBEsum trigger was adjusted in such a way that slightly more CBEsum triggers existed.

4.2.3 Multiplicity Trigger

In the second level trigger, it is possible to set an additional condition on the multiplicity of an event. With that, a rough requirement on the number of particles in the final state can be achieved. beamtimes which are aiming at having a π^0 or η in the final state require a multiplicity of two or more[4]. For the analyzed beamtime within this thesis, the multiplicity trigger is not selected because one of the studied final states is $n\pi^+$. The neutron can not always be detected in the calorimeters, especially at low beam photon energies. Therefore, only the π^+ is seen. Consequently, a multiplicity trigger of two or more would reject these kinds of events.

[3] A beamtime of the Basel group had a threshold of about 300 MeV to reject the π^0 channel and only be sensitive on the η channel [77].

[4] One multiplicity for each photon from the π^0/η decay.

4.2.4 Trigger Overview

An overview of the selected trigger adjustments can be seen in Tab. 4.2. As mentioned in Sec. 2.2.2, the tagger system has a maximum allowed rate for its elements. Therefore, tagger sections have been switched off in several beamtimes to maximize the luminosity for the desired final states. For an example, the reaction $\gamma p \to p\eta$ has a threshold production of 707 MeV and thus the low energetic tagger sections (F-H) are turned off in dedicated beamtimes[5]. In addition, for the extraction of the double polarization observable G, only beam photon energies in a defined region of the coherent edge are of interest and especially at high coherent edges, the low energetic sections of the tagger were turned off (see Tab. 4.2). The coherent edge is the position of maximum degree of linear polarization and is discussed in detail in Sec. 3.2. Besides adjusting the tagger sections, the trigger was selected as well for the coherent edge positions. Since coherent edges below 750 MeV do not play an important role in the extraction of the double polarization observable G in the $p\eta$ channel, the trigger thresholds for the lower edges are optimized for $p\pi^0/n\pi^+$ and are thus a bit lower than the $750/850$ MeV edge position. The May 15 beamtime was dedicated to optimize the statistics for the $p\eta$ channel and a high CBESum threshold was selected. Unfortunately, due to a gas leakage in the Čerenkov detector and a poor calibration of the TAPS LED1s, the TAPS Anti C trigger was dominating the readout. To compensate for this problem, the TAPS LED1 thresholds had to be increased to 120 MeV. This trigger configuration rejected a lot of possible $n\pi^+$ candidates and is discussed further in Sec. 8.1.2.3.

Table 4.2: Overview of the main settings of trigger thresholds and tagger sections for the beamtimes analyzed within this thesis.

Beamtime	Coh. Edge [MeV]	Tagger Sections	CBESum high threshold [MeV]	TAPS LED1 threshold [MeV]
November 13	350,450,550,650,750	A- H	40	40
April 14	350,450,550,650,750,850	A-F	90	60
May 14	850	A-F	90	60
May 15	750,850	A-G	120	120
September 15	450	A-G	70	60
	650	A-G	90	80
	850	A-G	90	80

4.3 Beamtimes

4.3.1 Overview

For the *G/E* measurements, five separate beamtimes were performed in total, namely in November 2013, April 2014, May 2014, May 2015, and September 2015. In the past, experiments for the double polarization observable G and E were mostly performed in two individual beamtimes. For the

[5]These are the tagger sections, which are far below the η production threshold.

extraction of the double polarization observable G and E, a longitudinally polarized target must be combined with linearly polarized photons for G and circularly polarized photons for E.
For the *G/E* measurements performed at the MAMI accelerator in Mainz with the A2 experiment, the beamtimes made use of the frozen spin butanol target which has been discussed in Sec. 2.3. To reduce systematic uncertainties, the polarization was set once in the direction of the beam and once in the opposite direction. Elliptically polarized photons, which are assumed to be circularly and linearly polarized at the same time, were produced via longitudinally polarized electrons impinging on a thin diamond radiator. Thereby, the electron beam was provided by MAMI with an incoming energy of 1557 MeV and an helicity flip of the electron spin with a frequency of 1 Hz. Special interest was paid to the degree of circular polarization of the photons and the influence of using elliptically polarized photons for the extraction of the double polarization observable E. Therefore, additional measurements with a Møller radiator were performed. With this radiator, only circularly polarized photons were produced serving as a reference measurement. In addition to the butanol target, data were taken in November 2013, April 2014, and September 2015 with a carbon foam target to study the unpolarized components inside the butanol target. Between the May 2014 and May 2015 beamtime, offline analysis of the author and F. Afzal [14] revealed that the carbon foam target alone is not able to describe the unpolarized components inside the butanol target. Therefore, additional tests were performed in September 2015 with the carbon target. In November 2013 and April 2014, no helium was included in the data taking of carbon, additional measurements with helium circulating inside the cryostat were performed in September 2015. To investigate the helium contribution in more detail, a few hours were used to take data with helium only. As a last check, the influence of the magnetic field of the holding coil was investigated by taking data with the magnetic field turned off and on. As will be seen later in the analysis, all of these performed tests are important for a reliable understanding of the experimental conditions. An overview of the beamtimes is given in Tab. 4.3. Note that between November 2013 and May 2014, the data acquisition readout was optimized. Therefore, in one hour data taking in May 2014, roughly 3.4 times more events were recorded than in November 2013. To compare the overall hours of data taking, the recorded hours of November 2013 are scaled by 1/3.4.

Table 4.3: Overview of the main settings and parameters of the *G/E* beamtimes. Target (+/-) indicates the target polarization vector in direction (+) and opposite direction (-) to the photon beam whereas hours(+/-) represents a rough estimation of the hours of good data taking with the two target polarization settings.

Beamtime	Radiator	Target	Coh. Edge [MeV]	Hours (+/-)
November 13	diamond	butanol (+/-)	350	7/4
	diamond	butanol (+/-)	450	4/6
	diamond	butanol (+/-)	550	11/9
	diamond	butanol (+/-)	650	8/12
	diamond	butanol (+/-)	750	4/4
	Møller	butanol (+/-)	-	5/5
November 13	diamond	carbon	350	1
	diamond	carbon	450	1
	diamond	carbon	550	3
	diamond	carbon	650	4
	diamond	carbon	750	4
	Møller	carbon	-	7
April 14	diamond	carbon	350	9
	diamond	carbon	450	13
	diamond	carbon	550	10
	diamond	carbon	650	16
	diamond	carbon	750	20
	diamond	carbon	850	13
	Møller	carbon	-	9
May 14	diamond	butanol (-)	850	0/86
	Møller	butanol (-)	-	0/36
May 15	diamond	butanol (+/-)	750	24/35
	diamond	butanol (+/-)	850	74/0
	Møller	butanol (+/-)	-	39/8
September 15	diamond	butanol (+/-)	450	27/18
	diamond	butanol (+/-)	650	44/25
	diamond	butanol (+/-)	850	18/0
	Møller	butanol (+/-)	-	33/25
September 15	diamond	He	850	28
	Møller	He	-	9
September 15	diamond	carbon+He	850	30
	Møller	carbon+He	-	11
September 15	diamond	carbon+no He	850	2
	Møller	carbon+no He	-	1

4.3.2 Problems

The *G/E* beamtimes were the first beamtimes after the DAQ upgrade, which caused several problems in the detector readout. In November 2013 and April/May 2014, the PID, in particular, was affected. During the DAQ upgrade in November 2013, the experimental trigger was roughly 140 ns delayed. Due to this delay, the PID gate came slightly later than the trigger window and thus the first part of the ADC signal was lost [112]. As a result, the whole deposited energy in the PID was not recorded, which compromises the $\Delta E - E$ spectrum resolution and the overall PID efficiency. This effect got even worse in May 2014 such that for the May 2014 analysis the PID $\Delta E - E$ spectrum was not used at all. In addition, the same problems occurred for the $PbW0_4$ of TAPS. In that case, a timing misalignment caused that the information from them was not reliable. Consequently, all events in the analysis including the $PbW0_4$ crystals are rejected. Finally, an offline analysis performed by F. Afzal and cross-checked by the author revealed a mistake in the measured target polarization degree. Since this mistake was discovered before the start of the September 2015 beamtime, only the beamtimes before September 2015 are affected. Due to an ice layer on the outer NMR coil of the target cell, the unpolarized background protons in the ice influenced the determination of the polarization inside the butanol target and resulted in a too low polarization degree [88]. A detailed analysis of the necessary correction factors are given in [14] and are summarized in Sec. 8.2.2.

4.4 Software

In the following sections, the main software packages for the analysis of the recorded data will be discussed. These include the main software package AcquRoot, the calibration software CaLib, and the final analysis software GoAT. In addition, the A2 simulation package will be explained, which has been used to simulate data.

4.4.1 AcquRoot

AcquRoot is an object-orientated analysis software written in C++ [113]. It is based on the CERN ROOT framework [114] and is used to decode the raw file information into physical quantities. AcquRoot consists of a hierarchy of classes. All detectors have the same base classes where common features and properties of all detectors are gathered. In addition, each detector has its own detector class. There the raw ADC and TDC information are converted into physical quantities (see Chap. 6) and particle tracks are built through reconstruction algorithms (see Chap. 5). The communication between the detectors is finally realized by additional apparatus classes, which are collections of detectors. For example, the Crystal Ball apparatus class combines the information from the detector classes of the NaI, PID, and MWPC detector classes. Details about the reconstruction can be found in Sec. 5.2.4.

4.4.2 CaLib

For the decoding of the raw ADC and TDC information of the detectors, pedestals and conversion gains of each detector element need to be known. In the past, the pedestals and gains of each element were read in by ASCII files. However, during a long data taking period, these pedestals and gains can vary over time and thus many ASCII files were needed. An easier approach to handle these instabilities of the calibration parameters is the CaLib software package by the Basel group [77]. The CaLib software is based on a SQL database system where the calibration parameters are given for a defined run number interval. During data taking, these parameters are read in by a special class that was included in the main AcquRoot interface. In addition, the CaLib software provides classes and functions which can be used to calibrate the recorded data. These will be further discussed in the calibration chapter (see Chap. 6). Several of the classes and functions have been optimized by the author and F. Afzal.

4.4.3 GoAT

GoAT is an extension of AcquRoot and stands for Generation of Analysis Trees [115]. It is used to preselect event patterns and reduce the size of the ROOT trees produced from AcquRoot. To do so, the preselection is divided into three stages. In the first stage, individual particle tracks are identified, i.e. if the particles are charged or neutral. The second stage allows for combining these particles to mesons and the final stage can be used to handle the amount of final state particles, i.e. the $p\pi^0$ requires three reconstructed particles where two of them are neutral and one of them is charged. Most importantly, the final selected information are stored in a ROOT tree structure which is optimized to perform a physical analysis. Within this thesis, only the first and last stage was used. The meson reconstruction was performed within a separate analysis script which makes use of the generated trees from GoAT.

4.4.4 A2 Simulations

As the complexity of the experimental setup in physics has increased in the last decades, Monte Carlo simulations were established as a commonly used tool to study the response of an experimental setup with respect to a desired reaction. The A2 simulation package consists on the first stage of an event generator, named AcquMC [113]. The generator produces the desired reactions which afterward can be fed into the A2 package [116]. It is based on the Geant4 libraries [117, 118] and includes all information on the A2 experimental setup (see Fig. 4.1 and App. A.2). In combination with physics classes that describe the interactions between the particles and the experimental setup, the simulations can be used to study the experimental results and further to understand the background contributions in a desired reaction. An overview of the used simulated data is shown in Tab. 4.4. Further studies of different available physics class and the inclusion of the charged reconstruction efficiency is given in App. A.2.

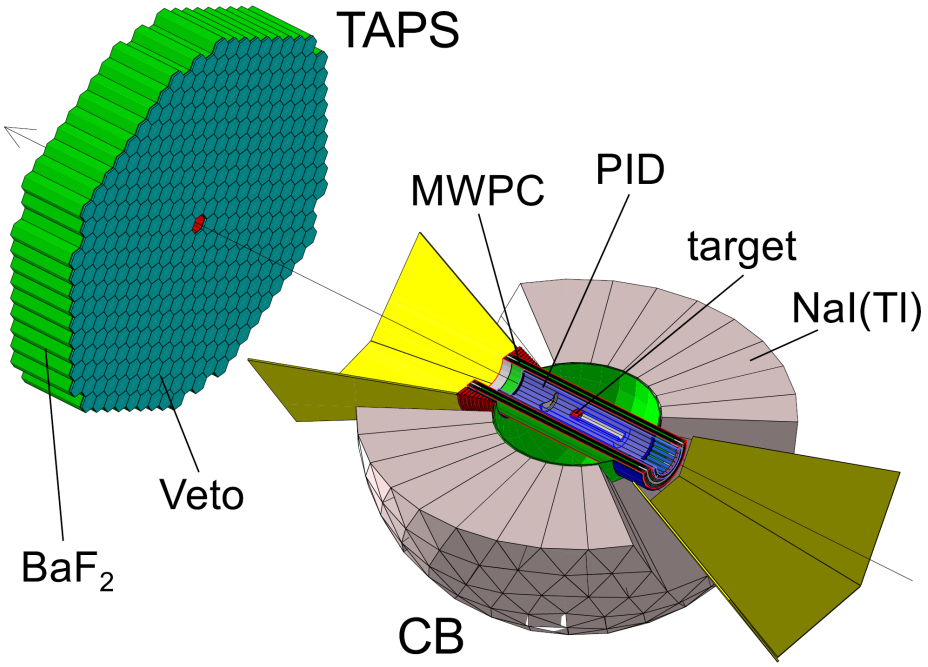

Fig. 4.1: Overview of the simulated A2 experiment. A schematic overview of the simulated setup based on Geant4 is shown. Note that the CB setup was cut in half to show the inner parts of the setup (figure taken from [77]).

Table 4.4: Overview of simulated data for the analysis.

Reaction	# Simulated Events
$\gamma p \to p\pi^0$	30×10^6
$\gamma p \to n\pi^+$	30×10^6
$\gamma p \to p\eta$	30×10^6
$\gamma p \to n\pi^+\pi^0$	15×10^6
$\gamma p \to p\pi^+\pi^-$	15×10^6
$\gamma p \to p\pi^0\pi^0$	15×10^6

Chapter 5

Reconstruction of Particles

To apply a calibration followed by the data analysis, the recorded data of the individual detectors need to be reconstructed first. For each detector, different algorithms are used to reconstruct the particles from their corresponding electronic signals. The reconstructed information is then combined into particle tracks. The principles of the reconstruction for the Crystal Ball setup, consisting of Crystal Ball (CB), the Particle-Identification Detector (PID) and the two Multi-Wire-Proportional Chambers (MWPCs), are described in this chapter. Tracks in forward direction are reconstructed using the TAPS and the TAPS Veto wall, which will be discussed as well.

5.1 Tagger

As described in Sec. 2.2.2, the tagger system consists of 353 overlapping plastic scintillators. If a scattered and deflected electron is detected in two neighboring elements, the hit is marked as a valid hit. For these hits, the corresponding channel number and all time information are stored. Events in which only one element has fired are rejected to reduce electronic noise and background coming from outside the tagger magnet, i.e. cosmic muons (see Fig. 5.1). As shown in Sec. 6.1.1, the tagger energy calibration connects the channel numbers with the electron energy E_e. Using energy conservation and knowing the initial electron energy E_0 of 1558 MeV from MAMI-C, the bremsstrahlung photon energy E_γ is given by:

$$E_\gamma = E_0 - E_e \ . \tag{5.1}$$

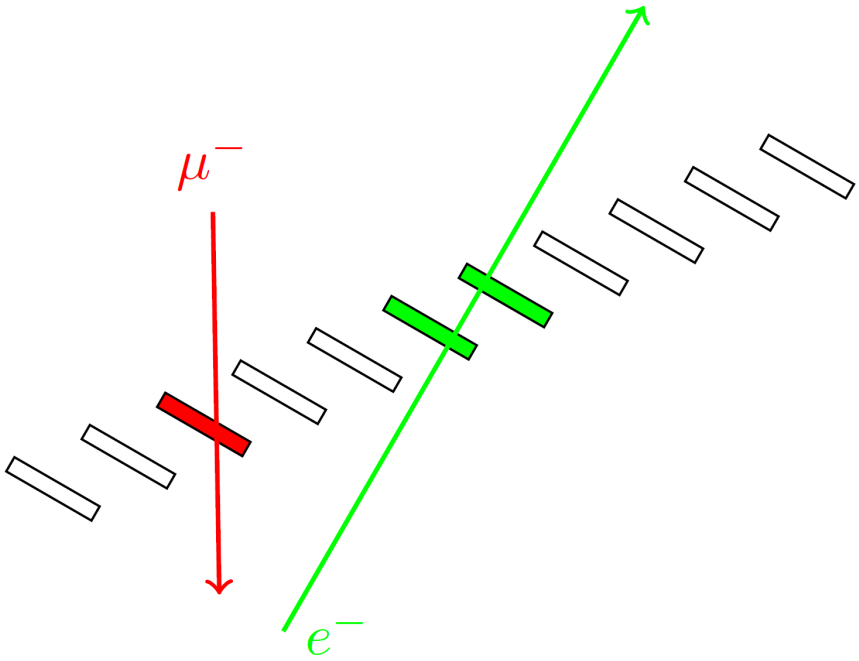

Fig. 5.1: Reconstruction of coincidence hits in neighboring plastic scintillators in the focal plane detector of the tagger. Electrons which have been scattered on the radiator and bent in the magnetic field of the tagger cause two neighboring elements to fire whereas cosmic muons from outside the Tagger system produce a hit in only one element. This coincidence condition reduces the amount of noise and background significantly (figure taken from [55]).

5.2 Crystal Ball Setup

5.2.1 CB

Particles detected in the CB typically do not deposit their whole energy in only one crystal. In fact, it has been found that photons typically distribute 98% of their deposited energy over up to 13 elements [84]. To detect also the remaining energy, additional 20 neighboring crystals would be required. Taking into account that these additional crystals would cause more possible noise signals and also overlapping reconstructed particles, only 13 neighboring elements are considered for the further reconstruction of a particle track. Therefore, an algorithm is applied to the detected hits in the CB which creates so-called clusters. A cluster is defined as a merger of neighboring crystal hits resulting in a track with a given energy, time and direction information. An example can be seen in Fig. 5.2 on the left. As a first step for the cluster formation, a threshold of 2 MeV is applied to each CB hit to reject noise and possible clusters resulting from it. Afterward, the remaining hits are sorted in a list by their energies. The crystal with the highest deposited energy is assumed to be the central crystal of the cluster. Starting from that, the clustering algorithm searches for neighboring crystals and adds them to the cluster. The final cluster energy E_{clust} is given by the energy sum of the central

and all contributing neighboring crystals. To reject also on this level clusters resulting from noise, the cluster energy has to exceed a threshold of 15 MeV to be accepted as a valid cluster. Finally, all hits contributing to the cluster are deleted from the list. The time information of the cluster is taken from the time of the central crystal. The direction of the cluster is determined by estimating the impact point $\vec{r_{cl}}$ which is defined as:

$$\vec{r_{cl}} = \frac{\sum_{i=1}^{n} \vec{r_i} \cdot \sqrt{E_i}}{\sum_{i=1}^{n} \sqrt{E_i}} \tag{5.2}$$

where E_i and $\vec{r_i}$ are the energy and direction information of the ith crystal in a cluster. This described method is applied iteratively to the remaining CB hits until no further clusters can be constructed.

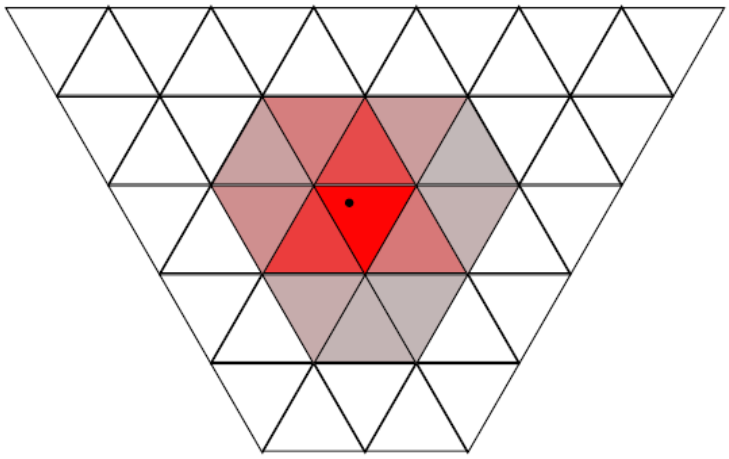

Fig. 5.2: Cluster formation in the CB. A typical cluster formation is shown. The black point indicates the reconstructed impact point whereas the intensity of red illustrates the amount of energy deposited in the individual crystals (figure taken from [55]).

5.2.2 PID

The PID, in contrast to the CB and the MWPCs, can only give information about the azimuthal angle of a charged track. Nevertheless, the energy information can significantly contribute to distinguish charged particles like protons and pions (see Sec. 7.9.1). Since charged particles with different polar angles have different path length through the scintillating plates, the energy is multiplied by $\sin(\theta)$ (see Fig. 5.3). Thereby, all tracks pass independently of the polar angle the same length through the scintillators.

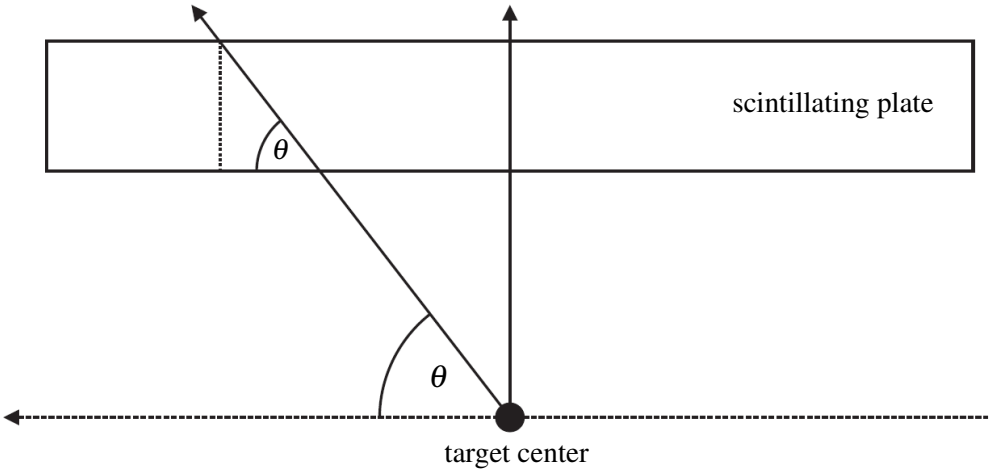

Fig. 5.3: PID energy correction. Due to the different path length of the charged tracks through the scintillating plates, the tracks are normalized to the track with $\theta = 90°$ (figure modified from [119]).

5.2.3 MWPCs

The two MWPCs allow to improve the tracking and angular resolution of charged particles. As mentioned in Sec. 2.4.3, both MWPCs consist of a layer of anode wires which are aligned parallel to the beam and are surrounded by an internal and external layer of cathode strips. As a first step of the reconstruction, the individual clusters of the fired strips and wires are calculated by determining the impact position. For the strips, the hit index s_i and charge amplitude distribution of adjacent strips A_i is used to determine the impact position $\bar{s}$ via:

$$\bar{s} = \frac{\sum_{i=1}^{N} A_i \cdot s_i}{\sum_{i=1}^{N} A_i} \,. \tag{5.3}$$

For the wires, only the hit index w_i is known and thus the impact position $\bar{w}$ of N neighboring wires is given by:

$$\bar{w} = \frac{1}{N} \sum_{i=1}^{N} \vec{w}_i \,. \tag{5.4}$$

Afterward, with the determined impact positions, the azimuthal angles $\phi_{I,E}$ of the internal-external strip interactions are constructed and compared to the azimuthal angles ϕ_W of the wire clusters. Since each pair of inner and outer strip cross each other at least twice (see Fig. 5.5), the best match of the ϕ angle difference with a limit of $\pm 10°$ among the possible combinations determines the intersection point (see Fig. 5.4 on the left).

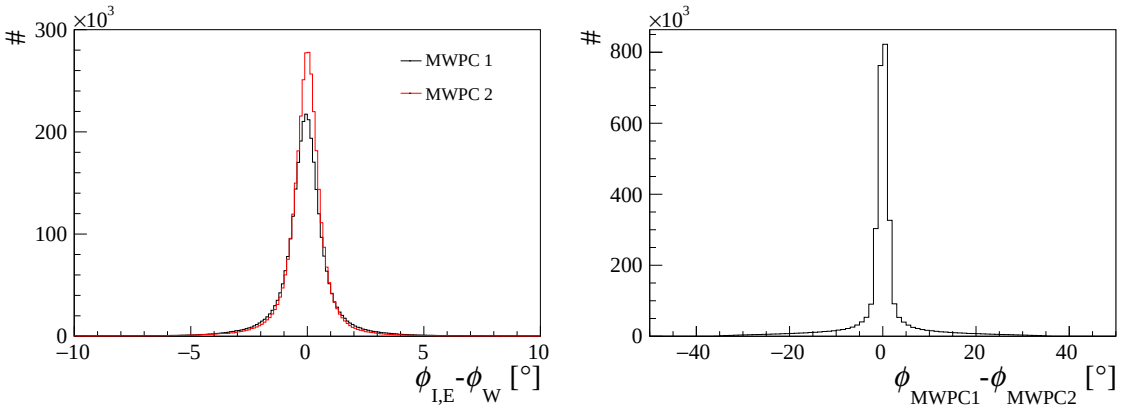

Fig. 5.4: Correlation of strips, wires and tracks. For all possible inner (I) and external (E) strip intersections, the correlation with fired wires (W) is checked as can be seen on the left side for both MWPCs. On the right side, the ϕ-correlation between intersections in the MWPC1 and MWPC2 are shown.

Approximately 75 % of all intersection possibilities are of these kind and are marked as true intersections. Intersections in which only two parts have fired and can be correlated are marked as candidate intersections. As a next step, the reconstruction correlates the intersection points of both MWPCs to construct tracks as can be seen in Fig. 5.4 on the right for the azimuthal angular correlation. Thereby, a track is marked as true track if both intersections are true intersections. If one of those intersections is a candidate intersection, the track is marked as a true-candidate track. All other tracks are marked as candidate tracks. An overview of all possibilities in the MWPC reconstruction and their contribution in a typical production run can be seen in appendix A.1. For each accepted track, the calculated pseudo vertex, which is the point of closest approach to {0,0,0}, must fulfill two additional conditions. The first one is that the radius R_{ps} of the pseudo vertex must be smaller than a maximum defined radius R_{max}. The radius is thereby selected in such a way that already on the first level of data selection events are rejected which are far away from the target cell. The second condition is that the reconstructed z-position Z_{ps} must be in the chamber length limits of the MWPC [94]. The track which fulfills these conditions and has, in addition, the minimal distance between the intersections of the MWPCs is chosen as the best track. As the last step, a maximum distance between the intersections of both MWPCs is applied to the best track by which the polar angular reconstruction range of the MWPC can be controlled. In the following analysis, a maximum distance of 0.55 cm was applied so that only tracks above 20° are possible. With this angular limit, the reconstruction ensures that a charged track is not counted twice since up to now no coincidence between the MWPCs and the TAPS is implemented. For the further analysis, events are also accepted in which the MWPCs can not construct a track. However, in these cases, a correlation with the CB and/or PID is required which is part of the next section.

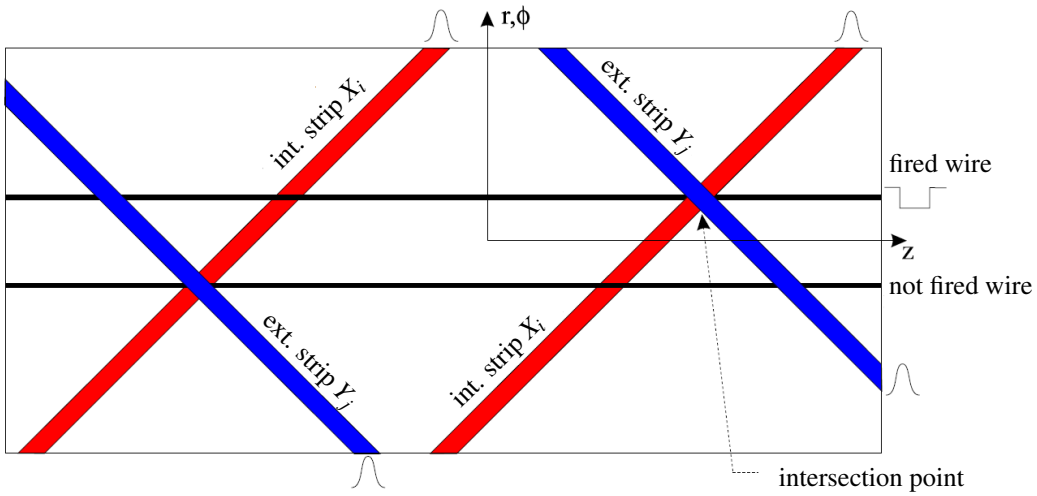

Fig. 5.5: Ambiguity of the MWPC intersection. As mentioned in the text, the internal and external strip cross each other at two position. The additional wire solves that problem and constructs the intersection point. (figure modified from [120]).

5.2.4 Charged tracks in the CB setup

After the cluster algorithm has constructed the clusters in the CB, several correlations between the CB and all MWPCs tracks/intersections and PID hits are checked. The hierarchy of the track reconstruction can be seen in Tab. 5.1.

Table 5.1: Overview of the possible charged tracks, their angular limits and their track number.

Track type	$\angle_{CB,MWPC}$ [°]	$\phi_{track,PID}$ [°]	Track number
CB + MWPC (both) + PID	[0-20]	[-50,50]	15
CB + MWPC (both)	[0-20]	-	14
MWPC (both) + PID	-	[-50,50]	7
MWPC (both)	-	-	6
CB + MWPC (1/2) + PID	[0-60]	[-50,50]	11/13
CB + MWPC (1/2)	[0-60]	-	10/12
MWPC (1/2) + PID	-	[-50,50]	3/5
CB + PID	-	[-15,15]	9
CB	-	-	8

First, all MWPC tracks are correlated with the CB clusters. Since the MWPC and the CB both provide azimuthal and polar angle information, a vector-angle correlation is constructed between the MWPC tracks and the CB clusters. A cut of [0-20]° is applied as shown in Fig. 5.6 on the top left in black. In red, the corresponding correlation for events with only one MWPC intersection is illustrated. The

different distributions, especially the width and the position of the maximum, can be explained by the fact that the vector-angle correlation assumes that the CB cluster originates from the center of the target, namely (0,0,0). In the case of only one MWPC intersection, the vector is also constructed from the position (0,0,0) whereas, in case of two intersections, a clear vertex with the intersections can be constructed. Based on that knowledge, the vector-angle correlation for the MWPC tracks is broader compared to the MWPC intersections since the MWPC tracks reconstruct the origin of the track inside the target more precisely compared to the CB track. Thus, after a correlation between the MWPC and the CB is ensured, the MWPC angular information is used for the further analysis. In the later analysis, it is helpful to have access to the $\Delta E - E$ spectrum which correlates a detected PID energy ΔE with a CB cluster energy E. Thus, a corresponding hit in the PID is searched. Since the PID only provides an azimuthal angle, a ϕ-correlation between the MWPC track and the PID hit is performed as can be seen in Fig. 5.6 on the top right in black.

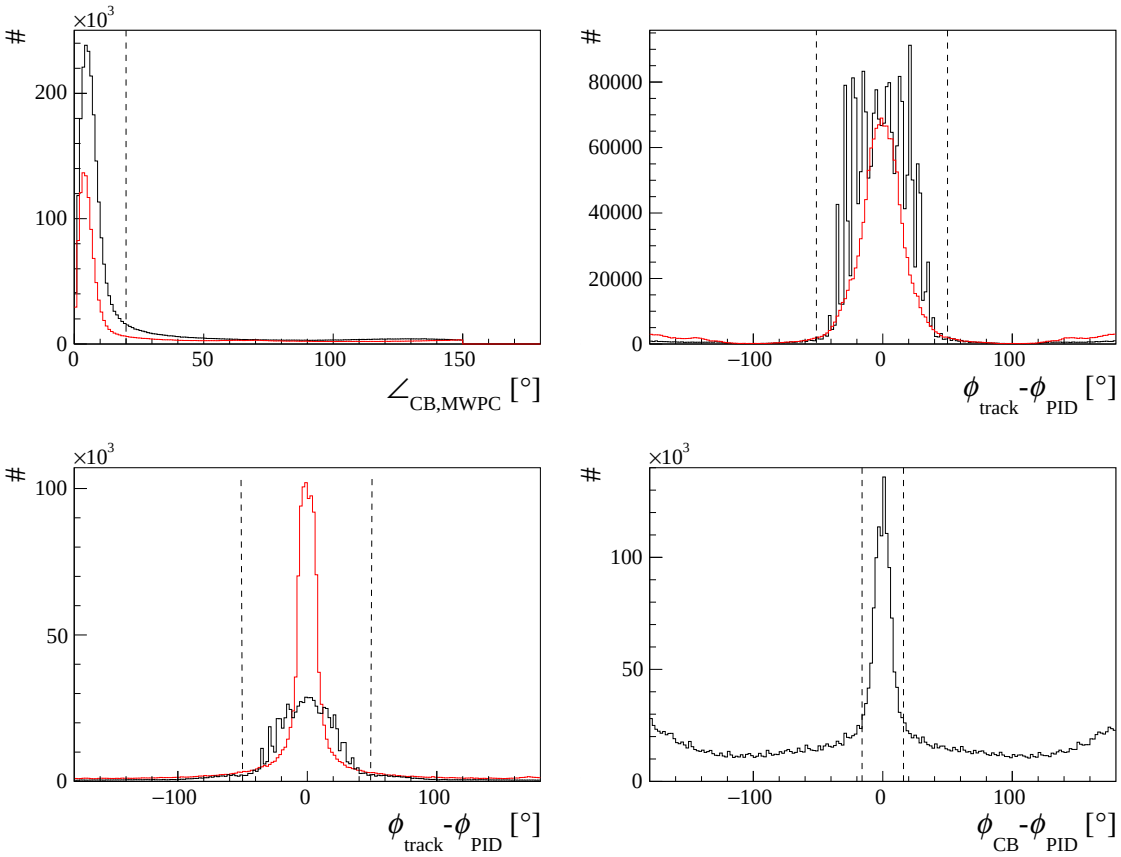

Fig. 5.6: Angular correlation for charged tracks in the CB setup. On the top left, the correlation between the MWPC and the CB track is presented. If both tracks correlate, the corresponding ϕ-correlation of the MWPC track with the PID hit is checked as shown in the top right. On the bottom left, the ϕ-correlation of a MWPC track and a PID hit is illustrated under the assumption that no correlated hit in the CB is available. If the MWPC does not correlate, the ϕ-correlation between the CB and the PID is checked as can be seen in the bottom right. The lines indicate the accepted angular limits for a charged track.

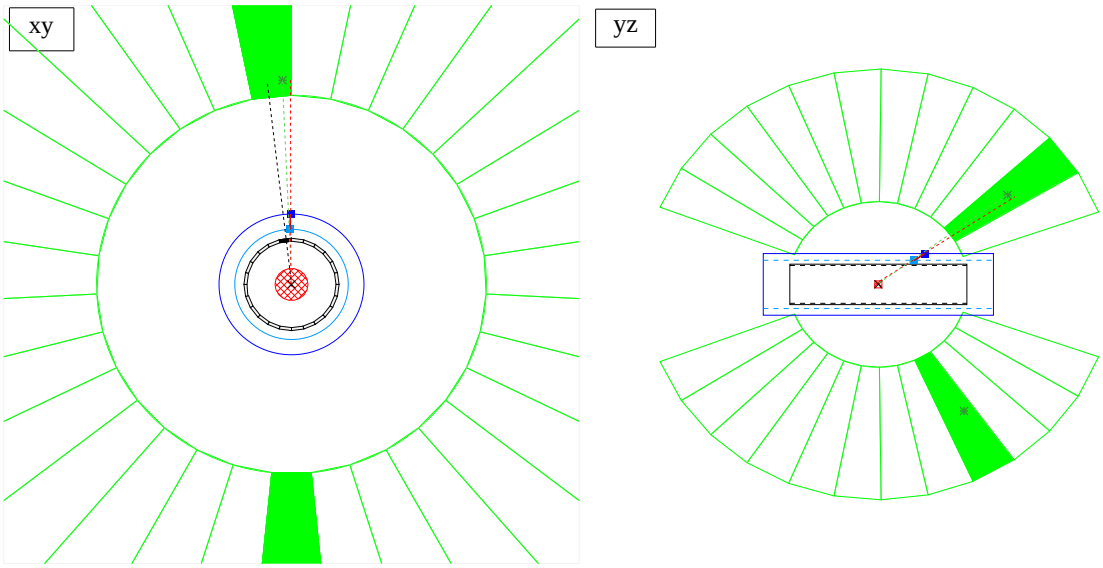

Fig. 5.7: Visualization of a $n\pi^+$ event in the CB charged reconstruction. On the left side, a cut through the detector system in the xy-plane is shown. The red circle indicates the target, surrounded by the PID (gray) and the two MWPCS (light blue/dark blue). In green, the CB sectors are shown whereas the filled green areas illustrate if an area has fired. In red, the reconstructed track is depicted whereas in green and black the track resulting from only CB or PID is depicted. On the right side, the corresponding yz-plane is presented in which the different polar angles can be seen.

For a better understanding of the above-mentioned arguments, Fig. 5.7 illustrates on the left side the xy-projection in the center of the CB detector system including the target, the PID, the MWPCs and the CB for a selected $n\pi^+$ event. In red, the reconstructed MWPC track is shown whereas the green line represents the CB track. The black line indicates the two-vector which is used for the correlation of the PID with the MWPC track. On the right side of Fig. 5.7, the corresponding yz-plane is presented in which the different polar angles of the tracks can be seen. In this event, both particles had enough energy to reach the CB. Nevertheless, it is also possible that a low energetic charged particle is stopped in the MWPCs. In that case, tracks are reconstructed with the MWPCs and PID alone. On the bottom left in Fig. 5.6, the correlation between MWPC tracks/intersections (black/red) and PID hits are shown. The structure of the correlation with MWPC tracks compared to the ones with intersections is caused by the discrete ϕ spacing of the wires of the MWPCs. The different widths can again be explained by the fact that the MWPC tracks can reconstruct the vertex inside the target more precisely compared to the events with only intersections. Up to now, only tracks have been considered in which the MWPCs have seen the charged particle. However, since the MWPCs have not an efficiency of 100% for the detection of charged tracks, the ϕ-correlation between the CB and PID can still be used to mark a track as charged as can be seen on the bottom right of Fig. 5.6. The overall contributing tracks are listed in Tab. 5.1 and their contribution in a typical production run is presented in Fig. 5.8. The highest contribution is coming from the CB alone standing events which indicates a high amount of reconstructed neutral particles, mostly photons coming from the decay of a neutral pion. The charged tracks are built up of many different combinations of the CB, the MWPCs

and the PID and thus already points out on this level that the acceptance of the MWPC/PID for the detection of charged particles is not 100 %.

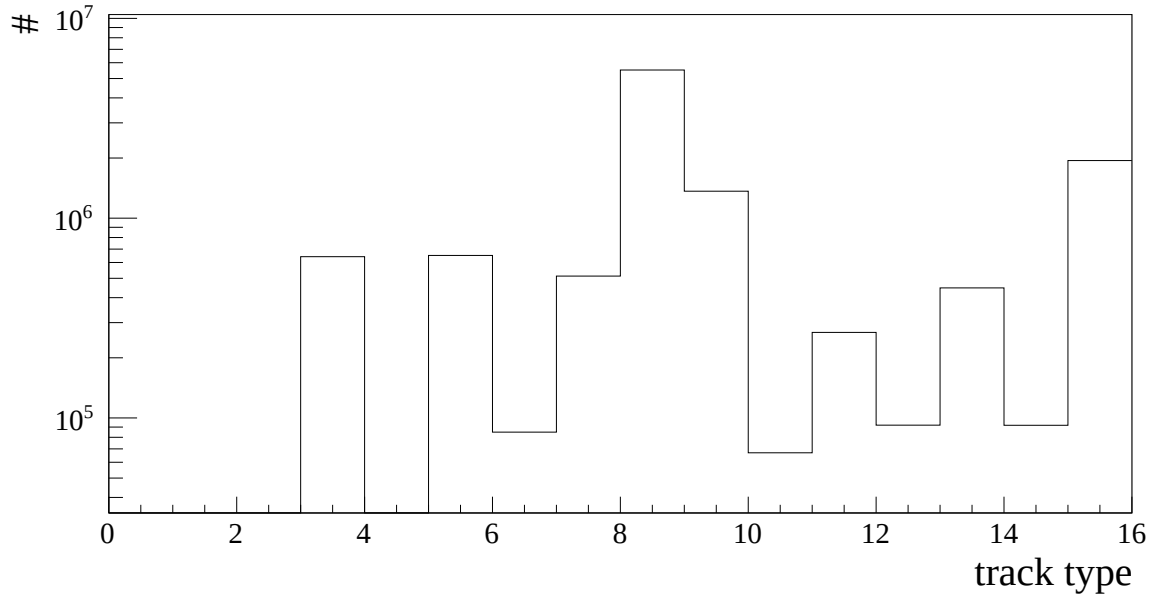

Fig. 5.8: Distribution of different track types in the Crystal Ball setup. The distribution of the tracks, as mentioned in Tab. 5.1, for a typical production run.

5.3 TAPS Setup

5.3.1 TAPS

Similar to the CB, the hits in the TAPS are merged into clusters. Thereby, as the first step for noise reduction, all hits below a defined software threshold of about 5 MeV are rejected from the clustering. From the list of passing hits, the hit with the maximum deposited energy is assumed to be the central crystal of the cluster. Afterward, analogous to the CB, the neighboring crystals are checked for an energy deposition and are added to the overall cluster energy (see Fig. 5.9). In contrast to the CB, the TAPS clustering algorithm also searches for hits in a defined distance from any created cluster and due its better time resolution also requires a time correlation withhin a 5 ns window with the central crystal. These hits are then added to the cluster until no further hits can be added to a cluster. For the final calculation of the impact point of the cluster, logarithmic weighting [121, 122] is used via:

$$W_i = max\left\{0.5 + log\left(\frac{E_i}{\sum_{i=1}^{n} E_i}\right)\right\}, \tag{5.5}$$

$$\vec{r_{cl}} = \frac{\sum_{i=1}^{n} \vec{r_i} \cdot W_i}{\sum_{i=1}^{n} W_i}, \tag{5.6}$$

where E_i is the energy deposition and $\vec{r_i}$ the position of the ith participating crystal in a cluster. In doing so, the transverse dropping exponential behavior of the electromagnetic shower is taken into account. Unfortunately, in contrast to the CB, the TAPS elements are not facing towards the target. Therefore, caused by the energy-dependent shower depth of the photons, an additional correction on the x and y coordinate of the impact point has to be applied [77]. The principles of the correction are illustrated in Fig. 5.10 on the left side and explained in [77].

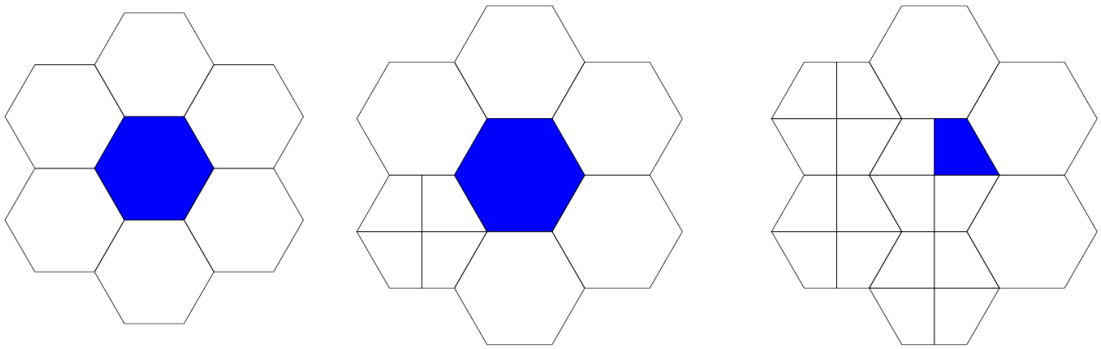

Fig. 5.9: Cluster formation in the TAPS. On the left side, a typical cluster formation is shown for only BaF_2 crystals. If also $PbWO_4$ participate in the cluster formation, the cluster size can increase from six neighboring clusters to up to 18 as can be seen in the middle and right panel (figure taken from [80]).

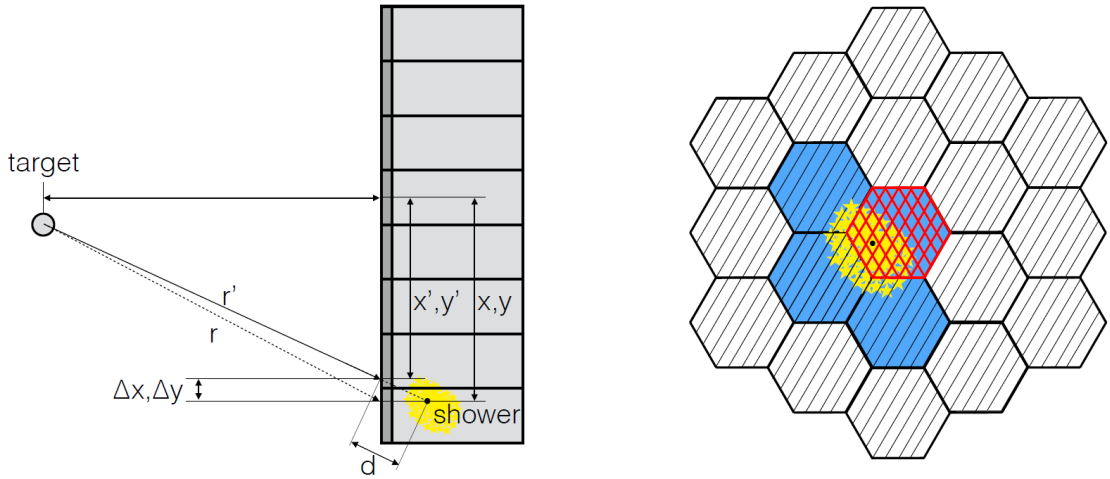

Fig. 5.10: Shower depth correction and correlation with the Veto-Wall in the TAPS. On the left side, the principles of the shower depth correction in the TAPS are shown. On the right side, the correlation for a reconstructed TAPS cluster (blue) with a Veto-Wall element (red) is shown (figure taken from [97]).

5.3.2 TAPS Veto Wall

The TAPS Veto Wall has the same purpose as the PID, namely the detection of charged particles. Whereas PID covers angles above 20°, the Veto Wall has the task to reconstruct charged particles in the forward direction. In combination with the TAPS, the Veto-Wall can further be used to distinguish charged particles (see Sec. 7.9.1). Similar to PID, the energy deposition in the Veto Wall is also normalized in such a way that all Veto elements see the same path length through the plates. Since the TAPS Veto Wall is tilted by 90° with respect to the scintillating plates of PID, all energies are multiplied by $\cos\theta$ instead of $\sin\theta$ where θ is the polar angle of the charged track.

5.3.3 Charged tracks in the TAPS setup

After the TAPS hits are formed into clusters, the correlation with the TAPS Veto Wall is performed. For each cluster, the algorithm checks if the Veto element in front of the central element of the TAPS cluster has fired. If this is not the case all neighboring Veto elements are checked (see Fig. 5.10 on the right). This is justified by the fact that charged tracks do not necessarily pass the Veto element in front of a crystal but instead the neighboring ones [77]. If at least one of these elements has fired, the track is marked as charged. For a further noise reduction and a correct assignment, a time correlation between the Veto element and the TAPS cluster time is performed as can be seen in Fig. 5.11. The second peak at approximately -10 ns is caused by the contribution of the Vetos in front of the $PbWO_4$ crystals and will be further discussed in Sec. 6.2.4.

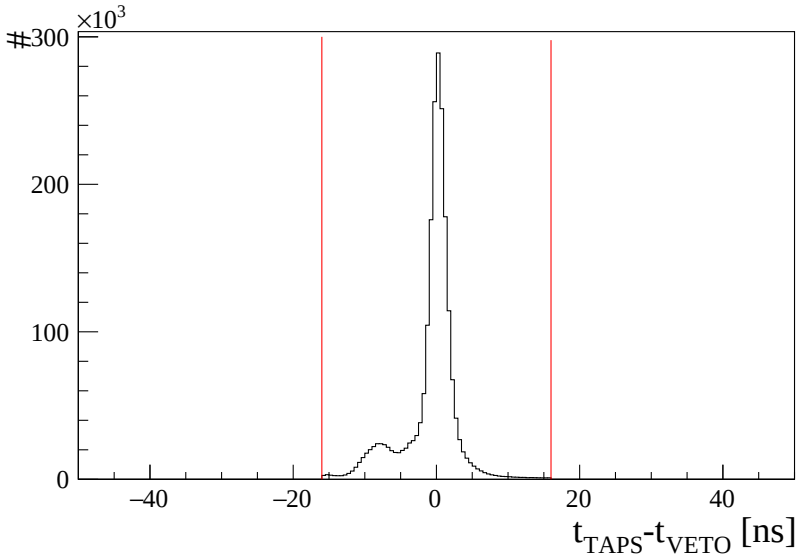

Fig. 5.11: TAPS-Veto time correlation. The time difference between the TAPS cluster time and its corresponding fired Veto time is shown. The red line indicates the limits in which a track is accepted as a charged track.

Chapter 6

Calibration

To perform a data analysis, the four-momentum of the particles involved in a given reaction and their relative times to each other need to be known. Therefore, the raw data are recorded with Analog-to-Digital Converters (ADCs) for the energy and Time-to-Digital Converters (TDCs) for the time information. Afterward, these information are converted via various calibration methods into physical quantities. These methods will be presented in this chapter for the September 2015 beamtime along with other important calibrations. Finally, an overview of the calibration and resolution optimization of the simulated data is given.

6.1 Energy Calibration

The deposited energy of a certain crystal is determined by using Charge-to-Digital Converters (QDCs) as ADCs which are integrating an analog input signal over a defined time window resulting in a digital charge output signal. The output signal is proportional to the deposited energy and digitized into channels which can be converted back into an energy E_{dep} [MeV] via:

$$E_{\mathrm{dep}} = g \cdot (A_{\mathrm{ch}} - A_{\mathrm{ped}}) \tag{6.1}$$

where g is the so-called conversion gain [MeV/channel] and A_{ped} [channel] the pedestal. Thereby, the pedestal corresponds to the channel in which no energy is deposited. Both, the conversion gain and the pedestal, need to be determined for each detector element individually which will be explained in the following subsections.

6.1.1 Tagger

The tagger calibration was performed by the Glasgow group in the past. To determine the calibration, MAMI-C provided low-intensity electron beams with well-known energies which are bent into the tagger magnet with varying magnetic field strengths. Afterward, the deflected electrons are detected in the tagger elements. By measuring with different electron energies and magnetic fields, a linear

relation between the energy and the tagger elements can be constructed and interpolated for all elements. Finally, small corrections were applied due to a slightly difference in the magnetic field strength. For this beamtime, the electron energy was set to 1557 MeV in combination with a stable magnetic field strength of the tagger dipole magnet. Applying the above-described calibration, a direct relation between tagger element and detected energy can be constructed which finally gives the energy of the bremsstrahlung photon.

6.1.2 CB

The energy calibration of Crystal Ball splits into two parts, namely the low energy and high energy calibration.

Low energy calibration

The low energy calibration is already important on the level of the data acquisition and thus is always performed before the start of a beamtime by J. Wettig of the A2 collaboration. In Sec. 4.2, the trigger electronic was explained and the importance of the leading edge discriminator (LED) threshold was underlined. Especially, the energy sum trigger in the CB was applied in our beamtimes and therefore a relative calibration of all elements to each other was mandatory. For the calibration, a ^{241}Am/^{9}Be source was used in which a chain reaction results in photons with a defined energy of 4.438 MeV [123]. To reach a uniform calibration of all elements, the source was placed in the center of the CB detector and photons are detected by the CB elements. A typical raw ADC spectrum, supplied by a defined high voltage, is shown in Fig. 6.1.

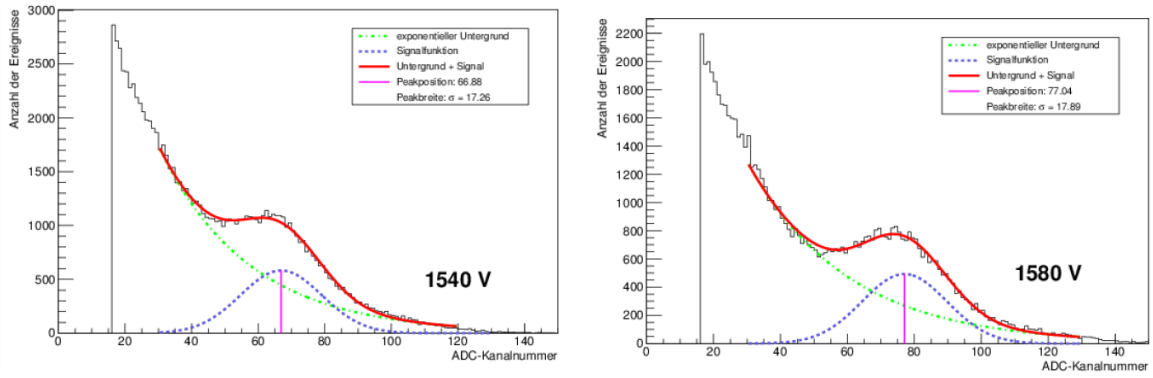

Fig. 6.1: Raw ADC spectrum of the CB element 239 for two different supplied high voltages. An exponential function (green line) is plotted in combination with a Gaussian function (blue line). The exponential function serves to describe the neutron background whereas the Gaussian function to describe the signal peak coming from the 4.438 MeV photons (figure taken from [123]).

A clear peak coming from the 4.438 MeV photons is visible. Furthermore, background originating from neutrons, which are produced in the chain reaction, are creating a smooth background. For 10 different applied high voltages of the PMTs, the peak position is determined. Afterward, the fitted

position, given in ADC channels, was plotted against the high voltage and a linear fit is applied. Finally, for all PMTs, the high voltage is adjusted in such a way that the peak is sitting at the same ADC channel for all elements. Thus an overall calibration is achieved.

High energy calibration

Photons produced in meson photoproduction reactions have typical energies in the region of several hundred MeV and thus an additional high energy calibration needs to be applied. For this purpose, a clean reaction signature is needed and found in the reaction $\gamma p \to p\pi^0$. Since the π^0 decays with a branching ratio of nearly 100% into two photons [7], the invariant mass of these photons can be used to calibrate the conversion gains of CB. Therefore, for each neutral cluster pair in the CB, the invariant mass was calculated and plotted against the central detector element of both clusters. The resulting two-dimensional plot is shown in Fig. 6.2 on the left side for both uncalibrated and calibrated data. For each element, the invariant mass distribution was fitted with a Chebyshev polynomial of the third order in combination with a Novosibirsk function[1]. For an illustration of the fit performance, the overall projection of all elements can be seen in Fig. 6.2 on the right panel. From the signal shape, the mean invariant mass $m_{\gamma\gamma}$ for a given crystal can be determined and compared to the rest mass of the π^0. For the determination of the new gain, the presented calibration method takes advantage of the fact that CB uses sampling ADCs (sADCs) for the read-out. By this, the pedestal of each element is already subtracted and a direct proportionality between gain and energy is given. As a result, the new conversion gain $g_{n,i}$ for each element i is given by Eq. (6.2):

$$g_{n,i} = g_{o,i} \frac{m^2_{\pi^0}}{m^2_{\gamma\gamma}} \tag{6.2}$$

where $g_{o,i}$ is the uncorrected gain factor. Since in the calculation of the invariant mass of two photons several elements are included for the particle reconstruction (see Sec. 5.2), the calibration needs to be done iteratively. After seven iterations, all gains have been adjusted in such a way that the invariant mass is aligned to the rest mass of the π^0. The resulting calibrated mean invariant mass lies at 135.01 MeV with a full width at half maximum of 20.67 MeV. Compared to the uncalibrated data, this is an improvement of 7% in the energy resolution and emphasizes the importance of a good calibration.

[1] The function are presented in App. B.

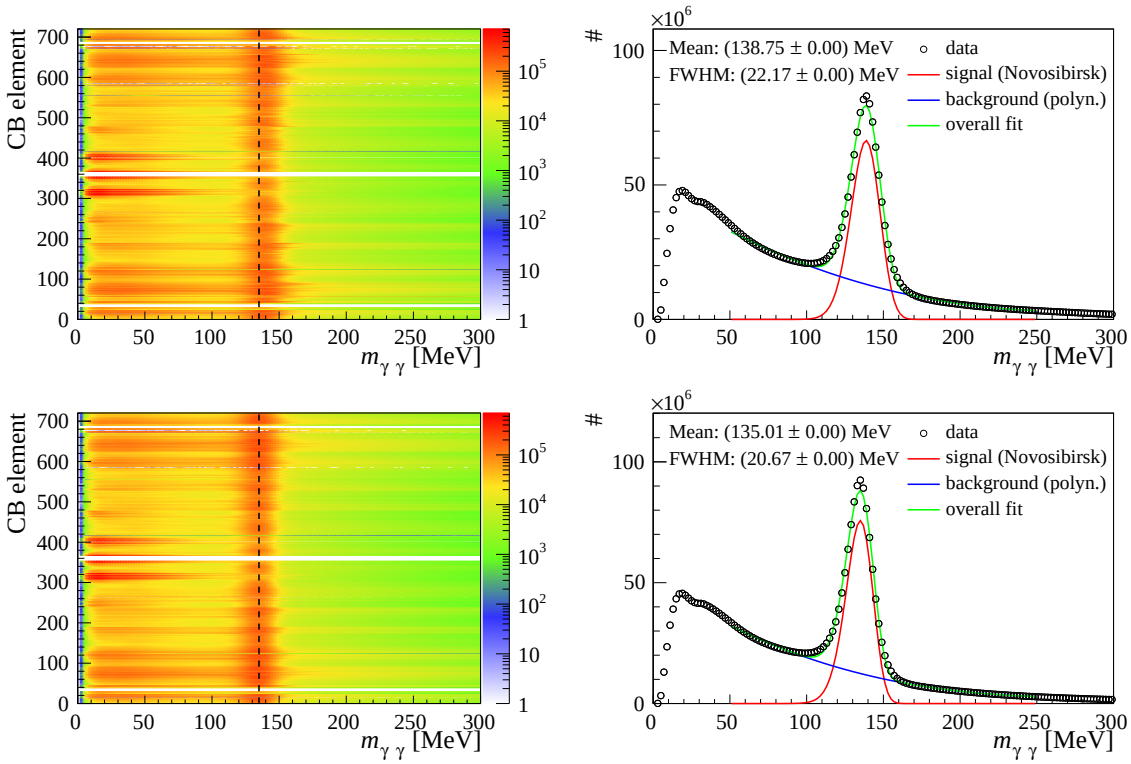

Fig. 6.2: CB energy calibration. On the left panel, the invariant mass of two photons in the CB as a function of their central cluster element is shown. The dotted line illustrates the position of the π^0 rest mass. On the right panel, the projection of all elements (black open circles) is presented in combination with several fit functions. The Novosibirsk function (red line) is used to describe the signal shape whereas a Chebyshev polynomial (blue line) for the background. The green line represents the sum of both signals. The upper row shows the uncalibrated data and the lower row the final calibrated data.

6.1.3 PID

The PID energy calibration was performed by Lorenzo Zana of the A2 collaboration. As a first step, the pedestal of each element was estimated by using special Pedestal runs and by determining the position of the first appearing peak (see as well Sec. 6.1.4). Afterward, to reach a uniform calibration, the proton band in the recorded data were matched with simulated data. To do so, a $p\pi^0$ selection on the recorded data was performed including an invariant mass, missing mass, coplanarity and time sideband cut. A further explanation of these cuts can be found in the Chap. 7. For the selected data, a two-dimensional histogram was constructed in which the raw ADC signal from each PID element is plotted as a function of the corresponding deposited energy in the CB. A typical example can be seen in Fig. 6.3 on the left side. Ten projections on the y-axis are produced for cluster energies smaller than 150 MeV in the CB. The range is thereby selected in such a way that a clear separation between the proton band and the pion band background is possible. A typical projection is illustrated on the right side of Fig. 6.3.

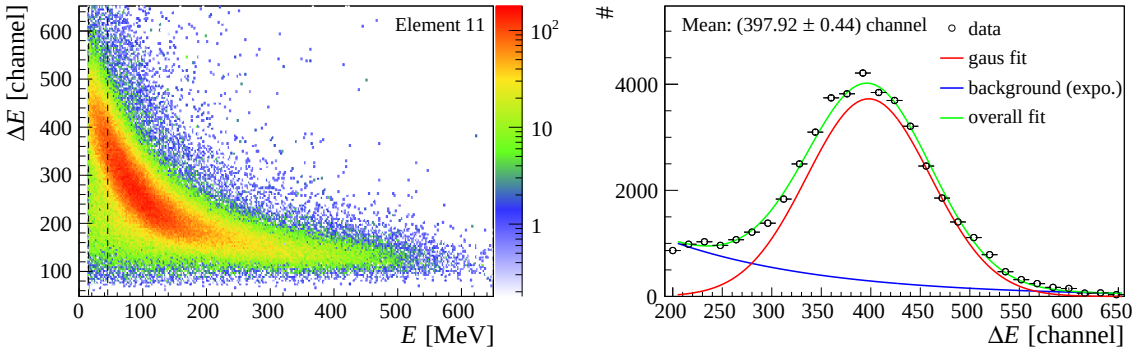

Fig. 6.3: PID energy calibration. On the left side, the raw ADC signal of PID element eleven as a function of the corresponding cluster energy in the CB is shown. The vertical dotted lines indicate the projection which is shown on the right panel. A clear peak coming from protons is visible. An exponential function in combination with a Gaussian function is used to determine the peak position of the proton peak.

Each projection was fitted with an exponential function for the background and a Gaussian function for the signal. The background thereby is mostly coming from charged pions in the proton band. The mean position of the Gaussian function, given in units of channel numbers, was extracted and compared to the corresponding projection of the equivalent constructed simulated spectra. Finally, ten points have been available which connect the experimental data with the simulated one. They were plotted against each other and a linear fit was applied (see Fig. 6.4). By this, the new conversion gain and pedestal were determined. Important to note is that the pedestal was already constrained by the Pedestal runs before the fit was applied.

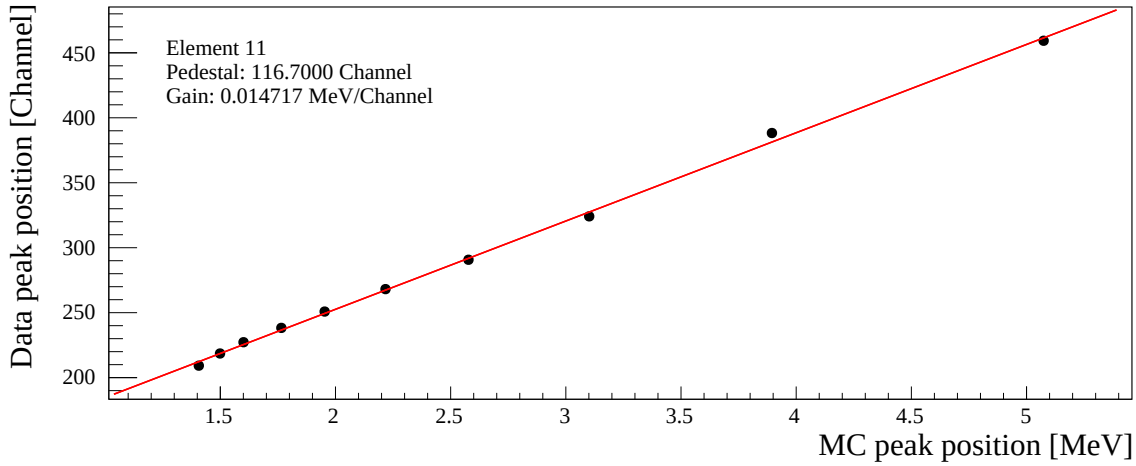

Fig. 6.4: Peak position of the proton band in recorded and simulated data for the PID energy calibration. Shown is the connection between the peak position in the experimental data of PID element 11 (as shown in Fig. 6.3) as a function of the corresponding position in the simulated data. A linear fit is applied to extract the new conversion gain and pedestal.

6.1.4 TAPS

As mentioned in Sec. 2.5.2, the TAPS consists of two different kinds of crystals, namely BaF_2 and $PbWO_4$. The $PbWO_4$ crystals have not performed satisfactorily during the beamtimes and thus will not be used for further analyses. The calibration, however, follows the same principles as for the BaF_2 crystals and thus all TAPS elements are calibrated simultaneously. Compared to CB, the analog signals of TAPS are split into two separate ADCs. One of the ADCs is integrated over a longer time period compared to the other one in order to take advantage of the two scintillation light components in BaF_2. The first is called Long Gate (LG) and the second Short Gate (SG) component. The LG component is comparable to the CB energy signal since the integration time is long enough to detect the whole signal of all particles. In the case of the SG component, the integration time is long enough to detect the total signal of photons but not of nucleons and pions. Therefore, the combination of SG and LG gives the possibility to distinguish between photons and neutrons via the application of the so-called Pulse Shape Analysis (PSA). In the following subsection, the calibration method for the LG and SG component will be presented.

Low energy calibration

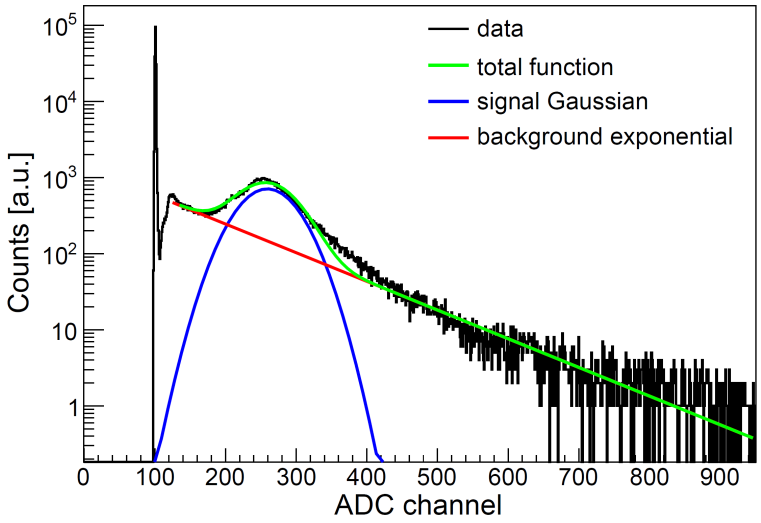

Fig. 6.5: Raw ADC spectrum of a TAPS element using cosmic rays. An exponential function (red line) is plotted in combination with a Gaussian function (blue line). The exponential function serves to describe the background whereas the Gaussian function to describe the signal peak coming from the 37.7 MeV MIPs (figure taken from [77]).

As discussed in Sec. 4.2, the trigger for these beamtimes was a combination of a CB trigger and a TAPS trigger. Therefore, the alignment of the thresholds of the LEDs of the TAPS was crucial to reject already electromagnetic background on the level of the data acquisition. Consequently, before the start of the beamtime, N. Walford of the A2 collaboration performed a low energy calibration. For the calibration, cosmic rays were used which deposit their energy in all crystals the same way.

It has been found that the mean deposited energy of minimizing ionizing particles (MIPs) in the TAPS elements is 37.7 MeV. Therefore, this information together with the raw ADC spectrum can be used to determine the pedestal and the conversion gain of each element. A typical spectrum with the corresponding fit functions for the extraction of the mean value for the MIP peak can be seen in Fig. 6.5. By this, a first rough calibration of each element to each other is achieved.

High energy calibration

Pedestals for LG and SG

Compared to the CB read-out electronics, TAPS does not use sampling ADCs as read-out. Thus, the pedestals of each element have to be determined first. For this purpose, special pedestal runs have been taken during the beamtime. The individual runs were tested on time stability of the pedestals and afterward were summed up. A Gaussian peak was fitted to the first visible peak in the corresponding raw ADC spectrum which determines the pedestal of each element. A typical LG raw ADC spectrum can be seen in Fig. 6.6. The spectra for the SG components look similar and the determination of the pedestals follows the same procedure.

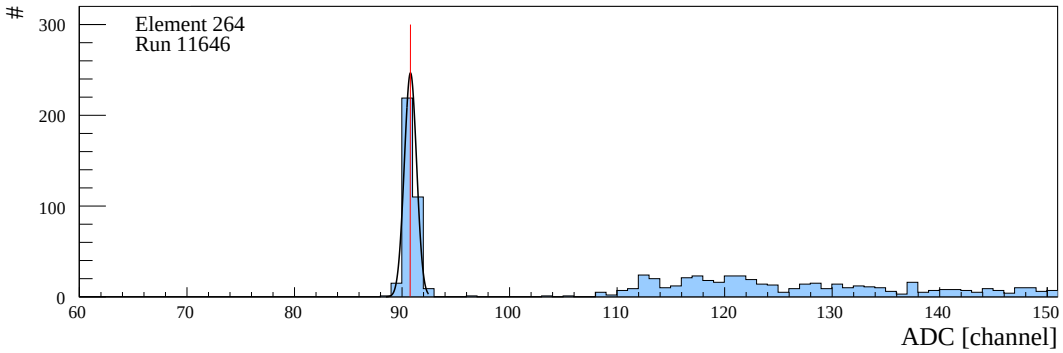

Fig. 6.6: Pedestal determination for the LG component of a TAPS element. The raw ADC spectrum for the LG component of crystal 264 of run 11646 is shown with a Gaussian fit (black line) to the first visible peak. The red line indicates the position of the determined pedestal value.

Long gate calibration

After the determination of all pedestals, the individual conversion gain values of the TAPS LG components can be determined. For this purpose, similar to the CB energy calibration, a two-dimensional histogram was constructed in which the invariant mass as a function of the central cluster element is plotted. Since the statistics are not sufficient for both photons being detected in the TAPS, one photon is detected in the CB and one in the TAPS. Consequently, the CB energy calibration must be performed before the TAPS energy calibration and the two-dimensional histogram was only filled for the central cluster element of the TAPS hit. The corresponding spectra for the uncalibrated and calibrated data are shown in Fig. 6.7. After several iterations, the calibrated mean invariant mass lies

at 135.15() MeV with a full width at half maximum (FWHM) of 20.51() MeV. Compared to the CB energy calibration, a similar energy resolution has been achieved.

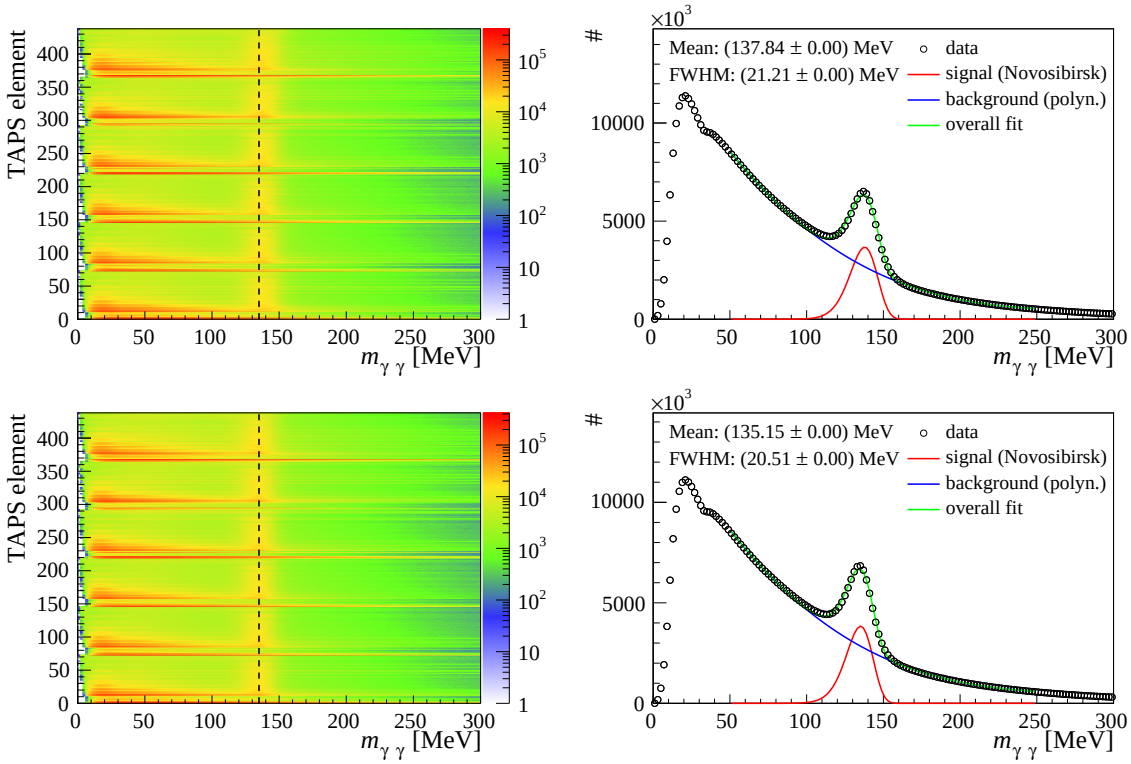

Fig. 6.7: TAPS energy calibration. On the left panel, the invariant mass of two photons (one in the CB and the other in the TAPS) as a function of the TAPS central cluster element is plotted. The dotted line illustrates the position of the π^0 rest mass. On the right panel, the projection of all elements (black open circles) is presented in combination with several fit functions. The Novosibirsk function (red line) is used to describe the signal shape whereas a Chebyshev polynomial (blue line) for the background. The green line represents the sum of both signals. The upper row shows the uncalibrated data and the lower row the final calibrated data.

Short gate calibration

The SG component calibration takes advantage of the fact that for photons the LG component can be clearly related to the SG. Therefore, the SG component must be performed after the LG calibration. For the calibration, two additional quantities, namely the PSA radius r_{PSA} and angle ϕ_{PSA}, are defined which connect the SG and LG components with each other. They are given by Eq. (6.3) and Eq. (6.4):

$$r_{\mathrm{PSA}} = \sqrt{E_{\mathrm{SG}}^2 + E_{\mathrm{LG}}^2}, \tag{6.3}$$

$$\phi_{\mathrm{PSA}} = \left(\frac{E_{\mathrm{SG}}}{E_{\mathrm{LG}}}\right). \tag{6.4}$$

For all central elements belonging to a cluster hit in the TAPS, a two-dimensional histogram was created in which the relation between the PSA radius and angle is plotted. An example is illustrated in Fig. 6.8 on the left side.

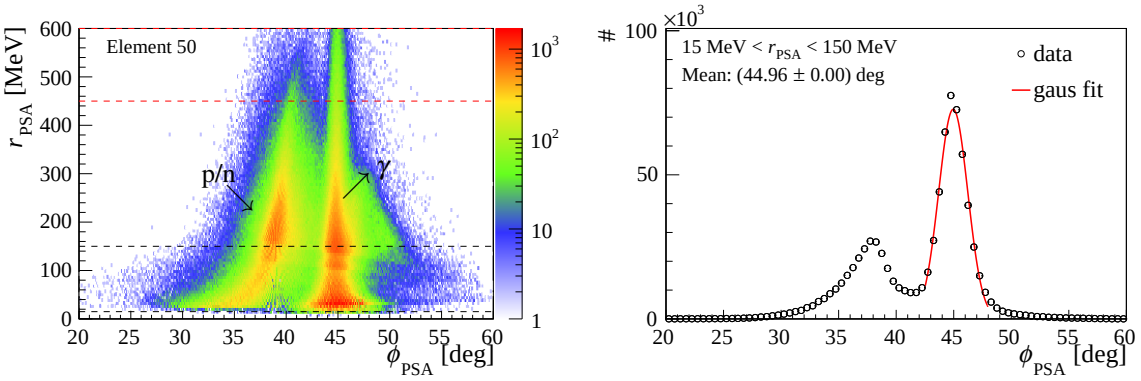

Fig. 6.8: Pulse shape analysis (PSA) for element 50 for the SG energy calibration of TAPS. On the left panel, the PSA radius is plotted as a function of the corresponding PSA angle for the TAPS Element 50. On the right panel, a y-projection for a cluster energy range 15 MeV to 150 MeV (indicated by the black dashed line in the left plot) is shown. A clear photon peak is visible which is fitted with a Gaussian function (red line) to determine its peak position.

First of all, a clear straight line at an angle of 45° is visible. This line corresponds to photons for which the SG components behave the same way as the LG components. This is not the case for nucleons and thus an additional banana-shaped band at lower angles appears. For two different PSA radius regions, the projected PSA angle distribution was fitted and the position of the photon peak was determined. An example can be seen on the right side of Fig. 6.8. By requiring that for these photons the SG and LG component are identical, new pedestal and gain values were determined for each crystal resulting in an overall calibration.

6.1.5 TAPS Veto wall

As a first step, the correlation between the TAPS elements and their corresponding Veto elements needs to be checked. Therefore, a two-dimensional histogram was plotted in which the relation between charged TAPS and Veto hits is plotted. If a charged track deposits energy in the TAPS elements, the Veto element in front of the TAPS element or its neighbors should have fired as well (see Sec. 5.3.3). As a result, a clear correlation between the TAPS and Veto elements should be visible. For this beamtime, all Veto elements were placed at the correct position which has been cross-checked with the CaLib software. After it has been assured that the correlation is correct, the Veto energy calibration can be performed. Therefore, similar to the pedestal calibration of the TAPS energy calibration, the pedestals of the Veto elements were calculated. As a next step, the conversion gains of each element need to be determined. To do so, a two-dimensional histogram is created in which the deposited energy E_{dep}^{Veto} in the Veto elements is plotted versus the deposited energy E_{dep}^{TAPS} in the TAPS. An example of the Veto element 15 is shown in Fig. 6.9.

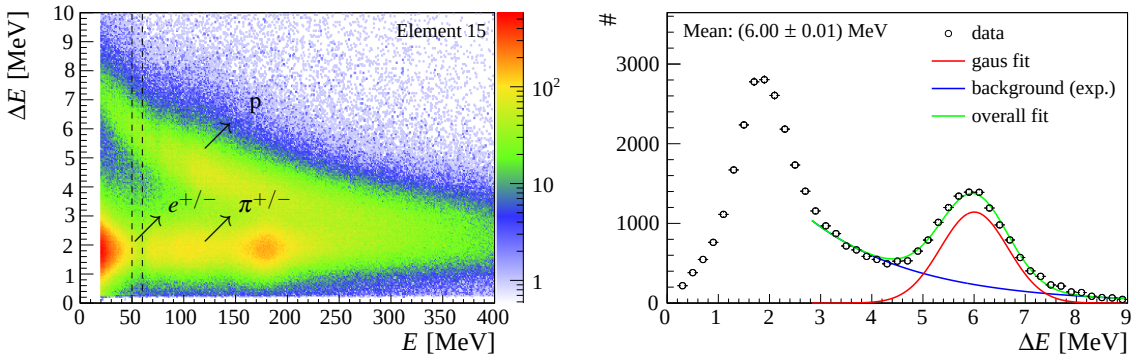

Fig. 6.9: TAPS Veto energy calibration. On the left panel, the TAPS veto energy is plotted as a function of the corresponding cluster energy for the Veto Element 15. On the right panel, a y-projection for a cluster energy range 50 MeV to 60 MeV (indicated by the dashed line in the left plot) is shown. A clear proton peak is visible which is fitted with a Gaussian function (red line) and an exponential background (blue line) to determine its peak position.

A clear "banana" band towards higher Veto energies and lower TAPS energies is visible. This band corresponds to protons which have been detected and stopped in the TAPS. An additional enhancement at about 200 MeV TAPS energy is present which is caused by fast charged pions and protons which only deposit a certain amount of their energy in the calorimeter. Finally, stopped pions in the calorimeter are responsible for the enhancement at about 100 MeV and below 50 MeV a high amount of electromagnetic background is seen. For each Veto element, a y-projection was performed integrated over a TAPS energy range where a clear separation between stopped protons and the other types is possible. A typical projection can be seen on the right side of Fig. 6.9. The background, coming from an overlap of the pion/electron band with the proton band, is described by an exponential function and the signal shape with a Gaussian function. The peak position can be determined from the mean position of the signal shape and was used to adjust the new proton band peak in such a way that the peak position agrees with the corresponding position in simulated data. By this, all elements were adjusted the same way. For this analysis, all peaks are aligned to 6 MeV as can be seen in Fig. 6.9 on the right side.

6.2 Time Calibration

All recorded detector times are measured relative to the trigger time. Thereby, depending on the detector, either the trigger signal or the detector signal serves as the start/stop signal of the TDCs. The time difference between the start and stop signal is afterward digitized into channel values. Analogous to the energy conversion (see Eq. (6.1)), the time [ns] is converted via:

$$t = g \cdot (A_{\mathrm{ch}} - A_{\mathrm{off}}) \tag{6.5}$$

where g is the so-called conversion gain [ns/channel] and A_{off} [channel] the time offset. The time offset originates from different cable lengths and electronics of the individual read-out parts of the detector elements. Thus, to reach an overall time alignment between detector hits corresponding to a given event, the detectors and also the individual detector elements have to be calibrated with respect to each other. This is always reached by looking at time differences of detector elements or detectors to each other. Thus, the trigger time is always canceled out which is of high importance since the trigger time is affected by jittering effects and thus decreases the resolution [77].

6.2.1 CB

The conversion gain for all elements is fixed to 0.117 ns/channel. Therefore, only the time offset of each element must be determined. To do so, for each event, a two-dimensional histogram was filled in which the time difference of all combinations of two neutral hits in the CB is plotted as a function of the central element of the individual clusters. Since this method selects only neutral hits, most of the particles are photons and thus their time difference is dominated by electronic delays. The resulting two-dimensional plot is illustrated in Fig. 6.10 on the left side.

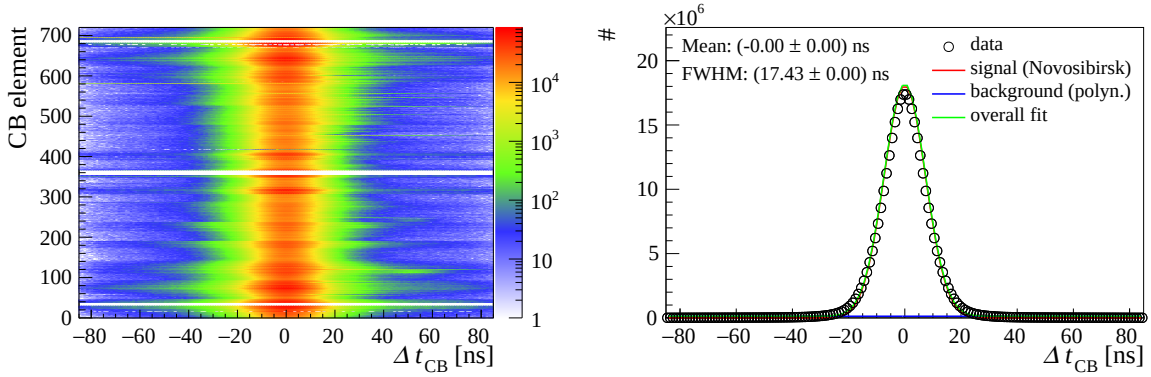

Fig. 6.10: CB time calibration. On the left side, the two-dimensional relation between the time difference of all CB hits as a function of the central cluster element is shown. On the right side, the overall projection of all elements is illustrated and fit to determine the peak position and FWHM.

For each element, the time difference was fitted with a Gaussian function to determine the peak position. An illustration of the fit performance is depicted in Fig. 6.10 on the right panel in which the overall sum of all time differences is plotted. With the new mean peak position m_i, the new time offset value $A_{\text{off},n,i}$ of element i can be determined via Eq. (6.6):

$$A_{\text{off},n,i} = A_{\text{off},o,i} + \frac{m_i}{g_i} \,. \tag{6.6}$$

Similar to the energy calibration, the time alignment of the individual elements depends on the other elements. Thus, the time calibration was done iteratively. After 6 iterations, all time offset were adjusted in such a way that two neutral hits corresponding to a given event, are detected in coincidence

with a time resolution of 18.62 ns. Note that the time resolution will be optimized in a final step with the Time Walk correction (see Sec. 6.3).

6.2.2 PID

Similar to the CB and the tagger, the conversion gains for the PID are fixed to 0.117 ns/channel. To calculate the time offset, for each event, the time difference of all charged particles detected in the PID was plotted against the corresponding PID elements as can be seen in Fig. 6.11 on the left side. Afterward, similar to the TAPS and CB time calibration, the resulting distribution was fitted and a new time offset was calculated. The resulting resolution is 3.75 ns.

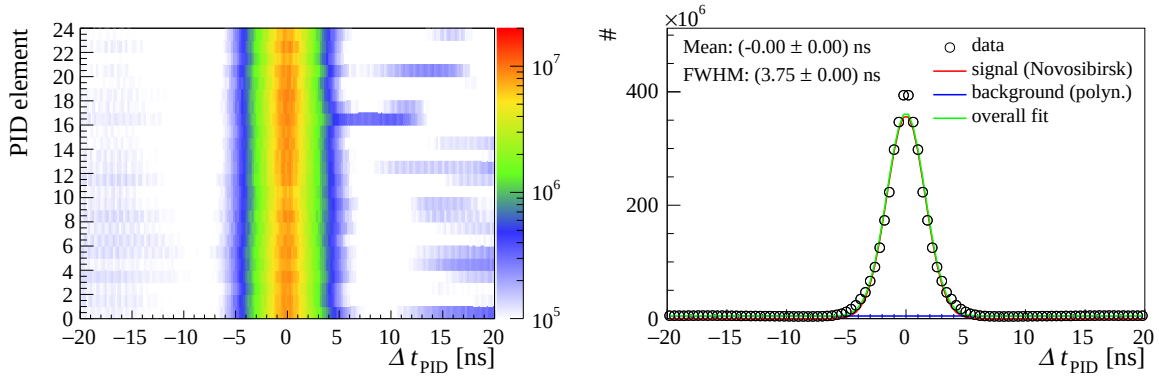

Fig. 6.11: PID time calibration. On the left side, the two-dimensional relation between the time difference of PID hits as a function of the corresponding PID hits is shown. On the right side, the overall projection of all elements is illustrated and fit to determine the peak position and FWHM.

6.2.3 TAPS

The TAPS time calibration follows the same procedure as the CB time calibration except that the conversion gains are not fixed. These have been determined by Tigran Rostoyman in November 2013. Thereby, special runs have been recorded in which various cables of known length have been included in the TAPS read-out. As a result, the stop signals of the TACs have been delayed by a known value which can be used to determine the gains for all elements using a program called TAPSMaintain [77]. After the gains have been determined, the time offset calibration can be performed. The resulting plots are shown in Fig. 6.12. For TAPS, the time alignment took 7 iterations and finally a time resolution of 0.55 ns was reached.

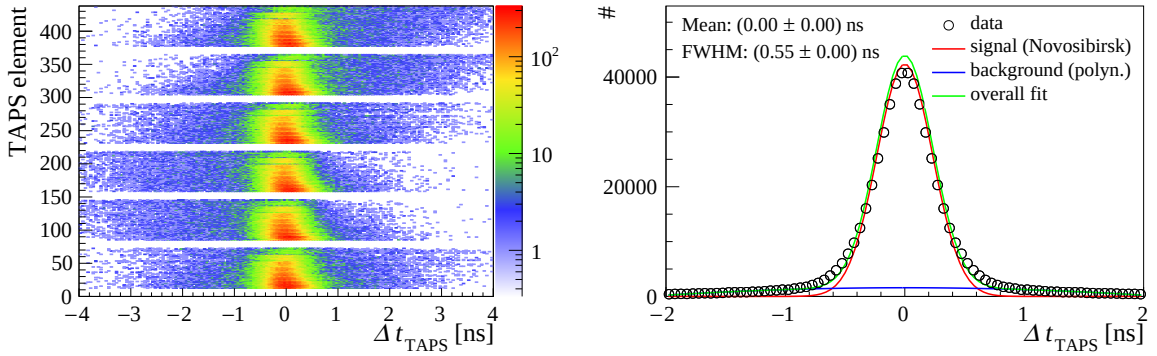

Fig. 6.12: TAPS time calibration. On the left side, the two-dimensional relation between the time difference of all TAPS hits as a function of the central cluster element is shown. On the right side, the overall projection of all elements is illustrated and fit to determine the peak position and FWHM.

6.2.4 TAPS Veto wall

The TAPS Veto wall time was calibrated in the same way as the PID time. The resulting plots are shown in Fig. 6.13.

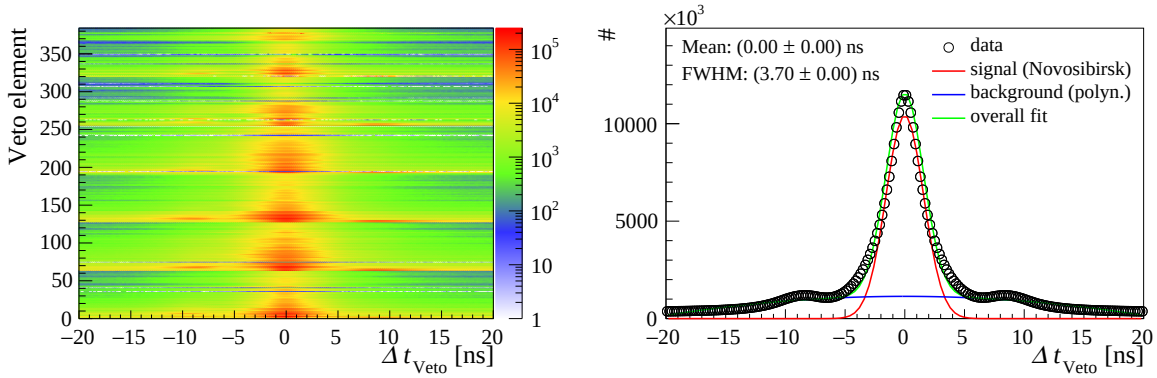

Fig. 6.13: TAPS Veto wall time calibration. On the left side, the two-dimensional relation between the time difference of Veto hits as a function of the corresponding Veto hits is shown. On the right side, the overall projection of all elements is illustrated and fit to determine the peak position and FWHM.

An additional peak at roughly -10 ns is visible which is caused by a time difference event between a Veto element in front of a $PbWO_4$ crystal and a BaF_2 crystal. Since all events in the region of the $PbWO_4$ are rejected in the analysis, the additional peak is not present in the later analysis.

6.2.5 Tagger

To ensure that the tagger time is independent of the beam photon energy, all tagger elements have to be calibrated relative to each other. Similar to the CB, all conversion gains are fixed to 0.117 ns/channel and thus only the time offset has to be adjusted. Unfortunately, the tagger is running with a high rate resulting in accidental hits in the tagger elements. As a result, a huge background is formed under the

coincidence peak. To eliminate most of this background, the tagger time was calibrated relative to the calorimeter with the best time resolution which is the TAPS. Since the individual TAPS elements have been already calibrated relative to each other, the whole tagger can be calibrated relative to the TAPS. Thus, again a two-dimensional histogram was created in which the time difference of tagger to TAPS hits is plotted as a function of the tagger element as can be seen in Fig. 6.14 on the left side. On the right side, the overall projection of all elements is shown. As mentioned, a huge background is visible which is fit with a polynomial (blue line) function. The signal is aligned to 0.05 ns with a resolution of 1.82 ns.

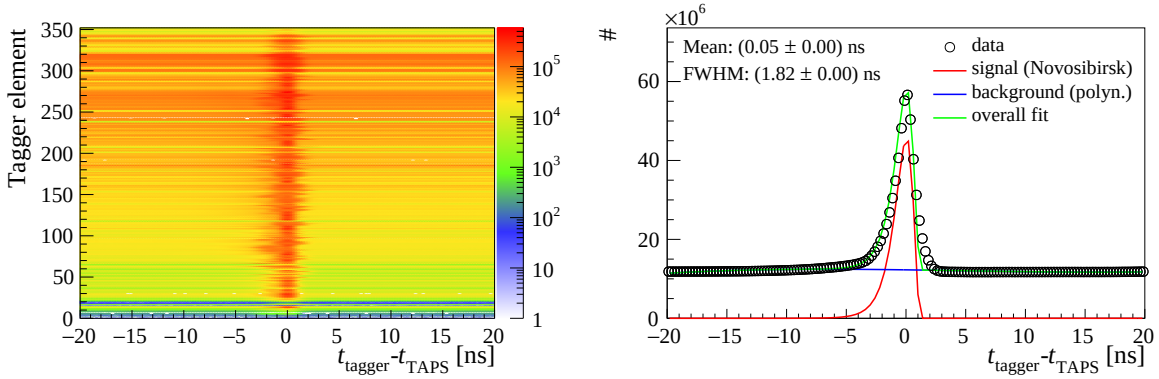

Fig. 6.14: Tagger time calibration. On the left side, the time difference between all Tagger and TAPS hits as a function of the Tagger element is shown. On the right side, the overall projection of all elements is illustrated and fit to determine the peak position and FWHM.

6.3 Further Calibrations

6.3.1 CB Time Walk Correction

The slow rise-time of the NaI crystals in combination with the used LEDs cause an energy-dependent time information, the so-called time walk effect. Thus, the time information of the CB hits need to be corrected to ensure the best possible time resolution. This is achieved by plotting for all CB elements the time difference between the CB hit and all tagger hits as a function of the deposited energy in the CB element. To reduce the amount of background, this is only performed for events that fulfill the kinematics of a π^0 photoproduction reaction. Therefore, only CB hits were used with an additional cluster in the CB which form together an invariant mass close to the π^0 rest mass. Additionally, the missing mass should be in the range of the proton rest mass. To reduce the time background, a sharp time cut between the CB hit and the tagger hit was applied in combination with a sideband subtraction. A detailed description of this technique is presented in Sec. 7.4.2. The resulting two-dimensional plot for each CB element was fitted with a 4-parameter function:

$$t(E) = a + \frac{b}{(E+c)^d}. \tag{6.7}$$

A typical example can be seen in Fig. 6.15 for the element 12.

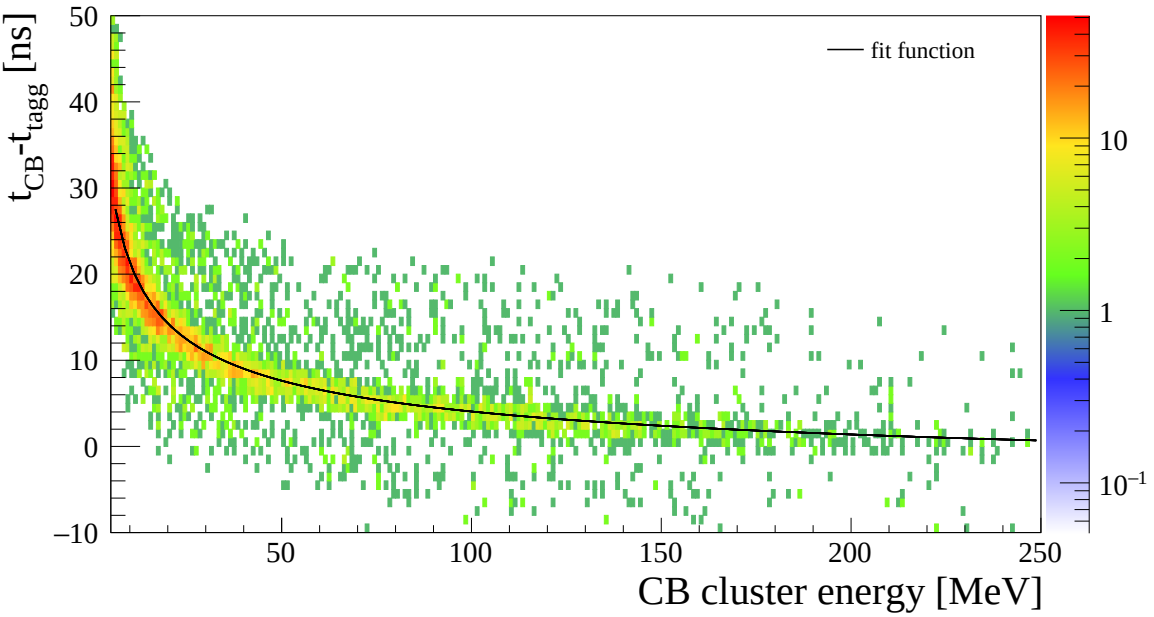

Fig. 6.15: Time walk correction of the CB. On the picture, the time difference between all CB times and tagger time of the CB element 12 as a function of the corresponding cluster energy is plotted. The fit, following Eq. (6.7), is depicted as the solid black line.

The resulting parameters were written to the database and all measured times were corrected by subtracting Eq. (6.6) with its individual parameters from the measured time. Since the tagger is used to calculate the corrections, the tagger and CB times are aligned to each other which can be seen in Fig. 6.16 on the right side in black. More importantly, the correction cancels the effect of the time walk which can be seen by the comparison of the time difference before (red) and after (black) the calibration. As a consequence, the time resolution of CB reduces from previously 18.62 ns to only 4.34 ns which is illustrated in Fig. 6.16 on the right.

6.3.2 CB Rise Time Correction

Due to a not perfectly working fit during the time walk calibration, the time difference between CB elements and tagger time can be slightly shifted to each other. To correct for this effect, a last final iteration has to be performed in which the peak position of the time difference has to be determined. By this, the rise time parameter a can be reevaluated and adjusted in such a way that the time difference peaks again at 0 ns.

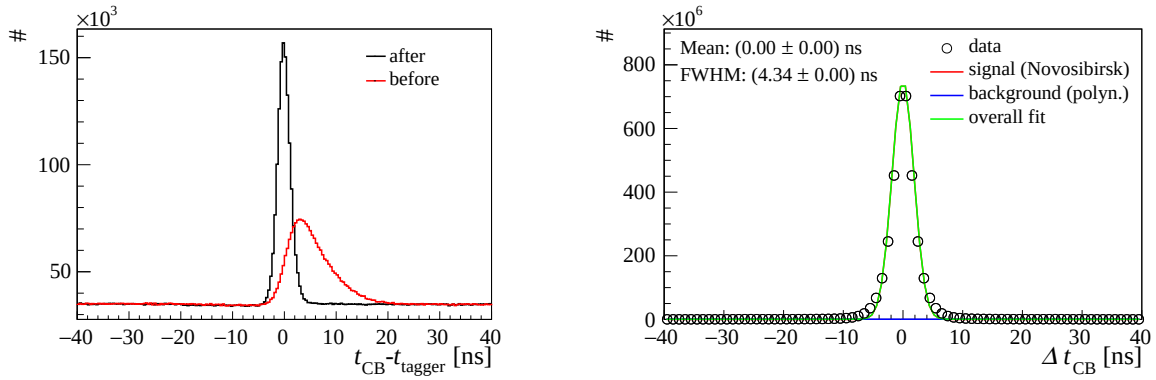

Fig. 6.16: CB Rise time and time walk correction. On the left side, the effect of the time walk correction is illustrated. The time difference between the CB and tagger hits is plotted once before the calibration is applied (red) and after the calibration (black). On the right side, the effect of the CB Rise time and time walk correction on the CB time calibration is illustrated. The FWHM is reduced from 18.62 ns to 4.34 ns (cf. Fig. 6.10).

6.3.3 PID Azimuthal Angle

To ensure that a charged track detected in the CB also provides a valid hit in the PID, the orientation of the PID inside the detector system must be determined. In doing so, events were selected with only one CB cluster in combination with one PID hit. Afterward, the PID element was plotted as a function of the azimuthal angle of the CB cluster and all projected elements are fit with a Gaussian function. A typical spectrum can be seen in Fig. 6.17 on the right. The resulting correlation between the PID element and the corresponding azimuthal angle is shown on the right and was saved to the database.

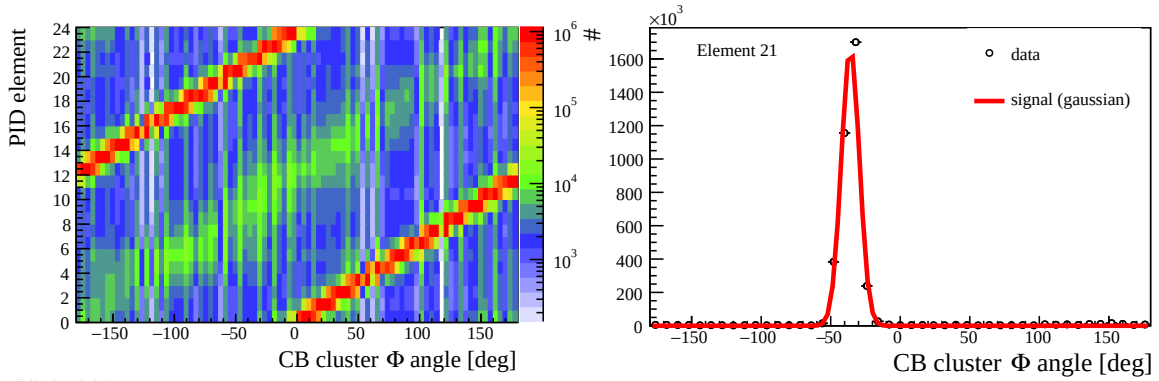

Fig. 6.17: PID azimuthal alignment. On the left side, for each track with a hit in the PID and a cluster in the CB, the ϕ angle of the CB cluster is plotted as a function of the corresponding PID element. Afterward, for each PID element, the ϕ angle distribution is fit with a Gaussian function to determine the correlation with the CB as can be seen on the right side for element 21.

6.3.4 Energy Loss Correction for Charged Pions

For a detailed analysis of the kinematics of a reaction, the four momenta of the initial state and the final state particles need to be known as precisely as possible. The initial state is well determined by

the energy of the beam photon traveling in z-direction towards the target. The target is assumed to be unbound protons at rest. The polar and azimuthal angles of the final state were calculated from the reconstructed tracks of the particles. The major problem, however, is the detected energy. Since particles traveling through the materials of the detector setup lose energy between the production point inside the target and the detection point, an energy correction must be applied. In section 6.1, the energies of the photons were calibrated by calculating the invariant mass of two photons. Iteratively, the invariant mass was corrected to the rest mass of the neutral pion. In that process, an energy loss correction was automatically performed for photons. The correct energy of the π^+ was found by calculating the energy of the π^+ in the $\gamma p \to n\pi^+$ reaction under the assumptions of an unbound-nucleon interaction by using Monte Carlo simulations followed by a final applied correction on data. For this purpose, the initial state and the measured polar angles of the particles in the final states are used to calculate the energy of the π^+ and the neutron (for a detailed calculation see App. B.3). Fig. 6.18 shows for MC simulations the two-dimensional relation between the calculated and reconstructed kinetic energy of the π^+ for three different polar angular ranges of the π^+. An angle-dependent correction is justified by the fact that different path lengths through the detector materials need to be taken into account. Additionally, in the edge regions of the detectors, parts of the energy can escape the detector system and thus the cluster does not reconstruct the whole energy.
First of all it should be noted that up to 300 MeV the calculated kinetic energy and reconstructed energy are except for ionization losses nearly the same. This means that the π^+ can completely be stopped in the calorimeter. In this region, an energy correction can be applied. However, above roughly 200 MeV the calculated kinetic energy becomes larger than the reconstructed because the π^+ does not deposit the whole energy in the calorimeter and thus can leave it (a so-called *Punch-Through*). At even higher energies, the π^+ becomes a minimal-ionizing particle (MIP) and consequently deposits only about 200 MeV in the calorimeter although the kinetic energy is much higher. Based on this problem, the measured kinetic energy of the π^+ does not correspond to the actual kinetic energy and an energy correction cannot be applied. For the events where an energy correction is possible, the reconstructed kinetic energy in a given calculated energy and polar angular range, was fitted with a Gaussian function. The maximum of all these fits as a function of the corresponding calculated energies was then fit with a polynomial of the third order. From the extrapolation of the fit functions towards zero reconstructed energy, the polar angle-dependent energy losses can be extracted. In high forward and backward regions, the calculated energy can be up to 40 MeV higher than the measured one. In the other regions, an overall energy loss of about 20 MeV is found. Overall, the reconstructed energy is slightly bigger than the calculated one which can be explained by an overcorrection of the reconstructed energy due to the calibration of the data and MC with photons. In Fig. 6.19, the energy difference between the reconstructed and calculated kinetic energy is presented for the corrected reconstructed energies. They are presented for the MC simulation on the left side and for the butanol data on the right side. A clear peak at 0 MeV is seen. Therefore, the energy correction performed efficiently and with the corrected energy several cuts can now be applied to the data to identify the $\vec{\gamma}\vec{p} \to n\pi^+$ reaction described in the next section.

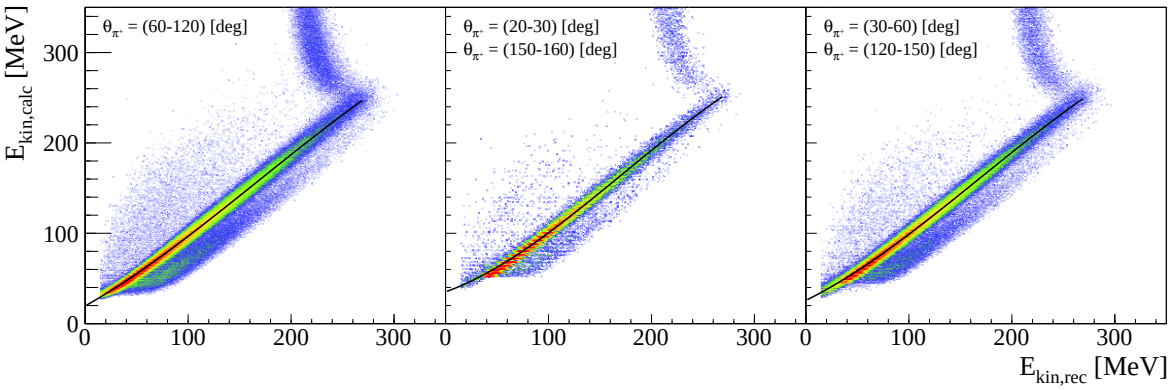

Fig. 6.18: two-dimensional relation between the reconstructed and calculated kinetic energy of the π^+ for different polar angular ranges. The relation between the reconstructed and calculated kinetic energy of the π^+ is fit with a polynomial of the third order (black line) as a function of the polar angle. The extrapolation of the fits towards zero reconstructed energy shows the different energy losses as a function of the polar angle.

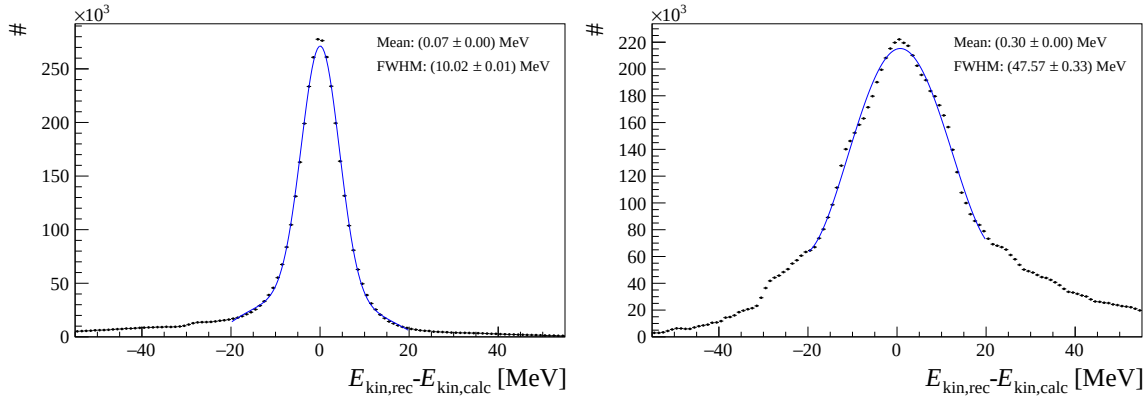

Fig. 6.19: Energy difference between the reconstructed and calculated kinetic energy of the π^+. Shown are the energy differences for the corrected cluster energy in blue. The distribution is fitted with a Gaussian function (blue curve). The left side presents the results for the MC simulations whereas the right side the results for the butanol data.

6.4 Overview of the Calibration Results

An overview of the final calibrated data is presented in Tab. 6.1.

Table 6.1: Overview of the FWHM of the calibrated data of the September 2015 beamtime.

Type	Quantity	ΔE [MeV] / Δ t [ns]
Energy	m_{π^0} (CB)	20.67
	m_{π^0} (CB/TAPS)	20.51
Time	CB-CB	4.34
	TAPS-TAPS	0.55
	PID-PID	3.75
	tagger-TAPS	1.82
	CB-tagger	2.9

6.5 Calibration of Simulated Data

For a later comparison of simulated and experimental data, the simulated data have to be calibrated in the same manner as the experimental data.

6.5.1 Energy Calibration

For all detectors, the energy calibration was performed as described in the previous sections. As an example to stress the importance of the calibration, Fig. 6.20 shows the comparison between uncalibrated and calibrated data of the TAPS energy calibration.

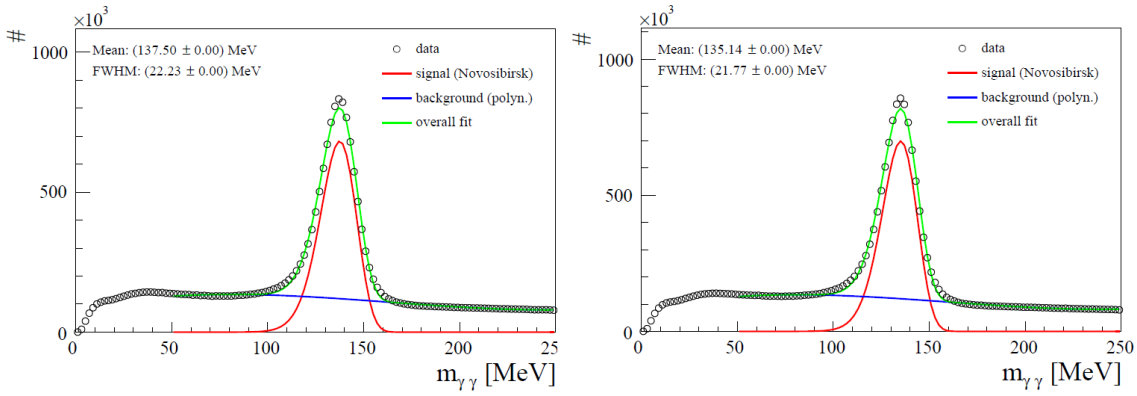

Fig. 6.20: TAPS Energy calibration for simulated data. On the left panel, the invariant mass of two photons (one in the CB and the other in the TAPS) as a function of the TAPS central cluster element is plotted. The description of the individual parts is similar to Fig. 6.2.

6.5.2 Energy Resolution

For a good comparison of experimental and simulated data, the energy resolution of both must be matched. For this purpose, the deposited energy in the simulated data are smeared to match the parameterized energy resolution of the experimental detectors given by Eq. (6.8):

$$\frac{\Delta E}{E_{dep}} = \begin{cases} \frac{0.2\%}{E[GeV]^{0.36}} & \text{for CB,} \\ 1.8\% + \frac{0.8\%}{E[GeV]^{0.5}} & \text{for TAPS.} \end{cases} \tag{6.8}$$

To do so, simulation of isotropically distributed photons of energies up to 1 GeV are generated. Afterward, as a function of the generated energy, the deposited energy was fitted with a Novosibirsk function and the energy resolution was extracted from the fit parameters. Iteratively, the deposited energy of the simulated data was folded with a Gaussian function of an energy-dependent FWHM given by Eq. (6.9):

$$\frac{\Delta E}{E_{dep}} = \begin{cases} 0.027\% \cdot E[GeV]^{0.795} & \text{for CB,} \\ 0.00225\% \cdot E[GeV]^{0.565} & \text{for TAPS.} \end{cases} \tag{6.9}$$

The resulting energy resolutions for the TAPS and the CB are depicted in Fig. 6.21 together with the experimental resolution, given by Eq. (6.8) in red.

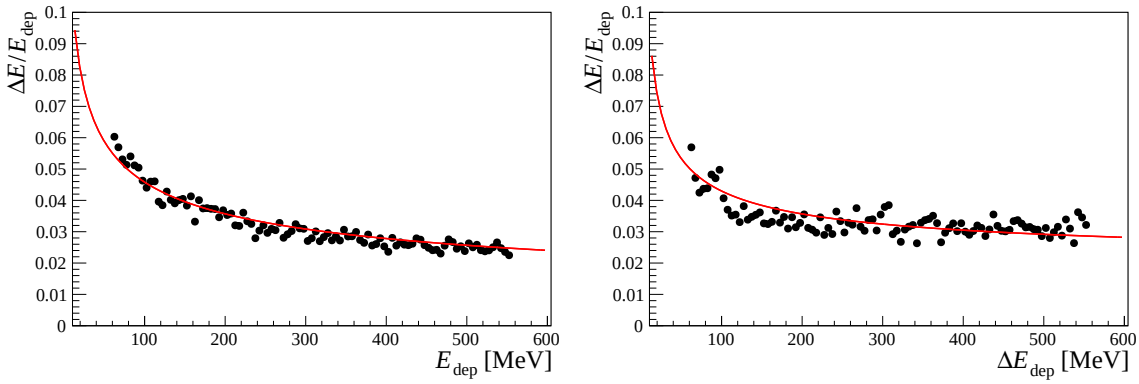

Fig. 6.21: Energy resolution adjustment for MC simulations. Shown are in black the energy resolution as a function of the deposited energy for both detectors. On the left, the resolution for the CB is presented whereas on the right for the TAPS. The red curve indicates the experimental resolution obtained with Eq. (6.8).

6.5.3 Angular Resolutions

For the later analysis of the $n\pi^+$ final state, a good understanding of the angular resolution for neutrons and charged pions in the Crystal Ball and TAPS is required. Therefore, neutrons and charged pions have been generated. Afterward, the angular difference between the reconstructed and generated angle is plotted as a function of the generated angles. For each generated angle, the angular difference is fit with a Gaussian function to extract the angular resolution. The angular resolution for neutrons and pions detected in the CB and the TAPS can be seen in Fig. 6.22. The peaks at about 20° are caused by

the transition region between the CB and the TAPS. The sharp peak close to 0° in the ϕ-resolution of the neutron and the overall decreasing resolutions below $\theta \leq 5°$ can be ignored as this range is covered by the $PbWO_4$ crystals which are ignored in the analysis.

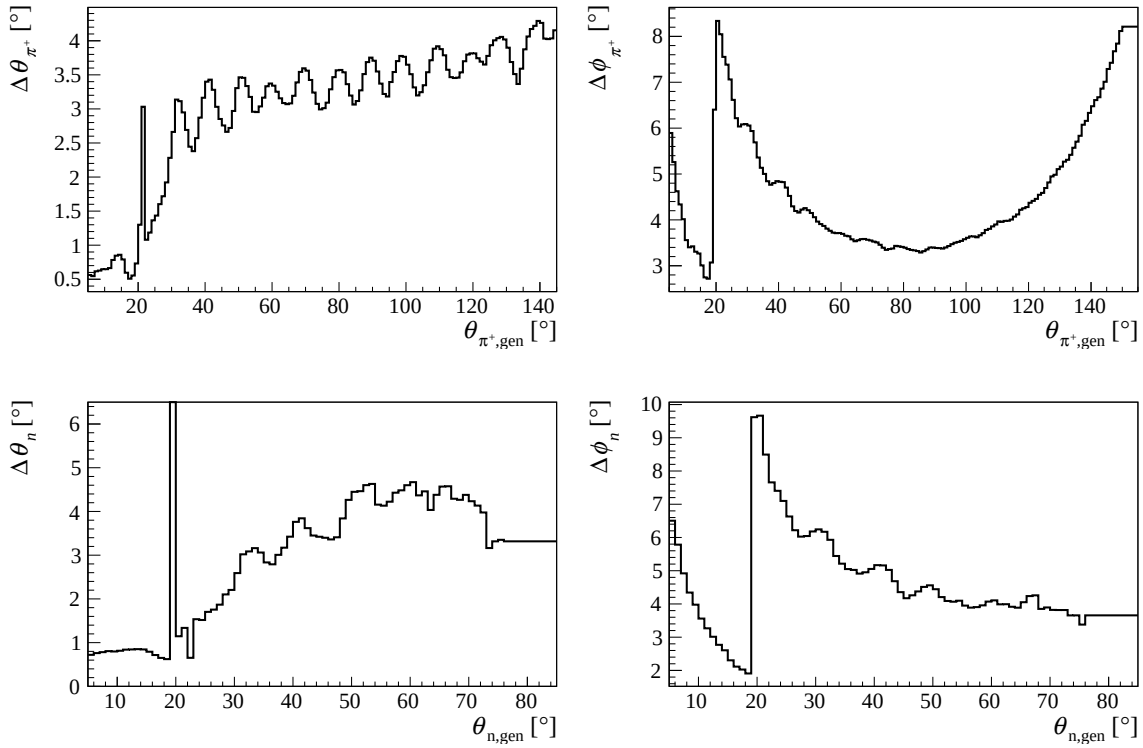

Fig. 6.22: Angular resolution for charged pions and neutrons. On the left side, the polar angular resolution is presented as a function of the generated polar angle for both particles. On the right side, the corresponding azimuthal angular resolution is depicted.

Chapter 7

Selection of the Reactions

For the extraction of the polarization observables G and E, the reactions $\vec{\gamma}\vec{p} \to p\pi^0$ and $\vec{\gamma}\vec{p} \to n\pi^+$ have to be selected from the experimental data. In this chapter, the selection process is described and applied with respect to the desired reaction. This includes a first preselection based on the signature of the reaction. To reduce the high amount of random events, the time coincidence between the initial state and the final state particles is required. Afterward, energy and momentum conservation are used to apply kinematic cuts which optimize the selection of the desired reaction and at the same time reject background. The different cuts are explained and are discussed with respect to the contribution of background reactions. Furthermore, background studies for the selected events are performed and are presented at the end of this chapter.

7.1 Carbon, Oxygen and Helium contribution inside the Butanol Target

For the measurement of the double polarization observables G and E, reactions on polarized nucleons are required. As mentioned in Sec. 2.3, only the hydrogen nucleons inside the butanol target can be polarized. Consequently, the contribution of the unpolarized nucleons from carbon, oxygen, and helium has to be subtracted from the data sample. This procedure allows for an optimal selection of the contribution coming only from hydrogen nucleons inside the butanol target. Therefore, in the following sections, all butanol and carbon beamtimes have been analyzed in the same way and the resulting carbon distributions for the kinematic cut variables of the examined reaction are scaled properly to match the unpolarized components inside the butanol target. Finally, the carbon distributions are subtracted from the butanol distributions which results in the reconstructed hydrogen distributions inside the butanol target. These distributions are used for determining the selection criteria for the kinematic cut variables. Further details about the carbon contribution will be discussed in this chapter and the proper scaling will be presented in Sec. 8.1.2.

7.2 CB Energy Sum Adjustment

As has been mentioned in Sec. 4.2.4, the different beamtimes had different energy sum thresholds for the CB trigger. Whereas most of the $\vec{\gamma}\vec{p} \to p\pi^0$ events have in total an energy far above the energy sum threshold, the situation is completely different for the $\vec{\gamma}\vec{p} \to n\pi^+$ reaction as will be further discussed in Sec. 8.1.2.3. In Fig. 7.1, the individual energy sum distributions of the different beam and times coherent edge positions are illustrated.

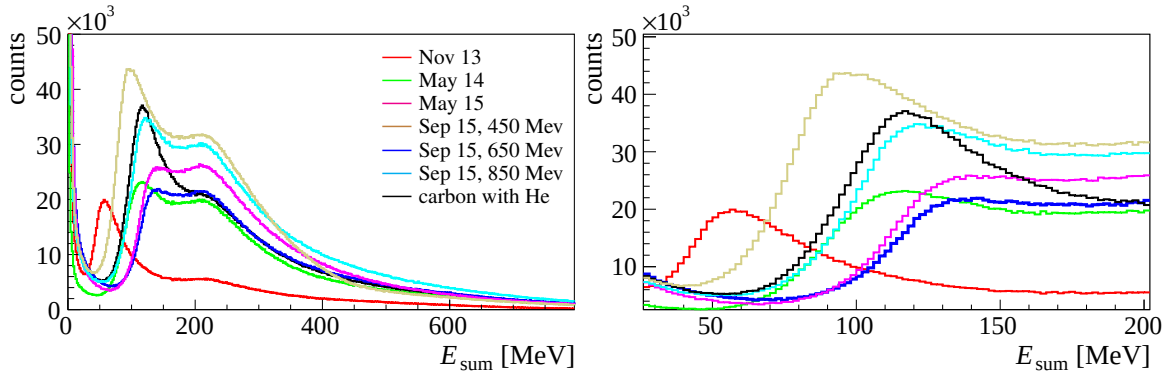

Fig. 7.1: Energy sum distribution of the different beamtimes. On the left side, the energy sum distributions for all recorded data of all different beamtimes and some individual coherent edge positions are presented. On the right side, a zoomed in area is depicted to show the different starting energy sum thresholds.

For the further investigation, it should be noted that the trigger setting of the carbon with helium measurement in September 2015 behaves similar to the butanol measurements with the coherent edge at 850 MeV in the same beamtime. The 450 MeV edge measurement of September 2015 and especially all the measurement with different coherent edges of the November 2013 increase earlier due to their lower energy sum threshold, whereas the 850 MeV edge measurement of May 2015 increases later. Since the carbon with helium measurement will be used to describe the unpolarized component inside the butanol target, it is crucial that the energy sum thresholds for the butanol measurements are set at the same value as the carbon with helium measurements. Therefore, as a first step, for all beamtimes and each different energy sum threshold setting, the energy sum is plotted. Afterward, the aim is to adjust all butanol settings to the reference settings which is the 850 MeV edge setting of the September 2015 beamtime. To avoid enhancements in the energy sum which are caused by different coherent edges, the adjustment is only performed with the Møller data. To do so, the two butanol energy sum distributions are first normalized to each other in the region above 300 MeV where no trigger effects are expected. An example of the 450 MeV edge of September 2015 is depicted in Fig. 7.2 on the left side. Afterward, the distributions which need to be adjusted are divided by the reference setting, resulting in a ratio histogram with values between 0 and 1. An example of the ratio plot of the butanol 450 MeV edge of the September 2015 beamtime is depicted in Fig. 7.2 on the right.

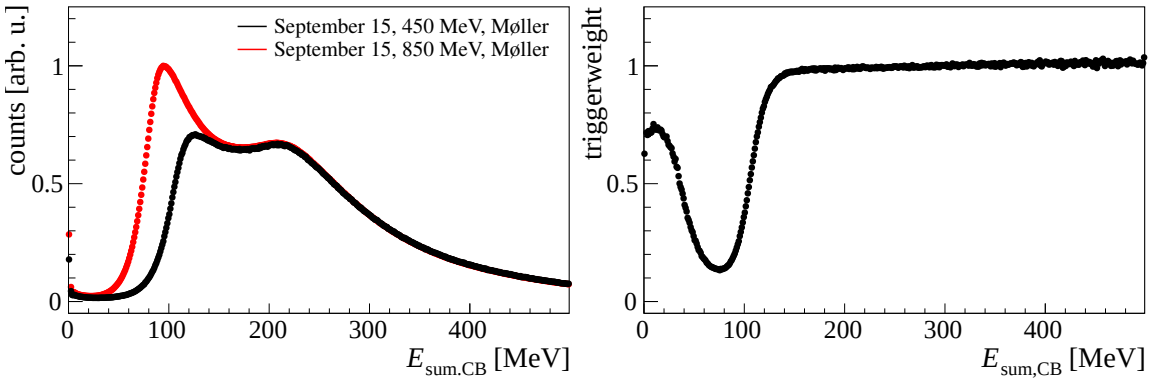

Fig. 7.2: Normalized energy sum distributions and their ratio. On the left side, the energy sum distribution of the 450 MeV and 850 MeV edge trigger setting of the September 2015 beamtime are shown. Note that only the Møller data have been used. On the right side, the ratio of both is plotted. The resulting values are later used to adjust the different trigger settings.

The final adjustment in the data analysis is achieved by giving each analyzed event a weighting factor according to their ratio plot. More details about the goodness and the uncertainty from the trigger adjustment are discussed in Sec. 8.1.2.3.

7.3 Signature of the Reactions

As a first step for the data analysis, a defined signature of the reactions is preselected within the GoAT framework. The signature of the reaction is given by the final state products. In the case of the reaction $\vec{\gamma}\vec{p} \rightarrow p\pi^0$, the main signature is given by the decay of the neutral pion into two photons with a branching ratio of 98.8% [7]. By that, two separate clusters are built in the main calorimeters. Together with a detected cluster formed by the proton, this signature is named *3 PED* event where PED stands for **P**article **E**nergy **D**eposition. At low beam photon energies, the proton can be lost due to its low energy and thus can not reach the main calorimeters or pass the detector thresholds. Further reasons for losing the proton are detector inefficiencies and small gaps in the detector setup, i.e. the transition between the CB and the TAPS (-0.8 $\leq \cos\theta_{\pi^0,\text{CMS}} \leq$ -0.6). As a result, only the clusters from the two photons can be detected. These kind of events are called *2 PED* events. A possible solution to detect also protons with low energies and in regions with low detector efficiency is to make use of the MWPCs with and without the PID. The events, where the proton is detected in this charge sensitive detectors are called *2.5 PED* events. Unfortunately, the MWPCs had to be repaired between the May 2015 and September 2015 beamtime. During the reinsertion for the September 2015, the two MWPCs were not exactly aligned in z-direction between themselves and thus do not show the same behavior as the previous beamtimes. As all beamtimes need the carbon with Helium measurement of the September 2015 beamtime as a reference, the angular information of the MWPC was not usable. In addition, as there is no fixed mechanical frame to hold the MWPCs inside the CB tunnel, the relative position of the CB center to the one of the MWPCs can be different for each beamtime. Consequently, the MWPC was only used as an additional charge identification detector.

However, as will be shown and explained later in the data analysis, the reaction can be selected by neglecting the charge information of the detectors. Thus, the reaction signature is simply given by two or three detected clusters in the main calorimeters. The detection efficiency together with the acceptance of the reaction of the different event types is illustrated as a function of the kinematic variable $\cos\theta_{\pi^0,\mathrm{CMS}}$ and the beam photon energy E_γ in Fig. 7.3.

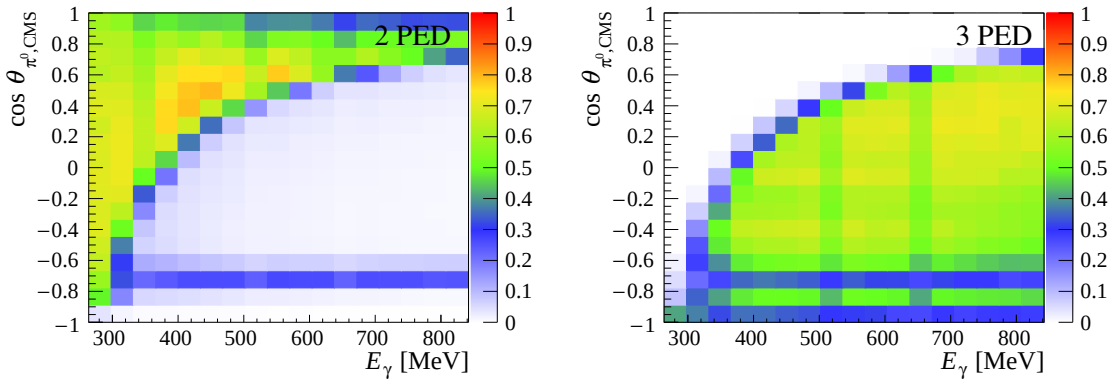

Fig. 7.3: Detection efficiency and acceptance for the reaction $\vec{\gamma}\vec{p}\to p\pi^0$. The detection efficiency and acceptance are presented for the 2 PED events on the left and for the 3 PED events on the right. They are depicted as a function of the kinematic variable $\cos\theta_{\pi^0,\mathrm{CMS}}$ and the beam photon energy E_γ.

For the $n\pi^+$ final state, the charge information of the detectors can not be neglected. As a selection criterion, a cluster in one of the main calorimeters must exist in combination with a correlated charge information (see Chap. 5). In the case of a cluster in the CB, a correlated charge information must be available in the PID and/or in the MWPCs whereas for the TAPS in the Veto Wall elements. These kind of events are called *1 PED* events and are mostly caused by the detection of a charged pion. At low beam photon energies, the neutron has not enough energy to be detected in the calorimeters. In addition, the detection efficiency of neutrons is estimated to be lower than 30% at kinetic energies below 100 MeV [124]. Thus, only the charged pion can be detected. However, as the detection efficiency of the neutron increases up to 40% at kinetic energies of about 200 MeV, the neutron can be detected at higher beam photon energies and consequently an additional neutral track can be selected in combination with the charged track. These events are called *2 PED* events. An overview of the distribution of the two event types is presented in Fig. 7.4. Note that the low acceptance is caused by the CB energy sum adjustment as the physical energy sum already starts at about 30 MeV[1] and the low detection efficiency of the neutrons.

[1] As previously mentioned, the G/E measurements were not optimized at all for the $n\pi^+$ channel. The major aim was the acquisition of data for the $p\pi^0$ and $p\eta$ channels which required a much higher energy sum.

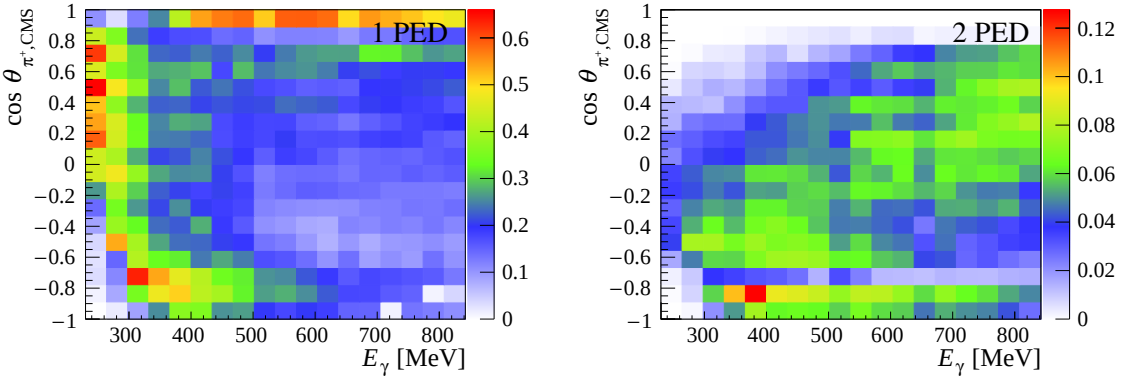

Fig. 7.4: Detection efficiency and acceptance for the reaction $\vec{\gamma}\vec{p}\to n\pi^+$. The detection efficiency and acceptance are presented for the 1 PED events on the left and the 2 PED events on the right. They are depicted as a function of the kinematic variable $\cos\theta_{\pi^+,\mathrm{CMS}}$ and the beam photon energy E_γ .

7.4 Time Coincidence Cuts

7.4.1 Time Coincidence of Final State Particles

The photons of the π^0 decay of the $p\pi^0$ channel are emitted at the same time and are traveling with nearly the speed of light. Therefore, the detected time information of photons, which originate from the decay of the π^0, should be in coincidence. Fig. 7.5 shows the time difference of the two photons as a function of the detector in which they have been detected. This is motivated by the fact that the time resolution of the TAPS is by a factor of roughly 7 better than the CB (cf. Sec. 6.4). Clean Gaussian-like time spectra are seen with only one defined peak at about 0 ns which emphasizes that two photons are correlated in time. Nevertheless, a combinatorial background of the reaction $\vec{\gamma}\vec{p}\to p\pi^0$ is possible where a photon is correlated with a proton. This effect should especially be seen if the proton candidate is detected in the TAPS. Due to its long flight distance and low kinetic energy, the proton has a significantly longer flight time. Although no hint of combinatorial background is present (blue curve), to ensure that a potential background is rejected for sure, a cut on the time coincidence of the photons from -3 ns to 3 ns is applied as can be seen by the narrow lines in the Fig. 7.5 on the left side. As the photons are now time coincidence, a final step is to correlate the final state proton with the meson time as can be seen in Fig. 7.5 on the right. Note the second peak at about 7 ns which corresponds to the low energetic protons in the TAPS. To ensure that these events are selected as well, a time window cut for the proton in the TAPS (blue curve) is selected from -3 ns to 15 ns and for the case in the CB (red curve) from -5 ns to 7 ns.

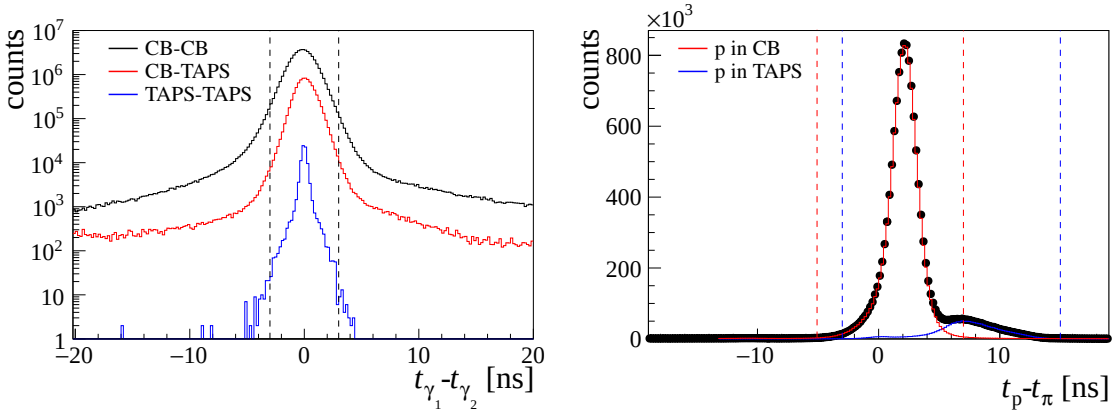

Fig. 7.5: Time coincidence of final state particles for $\vec{\gamma}\vec{p}\to p\pi^0$. On the left side, the time coincidence between the two photons of the π^0 decay is shown as a function of the detector in which they were detected. Black hereby indicates the case where both photons are detected in the CB, red the combination CB and TAPS whereas blue both in the TAPS. The black dashed lines indicate the applied time coincidence cut. On the right side, the time coincidence between the meson and the proton is illustrated with black points. Here, a distinction between the detection of the proton in the TAPS (blue) and the CB (red) was made. The selection criteria are indicated by the corresponding colored dashed lines.

For the $n\pi^+$ final state, the charged pion and the neutron are correlated in time. Hereby, the time correlation is as well studied as a function of the detectors. This can be seen in Fig 7.6 on the left side. If both particles are detected in the CB (black), a clear peak at about 2 ns is seen[2]. If the neutron is detected in the TAPS (red), the peak is shifted towards more positive values which can be explained by its high rest mass and the longer flight path. Finally, the detection of the charged pion in the TAPS (blue) peaks roughly at the same position as the case where both are detected in the CB. To only select final states which are in time coincidence, a conservative asymmetric cut from -10 ns to 20 ns is applied.

7.4.2 Random Tagger Hit Subtraction

After the above explained time cut ensures the time coincidence of the final state particles, the coincidence with the initial state is investigated. Therefore, the final state meson is correlated with the detected time information of the tagger hits $t_{\gamma,b}$:

$$\Delta t_{\text{reaction}} = t_\pi - t_{\gamma,b} \quad \text{with} \quad t_\pi = \begin{cases} 0.5\cdot(t_{\gamma_1}+t_{\gamma_2}) & \text{for } \vec{\gamma}\vec{p}\to p\pi^0 \\ t_{\pi^+} & \text{for } \vec{\gamma}\vec{p}\to n\pi^+ \end{cases} . \tag{7.1}$$

As mentioned in Sec. 5.1, the tagger hits are directly connected to the produced bremsstrahlung beam photons. Consequently, the beam photon that triggered the desired reaction should be in time coincidence with the averaged time information of the final state photon candidates. The A2

[2]Note that the time difference between both photons peaks at about 0 ns. Thus, if a huge contribution of the $n\pi^+$ is present in the $p\pi^0$ analysis, a second peak should be seen at about 2 ns in Fig. 7.5.

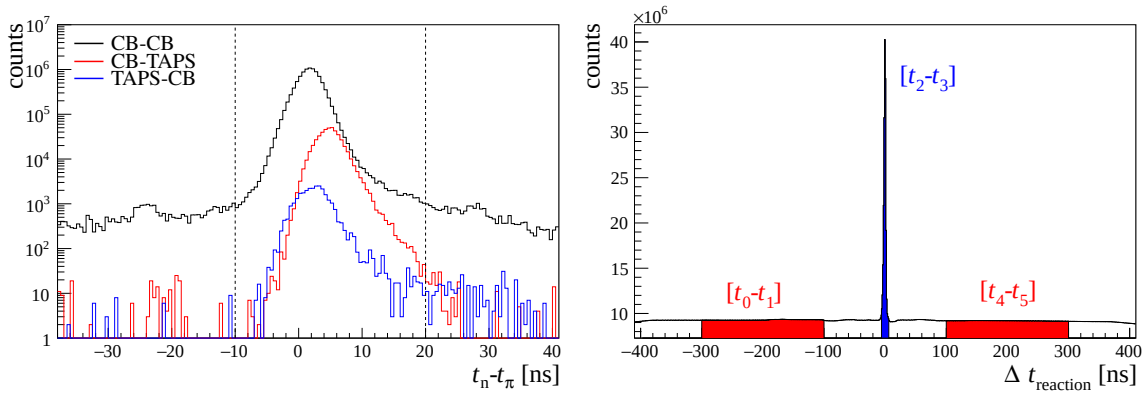

Fig. 7.6: Time coincidence of the $n\pi^+$ final state and the reaction time. On the left side, the time coincidence between the charged pion and the neutron is shown as a function of the detector in which they were detected. Hereby, the first detector in the legend corresponds to the detector where the charged pion is detected and the second where the neutron is detected. The black dashed lines indicate the applied time coincidence cut. On the right side, the reaction time $\Delta t_{\text{reaction}}$ is shown. The random time background events, which are indicated by the red area, are used to subtract the random time background beneath the coincidence time window (blue area).

experiment runs with a very high electron beam current of about 4 nA and thus up to 35 hits per event are recorded. This high intensity of electrons is causing the problem that also random time background is below the time coincidence signal as it is depicted in Fig. 7.6. To subtract the random time background events below the coincidence peak, the time window sideband subtraction is applied. The technique makes use of the fact that the random time background is constant, flat and random. Using these facts, the time background contribution should be equal for any selected time interval [77]. Therefore, only events in three different time windows are selected which are illustrated in Fig. The time window $[t_2,t_3]$ is the coincidence time window, which includes the random background events on top of the coincidence events. Two additional random time windows $[t_0,t_1]$ and $[t_4,t_5]$ are selected where only random time background is assumed. Finally, these three time windows can be used to subtract from a statistical point of view the time background beneath the coincidence peak. Whereas events in the prompt window are scaled by a factor $s_t = s_{\text{prompt}} = 1$, events in the random time windows are scaled by:

$$s_t = s_{\text{random}} = \frac{(t_3 - t_2)}{(t_1 - t_0) + (t_5 - t_4)} = \frac{6\,\text{ns} - (-6\,\text{ns})}{(-100\,\text{ns} - (-300\,\text{ns})) + (300\,\text{ns} - 100\,\text{ns})} = 0.03. \qquad (7.2)$$

With that, each histogram, which has been weighted according to the above scaling factor s_t, contains only the contribution of the coincidence time events. In the following, all shown distributions are time background subtracted.

7.5 Kinematic Cut Variables

7.5.1 Mass Cuts

7.5.1.1 Invariant Mass

The π^0 in the final state of the reaction $\vec{\gamma}\vec{p} \to p\pi^0$ decays with a branching ratio of almost 100% into two photons. Consequently, the invariant mass of these two photons can be used to identify if they belong to the decay of the π^0. In that case, the invariant mass should be in agreement with the rest mass of the π^0 ($m_{\pi^0} = 134.9766(6)\,\mathrm{MeV}$) [7]. Using the four-momenta p_γ of the photons, the invariant mass is given by:

$$\begin{aligned} m_{\gamma_1,\gamma_2} &= \sqrt{(p_{\gamma_1} + p_{\gamma_2})^2} \\ &= \sqrt{(E_{\gamma_1} + E_{\gamma_2})^2 - (\vec{p}_{\gamma_1} + \vec{p}_{\gamma_2})^2} \\ &= \sqrt{2 \cdot E_{\gamma_1} E_{\gamma_2} \cdot (1 - \cos\theta_{\gamma_1,\gamma_2})} \end{aligned} \tag{7.3}$$

where $\theta_{\gamma_1,\gamma_2}$ is the opening angle between the photons and $E_{\gamma_{1,2}}$ are the detected energies of the photons. The selection criterion is:

$$m_{\gamma_1,\gamma_2} \stackrel{!}{=} m_{\pi^0}. \tag{7.4}$$

For the $n\pi^+$ channel, the invariant mass of the π^+ and neutron system makes no sense as only information about the intermediate resonance state can be achieved.

7.5.1.2 Missing Mass

To identify the nucleon in the final state, the missing mass technique makes use of the fact that the four-momentum of the beam photon p_γ, the target proton p_p, and the final state pion p_π are known[3]. With respect to momentum- and energy conservation the missing mass of the system can then be calculated which is given by:

$$\begin{aligned} p_\gamma + p_p &= p_X + p_\pi \\ \begin{pmatrix} E_\gamma \\ \vec{p}_\gamma \end{pmatrix} + \begin{pmatrix} m_p \\ \vec{0} \end{pmatrix} &= \begin{pmatrix} E_X \\ \vec{p}_X \end{pmatrix} + \begin{pmatrix} E_\pi \\ \vec{p}_\pi \end{pmatrix} \\ \begin{pmatrix} E_X \\ \vec{p}_X \end{pmatrix} &= \begin{pmatrix} E_\gamma \\ \vec{p}_\gamma \end{pmatrix} + \begin{pmatrix} m_p \\ \vec{0} \end{pmatrix} - \begin{pmatrix} E_\pi \\ \vec{p}_\pi \end{pmatrix} \\ \to m_X &= \sqrt{(E_\gamma + m_p - E_\pi)^2 - (\vec{p}_\gamma - \vec{p}_\pi)^2}. \end{aligned} \tag{7.5}$$

[3] For the $n\pi^+$ channel, this is only true for the events which do not punch through the detector. Further details will be discussed in Sec. 7.7.2.

Hereby, the four-momentum p_π of the $p\pi^0$ channel is given by the sum of the four momenta of the final state photons whereas for the $n\pi^+$ channel by the charged pion. If the initial finite momentum of the target nucleon is neglected, the missing mass should be given by the rest mass of the nucleon N. Thus, the selection criterion is:

$$m_X \stackrel{!}{=} \begin{cases} m_p & \text{for } \vec{\gamma}\vec{p} \to p\pi^0, \\ m_n & \text{for } \vec{\gamma}\vec{p} \to n\pi^+, \end{cases} \tag{7.6}$$

with $m_p = 938.272\,081(6)\,\text{MeV}$ and $m_n = 939.565\,413\,3(60)\,\text{MeV}$ [7]. A deviation from the rest mass indicates either additional particles in the final states which are not detected or a detected particle which is not a pion.

7.5.2 Angular Cuts

7.5.2.1 Coplanarity

The first angular cut which can be performed is the coplanarity cut which is only applicable if both final state particles have been detected. Since the A2 experiment is a fixed target experiment and with the assumption of the beam photon only traveling in z-direction towards the target, the initial transverse momentum has to be zero. Thus, according to momentum conservation, the final state nucleon N and the meson π have to fly back-to-back which results in a vanishing total transverse momentum in the final state. Therefore, the difference between the azimuthal angle ϕ of the nucleon and the π is calculated and is given by:

$$\Delta\phi = \begin{cases} \phi_N - \phi_\pi & \text{if } \phi_N - \phi_\pi \geq 0 \\ \phi_N - \phi_\pi + 360^\circ & \text{if } \phi_N - \phi_\pi < 0. \end{cases} \tag{7.7}$$

If the reaction takes place on a nucleon at rest in the initial state, the kinematics should be fulfilled and the particles in the final state have to fly back-to-back. With that, the following selection criterion is given:

$$\Delta\phi \stackrel{!}{=} 180^\circ. \tag{7.8}$$

7.5.2.2 Polar Angle of the Nucleon

In the center of mass system (cms), the total momentum has to vanish. As already shown previously, the final state particles already fly back-to-back in the xy-plane in the lab frame and the transverse momentum is vanishing. Since the boost into the cms is in z-direction, only the longitudinal component needs to be considered in the cms. For a vanishing longitudinal component, the proton and the meson π need to fly back-to-back flight in z-direction. Consequently, the polar angular difference of the nucleon N and the meson π in the cms has to fulfill the condition:

$$\Delta\theta_{\text{cms}} = \theta_{N,\text{cms}} - \theta_{\pi,\text{cms}} \stackrel{!}{=} \pm 180^\circ. \tag{7.9}$$

Since the four momenta of the particles are given in the laboratory system, they first have to be boosted in the z-direction into the cms. To do so, an exact knowledge of the energy of the participating particles is mandatory. This is not guaranteed for the nucleons and the charged pions since at a certain energy these punch through the detector. Thus another selection condition must be found which is completely independent of the energies. A solution is given by the comparison of the reconstructed polar angle of the nucleon and the calculated angle. For the $p\pi^0$ final state, the initial state information and the photons from the π^0 decay are used for determining the calculated polar angle. For the $n\pi^+$ channel, the initial state information and the detected polar angle of the π^+ can determine the polar angle of the neutron under the assumption of the $\vec{\gamma}\vec{p} \to n\pi^+$ reaction kinematics. A detailed explanation of the calculations is presented in appendix B.3. Thus, a selection criterion is found which is completely independent of the critical proton and charged pion energy. If the reconstructed nucleon N belongs to the meson π in the reaction, the reaction kinematics should be fulfilled and the difference between the calculated and reconstructed nucleon polar angle should be compatible with $0°$ which leads to the final selection criterion:

$$\Delta\theta_N = \theta_{N,\text{calc}} - \theta_{N,\text{rec}} \stackrel{!}{=} 0°. \tag{7.10}$$

7.6 Iterative Selection of the Events

Since the distributions of the kinematic cut variables are contaminated by background reactions, the determination of the correct selection criteria for the variables is not straight-forward. As a first step, all kinematic variables are examined by eye and rough selection criteria are selected. Afterward, for all kinematic variables, all other selection criteria are applied and a first fit is applied to the reconstructed hydrogen distributions. Iteratively, the cut widths of the different kinematic variables are optimized with respect to an optimal signal to background ratio. While in the first iterations, the kinematic cut variables are integrated over all possible variables, in a second stage, the cut variables are investigated as a function of the incoming beam photon energy E_γ, referred as to the 2-dimensional cut criteria. In a final stage, the 3-dimensional cut criteria are applied by also considering the polar angle of the meson in the center of mass system. With that, the selection criteria are optimized in the dimension in which the double polarization observables are extracted. As will be seen in the following sections, the 3-dimensional cut criteria are mandatory. Consequently, in the following sections, they will be discussed with respect to the examined kinematic variable.

7.7 Application of Kinematic Cut Variables

7.7.1 Invariant Mass

For the $p\pi^0$ final state, Fig. 7.7 shows on the left side the invariant mass distribution of the butanol data as a function of the incoming beam photon energy E_γ after all other cuts. For the beam photon energy range from 400 MeV to 434 MeV the $\cos\theta_{\pi^0,\mathrm{CMS}}$ dependent invariant mass is depicted in Fig. 7.7 on the right side. A clear peak around the π^0 rest mass is visible which are the reactions of interest. An additional clear peak at an invariant mass of about 550 MeV is visible which starts at a beam photon energy of about 700 MeV. This peak belongs to the events where a η is detected instead of a π^0. The rest mass of the η is given by $547.862(17)$ MeV. The boundary conditions for the selection of the neutral pions, indicated by the black lines, are determined by fitting a Novosibirsk function[4] to the reconstructed hydrogen contribution inside the butanol target. Afterward, events within a 2σ range around the mean value of the fit are accepted as a signal event. Note, that under the assumption of a Gaussian distribution, a 2σ cut ensures that 95.45% of all valid events are selected. However, due to the low energy tail, a symmetric 2σ cut would select less than 95.45% of all events. Therefore, another method was tested, namely the selection via confidence intervals. The confidence interval selects all events within the smallest possible range where 95.45% of all events are located. As it turned out, this method takes the low energy tail into account. Unfortunately, the confidence interval method is very sensitive to background as the background events are also included in the calculation of the interval range for the 95.45%. Consequently, the normal symmetric 2σ range around the mean value is used as the selection criteria. Furthermore, this is motivated by the fact, that most of the

[4]The Novosibirsk function is used to take into account the low energy tail produced by the detector resolution [77].

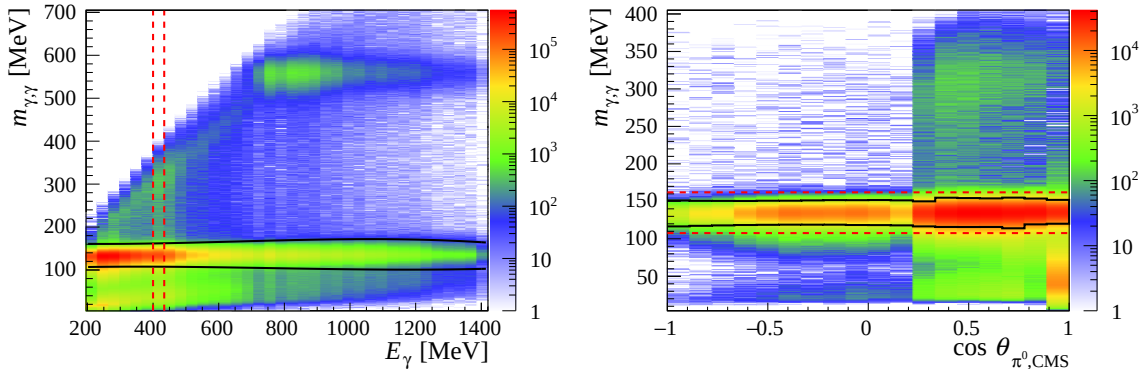

Fig. 7.7: Invariant mass distribution of the butanol data as a function of the beam photon energy E_γ and as a function of cos $\theta_{\pi^0,\mathrm{CMS}}$. On the left side, the invariant mass distribution is plotted as a function of the beam photon energy E_γ and integrated over the full angular coverage range. The 2-dimensional cut criteria limits are determined for each beam photon energy and are indicated by the black line. On the right side, the $\cos\theta_{\pi^0,\mathrm{CMS}}$ dependent invariant mass is illustrated for the beam photon energy range from 400 MeV to 434 MeV. The horizontal red dashed lines in the figure on the left hereby indicate the selected beam photon energy range. The dashed red line in the figure on the right shows the corresponding energy-dependent selection criteria whereas the black solid lines the $\cos\theta$ dependent. Note that all other cuts which are presented in this chapter are applied to these data and that the distributions with $\cos\theta_{\pi^0,\mathrm{CMS}} < 0.22$ only contain 3 PED events whereas for $\cos\theta_{\pi^0,\mathrm{CMS}} \geq 0.22$ also 2 PED events.

background is located at lower invariant masses which are mainly from $n\pi^+$ events or electromagnetic background. Ignoring the asymmetric energy tail towards lower invariant masses, therefore, rejects more possible background. Finally, it is important to optimize the overall statistic in combination with a low carbon contribution. A more detailed study has been performed in [60] and showed that a 2σ cut is the optimal cut range. An illustration of the different invariant mass distributions and the boundary conditions are shown in Fig. 7.8 for a beam photon energy range from 400 MeV to 434 MeV and as a function of the kinematic variable $\cos\theta_{\pi^0,\mathrm{CMS}}$. Note that the distributions with $\cos\theta_{\pi^0,\mathrm{CMS}} < 0.22$ have detected the proton and the distributions with $\cos\theta_{\pi^0,\mathrm{CMS}} \geq 0.22$ also include events where the proton is not detected. A remarkable observation is that the amount of reaction on bound nucleons is increasing dramatically if the proton is not detected. Unfortunately, the invariant mass alone can not be used to reject the contribution of bound protons since it only depends on the final state particles which are independent on the initial state. As will be shown later, the situation is different for the angular cuts which can reject a large portion of the reaction on bound protons. As these cuts are only available if all final state particles are detected, the increasing number of bound protons for $\cos\theta_{\pi^0,\mathrm{CMS}} \geq 0.22$ can be attributed to these missing angular cuts. Nevertheless, concerning the contamination with background reactions, the reconstructed hydrogen distribution is compared with Monte Carlo simulation for the signal reaction and can be nicely described by them. This already indicates a good signal to background ratio.

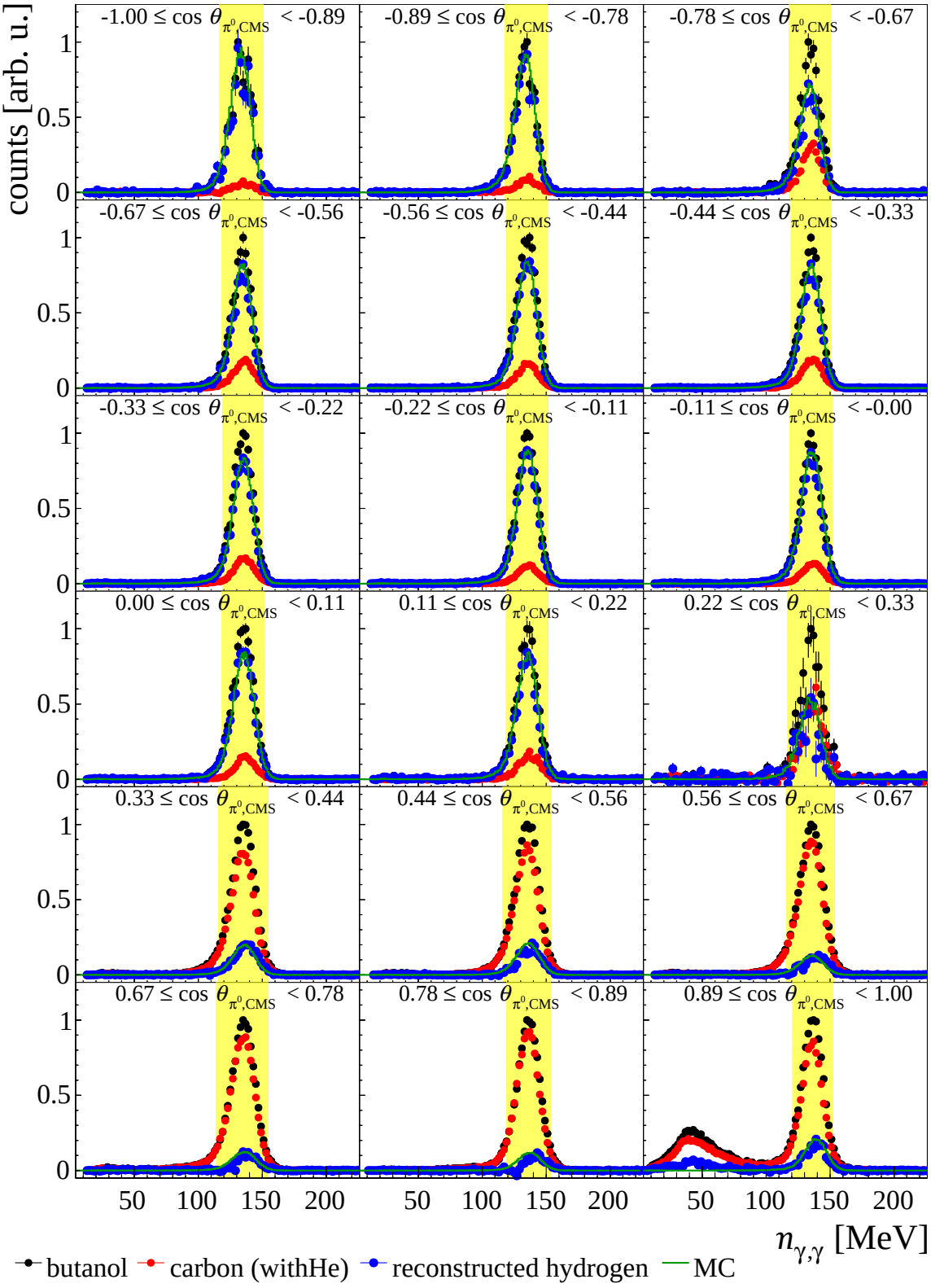

Fig. 7.8: Invariant mass distribution for E_γ = (400-434) MeV. The invariant mass distributions after all other cuts are shown as a function of $\cos\theta_{\pi^0,\mathrm{CMS}}$ for a given beam photon energy range. The yellow area hereby indicate the 2σ selection range. Note that the distributions with $\cos\theta_{\pi^0,\mathrm{CMS}} < 0.22$ only contain 3 PED events whereas for $\cos\theta_{\pi^0,\mathrm{CMS}} \geq 0.22$ also 2 PED events.

7.7.2 Missing Mass

Similar to the invariant mass cut, Fig. 7.9 shows on the left side the missing mass distribution of the butanol data after all cuts as a function of the incoming beam photon energy E_γ and on the right side as a function of $\cos\theta_{\pi^0,\mathrm{CMS}}$ and for a beam photon energy from 400 MeV to 434 MeV. The upper row presents the results of the $p\pi^0$ channel whereas the remaining two ones for the 1 PED and 2 PED events of the $n\pi^+$ channel. The butanol distributions clearly show an energy and $\cos\theta_{\pi,\mathrm{CMS}}$ dependence which can be explained by the energy resolution of the involved particles. Although the relative energy resolution of the particles gets better with increasing energy (cf. Sec. 6.5.2), the absolute resolution decreases and thus causes a broader missing mass distribution.
A detailed example of the 3-dimensional missing mass distribution is depicted in Fig. 7.13 for a beam photon energy from 400 MeV to 434 MeV. A similar example for the $n\pi^+$ final state is presented in Fig. 7.14 for the 1 PED events and in Fig. 7.15 for the 2 PED events. The boundary conditions are applied to the reconstructed hydrogen distribution and are shown in the form of the yellow area. Similar to the invariant mass, a Novosibirsk function is used to determine a 2σ range around the mean value of the fit. Note, that also here, the confidence interval was tested. In addition to the problems mentioned in Sec. 7.7.1, a not perfect carbon subtraction can artificially select a wrong confidence interval. Further problems concerning the carbon subtraction is presented in Chap. 8 in Sec. 8.1.2. Therefore, also for the missing mass, the 2σ fit was selected. In addition to the selection of the desired reaction, the boundary conditions reject contributions from the bound nucleons. This can be explained by the fact that the missing mass calculation assumes a target at rest. While this assumption is valid for reactions on unbound nucleons, bound nucleons carry an additional Fermi momentum. Consequently, reactions on bound nucleons trends towards higher missing masses. Similar to the invariant mass, 2 PED events are included for $\cos\theta_{\pi^0,\mathrm{CMS}} \geq 0.22$ in the $p\pi^0$ channel. Due to the missing angular cuts of the 2 PED events, an increasing amount of reactions on bound nucleons is seen. Similar argumentation holds for the 1 PED events of the $n\pi^+$ final state.
Nevertheless, the reconstructed hydrogen distribution is compared with MC simulations for both signal reactions and are in very good agreement with each other.
To emphasize the importance of the adjustment of the CB energy sum trigger in the $n\pi^+$ channel (see Sec. 7.2), Fig. 7.10 shows as an illustration of the problem the missing mass distribution for 1 PED events for a beam photon energy range $E_\gamma = (400 - 434)$ MeV and in the kinematic variable region $-0.44 \leq \cos\theta_{\pi^+,\mathrm{CMS}} < -0.33$. The missing mass distribution is depicted on the left side for the butanol measurements of the September 2015 beamtime with the coherent edge at 450 MeV and on the right side for the coherent edge at 850 MeV. The inspection of Fig. 7.10 clearly presents the problem of the different CB energy sum thresholds. Whereas the unpolarized component (red points) inside the butanol (black points) can be nicely described for the 850 MeV edge, the 450 MeV edge has significant problems in the carbon subtraction, especially the additional peak in the carbon subtracted distribution (blue points) towards higher missing masses. At first sight, the conclusion would be to assume that the second peak is coming from background events.

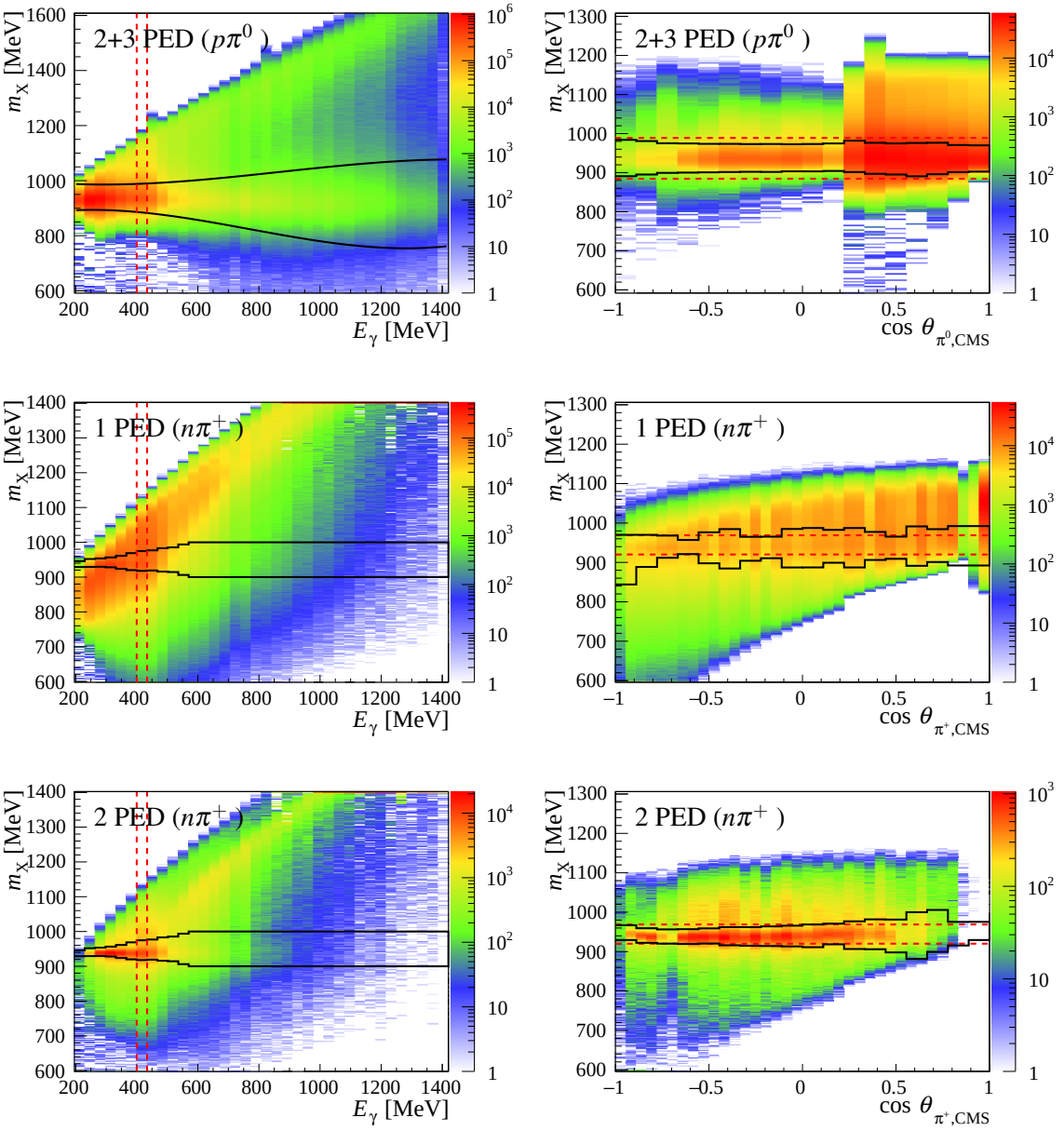

Fig. 7.9: Missing mass distribution of the butanol data as a function of the beam photon energy E_γ and as a function of cos $\theta_{\pi,\mathrm{CMS}}$. On the left side, the missing mass distribution is plotted as a function of the beam photon energy E_γ and integrated over the full angular coverage range. The 2-dimensional cut criteria limits are determined for each beam photon energy and are indicated by the black line. On the right side, the $\cos\theta_{\pi,\mathrm{CMS}}$ dependent missing mass is illustrated for the beam photon energy range from 400 MeV to 434 MeV. The horizontal red dashed lines in the figure on the left hereby indicate the selected beam photon energy range. The dashed red line in the figure on the right shows the corresponding energy-dependent selection criteria whereas the black solid lines the $\cos\theta$ dependent. Note that all other cuts which are presented in this chapter are applied to these data and that the distributions with $\cos\theta_{\pi^0,\mathrm{CMS}} < 0.22$ in the $p\pi^0$ analysis only contain 3 PED events whereas for $\cos\theta_{\pi^0,\mathrm{CMS}} \geq 0.22$ also 2 PED events.

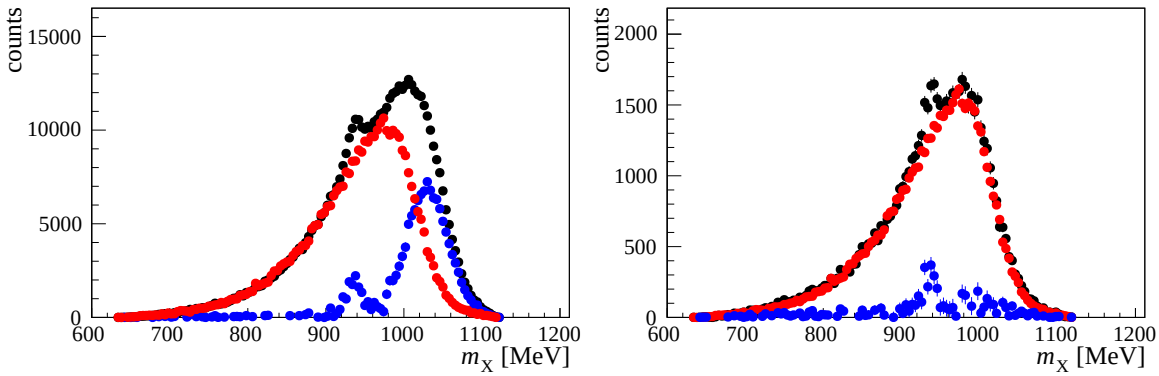

Fig. 7.10: Missing mass distribution for non-adjusted energy sums. Shown is on the left side the missing mass distribution of one kinematic bin (E_γ = (400-434) MeV, $-0.44 \leq \cos\theta_{\pi^+,\mathrm{CMS}} < -0.33$) of the 450 MeV edge trigger setting of the September 2015 beamtime. The similar bin is presented on the right side for the 850 MeV of the September 2015 beamtime. The black points represent the butanol distribution, the red one the scaled carbon with helium distribution and the blue on the reconstructed hydrogen distribution.

However, this assumption can be eliminated by the fact that the additional peak is not seen as well in the 850 MeV edge position and the MC simulations (cf. Fig. 7.14). The analysis of the coherent edge position are done in a similar way and thus should only enhance the amount of events in a defined beam photon energy range and not produce any coherent edge dependent background contamination. In conclusion, a CB energy sum adjustment is mandatory and is always applied in all spectra.

In contrast to the photon energies in the reaction $\vec{\gamma}\vec{p} \rightarrow p\pi^0$, the energy of the π^+ is only correct in the range where it is not punching through the detectors (cf. Sec. 6.3.4). For energies below the punch through energy of about 180 MeV, the missing mass cut can be applied and is compatible with the rest mass of the neutron. Above this region, the detected energy is much lower than the actual value. Consequently, a too low value is subtracted from the missing mass calculation and thus an additional broad distribution towards higher missing masses occurs. This is nicely seen in Fig. 7.9. Towards higher beam photon energies, the energy of the π^+ increases and thus its probability to punch through the detector increases. Above a beam photon energy of about 1000 MeV, all pions punch through the detectors and thus do not show any peak in the region of the rest mass of the neutron. As opposed to this, the missing mass distribution of the $p\pi^0$ channel always has a peak structure at the rest mass of the proton which can be explained by the fact that photons nearly never punch through the detectors. Finally, the $\cos\theta_{\pi^+,\mathrm{CMS}}$ dependence reflects the energy of the π^+ as well as high energetic pions more likely fly in forward direction. Thus, the missing mass distribution contains also a broader distribution towards higher missing masses for higher forward angles.

Of special interest is to investigate and understand the broad distribution towards higher missing masses. Here it is important to know if the distribution is caused by punch through pions from the signal reaction or from other background reactions. Fig. 7.11 shows the missing mass distribution of several simulated final states for a beam photon energy below 842 MeV and integrated over the kinematic variable $\cos\theta_{\pi^+,\mathrm{CMS}}$. Whereas the left side shows the π^+ candidates in the CB which do not punch through the detector, the right side does.

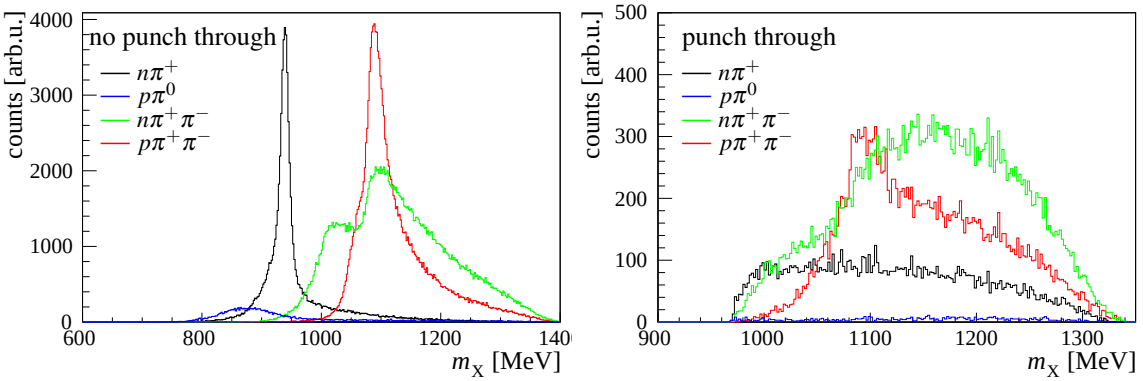

Fig. 7.11: Missing mass distribution for simulated data and their punch through behavior. The missing mass distributions for different simulated final states and charged particle being detected in the CB are shown. They have been integrated over all variables and up to a beam photon energy of 842 MeV. On the left side, charged particles that do not punch through the detector are shown whereas on the right side they do. Note the arbitrary unit for the y-axis since different amount of generated events were used.

In the case that the particles do not punch through the detector, the simulation can nicely be used to identify background reactions towards higher missing masses as both the $n\pi^+\pi^0$ (green) and the $p\pi^+\pi^-$ (red) channel show a peak like structure. As these structures are not seen in any reconstructed hydrogen distribution, the contribution of both these channels can be neglected for the not punch through events[5]. The $p\pi^0$ channel has no structure at all towards higher missing masses and thus can not be identified. Nevertheless, a broader peak below the missing mass peak is seen which contains a small shoulder towards lower missing masses as well.

For the punch through events, all different channels show a broad distribution with small structures towards higher missing masses. These structures, however, are not as pronounced which makes the selection of punch through particles more difficult. Further information about the background contribution will be given in Sec. 7.9.2.

Finally, the missing mass distributions in Fig. 7.9 show an additional broad distribution at lower missing masses which is mainly pronounced in the backward direction and is dominated by the carbon contribution. As will be shown later, these can be mostly assigned to background events on the carbon and oxygen inside the butanol with a proton in the final state. However, as carbon and oxygen are spinless particles, these background events do not contribute and affect the results of the double polarization observables. Even after the carbon subtraction, a small shoulder towards lower missing masses remains. Detail studies with simulations have shown that these features can be explained by the interaction of the π^+ within the scintillator crystal. If the π^+ is at rest within the crystals, the π^+ can decay with a branching ratio of nearly 100% into a μ^+ and a ν_μ. Therefore, due to the rest mass difference of about 34 MeV [7], additional energy can be detected. To proof this assumption, the energy balance between the generated π^+ energy and its reconstructed energy was investigated (see

[5] Although the missing mass distribution is shown here only integrated over all the variables, the distribution was studied as a function of the beam photon energy and the kinematic variable $\cos\theta_{\pi^+,\mathrm{CMS}}$ as well. Even the separation between punch through and not punch through pions was studied with respect to the reconstructed hydrogen distribution.

Fig. 7.12 on the right). As it turned out, the energy balance for the events belonging to the broad peak at lower missing masses showed a deviation from zero with a peak roughly at about 20 MeV. Taking into account that the μ^+ energy does not need to be detected completely within crystals and that the additional ν_μ can carry energy as well, the energy balance is a first hint for this assumption. The final proof nevertheless is given by studying the interaction of the μ^+ with MC simulation. Two MC sets were generated as illustrated in Fig. 7.12.

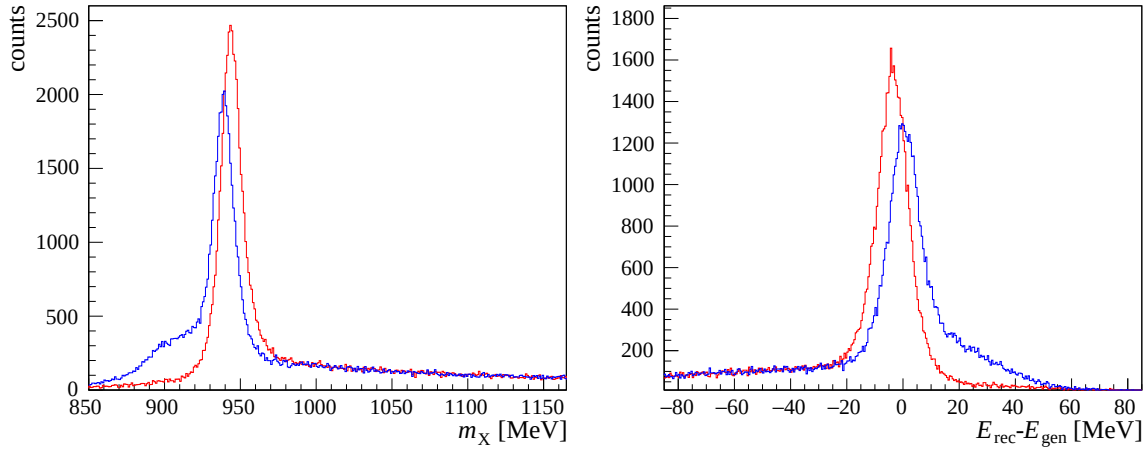

Fig. 7.12: Test of π^+ decay using simulated data. The two different MC samples for the missing mass distribution of both analyzed PED events are shown on the left side. On the right side, the corresponding energy balance between the reconstructed and generated energy is illustrated. The first sample is given by the blue distribution, the second one by the red one. For information about the different samples, see in the text below.

The first one includes all physical interactions for the π^+, including the decay of the π^+ before it reaches the detectors and the final decay at rest. The second one disallows the decay of the π^+ , including the decay within the crystals if the particle is at rest. As it turned out, the additional broad distribution in the missing mass distribution (see Fig. 7.12 on the left) vanishes and thus it can be explained by the decay of the π^+ within the crystals. Tests have further shown that nearly no π^+ decays before it reaches the detector. This is however expected as the mean travel path of the pion is in the order of 7.8045 m [7].

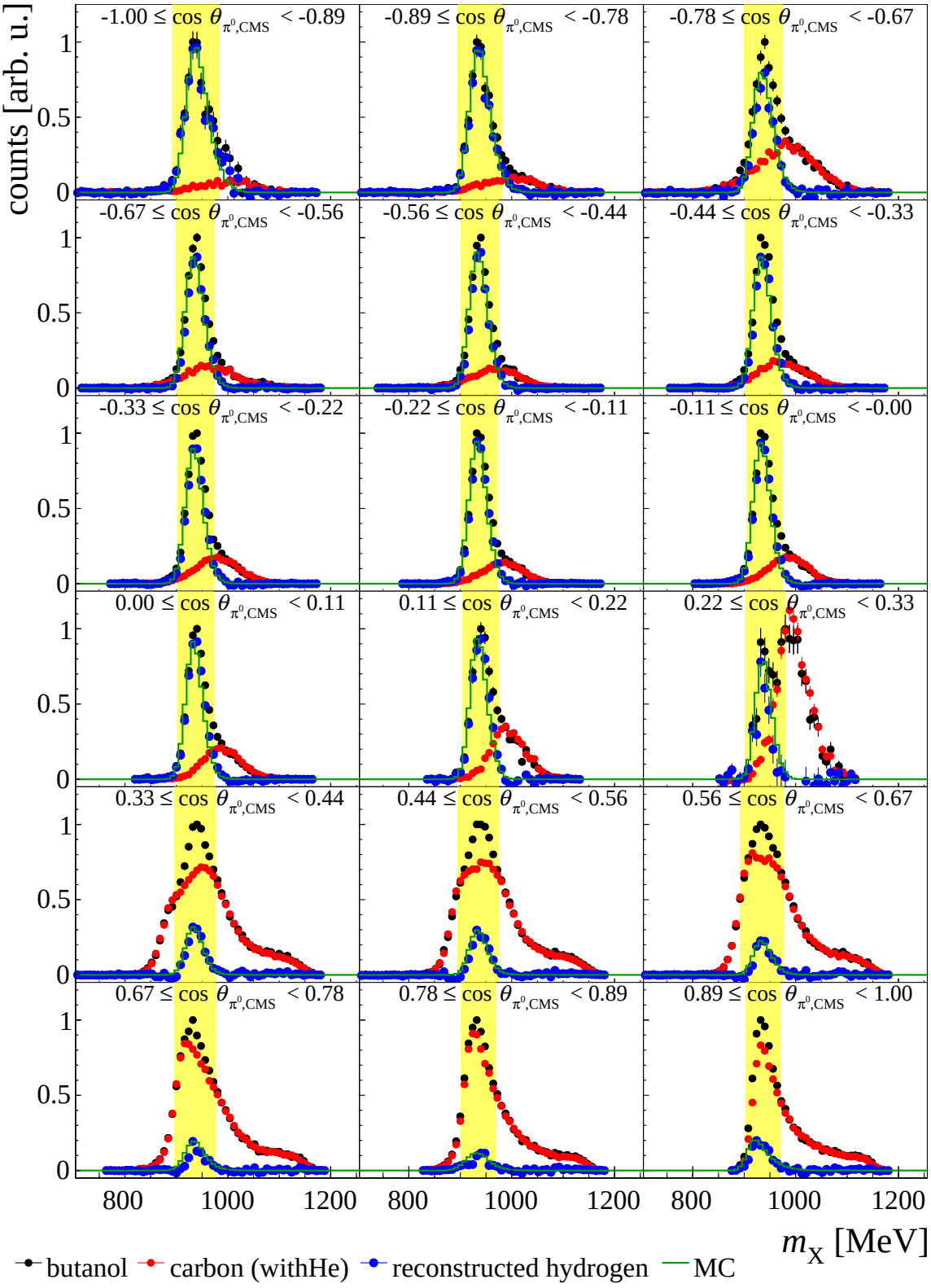

Fig. 7.13: Missing mass distribution for E_γ = (400-434) MeV for the $p\pi^0$ final state. The missing mass distributions after all other cuts are shown as a function of $\cos\theta_{\pi^0,\mathrm{CMS}}$ for a given beam photon energy range for the $p\pi^0$ final state. The yellow area hereby indicates the 2σ selection range. Note that the distributions with $\cos\theta_{\pi^0,\mathrm{CMS}} < 0.22$ only contain 3 PED events whereas for $\cos\theta_{\pi^0,\mathrm{CMS}} \geq 0.22$ also 2 PED events.

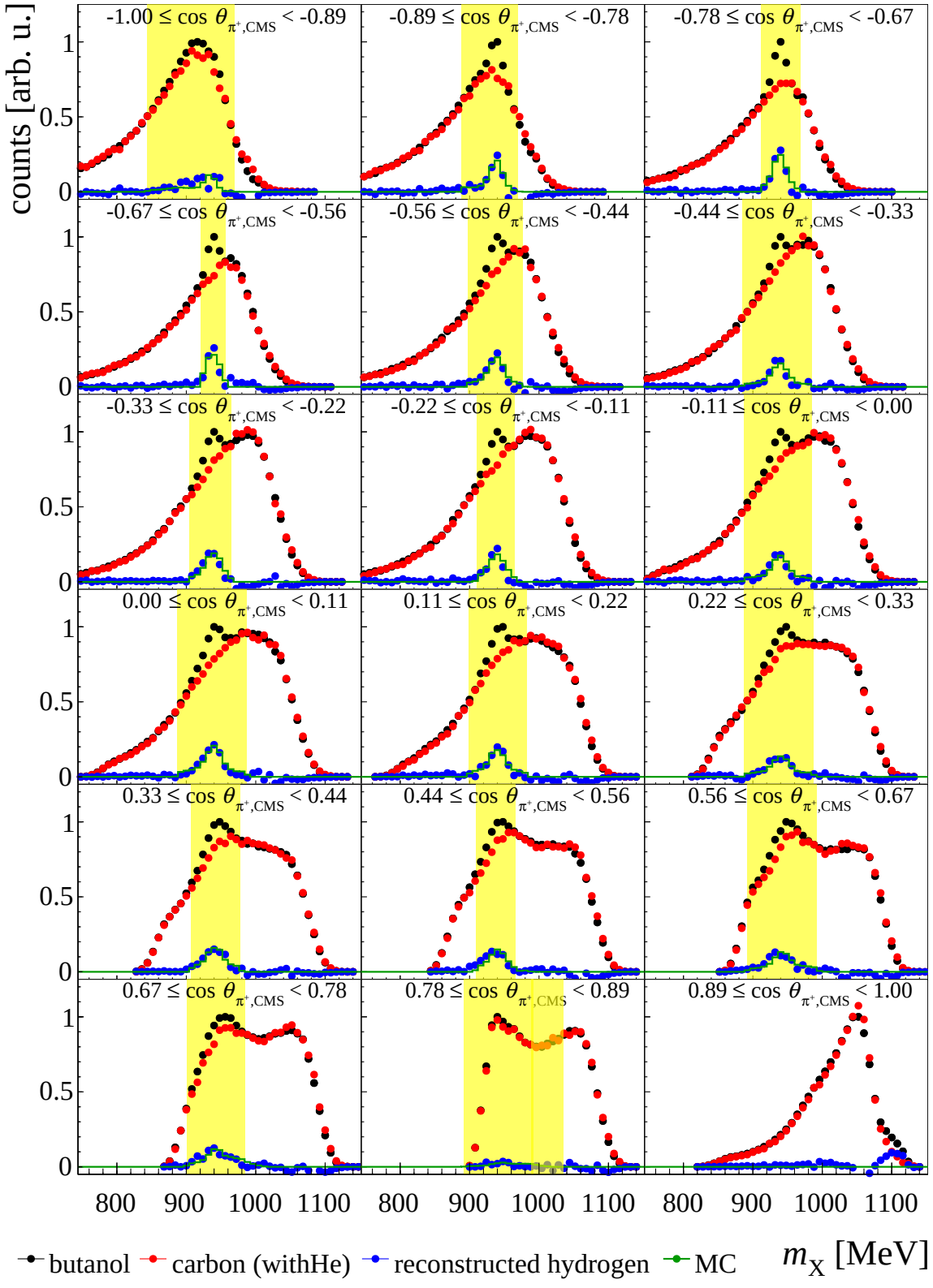

Fig. 7.14: Missing mass distribution for E_γ = (400-434) MeV for the $n\pi^+$ final state. The missing mass distributions of the 1 PED events after all other cuts are shown as a function of $\cos\theta_{\pi^+,\mathrm{CMS}}$ for a given beam photon energy range for the $n\pi^+$ final state. The yellow area hereby indicates the 2σ selection range.

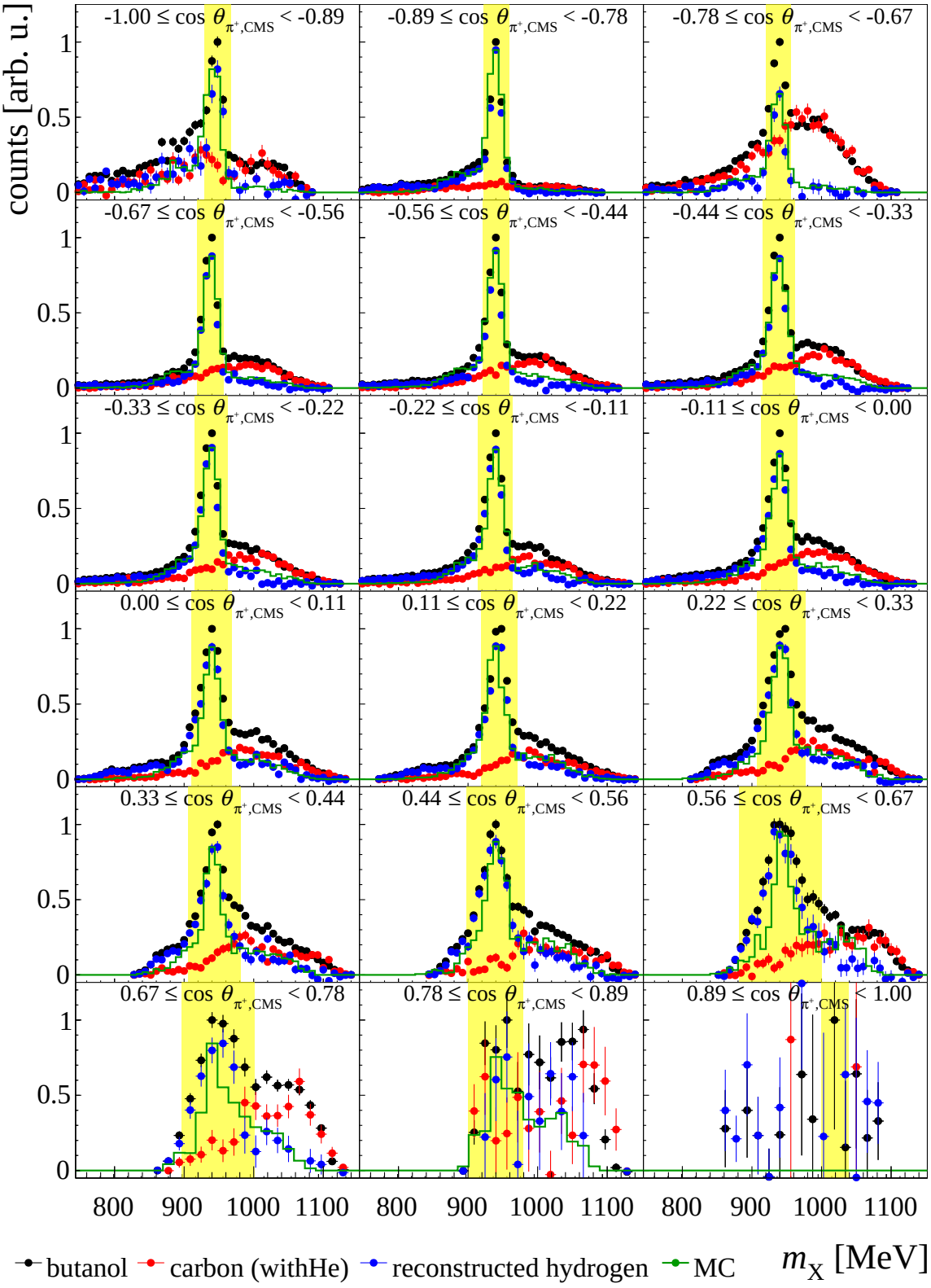

Fig. 7.15: Missing mass distribution for E_γ = (400-434) MeV for the $n\pi^+$ final state. The missing mass distributions of the 2 PED events after all other cuts are shown as a function of $\cos\theta_{\pi^+,\mathrm{CMS}}$ for a given beam photon energy range for the $n\pi^+$ final state. The yellow area hereby indicates the 2σ selection range.

7.7.3 Coplanarity

Fig. 7.16 shows on the left side the coplanarity distribution after all cuts as a function of the incoming beam photon energy E_γ and integrated over the variable $\cos\theta_{\pi,\mathrm{CMS}}$ for the butanol target. On the right side, the same distributions are presented as a function of $\cos\theta_{\pi,\mathrm{CMS}}$ and for a beam photon energy from 400 MeV to 434 MeV. The upper row belongs to the results of the $p\pi^0$ channel whereas the lower one to the 2 PED events of the $n\pi^+$ channel. A peak at about 180° can be seen. However, due

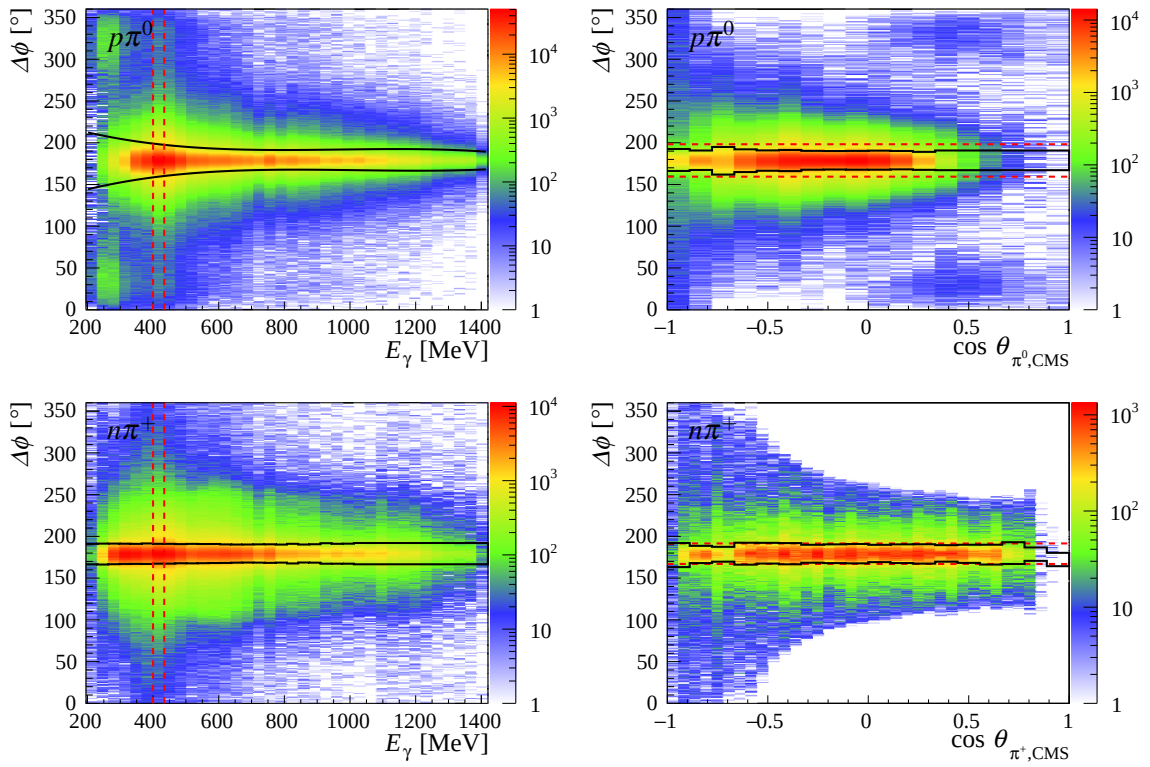

Fig. 7.16: Coplanarity distribution of the butanol data as a function of the beam photon energy E_γ and as a function of $\cos\theta_{\pi,\mathrm{CMS}}$. On the left side, the coplanarity distribution is plotted as a function of the beam photon energy E_γ and integrated over the full angular coverage range. The 2-dimensional cut criteria limits are determined for each beam photon energy and are indicated by the black line. On the right side, the $\cos\theta_{\pi,\mathrm{CMS}}$ dependent missing mass is illustrated for the beam photon energy range from 400 MeV to 434 MeV. The horizontal red dashed lines in the figure on the left hereby indicate the selected beam photon energy range. The dashed red line in the figure on the right shows the corresponding energy-dependent selection criteria whereas the black solid lines the $\cos\theta$ dependent. Note that all other cuts which are presented in this chapter are applied to these data.

to the internal holding magnetic field of the target and thus the deflection of charged particles, the maximum is not exactly located at 180°. Detailed studies with MC simulations, which have included the magnet field, revealed a deflection of the actual azimuthal angle of charged particle of about 0.6° for protons and 1° for charged pions. For further details, see App. A.2. The overall distribution is broader at lower beam photon energies compared to higher energies. The width dependence can be explained by the fact that the pion and the nucleon are low energetic at low beam photon energies

and thus are creating small clusters. As a result, the resolution in ϕ decreases which leads to a broader distribution. In addition, the sin θ dependence of the ϕ-resolution of the CB and the different resolutions of the CB and the TAPS play an important role. Finally, multiple scattering of the proton and the charged pion inside the target cause higher deflection angles. The inspection of Fig. 7.16 on the right side for the $p\pi^0$ channel reveals an additional very small enhancement at about 10° and 350° for $\cos\theta_{\pi^0,\mathrm{CMS}} > 0$. It has been found that these are caused by combinatorial background where the proton was falsely identified as a photon [14]. These events can be completely rejected in the analysis by the selection criteria which are indicated by the black and red lines in Fig. 7.16.
The different ϕ-distributions for a beam photon energy from 400 MeV to 434 MeV as a function of $\cos\theta_{\pi,\mathrm{CMS}}$ after all cuts is shown in Fig. 7.17 for the $p\pi^0$ channel and in Fig. 7.18 for the $n\pi^+$ channel. The nucleons in the butanol target carry a finite momentum and thus affect the kinematics which results in a broader ϕ-distribution. This effect is bigger for reactions on bound carbon/oxygen nucleons inside the butanol target due to their additional Fermi momentum. Consequently, the boundary conditions are determined by fitting a Gaussian distribution to the reconstructed hydrogen distribution and by selecting a 2σ range around the mean value. By that, a huge amount of the reaction on the bound nucleons can be rejected. The reconstructed hydrogen distributions are again compared with MC simulations for the signal reactions and are in very good agreement with each other. Note that for the $p\pi^0$ channel above $\cos\theta_{\pi^0,\mathrm{CMS}} > 0.22$ nearly no 3 PED events are present anymore and thus 2 PED need to be included in the analysis.

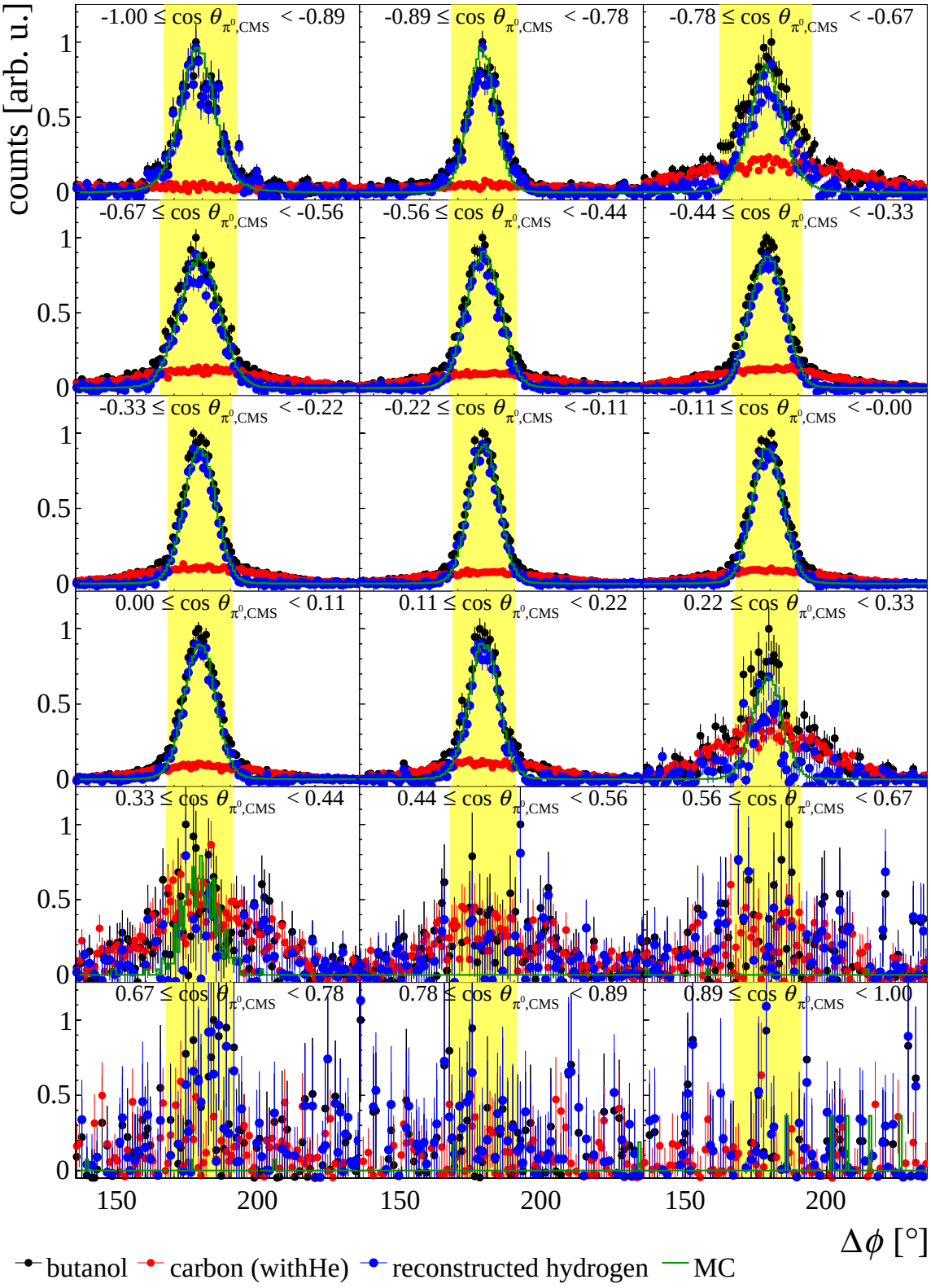

Fig. 7.17: Coplanarity distribution for E_γ = (400-434) MeV for the $p\pi^0$ final state. The coplanarity distributions after all other cuts are shown as a function of $\cos\theta_{\pi^0,\mathrm{CMS}}$ for a given beam photon energy range for the $p\pi^0$ final state. The yellow area hereby indicates the 2σ selection range.

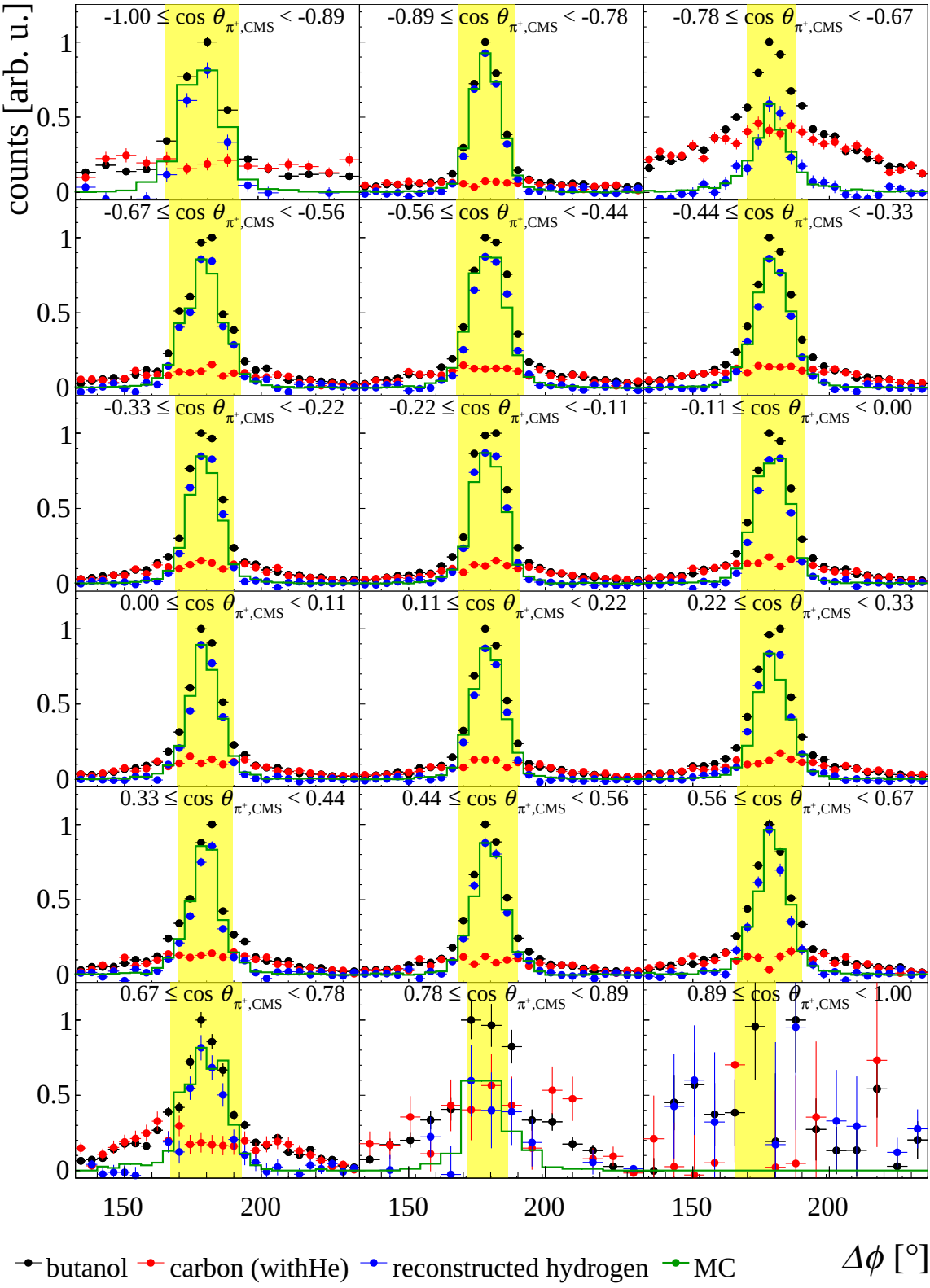

Fig. 7.18: Coplanarity distribution for E_γ = (400-434) MeV for the $n\pi^+$ final state. The coplanarity distributions after all other cuts are shown as a function of $\cos\theta_{\pi^+,\mathrm{CMS}}$ for a given beam photon energy range for the $n\pi^+$ final state. The yellow area hereby indicates the 2σ selection range.

7.7.4 Polar Angle of the Nucleon

Fig. 7.19 shows the $\Delta\theta_N$ distribution distribution after all cuts as a function of the incoming beam photon energy E_γ and integrated over the variable $\cos\theta_{\pi,\mathrm{CMS}}$ for the butanol target on the left side. On the right side, the same distributions are presented as a function of $\cos\theta_{\pi,\mathrm{CMS}}$ and for a beam photon energy from 400 MeV to 434 MeV. The upper row belongs to the results of the $p\pi^0$ channel whereas the lower one to the 2 PED events of the $n\pi^+$ channel.

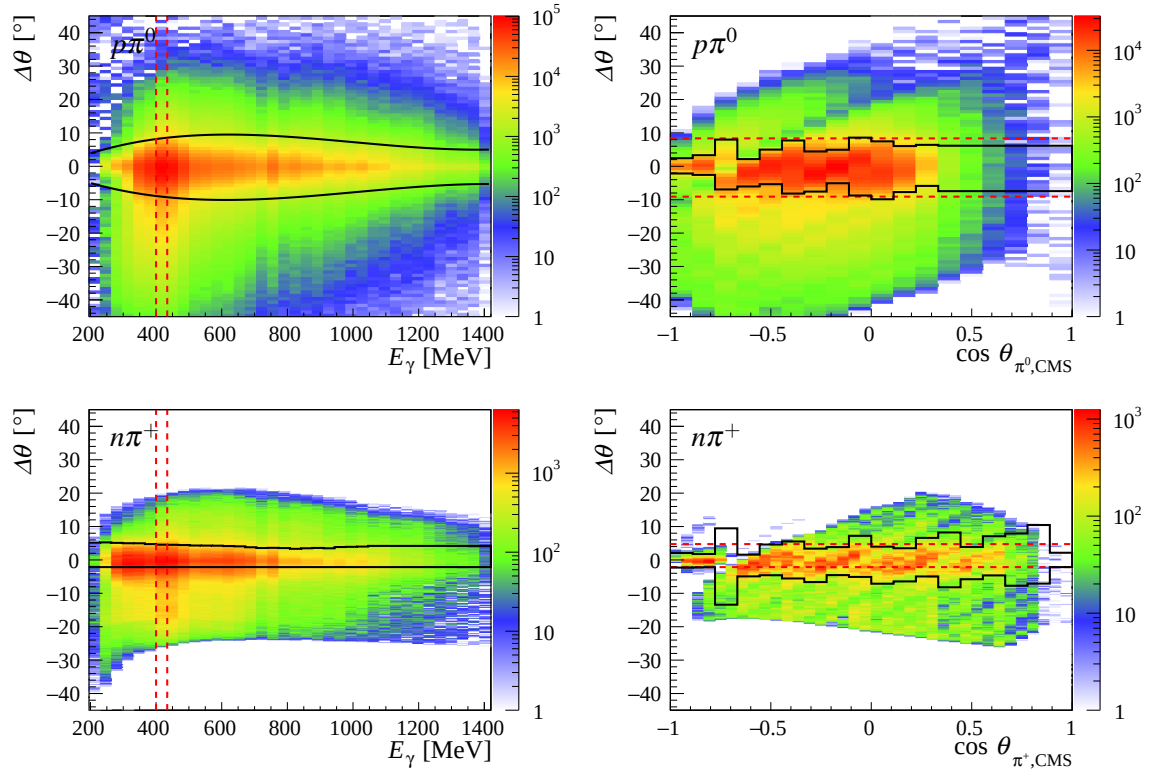

Fig. 7.19: $\Delta\theta_N$ distribution of the butanol data as a function of the beam photon energy E_γ and as a function of cos $\theta_{\pi,\mathrm{CMS}}$. On the left side, the $\Delta\theta_N$ distribution is plotted as a function of the beam photon energy E_γ and integrated over the full angular coverage range. The 2-dimensional cut criteria limits are determined for each beam photon energy and are indicated by the black line. On the right side, the $\cos\theta_{\pi,\mathrm{CMS}}$ dependent $\Delta\theta_N$ distribution is illustrated for the beam photon energy range from 400 MeV to 434 MeV. The horizontal red dashed lines in the figure on the left hereby indicate the selected beam photon energy range. The dashed red line in the figure on the right shows the corresponding energy-dependent selection criteria whereas the black solid lines the $\cos\theta$ dependent. Note that all other cuts which are presented in this chapter are applied to these data.

A deviation from 0° in the polar angular difference is seen which can be explained by the target center position. Detail studies can be found in Sec. 8.1.2.3 and App. A.3. The importance of a 3-dimensional selection is already visible in the selection criteria which are included in Fig. 7.19. The different $\Delta\theta_N$ distributions for a beam photon energy from 400 MeV to 434 MeV as a function of $\cos\theta_{\pi,\mathrm{CMS}}$ after all cuts is shown in Fig. 7.21 for the $p\pi^0$ channel and in Fig. 7.22 for the $n\pi^+$ channel. Of special interest is the transition region between the CB and the TAPS which can be seen in the third $\cos\theta_{\pi,\mathrm{CMS}}$ bin

and in more details in Fig. 7.20 where the energy and $\cos\theta_{\pi,\mathrm{CMS}}$ dependence is shown as a function of the polar angle of the proton in the $p\pi^0$ channel[6]. A well defined double-peak structure is visible which is caused by the fact that the calculated nucleon polar angle is determined within the gap region between the CB and the TAPS whereas the true nucleon is detected to some parts in the outer rings of the TAPS or the entrance area of the CB.

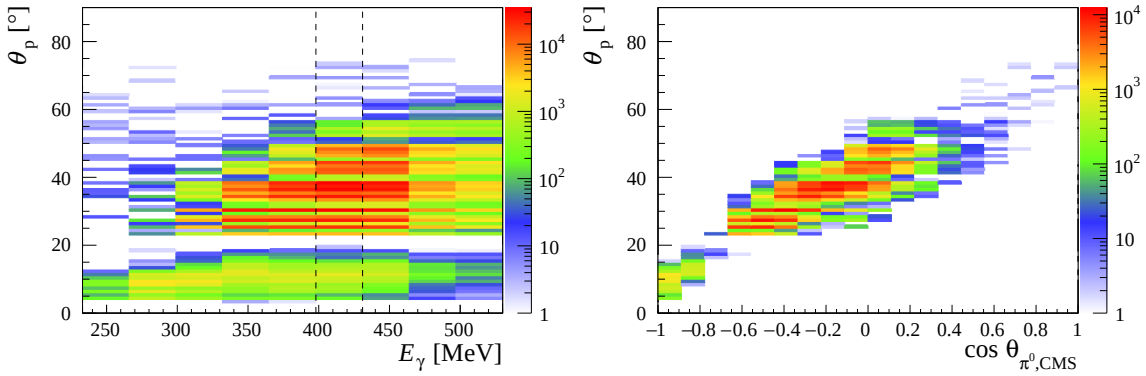

Fig. 7.20: Polar angle of the proton in the $p\pi^0$ channel. Shown is the polar angle Θ_p as a function of the beam photon energy E_γ on the left and on the right side as a function of $\cos\theta_{\pi^0,\mathrm{CMS}}$ for a beam photon energy range from 400 MeV to 434 MeV.

A further source of a double peak structure is the small cluster size of the nucleons. This is even more pronounced for the $n\pi^+$ channel as the neutron makes smaller cluster sizes compared to the proton. The two peaks are mostly seen for events where the nucleons deposit their whole energy in one crystal. By that, the impact point is reconstructed at the center of the crystal although the actual impact point could be at the edges of the crystals. In addition to the double peak structure, the $\Delta\theta_N$ distribution shows a 3-dimensional width dependence. This can be explained by the different detector resolution where the particles are detected. The polar angular resolution of the TAPS is better than the CB and thus shows as well a narrower $\Delta\theta$ distribution for $\cos\theta_{\pi,\mathrm{CMS}} < -0.78$. Finally, as for the calculation of the calculated nucleon angle, the initial proton was assumed to be at rest and bound nucleons inside the butanol target carry additional Fermi momentum, the $\Delta\theta_N$ distribution provides a good separation between the reaction on bound and unbound nucleons. Since the distribution can not be described by a Gaussian distribution, the boundary conditions are taken from the confidence interval method. By that, a huge amount of the reaction on the bound nucleons can be rejected. The reconstructed hydrogen distributions are again compared with MC simulations for the signal reaction and are in very good agreement with each other. Only small differences are visible between data and MC in the third $\cos\theta_{\pi,\mathrm{CMS}}$ bin. This can be explained by the tunnel region of the CB which is not perfectly included in the simulations. In detail, material is missing in the tunnel region and thus the amount of detected particles in this region differs between data and MC simulations. Investigations of solving this problem are ongoing [77].

[6]Similar behavior is seen for the neutron in the $n\pi^+$ channel.

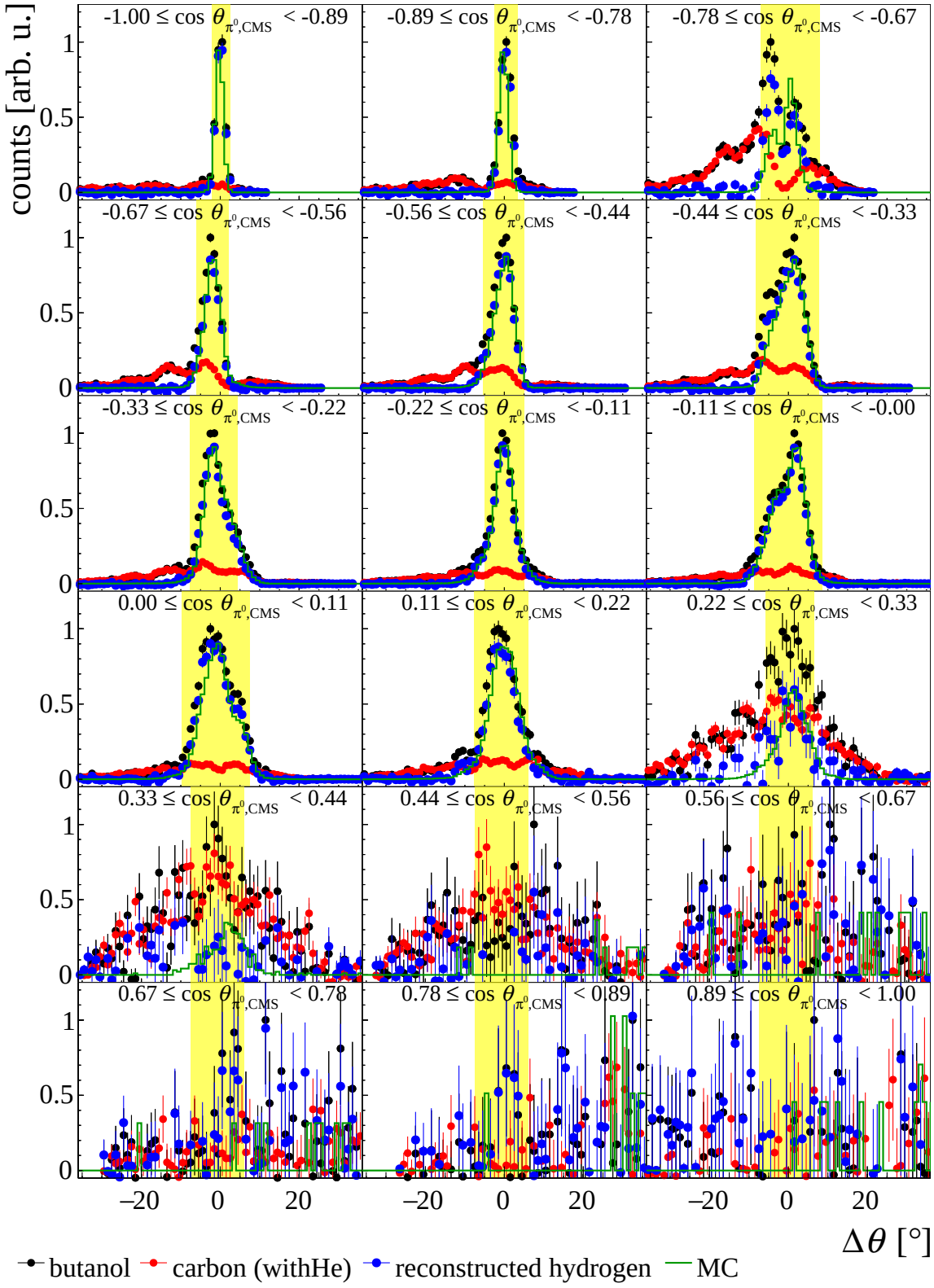

Fig. 7.21: $\Delta\theta_p$ distribution for E_γ = (400-434) MeV for the $p\pi^0$ final state. Shown are the $\Delta\theta_p$ distributions after all other cuts as a function of $\cos\theta_{\pi^0,\mathrm{CMS}}$ for a given beam photon energy range for the $p\pi^0$ final state. The yellow area hereby indicates the 2σ selection range.

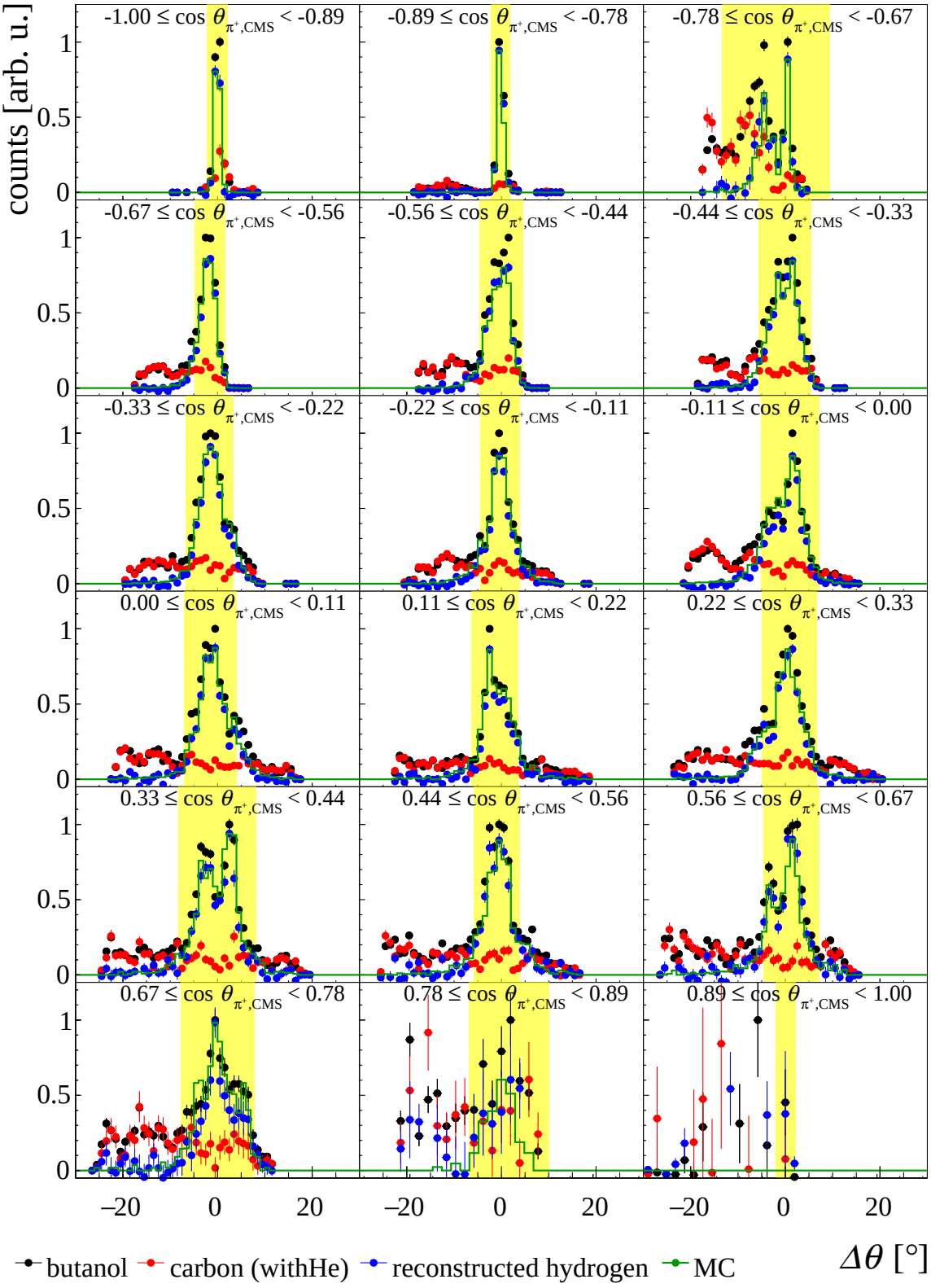

Fig. 7.22: $\Delta\theta_n$ distribution for E_γ = (400-434) MeV for the $n\pi^+$ final state. Shown are the $\Delta\theta_n$ distributions after all other cuts as a function of $\cos\theta_{\pi^+,\mathrm{CMS}}$ for a given beam photon energy range for the $n\pi^+$ final state. The yellow area hereby indicates the 2σ selection range.

7.8 Further Selection Cuts

7.8.1 Cluster Size

Whereas photons deposit their energy mostly via pair production and a cascading electromagnetic shower, the nucleons interact with the crystals via ionization and hadronic interactions. Therefore, the cluster sizes of photons are larger compared to the ones of nucleons and charged pions. This is illustrated in Fig. 7.23 where the cluster sizes of the individual particles are plotted as a function of their detector in which they have been detected.

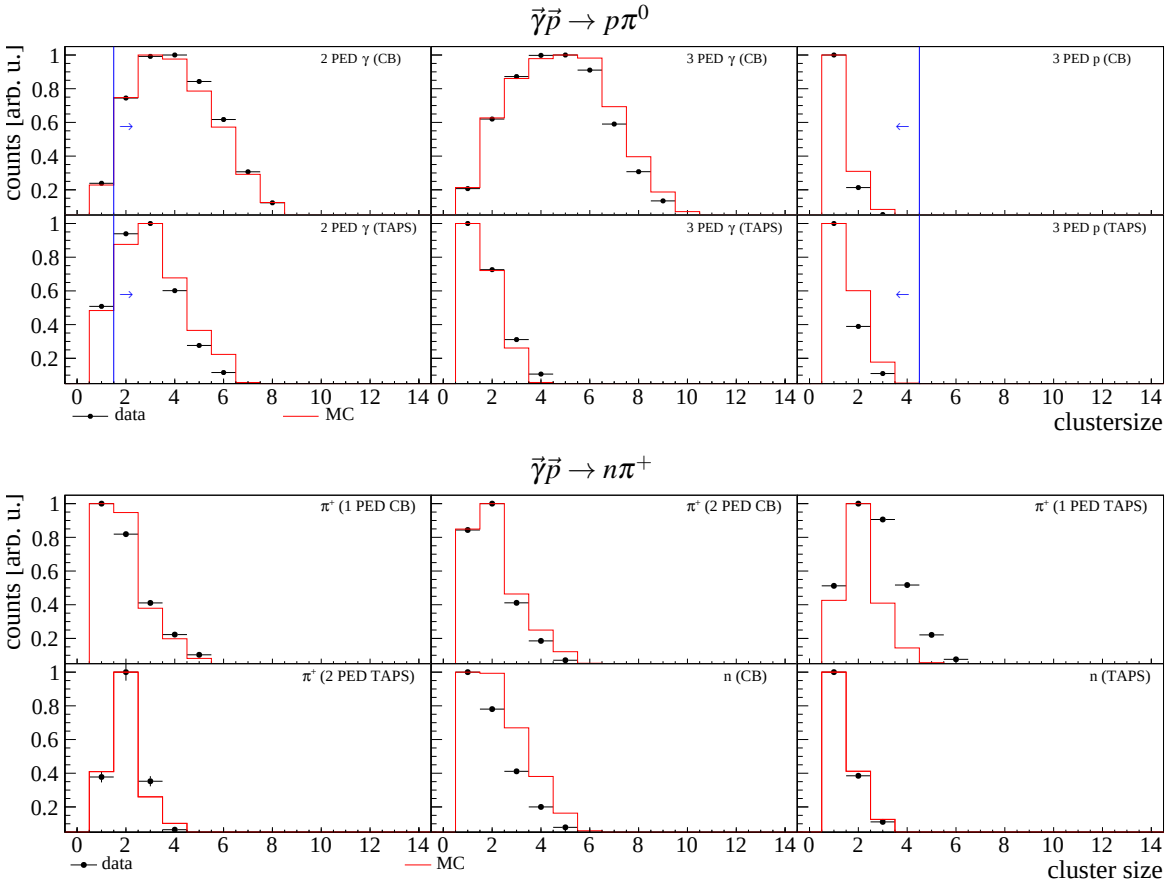

Fig. 7.23: Cluster sizes of different final state particles. Shown are the cluster sizes in black of the butanol data for the different particle candidates and as a function of the detector in which they have been detected. The upper two rows present the result for the $p\pi^0$ final state whereas the lower two ones for the $n\pi^+$ final state. The data are compared with their corresponding signal MC in red. The minimum or maximum cluster size is indicated by the blue line and the direction of the arrow.

Inspecting the detector dependence of the cluster sizes, the cluster sizes in the CB are in general a bit larger than the ones in the TAPS. This can be explained by the individual CFD/LED thresholds of the detectors. The CB had mostly LED thresholds in the region of 2 MeV and the TAPS CFD thresholds of 5 MeV. The data are compared to simulations and are in general in good agreement with the data. Difference between both can be traced back to a not exact matching of the CFD/LED thresholds of the

crystal, a not perfect adjusted CB energy sum trigger and especially in the $n\pi^+$ channel a not perfect description of the interaction of neutrons and charged pions in the crystals. Due to these problems, no cut on the maximum cluster size was applied. Comparing the cluster sizes of both analyzed channel, a high contribution of photons in the $n\pi^+$ final state, e.g., from the decay of the π^0 of the background channels $p\pi^0$ and $n\pi^+\pi^0$, can be ruled out. On the other hand, to reject contributions of the $n\pi^+$ final state in the 2 PED analysis of the $p\pi^0$ channel, a minimum cluster size of two is applied for the photon candidates.

7.8.2 Pulse-Shape Analysis (PSA)

As already described in previous chapters, the PSA technique can be used to distinguish nucleons from photons in the TAPS. The calibration of the short gate component of the TAPS BaF_2 crystals (cf. Sec. 6.1.4) ensures that photons are located at a PSA angle of $\phi_{\mathrm{PSA}} = 45°$ over the entire range of the PSA radius r_{PSA}. Therefore, the selection can be optimized by looking at the PSA technique of the selected photon candidates which are shown in Fig. 7.24 for the butanol data.

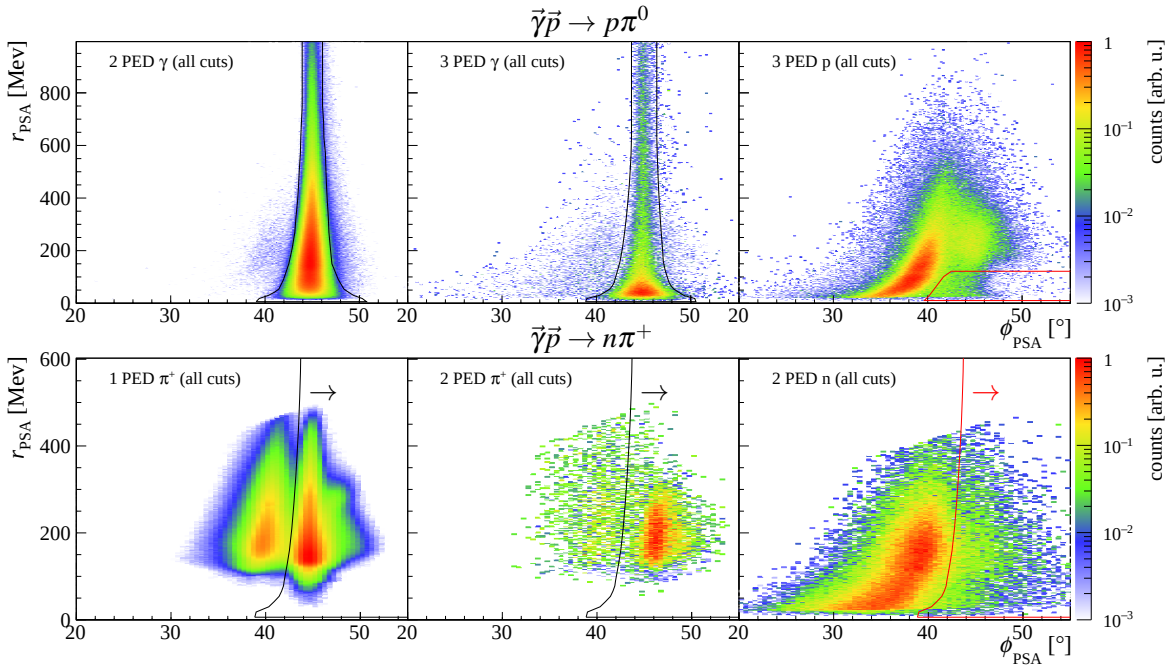

Fig. 7.24: Pulse-Shape-analysis (PSA) for the particle identification. Shown are the PSA spectra of the butanol data for the different particles and different channels. The upper row illustrates the photons and protons of the $p\pi^0$ final state whereas the lower row the once of the charged pion and the neutrons of the $n\pi^+$ final state. The black lines indicate a selection region whereas the red once a rejection region.

In the same way, the nucleon candidate can be identified by requiring a PSA behavior which is not compatible with the one of a photon candidate. The red areas in the corresponding PSA spectra of the proton and the neutron hereby indicate a rejection area for the nucleon candidates as here contribution of photons are expected. With that knowledge, not only the combinatorial background can be studied

for the 3 PED events of the $p\pi^0$ channel but also background reactions like $\vec{\gamma}\vec{p} \to n\pi^+$ in the 2 PED analysis. Comparing all distributions, a minimum number of neutrons contaminate the PSA spectra of the photons and vice versa. Similar argumentation holds for the combinatorial background. As no clear structure of the proton is seen, no combinatorial background is present as well[7]. Nevertheless, to select only photons in the $p\pi^0$ channel, the PSA angle is fitted with a Gaussian function as a function of the PSA radii. The resulting 2σ ranges are indicated by the black curve and are used as a selection criterion to reject any falsely identified particles.
For the identification of the proton it is important to note that the PSA technique can only be used to identify proton candidates if their kinetic energy is below the punch-through region. Above the punch-through region, as has been shown in [97, 14], the PSA band structure of protons crosses the one of the photons and consequently a discrimination of photons and protons is not possible.
The PSA behavior of the charged pions for the 1 PED events contains two structures that are well separated. To study the behavior of the π^+, the PSA spectra was investigated with the $\Delta E - E$ plot (see Sec. 7.9.1). Although the $\Delta E - E$ plot is only used as a cross-check, two data sets were built. In the first one, only events within the proton band were analyzed whereas in the second one only events in the pion band. As it turned out, the PSA spectra of the second set selected all the events which behave similarly to the photons. On the other hand, as expected, the first set selected the proton band structure which can be seen for the proton candidate in the $p\pi^0$ channel. Thus, to only select the π^+ candidates and reject the proton candidates, the left half of the photon band selection range is used which is indicated by the black curve. The cut to the right side of the Gaussian fit is not used because the pions, similar to the protons, can also punch through the detector which result in higher pulse shape angles. In fact, simulations and the data analysis have shown that nearly all π^+ of the 2 PED events in the TAPS are punch through particles that explain the straight line enhancement seen at about an angle of 47°. Contribution of proton can be rejected here as well by the same cut as for the 1 PED events. However, it is noteworthy that even punch through protons still might be contained in the enhancement. Their contribution is nevertheless assumed to be rather small as protons show a much broader enhancement compared to the pions.

7.8.3 Time-Of-Flight Analysis (TOF)

The Time-Of-Flight analysis is very useful to distinguish between massive charged particles and photons in the TAPS. The distance of the TAPS elements to the target center of about 180 cm in combination with a very good time resolution of the BaF_2 crystals, is perfectly suited to perform a TOF analysis. In contrast, the CB with only a distance of about 45 cm to the target center and a time resolution, which is roughly by a factor eight worse than TAPS time resolution (cf. Sec. 6.4), does not provide a good enough flight path distance and time resolution to distinguish between massive charged particles and photons.

[7] An additional check with simulations also has proven that in less than 1% of all signal events the proton was misidentified as a photon. Consequently, the charge information of the particles is not required for the $p\pi^0$ analysis.

To perform the TOF analysis, the deposited energy in the TAPS is plotted as a function of the time time-of-flight t_{TOF} which is given by:

$$t_{\mathrm{TOF}} = \frac{\Delta t}{s} + \frac{1}{c}, \tag{7.11}$$

where c is the speed of light, s is the flight path distance, and Δt is the time difference between the detected particle in the TAPS and the corresponding tagged beam photon[8]. Note that the 'time'-of-flight has not the unit s but is normalized with the flight path distance which leads to the unit $\frac{\mathrm{ns}}{\mathrm{m}}$. This is motivated by the fact that the flight path distance of the particles depends on their reconstructed polar angle[9]. Since all time calibrations were performed such that the time difference of photons is located at zero (cf. Sec. 6.2), the additional term $\frac{1}{c}$ ensures that photons are always located at the same position with the correct unit.

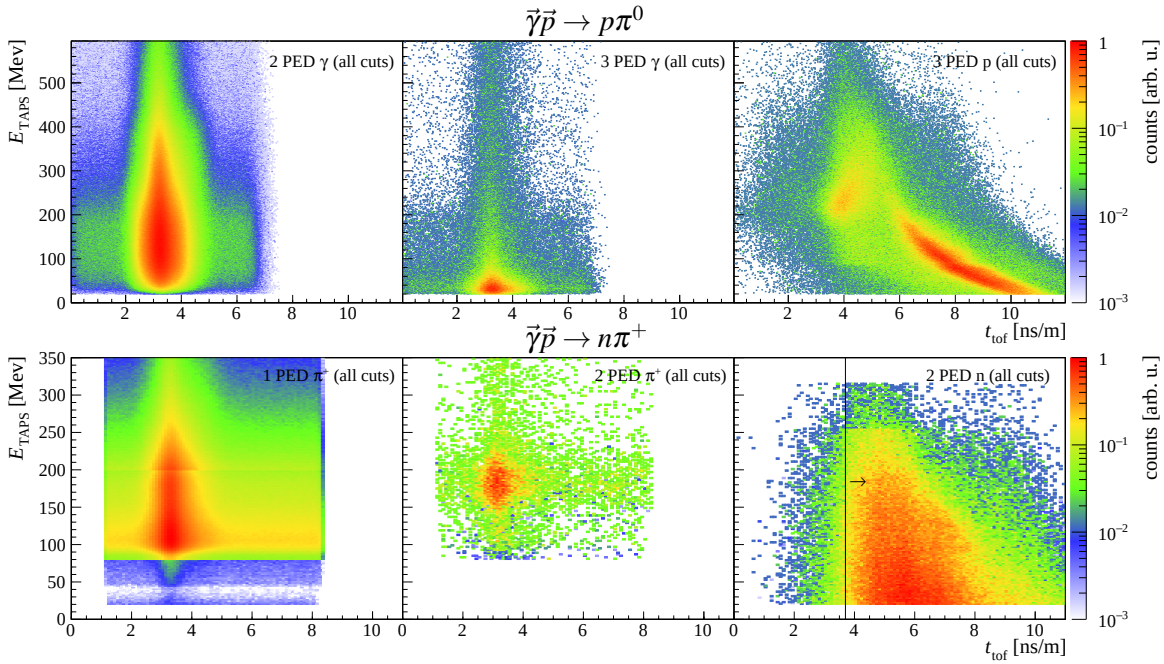

Fig. 7.25: Time-of-Flight Analysis (TOF) for the particle identification. Shown are the TOF analysis for the final state particles of the different analyzed channels. The upper row shows the photon and proton candidates in the TAPS for the $p\pi^0$ final state whereas the lower row the charged pion and neutron candidate in the TAPS for the $n\pi^+$ final state.

Fig. 7.25 illustrates the deposited energy in the TAPS as a function of the time time-of-flight t_{TOF} for different kinds of particles. Whereas photons always cause a straight line at about 3.3 $\frac{\mathrm{ns}}{\mathrm{m}}$ over the entire deposited energy range[10], charged particles, like the proton, show a clear energy dependence due to its high rest mass. The clear correlation between the deposited energy and the time-of-flight will be referred as the banana band in the following. With increasing kinetic energy, the time-of-flight

[8] The tagger provides a better time resolution than the CB.

[9] Higher polar angle corresponds to higher flight path distances.

[10] Photons always fly with the speed-of-light and thus do not show any energy dependence.

is getting smaller. Again at a certain kinetic energy, the proton starts to punch through the detector which leads to a deviation from the banana band and a trend towards the photon band. In contrast to the protons, neutrons cause a relatively broad and wide region in the time-of-flight and do not really correlate with their deposited energy. This can be explained by the fact that the neutron energy deposition in the crystals is much more complex than of charged particles. Additional secondary particles, which can be produced in inelastic and elastic scattering or even nuclear reactions, make it impossible to detect the entire initial energy. Nevertheless, although a nice correlation is not seen, a clear separation based on both analyzed channels is still possible between photons and neutrons. As neutron nearly always show a time-of-flight bigger than 3.7 $\frac{\text{ns}}{\text{m}}$, a cut was applied in the $n\pi^+$ channel to reject any contribution of photons in the analyzed.
Unfortunately, as has been shown already with the PSA technique, the pion rest mass of about 140 MeV is not enough to clearly separate pions from photons. Furthermore, due to the correlation of the beam photon with the charged pion[11], the random time background events can not be subtracted from the TOF spectra at all. This time background is, due to the lack of possible angular cuts for the 1 PED events, quite well pronounced and in combination with the huge contribution of carbon any separation cuts for pions is not feasible. Only the punch through pions of the 2 PED events show a clear bump at its punch through energy of about 200 MeV. Nevertheless, these pions are so high energetically that they nearly fly with speed of light and thus can not be distinguished from photons and protons at all.
In total, the TOF analysis does not help to distinguish protons and pions, especially for the 1 PED events of the $n\pi^+$ channel. Nevertheless, the TOF can be used to distinguish between photons and nucleons which helps to reject any contribution of photons from the $p\pi^0$ channel in the TAPS.

7.9 Quality of Event Selection

7.9.1 $\Delta E - E$ plot analysis

As mentioned in Sec. 2.4.2, the $\Delta E - E$ plot analysis can be used to distinguish different kinds of charged particles. For charged particles in the acceptance region of the CB, the technique makes use of the fact that electrons, charged pions, and protons deposit a different amount of their kinetic energy ΔE in the plastic scintillators of the PID. In the TAPS acceptance region, the deposited energy in the Veto Wall is used as a reference. The correlation with the cluster energy E is presented in Fig. 7.26 for both acceptance regions (CB and TAPS) and both charged particle candidates. Whereas the top row shows the figure with no applied cuts, the bottom row includes all previously mentioned cuts. Hereby, the second row corresponds to the proton candidate in the $p\pi^0$ final state whereas the remaining two to the charged pion candidate in the $n\pi^+$ final state.

[11] This explains also the reason why the TOF spectra is cut off at 8 ns because only the events in the time coincidence time window and the sidebands are analyzed.

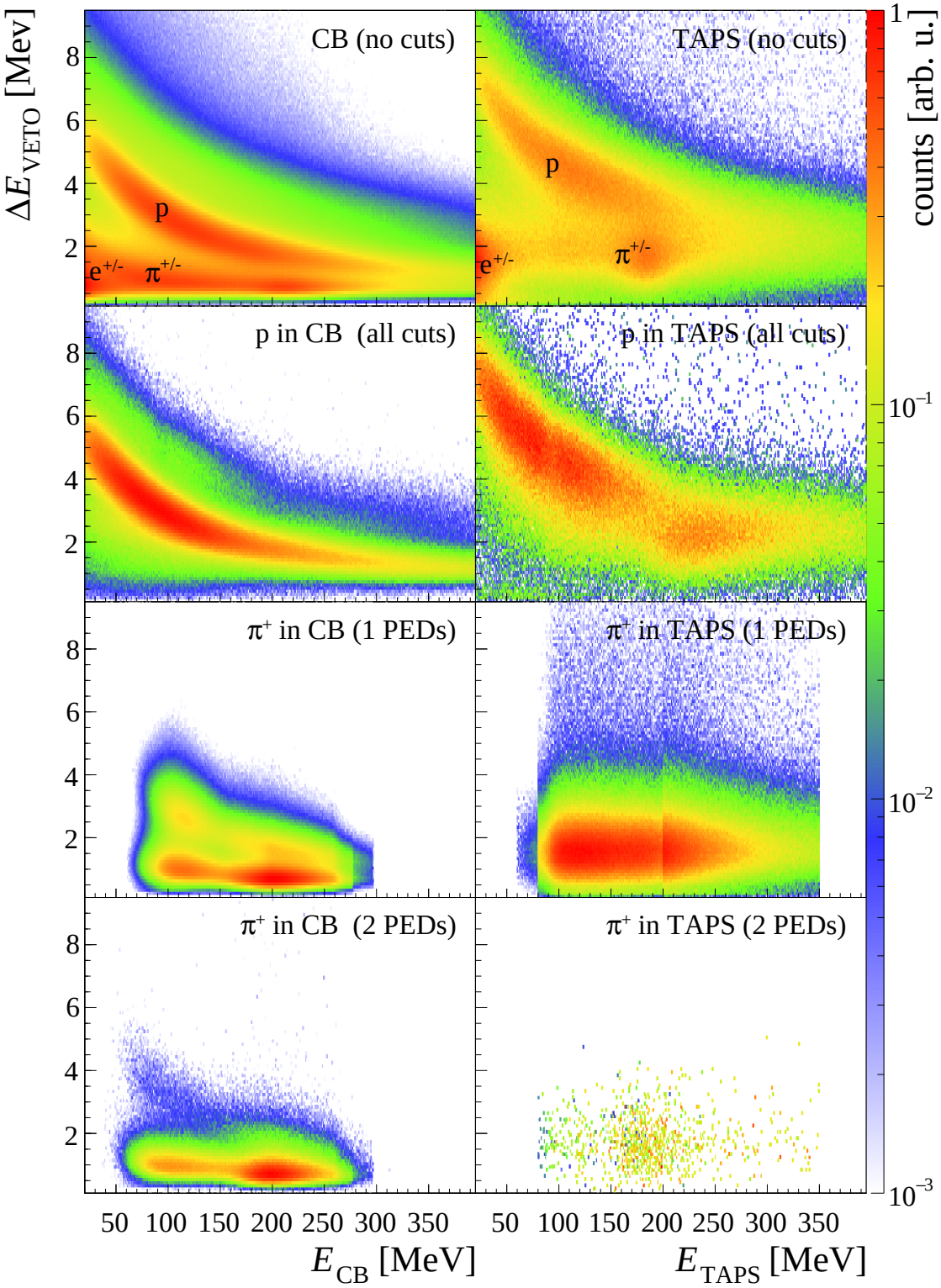

Fig. 7.26: ΔE - E plots for both analyzed channels. Shown are the $\Delta E - E$ plots for both acceptance regions (CB and TAPS) and for the different charged particles. Whereas the top row presents the case for no selected events, the second row corresponds to the proton candidate in the $p\pi^0$ analysis. The remaining ones illustrate the plots for the charged pion in the $n\pi^+$ analysis and for the different event patterns.

In the upper $\Delta E - E$ plot, three different main structures can be seen and are indicated within the plot. As protons are much more massive than electrons and charged pions, more energy is deposited in the PID/Veto Wall. Therefore, the band structure, which starts at low energies in the main calorimeters and high PID/Veto Wall energies, corresponds to detected protons and shows a strong energy dependence. An additional band is visible at lower PID/Veto Wall energies and has only a small energy dependence. This band corresponds to charged pions. It's low deposited energy in the PID/Veto Wall in combination with its small energy dependence can be explained by the fact that charged pions are almost always minimal ionizing particles in the detected kinetic energy region[12]. Furthermore, as shown in Sec. 6.3.4, charged pions punch through the detector at energies of about 180 MeV and thus cause an additional enhancement in the pion band. The enhancement at very low kinetic energies and PID/Veto Wall corresponds to electrons.

As has been already mentioned in Sec. 4.3.2, the PID was not working identically good in all beamtimes. In addition, it has been found that the overall resolution of the PID suffered from the internal holding magnetic field of the target. More details can be found in [125]. All the different problems in combination with the overall bad resolution lead to the decision to only use the $\Delta E - E$ plot as a cross-check of the quality of the selection. This is as well justified by the fact that a cut on the $\Delta E - E$ plot requires that the $\Delta E - E$ plot behaves similarly for the butanol and carbon beamtimes. As this is not the case, the contribution of the carbon/oxygen/helium inside the butanol is not selected correctly which results in a wrong carbon subtraction. Nevertheless, for the proton candidate in the $p\pi^0$ analysis, the $\Delta E - E$ plot contains only the proton band even though a charged particle was not required which emphasizes again the good selection of the 3 PED events. For the $n\pi^+$ final state, the charge information is used but again a cut on the spectra is not applied. At first sight, it seems that the selection is not good enough to reject protons in the CB as a clear banana band structure of the protons is still seen after all cuts. However, all $\Delta E - E$ plots are shown for the butanol data and integrated over all other variables. In addition, especially the 1 PED events have a huge contribution of reactions on the bound protons inside the butanol data. Thus, the $\Delta E - E$ spectra was carbon subtracted and plotted as a function of the beam photon energy. The carbon subtracted $\Delta E - E$ plot for the $n\pi^+$ final state of both event pattern are given in Fig. 7.28 whereas an example for the carbon subtraction method is presented in Fig. 7.27. The carbon subtraction was performed for each beam photon energy bin and the carbon scaling factor was taken from the energy-dependent scaling of the missing mass distribution for the 1 PED events and the coplanarity distribution for the 2 PED events. As can be seen from Fig. 7.27, the whole proton band can be described by the bound components inside the butanol target. As these are all unpolarized, they do not contribute as background contamination in the extraction of the double polarization observables G and E. A small remnant of the proton band in Fig. 7.28 is more likely due to a not perfect matching calibration of the butanol and carbon with helium data. As a final step, background contamination from reactions with an identified charged pion in the final state need to be investigated.

[12] Protons behave only like minimal ionizing particles at kinetic energies above 300 MeV.

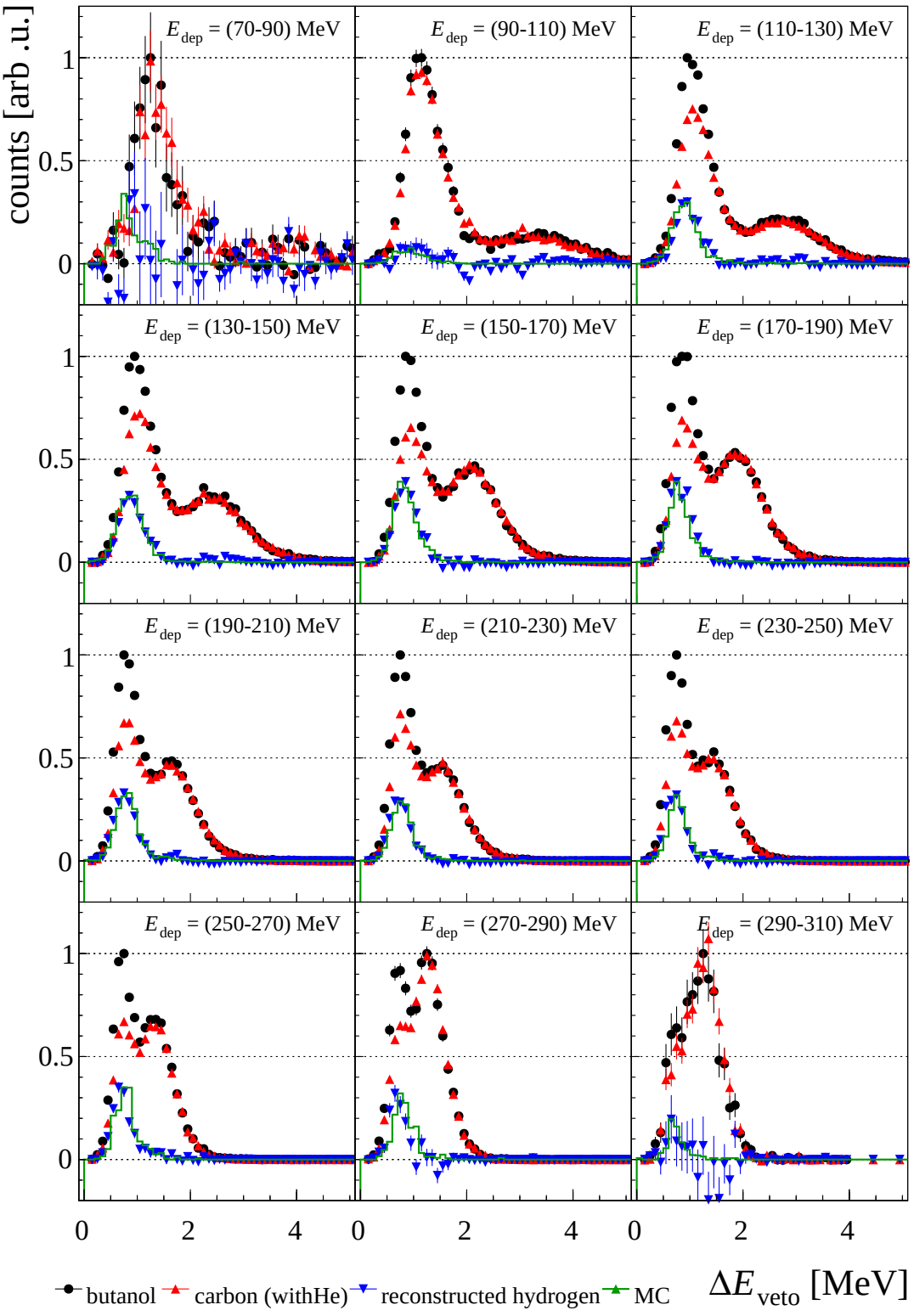

Fig. 7.27: ΔE - E projections. Shown are the y-projections for the $\Delta E - E$ plots for a beam photon energy from 400 MeV to 434 MeV. The $\Delta E - E$ correspond to the 1 PED events of the $n\pi^+$ channel. The carbon with helium distribution (red) was scaled to the butanol distribution (black) to obtain the reconstructed hydrogen distribution (blue). Thereby, the beam photon energy dependent scaling factor of the dilution factor was used to properly scale the carbon. The reconstructed hydrogen distribution is compared to simulations and is in perfect agreement with the data.

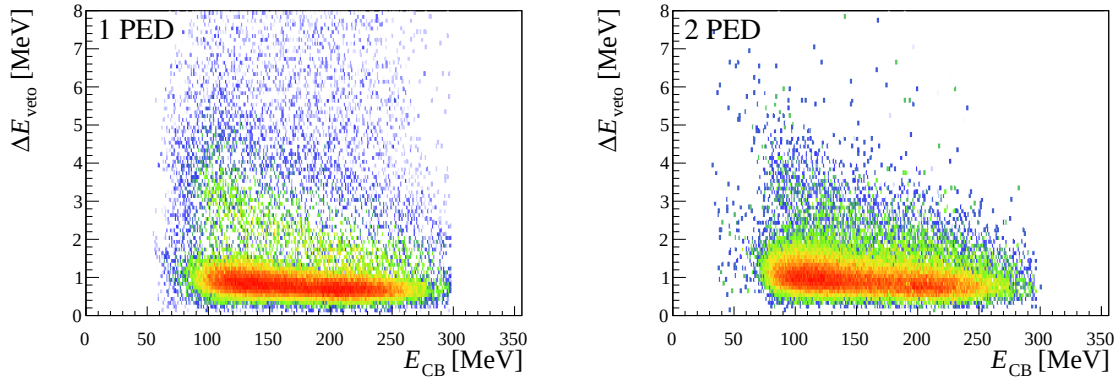

Fig. 7.28: Carbon subtracted ΔE - E plots of the $n\pi^+$ final state. Shown are the carbon subtracted $\Delta E - E$ plots in the CB acceptance regions of the butanol data for the two different event patterns of the $n\pi^+$ final state.

7.9.2 Background Contamination of Other Reactions

A final step is to investigate the background from other reactions which can pass the selection. For the $p\pi^0$ final state, the carbon subtracted invariant mass of the two photons is used to investigate the amount of background in the selected range. Therefore, as a first step, the behavior of all possible background reactions after all cuts was studied. These include the final states $n\pi^+$, $p\pi^+\pi^-$, $n\pi^+\pi^0$, $p\pi^0\pi^0$ and $p\eta$. It has been found that the background beneath the peak of the rest mass of the neutral pion can be modeled by a flat distribution. Thus, the distribution outside the peak range is fitted with a linear fit as can be seen by the red dashed lines in Fig. 7.29 for an energy range from 400 MeV to 434 MeV. The resulting background contamination as a function of the beam photon energy E_γ and the kinematic variable $\cos\theta_{\pi^0,\text{CMS}}$ is depicted in Fig. 7.30. Overall, the background shows nearly no energy dependence and is mostly far below 1%. Only in the high forward direction, where the 2 PED events dominate, bigger values are obtained. This can be traced down to the high amount of electromagnetic background at invariant masses of about 50 MeV (cf. the last bin in Fig. 7.29). Although their contribution below the peak is assumed to be small, the increase towards lower invariant masses affect the quality of the linear fit. Thus, the high amount of background should be treated as an upper limit for the amount of background. Furthermore, the background contamination in high forward directions exceeds 5% in a beam photon region where the extracted polarization observables have such a high statistical uncertainty that an exact knowledge of the amount of background is not further studied.

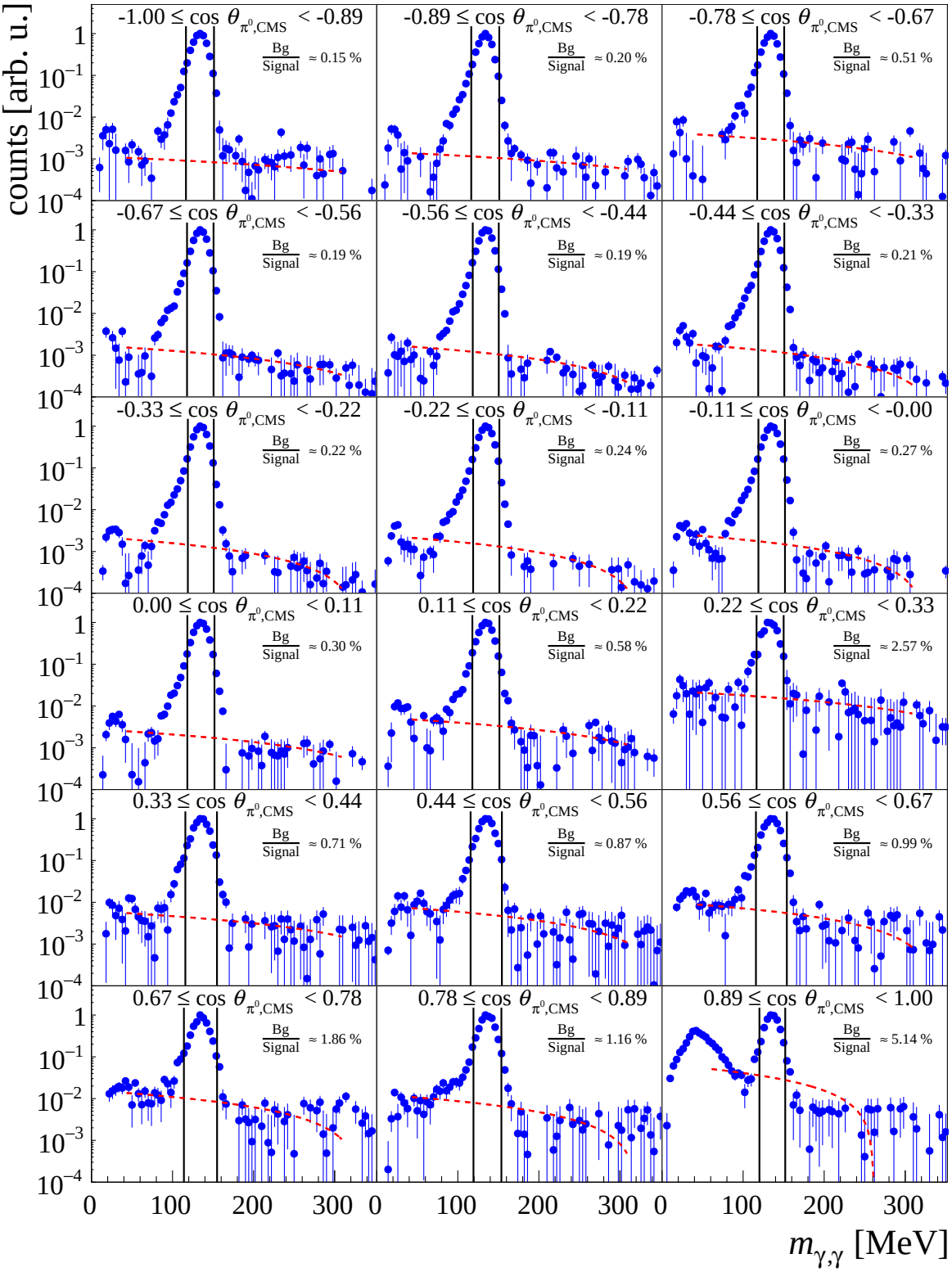

Fig. 7.29: Background estimation for the $p\pi^0$ final state. Shown are reconstructed hydrogen distributions of the invariant mass for a beam photon energy from 400 MeV to 434 MeV. The background contribution is described with a linear fit which is indicated by the red dashed line. The horizontal line indicate the 2σ selection range for which the background contamination is determined.

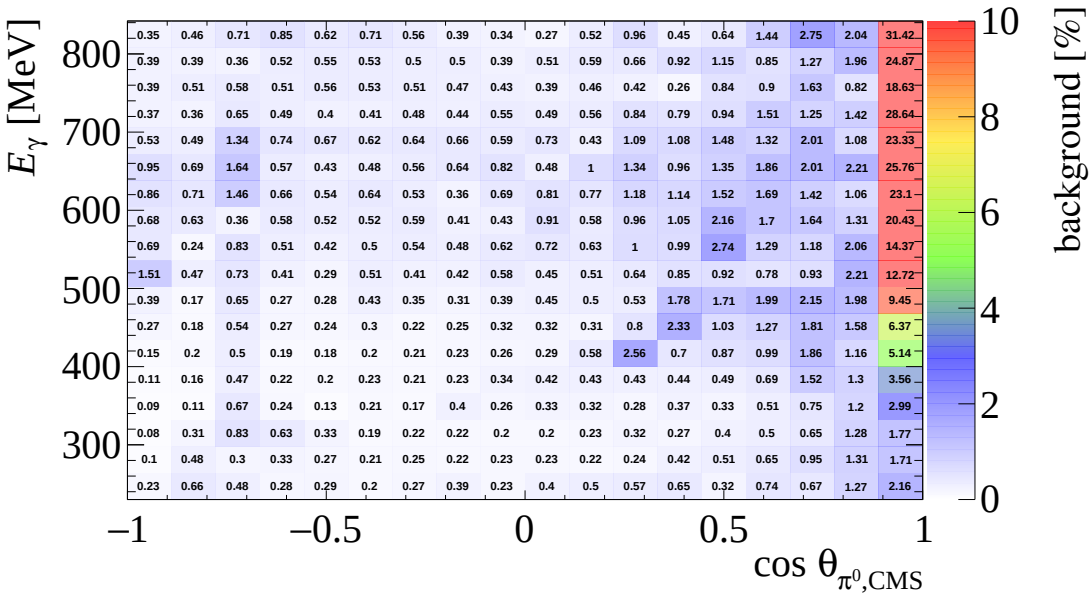

Fig. 7.30: Background contamination for the $p\pi^0$ final state. Shown is the background contamination as a function of the beam photon energy E_γ and the kinematic variable $\cos\theta_{\pi^0,\mathrm{CMS}}$.

For the $n\pi^+$ final state, the situation is a bit more complicated as no clear kinematic cut variables can be selected to determine the amount of background. As has been discussed in Sec. 7.7.2, the contribution of background contamination can be studied by investigating the structure of the missing mass distribution at higher missing masses. A try to fit the reconstructed hydrogen distribution with signal and background MC simulation however failed. This can be traced down to the not perfect matching of the charged pion and neutron interactions between data and MC. This includes a not perfect adjustment of the energy sum threshold, the individual crystal LED thresholds and the charge efficiency adjustments. In addition, the physical interactions are not perfect as well, i.e. the punch through behavior and the deposited energy at all. Nevertheless, the different missing mass distribution could be used to support the upper limit on the amount of background in the selected data. To estimate a value for the upper limit, the acceptance of the background MC reactions are compared to the one of the signal MC (see Fig. 7.31). Together with the approximated magnitude of the total cross section of the individual reactions[13], the ratio of both can give a statement of the size of possible background. As it turned out, the 2 PED events are nearly background free as the angular cuts reject most of the background. Only the $n\pi^+\pi^0$ final state pass these cuts and contribute above 500 MeV with an acceptance ratio in the order of 10^{-3}.

The 1 and 2 PED events have the strongest background contributions by the $n\pi^+\pi^0$ final state. Whereas below 434 MeV the 2 PED events are nearly background free, the 1 PED events have background contributions in the region where the π^+ is detected in higher backward direction ($\cos\theta_{\pi^+,\mathrm{CMS}} < -0.6$). In this kinematic region, the remaining particles either do not have enough energy to be detected or

[13] The total cross section is only an upper limit as the angular dependence should be taken into account as well. This is however not possible as the angular dependence of the background reactions is not well-known.

get lost in the transition region between the CB and the TAPS. However, the ratio of the acceptances is still in the order of 10^{-3} and the total cross section of the $n\pi^+\pi^0$ final state is in the order of only 1 µb [126] whereas the one of the $n\pi^+$ exceeds 100 µb [75]. Thus, as the cross section of $n\pi^+$ is by a factor of 100 bigger, the ratio with the inclusion of the cross section assumptions goes down to even 10^{-5} which is a clear hint to small background contamination in the selected data. Towards higher beam photon energies, the contribution of this channel in backward direction gets even smaller and thus can be ruled out completely. The situation is different towards higher forward angles, as the acceptance ratio increases up to 10^{-2} or even higher. The total cross section for the $n\pi^+\pi^0$ final state exceeds 20 µb at an energy of 600 MeV and has its first maximum with about 50 µb at roughly 750 MeV. Over this whole region, the total cross section of the $n\pi^+$ final state is still in the order of 100 µb. Thus, the cross section ratio is at least 0.5 and together with the acceptance ratio, a contribution above 5% can be ruled out. Furthermore, nearly all pions are punch through particles in that energy region and no clear evidence for a background contribution was seen in the missing mass distributions. Finally, the 1 PED events in this kinematic region are not analyzed. Due to the punch through behavior of the pions, no clear region is available for the carbon scaling and thus a proper determination of the dilution factor d is not possible. As this is however mandatory for both double polarization observables (see Sec. 8.1), these events are excluded from the analysis. Furthermore, this kinematic region is already covered by the 2 PED events which have in comparison to the 1 PED events a much higher dilution factor and thus lower systematic uncertainties as well.

The contribution of the $p\pi^+\pi^-$ channel in the analyzed regions is negligibly small in both event patterns. First, the acceptance ratio is in the order of 10^{-4} or even lower. Second, the total cross section below 434 MeV never exceeds 10 µb [127] and thus the ratio between the $n\pi^+$ and $p\pi^+\pi^-$ final state is in the order of 10^{-5}. The low acceptance ratio can be mainly assigned to the number of tracks that have been seen in the MWPCs. The analysis required only one track in the MWPC which correlates with a hit in the CB. Simulations have shown that in the energy region below 500 MeV, one or even two additional tracks in the MWPCs were seen in more than 95% of the cases. These tracks correspond to the remaining two charged particles of the $p\pi^+\pi^-$ channel. Thus, limiting the number of tracks in the MWPCs to only one rejected nearly all the background from this channel. Only in very high forward directions, where the π^+ is detected in the TAPS, the acceptance ratio increases. As the forward point is nearly completely dominated by carbon and the missing mass distribution can also not be described by the signal MC, the last bin is rejected from the L_{max} fit procedure which will be presented in Sec. 9.2. Nevertheless, for completeness reasons, the results will also be shown for the last bin in the forward direction.

Although the cross section of the $p\pi^0$ channel is in the same order as the $n\pi^+$ channel, the overall ratio is in the order of 10^{-3} or even lower in the analyzed kinematic region. In contrast to the final states where the π^+ is detected, the quality of the background contamination of $p\pi^0$ channel can be tested by the carbon subtracted $\Delta E - E$ plots. As no proton band is seen, the $p\pi^0$ channel with an identified proton in the final state can be ruled out as a possible background. In addition, under the assumption of $p\pi^0$ kinematics, the proton from the $p\pi^0$ background channel can not be above a polar

angle of 90° in the laboratory system. Thus, protons from the $p\pi^0$ channel in backward direction can be ruled out as a possible background source. In fact, it has been found that even a small amount of $n\pi^+$ events showed a structure inside the proton band. Finally, the missing mass can reject all contribution of a detected proton as the rest mass difference of about 800 MeV results in a missing mass in the region of about 1400 MeV or even higher. The only possibility is that a photon is falsely identified as a charged particle. To test this effect, the charge identification was not applied in the MC simulation of the $p\pi^0$ channel and again the acceptance ratio has been compared. As the ratio was still in the order of 10^{-3}, the contribution of the $p\pi^0$ channel is assumed to be low as well.
Finally, simulations have shown that the $p2\pi^0$ final state have a similar acceptance ratio as the $p\pi^0$ and $p\pi^+\pi^-$ final state. Together with a maximum of 10 µb in the analyzed beam photon energy region, a significant contribution of this channel can be ruled out [126].
In total, the acceptance ratios of all these final states with respect to the signal reaction together with the not seen clear structure in the missing mass distribution lead to the conclusion that an upper limit of 3% of these background reactions can be assumed. The comparison of the results of the 1 PED events with the 2 PED events in App. A.9 strengthens these assumptions as no huge deviations are seen.

In Tab. 7.1, the number of selected events within the analyzed energy- and acceptance region after all cuts are presented for each beamtime, both radiators and for the individual event patterns. For the $p\pi^0$ final state, 11.9×10^6 events are selected for the 2 PED events and 20.0×10^6 for the 3 PED events. For the $n\pi^+$ final state, 4.1×10^6 events are selected for the 2 PED events and 37.0×10^6 for the 1 PED events.

Table 7.1: Overview of the number of selected events. Shown are the number of selected events in the butanol data for each beamtime, target, radiator type and event pattern. Note that all all cuts which have been introduced in this chapter are applied and that only events are selected within the analyzed energy- and acceptance region.

Beamtime	Target	Radiator	$\vec{\gamma}\vec{p} \to p\pi^0$		$\vec{\gamma}\vec{p} \to n\pi^+$	
			2 PED	3 PED	1 PED	2 PED
November 2013	butanol	diamond	5.21×10^6	1.61×10^6	9.87×10^6	5.46×10^5
	butanol	Møller	-	-	8.94×10^5	3.88×10^4
May 2014	butanol	diamond	1.28×10^6	8.91×10^5	2.74×10^6	3.09×10^5
	butanol	Møller	-	-	2.81×10^5	1.63×10^5
May 2015	butanol	diamond	9.26×10^6	3.24×10^6	2.14×10^7	1.10×10^6
	butanol	Møller	-	-	6.60×10^6	3.00×10^5
September 2015	butanol	diamond	1.14×10^7	3.77×10^6	2.43×10^7	1.22×10^6
	butanol	Møller	-	-	6.64×10^6	3.86×10^5
	carbon (withHe)	diamond/Møller	2.03×10^5	2.36×10^6	5.22×10^6	8.95×10^4

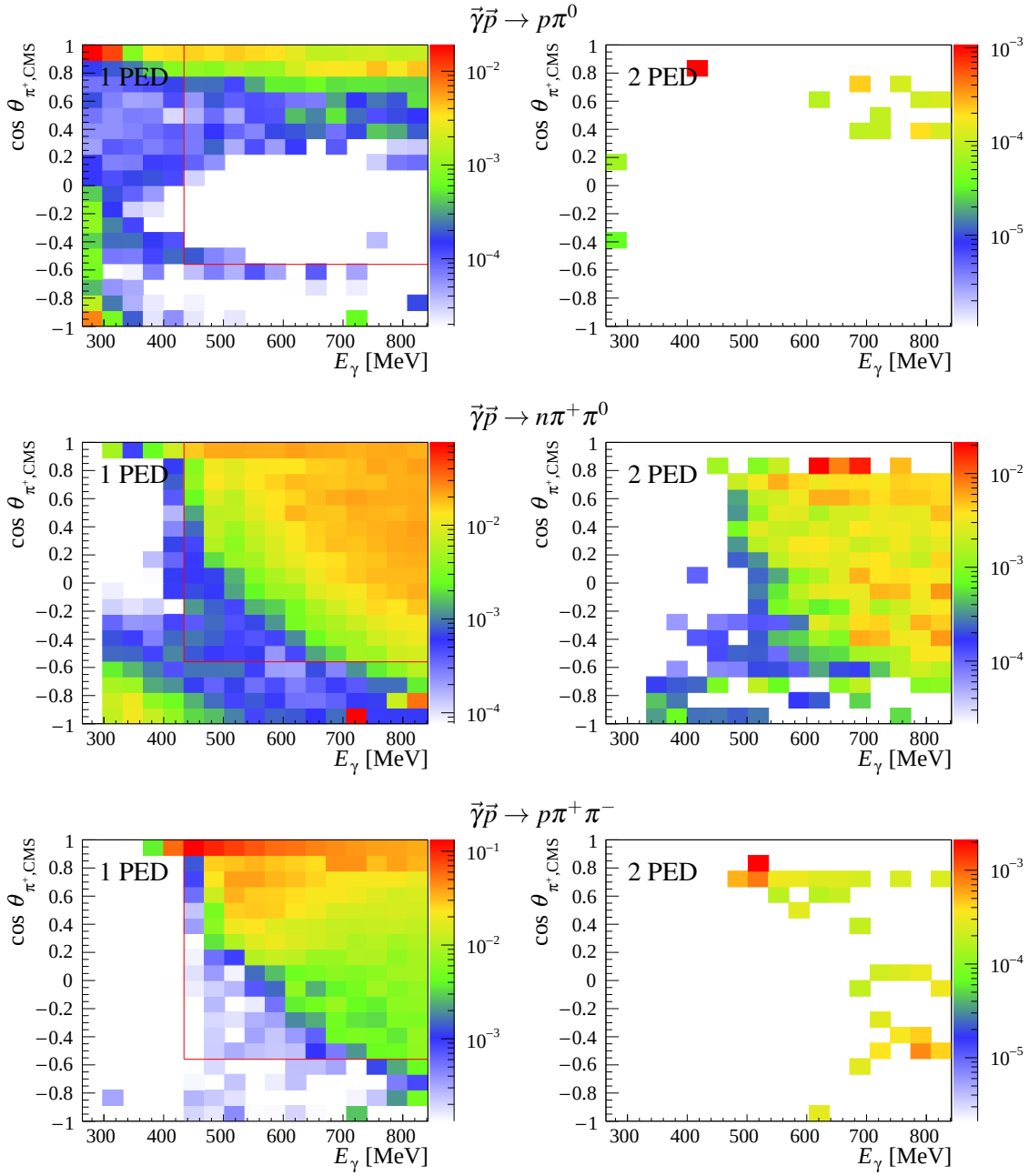

Fig. 7.31: Background estimation for the $n\pi^+$ final state. Shown are the ratios of the acceptances of the background channel to the signal reaction $\vec{\gamma}\vec{p} \to n\pi^+$ on the left side for the 1 PED events and on the right side for the 2 PED events. The red line starting at 434 MeV indicates the starting position from where on the 1 PED events are not included in the analysis anymore.

Chapter 8

Extraction of the Polarization Observables

As introduced in Sec. 4.3.1, the G/E measurements used a longitudinally polarized electron beam which interacts with a diamond radiator to produce linearly and circularly polarized photons at the same time. The differential cross section for linearly polarized photons in combination with a longitudinally polarized target is given by:

$$\frac{d\sigma}{d\Omega}(E_\gamma, \cos\theta, \varphi) = \left.\frac{d\sigma}{d\Omega}\right|_0 (E_\gamma, \cos\theta) \cdot \Big(1 - p_L \Sigma \cos 2\varphi + p_L p_z G \sin 2\varphi\Big), \tag{8.1}$$

whereas the one for circularly polarized photons in combination with a longitudinally polarized target is:

$$\frac{d\sigma}{d\Omega}(E_\gamma, \cos\theta) = \left.\frac{d\sigma}{d\Omega}\right|_0 (E_\gamma, \cos\theta) \cdot \Big(1 - p_C p_Z E\Big). \tag{8.2}$$

$\left.\frac{d\sigma}{d\Omega}\right|_0 (E_\gamma, \cos\theta)$ is the unpolarized differential cross section, which does not depend on the azimuthal angular distribution, $p_{L/C}$ are the polarization degrees of the linearly/circularly polarized photons, p_Z is the polarization degree of the longitudinally polarized target, and φ is the angle between the beam photon plane and the reaction plane. For the studies of systematic effects and detector inefficiencies, the target polarization was measured with two polarization orientations. Thereby, $p_z^{\uparrow}$ indicates the polarization vector which lies in the beam direction whereas $p_z^{\downarrow}$ is against it. In addition, the linearly polarized photons were produced with two different angles φ_0 of the beam photon plane with respect to the laboratory system plane, namely parallel ($\|$) and perpendicular ($\perp$) (see Fig. 8.2 on the left side). Thus, by using Eq. (8.1), in total four possible distributions are possible, which are given by[1]:

$$\left.\frac{d\sigma}{d\Omega}\right|_{T(\uparrow/\downarrow)}^{L(\|/\perp)} = \left.\frac{d\sigma}{d\Omega}\right|_0 \cdot \Big(1 - p_L^{\|/\perp} \Sigma \cos 2(\phi + \varphi_0) + p_L^{\|/\perp} p_Z^{\uparrow/\downarrow} G \sin 2(\phi + \varphi_0)\Big) \tag{8.3}$$

[1] In all following equations, the dependencies of the cross-sections will be neglected.

where φ_0 is 45° for the parallel setting and −45° for the perpendicular setting. The angle ϕ thereby is the angle between the laboratory system plane and the reaction plane. The definition of the angles are illustrated in Fig. 8.1 As an example, Fig. 8.2 depicts on the right side normalized ϕ-distributions,

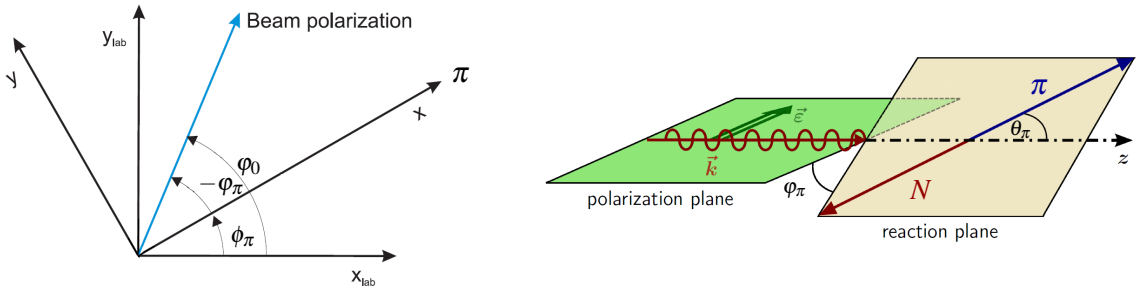

Fig. 8.1: Definition of the angles for the differential cross section. The reaction frame (x, y) for the *pi*-system and the laboratory frame (x_{lab}, y_{lab}) with their respective angles to each other are shown. In addition, the beam photon polarization vector and its angle φ_0 are presented. The negative value for φ_π is selected so that it agrees with the definition in [42] (figure adapted from [128]).

following Eq. (8.3), for the $\vec{\gamma}\vec{p} \to p\pi^0$ final state in a given kinematic range. The red line indicates thereby the beam polarization plane. The left side of the figure illustrates the orientation of φ_0 and the target polarization vector p_Z.

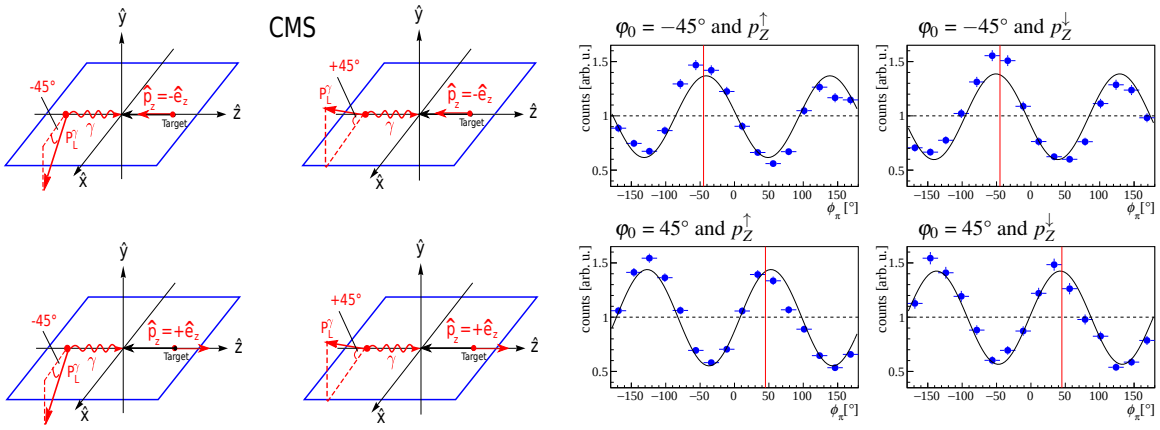

Fig. 8.2: Normalized ϕ-distributions for the four different settings. The left side presents coordinate sytems for the four different configurations of the linear polarization and target polarization orientations which are defined by Eq. (8.3). The reaction plane is hereby indicated by the blue box. On the right side, corresponding normalized ϕ-distributions are shown for the $p\pi^0$ final state in the kinematic region $E_\gamma = 400 - 434$ MeV and $0.11 < \cos\theta_{\pi^0,\mathrm{CMS}} \leq 0.22$. The amplitude of the $\cos 2\varphi$ distribution gives access to the contribution of the beam asymmetry Σ_B, whereas the shift of this $\cos 2\varphi$ modulation from the beam polarization plane (red line) indicates the contribution of the double polarization observable G (figure on the left taken from [129]).

Taking into account the additional distribution of the circularly polarized photons, which can either be produced in the helicity up state ($p_C^\uparrow$) or in the down state ($p_C^\downarrow$), the overall number of combinations becomes eight. The helicity dependent cross-section can be split into two parts: the anti-parallel (1/2), which is given by Eq. (8.4), and the parallel spin configuration (3/2) of the photon helicity and proton

target spin, given by Eq. (8.5).

$$\left.\frac{d\sigma}{d\Omega}\right|^{1/2} = \left.\frac{d\sigma}{d\Omega}\right|^{L(\parallel/\perp),H(\uparrow/\downarrow)}_{T(\downarrow/\uparrow)} = \left.\frac{d\sigma}{d\Omega}\right|^{L(\parallel/\perp)}_{T(\downarrow/\uparrow)} + \left.\frac{d\sigma}{d\Omega}\right|_{0} \cdot \left(1 + p_C^{\uparrow/\downarrow} p_Z^{\downarrow/\uparrow} E\right) \tag{8.4}$$

$$\left.\frac{d\sigma}{d\Omega}\right|^{3/2} = \left.\frac{d\sigma}{d\Omega}\right|^{L(\parallel/\perp),H(\uparrow/\downarrow)}_{T(\uparrow/\downarrow)} = \left.\frac{d\sigma}{d\Omega}\right|^{L(\parallel/\perp)}_{T(\uparrow/\downarrow)} + \left.\frac{d\sigma}{d\Omega}\right|_{0} \cdot \left(1 - p_C^{\uparrow/\downarrow} p_Z^{\uparrow/\downarrow} E\right) \tag{8.5}$$

Note that in Eq. (8.5) $p_Z^{\downarrow} = |p_Z^{\downarrow}|$ has been assumed and note the resulting sign change in the term in front of E. Since the A2 butanol target (see Sec. 2.3.1) consists of hydrogen, carbon, and oxygen, the overall cross section is split into a polarizable hydrogen contribution and an unpolarizable carbon/oxygen contribution. The combination of Eq. (8.1) and Eq. (8.2) results in the hydrogen cross section. Since the nucleons in carbon and oxygen are spinless and thus unpolarized, the $\sin 2\varphi$ modulation, and thus G, vanishes. In addition, as no coupling of the photon helicity with the target spin is available, the cross section shows no E contribution. Taking into account that the differential cross sections behave almost similarly for different nuclei with increasing mass number [93], the carbon differential cross-section, given by Eq. (8.6), can be used to describe the unpolarizable contributions.

$$\left.\frac{d\sigma}{d\Omega}\right|_{C} = \left.\frac{d\sigma}{d\Omega}\right|_{C0} \cdot \left(1 - p_L \Sigma_C \cos 2\varphi\right). \tag{8.6}$$

The differential cross section of the carbon and oxygen contribution is solely a $\cos 2\varphi$ modulation of the unpolarized cross section with an amplitude proportional to the beam asymmetry Σ_C for bound nucleons. Combining the unpolarized and polarized differential cross section, the overall cross section for the butanol target results in:

$$\begin{aligned}
\left.\frac{d\sigma}{d\Omega}\right|_{B} = & \left.\frac{d\sigma}{d\Omega}\right|_{H} + \left.\frac{d\sigma}{d\Omega}\right|_{C} \\
= & \left.\frac{d\sigma}{d\Omega}\right|_{H0} \cdot \left(1 - p_L \Sigma_H \cos 2\varphi + p_L p_Z G \sin 2\varphi - p_C p_Z E\right) \\
& + \left.\frac{d\sigma}{d\Omega}\right|_{C0} \cdot \left(1 - p_L \Sigma_C \cos 2\varphi\right) \\
= & \left(\left.\frac{d\sigma}{d\Omega}\right|_{H0} + \left.\frac{d\sigma}{d\Omega}\right|_{C0}\right) \cdot \left(1 - p_L \frac{\left.\frac{d\sigma}{d\Omega}\right|_{H0} \Sigma_H + \left.\frac{d\sigma}{d\Omega}\right|_{C0} \Sigma_C}{\left.\frac{d\sigma}{d\Omega}\right|_{H0} + \left.\frac{d\sigma}{d\Omega}\right|_{C0}} \cos 2\varphi \right. \\
& \left. + \frac{\left.\frac{d\sigma}{d\Omega}\right|_{H0}}{\left.\frac{d\sigma}{d\Omega}\right|_{H0} + \left.\frac{d\sigma}{d\Omega}\right|_{C0}} \left(p_L p_Z G \sin 2\varphi - p_C p_Z E\right)\right) \\
= & \left.\frac{d\sigma}{d\Omega}\right|_{B0} \cdot \left(1 - p_L \Sigma_B \cos 2\varphi + d p_L p_Z G \sin 2\varphi - d p_C p_Z E\right).
\end{aligned} \tag{8.7}$$

Hence, the butanol differential-cross section can be used to extract the unpolarized cross-section, the beam asymmetry Σ_B, and the double polarization observables G and E. Please note that the beam asymmetry Σ is defined for the reaction on unbound nucleons Thus, the results of the beam asymmetry Σ_B are only considered as a cross-check and will not further be used as new input for the complete experiment.
As a first step, the following section will introduce the prerequisites, which include the polarization degrees of the polarized photons $p_{L/C}$ and the target protons p_Z, and the number of polarizable protons inside the analyzed butanol data. The latter one is referred to as the dilution factor d. Afterward, two different methods for the extraction of the polarization observables will be presented. The latter one is referred to as the dilution factor d. Afterward, the extraction of the polarization observables will be performed using two different approaches. As will be described in Sec. 8.3.1, binned event yield asymmetries are fit based on a χ^2 minimization. Finally, Sec. 8.3.2 will present an unbinned event-based maximum likelihood fit.

8.1 Dilution Factor

8.1.1 Definition

As already mentioned in the introduction of this chapter, the butanol target consists of hydrogen, carbon and oxygen. However, for the determination of the double polarization observables G and E, a good knowledge of the amount of reactions on unbound polarizable protons is mandatory. Within the butanol target, the hydrogen nuclei provide the unbound protons, whereas the carbon and oxygen nuclei provide bound protons and neutrons. The bound ones are both spinless and thus can not be polarized. Moreover, coherent meson photoproduction off the carbon and oxygen nuclei contributes, though with a negligible cross section compared to the incoherent processes [60]. In Eq. (8.7), the dilution factor d has already been introduced and is given by:

$$d = \frac{\frac{d\sigma}{d\Omega}\big|_{H0}}{\frac{d\sigma}{d\Omega}\big|_{H0} + \frac{d\sigma}{d\Omega}\big|_{C0}} = \frac{\frac{d\sigma}{d\Omega}\big|_{B0} - \frac{d\sigma}{d\Omega}\big|_{C0}}{\frac{d\sigma}{d\Omega}\big|_{B0}} = \frac{\frac{d\sigma}{d\Omega}\big|_{\text{unbound}}}{\frac{d\sigma}{d\Omega}\big|_{\text{unbound}} + \frac{d\sigma}{d\Omega}\big|_{\text{bound}}}. \tag{8.8}$$

Please note that carbon can represent the oxygen contribution, and therefore the sum of hydrogen and carbon can describe butanol. Inspecting Eq. (8.8), the dilution factor can, therefore, be interpreted as a probability that a beam photon initialized a reaction off an unbound polarizable proton inside the butanol target. Up to now, the dilution factor has been written as a ratio of differential cross sections. In general, a differential cross section can be written as:

$$\frac{d\sigma}{d\Omega}(E_\gamma, \cos\theta) = \frac{N(E_\gamma, \cos\theta, \varphi)}{\varepsilon_{\text{det}}(E_\gamma, \cos\theta, \varphi) \cdot A(E_\gamma, \cos\theta, \varphi) \cdot n_\gamma(E_\gamma) \cdot n_t \cdot \Gamma(M \to X)}, \tag{8.9}$$

where N is the event yield, ε_{det} the detector efficiency, A the acceptance of the considered reaction, n_γ the photon flux, n_t the target area density and $\Gamma(M \to X)$ the branching ratio of meson M to decay

into X. As the butanol and carbon measurements were performed for the same reaction, the branching ratio $\Gamma(M \to X)$ cancels out, leading with Eq. (8.8) and Eq. (8.9) to:

$$d = \frac{\left(\frac{N_B}{\varepsilon_{\text{det},B} \cdot A_B \cdot n_{\gamma,B} \cdot n_{t,B}}\right) - \left(\frac{N_C}{\varepsilon_{\text{det},C} \cdot A_C \cdot n_{\gamma,C} \cdot n_{t,C}}\right)}{\left(\frac{N_B}{\varepsilon_{\text{det},B} \cdot A_B \cdot n_{\gamma,B} \cdot n_{t,B}}\right)} = \frac{N_B - \left(\frac{\varepsilon_{\text{det},B} \cdot A_B \cdot n_{\gamma,B} \cdot n_{t,B}}{\varepsilon_{\text{det},C} \cdot A_C \cdot n_{\gamma,C} \cdot n_{t,C}}\right) \cdot N_C}{N_B} = \frac{N_B - s_C \cdot N_C}{N_B} \tag{8.10}$$

In Eq. (8.10), the carbon scaling factor s_C has been introduced which can be determined via two independent methods. They will be presented in the following section.

8.1.2 Carbon Scaling Factor

8.1.2.1 Determination via Photon Flux Normalization

The first method is already written down in Eq. (8.10) and will be referred to as the Flux Normalization Scaling and is given by:

$$s_C = \frac{\varepsilon_{\text{det},B} \cdot A_B \cdot n_{\gamma,B} \cdot n_{t,B}}{\varepsilon_{\text{det},C} \cdot A_C \cdot n_{\gamma,C} \cdot n_{t,C}}. \tag{8.11}$$

It requires an absolute normalization of the butanol and carbon measurement, including the knowledge of the target area densities of the bound nucleons in both targets and their corresponding photon fluxes. The target area density of the bound nucleons inside the butanol target is given by $n_{t,B}^{\text{bound}} = 0.5875\ \text{b}^{-1}$ whereas the one of the carbon target by $n_{t,C} = 0.6798\ \text{b}^{-1}$. As both targets are cooled down by helium, the additional contribution of the flowing helium with $n_{t,B}^{\text{He}} = 0.0843\ \text{b}^{-1}$ needs to be taken into account. Therefore, the ratio of the target area densities, defined in Eq. (8.11), is given by:

$$\frac{n_{t,B}}{n_{t,C}} = \frac{n_{t,B}^{\text{bound}}}{n_{t,C}} = \frac{0.5875 + 0.0843}{0.6798 + 0.0843} = 0.882. \tag{8.12}$$

More detailed derivations and explanations are presented in [14].
The photon flux n_γ was determined by P. Pauli for all beamtimes and can be calculated by the number of detected electrons $n_e(c)$ in the tagger channel c and their corresponding tagging efficiency $\varepsilon_{\text{tagg}}(c)$ via [102]:

$$n_\gamma(c) = \varepsilon_{\text{tagg}}(c) \cdot n_e(c). \tag{8.13}$$

As mentioned in Sec. 4.1, the tagger hits are read out by scalers, which are not inhibited by the experimental trigger. Thus, electrons are also counted by the scalers in the time window when digitization is taking and no further events can be recorded. In order to account for that, additional correction factors in the offline analysis need to be applied on the electron scalers, namely the lifetime factors. This achieved by determining the ratio of a free-running clock and an inhibited clock, which is halted if the data digitization is taking place. As has been discussed in [14] and [102], different beamtimes need an additional correction factor for the lifetime since these were not recorded correctly during the beamtimes. Consequently, this method is only used as a rough estimation of the

systematic uncertainty of the determination of the scaling factor, which has been performed by two A2 collaboration members [14, 102]. Comparison with the determination of the scaling factor using the event yield method showed that the deviations between the methods are less than 3%.

8.1.2.2 Determination via Event Yields

Another method, which requires no absolute normalization, takes advantage of the additional carbon data along with the butanol data. It was already partly introduced in Sec. 7.1. The aim is to scale the carbon data to the reactions of the bound nucleons inside the butanol data. Therefore, a kinematic variable distribution was selected in which the reactions off the unbound protons inside the butanol target can nicely be separated from the bound protons. For the 3 PED events in the $\vec{\gamma}\vec{p} \to p\pi^0$ analysis and the 2 PED events in the$\vec{\gamma}\vec{p} \to n\pi^+$ analysis, the coplanarity distribution was selected. As the nucleon angular information is not available for the 2 PED events in the $\vec{\gamma}\vec{p} \to p\pi^0$ analysis and the 1 PED events in the $\vec{\gamma}\vec{p} \to n\pi^+$ analysis, the kinematic variable of choice here is the missing mass. Since bound protons carry additional Fermi momentum, the coplanarity and missing mass distributions for bound protons are broader compared to the unbound ones. In Chap. 7, the selection criteria for the coplanarity and missing mass distributions were optimized to select the reactions off the unbound protons. Taking the extracted σ of the Gaussian fit, a 3σ anti-cut [2] around the mean value was applied to only select the reactions off bound protons. As has been in Sec. 7.7.2, an additional problem arises in the 1 PED events of the $n\pi^+$ channel because the selection of the reaction on the unbound protons is more complex, especially at lower missing masses. It has been shown that simulations can explain the shoulder towards lower missing masses but can not perfectly model the data. Furthermore, the background from the $p\pi^0$ channel can also contribute to this region. Thus, 1 PED events need to be selected carefully to not scale background reactions as well. In regions where a clear separation between signal and background reactions is not 100% guaranteed, an additional systematic uncertainty of 5% in the scaling factor is included to account for the small discrepancies between the reconstructed hydrogen distribution and the signal MC, and the possibility of small background contamination. Afterward, the scaling factor can be determined by matching the integral of the selected events in a given kinematic range of the butanol data with the integral of the carbon data. The advantage of this method compared to the Photon Flux Normalization is that it can be determined not only as a function of the incoming beam photon energy E_γ but also as a function of the kinematic variable $\cos\theta_{\mathrm{M,\,CMS}}$ of the meson M. In fact, the scaling factor should only be energy-dependent as shown in the Photon Flux Normalization. A $\cos\theta_{\mathrm{M,CMS}}$ dependence would indicate that the product of the detector efficiency and the reaction acceptance of the butanol and carbon target data are not similar. Therefore, in the following section possible sources of the $\cos\theta_{\mathrm{M,CMS}}$ dependence and their impact on the acceptance will be discussed.

[2] Assuming a normal Gaussian distribution for the reconstructed reactions off the unbound protons, 99.73% of all reactions on unbound protons are rejected.

8.1.2.3 Studies of the Acceptance and their Impact on the Scaling Factor

Three major problems have been found which can cause a difference in the acceptance, namely:

- Different PMT holes in the CB cause a change in the detector efficiency,
- Different positions of the target center change the selection criteria and thus the reaction acceptance,
- Different trigger conditions in the data acquisition change the selection criteria and the detector efficiency as well.

Reconstruction Holes

One problem of the individual beamtimes is the PMTs of the CB, e.g., several PMTs were dead in May 2014 and thus create holes in the CB cluster reconstruction. An overview of the $\phi - \theta$ distribution of all recorded clusters in the four analyzed beamtimes is depicted in Fig. 8.3. It is clearly visible

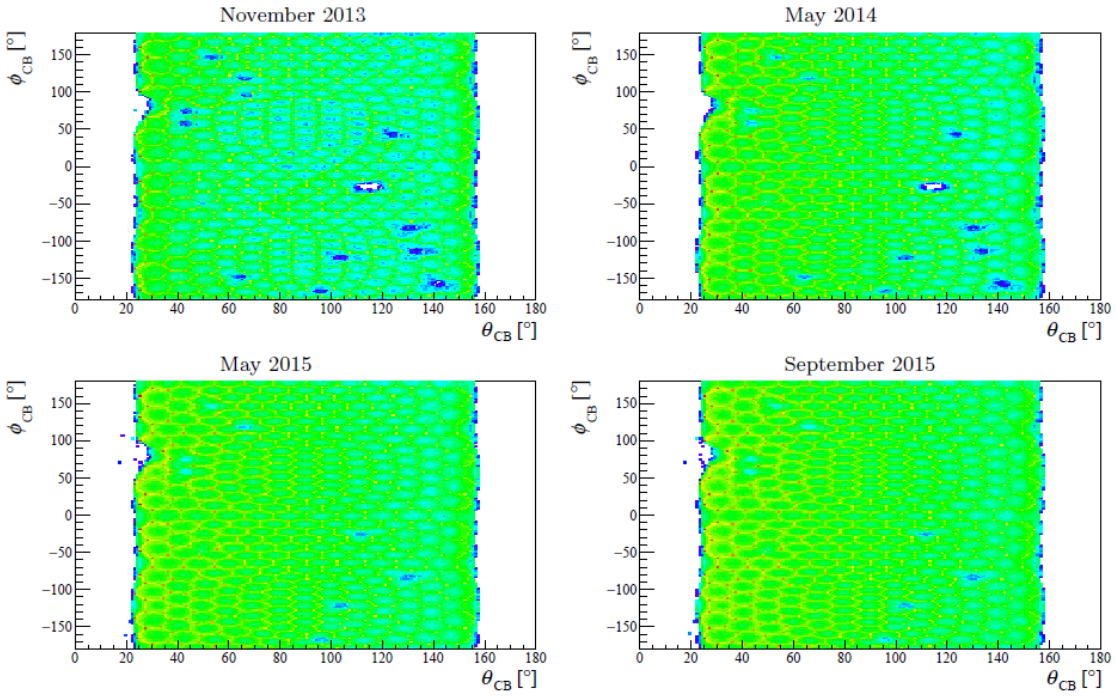

Fig. 8.3: Cluster map distribution in the CB. The $\phi - \theta$ distribution of all recorded clusters of the different beamtimes are shown. As can be seen, especially for the November 2013 and May 2014 beamtimes, noisy or broken PMTs cause holes in the cluster map (figure taken from [14]).

that more holes are present in the November 2013 and May 2014 beamtime compared to the May 2015 and September 2015 beamtime, especially at higher polar angles. As the carbon measurements were performed in September 2015, the influence of the CB holes on the acceptance is studied by

comparing the CB holes of September 2015 with the ones of May 2014. To do so, two Monte Carlo simulation sets have been produced where one has the holes of the May 2014 and the other the ones of the September 2015 beamtimes.

Target Center Position

In the experiment, the CB detector system is moved over the target. The aim is that the target cell center is located exactly at the center of the CB. Unfortunately, as the CB is moved mechanically over the target, a precision of several millimeters is only achieved. However, as the target cell length is only 2 cm, a few millimeters deviation in the placement of the target cell already causes noticeable changes in the kinetic variables as will be shown later. As a first estimation of the target center position, the z-vertex reconstruction of the MWPCs can be used. Therefore, P. Pedroni from the A2 Collaboration determined the z-vertex position using only a calibration of the MWPCs relative to each other in which the center of the second MWPC was chosen as the reference z= 0 mm position. For November 2013 and May 2014, a value of -0.63 mm was obtained whereas for May 2015 a value of 3.1 mm. The obtained value for September 2015, unfortunately, can not be used as reparations between May 2015 and September 2015 were performed. Although a not perfect alignment in the z-direction between both MWPCs can be corrected with a calibration, the overall misalignment of the MWPCs with respect to the CB can be not be corrected to a precision of less than a few millimeters. The overall misalignment can be traced back to the fact that the MWPCs are not mechanically fixed by a frame inside the CB tunnel. Furthermore, a precise correction with a calibration is not possible since the reference z= 0 mm position of the CB is not known accurately as the CB is not a perfectly spherical ball. Nevertheless, a first conclusion from the vertex position test is that the target positions of the November 2013 and May 2014 beamtimes are similar and that the May 2015 beamtime is shifted by about 4 mm.

To determine the position of the target cell independently from the MWPCs, a detailed study of the polar angular difference $\Delta\theta_p = \theta_{p,\text{calc}} - \theta_{p,\text{rec}}$ between the calculated and reconstructed proton polar angle in the reaction $\vec{\gamma}\vec{p} \to p\pi^0$ is used. The calculated proton polar angle is determined from the four momenta of the incoming beam photon, the target at rest and the photons in the final state. As the photons are reconstructed and calibrated under the assumption that the target cell is located at the center of the CB, a deviation from 0° in the polar angular difference indicates that the actual reaction is produced at a different z-position inside the target cell. The position of the target cell was determined by simulating Monte Carlo data sets with the target cell center sitting at different z-positions. It has been found that the November 2013 and May 2014 beamtimes had the target cell located at about 0 mm whereas the May 2015 and September 2015 beamtimes at about -3.3 mm. Fig. 8.4 shows the polar angular difference $\Delta\theta_p$ for November 2013 (left side) and September 2015 (right side) for the beam photon energy range from 400 MeV to 434 MeV and the kinematic variable range $-0.44 \leq \cos\theta_{\pi^0,\text{CMS}} < -0.33$. The simulations for the corresponding target position of the beamtimes is indicated by the green line whereas the one of the other in violet. It is clearly visible that both

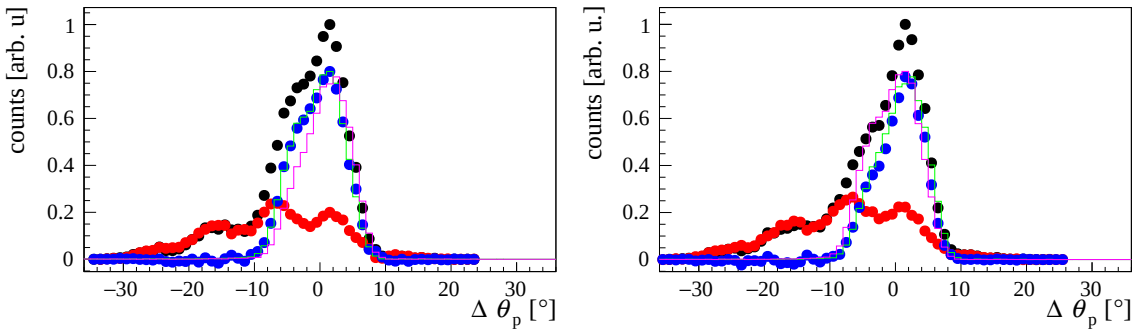

Fig. 8.4: $\Delta\theta_p$ distributions of different target center positions. On the left side, the different distributions of the November 2013 beamtime for butanol (black), scaled carbon (red), and reconstructed hydrogen (blue) are shown for the kinematic region E_γ = (400-434) MeV and $-0.44 \leq \cos\theta_{\pi^0,\mathrm{CMS}} < -0.33$. This beamtime corresponds to the target position center at z = 0 mm with its simulated MC indicated by the green line. The MC simulation of the other target position center at z = -3 mm is included as the violet line. On the right side, the same distributions are depicted for the September 2015 beamtime with its connected simulation in green and the one of the other setting in violet.

reconstructed hydrogen distributions (blue dots) do not agree with each other and that the individual MC simulations can nicely reproduce the distributions. In App. A.3, all butanol distributions are scaled to each other for all $\cos\theta_{\pi^0,\mathrm{CMS}}$ bins for the beam photon energy range 400 MeV to 434 MeV. Inspecting these distributions, a clear conclusion is that September 2015 and May 2015 behave similarly and thus have the same target position with $z \approx -3.3$ mm [3]. A similar argumentation holds for the May 2014 and November 2013 beamtime with a target center sitting at $z \approx 0$ mm.

Influence on the Acceptance

To study the influence of the target position and the CB holes on the acceptance [4], the May 2014 simulations have been produced at a target cell center position of 0 mm whereas the September 2015 at a position of -3 mm. Note that these simulations also have the corresponding CB holes of the beamtimes included. Fig. 8.5 shows the ratio of the acceptance for the $p\pi^0$ final state as a function of the beam photon energy E_γ and the kinematic variable $\cos\theta_{\pi^0,\mathrm{CMS}}$ on the left side, and one beam photon energy projection on the right side. It can be seen that the wrong target position and the CB holes of the butanol May 2014 beamtime relative to the carbon September 2015 beamtime cause a relative change of the acceptance of up to 5%. To take this effect into account, the energy dependent scaling factor is modified by these relative changes via:

$$s_C(E_\gamma, \cos\theta_{M,\mathrm{CMS}}) = s_C(E_\gamma) \cdot \frac{\varepsilon_{\mathrm{MC},0mm}}{\varepsilon_{\mathrm{MC},-3mm}}(\cos\theta_{M,\mathrm{CMS}}) \text{ with } M = \pi^0/\pi^+. \tag{8.14}$$

[3] Similar behavior was observed for all beam photon energies and over the whole kinematic range.

[4] In the following, acceptance means the product of detection efficiency and reconstruction efficiency.

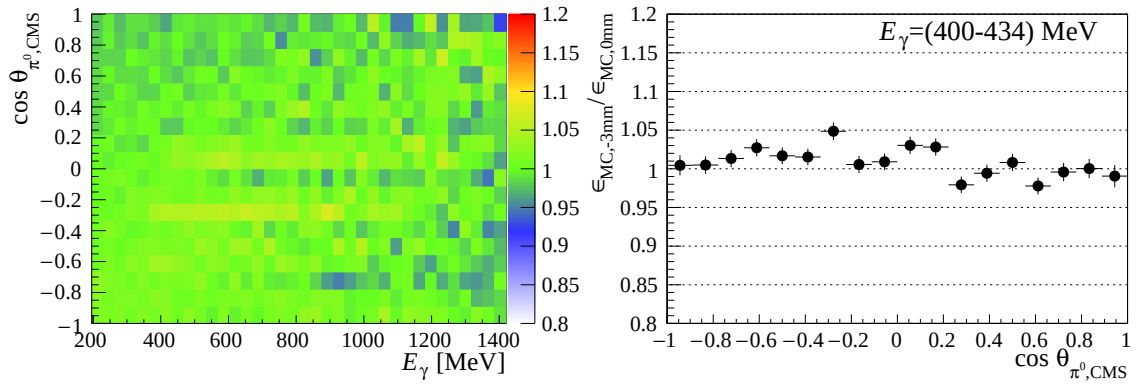

Fig. 8.5: Ratio of the acceptance of the two detector configurations. On the left side, the ratio of the acceptances of the first setting (target position at z = −3 mm and the CB holes of September 2015) and the second setting (target position at z = 0 mm and the CB holes of May 2014) is shown. For a further illustration, the right side depicts one beam photon energy projection.

Trigger Conditions

As has been mentioned in Sec. 4.3.1, the CB energy sum thresholds and TAPS LED1 thresholds of all beamtimes were set to different values. Consequently, different threshold values between the butanol and carbon data would cause different acceptances. The physical energy sum for the 3 PED events of the $\vec{\gamma}\vec{p} \to p\pi^0$ reaction starts far away from any trigger effects. The situation is different for the 2 PED events in the forward direction[5] and especially for all 1 PED/2 PED events in the $n\pi^+$ final state. To illustrate this effect, Fig. 8.6 shows a two-dimensional map of the starting position of the energy sum for the 3 PED and 2 PED events in the $p\pi^0$ channel in the top row for the butanol 450 MeV edge position of the September 2015 beamtime. Similarly, the bottom row presents the 2 PED and 1 PED events of the $n\pi^+$ channel. Since the energy sums need to be adjusted to the carbon with helium setting which has an energy sum trigger of about 90 MeV, it becomes clear that the 3 PED events of the $p\pi^0$ channel are not affected by any trigger effects. The 2 PED events of the $p\pi^0$ channel start at an energy sum of about 120 MeV and thus only minor adjustments were needed. The situation is different for the 1 PED and 2 PED events of the $n\pi^+$ channel, especially at lower beam photon energies E_γ. Here the energy sum already starts at about 60 MeV and thus an adjustment of the trigger is mandatory. It is noteworthy that the energy sum of the November 2013 beamtime starts already at 30 MeV. As has been shown in Sec. 7.2, it was nevertheless possible to adjust the different energy sum thresholds of the individual beamtimes to each other. To estimate the remaining uncertainty from the trigger adjustments, the energy sum distributions of the adjusted settings are normalized to the reference setting. Afterward, the ratio of the integral of both settings is used as an estimator of the uncertainty coming from the trigger adjustment[6] Fig. 8.7 shows the case for the 1

[5] Note that the smaller CB energy sum in the forward direction is caused by the TAPS trigger where the CB energy sum did not trigger.

[6] If the adjustment was performed and worked perfectly, both distributions should be identical and should result in a ratio of 1.

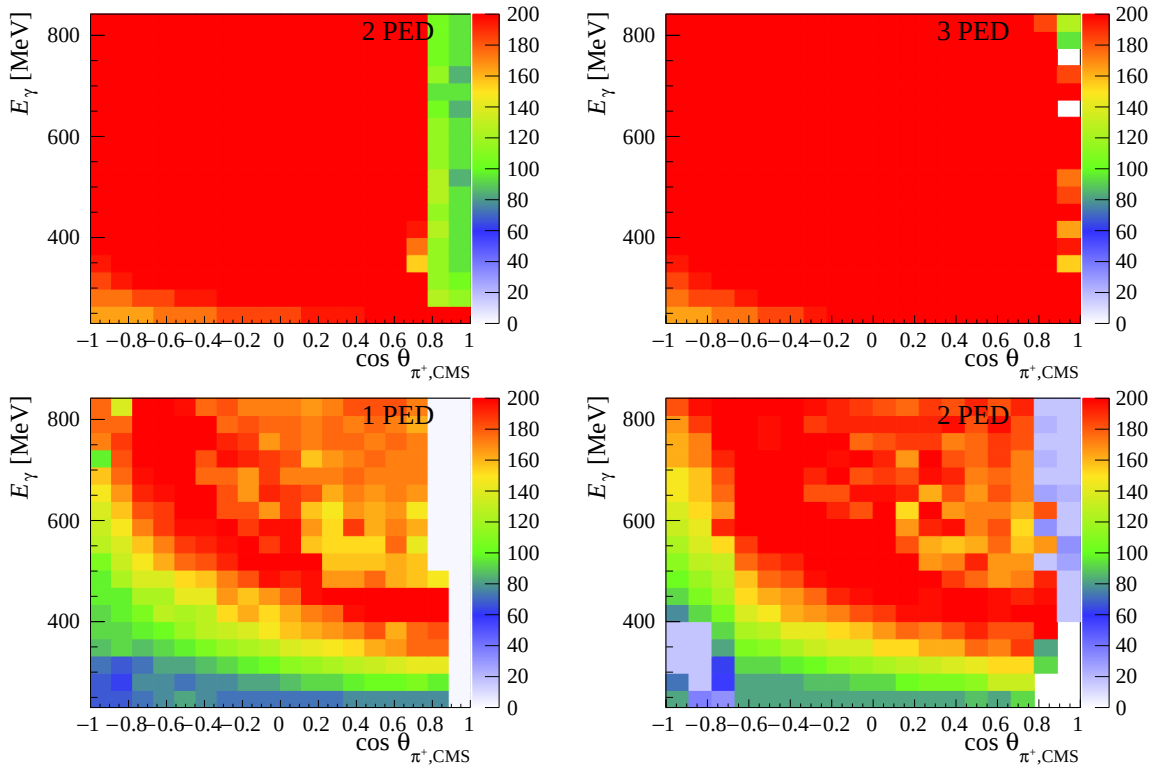

Fig. 8.6: Physical CB energy sum of different event patterns for both analyzed channels. The starting points of the physical energy sums of the different event patterns are shown as a function of the beam photon energy E_γ and the kinematic variable $\cos\theta_{M,\mathrm{CMS}}$ with $M = \pi^0/\pi^+$. The upper row shows the 2 PED and 3 PED events of the $p\pi^0$ channel whereas the lower row the 1 PED and 2 PED events of the $n\pi^+$ channel.

PED events of the $n\pi^+$ channel. Only small deviations between the ratio of the carbon with helium and the corresponding butanol integral are seen which can be explained by an imperfect adjustment of the energy sum triggers due to the lack of statistics. As these deviations are only on the order of 5%[7] in the region where the carbon scaling is performed, an uncertainty of 5% is assumed for effects coming from the trigger adjustment in the energy-dependent scaling factor.

8.1.3 Determination of the Dilution Factor

With the count rates of butanol N_B and the scaled count rates of carbon $s_C \cdot N_C$, it is now possible to determine the dilution factor as a function of the incoming beam photon energy E_γ and the kinematic variable $\cos\theta_{\mathrm{M,\,CMS}}$ via:

$$d(E_\gamma, \cos\theta_{\mathrm{M,\,CMS}}) = 1 - s_C(E_\gamma) \cdot \frac{N_C(E_\gamma, \cos\theta_{\mathrm{M,\,CMS}})}{N_B(E_\gamma, \cos\theta_{\mathrm{M,\,CMS}})}. \tag{8.15}$$

As already mentioned in Sec. 4.3.1, it is crucial that the determination is performed with the carbon measurements including the helium mixture in the cryostat. An analysis by F. Afzal [14], and

[7] Similar results were obtained for the 2 PED events.

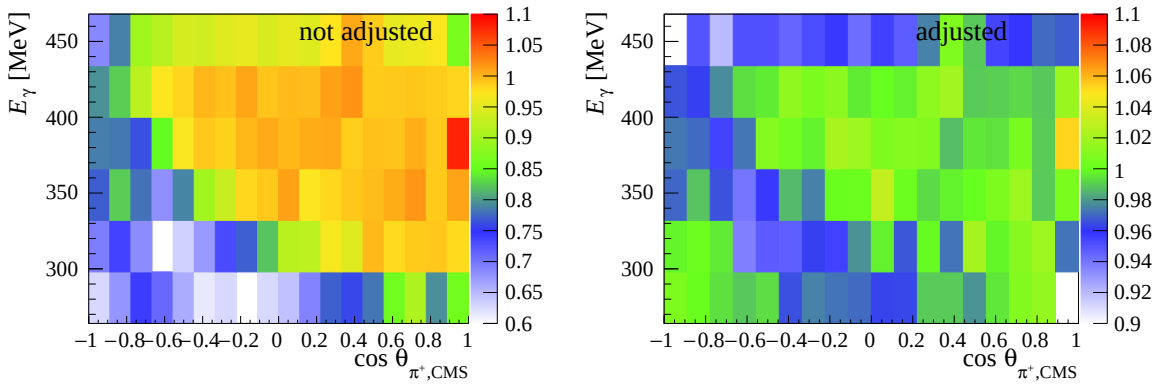

Fig. 8.7: Quality test of the trigger adjustment. Shown is the ratio of the adjusted butanol distribution to the carbon with helium reference distribution as a function of the beam photon energy E_γ and the kinematic variable $\cos\theta_{\pi^+,\mathrm{CMS}}$ for the 1 PED events. The left side presents the unadjusted situation whereas the right side the adjusted one. Clearly seen is that the ratio varies only within 5% of 1. Note that only the beam photon energy range is shown where the 1 PED events are analyzed and that the z-axis is zoomed in for the adjusted case.

confirmed in this analysis, revealed that the Fermi momentum and the final state interaction of carbon and helium differ. Consequently, the forms of the coplanarity and the missing mass distributions differ for carbon and helium. With that, it was shown that the carbon measurements without helium overestimated the dilution factor by about 10-15%.

To handle the effects of different acceptances of the beamtimes, the energy-dependent scaling factor $s_C(E_\gamma)$ and thus the dilution factor $d(E_\gamma, \cos\theta_{\mathrm{M,\,CMS}})$ were first determined for the coherent edge setting at 850 MeV of the September 2015 beamtime. The main advantage of just taking this setting as a reference is that it has the same trigger conditions as the carbon with helium measurement. Furthermore, effects from an incorrect target position and reconstruction holes do not appear as the data are taken within the same beamtime. As a next step, the obtained dilution factor can be used to constrain the scaling factors of all other coherent edges by rewriting Eq. (8.15) to:

$$s_C(E_\gamma, \cos\theta_{\mathrm{M,\,CMS}}) = \left(1 - d(E_\gamma, \cos\theta_{\mathrm{M,\,CMS}})\right) \cdot \frac{N_B(E_\gamma, \cos\theta_{\mathrm{M,\,CMS}})}{N_C(E_\gamma, \cos\theta_{\mathrm{M,\,CMS}})}. \tag{8.16}$$

Taking into account the uncertainties which are mentioned above, the scaling factor of the other coherent edge settings should only vary within these uncertainties. The statistical error of the dilution factor is determined via Gaussian error propagation and is given by:

$$\Delta d_{\mathrm{stat}} = s_C \cdot \sqrt{\left(\frac{\Delta N_C}{N_B}\right)^2 + \left(\frac{N_C \cdot \Delta N_B}{N_B^2}\right)^2}. \tag{8.17}$$

As the statistical uncertainty is given by $\Delta N = \frac{1}{\sqrt{N}}$ and $N_B \gg N_C$, the contribution of ΔN_B to the statistical error of the dilution can be neglected which results in the approximation:

$$\Delta d_{\text{stat}} \approx s_C \cdot \left(\frac{\Delta N_C}{N_B} \right). \tag{8.18}$$

With that, due to the vanishing contribution of the butanol data, no correlation between the dilution factor and the butanol data needs to be respected [60]. The systematic uncertainty of the dilution factor is given by the systematic uncertainty of the scaling factor s_C via:

$$\Delta d_{\text{syst}} = \Delta s_{C_{\text{syst}}} \cdot \frac{N_C}{N_B} = \frac{\Delta s_{C_{\text{syst}}}}{s_C} \cdot (1 - d). \tag{8.19}$$

Consequently, the systematic uncertainty of the dilution factor increases with a decreasing dilution factor. In fact, the biggest systematic uncertainty contribution to the double polarization observables for the 2 PED events in the $\vec{\gamma}\vec{p} \to p\pi^0$ analysis and the 1 PED events in the $\vec{\gamma}\vec{p} \to n\pi^+$ is dominated by the dilution factor uncertainty. In App. A.4, the resulting dilution factors of all beamtimes and coherent edges together with their systematic uncertainties for both analyzed channels are included. Indeed only small deviations between the dilution factors of the individual coherent edges and beamtimes are seen. Therefore, the systematic uncertainties are well understood. The mean dilution factors of all coherent edges and beamtimes are illustrated as a two-dimensional map in Fig. 8.8 for both analyzed channels and the different event types. It is clearly visible that the 3 PED events in the $\vec{\gamma}\vec{p} \to p\pi^0$ analysis have a much higher dilution factor compared to the 2 PED events. This can be explained by the non-existing angular cuts in the 2 PED events. Especially, the proton polar angular difference cut significantly decreases the contribution of reactions off bound proton as has been discussed in Chap. 7. In addition, the transition region between the CB and the TAPS (third $\cos\theta_{\pi^0,\text{CMS}}$ bin) is clearly visible as the dilution factor suddenly decreases within one bin and afterward increases again. This can be explained by the lack of detected protons within the transition region between the CB and TAPS. The lack of angular cuts also shows a huge effect on the dilution factor values for the 2 and 1 PED events in the $\vec{\gamma}\vec{p} \to n\pi^+$ analysis which are shown in the lower column in Fig. 8.8. Special attention should be given to the 1 PED events in the backward direction. As can be seen, the dilution factor here is close to zero. A possible explanation is that only events with an additional Fermi momentum can overcome the CB energy sum trigger. In fact, simulations have shown that most of the possible $n\pi^+$ events in this kinetic region have energies far below the adjusted energy sum of about 90 MeV. The same argument holds for the π^+ in the forward direction where they are detected in the TAPS. The TAPS LED1 thresholds were set to 90 MeV which are as well far above the physical energy sum of the $n\pi^+$ channel[8]. In addition, it is important to mention that the dilution factor for the 1 PED events can only be determined for events where the actual energy of the π^+ is known. If this is not the case, the scaling factor can not be determined accurately as the reactions on unbound protons can not be distinguished from the bound ones. Therefore, all events with a beam photon energy above

[8] Note again that the G/E measurements were not optimized for the $n\pi^+$ channel.

434 MeV and towards forwarding angles are rejected within this analysis. Fortunately, the 2 PED events can cover the lost acceptance region.

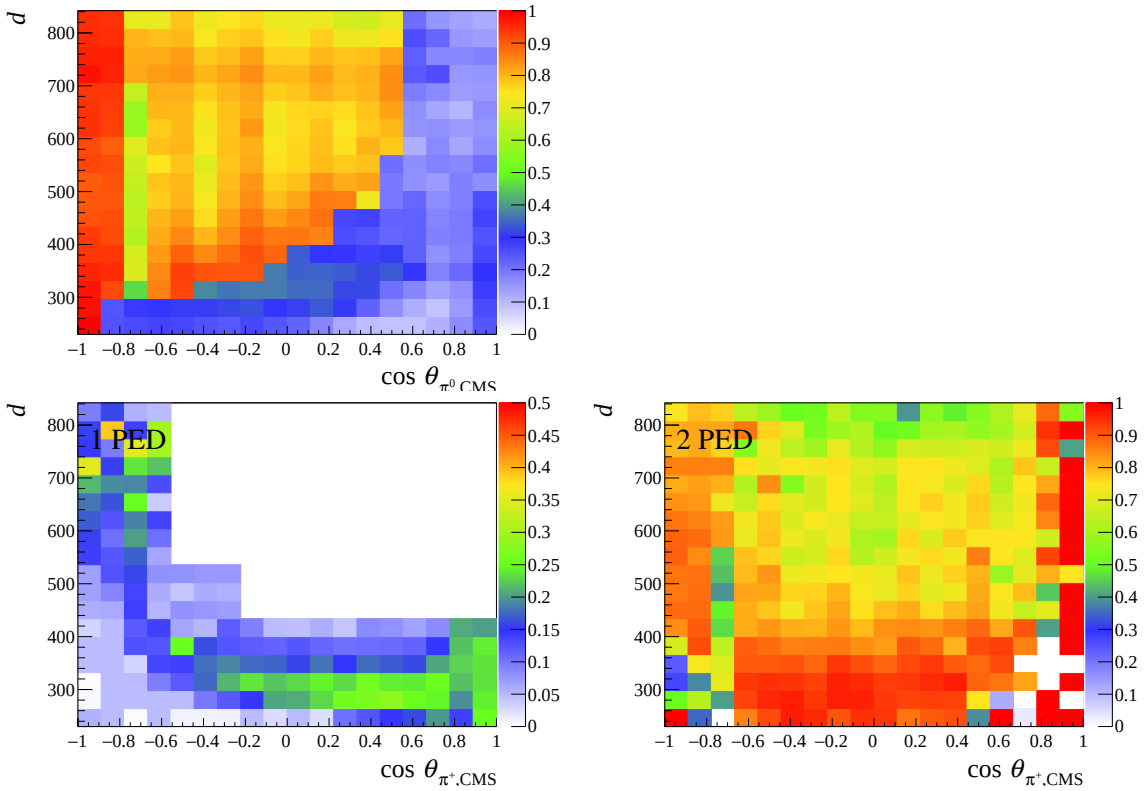

Fig. 8.8: Dilution factor *d*. The mean dilution factors d for the different final states and event patterns are shown as a function of the beam photon energy E_γ and the kinematic variable $\cos\theta_{\pi,\mathrm{CMS}}$. The upper row corresponds to the $p\pi^0$ channel whereas the lower ones to the $n\pi^+$ channel. The white area in the 1 PED distribution for the $n\pi^+$ channel indicates the rejected kinematic region in the analysis.

8.2 Polarization Degrees

8.2.1 Beam Polarization

8.2.1.1 Linearly Polarized Photons

The production and determination of the linearly polarized photons have been explained in detail in Sec. 3.2.5. To ensure the optimal statistics in certain beam photon energy ranges in combination with a high polarization degree, the linearly polarized photons have been produced at different positions of the coherent edge. Tab. 8.1 gives an overview of the combined coherent edges for the different beam photon energy ranges in combination with the highest achievable polarization degree. Fig. 8.9 shows an overview of the different polarization tables, starting with a coherent edge at 350 MeV and ending with an edge at 850 MeV. Consequently, the beam asymmetry Σ_B and the double polarization observable G are extracted in the beam photon energy range from 230 MeV to 842 MeV.

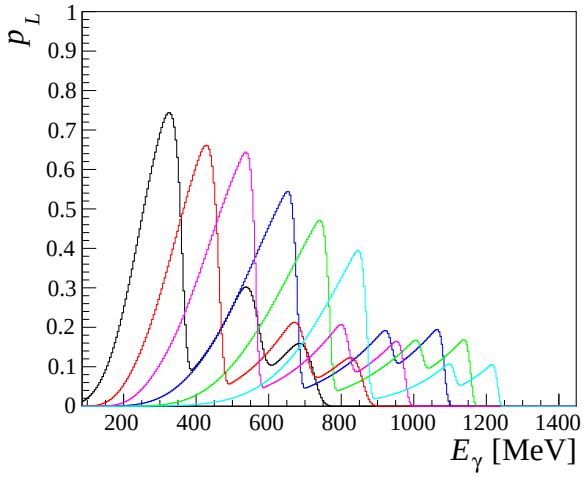

E_γ [MeV]	Coh. edges [MeV]	$p_{L,max}$
230–332	350+450	0.7
332-434	450	0.64
434–468	450+550	0.64
468-536	550+650	0.62
536-604	650	0.49
604-638	650+750	0.55
638-740	750	0.45
740-842	850	0.37

Fig. 8.9 & Table 8.1: Coherent edges for the different beam photon energy ranges. The linear polarization degrees for different coherent edges starting at 350 MeV and ending at 850 MeV are shown on the left side. The right side presents an overview of the combined coherent edges as a function of the beam photon energy.

Moreover, the beam polarization is split into the two diamond settings, namely parallel (∥) and perpendicular (⊥). Since the coherent edge positions of both these settings are not always adjusted completely at the same coherent edge position during data taking, small deviations in the polarization degree can occur. Fig. 8.10 shows the obtained polarization degrees for a coherent edge of 450 MeV for the parallel (red) and perpendicular (black) setting on the left side. On the right side, the ratio between both settings is illustrated. As already has been stated in [104], the uncertainty in the polarization degree increases further away from the coherent edge position as in this area the systematic uncertainty of the fit has the biggest effect. Nevertheless, these deviations are less than 5%. In addition, as will be shown later in Sec. 8.3, the extraction methods of the polarization observables are able to handle the effects of the small deviations in the polarization degrees of both settings.

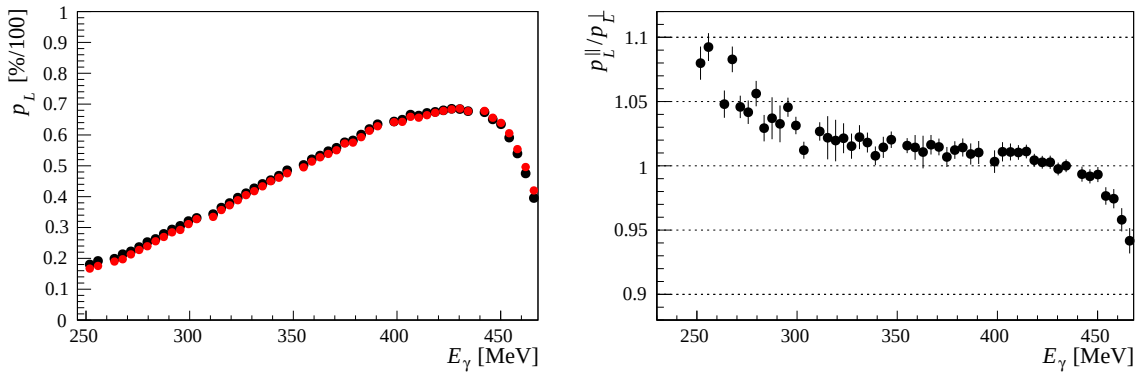

Fig. 8.10: Polarization degrees for the parallel and perpendicular settings of the 450 MeV edge. The left panel shows the obtained polarization degrees for the parallel (red) and perpendicular (black) settings whereas the right panel presents their ratio.

The systematic error of the linear polarization degree is mainly dominated by the active edge fitting,

which has been introduced in Sec. 3.2.5. A significant source of systematic error in the polarization degree is the production of the enhancement which is used to obtain the polarization degrees (cf. Sec. 3.2.5). Thereby, the major source of uncertainty comes from the normalization of the enhancement and the determination of its baseline. The baseline indicates the level where no coherent bremsstrahlung contribution is present and thus the ratio between the distribution of the diamond and amorphous radiator should be once. It is located between the first and second enhancement. However, as the collimation of the photon beam was not narrow enough, the coherent contribution between both enhancement regions could not be suppressed completely. The systematic uncertainty due to a wrong baseline fit can be estimated with the relation between the enhancement ε and the resulting polarization degree p_L [103]:

$$\frac{\Delta p_L}{p_L} = \frac{1}{(\varepsilon - 1)} \cdot \frac{\Delta \varepsilon}{\varepsilon}. \tag{8.20}$$

Therefore, a larger enhancement maximum results in a lower fractional error in the polarization degree. As the enhancement decreases with increasing coherent edge positions, the fractional error of the polarization degree grows with the increasing coherent edge. The enhancement of the coherent edge at 450 MeV has a maximum of 4. whereas at 850 MeV it has a maximum of 2.5. Further studies and comparison with previous works [115] show that an upper limit of 5% can be assumed for the enhancement uncertainty. Therefore, the fractional error of the polarization degree is in the range from 2.5% to 5%.

The second source of systematic errors lies in the proper fitting and determination of the actual coherent edge position. In the past, the coherent edge position in the active determination of the polarization degree was performed by fitting a Gaussian function with a baseline close to the falling edge of the coherent edge. Afterward, the derivation of the Gaussian function was calculated and its maximum position was chosen to be the coherent edge position. To ensure that the fit is performed close to the falling edge, a starting point for each coherent edge setting was defined in a config file. Starting from there, the bin content with the highest count rate was chosen as the starting point of the fitting routine and the endpoint of the fit was set at roughly the starting point plus 40 MeV. A drawback of this method is finding the correct starting point of the fit. Missing or noisy channels can artificially select a wrong starting point of the fitting routine and thus often cause an incorrect determination of the coherent edge position. Therefore, within the thesis, a new fitting routine was developed with collaborators in Bonn. Under perfect conditions, the enhancement can be approximated by a linearly increasing function with a sharp discontinuity at the coherent edge position d and afterward a flat distribution. Therefore, the function is given by:

$$f(x) = \begin{cases} a + b \cdot x & \text{if } x < d \\ c & \text{if } x \geq d. \end{cases} \tag{8.21}$$

However, as experimental aspects like beam divergence and multiple scattering need to be taken into account, the function is smeared out. This smearing can be respected by convoluting the linear function

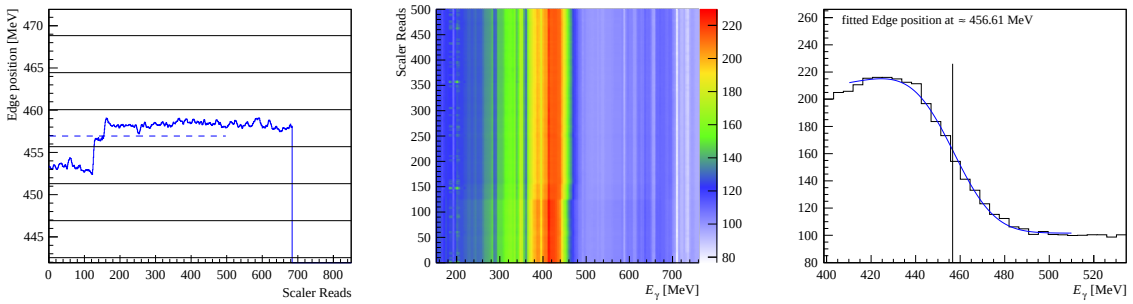

Fig. 8.11: Stability check of the determination of the coherent edge position. The left side shows the fitted coherent edge position as a function of the scaler reads of a run. The middle represents the corresponding enhancement as a function of the scaler read whereas the right side illustrates one projection together with the fit function $h(x)$. The plots are represented for a run with a coherent edge setting at 450 MeV.

with a gaussian function $g(x)$ and solving the convolution $h(x) = (f * g)(x)$ with MATHEMATICA [130]. Compared to the previous fitting routine, this method has two major advantages. First of all, the new routine is much faster in the fitting because the parameter d directly gives the coherent edge position without searching for the largest slope of the Gaussian function. Most importantly, however, the linear part of the new fitting routine stabilizes the fit if statistical fluctuations in the enhancement spectrum would set a wrong starting position for the previous fit routine.

To ensure the stability of the fitting routine for each run, a script was written. It creates three histograms as can be seen in Fig. 8.11. The left one depicts the fitted edge position as a function of the scaler read of a run whereas the right one illustrates the non-normalized enhancement for one scalar read together with its fitted edge position. From the inspection of the figure, it becomes directly visible how important the active fitting routine is. For the upper row, the coherent edge position suddenly jumped from roughly 452 MeV to 457 MeV. To ensure that this jump is not caused by a wrong fit, the middle panel is included in the check routine as a jump in the enhancement distribution is seen. This can be explained by the fact that shift members were able to nudge and readjust the coherent edge within a run. Although this was not desired, it was sometimes not avoidable. Another possible explanation could be sudden jumps in the beam position. Nevertheless, in most cases, the coherent edge position was very stable and oscillated only within one tagger channel. The tagger channels hereby are indicated by the horizontal lines. To estimate an upper limit of the contribution of the fitting routine to the overall systematic error, the enhancements were artificially shifted from their fitted position by $\pm$ 2 MeV and the polarization degrees were extracted. An example can be seen in Fig. 8.12 on the left where the black line indicates the fitted coherent edge position and the red and blue lines the distribution where the position was shifted by $\pm$ 2 MeV. On the right side, the fraction between the non-shifted polarization degrees and the shifted one is depicted. A conclusion of the figure is that the data should only be analyzed below the coherent edge position as the fractional error increases dramatically due to the large change in the absolute polarization degree. Therefore, only events within the yellow region are analyzed. In addition, the figure reveals that an uncertainty in the fitting of the edge position by $\pm$ 2 MeV is in the order of about 2%. Similar results were obtained

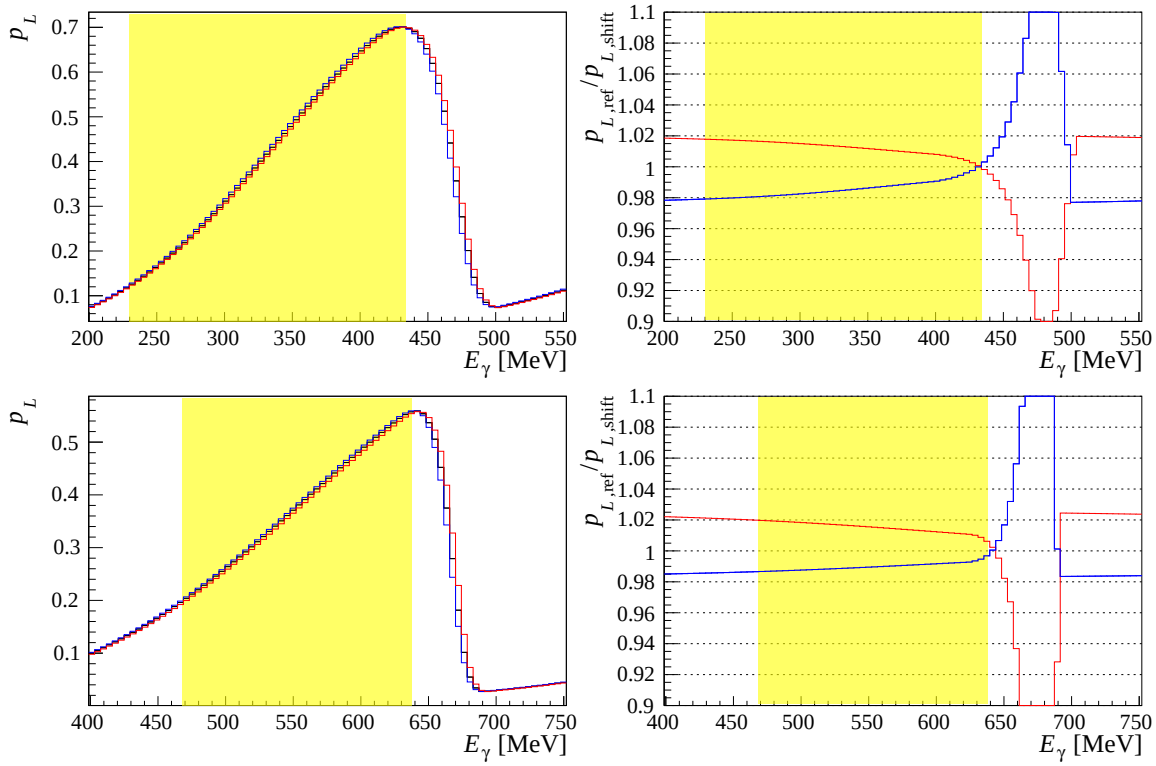

Fig. 8.12: Systematic uncertainty test due to a shift of the coherent edge. The black line indicates the fitted coherent edge distribution and the red and blue lines the distributions where the edge position was shifted by $\pm$ 2 MeV. On the right side, the fraction between the non-shifted polarization degrees and the shifted one is depicted. The yellow region depicts the energy range in which the polarization observables are extracted. The upper row shows the case for the coherent edge position at 450 MeV while the lower depicts the one for the edge position at 650 MeV.

for other coherent edge positions which can be found in App. A.5. As the actual oscillation of the final fit and the difference in both fitting models is mostly only in the order of 1 to 2 MeV, an upper limit of 2% is assumed for the systematic uncertainty coming from the determination of the edge position in data. These upper limits will later be strengthened by a comparison of the results of the beam asymmetry Σ_B for different coherent edge fit positions within a single coherent edge setting (cf. App. A.5).

Combining this uncertainty in quadrature with the uncertainty mentioned above, an overall uncertainty of about 3% is achieved for the 450 MeV coherent edge which increases to 5% for the 850 MeV coherent edge.

8.2.1.2 Circularly Polarized Photons

In Sec. 3.3, the determination of the circular polarization degree was introduced. After each tagging efficiency measurement in the individual beamtimes, Mott measurements were performed by the MAMI group to determine the polarization degree of the electrons. An overview of the measured

values as a function of the run number and the beamtimes is given in Fig. 8.13. These values are used to determine a linear interpolation for the extraction of the electron polarization as a function of the run number. In combination with the incoming electron energy E_e and Eq. (3.15), the circular polarization degree for each event can be determined. The overall systematic uncertainty for the circular polarization degree is 2.7%. Further details can be found in references [84] and [106].

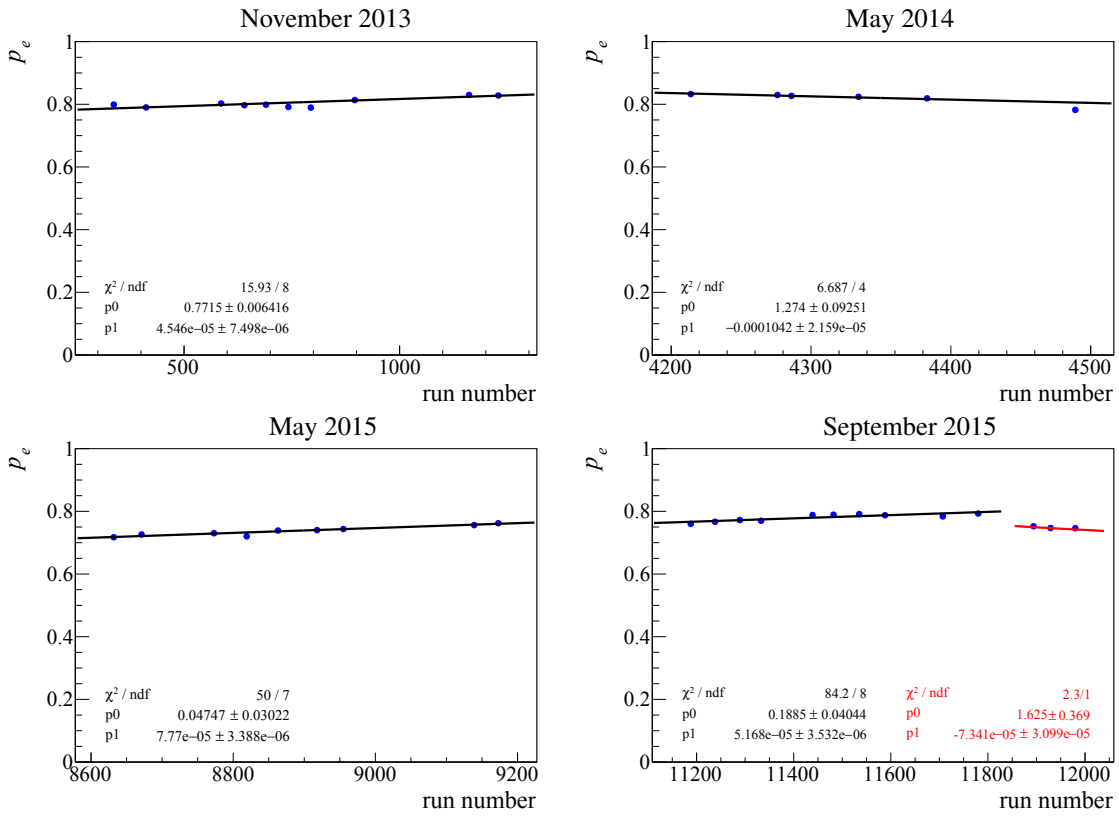

Fig. 8.13: Electron polarization degree as a function of the run number of each bean time. The Mott measurements of the MAMI group for the individual beamtimes are shown in blue. In addition, a linear interpolation between the points is performed and the resulting fit results are given (figure taken from [14]).

8.2.2 Target Polarization

In Sec. 2.3.1, the procedure for the determining target polarization has been explained. The target polarization was measured at the beginning and at the end of a data taking period using the NMR technique. Thereby, a data taking period can either be a repolarization of the target, a change of the polarization orientation[9] or a new measurement of the polarization degree. Afterward, the initial polarization degrees p_Z^i and the final polarization degrees p_Z^f can be used to determine the relaxation time $\Delta\tau$. An overview of the individual polarization degrees and relaxation times of the four beamtimes is given in Tab. 8.2. Special attention needs to be paid to the smaller relaxation times

[9] Indicated in Tab. 8.2 by the sign change.

Table 8.2: Overview of the main parameters for the determination of the target polarization run by run. The initial target polarization measurements p_Z^i and final target polarization values p_Z^i and their corresponding relaxation times $\Delta\tau$ obtained by the A2 target group are shown. Furthermore, the run number of the run directly after the polarization measurements is given. Note that a repolarization of the target was not performed each time between a NMR measurement. The smaller relaxation times of the May 2015 beamtime can be explained by a small helium leak which caused a sub-optimal cooling of the target.

Beamtime	Run number	p_Z^i [%]	p_Z^f [%]	$\Delta\tau$ [h]
November 2013	320	63.00	59.25	3707
	860	-64.69	-53.14	1223
May 2014	4181	-62.90	53.14	1082
May 2015	8607	70.50	66.40	472
	8642	66.40	52.75	307
	8790	64.20	54.70	699
	9030	66.10	58.30	548
	9098	-70.50	-66.90	995
	9178	-66.90	-65.44	974
September 2015	11159	-84.90	-81.65	1038
	11203	-80.50	-73.90	1038
	11390	87.15	79.02	1736

of the May 2015 beamtime compared to the others. This can be explained by a helium leak in the refrigerator system which caused a sub-optimal cooling of the target cell and consequently smaller relaxation times. With the values obtained in Tab. 8.2, and assuming an exponential behavior between the data taking periods, the target polarization degree of each run can be calculated via:

$$p_Z(t) = p_Z^i \cdot \exp(-t/\Delta\tau), \tag{8.22}$$

where t is the time that has passed from the beginning of the data taking period to the start of the considered run. The resulting target polarization degrees as a function of the run number and their corresponding beamtime are shown in Fig. 8.14. As already mentioned in Sec. 4.3.2, in all beamtimes except September 2015 the target polarization degree was not measured correctly. The problem was detected in an offline analysis performed by F. Afzal in which the double polarization observable E was extracted in the $\vec{\gamma}\vec{p} \to p\pi^0$ and $\vec{\gamma}\vec{p} \to p\eta$ final state [14]. Two major observations in the results suggest a problem with the target polarization, namely:

- a large discrepancy between the extracted double polarization observable E and the PWA solutions in the $\Delta(1232)3/2^+(P_{33})$ -region for the reaction $\vec{\gamma}\vec{p} \to p\pi^0$ ($E_\gamma \approx 320\,\text{MeV}$ to $360\,\text{MeV}$),
- a value for E above 1 for the $\vec{\gamma}\vec{p} \to p\eta$ final state in the η photoproduction threshold region ($E_\gamma \approx 700\,\text{MeV}$ to $900\,\text{MeV}$).

First of all, the double polarization observable E has a large amplitude in the $\Delta(1232)3/2^+(P_{33})$ region for the $\vec{\gamma}\vec{p} \to p\pi^0$ final state and the resonance is quite well understood from the different PWA groups.

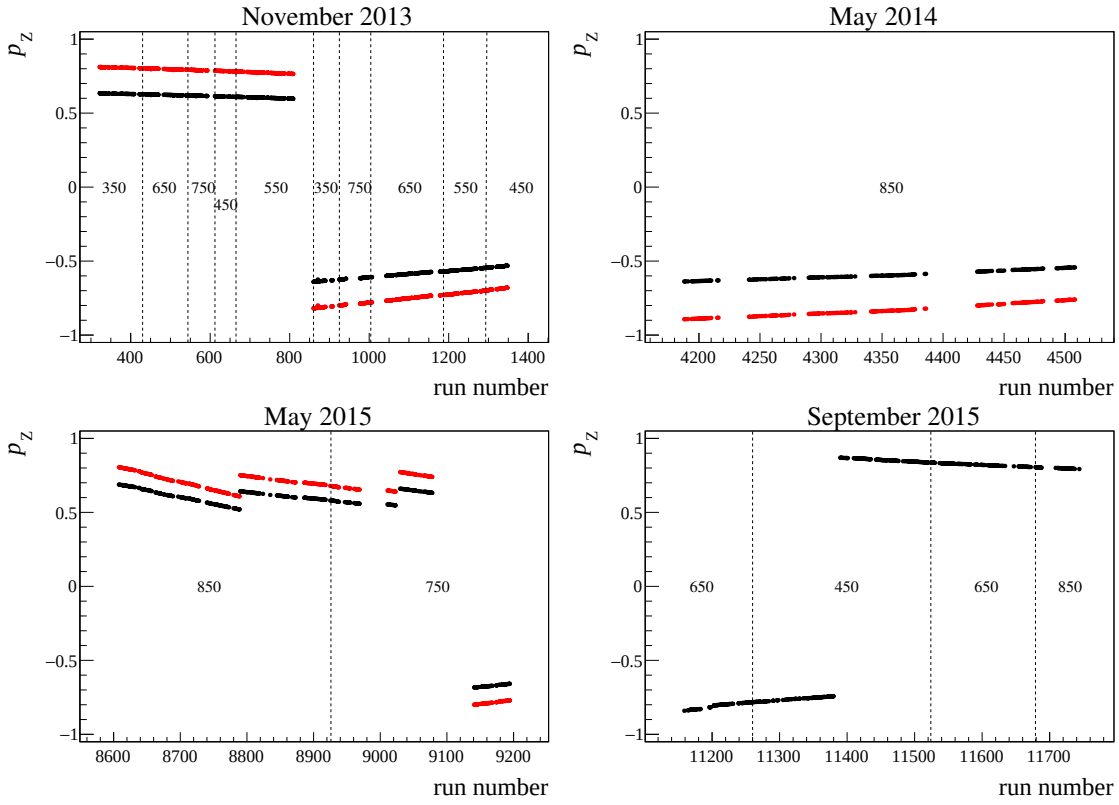

Fig. 8.14: Target polarization degree as a function of the run number of each bean time. By using the values in Tab. 8.2 in combination with Eq. (8.22), the target polarization degree values are obtained and are shown in black. The corrected target polarization values (see text) are depicted by the red points. In addition, the coherent edge settings are included by the vertical, dashed lines.

Second, from theory it is well known that the observable E for the $\vec{\gamma}\vec{p} \to p\eta$ final state in the η photoproduction threshold region is 1 and should not exceed 1[10]. Inspecting Eq. (8.7), the double polarization observable E depends on the dilution factor d, the circular polarization degree of the photon p_C and the polarization degree of the target p_Z. Each contribution will be discussed shortly within this thesis. For more details see [14].

Dilution factor Detailed studies were performed by F. Afzal and within this thesis to show that the dilution factor is well understood. An independent analysis was performed by Prof. P. Pedroni of the A2 collaboration. The difference of the helicity dependent cross sections $\Delta\sigma = \sigma_{3/2} - \sigma_{1/2}$ was extracted for the November 2013 beamtime and compared to recent GDH data (see Fig. 8.15). This method is independent of the dilution factor and needs similar target polarization correction factors as have been found in [14].

Circular polarization degree of the photons The circular polarization degree is well understood from QED calculations. The systematic uncertainties of the polarization degree of the incoming

[10]The dominant resonance contribution near threshold comes from the $N(1535)1/2^-(S_{11})$ resonance. From the definition of E (cf. Sec. 8.4), it follows that the observable E must be 1.

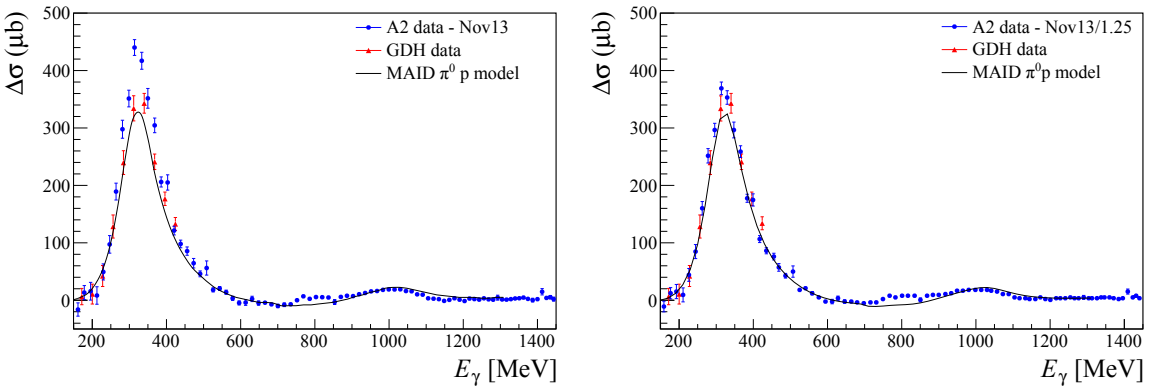

Fig. 8.15: Helicity dependent cross section $\Delta\sigma = \sigma_{3/2} - \sigma_{1/2}$. Shown is the difference of the helicity dependent cross section $\Delta\sigma = \sigma_{3/2} - \sigma_{1/2}$ as a function of the beam photon energy. The blue data points indicate the results for the $p\pi^0$ channel of the November 2013 beamtime. They are compared to existing GDH data [131]. The black line shows the PWA solution of MAID 2007. The left side presents the case without any target correction factor whereas the right side includes a target correction factor of 1.25 (figure taken from [14]).

electrons are in the order of 3%, whereas the uncertainties of the incoming electron energy and the tagged photon energy can be neglected in the calculation. The only remaining concern has been that the linear polarization degree of the photons can affect the circular polarization degree. Fortunately, data were taken with a Møller radiator, where only circular polarized photons are produced. A study has proven that the polarizations do not affect each other [14].

Polarization degree of the target The only remaining source can be the target polarization degree. As briefly mentioned in Sec. 4.3.2, the A2 target group has already proven that the target polarization degree was not determined correctly for all beamtimes before September 2015. Due to an ice layer on the outer NMR coil of the target cell, the unpolarized background protons in the ice influenced the determination of the polarization inside the butanol target and resulted in a too low polarization degree [88]. To solve this problem, in September 2015 the outer NMR coil was replaced with an inner NMR coil. Note that September 2015 does not need any correction factors for the target polarization degree. As a final cross-check, it is also important to mention that all the results presented in this thesis, including G which is also sensitive to the target polarization degree, include the correction factors which have been found in [14]. Especially, the double polarization observable G in the $n\pi^+$ channel is so large that the target factors can be seen there as well (cf. Sec. 8.3.6). For a further cross-check of the analysis performed in [14], the double polarization observable E has been extracted in an independent analysis within this thesis for the reactions $\vec{\gamma}\vec{p} \to p\pi^0$ and $\vec{\gamma}\vec{p} \to n\pi^+$. As will be shown in Sec. 9.1.3, recent data for the observable E have been published by the CLAS collaboration [68]. These data are perfectly suited to be compared with the results obtained within this analysis. Note that here target correction factors were also needed to match both data sets.

To determine the correction factors, the E results of the individual beamtimes were normalized by the unaffected E results of the September 2015 beamtime. Afterwards, each point is filled in a histogram. A Gaussian fit to the distribution finally gives a mean value for the correction factors. The correction factors were determined for the $p\pi^0$ and $p\eta$ channel by F. Afzal and are summarized in Tab. 8.3 and are illustrated in Fig. 8.16 in the upper and middle row [14].

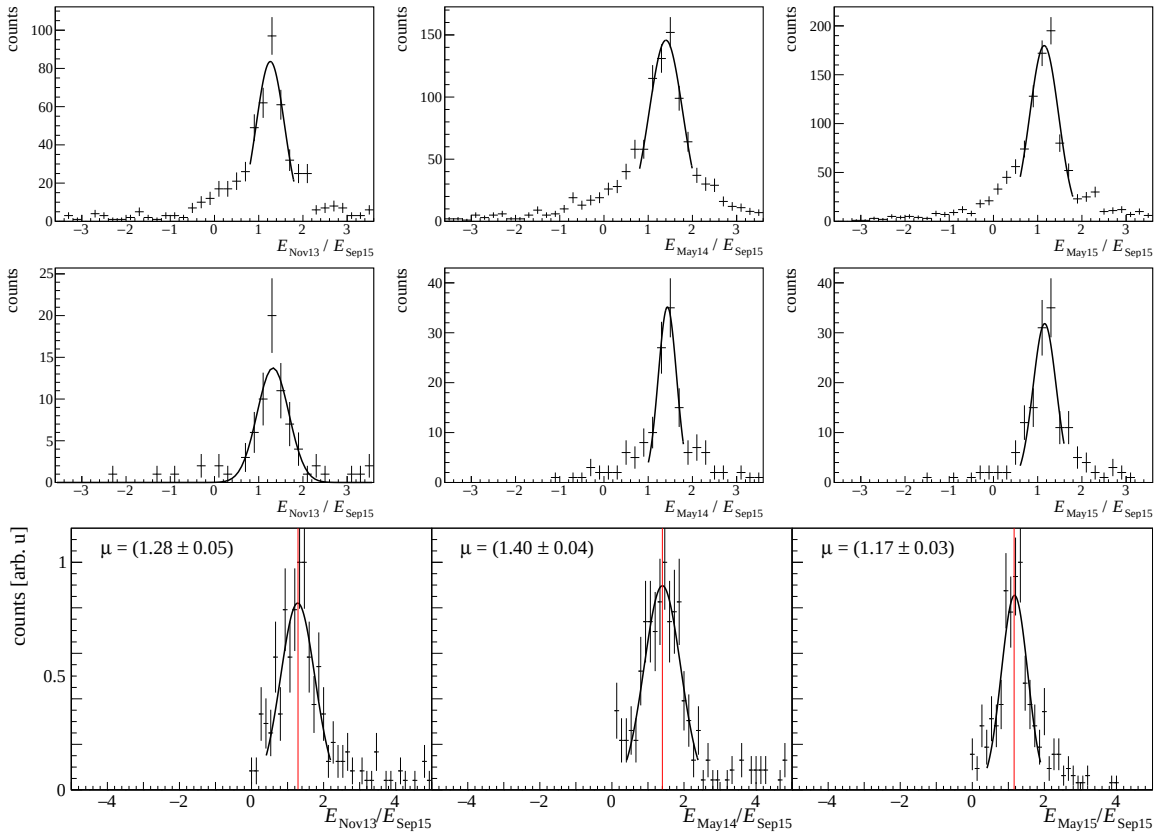

Fig. 8.16: Target correction factors obtained by the double polarization observable *E*. The ratios of the extracted polarization observable values of the November 2013, May 2014 and May 2015 beamtimes are shown with respect to the September 2015 beamtime. The upper row presents the results from the $p\pi^0$ channel whereas the middle row for the $p\eta$. Both are determined within the thesis of F. Afzal [14]. The lower row depicts the results for the $n\pi^+$ channel which have been determined within this thesis. The black gaussian functions are used to determine the correction factors. The red line in the lower column indicates the position of the correction factors which have been determined within the thesis of F. Afzal [14].

The histograms and the corresponding correction factors for the $n\pi^+$ final state are illustrated for the 2 PED events in the lower row in Fig. 8.16. Thereby, the correction factors were only determined for the 2 PED events because the contribution of the systematic uncertainty, coming from the dilution factor, is negligible in this case. Inspecting Tab. 8.3 and Fig. 8.16, it can be concluded that these

Table 8.3: Overview of the target polarization correction factors. The obtained correction factors for the individual final states and beamtimes are shown. The values for the $p\pi^0$ and $p\eta$ channel were taken from [14] .

Channel	Beamtime		
	November 2013	May 2014	May 2015
$p\pi^0$	1.27±0.03	1.40±0.03	1.15±0.02
$p\eta$	1.30±0.05	1.39±0.04	1.17±0.03
$n\pi^+$	1.28±0.05	1.40±0.04	1.17±0.03

correction factors are, within their statistical uncertainties, independent of the analyzed channel[11] which emphasizes again the incorrect determination of the target polarization degree.

8.3 Beam Asymmetry Σ_B and Double Polarization Observable G

To extract the contribution of the beam asymmetry Σ_B and the double polarization observable G from the selected data, a detailed inspection of Eq. (8.4) and Eq. (8.5) is mandatory. As mentioned in the introduction of the chapter, the helicity dependent cross section cause a change in the sign in the contribution of the double polarization observable E. Thus, the summation over both helicity states for both target settings should cancel the contribution of E, as can be seen in Eq. (8.23).

$$\begin{aligned}
\left.\frac{d\sigma}{d\Omega}\right|_{T\uparrow}^{H\uparrow} + \left.\frac{d\sigma}{d\Omega}\right|_{T\uparrow}^{H\downarrow} &= \left.\frac{d\sigma}{d\Omega}\right|_{B0} \cdot (2 - \ldots - \dot{d}p_C^{\uparrow}\dot{p}_Z^{\uparrow}E + \dot{d}p_C^{\downarrow}\dot{p}_Z^{\uparrow}E) \stackrel{!}{=} \left.\frac{d\sigma}{d\Omega}\right|_{0} \cdot (2 - \ldots) \\
\left.\frac{d\sigma}{d\Omega}\right|_{T\downarrow}^{H\uparrow} + \left.\frac{d\sigma}{d\Omega}\right|_{T\downarrow}^{H\downarrow} &= \left.\frac{d\sigma}{d\Omega}\right|_{B0} \cdot (2 - \ldots + \dot{d}p_C^{\uparrow}\dot{p}_Z^{\downarrow}E - \dot{d}p_C^{\downarrow}\dot{p}_Z^{\downarrow}E) \stackrel{!}{=} \left.\frac{d\sigma}{d\Omega}\right|_{0} \cdot (2 - \ldots)
\end{aligned} \tag{8.23}$$

For a better overview within the equations, the contribution terms of the linear polarization degree of the photons are marked with dots.

The inspection of Eq. (8.23) shows that the circular polarization degrees of the photons need to be similar in both helicity states. In that case, the contribution of the double polarization observable E vanishes. The agreement of the electron polarization degree in both helicity states can be used as a simple cross-check since the circular polarization degree of the photons is determined with the incoming electron polarization degree. The MAMI accelerator group provides this information, and the electron polarization degree in both helicity states agrees within 3%. Consequently, $p_C^{\uparrow} = p_C^{\downarrow}$ is a very good approximation. In addition, it needs to be shown that the helicity of the electron spin was switched with a frequency of 1 Hz within a run. Otherwise, an artificial count rate asymmetry would be produced. Each individual run was tested if the spin-flip between the helicity states $H\uparrow$ and $H\downarrow$ took place. As illustrated in Fig. 8.17, the helicity flip was not working for recent runs, and thus they need to be rejected from the complete analysis. Therefore, after summation over both helicity states,

[11] Since the target correction factor is a global correction, it is also expected to see no dependency on the analyzed reaction channel.

the differential cross section is given by:

$$\left.\frac{d\sigma}{d\Omega}\right|^{L(\parallel/\perp)}_{T(\uparrow/\downarrow)} = \left.\frac{d\sigma}{d\Omega}\right|_{B0} \cdot \left(1 - p_L^{\parallel/\perp}\Sigma_B \cos 2(\phi+\varphi_0) + d p_L^{\parallel/\perp} p_Z^{\uparrow/\downarrow} G \sin 2(\phi+\varphi_0)\right). \tag{8.24}$$

Based on Eq. (8.24), different methods for the extraction of Σ_B and G will be presented in the following sections.

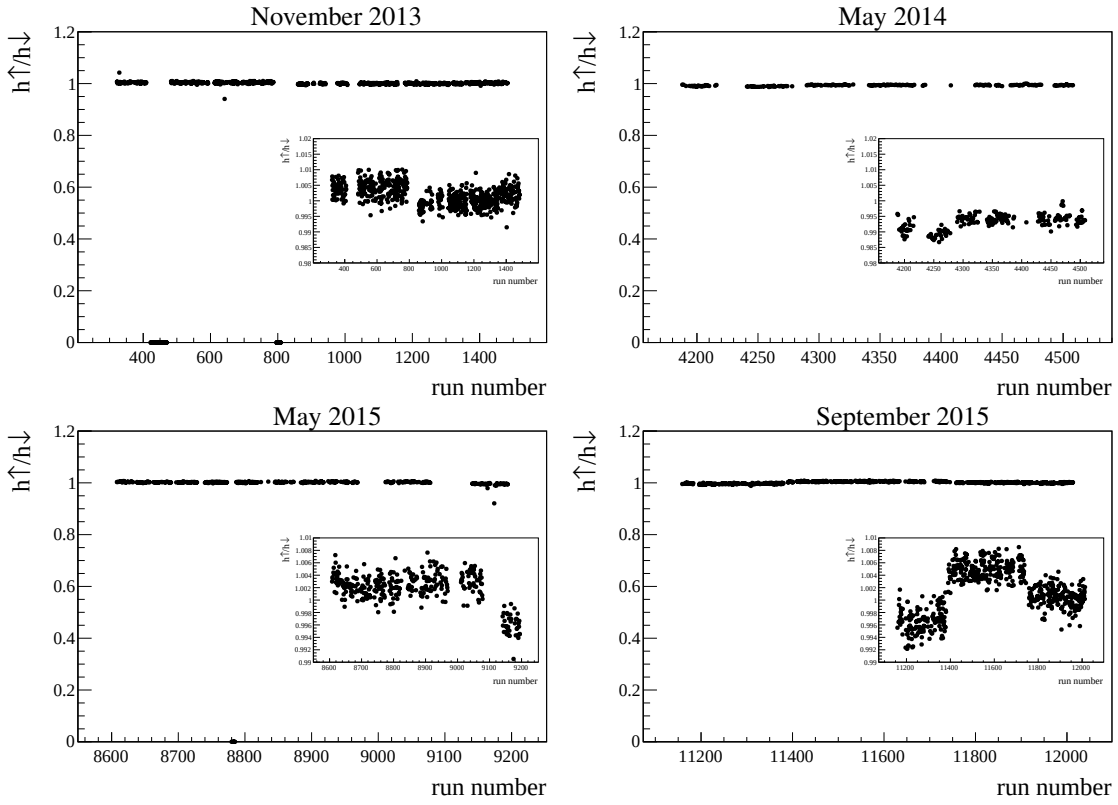

Fig. 8.17: Ratio of the helicity states. The ratios of the helicity states are shown as a function of the run number of each run. It is clearly visible that the ratio is close to 1 with a fluctuation of only 0.01. In addition, runs with no helicity flip can be identified as their ratio is zero.

8.3.1 Determination using a Binned Event Yield Asymmetries

One method for the extraction of the polarization observables is to make use of the orthogonality of the parallel and perpendicular setting of the beam polarization plane in combination with the target polarization direction in and against the beam direction. With that, changes in the sign are produced in the $\sin 2\phi$ and $\cos 2\phi$ modulations of the cross section, which makes it possible to combine the

settings in such a way that only one modulation is left. The following four settings are defined as:

$$\left.\frac{d\sigma}{d\Omega}\right|_{\parallel}^{\uparrow} = \left.\frac{d\sigma}{d\Omega}\right|_{B0} \cdot \left(1 - p_L^{\parallel}\Sigma_B \cos 2\varphi_{\parallel} + d p_L^{\parallel} p_Z^{\uparrow} G \sin 2\varphi_{\parallel}\right) \tag{8.25}$$

$$\left.\frac{d\sigma}{d\Omega}\right|_{\perp}^{\uparrow} = \left.\frac{d\sigma}{d\Omega}\right|_{B0} \cdot \left(1 + p_L^{\perp}\Sigma_B \cos 2\varphi_{\parallel} - d p_L^{\perp} p_Z^{\uparrow} G \sin 2\varphi_{\parallel}\right) \tag{8.26}$$

$$\left.\frac{d\sigma}{d\Omega}\right|_{\parallel}^{\downarrow} = \left.\frac{d\sigma}{d\Omega}\right|_{B0} \cdot \left(1 - p_L^{\parallel}\Sigma_B \cos 2\varphi_{\parallel} - d p_L^{\parallel} p_Z^{\downarrow} G \sin 2\varphi_{\parallel}\right) \tag{8.27}$$

$$\left.\frac{d\sigma}{d\Omega}\right|_{\perp}^{\downarrow} = \left.\frac{d\sigma}{d\Omega}\right|_{B0} \cdot \left(1 + p_L^{\perp}\Sigma_B \cos 2\varphi_{\parallel} + d p_L^{\perp} p_Z^{\downarrow} G \sin 2\varphi_{\parallel}\right) \tag{8.28}$$

with $\varphi_{\parallel} = \phi + \varphi_0$, $\varphi_{\perp} = \varphi_{\parallel} - 90°$, and $p_Z^{\downarrow} = |p_Z^{\downarrow}|$.

As already mentioned in the introduction of this chapter, the different cross sections can be replaced by a normalized event yield. Thereby, each cross section needs to have a similar acceptance of the analyzed reaction and detector efficiency. Within one target setting, data taking has been switched with a constant frequency between the parallel and perpendicular beam polarization plane. Thus, if the detector or reaction efficiency has changed, both settings would be affected in the same way. Between both target settings, a change in the acceptance or efficiency would cause bigger problems in building the asymmetry. However, a detailed study of the detector performance within a beamtime showed no evidence for a change. Thus, within a beamtime, the product of the detector and the reconstruction efficiency is assumed to be similar for all settings.

The product of both efficiencies, defined as the acceptance of the reaction, is unknown but can be modeled by a Fourier decomposition via:

$$\varepsilon(\phi) = \frac{1}{\varepsilon_{\text{det}}(\phi) \cdot A(\phi)} = 1 + \sum_{i=1}^{\infty} s_i \sin(i\phi) + c_i \cos(i\phi). \tag{8.29}$$

The normalization factor N_0 of each setting is then given by the inverse of the integral of each setting. As an example, the calculation for the setting, following Eq. (8.25), is presented. Using the orthogonality of the sin and cos functions, only the coefficients s_2 and c_2 from Eq. (8.29) contribute to the normalization. Thus, the integral of Eq. (8.25) is given by:

$$\begin{aligned}
\int_{-\pi}^{\pi} \left.\frac{d\sigma}{d\Omega}\right|_{\parallel}^{\uparrow} \mathrm{d}\phi &= \int_{-\pi}^{\pi} a \cdot \varepsilon(\phi) \cdot \left(1 - p_L^{\parallel}\Sigma_B \cos 2\varphi_{\parallel} + d p_L^{\parallel} p_Z^{\uparrow} G \sin 2\varphi_{\parallel}\right) \mathrm{d}\phi \\
&= 2\pi \cdot a \cdot \left(1 - p_L^{\parallel}\Sigma_B s_2 + d {p_L}^{\parallel} p_Z^{\uparrow} G c_2\right) \\
&= 2\pi \cdot a \cdot (1 + f_{\text{corr}})
\end{aligned} \tag{8.30}$$

where a includes the ϕ-independent contributions, namely the target area density n_B, the photon flux n_γ, and the event count rates N (cf. Eq. (8.9)). Rewriting Eq. (8.30) finally gives the normalization:

$$N_0 = \frac{1}{2\pi \cdot a} = \frac{(1+f_{\text{corr}})}{\int_{-\pi}^{\pi} \frac{d\sigma}{d\Omega}\big|_{\parallel}^{\uparrow} \, \mathrm{d}\phi}. \tag{8.31}$$

As will be shown later, the mean value of the coefficients s_2 is -0.012×10^{-2} and c_2 has a value of -0.046×10^{-2} (cf. Fig. 8.32). To give an upper limit for the correction factors, the highest possible values for the contributing parameters is assumed, leading to:

$$f_{\text{corr}} \leq +0.75 \cdot (\pm 1) \cdot (-0.012 \times 10^{-2}) + 1 \cdot 0.75 \cdot 0.85 \cdot (\pm 1) \cdot (-0.046 \times 10^{-2}) \approx \mp 3.810^{-3}. \tag{8.32}$$

Thus the correction factor f_{corr} in Eq. (8.31) can be neglected as it is in the order of 10^{-3}. Therefore, the normalization of each setting is finally determined by the inverse of the integral over ϕ of each setting by what the target area density n_B, the photon flux n_γ, and the event count rates N are taken into account (cf. Eq. (8.9)).

A further problem to investigate is the polarization degree of the individual settings. As the beam polarization plane was constantly switched, the target polarization degree can be assumed to be independent of the beam polarization plane. Under perfect conditions, the absolute values of the target polarization in and against the beam direction should be similar as well. However, as has been shown in Sec. 8.2.2, the butanol target was not polarized back to similar polarization degrees. Moreover, the data taking after the repolarization was not always started with the same coherent edge position. Combining both these facts, a relative deviation of up to 10% in the polarization degree between both target settings is present.

Concerning the beam polarization settings, Sec. 8.2.1.1 has proven that the coherent edge positions of both settings were not always sitting perfectly at the same position. Already a shift of only 2 MeV, cause a relative difference of about 2-3%. Therefore, the difference between both these polarizations needs to be respected as well.

To compensate for all these effects, a polarized weighted asymmetry is needed which is achieved by normalizing the individual settings by their polarization degrees and integrals. In the following, a detailed calculation of the polarized weighted asymmetries will be presented.

8.3.1.1 Artificial Asymmetries

As the polarization observables are extracted through the analysis of the different ϕ-distributions, it is crucial that the distributions are not affected by artificial asymmetries. These artificial asymmetries are caused by inefficiencies in the detector system and reaction inefficiencies of the desired reaction and can be studied by the unpolarized cross section $\frac{d\sigma}{d\Omega}\big|_0$ which includes the acceptance ε (cf. Eq. (8.29)). Inspecting Eqs. 8.25-8.28, the sum of all settings should cancel all contributions of the polarization observables and only the acceptance ε should remain. However, this is only the case if all polarization

degree values are the same. To ensure that the normalized event yields are independent of their polarization degree values, the settings are divided by the product of their beam and target polarization value.

$$\begin{aligned}\frac{N_{\parallel}^{\uparrow}}{p_L^{\parallel}p_Z^{\uparrow}}+\frac{N_{\parallel}^{\downarrow}}{p_L^{\parallel}p_Z^{\downarrow}}+\frac{N_{\perp}^{\uparrow}}{p_L^{\perp}p_Z^{\uparrow}}+\frac{N_{\perp}^{\downarrow}}{p_L^{\perp}p_Z^{\downarrow}} &= \varepsilon\cdot\left(\frac{1}{p_L^{\parallel}p_Z^{\uparrow}}+\frac{1}{p_L^{\parallel}p_Z^{\downarrow}}+\frac{1}{p_L^{\perp}p_Z^{\uparrow}}+\frac{1}{p_L^{\perp}p_Z^{\downarrow}}\right.\\ &\quad+\left(\frac{1}{p_Z^{\uparrow}}+\frac{1}{p_Z^{\downarrow}}\right)\Sigma_B\cos 2\varphi_{\parallel}-\left(\frac{1}{p_Z^{\uparrow}}+\frac{1}{p_Z^{\downarrow}}\right)\Sigma_B\cos 2\varphi_{\parallel}\\ &\quad\left.+d(G-G-G+G)\sin 2\varphi_{\parallel}\right)\\ &= \varepsilon\cdot\left(\frac{1}{p_L^{\parallel}p_Z^{\uparrow}}+\frac{1}{p_L^{\parallel}p_Z^{\downarrow}}+\frac{1}{p_L^{\perp}p_Z^{\uparrow}}+\frac{1}{p_L^{\perp}p_Z^{\downarrow}}\right).\end{aligned} \tag{8.33}$$

Therefore, the acceptance ε is given by:

$$\varepsilon=\left(\frac{N_{\parallel}^{\uparrow}}{p_L^{\parallel}p_Z^{\uparrow}}+\frac{N_{\parallel}^{\downarrow}}{p_L^{\parallel}p_Z^{\downarrow}}+\frac{N_{\perp}^{\uparrow}}{p_L^{\perp}p_Z^{\uparrow}}+\frac{N_{\perp}^{\downarrow}}{p_L^{\perp}p_Z^{\downarrow}}\right)\cdot\left(\frac{1}{p_L^{\parallel}p_Z^{\uparrow}}+\frac{1}{p_L^{\parallel}p_Z^{\downarrow}}+\frac{1}{p_L^{\perp}p_Z^{\uparrow}}+\frac{1}{p_L^{\perp}p_Z^{\downarrow}}\right)^{-1}. \tag{8.34}$$

8.3.1.2 Beam Asymmetry Σ_B

Inspecting Eqs. 8.25-8.28, it can be directly seen that the summation over both target settings cancels the contribution of the double polarization observable G. To take into account the effect of the different target polarization degrees, the settings are divided by their individual target polarization degrees, resulting in the following conditions for both diamond orientations:

$$\begin{aligned}N_{\parallel}:=\frac{N_{\parallel}^{\uparrow}}{p_Z^{\uparrow}}+\frac{N_{\parallel}^{\downarrow}}{p_Z^{\downarrow}} &= \varepsilon\cdot\left[\frac{1}{p_Z^{\uparrow}}+\frac{1}{p_Z^{\downarrow}}-\left(\frac{1}{p_Z^{\uparrow}}+\frac{1}{p_Z^{\downarrow}}\right)p_L^{\parallel}\Sigma_B\cos 2\varphi_{\parallel}\right]\\ &= \varepsilon\cdot\left(\frac{1}{p_Z^{\uparrow}}+\frac{1}{p_Z^{\downarrow}}\right)\cdot\left(1-p_L^{\parallel}\Sigma_B\cos 2\varphi_{\parallel}\right),\end{aligned} \tag{8.35}$$

$$\begin{aligned}N_{\perp}:=\frac{N_{\perp}^{\uparrow}}{p_Z^{\uparrow}}+\frac{N_{\perp}^{\downarrow}}{p_Z^{\downarrow}} &= N_0\cdot\left[\frac{1}{p_Z^{\uparrow}}+\frac{1}{p_Z^{\downarrow}}+\left(\frac{1}{p_Z^{\uparrow}}+\frac{1}{p_Z^{\downarrow}}\right)p_L^{\perp}\Sigma_B\cos 2\varphi_{\parallel}\right]\\ &= \varepsilon\cdot\left(\frac{1}{p_Z^{\uparrow}}+\frac{1}{p_Z^{\downarrow}}\right)\cdot\left(1+p_L^{\perp}\Sigma_B\cos 2\varphi_{\parallel}\right).\end{aligned} \tag{8.36}$$

As a next step, Eq. (8.36) will be subtracted from Eq. (8.35) and divided by the normalized and polarized weighted acceptance ε , given by Eq. (8.34), and the target polarization degrees. Therefore, the beam asymmetry can be extracted by the amplitude of a $\cos 2\phi$ dependent ϕ-asymmetry distribution

which is created via:

$$A^*_{\Sigma_B} := \frac{N_\perp - N_\parallel}{\varepsilon \cdot \left(\frac{1}{p_Z^\uparrow} + \frac{1}{p_Z^\downarrow}\right)} = \left(p_L^\perp + p_L^\parallel\right) \Sigma_B \cos 2\varphi_\parallel$$
$$\rightarrow A_{\Sigma_B} := \frac{A^*_{\Sigma_B}}{p_L^\perp + p_L^\parallel} = \Sigma_B \cos 2\varphi_\parallel. \tag{8.37}$$

8.3.1.3 Double Polarization Observable G

For the extraction of the double polarization observable G, the following asymmetries need to be built:

$$\left(\frac{N_\parallel^\uparrow}{p_L^\parallel p_Z^\uparrow} + \frac{N_\perp^\downarrow}{p_L^\perp p_Z^\downarrow}\right) - \left(\frac{N_\parallel^\downarrow}{p_L^\parallel p_Z^\downarrow} + \frac{N_\perp^\uparrow}{p_L^\perp p_Z^\uparrow}\right) = \varepsilon \cdot \left(\frac{1}{p_L^\parallel p_Z^\uparrow} + \frac{1}{p_L^\perp p_Z^\downarrow} - \frac{1}{p_L^\parallel p_Z^\downarrow} - \frac{1}{p_L^\perp p_Z^\uparrow} + 2\left(\frac{1}{p_Z^\uparrow} - \frac{1}{p_Z^\downarrow}\right)\Sigma_B \cos 2\varphi_\parallel + 4dG \sin 2\varphi_\parallel\right) \tag{8.38}$$

Rewriting Eq. (8.38) and including Eq. (8.37), the final asymmetry for the extraction of G is given by:

$$\begin{aligned} A^*_G = \quad & \frac{1}{4\varepsilon} \cdot \left[\left(\frac{N_\parallel^\uparrow}{p_L^\parallel p_Z^\uparrow} + \frac{N_\perp^\downarrow}{p_L^\perp p_Z^\downarrow}\right) - \left(\frac{N_\parallel^\downarrow}{p_L^\parallel p_Z^\downarrow} + \frac{N_\perp^\uparrow}{p_L^\perp p_Z^\uparrow}\right)\right] \\ & - \frac{1}{4} \cdot \left(\frac{1}{p_L^\parallel} - \frac{1}{p_L^\perp}\right) \cdot \left(\frac{1}{p_Z^\uparrow} - \frac{1}{p_Z^\downarrow}\right) + \frac{1}{2} \cdot \left(\frac{1}{p_Z^\uparrow} - \frac{1}{p_Z^\downarrow}\right) A_{\Sigma_B} \\ = \quad & dG \sin 2\varphi_\parallel \end{aligned}$$

$$\rightarrow A_G := \frac{A^*_G}{d} = G \sin 2\varphi_\parallel. \tag{8.39}$$

Thus, the double polarization observable G can be extracted by the amplitude of a $\sin 2\varphi_\parallel$ dependent ϕ-asymmetry distribution which is created via Eq. (8.39).

8.3.1.4 Determination of the Beam Polarization Offset Angle φ_0

Within this thesis, two possible ways for the determination of the offset angle φ_0 were studied. It should be noted that the parallel and perpendicular orientation of the diamond crystal is perfectly orthogonal to each other because the lattice of a diamond has a four-fold symmetry. Thereby, the parallel setting uses the orthogonal set of planes from the perpendicular setting. Consequently, it is sufficient to measure the beam polarization offset angle φ_0 for only one setting and also independent from the coherent edge position [132]. The first determination makes use of the carbon measurements performed in November 2013 and September 2015. As mentioned in the introduction of this chapter, the carbon angular distribution shows no contribution of the double polarization observables G and E. Therefore, the cross section is only given by Eq. (8.6). By building an asymmetry, based on Eq. (8.37),

the φ_0 offset angle can be treated as a free parameter in the fit. The second method is to determine the offset angle directly from the butanol data using the beam asymmetry which is given by Eq. (8.37). The resulting asymmetries are illustrated in Fig. 8.18.

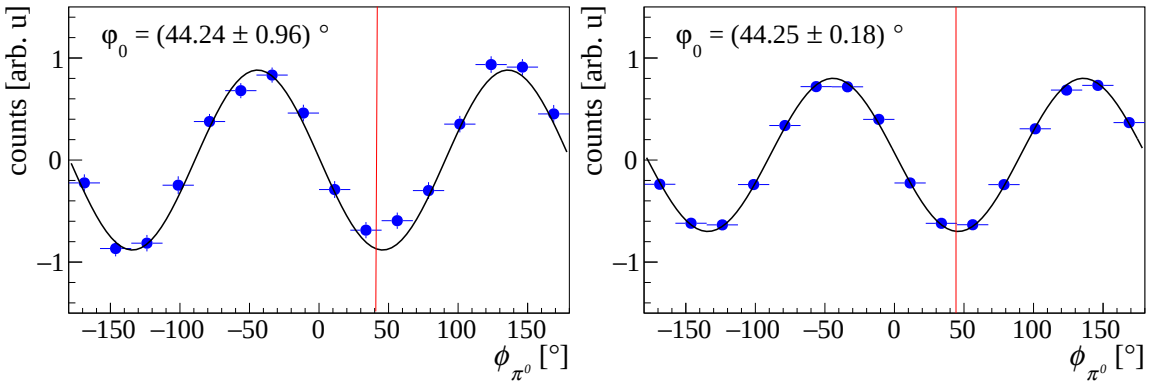

Fig. 8.18: Asymmetries for the determination of the beam polarization offset angle φ_0. Two asymmetries are shown which are determined via Eq. (8.37) and integrated over all kinematic variables. On the left side, the asymmetry for the September 2015 butanol data of the 450 MeV edge is shown whereas on the right side the one for the September 2015 carbon with helium data. Both methods result in a fitted offset angle φ_0 of about 44.24°.

Both methods result in a similar offset angle of about 44.24°. A value of 44.3° was also reported for the same data set in [104] and for a different data set a value was estimated to be 44.15° [115]. As all these values perfectly agree with each other, a strong conclusion is that the offset angle is determined accurately. The importance of the correct determination of the offset angle becomes clear in the analysis of data sets with only one target polarization orientation. In that case, the determination of the double polarization G without the contribution of the beam asymmetry Σ_B becomes impossible. Whereas the amplitude of the $\cos 2\varphi_{\parallel}$ distribution gives access to the contribution of the beam asymmetry Σ_B, the shift of this $\cos 2\varphi_{\parallel}$ modulation from the beam polarization plane, which is given by the offset angle, indicates the contribution of the double polarization observable G. In case the beam polarization plane is not known accurately, it is not clear if the shift is caused by the contribution of the double polarization observable G or not. Especially for the May 2014 beamtime an accurate determination of the offset angle was not possible. In addition, the interaction point of the beam spot and the diamond crystal was sitting at the corner of the crystal and thus caused high instabilities in the correct adjustment of the coherent edge position. To test the influence of the offset angle on the extracted polarization observable G, the determined offset angle was varied by $\pm 1°$ and the observable were determined. Fig. 8.19 shows in the top row the G results for the May 2015 beamtime for the coherent edge at 750 MeV and a beam photon energy $E_\gamma = (706 - 740)$ MeV while the second row presents the results for the May 2014 beamtime for the coherent edge at 850 MeV and a beam photon energy $E_\gamma = (774 - 808)$ MeV. For the May 2015 beamtime where both target polarization orientations are available, the results have a relative change in the order of 2%. Only the χ^2/ndf got worse due to a not perfect $\sin 2\varphi_{\parallel}$ modulation anymore. The situation was different for the May

2014 beamtime. As G can not be determined by the amplitude of the $\sin 2\varphi_{\|}$ modulation, the relative changes between the three offset angle setting were huge. Thus, it has been decided to reject the May 2014 beamtime for the extraction of the double polarization observable G.

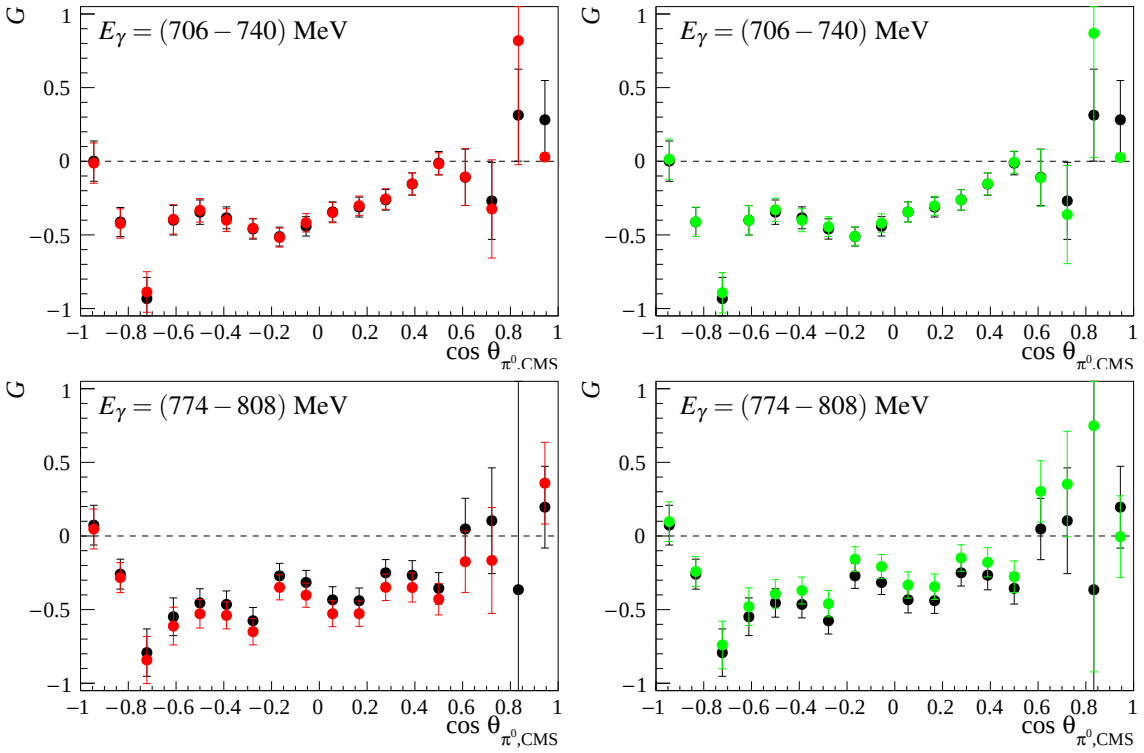

Fig. 8.19: Systematic uncertainty test due to a shift of beam polarization offset angle. The black points indicate the results for the double polarization observable G which have been determined with the extracted beam offset angle. The green and red points correspond to the results where the offset angle was shifted by $\pm$ 1°, respectively. The first row corresponds to the results of the May 2015 beamtime for the coherent edge at 750 MeV and a beam photon energy $E_\gamma = (706 - 740)$ MeV while the second row to the May 2014 beamtime for the coherent edge at 750 MeV and a beam photon energy $E_\gamma = (774 - 808)$ MeV.

8.3.2 Determination using an Unbinned Maximum Likelihood Fit

For the determination of the statistical error, the binned event yield method assumes a Gaussian error distribution. However, the underlying distribution of the data follows a Poisson distribution, which segues, according to the central limit theorem, into a Gaussian distribution for only high data samples ($n \to \infty$). Especially for higher beam photon energies E_γ, the data sample in a given $(E_\gamma, \cos\theta, \varphi)$ bin does not fulfill this condition and thus the binned event yield method does not determine the correct statistical errors. In addition, the binned event yield method uses weighted averaged polarization degrees for the beam and target. In combination with the differences in the polarization degrees of each setting, one additional uncertainty is included in the extraction. Finally, due to the binning of the azimuthal angle ϕ, additional information gets lost. To avoid these problems, an unbinned maximum

likelihood fit was performed in addition to the binned method. Therefore, in the following section, the basic idea and the implementation of the unbinned maximum likelihood fit will be presented.

8.3.2.1 Definition of the Likelihood Function

The probability of observing an event i at a given value x is given by a probability density function (PDF) $F(x;p)$ with $\vec{p}$ being the model/theory parameters. The likelihood $\mathscr{L}(\vec{p})$ is the product of the values of $F(x;\vec{p})$ evaluated at the measured values x_i of the observables $\vec{p}$:

$$\mathscr{L}(\vec{p}) = \prod_{i=1}^{N} F(x_i;\vec{p}). \tag{8.40}$$

As the values of $\mathscr{L}(\vec{p})$ are very small, the best values for the observables $\vec{p}$ for a data set consisting of N events with given values x_i are determined by minimizing the function

$$-\ln(\mathscr{L}(\vec{p})) = -\sum_{i=1}^{N} \ln(F(x_i;\vec{p})). \tag{8.41}$$

In case of high statistics, the likelihood $\mathscr{L}$ is a Gaussian function of the parameters $\vec{p}$ and therefore the $-\ln(\mathscr{L})$ can be approximated by a parabolic function. A good estimate of the errors for a 1σ confidence interval are those values for which the $\ln(\mathscr{L})$ changes by 0.5 from its minimum value:

$$\ln(\mathscr{L}) < -\ln(\mathscr{L})_{min} + 0.5. \tag{8.42}$$

The interval can be calculated with the second derivative at the minimum. Thus, the main advantage of this method is the possibility to have also asymmetric errors which are of special interest at low statistics. For this work, the theory/model parameters $\vec{p}$ are the beam asymmetry Σ_B and the double polarization observable G. They are extracted through studying the azimuthal angular distribution of the reconstructed pion as a function of the beam photon energy E_γ and $\cos\theta_{\mathrm{CMS}}$. Thus, the measured variable x is in the following the azimuthal angle ϕ. As shown previously, the distribution of a given event is given by the cross sections defined in Eq. (8.25)-(8.28). The normalized PDF for a given event is therefore:

$$F_{T(\uparrow/\downarrow)}^{L(\parallel/\perp)}(\phi;\Sigma_B,G) = \frac{1}{2\pi}\left(1 - p_L^{\parallel/\perp}\Sigma_B\cos 2(\phi+\varphi_0) + d\,p_L^{\parallel/\perp}p_Z^{\uparrow/\downarrow}G\sin 2(\phi+\varphi_0)\right). \tag{8.43}$$

Thereby, the factor $\frac{1}{2\pi}$ is the result of the normalization of the function in the brackets. Moreover, in this PDF, it has been assumed that the unpolarized cross section component has no ϕ-dependence which corresponds to a flat detector and reconstruction efficiency. As already shown in the Sec. 8.1.2.3, this is not the case and the overall acceptance can be modeled by the Fourier series which is given by Eq. 8.29. Although the Fourier series is truncated at four, the truncated series was able to model any simulated acceptances as will be shown later in this section and as well in the references [14]

and [60]. Since the overall acceptance is now ϕ-dependent, the normalization of the PDF is more complicated and is given for the four different settings by:

$$\begin{aligned}
\tilde{F}_{\parallel}^{\uparrow}(\phi;\vec{p}) &:= F^1 = \frac{F_{\parallel}^{\uparrow}(\phi;\vec{p})\cdot\varepsilon(\phi)}{2\pi+0.5\cdot\pi\cdot\left(p_L^{\parallel}\Sigma_B s_2 + d p_L^{\parallel} p_Z^{\uparrow} G c_2\right)} \\
\tilde{F}_{\perp}^{\uparrow}(\phi;\vec{p}) &:= F^2 = \frac{F_{\perp}^{\uparrow}(\phi;\vec{p})\cdot\varepsilon(\phi)}{2\pi+0.5\cdot\pi\cdot\left(-p_L^{\perp}\Sigma_B s_2 - d p_L^{\perp} p_Z^{\uparrow} G c_2\right)} \\
\tilde{F}_{\parallel}^{\downarrow}(\phi;\vec{p}) &:= F^3 = \frac{F_{\parallel}^{\downarrow}(\phi;\vec{p})\cdot\varepsilon(\phi)}{2\pi+0.5\cdot\pi\cdot\left(p_L^{\parallel}\Sigma_B s_2 - d p_L^{\parallel} p_Z^{\downarrow} G c_2\right)} \\
\tilde{F}_{\perp}^{\downarrow}(\phi;\vec{p}) &:= F^4 = \frac{F_{\perp}^{\downarrow}(\phi;\vec{p})\cdot\varepsilon(\phi)}{2\pi+0.5\cdot\pi\cdot\left(-p_L^{\perp}\Sigma_B s_2 + d p_L^{\perp} p_Z^{\downarrow} G c_2\right)}
\end{aligned} \tag{8.44}$$

with $\vec{p} = (\Sigma_B, G, s_1, \cdots, s_4, c_1, \cdots, c_4)$.
Note that due to the different settings, the normalization introduces sign changes in the denominator. As a consequence, the correlation between the polarization observables Σ_B and G and their corresponding Fourier coefficients s_2 and c_2 is removed and thus they can be determined independently from each other. The final function to be minimized is then given by:

$$\mathscr{L}(\vec{p}) = \prod_{k=1}^{4}\left(\prod_{i=1}^{N_k} F^k(\phi_i;\vec{p})\right) \tag{8.45}$$

with k being the 4 settings defined above and N_k the number of events in each setting. Lastly, the time background subtraction needs to be accounted for in the likelihood function which is defined in Eq. (8.45). Within this thesis, two different approaches have been implemented. The first one will be referred to as the background-subtracted method, the latter one as the background fitted method.

8.3.2.2 Implementation of Different Methods

Background-subtracted Method

The background-subtracted method aims to construct a likelihood which only fits the signal events in the prompt peak. The prompt likelihood consists of the prompt signal events, described by the PDF $F^k_{\text{signal}}(\phi;\vec{p}_{\text{signal}})$, and the random time background events beneath the peak, described by the PDF $F^k_{\text{back}}(\phi;\vec{p}_{\text{back}})$. Therefore, the overall likelihood is given by:

$$\begin{aligned}
\mathscr{L}_{\text{prompt}}(\vec{p}_{\text{signal}},\vec{p}_{\text{back}}) &= \prod_{k=1}^{4}\left(\prod_{i=1}^{N_{k,\text{prompt,signal}}} F^k_{\text{signal}}(\phi_i;\vec{p}_{\text{signal}})\cdot\prod_{j=1}^{N_{k,\text{prompt,back}}} F^k_{\text{back}}(\phi_j;\vec{p}_{\text{back}})\right) \\
&= \prod_{k=1}^{4}\left(\mathscr{L}^k_{\text{signal}}(\vec{p}_{\text{signal}})\cdot\mathscr{L}^k_{\text{back}}(\vec{p}_{\text{back}})\right).
\end{aligned} \tag{8.46}$$

Similar to the binned χ^2-fit method, the scaled sideband events can be used to subtract the random time background beneath the prompt peak. Thus, by taking the factor s_t, which is defined in Eq. (7.2), the contribution of the random time background beneath the prompt peak can be described with the sideband events leading to:

$$\mathscr{L}^k_{\text{back}}(\vec{p}_{\text{back}}) = \prod_{i=1}^{N_{k,\text{prompt,back}}} F^k_{\text{back}}(\phi_i;\vec{p}_{\text{back}}) = \left(\prod_{i=1}^{N_{k,\text{sideband}}} F^k_{\text{back}}(\phi_i;\vec{p}_{\text{back}})\right)^{s_t}. \tag{8.47}$$

Finally, the likelihood of the signal events in the prompt peak is given by:

$$\mathscr{L}_{\text{signal}}(\vec{p}_{\text{signal}}) = \frac{\mathscr{L}_{\text{prompt}}(\vec{p}_{\text{signal}},\vec{p}_{\text{back}})}{\mathscr{L}_{\text{back}}(\vec{p}_{\text{back}})} \tag{8.48}$$

and the function to be minimized is:

$$\begin{aligned}
-\ln\left(\mathscr{L}_{\text{signal}}(\vec{p}_{\text{signal}})\right) = \sum_{k=1}^{4}\Bigg(& -\sum_{i=1}^{N_{k,\text{prompt,signal}}} \ln\left(F^k_{\text{signal}}(\phi_i;\vec{p}_{\text{signal}})\right) \\
& \underbrace{-\sum_{i=1}^{N_{k,\text{prompt,back}}} \ln\left(F^k_{\text{back}}(\phi_i;\vec{p}_{\text{back}})\right) + s_t\cdot\sum_{j=1}^{N_{j,\text{sideband}}} \ln\left(F^k_{\text{back}}(\phi_k;\vec{p}_{\text{back}})\right)}_{=0}\Bigg) \\
= -\sum_{k=1}^{4}\Bigg(& \sum_{i=1}^{N_{k,\text{prompt,signal}}} \ln\left(F^k_{\text{signal}}(\phi_i;\vec{p}_{\text{signal}})\right)\Bigg).
\end{aligned} \tag{8.49}$$

Background-fitted Method

Instead of subtracting the time background beneath the prompt peak, it is also possible to fit the signal and background events simultaneously [60]. To do so, the exact amount of signal events beneath the prompt peak in each setting k needs to be known and can be calculated via:

$$\zeta^k = \frac{N_{k,\text{prompt}} - s_t\cdot N_{k,\text{sideband}}}{N_{k,\text{prompt}}} \tag{8.50}$$

where $N_{k,\text{prompt}}$ and $N_{k,\text{sideband}}$ are the total number of events for the given setting k in their individual time windows (cf. Sec. 7.4.2). Therefore, the likelihood in Eq. (8.45) can be rewritten to:

$$\mathscr{L}_{\text{prompt}}(\vec{p}_{\text{signal}},\vec{p}_{\text{back}}) = \prod_{k=1}^{4}\left(\prod_{i=1}^{N_{k,\text{prompt}}} \zeta^k\cdot F^k_{\text{signal}}(\phi_i;\vec{p}_{\text{signal}}) + (1-\zeta^k)\cdot F^k_{\text{back}}(\phi_i;\vec{p}_{\text{back}})\right). \tag{8.51}$$

As the time background events beneath the prompt peak can not be distinguished from the signal events, the sideband events can be used to describe the time background, leading to the time background

likelihood

$$\mathscr{L}_{\text{back}}(\vec{p}_{\text{back}}) = \prod_{k=1}^{4} \left(\prod_{i=1}^{N_{k,\text{sideband}}} F^k_{\text{back}}(\phi_i; \vec{p}_{\text{back}}) \right). \tag{8.52}$$

Thus, the total likelihood is the product of both leading to:

$$\mathscr{L}_{\text{total}}(\vec{p}_{\text{signal}}, \vec{p}_{\text{back}}) = \mathscr{L}_{\text{prompt}}(\vec{p}_{\text{signal}}, \vec{p}_{\text{back}}) \cdot \mathscr{L}_{\text{back}}(\vec{p}_{\text{back}}) \tag{8.53}$$

and the function to be minimized is given by:

$$\begin{aligned} -\ln\left(\mathscr{L}_{\text{total}}(\vec{p}_{\text{signal}}, \vec{p}_{\text{back}})\right) = \sum_{k=1}^{4} \Bigg(& - \sum_{i=1}^{N_{k,\text{prompt}}} \ln\left(\zeta^k \cdot F^k_{\text{signal}}(\phi_i; \vec{p}_{\text{signal}}) + (1-\zeta^k) \cdot F^k_{\text{back}}(\phi_i; \vec{p}_{\text{back}})\right) \\ & - \sum_{j=1}^{N_{k,\text{sideband}}} \ln\left(F^k_{\text{back}}(\phi_j; \vec{p}_{\text{back}})\right) \Bigg). \end{aligned} \tag{8.54}$$

Comparing Eq. (8.49) with Eq. (8.54), the main disadvantage of this method is the number of additional fit parameters. Whereas the background-subtracted method fits the signal events with only ten fit parameters $\vec{p}_{\text{signal}}$, the background-fitted method needs ten fit parameters $\vec{p}_{\text{back}}$ in addition, resulting in a total of 20 parameters.

8.3.3 Application of Methods to Toy Monte Carlo simulations

It is mandatory to make sure that both introduced unbinned likelihood fit methods above and the binned χ^2 fit method are working properly before they are applied to real data. A common tool to test the quality of the methods is to generate so-called Toy Monte Carlo simulations. Thereby, events are generated according to the cross sections given by Eqs. 8.25-8.28. Different samples of toy MC are produced to study the effect of artificial asymmetries in the real data (cf. Sec. 8.3.1.1), the effect of different polarization degrees and differences in the statistics of the individual setting[12]. The setting 1 and 2 represent the ideal case where all settings have roughly the same statistic, the polarization degree values are similar, and no detector inefficiency is included. Hereby, setting 1 is simulated for a region of low statistic whereas setting 2 for high statistic. Setting 3 and 4 include strong artificial asymmetries, different polarization degrees, and differences in the statistics of the individual setting. An overview of the different setting is given in Tab. 8.4. For all settings, the data sample consists of prompt peak events and random time background events. The number of events is hereby selected in such a way that the amount of prompt to random time background events matches the number of the real data. Moreover, the polarization observables are created with different values for both kinds of events as can be seen in Tab. 8.4 as well.

For the illustration of the parabolic shape of the likelihood function, which has been defined in

[12] Although only four MC sample are presented here, many other configuration were tested and all gave the same result.

Table 8.4: Overview of the parameters for the toy MC studies. Four MC samples were generated with different configurations for the target polarization p_Z with their polarization vector orientation in (↑) and against the beam direction (↓) and the linear polarization degrees p_L with their two beam polarization planes perpendicular (⊥) and parallel (‖). In addition, inefficiencies were included in sample 3 and 4. The number of events for each setting (in total 4) is generated under the assumption of Poisson distributions for a low statistic region in both analyzed channels in data with about 500 events per setting and a high statistic region with about 5000 events. Note that all number of events are smeared with a Gaussian function with a width of 50(500) to allow differences in statistics-. For each MC sample, 2500 independent experiments were generated with 95% prompt events with the beam asymmetry $\Sigma_{B,sig}$ = 0.7 and double polarization observable G_{sig} = -0.4. The remaining 5% random time background events have the exact opposite sign $\Sigma_{B,bg}$ = -0.7 and G_{sig} = 0.4.

MC sample	p_Z [%]		p_L [%]		Inefficiency	#Events
	↑	↓	⊥	‖		
1	84	84	60	60	no	500
2	84	84	60	60	no	5000
3	84	73	70	60	yes	500
4	84	73	70	60	yes	5000

Eq. (8.49), Fig. 8.20 illustrates the resulting likelihood function for a Toy Monte Carlo simulation of data sample four for the background-subtracted method. The theory parameters $\vec{p}$ are the polarization observables Σ_B and G which have been generated with a value of 0.7 and -0.4, respectively. Fig. 8.20 clearly shows that only one minimum exists and that the extracted values for the polarization observables are well in agreement with the generated once. In addition, the parabolic behavior of the likelihood function is nicely seen in both dimensions. Since these results are presented for a MC toy experiment of sample four, a direct conclusion would be to assume that this extraction method can handle strong artificial asymmetries. To prove this theory, the sum of all four cross section settings, given by Eqs. 8.25-8.28, is plotted in a binned histogram as a function of the azimuthal angular distribution of the reconstructed meson. Since the unbinned extraction methods can model the artificial asymmetries via Eq. (8.29), the comparison of the binned histogram with the obtained artificial asymmetry function from the unbinned extraction methods can ensure that artificial asymmetries do not affect the polarization observable values. Fig. 8.21 depicts an example of the binned sum of all cross section settings together with the obtained artificial asymmetry fit function of the unbinned extraction method for a MC experiment with strong artificial asymmetries on the left and without on the right. From the inspection of this comparison, a striking conclusion is that the unbinned method can handle huge detection inefficiencies and thus can even extract the polarization observables under these kind of conditions. The results of all obtained Fourier coefficients is depicted in Fig. 8.22. Whereas the Fourier coefficient are close to zero for the case without any artificial asymmetries (red distributions), the coefficients for the case with artificial asymmetries are not negligible (blue distributions).

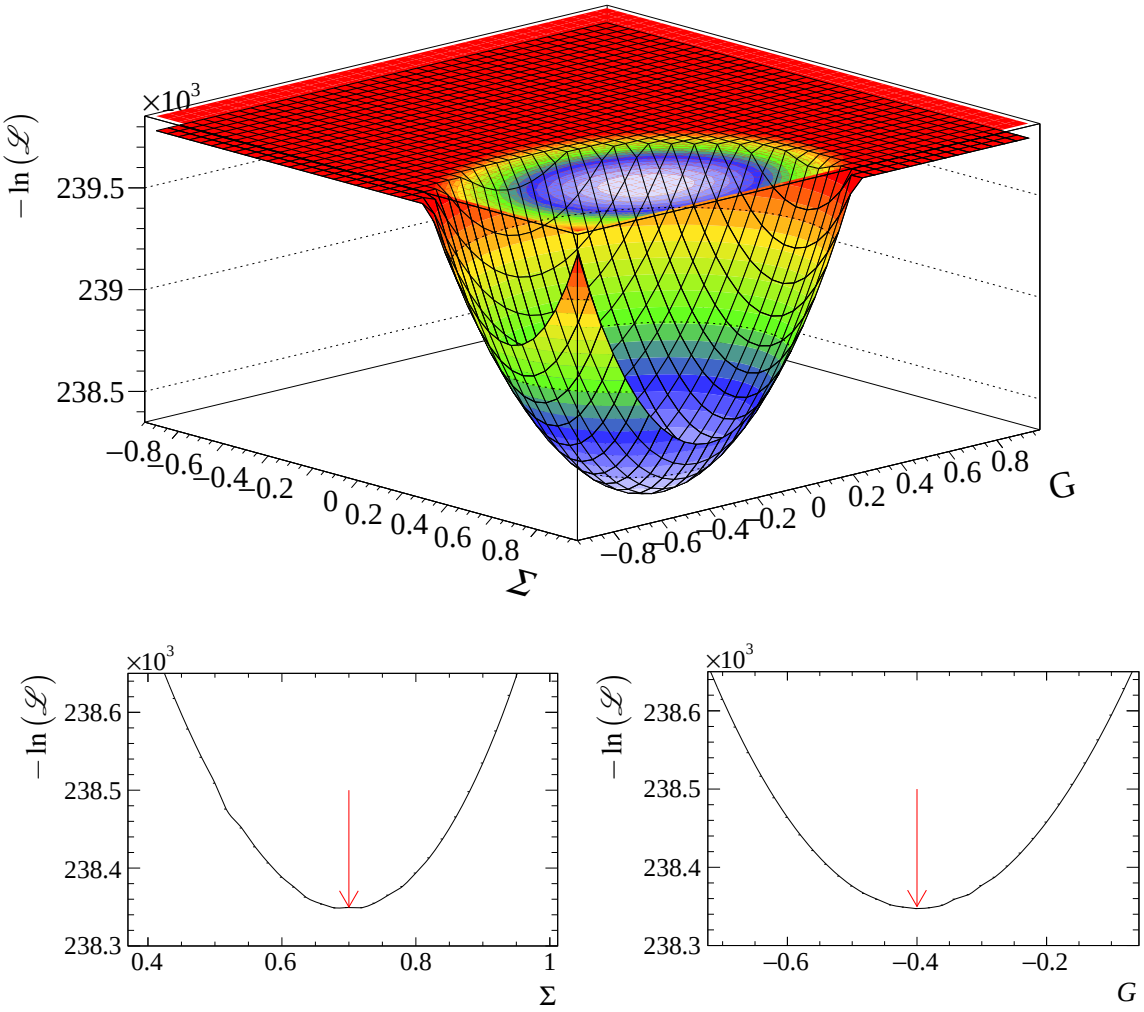

Fig. 8.20: The two dimensional $-\ln\left(\mathscr{L}_{\mathbf{signal}}(\vec{p}_{\mathbf{signal}})\right)$ function of the background subtracted method. The 2-dimensional likelihood function, defined in Eq. (8.49), for a Toy MC simulation experiment of MC sample four with the beam asymmetry Σ_B generated at 0.7 and the double polarization observable G at -0.4 is presented. The parabolic shape is clearly seen and the obtained minimum of the function is located at the generated values. To show the parabolic behavior of the likelihood function, the projection of the individual theory parameters is performed. To do so, one theory parameter was kept at its minimum whereas the other one was changed. The red arrow hereby indicates the position of the generated values.

Especially the parameter s_2 and c_2 need to be respected as they are contributing to the normalization of the individual settings for the binned extraction method. Nevertheless, the artificial asymmetries can be controlled by allowing an additional offset parameter p_0 in the asymmetry functions defined in Eq. (8.37) and Eq. (8.39) [14, 55]. The obtained offset parameter p_0 for the two MC samples with and without artificial asymmetries can be seen in Fig. 8.23.

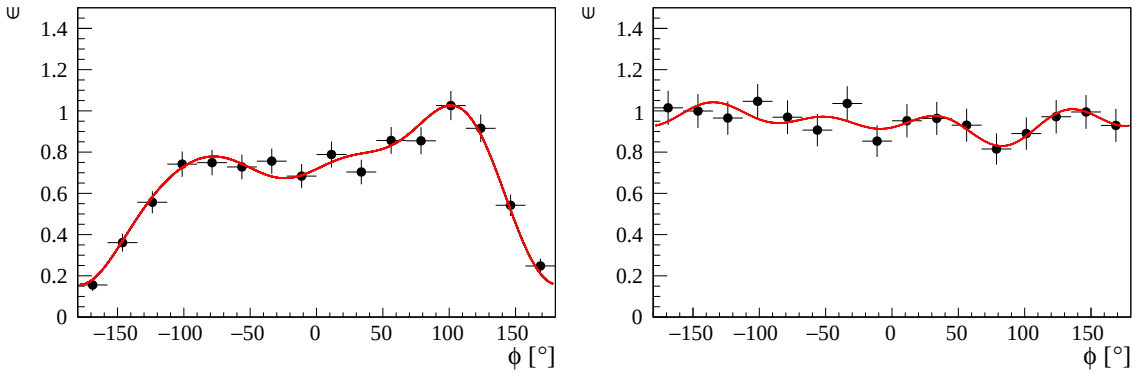

Fig. 8.21: Sum off all settings with their corresponding artificial asymmetry fit function. Shown is the sum of all settings, based on Eq. (8.34), together with the obtained artificial asymmetry fit function (red line) from the unbinned maximum likelihood fit. On the left side, an example of MC sample four is shown which includes strong artificial asymmetries whereas on the right side an example of MC sample one without any artificial asymmetries.

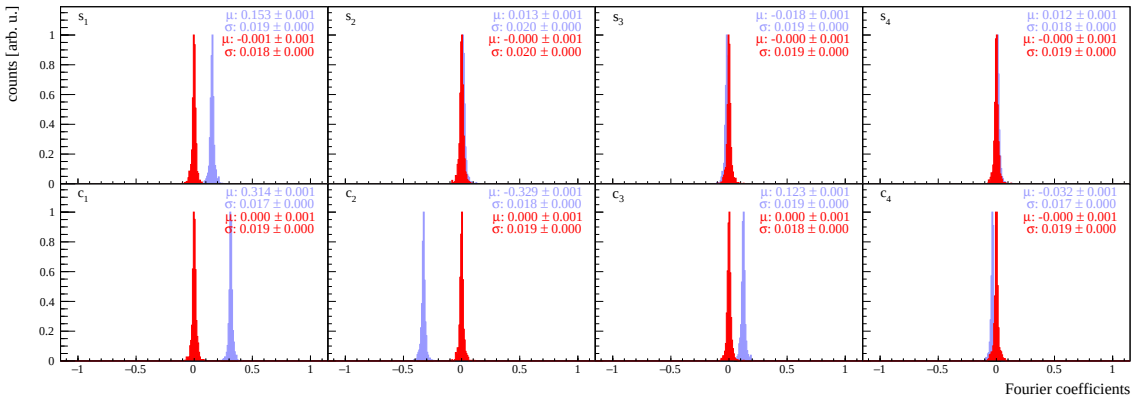

Fig. 8.22: All Fourier coefficients obtained by the artificial asymmetry fit for MC. All fitted Fourier coefficients which are based on Eq. (8.34) are shown. The blue distributions correspond to the coefficients of MC sample four which includes strong artificial asymmetries whereas the red distribution of MC sample one without any artificial asymmetries.

For the case without artificial asymmetries, the offset is distributed around zero whereas for the case of strong artificial asymmetries a small offset towards negative values is seen which is nevertheless negligible compared to the amplitudes from the polarization observables. Under the assumption of no offset parameter in the fit functions, tests have shown that the polarization observable changed from -0.4 to -0.392 for the case with strong artificial asymmetries, These discrepancy however was corrected with the inclusion of the additional offset parameter. A final test of the quality for the fit parameter is to investigate the normalized residual r_p which can be calculated via:

$$r_p = \frac{p_{\text{output}} - p_{\text{input}}}{\sigma_{p_{\text{output}}}} \text{ with } p \in \{\Sigma_B, G\}. \tag{8.55}$$

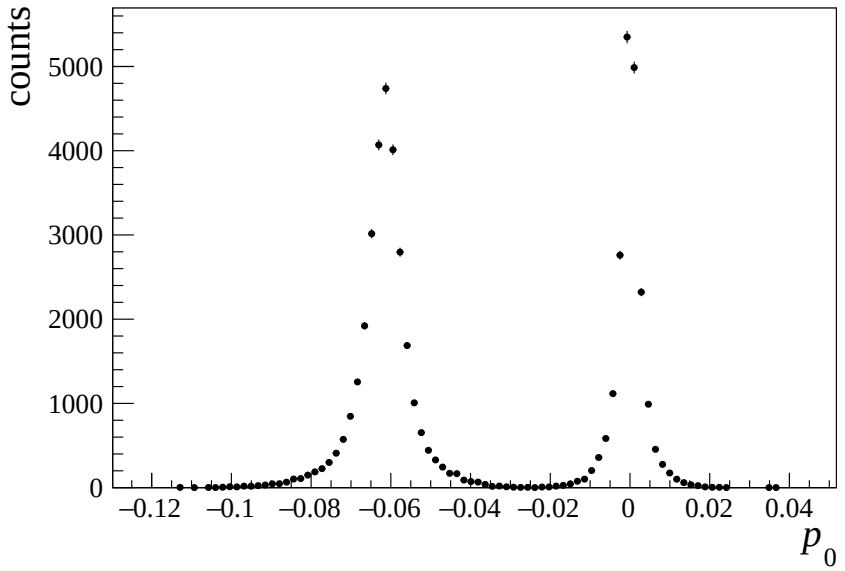

Fig. 8.23: Offset parameter p_0 for the correction of artificial asymmetries in MC. The additional offset parameter p_0 which can be included in the asymmetry functions defined in Eq. (8.37) and Eq. (8.39) is shown. Two defined peaks are visible which corresponds to the case with artificial asymmetries (left peak) and without artificial asymmetries (right peak).

Thereby, p_{input} is the value of the polarization observable which was implemented in the Toy MC samples and p_{output} and $\sigma_{p_{\text{output}}}$ are the obtained polarization observable value from the applied methods and the statistical errors, respectively. In case the method is unbiased, the mean value of the normalized residuals should be compatible with 0. In addition, if the statistical errors are correctly determined, the width of the residuals should be 1. An overestimated statistical error thereby would lead to a width smaller than 1, whereas an underestimated one a value bigger than one. For all settings mentioned above, Fig. 8.24 shows the resulting residuals of the double polarization observable G for all extraction methods whereas Fig. 8.25 illustrates the output value for the double polarization G[13]. Hereby, the row number indicates the individual MC samples introduced in Tab. 8.4. The inspection of Fig. 8.24 clearly shows that all residuals are compatible with a mean value of 0 and a width of 1. Consequently, all extraction methods are unbiased and are determining the correct statistical uncertainties. It is also noteworthy that both unbinned maximum likelihood functions for the treatment of the background events beneath the prompt peak are working properly and that the background events are fitted correctly as can be seen in Fig. 8.25 in the middle columns in red. In addition, the residuals of the data samples 2 and 4 clearly show that the extraction methods can handle the differences in the polarization degrees and also huge detection inefficiencies.

[13]The corresponding figures for the beam asymmetry Σ_B can be found in App. A.7.

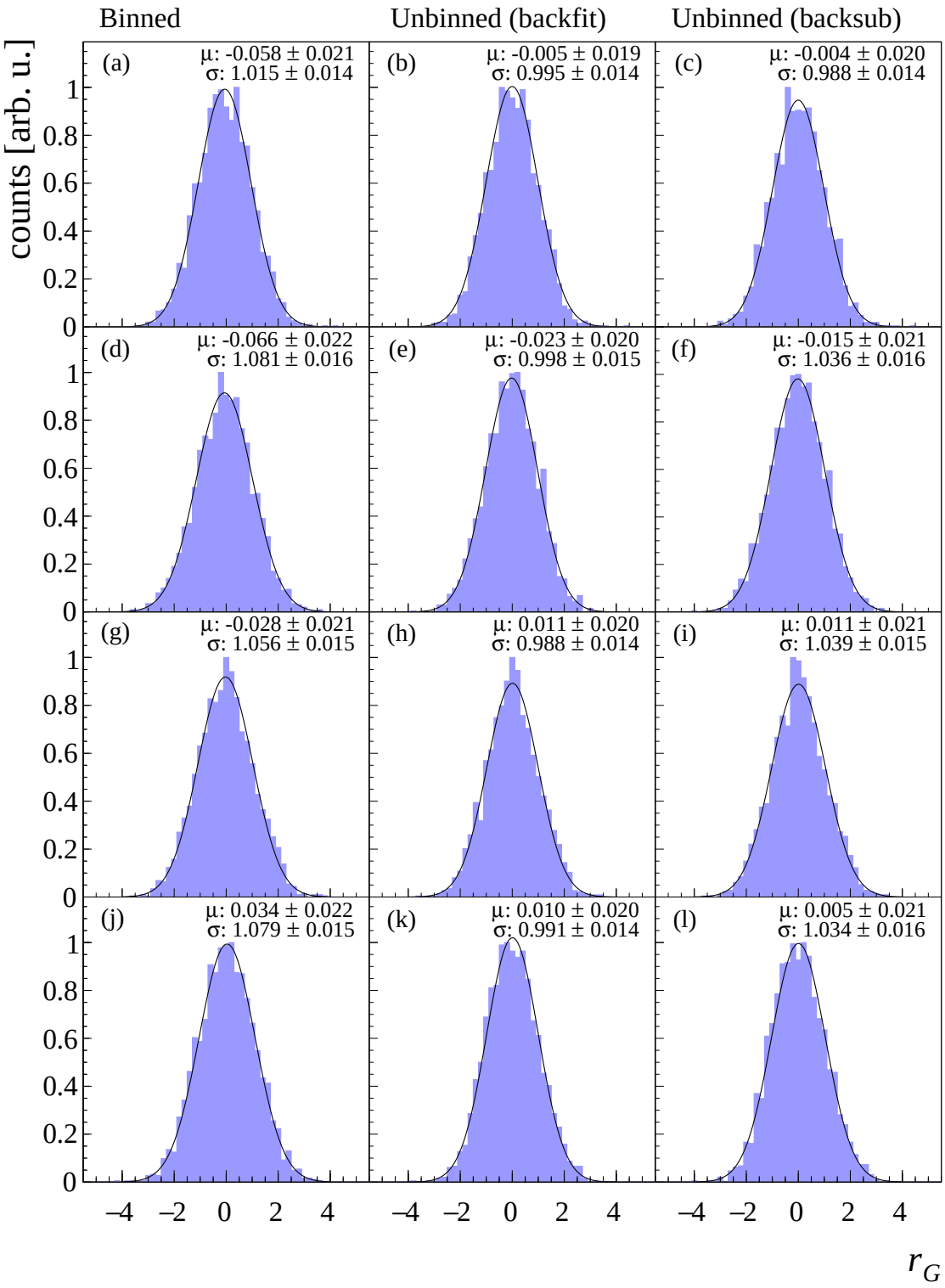

Fig. 8.24: Normalized residuals for the results of the double polarization observable *G* for the different Toy MC samples. The residuals for the different MC samples, defined in Tab. 8.4, and the different extraction methods are shown. Hereby, the row number indicates the MC sample number and the column the three extraction methods. All distributions are in agreement with a normal distribution.

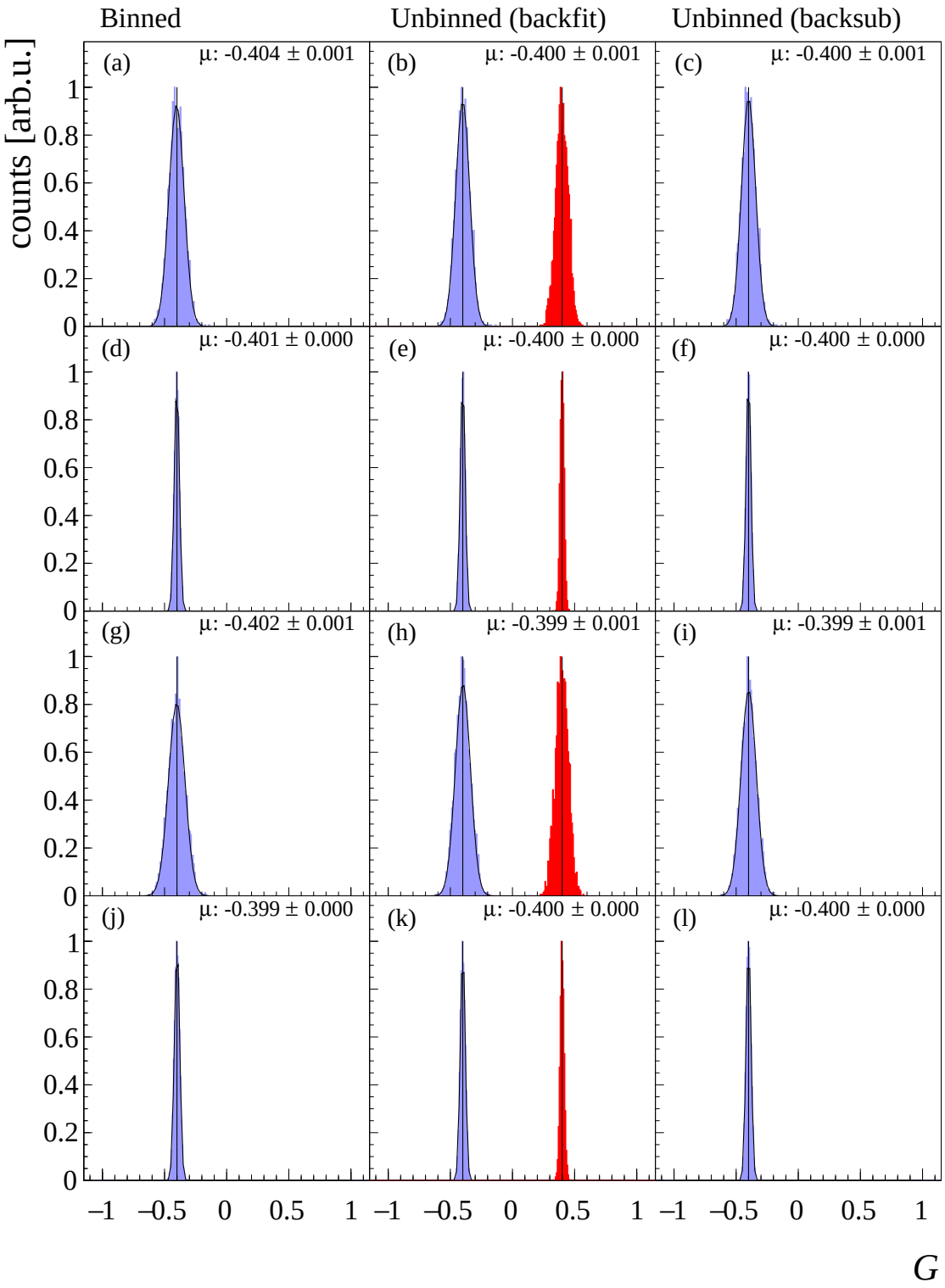

Fig. 8.25: Results of the double polarization observable G for the different Toy MC samples. The extracted polarization observable for the different MC samples, defined in Tab. 8.4, and the different extraction methods are shown. Hereby, the row number indicates the MC sample number and the column the three extraction methods. The extracted polarization observables for the signal events (blue) are distributed around their input value of -0.4 and the extracted once for the background events (red) around their input value of 0.4.

8.3.4 Application of Methods to Data

Since the Toy MC studies have proven that the different extraction methods are able to determine the polarization observable values, the final step is to apply and test the methods on real data. Therefore, similar to the Toy MC studies, the resulting polarization observables of both methods are compared. For the binned event yield method, Fig. 8.26 and Fig. 8.27 show typical asymmetries, following Eq. (8.39), for the reaction $\vec{\gamma}\vec{p} \to p\pi^0$ and $\vec{\gamma}\vec{p} \to n\pi^+$. They belong to a beam photon energy range from 400 MeV to 434 MeV and are presented as a function of the kinematic variable $\cos\theta_{M,CMS}$ with $M = \pi^0/\pi^+$.

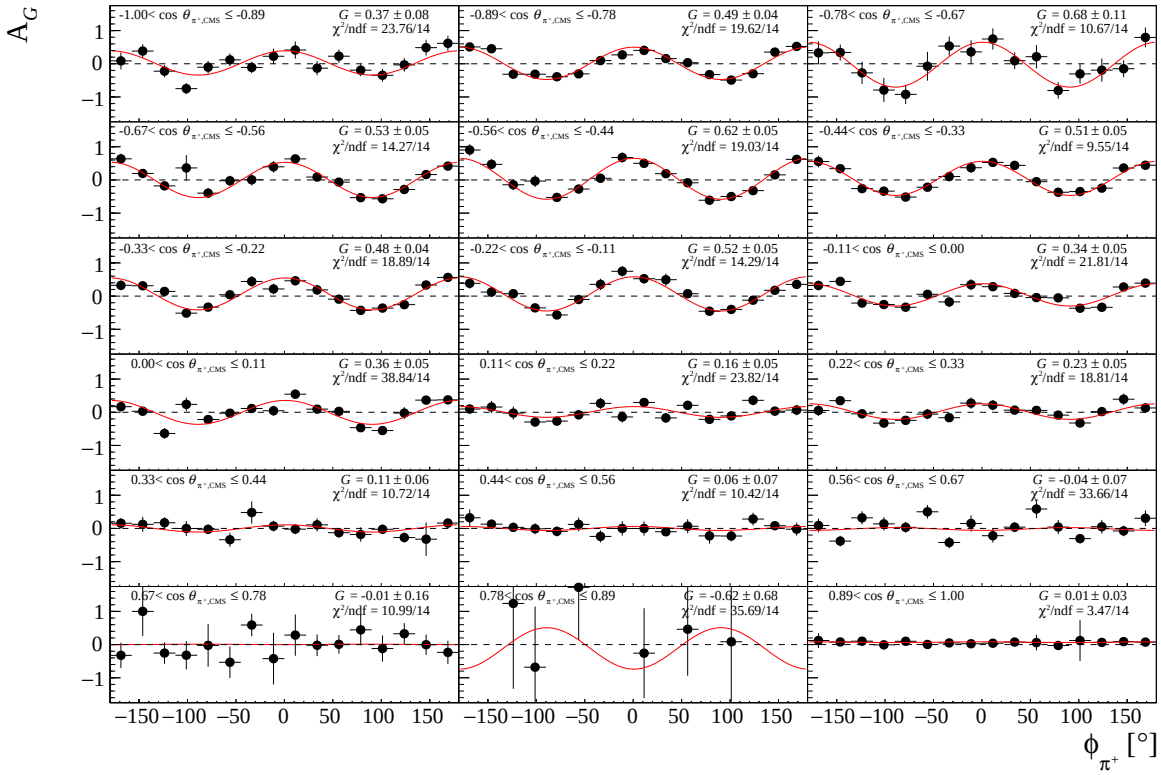

Fig. 8.26: Asymmetry A_G for the extraction of the double polarization observable G. The resulting asymmetries for a beam photon energy range from 400 MeV to 434 MeV are shown as a function of the kinematic variable $\cos\theta_{\pi^+,\mathrm{CMS}}$ for the reaction $\vec{\gamma}\vec{p} \to n\pi^+$. The distributions are fitted with a function (red line) which follows Eq. (8.39). The obtained polarization observable are extracted through the amplitude of the fit.

Similar to the MC studies, a possible offset parameter p_0 is included in the fit function to respect the artificial asymmetries. The resulting offset parameters are depicted in Fig. 8.28 on the left for the $p\pi^0$ channel whereas on the right for $n\pi^+$. From the inspection of the Fig. 8.28, a first hint of small artificial asymmetries is given as the offset parameter p_0 is close to zero.

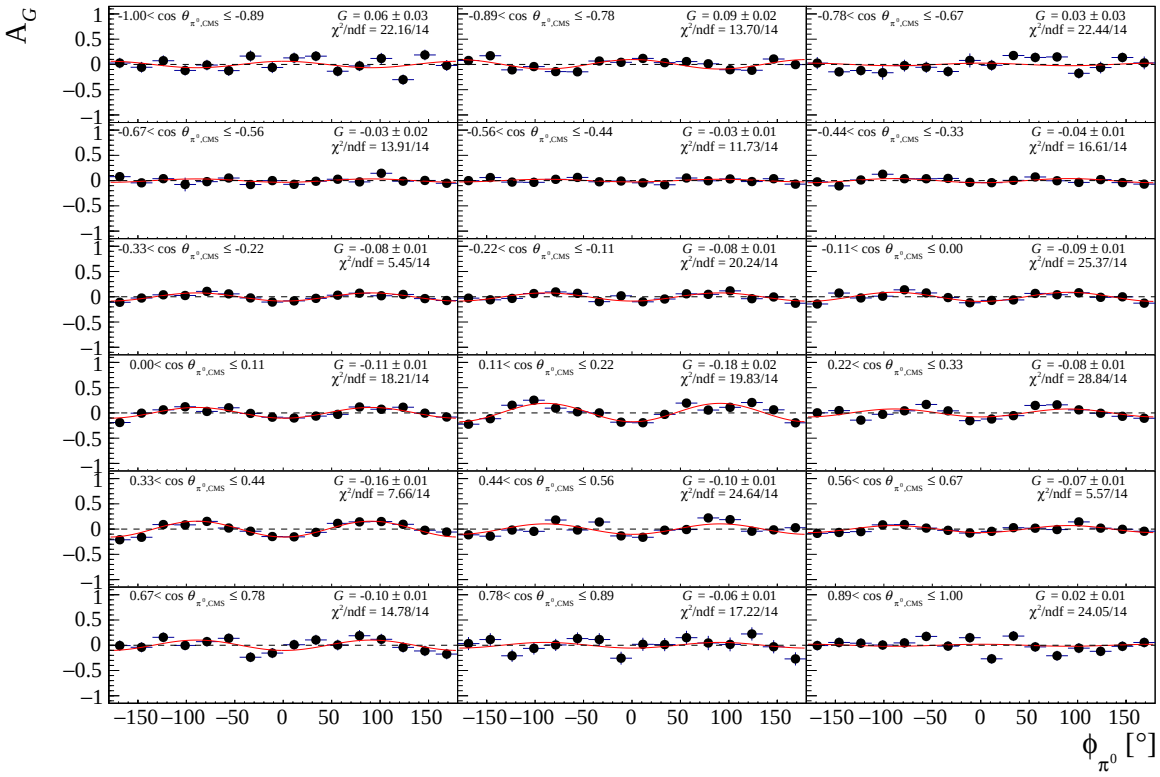

Fig. 8.27: Asymmetry A_G for the extraction of the double polarization observable G. The resulting asymmetries for a beam photon energy range from 400 MeV to 434 MeV are shown as a function of the kinematic variable $\cos\theta_{\pi^0,\mathrm{CMS}}$ for the reaction $\vec{\gamma}\vec{p} \to p\pi^0$. The distributions are fitted with a function (red line) which follows Eq. (8.39). The obtained polarization observable are extracted through the amplitude of the fit.

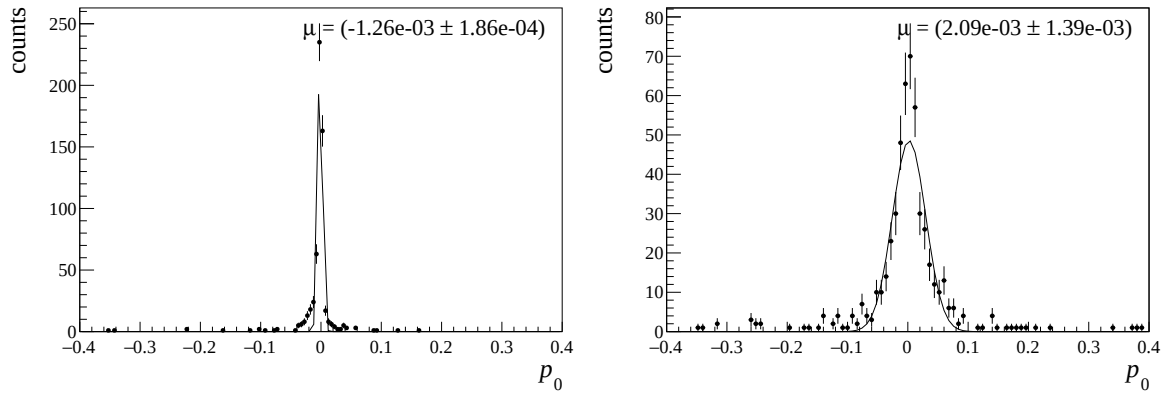

Fig. 8.28: Offset parameter p_0 for the correction of artificial asymmetries in data. Shown is the additional offset parameter p_0 which can be included in the asymmetry functions defined in Eq. (8.37) and Eq. (8.39). On the left side, the result is shown for the $p\pi^0$ whereas on the right for $n\pi^+$ channel. Both values are compatible with zero and thus indicate small detector inefficiencies.

For the unbinned maximum likelihood method, Fig. 8.29 presents the resulting likelihood function for the $\cos\theta_{\pi^0,\mathrm{CMS}}$ bin $0.11 \leq \cos\theta_{\pi^0,\mathrm{CMS}} < 0.22$ in the same beam photon energy region as the binned

method. The red arrows in the projections indicate the results of the binned extraction methods. The minimum, obtained with the unbinned maximum likelihood method, is perfectly in agreement with it.

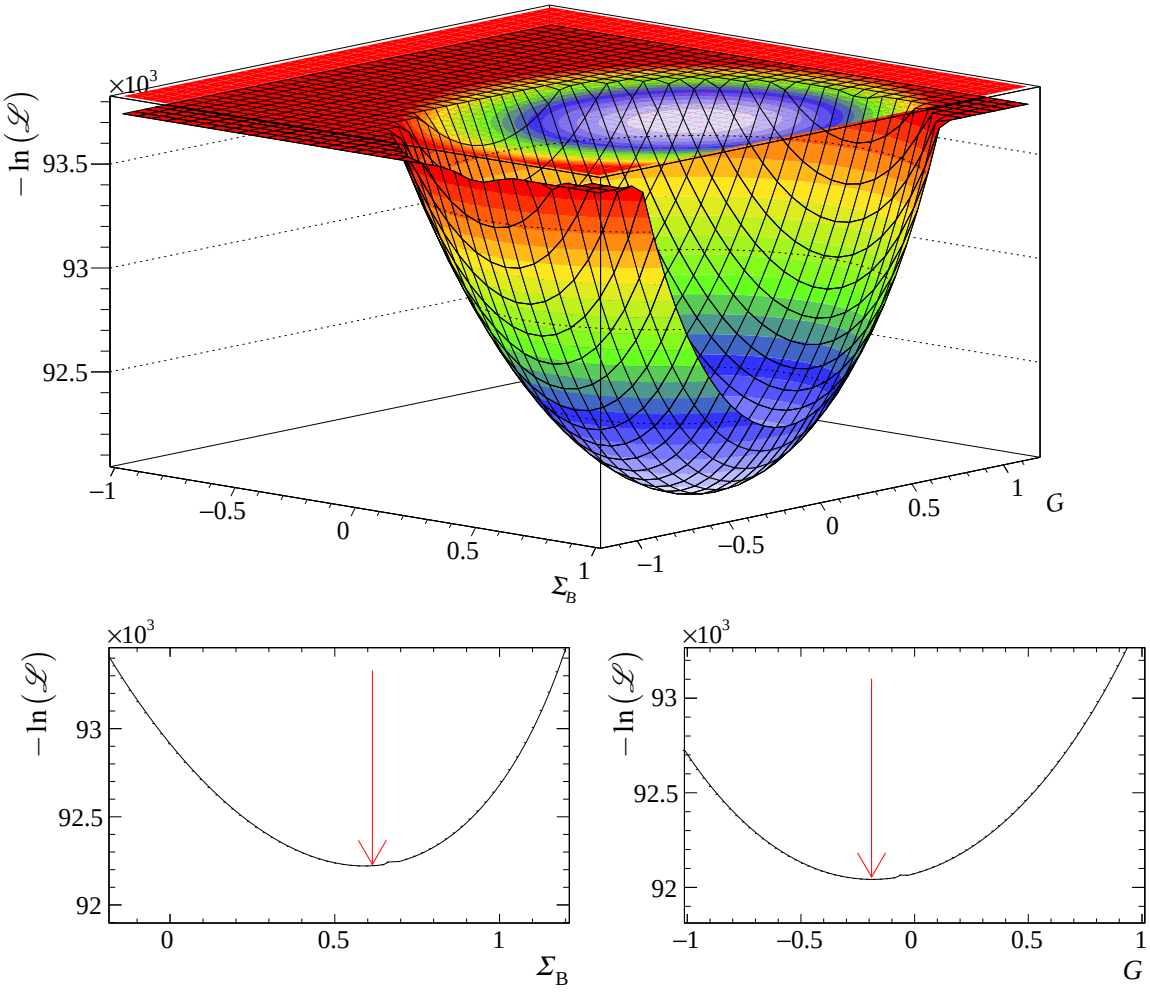

Fig. 8.29: The $-\ln\left(\mathscr{L}_{\text{signal}}(\vec{p}_{\text{signal}})\right)$ function of the background-subtracted method for data. In the upper row, the resulting 2-dimensional likelihood function, defined in Eq. (8.49), for a beam photon energy E_γ from 400 MeV to 434 MeV and the kinematic range $0.11 \leq \cos\theta_{\pi^0,\text{CMS}} < 0.22$. The parabolic shape is clearly seen. To show the parabolic behavior of the likelihood function, the projection of the individual theory parameters is shown in the lower row. To do so, one theory parameter was kept at its minimum whereas the other one was changed. The red arrow hereby indicates the position of the values obtained with the binned event yield asymmetries.

As a further cross-check and comparison of both methods, Fig. 8.30 shows the resulting statistical uncertainty of both methods for all extracted polarization observables values within the analyzed kinematic regions. These will be presented in Sec. 8.3.6. In addition, Fig. 8.30 shows the extracted polarization observable values for both methods. As expected, the unbinned extraction method always shows at least similar or even better statistical uncertainties as the binned method. In addition, both

methods obtain the same results for the polarization observable values and thus in the following only the results of the unbinned extraction method will be presented.

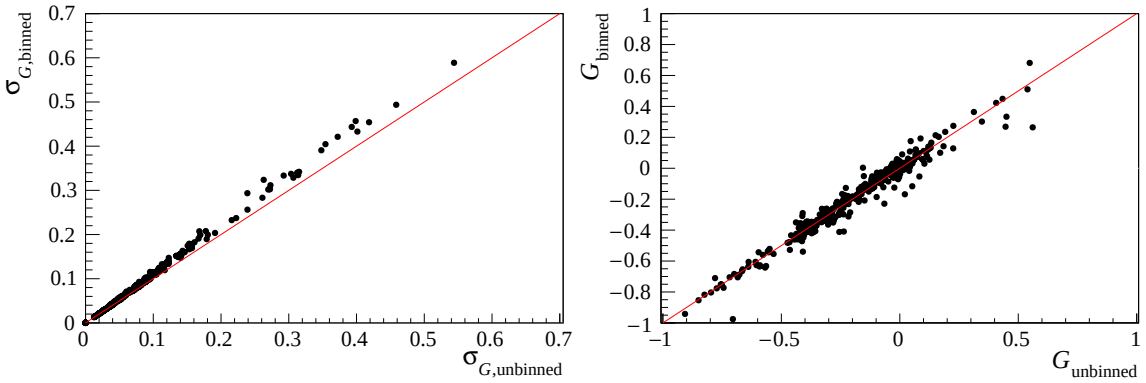

Fig. 8.30: Comparison of the statistical uncertainty and the extracted polarization observable value G for both extraction methods. The resulting statistical uncertainty of both methods for all extracted polarization values is shown on the left. On the right side, all extracted polarization observable values for both methods is depicted. The red line in the plots indicates the line where values are the same.

A final step is to test if the overall acceptance can be modeled with the artificial asymmetry function of the unbinned extraction method. Therefore, the artificial asymmetry function is again compared to the sum of all settings. The results are shown for one selected region in both analyzed channels in Fig. 8.31. From the inspection of the Fig. 8.31 it becomes clear that the unbinned extraction method can also handle the artificial asymmetries in data.

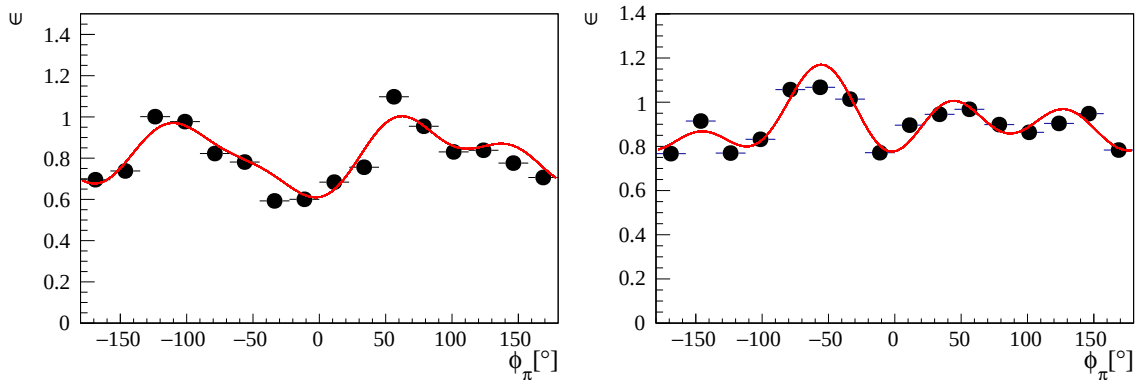

Fig. 8.31: Sum off all settings with their corresponding artificial asymmetry fit function. Shown is the sum of all settings, based on Eq. (8.34), together with the obtained artificial asymmetry fit function (red line) from the unbinned maximum likelihood fit. On the left side, an example bin (E_γ = (400-434) MeV and $-0.11 \leq \cos\theta_{M,\mathrm{CMS}} < 0$) for the $p\pi^0$ analysis is shown whereas on the right side the same kinematic bin for the $n\pi^+$ analysis.

The resulting coefficients of all fitted artificial asymmetry functions for both analyzed channels are depicted in Fig. 8.32. Note that the important parameters s_2 and c_2, which contribute in the

normalization of the settings (cf. Sec. 8.3.1), are in the order of 10^{-2} and thus their contribution to the normalization, defined in Eq. (8.30), can be neglected.

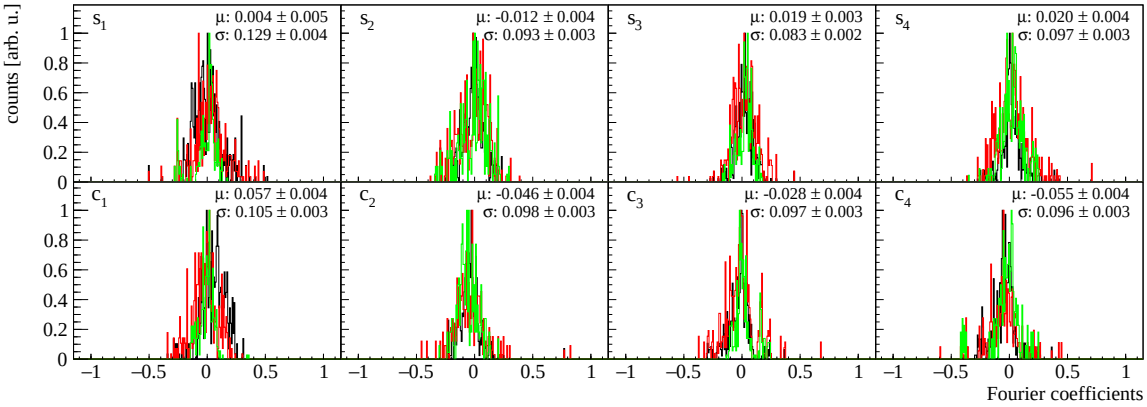

Fig. 8.32: All Fourier coefficients obtained by the artificial asymmetry fit. All fitted Fourier coefficients which are based on Eq. (8.34) are shown. The black distribution indicate the obtained values from the $p\pi^0$ analysis, the red for the 2 PED events of the $n\pi^+$ analysis, and the blue for the 1 PED events of the $n\pi^+$ analysis.

8.3.5 Error Analysis

8.3.5.1 Statistical Uncertainty

The statistical error of the polarization observables for the event yield method is determined via Gaussian error propagation and is mainly dominated by the statistical uncertainties of the four event yield settings of the butanol data with a small contribution of the dilution factor d. Note that a correlation between the dilution factor and the butanol data does not need to be respected as has been shown in Sec. 8.1. In addition, the statistical error of the linear and target polarization degree is negligible small and thus can be ignored. Therefore, the overall statistical uncertainty of the observable p with $p \in \{\Sigma_B, G\}$ is given by[14]:

$$\Delta p_{\text{stat}} = \sqrt{\left(\frac{\partial A_p}{\partial N_{\parallel}^{\uparrow}}\,\Delta N_{\parallel}^{\uparrow}\right)^2 + \left(\frac{\partial A_p}{\partial N_{\parallel}^{\downarrow}}\,\Delta N_{\parallel}^{\downarrow}\right)^2 + \left(\frac{\partial A_p}{\partial N_{\perp}^{\uparrow}}\,\Delta N_{\perp}^{\uparrow}\right)^2 + \left(\frac{\partial A_p}{\partial N_{\perp}^{\downarrow}}\,\Delta N_{\perp}^{\downarrow}\right)^2 + \left(\frac{\partial A_p}{\partial d}\,\Delta d_{\text{stat}}\right)^2}. \tag{8.56}$$

The statistical uncertainty from the unbinned maximum likelihood extraction method was already discussed in detail in Sec. 8.3.2.1. As different coherent edges and data sets were merged after their were checked for consistency, a final error weighted statistical error can be determined for the merged

[14] Note that for the observable Σ_B the contribution of the dilution factor d is not included.

results via:

$$p_{\text{merged}} = \frac{\sum_{i=1}^{N} p_i/\Delta p_{i,\text{stat}}^2}{\sum_{i=1}^{N} 1/\Delta p_{i,\text{stat}}^2} \quad \text{and} \quad \Delta p_{\text{merged}} = \sqrt{\frac{1}{\sum_{i=1}^{N} 1/\Delta p_{i,\text{stat}}^2}} \tag{8.57}$$

where N is the number of individual results to merge.

8.3.5.2 Systematic Uncertainty

Background Reactions

The background contribution from other reactions have been already intrdocued and explained in Sec. 7.9. As has been shown in [14] and [60], the absolute contribution to the overall systematic uncertainty of the observable p is given by the relative background contamination δ_{bg} and thus:

$$\Delta p_{syst,bg} \lesssim \delta_{bg}. \tag{8.58}$$

Linear Polarization Degree

As already been discussed in Sec. 8.2.1.1, the overall uncertainty of the linear polarization degree is in the order of 2.5% for the 450 MeV MeV edge and increases to a maximum of about 5% for the 850 MeV. Therefore, the relative uncertainty is given by:

$$2.5\% \leq \frac{\Delta p_L}{p_L} \leq 5\%. \tag{8.59}$$

Target Polarization Degree

The overall systematic uncertainties of the target polarization degree is in the order of 2%. The main contribution comes from the NMR signal evaluation at thermal equilibrium and is assigned with 1%. The remaining sources are temperature stability, electronics and non-linearities. As the target polarization degree values needed to be corrected with correction factors (see Sec. 8.2.2) which have as well their own systematic uncertainty, an additional 2% relative error needs to be taken into account. Thereby, the value is estimated from the averaged correction factors as has been shown in [14]. Finally, the overall systematic uncertainty from the target polarization degree is given by:

$$\frac{\Delta p_Z}{p_Z} = \sqrt{2\%^2 + 2\%^2} = 2.8\%. \tag{8.60}$$

Dilution Factor

As has been already mentioned in Sec. 8.15, the uncertainty of the dilution factor is determined by the uncertainty of the scaling factor. One source of systematic uncertainty is given by the determination method of the scaling factor. In reference [14], it has been shown that a systematic deviation of about

3% was found between the determination via the photon flux and the event yields method. Additional uncertainties come from the filling factor of the butanol target and whether the amount of helium is similar in the butanol and carbon measurements. This uncertainty is stated with an additional 1.5% [14].

For the $n\pi^+$ channel, a beam photon energy-dependent uncertainty is produced by the small discrepancy between the reconstructed hydrogen distribution and the signal MC which can either be explained by background contamination of the $p\pi^0$ channel or a not perfect description of the interactions of the π^+ at rest within the detector crystals. It contributes with a maximum of additional 5% to the systematic uncertainty of the scaling. This uncertainty mainly contributes to the 1 PED events of the $n\pi^+$ final state and especially in the backward direction in the CB (cf. Sec 7.7.2). For all events in the TAPS, an additional uncertainty of 5% is assumed. The reason lies in the LED1 threshold adjustments between all beamtimes and the MC, the very low hydrogen distribution and the fact that nearly all events are punch-through particles. Therefore, especially the energy correction of the π^+ in the TAPS was more complex and a matching of data and MC simulation was difficult. As a result, only an upper limit on the background contamination was possible. The additional 5% to the systematic uncertainty respects these problems. The 2 PED events of the $n\pi^+$ and the 3 PED events of the $p\pi^0$ channel do not need these additional uncertainties. The reason lies in the available angular selection criteria which were able to reject a lot of background reactions. Furthermore, the scaling is performed with the coplanarity distribution which is completely independent of the π^+ energy correction. Finally, for the $n\pi^+$ channel, the trigger adjustment contributes with a maximum of 5% to the systematic uncertainties (cf. Fig. 8.7). Combining all these information, the overall systematic uncertainty of the scaling factor is given by:

$$3.4\% \approx \sqrt{(3\%)^2 + (1.5\%)^2} \leq \frac{\Delta s_C}{s_C} \leq \sqrt{(3\%)^2 + (1.5\%)^2 + 3 \cdot (5\%)^2} \approx 9.3\%. \tag{8.61}$$

The relative error of the dilution factor is finally given by:

$$\frac{\Delta d}{d} = \frac{\Delta s_C}{s_C} \cdot \frac{(1-d)}{d}. \tag{8.62}$$

As already mentioned several times, the contribution of the dilution factor to the overall systematic error has its maximum contribution for low dilution factor values. This is especially given for the 1 PED events in the $n\pi^+$ channel and the 2 PED events in the $p\pi^0$ channel.

Overall

The overall systematic uncertainty is built of all mentioned uncertainties above and is given by[15]:

$$\Delta p_{\text{syst,all}} = \sqrt{\left[\left(\frac{\Delta p_L}{p_L}\right)^2 + \left(\frac{\Delta p_Z}{p_Z}\right)^2 + \left(\frac{\Delta d}{d}\right)^2\right] \cdot p^2 + \Delta p^2_{\text{syst,bg}}}. \tag{8.63}$$

Note that all individual uncertainties are uncorrelated and thus can be added up in quadrature. To take into account the different systematic uncertainties of the 1 and 2 PED events of the $n\pi^+$ channel, the systematic uncertainty of the merged result of the observable p is calculated similar to the statistical error and is therefore:

$$\Delta p_{\text{syst,all,merged}} = \frac{\sum_{i=1}^{N} \Delta p_{i,\text{syst,all}} / \Delta p^2_{i,\text{stat}}}{\sum_{i=1}^{N} 1/\Delta p^2_{i,\text{stat}}}. \tag{8.64}$$

In the following, the overall systematic uncertainty of the extracted polarization observable is indicated by gray boxes.

8.3.6 Results

The final obtained results of the new A2 data for the double polarization observable G in the reaction $\vec{\gamma}\vec{p} \to p\pi^0$ are given by the black points together with their statistical uncertainty in Fig. 8.33 and Fig. 8.34 whereas in Fig. 8.35 and Fig. 8.36 for the reaction $\vec{\gamma}\vec{p} \to n\pi^+$. They have been determined in a beam photon energy range from 230 MeV to 842 MeV ($W = 1145$ MeV $- 1569$ MeV) with a 34 MeV broad energy bin window and 18 angular bins. The gray box presents the systematic uncertainties. The corresponding results for the beam asymmetry Σ_B can be found in App. A.8.

[15] For the observable Σ_B the systematic uncertainties of the target polarization p_Z and the dilution factor d do not contribute.

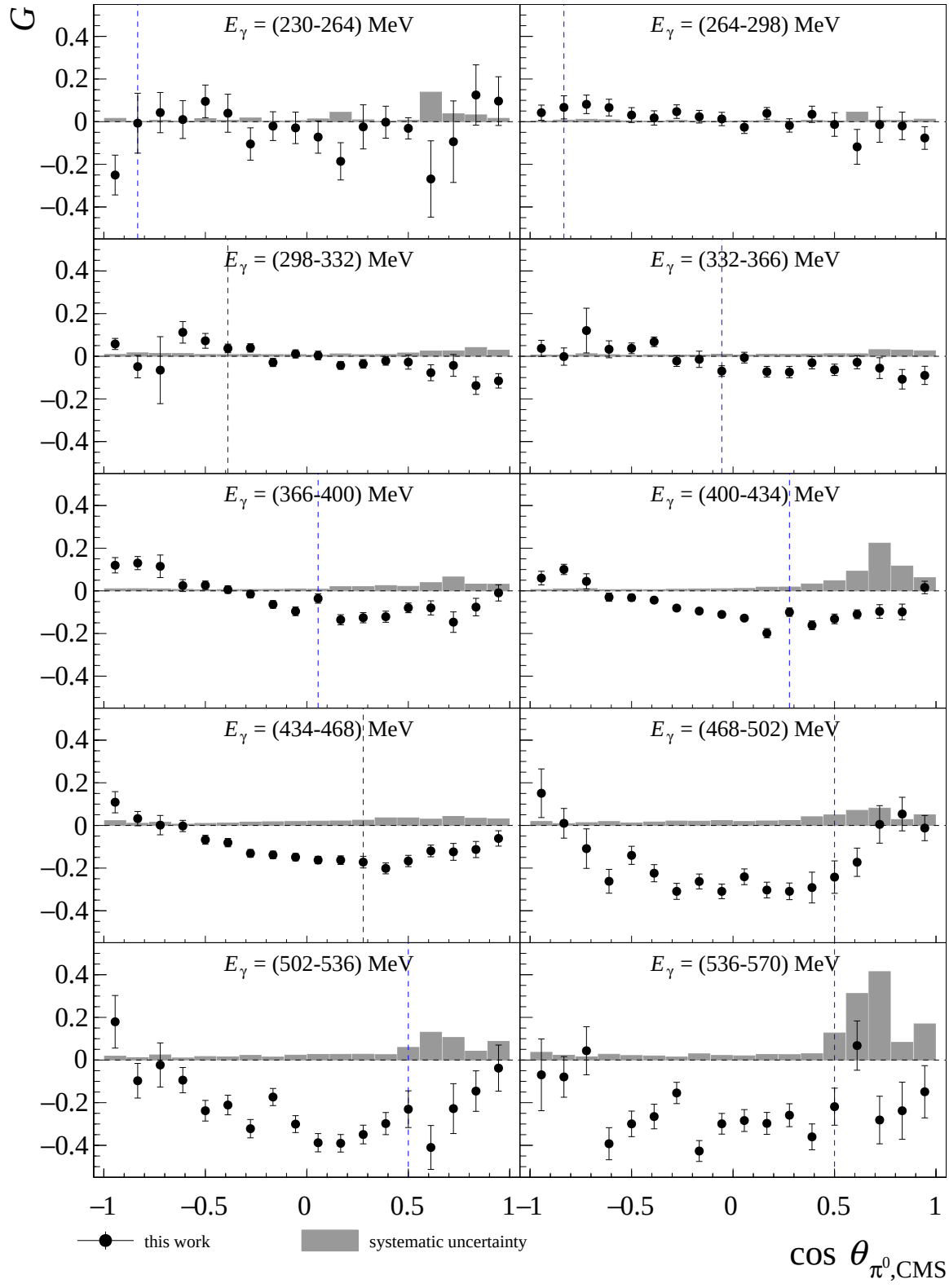

Fig. 8.33: Double polarization observable *G* for the reaction $\vec{\gamma}\vec{p}\rightarrow p\pi^0$. The results of the double polarization observable *G* are shown as a function of $\cos\theta_{\pi^0,\mathrm{CMS}}$ for the beam photon energy from 230 MeV to 570 MeV. They are plotted as black dots together with their statistical uncertainties whereas the gray boxes represent the systematic uncertainties. The blue dashed line indicates the position where the 2 PED events are added to the 3 PED events.

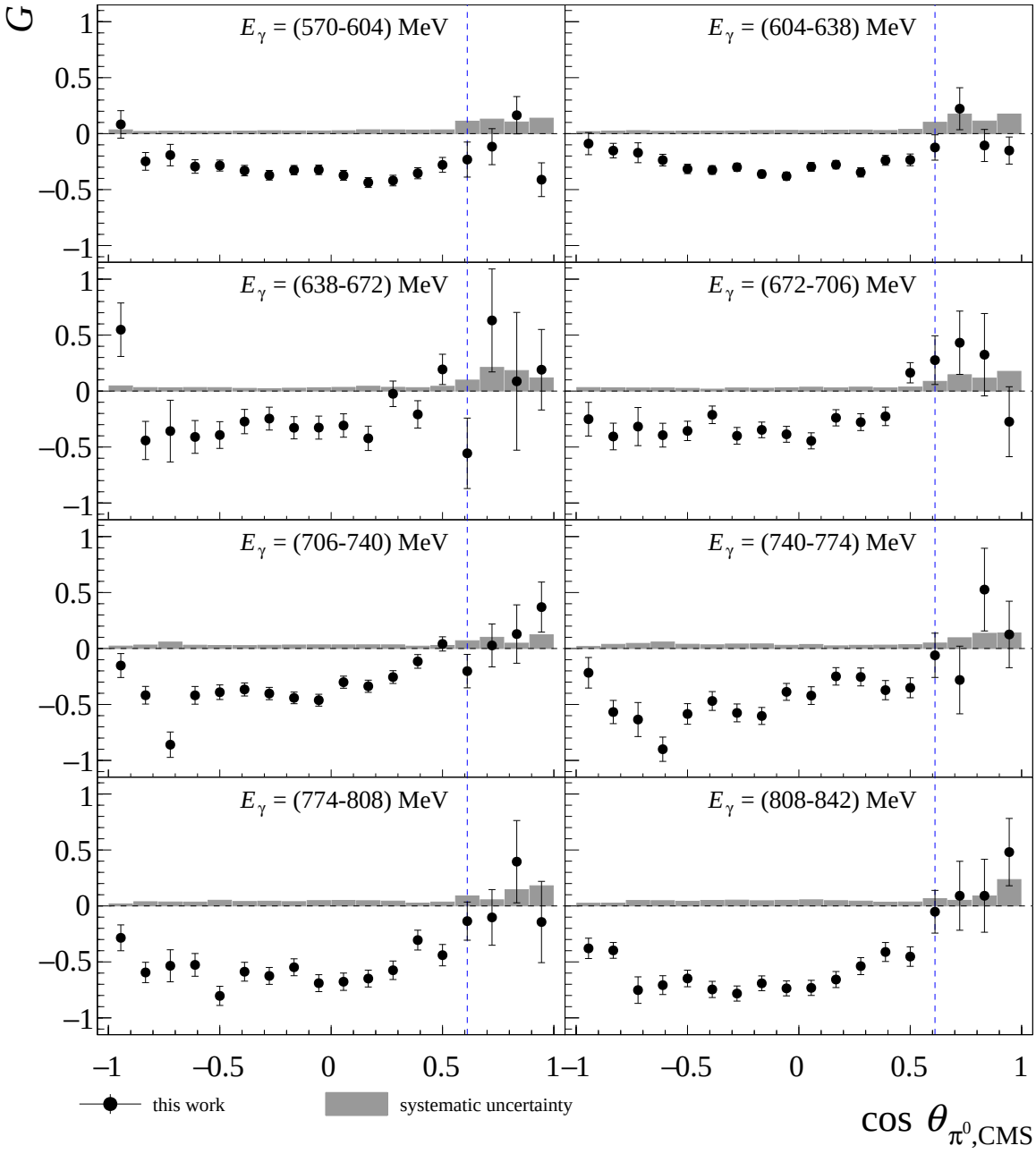

Fig. 8.34: Double polarization observable G for the reaction $\vec{\gamma}\vec{p}\to p\pi^0$. The results of the double polarization observable G are shown as a function of $\cos\theta_{\pi^0,\mathrm{CMS}}$ for the beam photon energy from 570 MeV to 842 MeV. They are plotted as black dots together with their statistical uncertainties while the gray boxes represent the systematic uncertainties. The blue dashed line indicates the position where the 2 PED events are added to the 3 PED events.

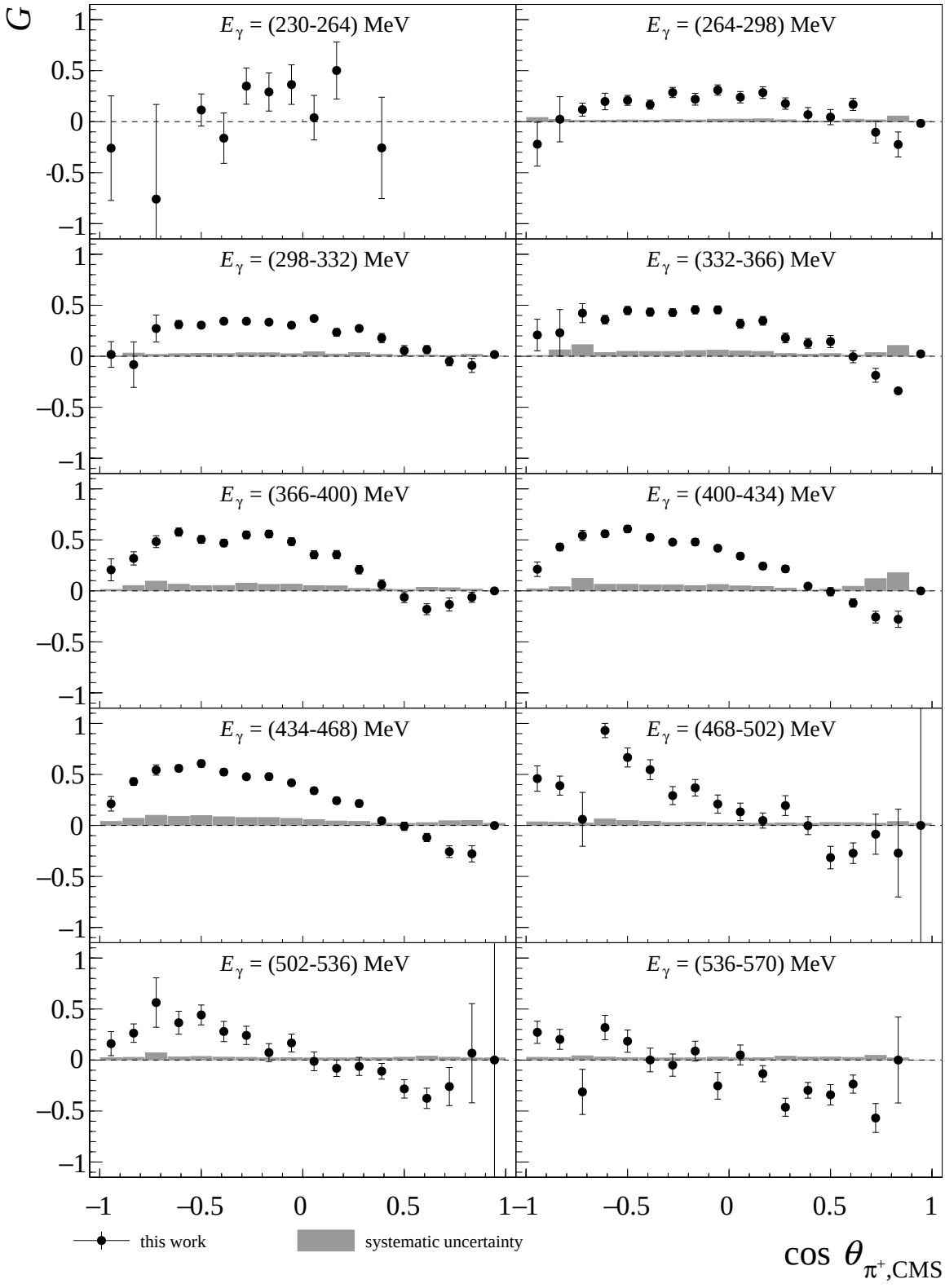

Fig. 8.35: Double polarization observable *G* for the reaction $\vec{\gamma}\vec{p}\to n\pi^+$. The results of the double polarization observable *G* are shown as a function of $\cos\theta_{\pi^+,\mathrm{CMS}}$ for the beam photon energy from 230 MeV to 570 MeV. They are plotted as black dots together with their statistical uncertainties while the gray boxes represent the systematic uncertainties.

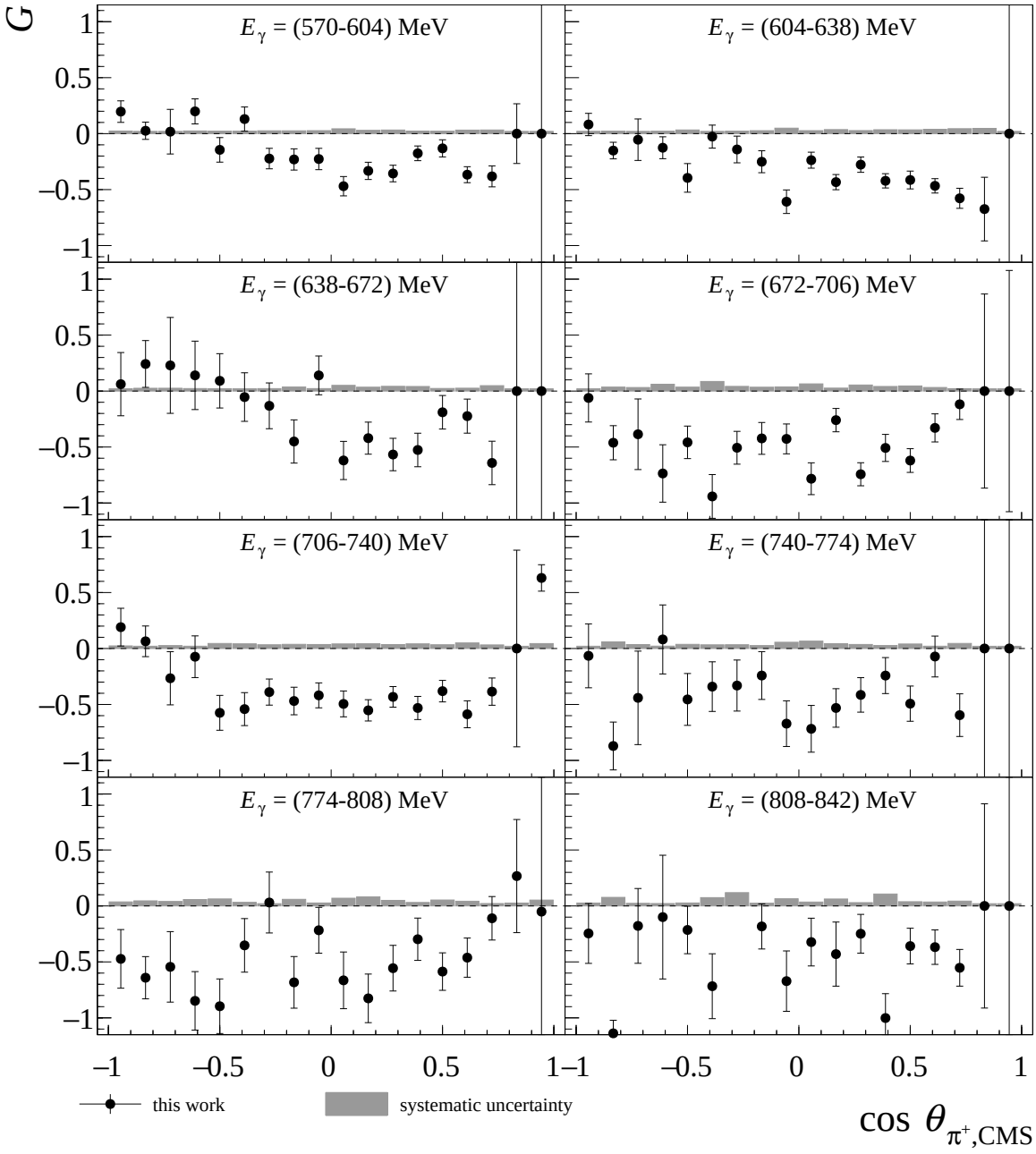

Fig. 8.36: Double polarization observable G for the reaction $\vec{\gamma}\vec{p}\to n\pi^+$. The results of the double polarization observable G are shown as a function of $\cos\theta_{\pi^+,\mathrm{CMS}}$ for the beam photon energy from 570 MeV to 842 MeV. They are plotted as black dots together with their statistical uncertainties while the gray boxes represent the systematic uncertainties.

8.4 Double Polarization Observable *E*

As already mentioned in the introduction of this chapter, the measurement of elliptically polarized photons in combination with a longitudinally polarized target lead to a total of eight possible configurations for the polarized cross section (cf. Eq. (8.4) and Eq. (8.5)). To only get access to the double polarization observable E, the dependence of the cross sections on the observables Σ_B and G need to be canceled. This is achieved by integrating all settings over the entire azimuthal angle ϕ because it holds:

$$\int_0^{2\pi} \cos 2\phi \, \mathrm{d}\phi = \int_0^{2\pi} \sin 2\phi \, \mathrm{d}\phi = 0. \tag{8.65}$$

Unfortunately, as has been shown already in the extraction of the polarization observables Σ_B and G, the acceptance $\varepsilon(\phi)$ shows a small ϕ dependence and thus its dependence needs to be respected as well in the integration of the individual cross section configurations. As an example, the calculation of the setting in the helicity down state ($H(\downarrow)$), target polarization orientation in beam direction ($T(\uparrow)$) and beam polarization plane parallel to the reaction plane ($L(\parallel)$) is depicted:

$$\begin{aligned}\int_0^{2\pi} \frac{d\sigma}{d\Omega}\bigg|_{T(\uparrow)}^{L(\parallel),H(\downarrow)} \mathrm{d}\phi &= \frac{d\sigma}{d\Omega}\bigg|_0 \cdot \varepsilon(\phi) \cdot \left(1 + d p_C^{\downarrow} p_Z^{\uparrow} E + p_L^{\parallel} \Sigma_B \sin 2\phi + d p_L^{\parallel} p_Z^{\uparrow} G \cos 2\phi\right) \mathrm{d}\phi \\ &= \frac{d\sigma}{d\Omega}\bigg|_0 \cdot 2\pi \cdot \left(1 + d p_C^{\downarrow} p_Z^{\uparrow} E + 0.5 p_L^{\parallel} \Sigma_B s_2 + 0.5 d p_L^{\parallel} p_Z^{\uparrow} G c_2\right).\end{aligned} \tag{8.66}$$

Thereby, s_2 and c_2 are the Fourier coefficients which are defined in Eq. (8.29). The helicity dependent cross section can be split into an anti-parallel (1/2) and parallel spin configuration (3/2) of the photon and proton target spin. Summing over both beam polarization orientations, both configuration are defined by:

$$\frac{d\sigma}{d\Omega}\bigg|^{1/2} = \int_0^{2\pi} \left(\frac{d\sigma}{d\Omega}\bigg|_{T(\uparrow)}^{L(\parallel),H(\downarrow)} + \frac{d\sigma}{d\Omega}\bigg|_{T(\uparrow)}^{L(\perp),H(\downarrow)} + \frac{d\sigma}{d\Omega}\bigg|_{T(\downarrow)}^{L(\parallel),H(\uparrow)} + \frac{d\sigma}{d\Omega}\bigg|_{T(\downarrow)}^{L(\perp),H(\uparrow)} \right) \mathrm{d}\phi, \tag{8.67}$$

$$\frac{d\sigma}{d\Omega}\bigg|^{3/2} = \int_0^{2\pi} \left(\frac{d\sigma}{d\Omega}\bigg|_{T(\uparrow)}^{L(\parallel),H(\uparrow)} + \frac{d\sigma}{d\Omega}\bigg|_{T(\uparrow)}^{L(\perp),H(\uparrow)} + \frac{d\sigma}{d\Omega}\bigg|_{T(\downarrow)}^{L(\parallel),H(\downarrow)} + \frac{d\sigma}{d\Omega}\bigg|_{T(\downarrow)}^{L(\perp),H(\downarrow)} \right) \mathrm{d}\phi. \tag{8.68}$$

Solving the individual integrals, similar to Eq. (8.66), the final two configurations are given by[16]:

$$\begin{aligned}\frac{d\sigma}{d\Omega}\bigg|^{1/2} = \frac{d\sigma}{d\Omega}\bigg|_0 \cdot 8\pi \cdot \Big(1 &+ 0.5 \cdot d \cdot (p_C^{\uparrow} \cdot p_Z^{\downarrow} + p_C^{\downarrow} \cdot p_Z^{\uparrow}) \cdot E \\ &+ 0.25 \cdot (p_L^{\parallel} - p_L^{\perp}) \cdot \Sigma_B \cdot s_2 \\ &+ 0.125 \cdot d \cdot (p_L^{\parallel} - p_L^{\perp}) \cdot (p_Z^{\uparrow} - p_Z^{\downarrow}) \cdot G \cdot c_2\Big),\end{aligned} \tag{8.69}$$

[16] The individual integrals including the acceptance $\varepsilon(\phi)$ have been already calculated in Eq. (8.44).

$$\begin{aligned}\left.\frac{d\sigma}{d\Omega}\right|^{3/2} = \left.\frac{d\sigma}{d\Omega}\right|_0 \cdot 8\pi \cdot \Big(1 - 0.5 \cdot d \cdot (p_C^{\uparrow} \cdot p_Z^{\uparrow} + p_C^{\downarrow} \cdot p_Z^{\downarrow}) \cdot E \\ + 0.25 \cdot (p_L^{\parallel} - p_L^{\perp}) \cdot \Sigma_B \cdot s_2 \\ + 0.125 \cdot d \cdot (p_L^{\parallel} - p_L^{\perp}) \cdot (p_Z^{\uparrow} - p_Z^{\downarrow}) \cdot G \cdot c_2\Big).\end{aligned} \tag{8.70}$$

Inspecting the Eq. (8.69) and Eq. (8.70), it can be seen that the only difference is given by the sign change in front of the double polarization observable E part. Therefore, the difference of the anti-parallel (1/2) and parallel (3/2) settings eliminates the contribution of Σ_B and G which results in:

$$\left.\frac{d\sigma}{d\Omega}\right|^{1/2} - \left.\frac{d\sigma}{d\Omega}\right|^{3/2} = \left.\frac{d\sigma}{d\Omega}\right|_0 \cdot 4\pi \cdot d \cdot (p_C^{\uparrow} + p_C^{\downarrow}) \cdot (p_Z^{\uparrow} + p_Z^{\downarrow}) \cdot E. \tag{8.71}$$

For the sum of both settings, the terms coming from Σ_B and G remain which leads to:

$$\begin{aligned}\left.\frac{d\sigma}{d\Omega}\right|^{1/2} + \left.\frac{d\sigma}{d\Omega}\right|^{3/2} = \left.\frac{d\sigma}{d\Omega}\right|_0 \cdot 16\pi \cdot \Big(1 - 0.5 \cdot d \cdot (p_C^{\uparrow} - p_C^{\downarrow}) \cdot (p_Z^{\uparrow} - p_Z^{\downarrow}) \cdot E \\ + 0.25 \cdot (p_L^{\parallel} - p_L^{\perp}) \cdot \Sigma_B \cdot s_2 \\ + 0.125 \cdot d \cdot (p_L^{\parallel} - p_L^{\perp}) \cdot (p_Z^{\uparrow} - p_Z^{\downarrow}) \cdot G \cdot c_2\Big).\end{aligned} \tag{8.72}$$

As already the normalization correction in Eq. (8.32) is in the order of 10^{-3}, the contribution of the beam asymmetry Σ_B and G can be neglected here. Even a difference of 5% in the linear polarization degrees and a maximum of 10% in the target polarization degrees result in a minimal correction in the order of 10^{-5}. Thus, their contribution can be neglected. As has been shown in [14], the difference in the circular polarization degree of both helicity states is less than 3%. Combining this with a maximum target polarization difference of about 10% the maximum contribution of the E term is in the order of 10^{-3}. Consequently, the contribution of E in the sum of both helicity configurations can be neglected as well so that the sum is given by:

$$\left.\frac{d\sigma}{d\Omega}\right|^{1/2} + \left.\frac{d\sigma}{d\Omega}\right|^{3/2} = \left.\frac{d\sigma}{d\Omega}\right|_0 \cdot 16\pi. \tag{8.73}$$

The double polarization observable E is defined as:

$$E := \frac{\left.\frac{d\sigma}{d\Omega}\right|^{1/2} - \left.\frac{d\sigma}{d\Omega}\right|^{3/2}}{\left.\frac{d\sigma}{d\Omega}\right|^{1/2} + \left.\frac{d\sigma}{d\Omega}\right|^{3/2}}. \tag{8.74}$$

Using Eq. (8.9) with the assumption of a similar acceptance and photon flux of both helicity configurations[17], E can be described by the two event yields $N^{1/2}$ and $N^{3/2}$. In addition, the definition of the

[17] Although the photon flux of each individual configuration is not the same, the combined flux in the helicity states are. This can be explained by the fact that in both helicity configurations a sum of positive and negative target orientation is included (cf. Eq. (8.67) and Eq. (8.68)). The only requirement is that the photon flux of the helicity states is fulfilled which has been proven in Sec. 8.3.

observable E in Eq. (8.74) assumes polarization degrees of the photons and the target of 100%. The measured observable E corrects the polarization degrees and is finally given by:

$$E := \left(\frac{N^{1/2} - N^{3/2}}{N^{1/2} + N^{3/2}}\right)\left(\frac{4}{d \cdot (p_C^{\uparrow} + p_C^{\downarrow}) \cdot (p_Z^{\uparrow} + p_Z^{\downarrow})}\right). \tag{8.75}$$

8.4.1 Error analysis

The statistical and systematic uncertainties are calculated in the same way as for the double polarization observable G. Only the systematic uncertainties of the linear polarization degree need to be exchanged with the uncertainty of the circular polarization degree. The background contamination and the uncertainty on the dilution factor are the same since E is extracted from the same selected events as the polarization observables Σ_B and G. The extraction on the same selected events was chosen on purpose, especially for the $n\pi^+$ channel. As will be shown in Chap. 9, the data base for the observable G is oversee-able whereas for E data are already published by the CLAS collaboration [68]. Therefore, the correctness of the target polarization degree, the dilution factor, and the background contamination can be cross-checked with the comparison of the obtained E results with the CLAS data. If any of these uncertainties cause a deviation between both results, the effect should as well be seen in the G results.

8.4.2 Comparison between Diamond and Møller Data

One goal of the G/E measurements is to investigate if a simultaneous measurement of the double polarization observables G and E is possible. These measurements make use of a longitudinally polarized electron beam which interacts with a diamond radiator. Thereby, elliptically polarized photons are produced, having a linear and circular polarization component at the same time. It is important to check if the linearly polarized component affects the circularly polarized component. In the case of coherent bremsstrahlung and thus linear polarization contributions, a full calculation of the circular polarization degree is possible. It can be compared to an approximated calculation which uses only the assumption of incoherent bremsstrahlung based on Eq. (3.15). Fig. 8.37 shows the comparison of these calculations for two different configurations of the incoming electron energy E_0 and coherent edge position. The inspection of the figure presents some dip structures in the full calculation of the circular polarization degree. The maximum dip is located at the coherent edge position, whereas additional dips towards higher electron energies correspond to the higher lattice contributions. According to the model calculations presented in [133], the relative change for a coherent edge sitting at $E_\gamma \approx E_0/2$ with a maximum linear polarization degree of about 40% is in the order of 2% [14]. These relative changes in the circular polarization degree are studied by the comparison of two measurements. The first one used a diamond radiator, which produced the elliptically polarized photons. The second one exchanged the diamond radiator with a Møller radiator. In doing so, only circularly polarized photons are created. Furthermore, high sensitivity to the relative

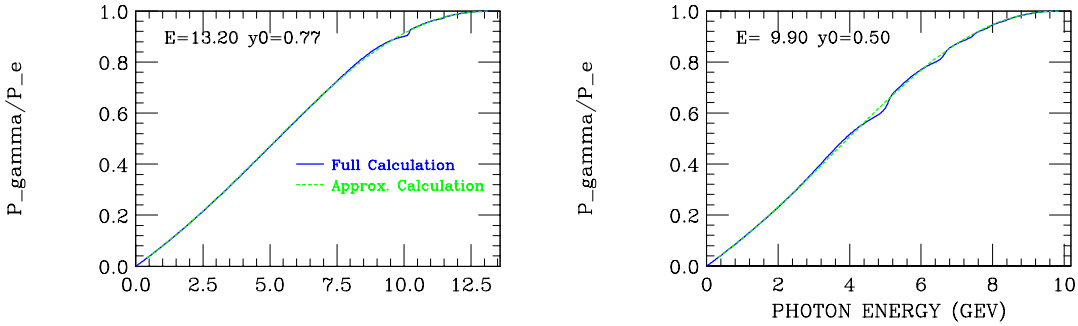

Fig. 8.37: Calculation of the circular polarization degrees. The ratio of the circular polarization to the electron polarization degree is plotted as a function of the beam photon energy E_γ for two different incoming electron energies E_0 and position of the coherent edges of the SCLAC E159 experiment. The parameter $y0 = E_\gamma/E_0$ defines the position of the coherent edges. The full calculation of the circular polarization degree of the coherent bremsstrahlung, which includes the linearly polarized component, is depicted in blue. The calculation of incoherent bremsstrahlung, based on Eq. (3.15), is presented in green (figure taken from [133]).

changes is only achievable if differences in the systematic uncertainties are negligible. They are minimized by comparing data sets of one beamtime with a similar trigger. This is only given for the 450 MeV coherent edge setting of September 2015 as these were taken together with a high statistic data set for the Møller radiator. The relative changes between the circular polarization degrees is obtained in the region of maximum linear polarization degree. For the September 2015 beam time, the linear polarization component of the elliptically polarized photons has a maximum polarization of about 70% at the coherent edge position. Hence, both data sets are compared in the region from 230 MeV to 434 MeV. The results for the double polarization observable E in the $n\pi^+$ channel, using a diamond and Møller radiator, are shown in Fig. 8.38. They are presented for the two closest energy bins to the coherent edge.

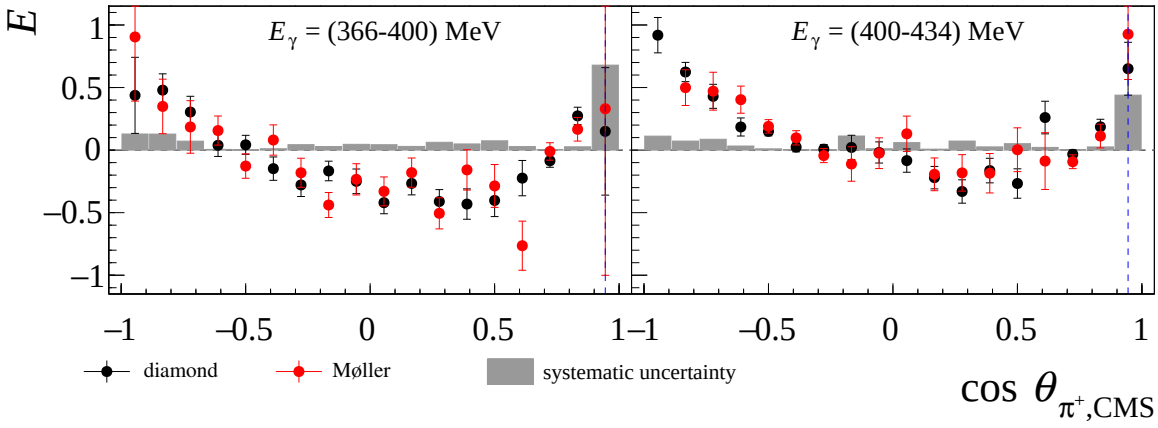

Fig. 8.38: Comparison of diamond and Møller results for the double polarization observable E for the reaction $\vec{\gamma}\vec{p}\to n\pi^+$. The results of the double polarization observable E for the diamond radiator (black) and Møller radiator (red) is presented for two beam photon energy. They have been determined for the 450 MeV coherent edge setting of September 2015. The gray box presents the systematic uncertainties of the diamond radiator. The systematic uncertainties of the Møller radiator are almost similar, since only the value of E in Eq. (8.63) is different.

Fig. 8.39 depicts the ratio of both of these results along with the remaining energy bins in the beam photon energy range from 230 MeV to 434 MeV.

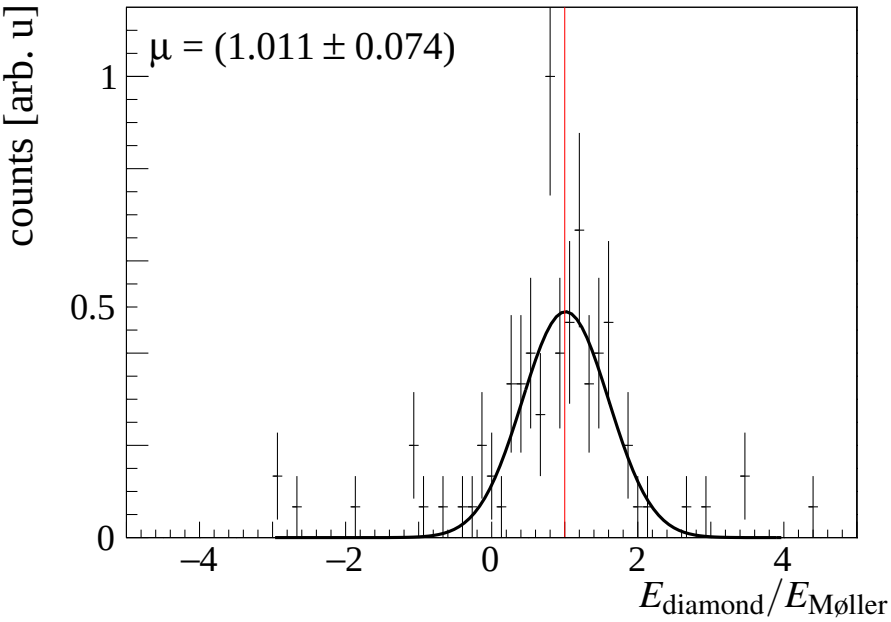

Fig. 8.39: Ratio of diamond to Møller results for the double polarization observable *E* for the reaction $\vec{\gamma}\vec{p}\rightarrow n\pi^+$. The diamond data of the 450 MeV edge setting of September 2015 and the corresponding Møller data were used to extract the double polarization observable E. The ratio of the diamond to Møller results are shown for the beam photon energies from 230 MeV to 434 MeV. The distribution was fit a Gaussian function to obtain the mean value of (1.01±0.07).

A very good agreement (1.01±0.07) is obtained by fitting a Gaussian function to the distribution. Within the PhD work of F. Afzal, the results of the double polarization observable E in the $p\pi^0$ channel revealed a ratio of 1.02±0.03 between the diamond and Møller radiator [14]. Both results clearly show the first experimental indication that the linear polarization component of the elliptically polarized photons does not affect the circular polarization component. Consequently, the results of both radiators will be combined in the following.

8.4.3 Results of the Complete Data

The final obtained results of the new A2 data for the double polarization observable E in the reaction $\vec{\gamma}\vec{p} \rightarrow n\pi^+$ are given by the black points together with their statistical uncertainty in Fig. 8.40 and Fig. 8.40. They have been determined in a beam photon energy range from 230 MeV to 842 MeV ($W = 1145$ MeV $-$ 1569 MeV) with a 34 MeV broad energy bin window. The gray box presents the systematic uncertainties.

The observable E of the new A2 data for the reaction $\vec{\gamma}\vec{p} \rightarrow p\pi^0$ was studied and investigated in more detail within the PhD thesis of F. Afzal. More details can be found in [14].

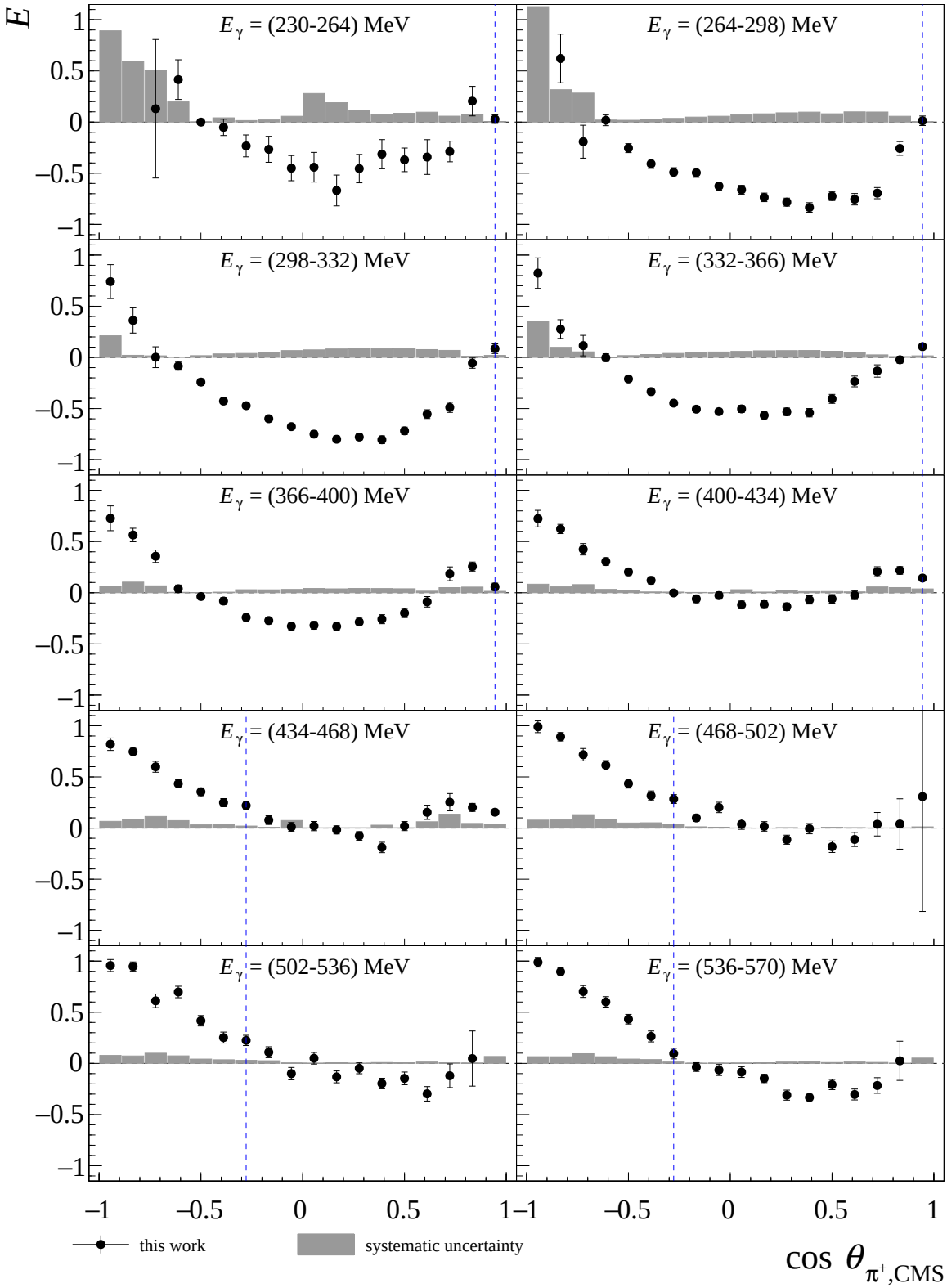

Fig. 8.40: Double polarization observable E for the reaction $\vec{\gamma}\vec{p}\to n\pi^+$. The results of the double polarization observable E are shown as a function of $\cos\theta_{\pi^+,\mathrm{CMS}}$ for the beam photon energy from 230 MeV to 570 MeV. They are plotted as black dots together with their statistical uncertainties while the gray boxes represent the systematic uncertainties. The blue dashed line indicates the position up to which point the 1 PED events are added to the 2 PED events.

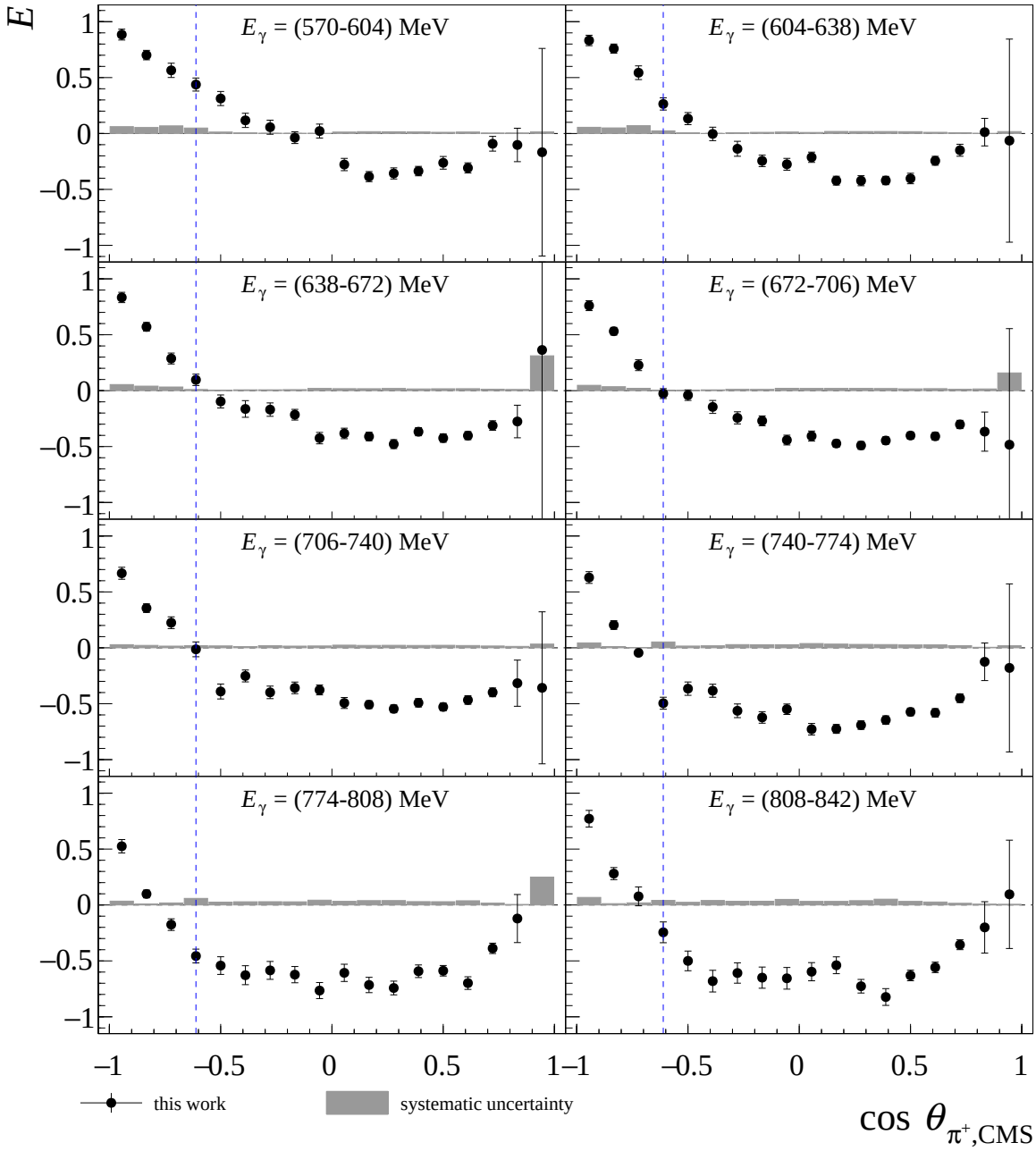

Fig. 8.41: Double polarization observable *E* for the reaction $\vec{\gamma}\vec{p}\to n\pi^+$. The results of the double polarization observable *E* are shown as a function of $\cos\theta_{\pi^+,\mathrm{CMS}}$ for the beam photon energy from 570 MeV to 842 MeV. They are plotted as black dots together with their statistical uncertainties while the gray boxes represent the systematic uncertainties. The blue dashed line indicates the position up to which point the 1 PED events are added to the 2 PED events.

Chapter 9

Discussion of the Results

The following chapter discusses the results. After a comparison of the results with the most recent data base, the dominant partial wave contributions are determined using a truncated partial wave analysis (PWA). Finally, the results are compared to different PWA solutions.

9.1 Comparison with Recent Results

9.1.1 Double Polarization Observable *G* for the reaction $\vec{\gamma}\vec{p} \to p\pi^0$

The final obtained results of the new A2 data for the double polarization observable G in the reaction $\vec{\gamma}\vec{p} \to p\pi^0$ have been determined in a beam photon energy range from 230 MeV to 842 MeV ($W = 1145\,\text{MeV} - 1569\,\text{MeV}$) with a 34 MeV energy bin window. The first possible data for comparison start at a beam photon energy of 617 MeV ($W = 1428\,\text{MeV}$)[1] with a 33.33 MeV energy bin window and have been published by the CBELSA/TAPS collaboration [45, 64]. Only the results of the overlapping beam photon energy range are presented here.
Fig. 9.1 shows the comparison of the new A2 data in black with the published CBELSA/TAPS data in red as a function of the kinematic variable $\cos\theta_{\pi^0,\text{CMS}}$. The corresponding beam photon energy ranges of the compared data are depicted in the same color scheme. Due to different positions of the coherent edges and the requirement to reject data with energies above the falling coherent edges, it was not possible to use the exact same energy binning for the A2 data as for the CBELSA/TAPS data. The CBELSA/TAPS collaboration took data with three coherent edge positions at 950 MeV, 1150 MeV, and 1350 MeV, respectively. The A2 collaboration recorded data for a coherent edge position starting at 350 MeV and ending at 850 MeV with a step size of about 100 MeV. Thus, the A2 data needed to respect the requirements of the falling coherent edge positions (cf. Sec. 8.2.1.1). Although the fist energy bin has a deviation of 12 MeV, the following bin deviation decreases per each energy bin with a minimum deviation of 8 MeV for the last energy bin.

[1] Additionally, three data points from the A2/GDH collaboration are available in the beam photon energy range from 326 MeV to 354 MeV [67]. However, due to their low angular coverage in combination with high statistical uncertainties, a comparison is not useful.

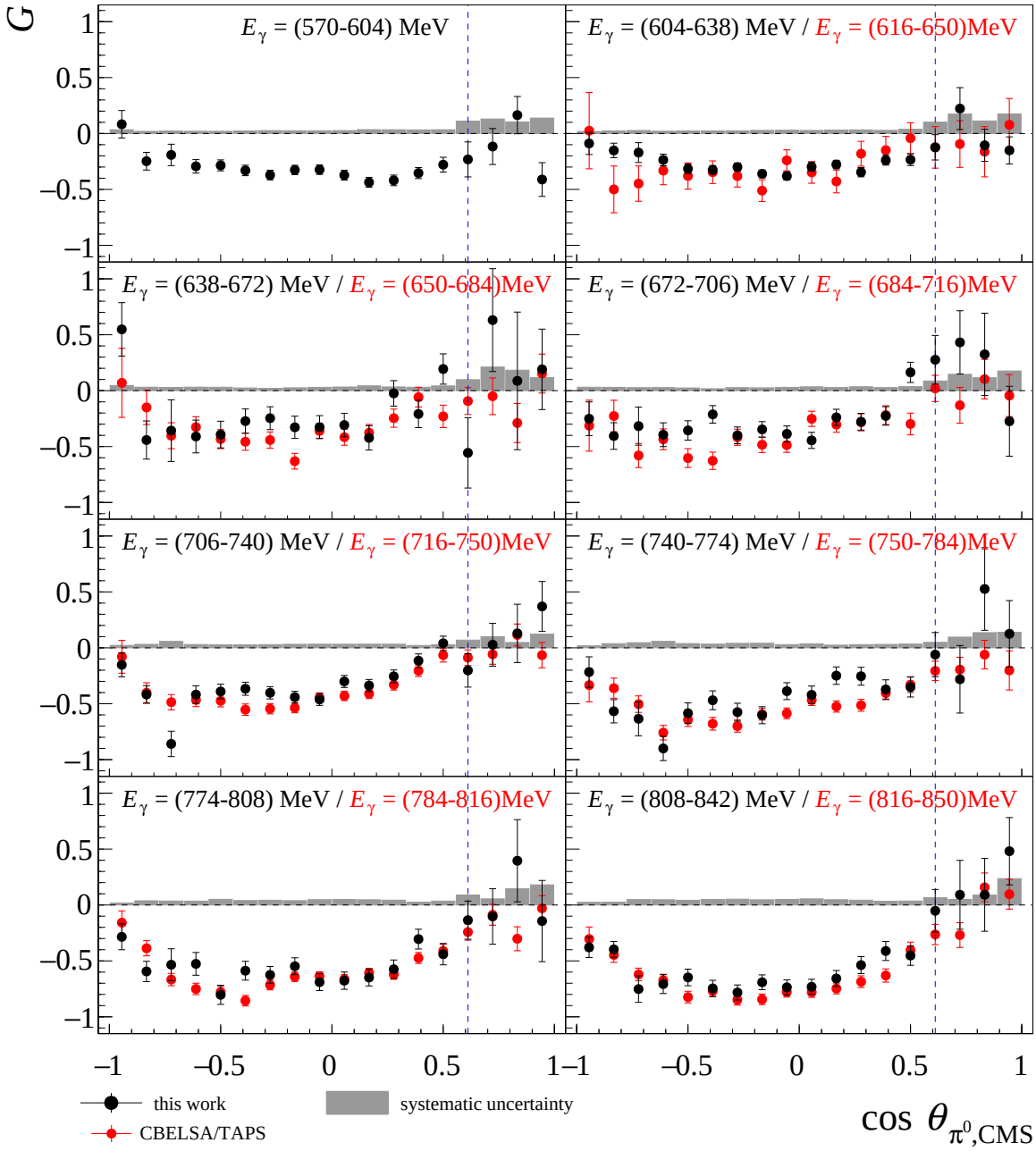

Fig. 9.1: Comparison of the results for the double polarization observable G with previous data for $\vec{\gamma}\vec{p}\to p\pi^0$. The results of the double polarization observable G are shown as a function of $\cos\theta_{\pi^0,\mathrm{CMS}}$ for the beam photon energy from 570 MeV to 842 MeV. The black points represent the results of the new A2 data together with their statistical uncertainties whereas the red points the CBELSA/TAPS data [45, 64]. The blue dashed line indicates the position where the 2 PED events are added to the 3 PED events while the gray boxes show the systematic uncertainties.

Therefore, a direct comparison should be treated with caution. Nevertheless, a good agreement between the A2 and CBELSA/TAPS data is present within their statistical uncertainties. Only a few

data points disagree with each other. An example is the third $\cos\theta_{\pi^0,\mathrm{CMS}}$ bin in the beam photon energy range from 706 MeV to 740 MeV, where even the systematic uncertainties of about 8% of both data set can not explain this deviation. The bin of the A2 data corresponds to the more challenging kinematic region due to the transition region between the TAPS and the CB where the dilution factor drops (cf. Fig. A.8) and higher sensitivities to the exact target center position and trigger adjustments are present (cf. Sec. 8.3.5).

To avoid deviations, which are caused by a different energy binning between both data sets, the data are compared in another representation where the individual 18 $\cos\theta_{\pi^0,\mathrm{CMS}}$ bins are plotted as a function of the mean value of the beam photon energy bin E_γ. Since the $\cos\theta_{\pi^0,\mathrm{CMS}}$ binning is independent of the coherent edge positions, the same number of bins was selected for the A2 data as for the CBELSA/TAPS data. Thus, a better direct comparison is reached. Fig 9.2 and Fig. 9.3 depicts the results of the double polarization observable G for the different $\cos\theta_{\pi^0,\mathrm{CMS}}$ bins as a function of the mean value of the beam photon energy window E_γ. The inspection of both figures shows a very good agreement between both data within their statistical uncertainties as well. Special attention should be given to the sixth $\cos\theta_{\pi^0,\mathrm{CMS}}$ bin ($-0.44 \leq \cos\theta_{\pi^0,\mathrm{CMS}} < -0.33$) where a notable difference between both data sets is present for the second (E_γ = (650-684) MeV) and third beam photon energy bin (E_γ = (684-716) MeV) of the CBELSA/TAPS. In this kinematic region, the proton polar angle in the CBELSA/TAPS setup lies in the transition region between the forward plug detector and the Crystal Barrel detector [45]. As shown in the reference, the acceptance of the 3 PED events drops in this region as the proton is not detected by the main calorimeters in this region. To compensate for this acceptance hole, additional events are included in the analysis of the CBELSA/TAPS data, namely the 2 PED events. As 2 PED events can not be selected as good as 3 PED events[2], the results of the 2 PED events can be subjected to higher systematic uncertainties. While all these problems of this CBELSA/TAPS data only give a hint to explain these deviations, the A2 data for this kinematic region can be discussed in detail regarding this deviations. Possible explanations for the deviations are the dilution factor, the polarization degrees of the photon and the target, and background contamination. A wrong target polarization degree would affect all bins as the target correction factors are global factors. In addition, the polarization needed to be corrected by a factor that would result in a polarization degree above 100%. As a conclusion, the target polarization degree can be excluded. The linear polarization degree is only depending on the beam photon energy and not the $\cos\theta_{\pi^0,\mathrm{CMS}}$ binning. Therefore, if the problems arise from the beam photon polarization degree, the deviation should be seen in all $\cos\theta_{\pi^0,\mathrm{CMS}}$ bins. As this is not the case, the beam polarization degree can be ruled out as well. However, the dilution factor reveals a $\cos\theta_{\pi^0,\mathrm{CMS}}$ dependence as has been shown in Sec. 8.1.3, and thus could perhaps explain this deviation. The data in this $\cos\theta_{\pi^0,\mathrm{CMS}}$ bin are only 3 PED events and thus the dilution factor can be determined via the coplanarity distributions with small systematic uncertainties. The inspection of the dilution factors in Fig. A.8 give a dilution factor value d of about 0.8 for both of these bins and a quite flat distribution of the surrounding bins.

[2]The angular cuts are missing (cf. Sec. 7.5.2).

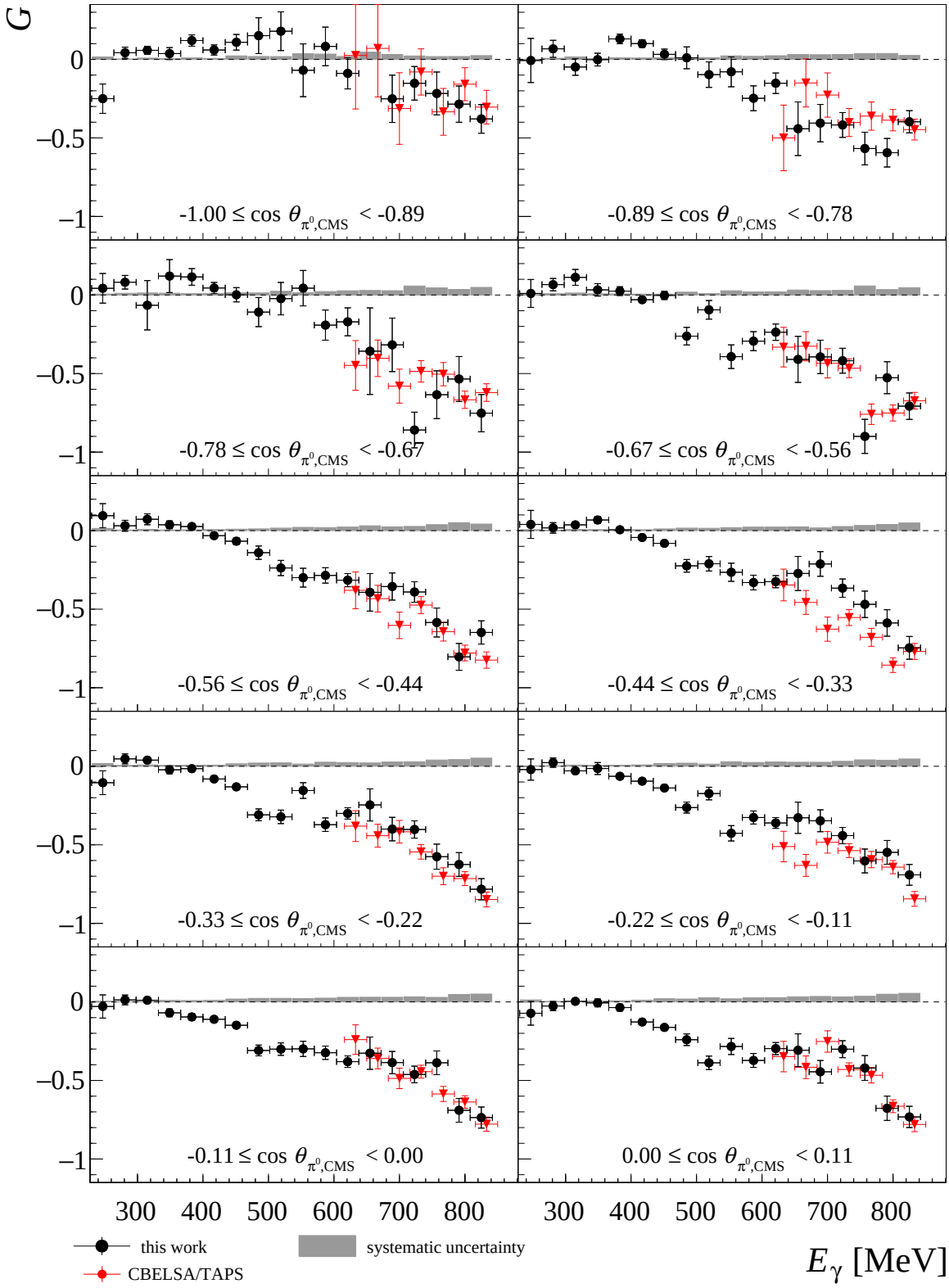

Fig. 9.2: Comparison of the results for the double polarization observable G with previous data for $\vec{\gamma}\vec{p}\to p\pi^0$ as a function of the beam photon energy E_γ. The results of the double polarization observable G are shown as a function of the mean value of the beam photon energy bin E_γ for the kinematic range $-1.00 \leq \cos\theta_{\pi^0,\mathrm{CMS}} < 0.11$. The black points represent the results of the new A2 data together with their statistical uncertainties whereas the red points the CBELSA/TAPS data [45, 64]. The gray boxes show the systematic uncertainties.

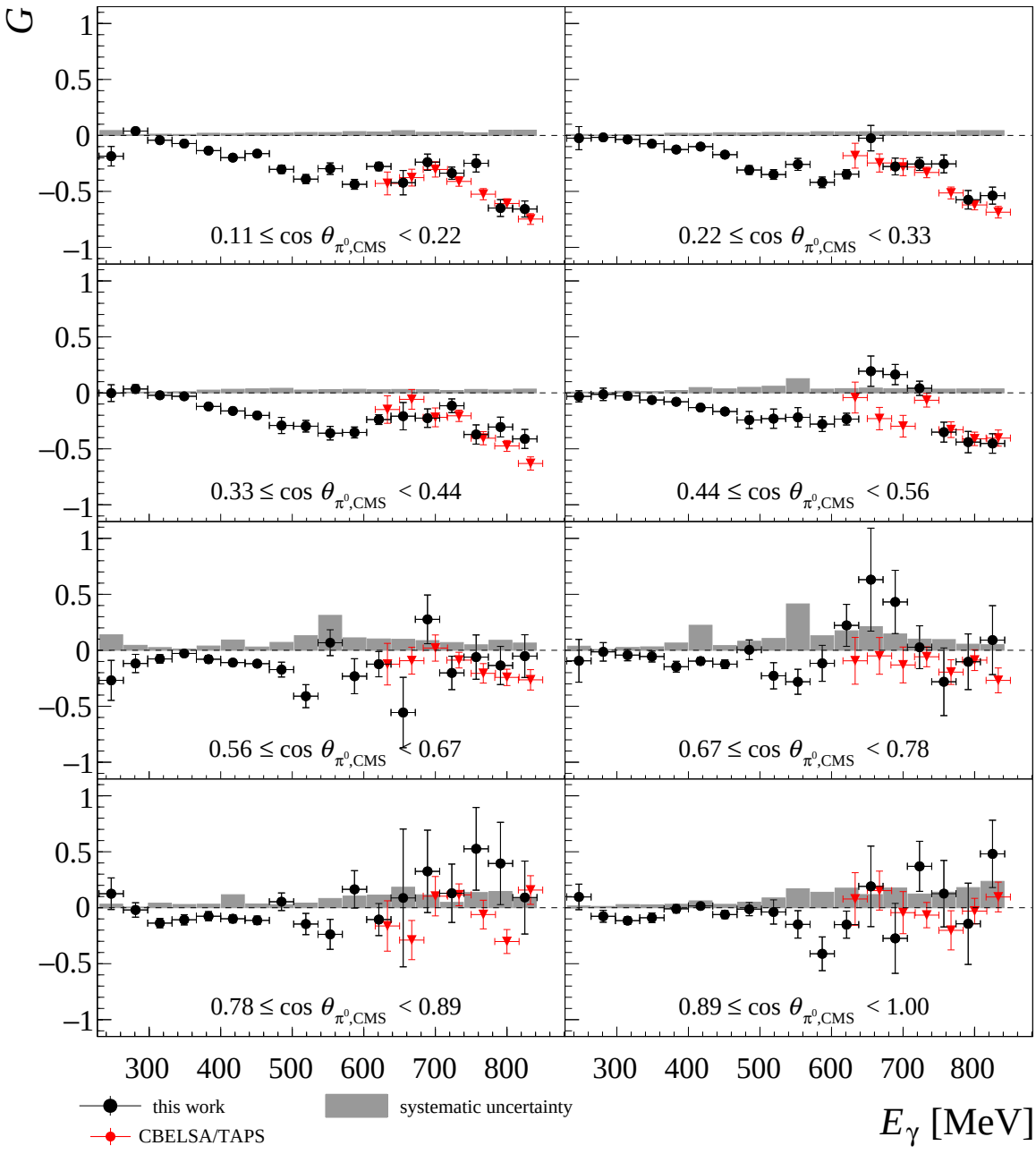

Fig. 9.3: Comparison of the results for the double polarization observable G with previous data for $\vec{\gamma}\vec{p}\rightarrow p\pi^0$ as a function of the beam photon energy E_γ. The results of the double polarization observable G are shown as a function of the mean value of the beam photon energy bin E_γ for the kinematic range $0.11 \leq \cos\theta_{\pi^0,\mathrm{CMS}} < 1.00$. The black points represent the results of the new A2 data together with their statistical uncertainties whereas the red points the CBELSA/TAPS data [45, 64]. The gray boxes show the systematic uncertainties. Note the different y-axis range compared to Fig. 9.2.

To match the considered A2 point with the CBELSA/TAPS point, the dilution factor needs to be decreased. Nevertheless, a smaller dilution factor d directly requires an increasing scaling factor s_C.

As the obtained scaling with the required matching dilution factor would result in an overall negative reconstructed hydrogen distribution, the dilution factor can not be the source of the deviation. The final possible source is the background contamination. The CBELSA/data collaboration quoted an overall background contamination of less than 3% [64]. The A2 data also contain background of less than 2% in this kinematic region. Even if the background contributes with the maximal possible polarization observable value of ± 1, the deviation could not explain these effects.
A final remarkable observation is seen in the 14th $\cos\theta_{\pi^0,\mathrm{CMS}}$ bin ($0.44 \leq \cos\theta_{\pi^0,\mathrm{CMS}} < 0.56$) for the same energy bins as above. In that case, even a different sign of the extracted polarization observable values is observed. Whereas the data points in this analysis are only given by the 3 PED event yields, the points in the CBELSA/TAPS data are already dominated by the 2 PED events. As the angular cuts for the selection are missing, 2 PED events are more sensitive to background contamination.
Nevertheless, besides these small deviations, a very good agreement between the new A2 data and the CBELSA/TAPS data is seen and for the first time, precise measurement of the double polarization observable G below 600 MeV are available.

9.1.2 Double Polarization Observable G for the reaction $\vec{\gamma}\vec{p} \to n\pi^+$

The final obtained results of the new A2 data for the double polarization observable G in the reaction $\vec{\gamma}\vec{p} \to n\pi^+$ have been determined in a beam photon energy range from 264 MeV to 842 MeV ($W = 1145\,\mathrm{MeV} - 1569\,\mathrm{MeV}$) with a 34 MeV energy bin window and are indicated by the black points in Fig. 9.4 and Fig. 9.5. Up to now, the data base for the polarization observable G in the reaction $\vec{\gamma}\vec{p} \to n\pi^+$ is with a total of only 23 other data points within the analyzed energy region quite oversee-able. Past data were published by the A2/GDH collaboration with six $\cos\theta_{\pi^+,\mathrm{CMS}}$ bins which cover the kinematic range $-0.64 \leq \cos\theta_{\pi^+,\mathrm{CMS}} < 0.86$ in the beam photon energy range from 326 MeV to 354 MeV [67]. The remaining 17 data points were recorded during the 90s with four data points for a beam photon energy range from 320 MeV to 380 MeV [69] and 13 data points in the range from 700 MeV to 850 MeV [70].
The corresponding old A2/GDH data are included in Fig. 9.4 and are given by the red points, whereas the data points from Belayey et al. [69] are indicated by the blue dots. Both data sets agree very good with the new A2 data within their statistical uncertainties. Most importantly, the new precise A2 data cover also the $\cos\theta_{\pi^+,\mathrm{CMS}}$ bins in the forward direction and backward direction. These points are of major importance for the $\mathrm{L_{max}}$-fit procedure which will be presented in Sec. 9.2 [43]. Finally, the overall statistic is improved significantly by a factor of more than four. At higher energies ($E_\gamma > 700$ MeV), a comparison with data from Bussey et al. [70], indicated by the green points in Fig. 9.5, is possible. The first remarkable observation can be seen in the beam photon energy range from 672 MeV to 706 MeV. Whereas the old data show a positive sign, the new A2 data clearly have a parabolic behavior with negative values. The remaining energy bins behave similar as the new A2 data, and both data sets agree very good with each other within their statistical errors.

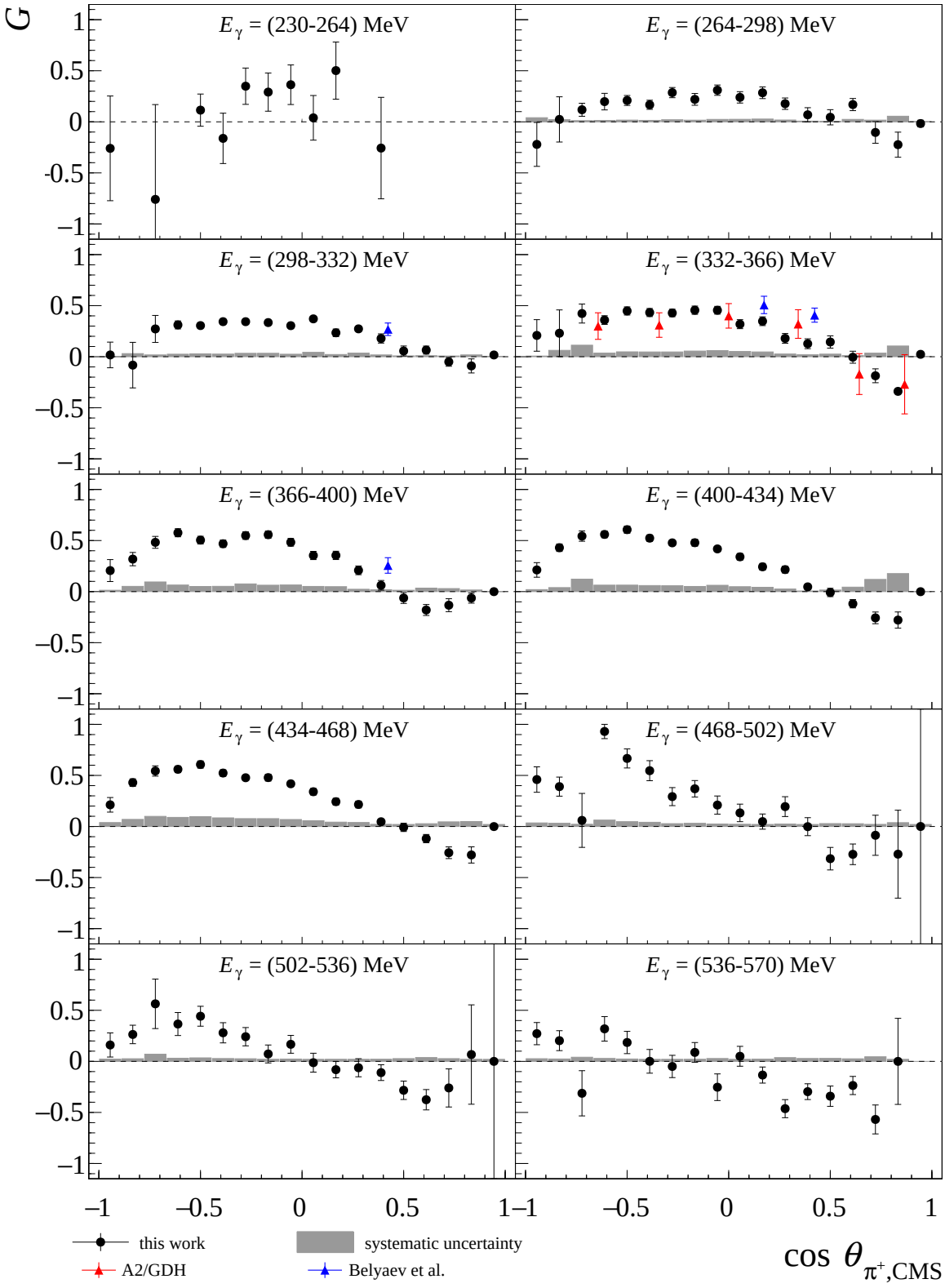

Fig. 9.4: Comparison of the results for the double polarization observable *G* with previous data for $\vec{\gamma}\vec{p}\to n\pi^+$. The results of the double polarization observable *G* are shown as a function of $\cos\theta_{\pi^+,\mathrm{CMS}}$ for the beam photon energy from 230 MeV to 570 MeV. The black points represent the results of the new A2 data together with their statistical uncertainties whereas the gray boxes show the systematic uncertainties. The new A2 data are compared to the recent data base which consists of the A2/GDH data [67] in red and Belayev et al. [69] in blue.

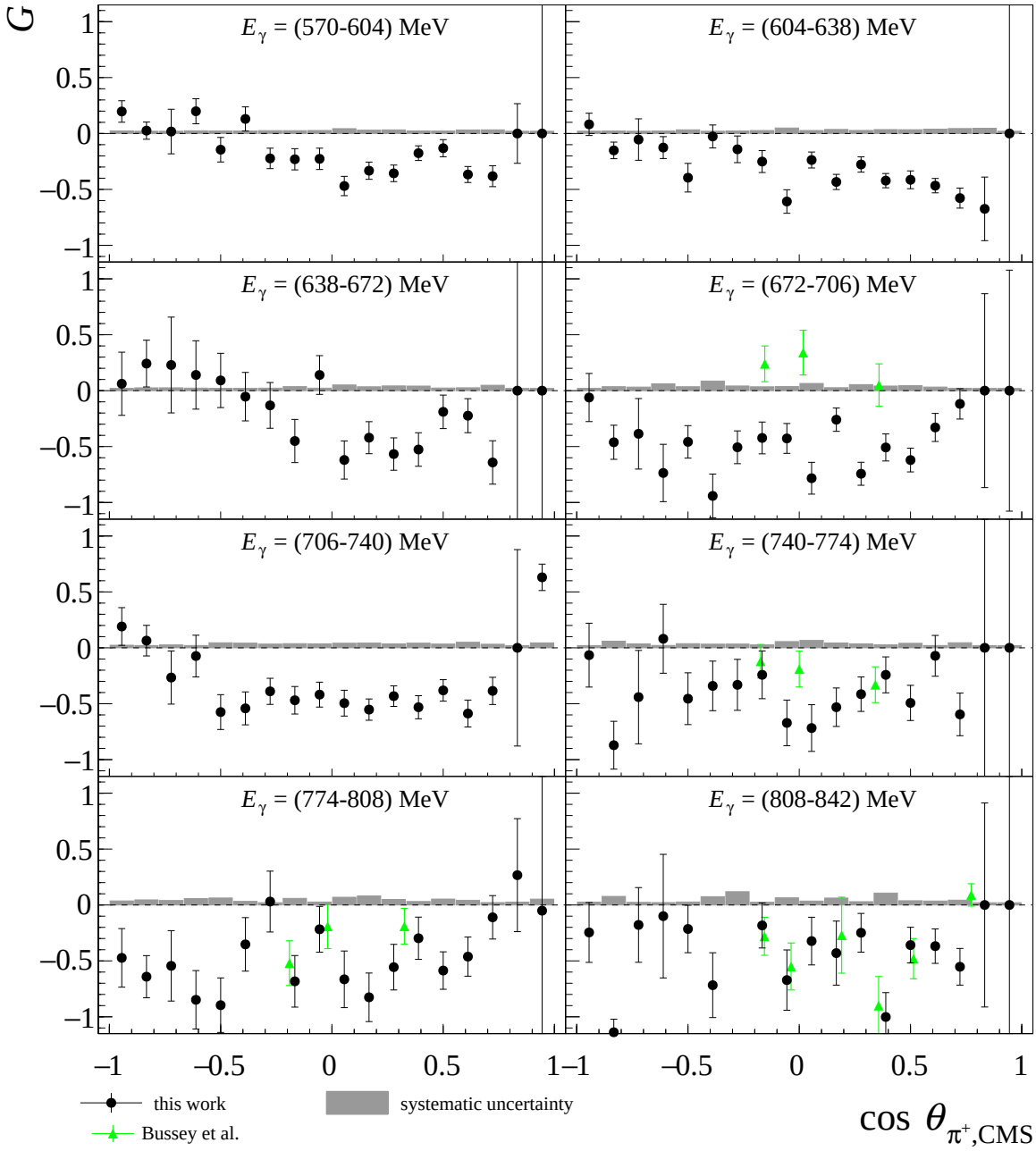

Fig. 9.5: Comparison of the results for the double polarization observable G with previous data for $\vec{\gamma}\vec{p}\to n\pi^+$. The results of the double polarization observable G are shown as a function of $\cos\theta_{\pi^+,\mathrm{CMS}}$ for the beam photon energy from 570 MeV to 842 MeV. The black points represent the results of the new A2 data together with their statistical uncertainties whereas the gray boxes show the systematic uncertainties. The new A2 data are compared to the recent data base which consists of Bussey et al. [70] in green.

As a conclusion, the comparison of the new A2 data with the existing data clearly show that an improvement of the overall data base was reached with high precision quality data which can be used to further constrain the PWAs at beam photon energies below 842 MeV.

9.1.3 Double Polarization Observable *E* for the reaction $\vec{\gamma}\vec{p} \to n\pi^+$

The final results of the new A2 data for the double polarization observable E in the reaction $\vec{\gamma}\vec{p} \to n\pi^+$ have been determined in a beam photon energy range from 230 MeV to 842 MeV ($W = 1145\,\text{MeV} - 1569\,\text{MeV}$) with a 34 MeV energy bin window and are indicated by the black points in Fig. 9.6 and Fig. 9.7. In contrast to the double polarization observable G, the data base for the E observable is much better as the CLAS collaboration published in 2015 data which cover the beam photon energy range from 350 MeV to 2370 MeV with a minimum energy bin window of 27 MeV. The kinematic region $-0.9 \leq \cos\theta_{\pi^+,\text{CMS}} < 0.9$ is covered by up to 27 points [68]. They are indicated by the red points, and their corresponding beam photon energy range is depicted in the same color scheme.

At first sight, both data sets agree very good with each other within their statistical and systematic uncertainties. Nevertheless, it should be kept in mind that the energy bins are not exactly the same. Therefore, energy ranges where the change in the polarization observables values between two energy bins is huge should be treated with caution, e.g., E_γ = (332-364) MeV. Although the A2 data lie systematically below the CLAS data, the discrepancies can be ascribed to the energy difference of the inspected bin. Whereas the A2 bin already starts at E_γ = 332 MeV, the CLAS bin begins at E_γ = 350 MeV which corresponds to an energy difference of 18 MeV. Taking the behavior of all surrounding energy bins into account, it becomes clear that the A2 data need to lie below the CLAS data. A final striking argument is the total cross section as the energy bin lies in the falling slope of the $\Delta(1232)3/2^+(P_{33})$ resonance [20]. Therefore, the cross section for the A2 energy bin is still higher compared to the CLAS energy bin, and thus E is negatively higher for the A2 bin by definition. Small deviation at higher energy bins can be assigned to the second resonance region. Small deviation at higher energy bins can be assigned to the second resonance region.

To avoid energy binning effects, a better representation is again to compare the results as a function of the mean value of the beam photon energy window E_γ. Since the CLAS data have a finer binning in $\cos\theta_{\pi^+,\text{CMS}}$ [3], the bin with the smallest deviation to the A2 bin is chosen. The resulting E observable for the 18 $\cos\theta_{\pi^+,\text{CMS}}$ bins of the A2 data as a function of the mean value of the beam photon energy window is depicted in Fig. 9.8 and Fig.9.9. In this representation, no energy binning effects contribute. Both data agree very well with each other within the statistical uncertainty, which indicates that both experiments have their systematic effects under control. Overall, the statistics of the CLAS data set is better than the new A2 data. However, the main advantage of the new A2 data are the additional points in the backward direction and beam photon energies below 350 MeV which can be used as a new input for the L_{max}-fit procedure and new PWA fits.

[3] The best comparison would have been to adjust the energy binning to the CLAS data. However, it has been decided to extract the double polarization observable E in the same binning as the double polarization observable G. The reason lies in the comparison of the A2 result with each other as the observables are extracted from the same data and with the same selection and analysis procedure.

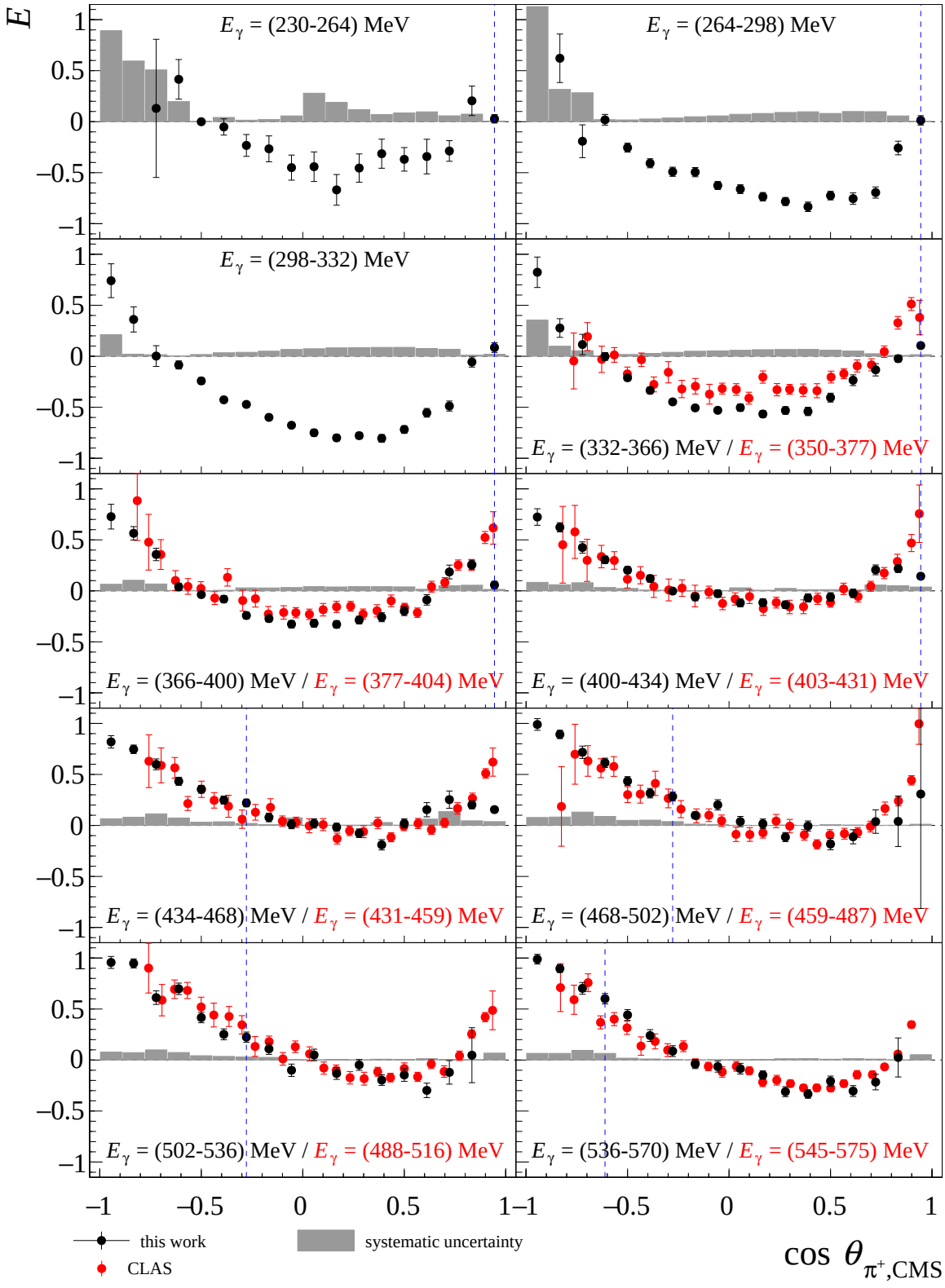

Fig. 9.6: Comparison of the results for the double polarization observable *E* with previous data for $\vec{\gamma}\vec{p}\to n\pi^+$. The results of the double polarization observable *E* are shown as a function of $\cos\theta_{\pi^+,\mathrm{CMS}}$ for the beam photon energy from 230 MeV to 570 MeV. The black points represent the results of the new A2 data together with their statistical uncertainties whereas the red points the CLAS data [68]. The blue dashed line indicates the position up to which point the 1 PED events are added to the 2 PED events while the gray boxes shows the systematic uncertainties.

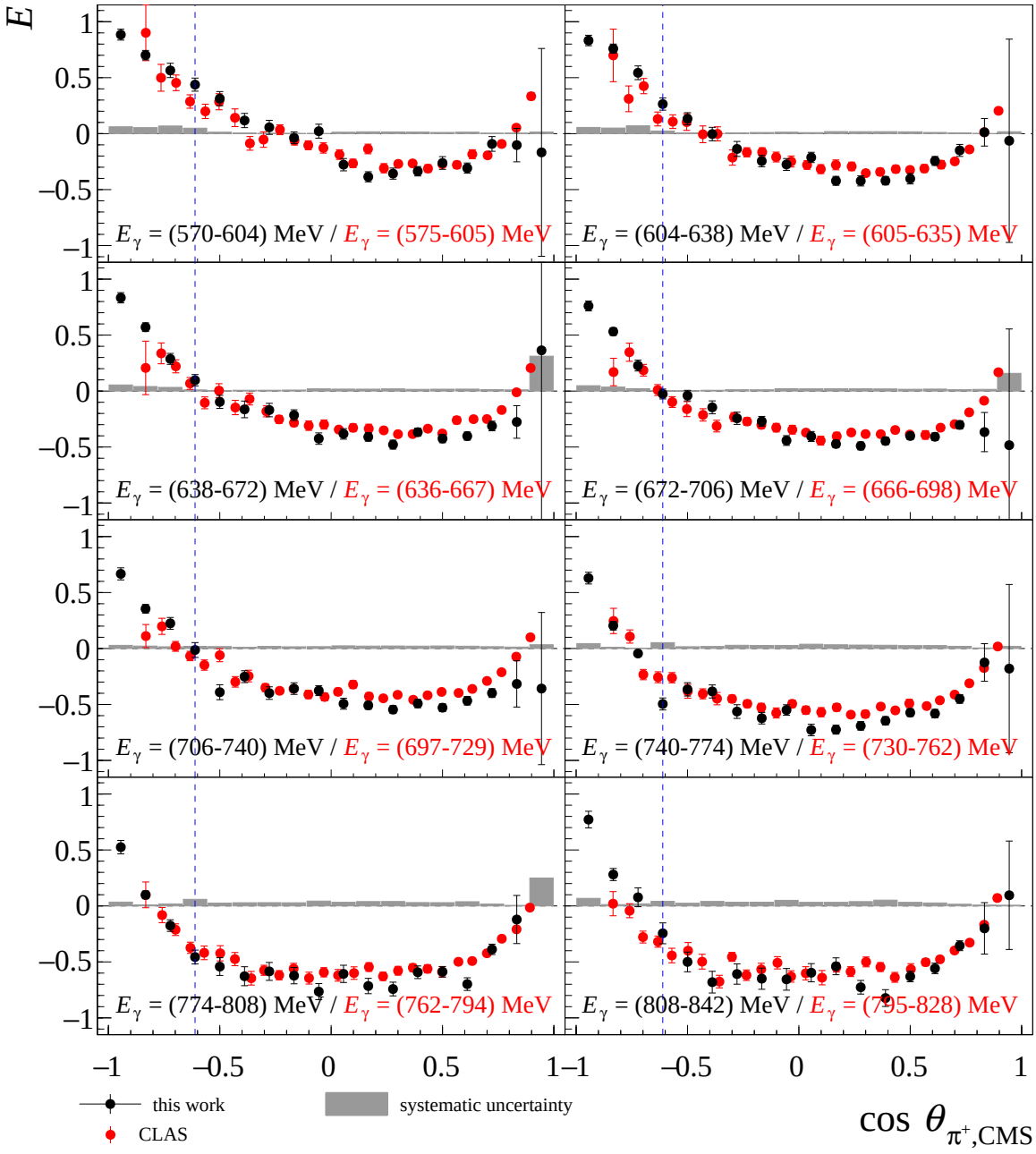

Fig. 9.7: Comparison of the results for the double polarization observable *E* with previous data for $\vec{\gamma}\vec{p}\to n\pi^+$. The results of the double polarization observable *E* are shown as a function of $\cos\theta_{\pi^+,\mathrm{CMS}}$ for the beam photon energy from 570 MeV to 842 MeV. The black points represent the results of the new A2 data together with their statistical uncertainties whereas the red points the CLAS data [68]. The blue dashed line indicates the position up to which point the 1 PED events are added to the 2 PED events while the gray boxes shows the systematic uncertainties.

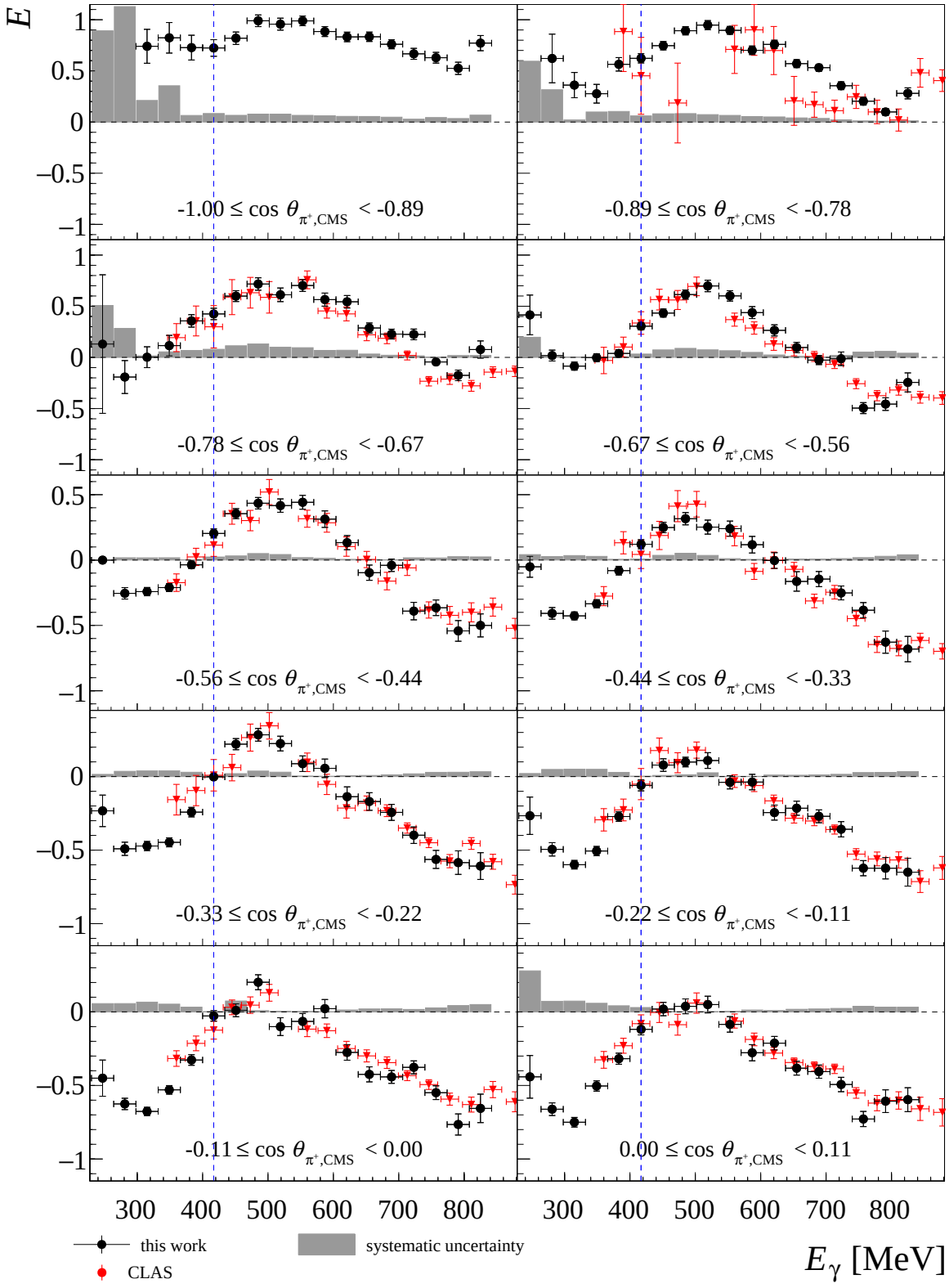

Fig. 9.8: Comparison of the results for the double polarization observable E with previous data for $\vec{\gamma}\vec{p}\to n\pi^+$ as a function of the beam photon energy E_γ. The results of the double polarization observable E are shown as a function of the mean value of the beam photon energy bin E_γ for the kinematic range $-1.00 \leq \cos\theta_{\pi^+,\mathrm{CMS}} < 0.11$. The black points represent the results of the new A2 data together with their statistical uncertainties whereas the red points the CLAS data [68]. The gray boxes show the systematic uncertainties. Note the different y-axis range between the different rows.

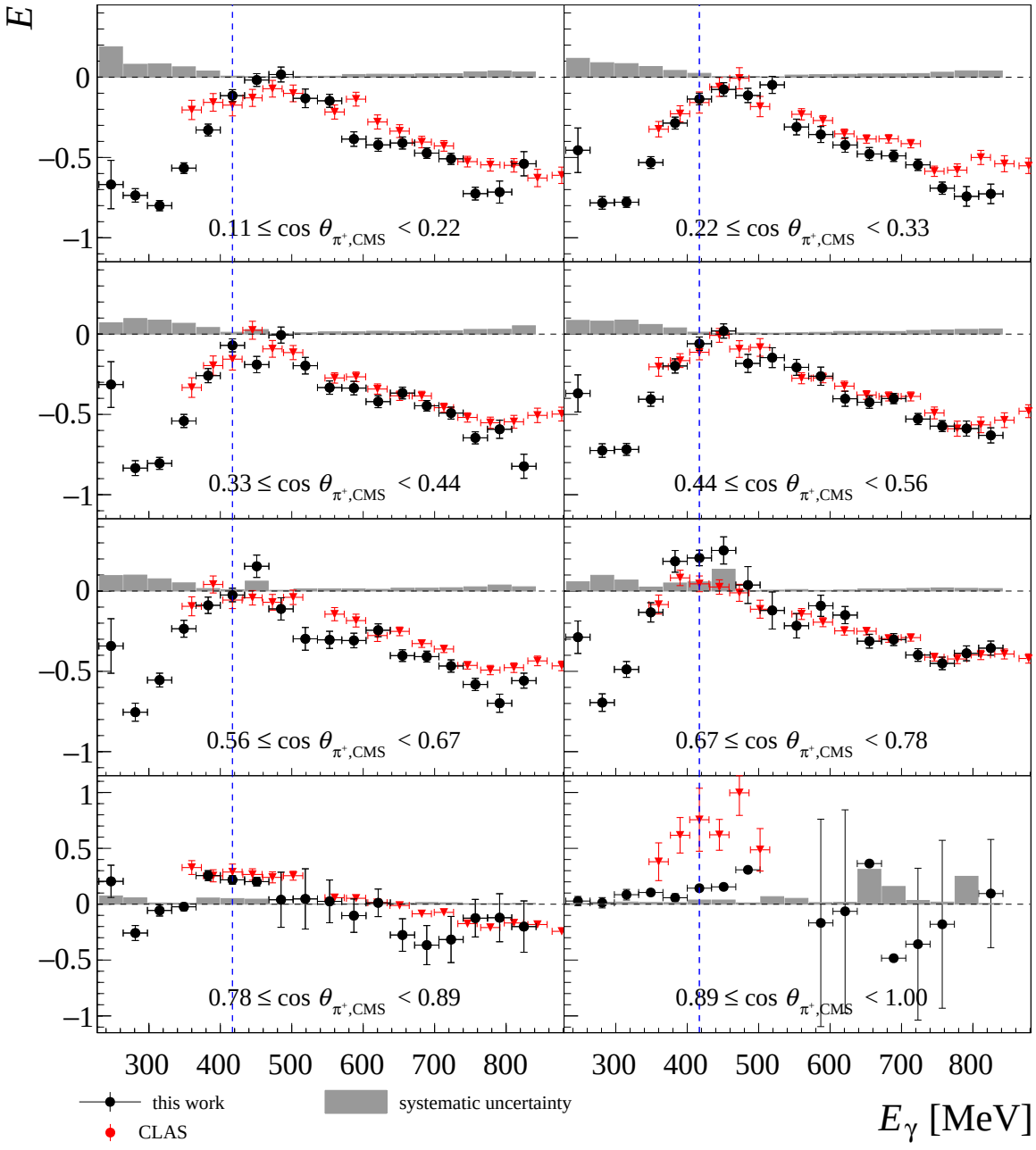

Fig. 9.9: Comparison of the results for the double polarization observable E with previous data for $\vec{\gamma}\vec{p}\to n\pi^+$ as a function of the beam photon energy E_γ. The results of the double polarization observable E are shown as a function of the mean value of the beam photon energy bin E_γ for the kinematic range $0.11 < \cos\theta_{\pi^+,\mathrm{CMS}} \leq 1.00$. The black points represent the results of the new A2 data together with their statistical uncertainties whereas the red points the CLAS data [68]. The gray boxes show the systematic uncertainties. Note the different y-axis range between the different rows.

9.2 Dominant Partial Wave contributions

As already mentioned in the introduction of this thesis, a truncated PWA decomposition can be performed with the obtained polarization observable data to determine the dominant partial wave contributions. As a first step, the polarization observables are multiplied by the differential cross section to obtain the profile functions $\check{\mathrm{G}} = G \cdot \frac{d\sigma}{d\Omega}$ and $\check{\mathrm{E}} = E \cdot \frac{d\sigma}{d\Omega}$ which are given as a partial wave expansion, which is truncated at $\mathrm{L}_{\max}$, by [43]:

$$\check{\mathrm{G}}(W, \cos\theta) = \rho \sum_{k=2}^{2\mathrm{L}_{\max}} (a_{\mathrm{L}_{\max}})_k^{\check{\mathrm{G}}}(W)\, P_k^2(\cos\theta)\,, \tag{9.1}$$

$$\check{\mathrm{E}}(W, \cos\theta) = \rho \sum_{k=0}^{2\mathrm{L}_{\max}} (a_{\mathrm{L}_{\max}})_k^{\check{\mathrm{E}}}(W)\, P_k^0(\cos\theta)\,. \tag{9.2}$$

Thereby, ρ is the phase space factor, $(a_{\mathrm{L}_{\max}})_k^{\check{\Omega}}$ are the energy-dependent real expansion coefficients for a defined $\mathrm{L}_{\max}$, and $P_k^m(\cos\theta)$ are the angular-dependent associated Legendre polynomials. The information about the contributing multipoles is included in the expansion coefficients. Some examples of the coefficients are given in the introduction of this thesis. As the terms for the expansion coefficients are quite large, the contributing partial waves are presented only for their corresponding l_M, i.e. an interference between the partial wave S_{11} and the P_{11} is contained in the $\langle S, P\rangle$ term whereas an interference between P_{11} and P_{33} in $\langle P, P\rangle$. The connection between photoproduction multipoles and the partial waves is given in Tab. 1.5. The extracted expansion coefficients are compared to continuous curves which have been determined from the multipole solutions of the latest BnGa-2016 PWA solution [46].

9.2.1 The reaction $\vec{\gamma}\vec{p} \to p\pi^0$

Fig. 9.10 shows six profile functions for different center of mass energies W as a function of the kinematic variable $\cos\theta_{\pi^0,\mathrm{CMS}}$. They have been fitted with associated Legendre polynomials up to a maximum of $\mathrm{L}_{\max} = 4$. In the top row, the corresponding χ^2/ndf distribution for the different $\mathrm{L}_{\max}$ truncation is presented.

Under the assumption of $\mathrm{L}_{\max} = 1$, the angular dependence of the profile functions follow a parabolic shape. However, it is clearly visible that the profile functions already need higher orders of L at low energies. This can be seen as well in the χ^2/ndf where only the first two energy bins are compatible with $\chi^2/\mathrm{ndf} = 1$. Starting at $W = 1200\,\mathrm{MeV}$, the χ^2/ndf of the $\mathrm{L}_{\max} = 1$ fit starts to increase and only the inclusion of higher waves up to $\mathrm{L}_{\max} = 3$ (F-waves) can describe the data from thereon.

Fig. 9.11 and Fig. 9.12 present the energy-dependent real expansion coefficients truncated at $\mathrm{L}_{\max} = 3$. Below $W = 1400\,\mathrm{MeV}$, the first coefficient $(\mathrm{a}_3)_2^{\check{\mathrm{G}}}$ is dominated by the interference term $\langle P, P\rangle$. This can be explained by the dominance of the $\Delta(1232)3/2^+(P_{33})$ resonance which does not interfere with S-, D- or F-waves in this coefficient. Starting at about $W = 1400\,\mathrm{MeV}$, the contribution of S- and D-waves is seen in form of the interference terms $\langle S, D\rangle$ and $\langle D, D\rangle$. Although their inclusion helps to

describe the behavior of the extracted expansion coefficient, deviations are still present which already indicates in this coefficient that modification in the S- and/or D-waves might be needed. In the $\langle S,D\rangle$ term, a small $p\eta$ cusp effect occurs at the photoproduction threshold of the $p\eta$ channel which is indicated by the dashed line. It is seen as a sudden drop or increase in the expansion coefficient. For the first time, the cusp effect in the $p\pi^0$ channel was observed in the differential cross section[134]. However, the A2 data in this region are not precise enough to confirm the cusp. For that, a finer energy binning is mandatory which however would result in higher statistical uncertainties. The cusp is most pronounced in this coefficient due to the $\langle S,D\rangle$ interference term. First of all, the S-waves with the $N(1535)1/2^-(S_{11})$ resonance dominate the $p\eta$ photoproduction at threshold which explains the seen cusp effect. The strength of the cusp in the coefficient is finally given by its interference partner. For the first coefficient, the partner is the D-waves which have the dominant $N(1520)3/2^-(D_{13})$ resonance in that region.

The importance of D-waves at low center of mass energies W can be seen in the second coefficient $(a_3)_3^{\check{G}}$ due to the interference of the D-waves with the P-waves. Here already starting at about $W = 1300\,\text{MeV}$ the interference between the P- and D-waves is not sufficient to describe the data at all. Here already starting at about $W = 1300\,\text{MeV}$ the interference between the P- and D-waves is not sufficient to describe the data at all. Only the inclusion of F-waves can match the data with the BnGa solution. The cusp effect is also seen in the continuous curves of this coefficient by the $\langle S,F\rangle$ interference term but it is again too small to give a further statement.

The necessity of F-waves at even low center of mass energies becomes clear in the next coefficient $(a_3)_4^{\check{G}}$ where interference between $\langle P,F\rangle$ and $\langle F,F\rangle$ occur. Although the amplitude is close to zero, a clear deviation from zero is visible for the coefficient and the BnGa solution. This coefficient has also a feature compared to the first coefficient concerning the $\langle D,D\rangle$ term. In the third coefficient, only interference terms between different total angular momentum contribute whereas in the first one does not. Therefore, the contribution of the term is higher in the first coefficient due to the interference of two multipoles to which the dominant $N(1520)3/2^-(D_{13})$ resonance couples. Since the latter does not exist in the third coefficient, some sensitivities to weakly contributing D-wave resonances might be accessible, e.g., the $N(1675)5/2^-(D_{15})$. Coming to the next coefficient $(a_3)_5^{\check{G}}$, a small hint of G-waves in the $\Delta(1232)3/2^+(P_{33})$ region is visible via the $\langle P,G\rangle$ term. Whereas the BnGa solution shows no deviation from zero in this region, the data does. A similar peak like structure has been seen in the higher expansion coefficients of the differential cross section as well [43]. However, the authors quote that the structure is caused by systematic uncertainties in the analyzed data[4]. To take into account systematic effects in the extracted expansion coefficient in this analysis, another fit was performed where the total error is given by:

$$\Delta\Omega = \sqrt{\Delta\Omega_{\text{stat}}^2 + \Delta\Omega_{\text{syst}}^2}. \tag{9.3}$$

[4]It is noteworthy that the data were recorded with the A2 experiment. Thus, a possible explanation could be that the peak is caused by a not understood systematic effect of the detector setup

Even after the inclusion of the systematic uncertainties, a deviation from zero is visible. However, the data are not precise enough to give a clear statement as only two data points deviate from zero. Therefore, to rule out contributions of G-waves, a more precise measurement of the observable G is needed.

A more robust statement can be made for the higher center of mass energies where the expansion coefficients start to deviate from zero at about $W = 1460\,\mathrm{MeV}$ while the BnGa solution first at $W = 1520\,\mathrm{MeV}$. Together with the observation of the other coefficients, the contribution of the D-waves in the $\langle D, F\rangle$ term could be wrong. Note that a similar observation is seen in the expansion coefficient $(a_4)_5^{\check{\mathrm{E}}}$ which has been determined within the thesis of F. Afzal [14].

Overall, due to the sensitivity of the profile function $\check{\mathrm{G}}$ to only interference terms in all expansion coefficients, the $\mathrm{L_{max}}$-fit procedure can extract even small contributing multipoles with high angular momentum l_M at low center of mass energies. Especially, the interference with the P-waves is well pronounced as here the dominant $\Delta(1232)3/2^+(P_{33})$ contributes.

To study the Roper resonance in more detail, the different contributing interference terms of the $\langle P, P\rangle$ block are plotted separately for the first coefficient as can be seen in Fig. 9.13. From the inspection of the Fig, two important information can be extracted. On the one hand, the interference between the E_{1+} and the M_{1-} multipole is negligible. On the other hand, the interference between the M_{1+} with the E_{1+} and M_{1-} multipole has the same strength ,and they interfere destructively. Because only small deviations to the extracted expansion coefficient are seen, the new data may help to further constrain this interference terms. As already concluded previously, problems might be present in the D-wave interference terms. However, since the strength of the contribution of the interference of $\langle S, D\rangle$ and $\langle D, D\rangle$ are in the same order, the deviation can not easily be traced back to the D-wave contribution.

For a final cross-check of the quality of the new A2 data, the CBELSA/TAPS data are used to determine the expansion coefficient in a similar way. These are indicated by the red points in the Fig. 9.14 and 9.15. In total, a good agreement between both data sets is seen which supports the quality of the new A2 data.

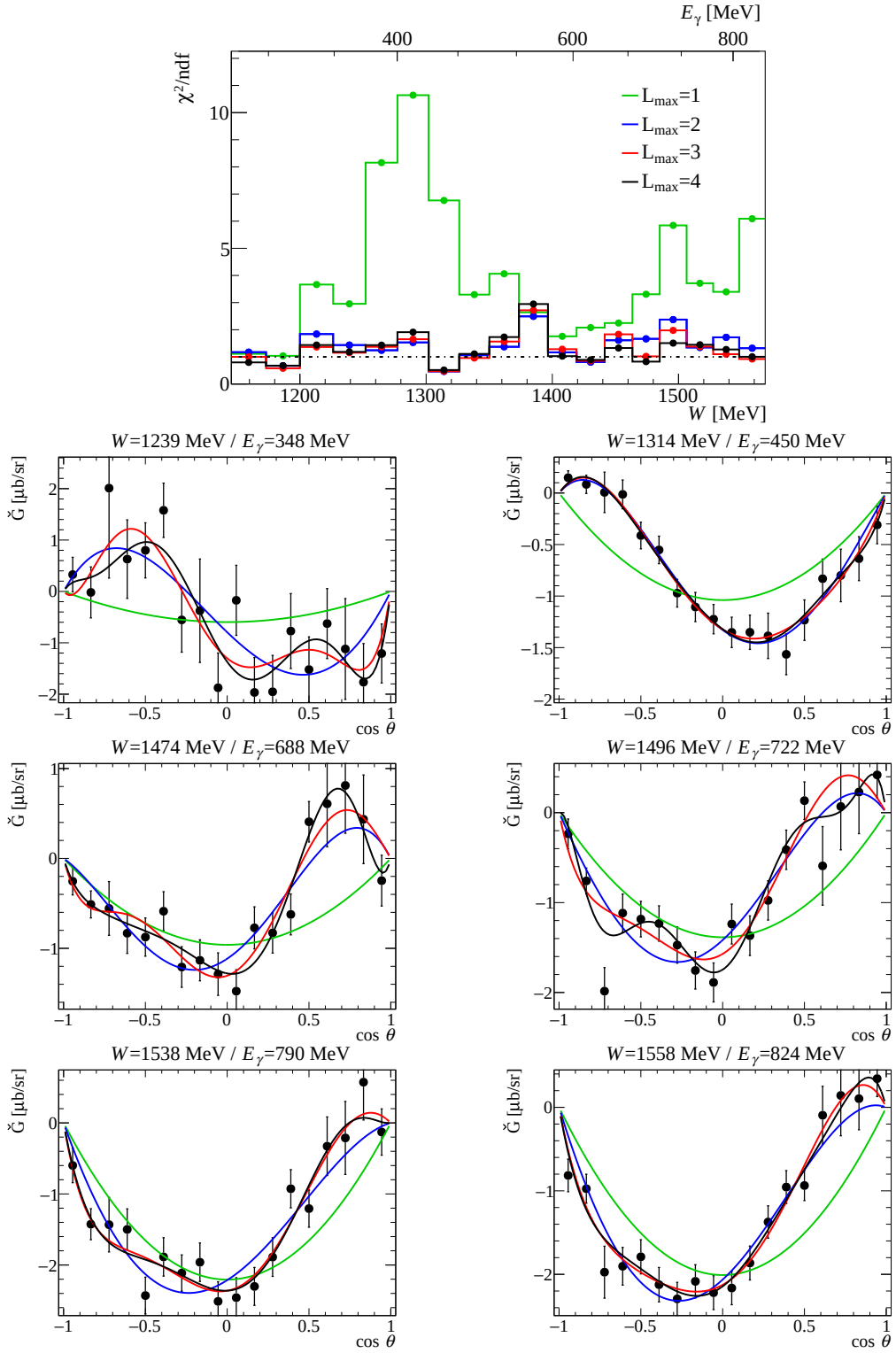

Fig. 9.10: Associated Legendre polynomial fits to the profile function Ğ for $\vec{\gamma}\vec{p}\to p\pi^0$. The profile function Ğ as a function of the kinematic variable $\cos\theta_{\pi^0,\mathrm{CMS}}$ were fitted with associated Legendre polynomials which are described by Eq. (9.2). The fits have been truncated at different L_{max}. Hereby, the green line corresponds to $L_{max} = 1$, the blue line to $L_{max} = 2$, the red line to $L_{max} = 3$, and the black line to $L_{max} = 4$. As an illustration of the fits, six profile functions (black points) are presented in the second to fourth row together with the different truncated L_{max}-fits. The corresponding χ^2/ndf of all fits is depicted in the top row as a function of the center of mass energy W and the beam photon energy E_γ.

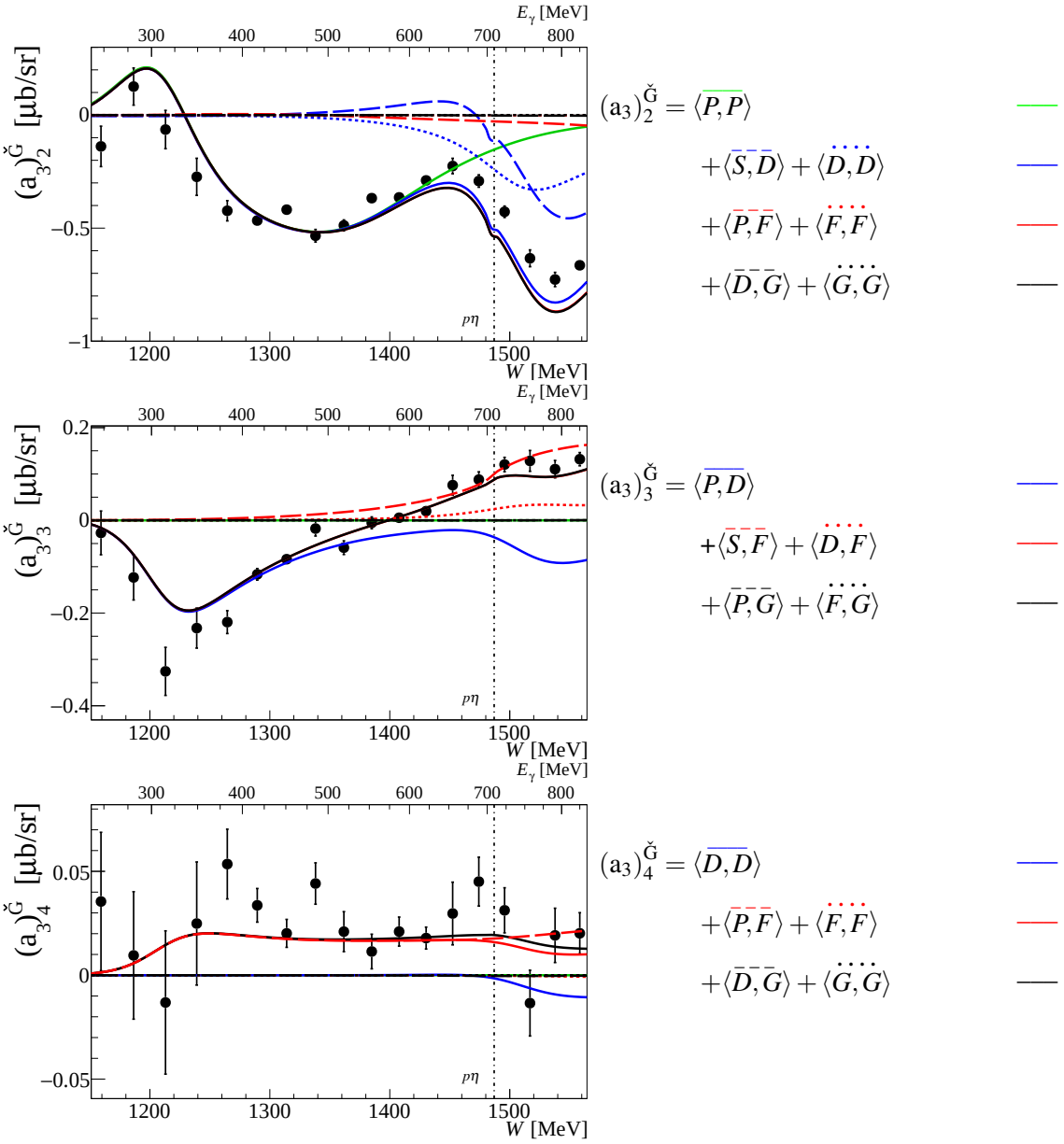

Fig. 9.11: Fit coefficients $(a_3)^{\check{G}}_{2\cdots4}$ for $\vec{\gamma}\vec{p}\to p\pi^0$ as a function of the center of mass energy W. The resulting fit coefficients, indicated by the black points, are plotted on the left side. They are compared to continuous curves which have been determined from the multipole solutions of the BnGa-2016 PWA solution [46]. The solution have been truncated at different L_{max}. Hereby, the green solid curve corresponds to $L_{max} = 1$, the blue solid curve to $L_{max} = 2$, the red solid curve to $L_{max} = 3$, and the black solid curve to $L_{max} = 4$. On the right panel, the contributing partial wave interference terms are given for the different L_{max} values. Thereby, $L_{max} = 1$ only contains the contribution of S-and P-waves, $L_{max} = 2$ additionally D-waves, $L_{max} = 3$ additionally F-waves, and $L_{max} = 4$ additionally G-waves. The individual interference terms are included as well and are indicated by their color and dashed or dotted curves. The dashed-dotted line marks the photoproduction threshold of the $p\eta$ channel.

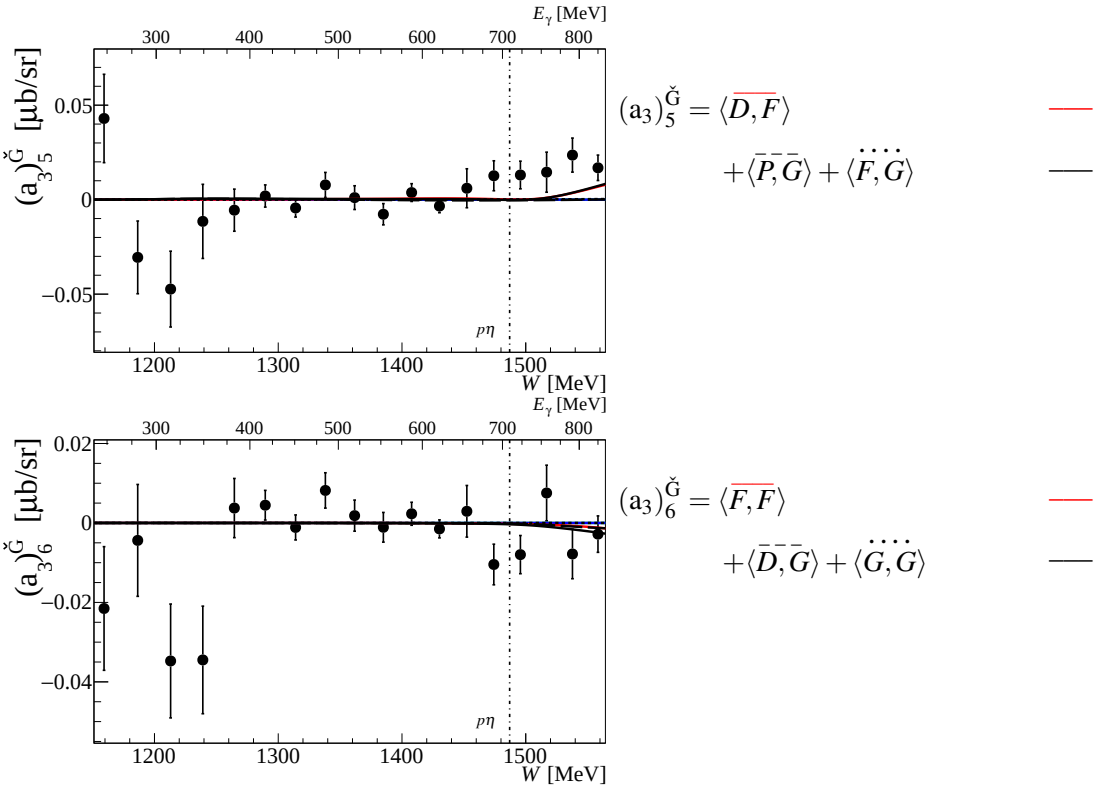

Fig. 9.12: Fit coefficients $(a_3)^{\check{G}}_{5\ldots6}$ for $\vec{\gamma}\vec{p}\to p\pi^0$ as a function of the center of mass energy W. The remaining plot which correspond to Fig. 9.11. For further information, see caption of Fig. 9.11.

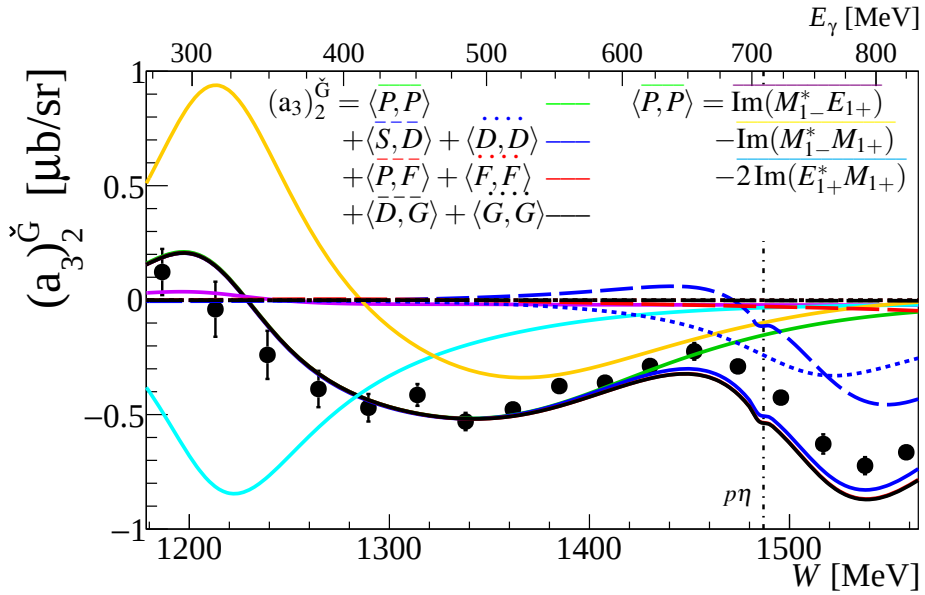

Fig. 9.13: Contributing interference terms for the $\langle \mathbf{P}, \mathbf{P}\rangle$ block in the fit coefficient $(a_3)^{\check{G}}_2$ for the $p\pi^0$ channel. The different interference terms for the $\langle P, P\rangle$ block are plot together with the extracted expansion coefficients which are indicated by the black points. The remaining curves are similar to the ones defined in Fig. 9.11.

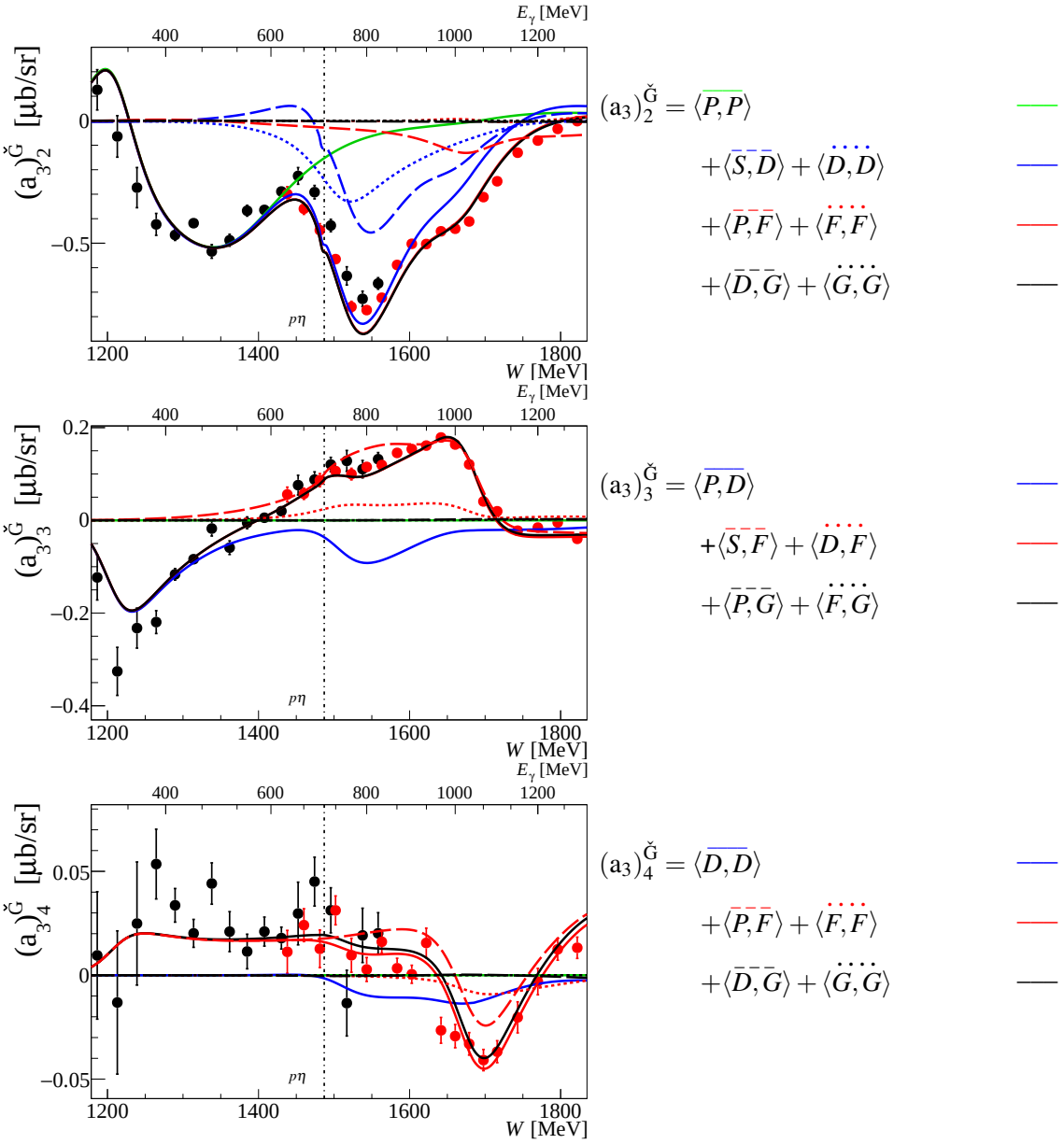

Fig. 9.14: Comparison of the fit coefficients $(a_3)^{\check{G}}_{2\cdots4}$ for $\vec{\gamma}\vec{p}\to p\pi^0$ as a function of the center of mass energy *W*. The resulting fit coefficients, indicated by the black points, are plotted on the left side together with the obtained once with the CBELSA/TAPS data in red [45, 64]. They are compared to continuous curves which have been determined from the multipole solutions of the BnGa-2016 PWA solution [46]. The solution have been truncated at different L_{max}. Hereby, the green solid curve corresponds to $L_{max} = 1$, the blue solid curve to $L_{max} = 2$, the red solid curve to $L_{max} = 3$, and the black solid curve to $L_{max} = 4$. On the right panel, the contributing partial wave interference terms are given for the different L_{max} values. Thereby, $L_{max} = 1$ only contains the contribution of *S*-and *P*-waves, $L_{max} = 2$ additionally *D*-waves, $L_{max} = 3$ additionally *F*-waves, and $L_{max} = 4$ additionally *G*-waves. The individual interference terms are included as well and are indicated by their color and dashed or dotted curves. The dashed-dotted line marks the photoproduction threshold of the $p\eta$ channel.

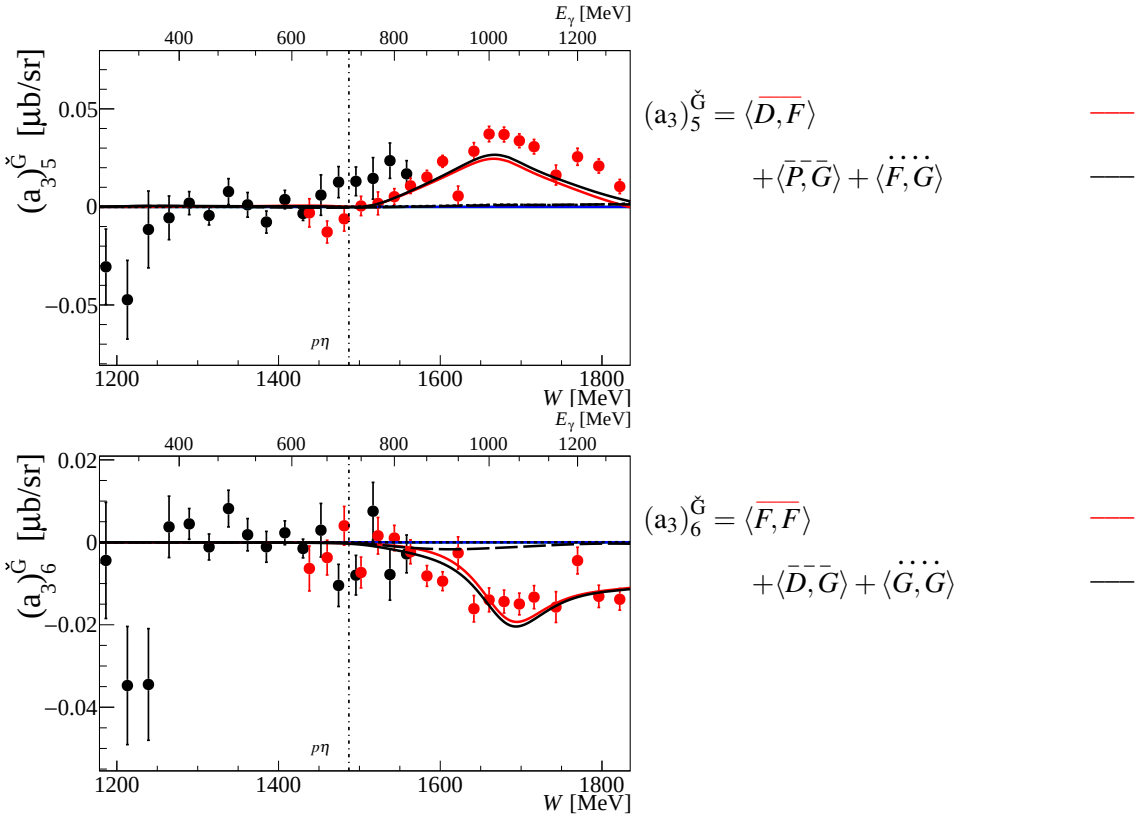

Fig. 9.15: Comparison of the fit coefficients $(a_3)^{\check{G}}_{5\ldots6}$ for $\vec{\gamma}\vec{p}\to p\pi^0$ as a function of the center of mass energy W. The remaining plot which correspond to Fig. 9.14. For further information, see caption of Fig. 9.14.

9.2.2 The reaction $\vec{\gamma}\vec{p} \to n\pi^+$

Fig. 9.16 shows six profile functions for different center of mass energies W as a function of the kinematic variable $\cos\theta_{\pi^+,\mathrm{CMS}}$ for the $n\pi^+$ channel. They have been fitted with associated Legendre polynomials up to a maximum of $\mathrm{L}_{\max} = 4$. In the top row, the corresponding χ^2/ndf distribution for the different $\mathrm{L}_{\max}$ truncation is presented.

Inspecting the χ^2/ndf distribution and the profile functions, a first conclusion is again that only S- and P-waves are not able to describe the data at all. In contrast to the $p\pi^0$ channel, the addition of D-waves in the region between roughly $W = 1260\,\mathrm{MeV}$ and $W = 1360\,\mathrm{MeV}$ is not sufficient as well. This can be seen not only in the χ^2/ndf but also in the profile function, e.g., the second profile function for $W = 1290\,\mathrm{MeV}$. Finally, the expansion coefficients demonstrate that higher orders of L contribute already at low energies. Therefore, Fig. 9.17 and Fig. 9.18 illustrate the energy-dependent real expansion coefficients truncated at $\mathrm{L}_{\max} = 3$.

Already the first coefficient $(a_3)^{\check{G}}_2$ leads to the conclusion that at least F-waves are needed to match the BnGa solutions to the extracted expansion coefficients. Whereas only S-, P- and D-waves alone overestimates the expansion coefficient, the interference of the F-waves with the D-waves and itself correct the deviation between the coefficient and the BnGa solution. This correction can mainly

be assigned to the $\langle P,F\rangle$ interference term due to the dominant $\Delta(1232)3/2^+(P_{33})$ resonance in the P-waves.

A final remarkable observation in this coefficient is the well pronounced $p\eta$-cusp which is seen close to the η photoproduction threshold (solid line) by a sudden and discontinuous change in the data but also in the BnGa solution. The cusp is most pronounced in this coefficient due to the $\langle S,D\rangle$ interference term. The $p\eta$-cusp is stronger in the $n\pi^+$ channel compared to the $p\pi^0$ channel which is in agreement with the findings in [134]. Another interference term with S-waves is given in the second coefficient $(\mathrm{a}_3)_3^{\check{\mathrm{G}}}$ by the F-waves. Although the statistics of the A2 data is quite poor to constrain the behavior of the $p\eta$- cusp in this coefficient, a sudden jump in the coefficient is present. Overall, the coefficient also confirms the necessity of F-waves but further indicates already sensitivities to G-waves. Only the inclusion of G-waves, mainly due to the $\langle P,G\rangle$ term, can describe the data. This claim is supported by the next two coefficient $(\mathrm{a}_3)_4^{\check{\mathrm{G}}}$ and $(\mathrm{a}_3)_5^{\check{\mathrm{G}}}$ which are only sensitive to interference between F-and G-waves below $W = 1400\,\mathrm{MeV}$. Combining these information with the extracted expansion coefficients, a final conclusion is that small contributions of F- and G-waves are visible at low energies. This can be assigned to the non-resonant background terms, including the pion-pole and Kroll-Ruderman term, and the interference behavior of the multipoles of the profile function of G .

To study the sensitivity to the Roper resonance in the $n\pi^+$ channel, the different contributing interference terms of the $\langle P,P\rangle$ block are plotted separately for the first coefficient in Fig. 9.19. It has been shown in Fig. 9.17 that the P-waves alone are not enough to describe the data at all which can be assigned to the strong contribution of higher waves at even lower energies. Therefore, in contrast to the $p\pi^0$ channel, the sensitivity to the Roper resonance is already not given in the $\Delta(1232)3/2^+(P_{33})$ region. Hereby, the difference between a truncation at $\mathrm{L}_{\mathrm{max}} = 1$ and $\mathrm{L}_{\mathrm{max}} = 2$ can be traced down to the dominant $\langle S,D\rangle$ term[5] whereas the difference between the truncation at $\mathrm{L}_{\mathrm{max}} = 2$ and $\mathrm{L}_{\mathrm{max}} = 3$ to the $\langle P,F\rangle$ term.

Fig. 9.20 shows six profile functions for different center of mass energies W as a function of the kinematic variable $\cos\theta_{\pi^+,\mathrm{CMS}}$ for the double polarization observable E together with the fitted associated Legendre polynomials up to a maximum of $\mathrm{L}_{\mathrm{max}} = 4$. Fig. 9.21 and Fig. 9.22 illustrates the energy-dependent real expansion coefficients truncated at $\mathrm{L}_{\mathrm{max}} = 3$.

For the double polarization observable E in the $n\pi^+$ channel, the S- and P-waves of the BnGa solution alone are not able to describe any coefficient at all. Already in the first coefficient $(\mathrm{a}_3)_0^{\check{\mathrm{E}}}$, the $\langle D,D\rangle$ term is needed to match the data with the multipole solutions. Minor corrections of F- and G-waves are seen as well. These are, however, very small as they interfere only with themselves in this coefficient. Even their inclusion shows a clear deviation to the expansion coefficient starting at about $W = 1400\,\mathrm{MeV}$. Stronger contributions of F-waves are visible in the next coefficient $(\mathrm{a}_3)_1^{\check{\mathrm{E}}}$. Here, the D-waves interfere with the F-waves which results in a significant correction between $\mathrm{L}_{\mathrm{max}} = 2$ and $\mathrm{L}_{\mathrm{max}} = 3$. The inclusion of G-waves has a minor correction due to the interference with only

[5] S-waves are given by the E_{0+} multipole. Due to the t-channel pion exchange which is forbidden in the $p\pi^0$ channel, especially the real part of the $n\pi^+$ multipole is huge compared to the one of the $n\pi^+$ channel.

F-waves. The second extracted coefficient shows an additional peak structure in the region of the $N(1440)1/2^+(P_{11})$ resonance which is not at all seen by the BnGa solution. Therefore, the coefficients are investigated in more detail. As a first step, the CLAS data were used to extract the coefficients similarly. At first sight, the inspection of Fig. 9.23 might suggest that both results do not match at all, e.g., the peak structure is not seen with the CLAS data. The discrepancy between both results, however, can be traced back to the CLAS points in the forward direction ($\cos\theta_{\pi^+,\mathrm{CMS}} > 0.7$) which have a much higher precision than the A2 data in that region. After excluding these points in the fit of the data and therefore achieving a similar angular coverage, both results show the peak structure as can be seen in Fig. 9.25. The high sensitivity to the forward points can be explained by the fact that the observable E is constrained to 1 for the extreme angles $\cos\theta_{\pi^+,\mathrm{CMS}} = \pm 1$ whereas G to 0. As a result, the profile function $\check{\mathrm{G}}$ is fixed to 0 whereas the profile function $\check{\mathrm{E}}$ is not. Thus, due to the non-existing constrains in the forward direction together with the CLAS points in the forward direction with high statistics, the huge deviation between both data set seems plausible and the peak structure could simply be an artifact due to the lack of information in the forward direction. Nevertheless, as can be seen in Fig. 9.23, the extracted coefficient with the CLAS data can not be described by the BnGa solution as well. This is especially pronounced in the region of the $N(1680)3/2^+(F_{15})$ resonance due to the interference terms $\langle D,F\rangle$ and $\langle F,G\rangle$. The coefficient $(\mathrm{a}_3)_2^{\check{\mathrm{E}}}$ illustrates again the need of D-waves at low energies. Besides that, the $\langle D,D\rangle$ term causes a peak structure with a maximum at about $W = 1480\,\mathrm{MeV}$ which is not in agreement with the A2 data. The CLAS data have this peak structure, however, the BnGa solution is not able to describe the data even with the inclusion of partial waves up to $\mathrm{L}_{\max} = 4$. Similar statement can be made for the $(\mathrm{a}_3)_3^{\check{\mathrm{E}}}$ coefficient. Although the statistics are not sufficient enough to give any strong conclusion anymore, the expansion coefficient over the whole analyzed energy region is smaller than the BnGa solution. Additionally, this is visible in the expansion coefficient extracted with the CLAS data (cf. Fig. 9.24) towards higher energies, especially again in the $N(1680)3/2^+(F_{15})$ region. For the higher coefficients, the statistic of the new A2 data is not sufficient to give any statement. Overall, a conclusion is that, although the CLAS data are included in the BnGa solutions, huge deviations between the coefficients and the BnGa solutions are still appearing. As a final test, preliminary results of the higher beam photon energies of the new A2 data are presented in App. A.10 which strengthen the expansion coefficient of the CLAS data and give also a final hint that the $n\pi^+$ final state is up to now not well understood by the PWAs.

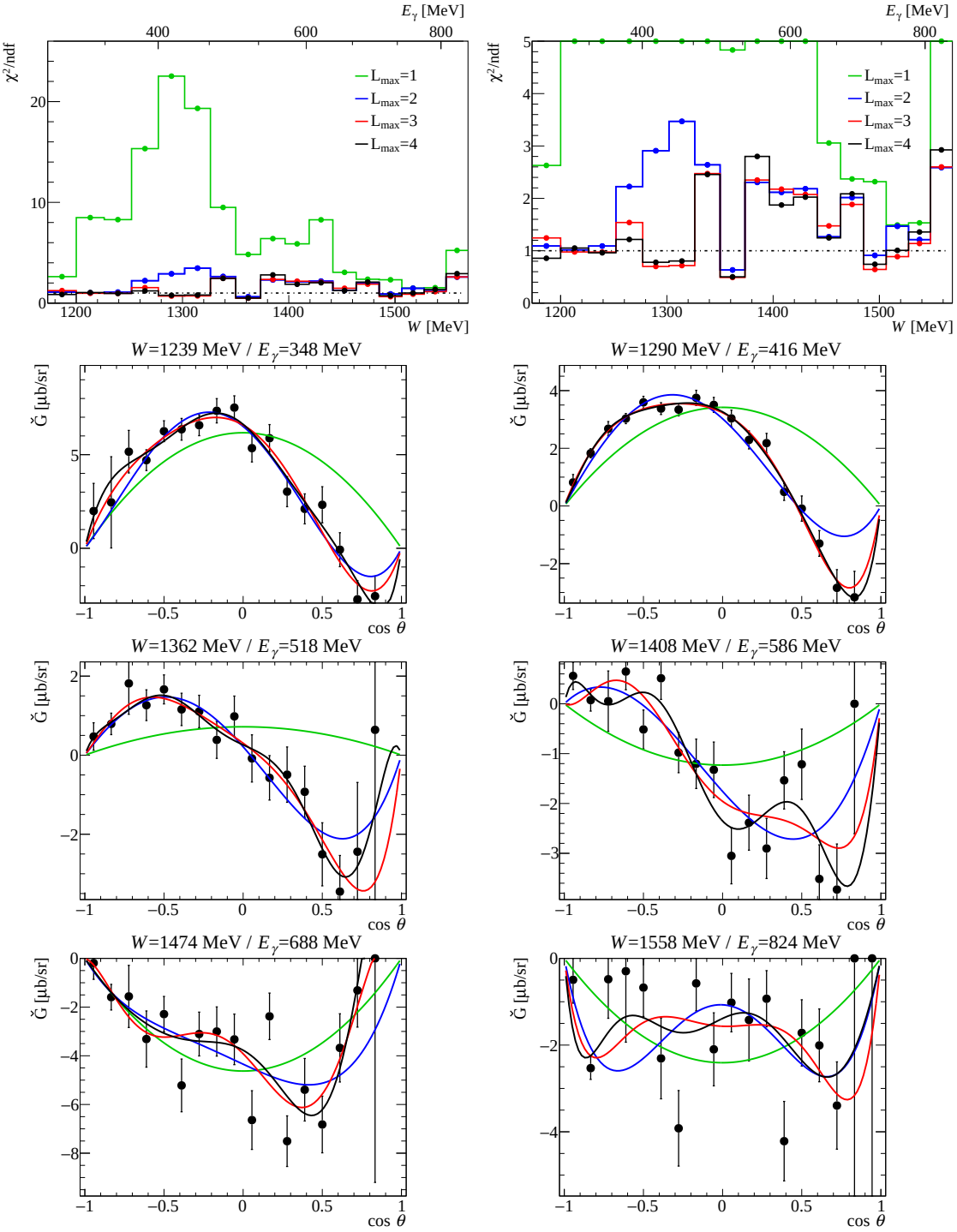

Fig. 9.16: Associated Legendre polynomial fits to the profile function $\check{G}$ for $\vec{\gamma}\vec{p}\to n\pi^+$. The profile function $\check{G}$ as a function of the kinematic variable $\cos\theta_{\pi^+,\mathrm{CMS}}$ were fitted with associated Legendre polynomials which are described by Eq. (9.2). The fits have been truncated at different L_{max}. Hereby, the green line corresponds to $L_{max}=1$, the blue line to $L_{max}=2$, the red line to $L_{max}=3$, and the black line to $L_{max}=4$. As an illustration of the fits, six profile functions (black points) are presented in the second to fourth row together with the different truncated L_{max}-fits. The corresponding χ^2/ndf of all fits is depicted in the top row as a function of the center of mass energy W and the beam photon energy E_γ.

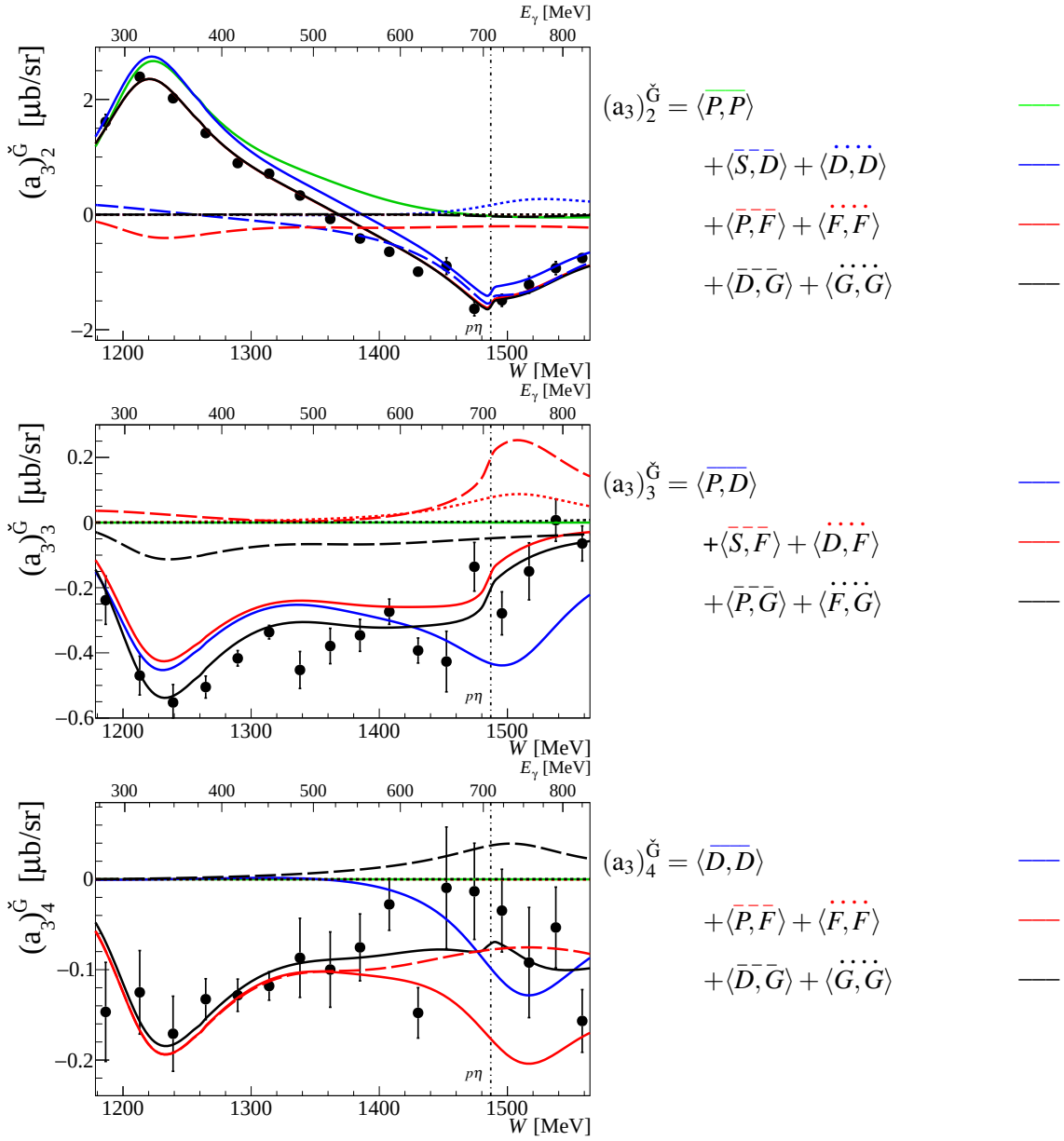

Fig. 9.17: Fit coefficients $(\mathbf{a_3})^{\check{G}}_{2\cdots4}$ for $\vec{\gamma}\vec{p}\to n\pi^+$ as a function of the center of mass energy W. The resulting fit coefficients, indicated by the black points, are plotted on the left side. They are compared to continuous curves which have been determined from the multipole solutions of the BnGa-2016 PWA solution [46]. The solution have been truncated at different L_{max}. Hereby, the green solid curve corresponds to $L_{max} = 1$, the blue solid curve to $L_{max} = 2$, the red solid curve to $L_{max} = 3$, and the black solid curve to $L_{max} = 4$. On the right panel, the contributing partial wave interference terms are given for the different L_{max} values. Thereby, $L_{max} = 1$ only contains the contribution of S-and P-waves, $L_{max} = 2$ additionally D-waves, $L_{max} = 3$ additionally F-waves, and $L_{max} = 4$ additionally G-waves. The individual interference terms are included as well and are indicated by their color and dashed or dotted curves. The dashed-dotted line marks the photoproduction threshold of the $p\eta$ channel.

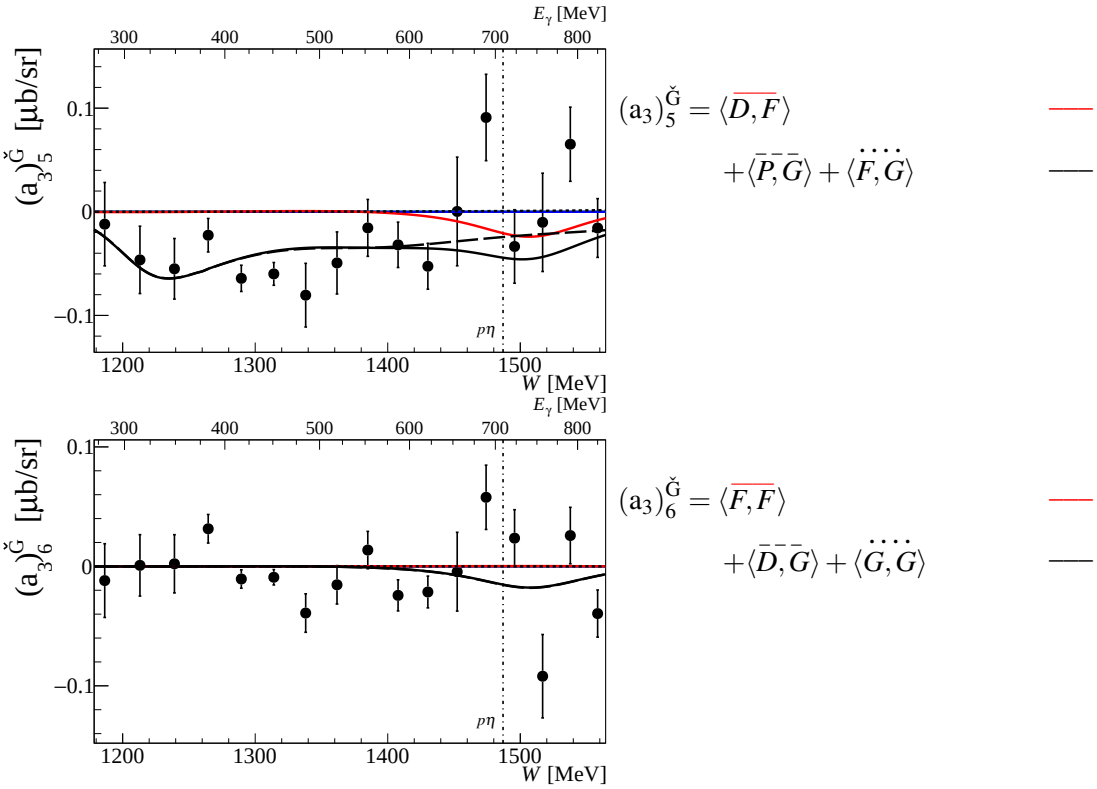

Fig. 9.18: Fit coefficients $(a_3)^{\check{G}}_{5\cdots6}$ for $\vec{\gamma}\vec{p}\to n\pi^+$ as a function of the center of mass energy W. The remaining plot which correspond to Fig. 9.17. For further information, see caption of Fig. 9.17.

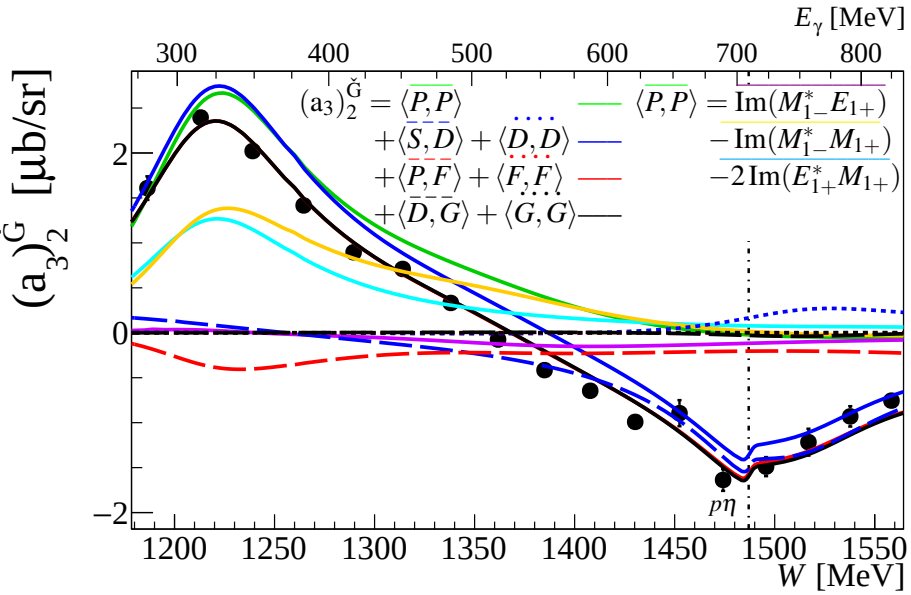

Fig. 9.19: Contributing interference terms for the $\langle \mathbf{P},\mathbf{P} \rangle$ block in the fit coefficient $(a_3)^{\check{G}}_2$ for the $n\pi^+$ channel. The different interference terms for the $\langle P,P \rangle$ block are plot together with the extracted expansion coefficients which are indicated by the black points. The remaining curves are similar to the once defined in Fig. 9.17.

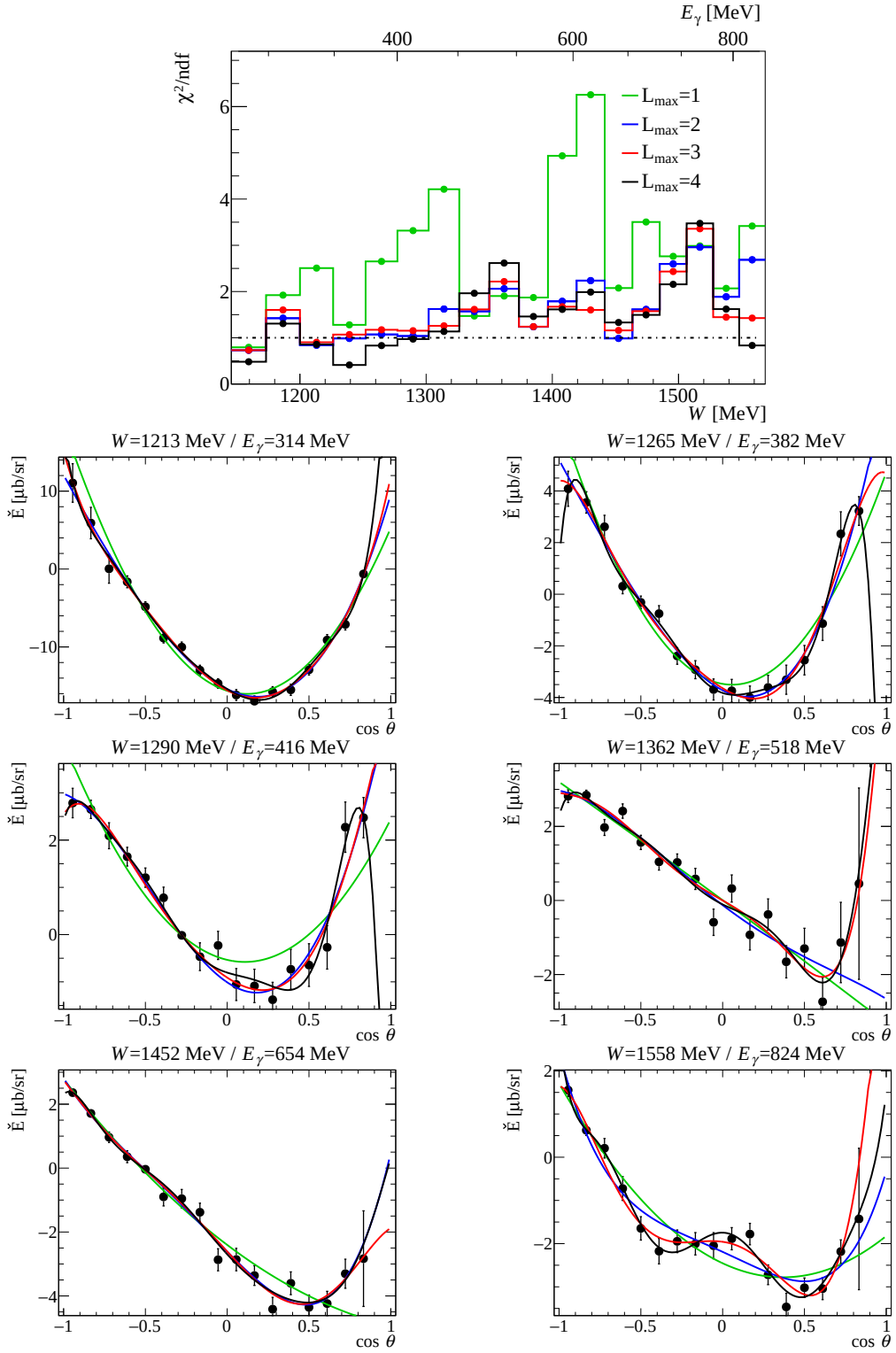

Fig. 9.20: Associated Legendre polynomial fits to the profile function Ě for $\vec{\gamma}\vec{p}\to n\pi^+$. The profile function Ě as a function of the kinematic variable $\cos\theta_{\pi^+,\mathrm{CMS}}$ were fitted with associated Legendre polynomials which are described by Eq. (9.2). The fits have been truncated at different L_{max}. Hereby, the green line corresponds to $L_{max} = 1$, the blue line to $L_{max} = 2$, the red line to $L_{max} = 3$, and the black line to $L_{max} = 4$. As an illustration of the fits, six profile functions (black points) are presented in the second to fourth row together with the different truncated L_{max}-fits. The corresponding χ^2/ndf of all fits is depicted in the top row as a function of the center of mass energy W and the beam photon energy E_γ.

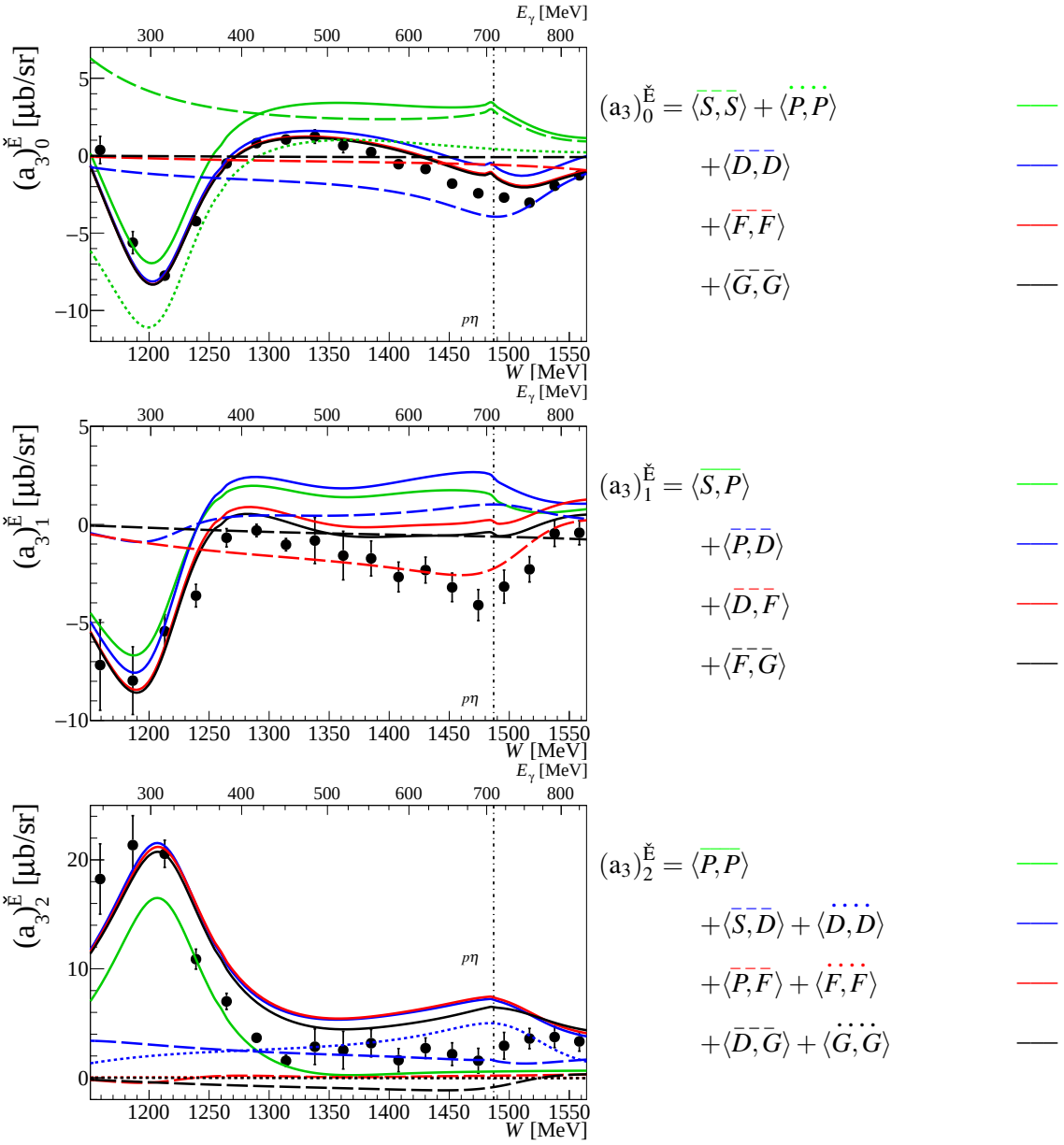

Fig. 9.21: Fit coefficients $(a_3)^{\check{E}}_{0\cdots2}$ for $\vec{\gamma}\vec{p}\to n\pi^+$ as a function of the center of mass energy W. The resulting fit coefficients, indicated by the black points, are plotted on the left side. They are compared to continuous curves which have been determined from the multipole solutions of the BnGa-2016 PWA solution [46]. The solution have been truncated at different L_{max}. Hereby, the green solid curve corresponds to $L_{max} = 1$, the blue solid curve to $L_{max} = 2$, the red solid curve to $L_{max} = 3$, and the black solid curve to $L_{max} = 4$. On the right panel, the contributing partial wave interference terms are given for the different L_{max} values. Thereby, $L_{max} = 1$ only contains the contribution of S-and P-waves, $L_{max} = 2$ additionally D-waves, $L_{max} = 3$ additionally F-waves, and $L_{max} = 4$ additionally G-waves. The individual interference terms are included as well and are indicated by their color and dashed or dotted curves. The dashed-dotted line marks the photoproduction threshold of the $p\eta$ channel.

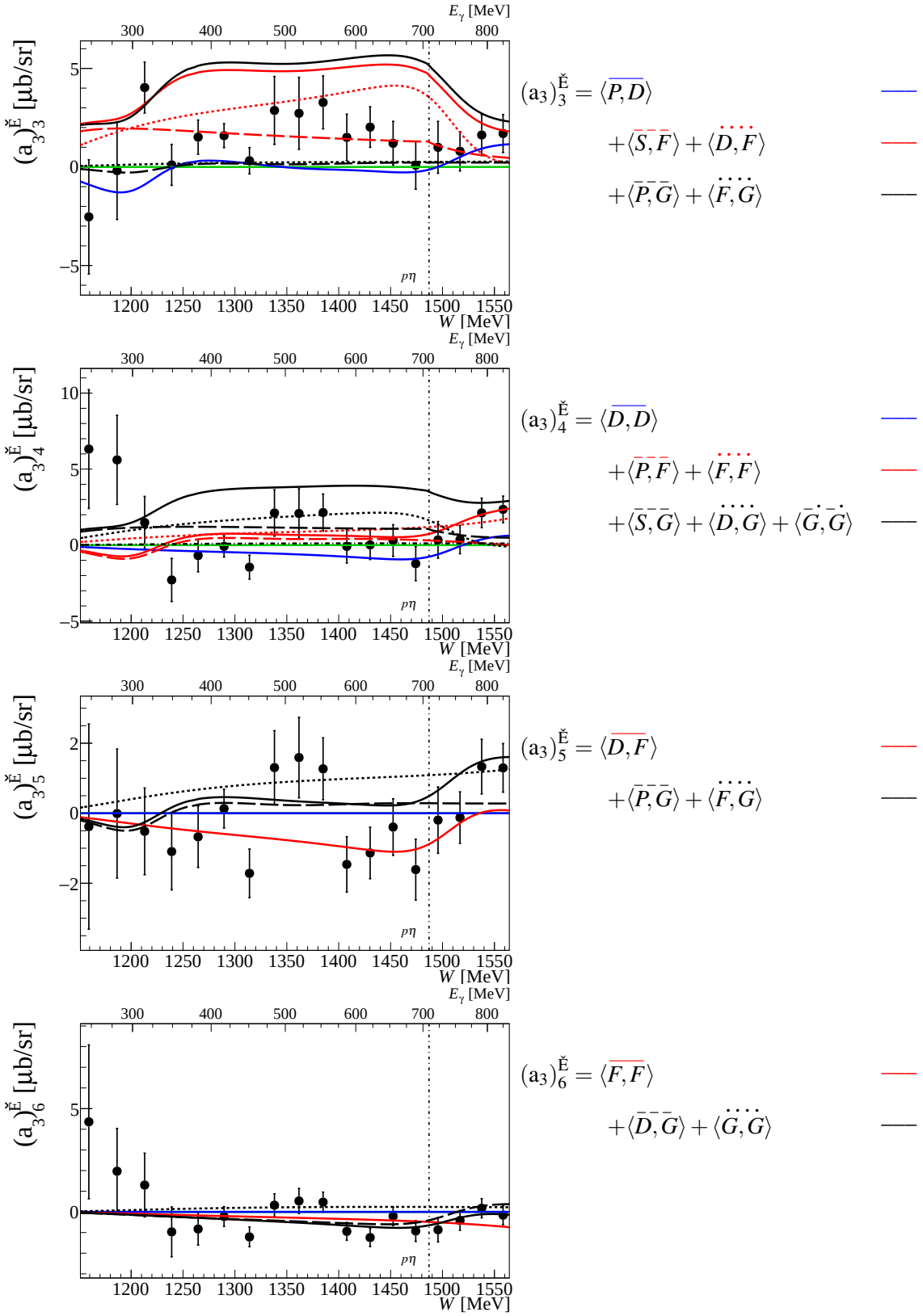

Fig. 9.22: Fit coefficients $(a_3)^{\check{E}}_{3...6}$ for $\vec{\gamma}\vec{p}\to n\pi^+$ as a function of the center of mass energy W. The remaining plots which correspond to Fig. 9.21. For further information, see caption of Fig. 9.21.

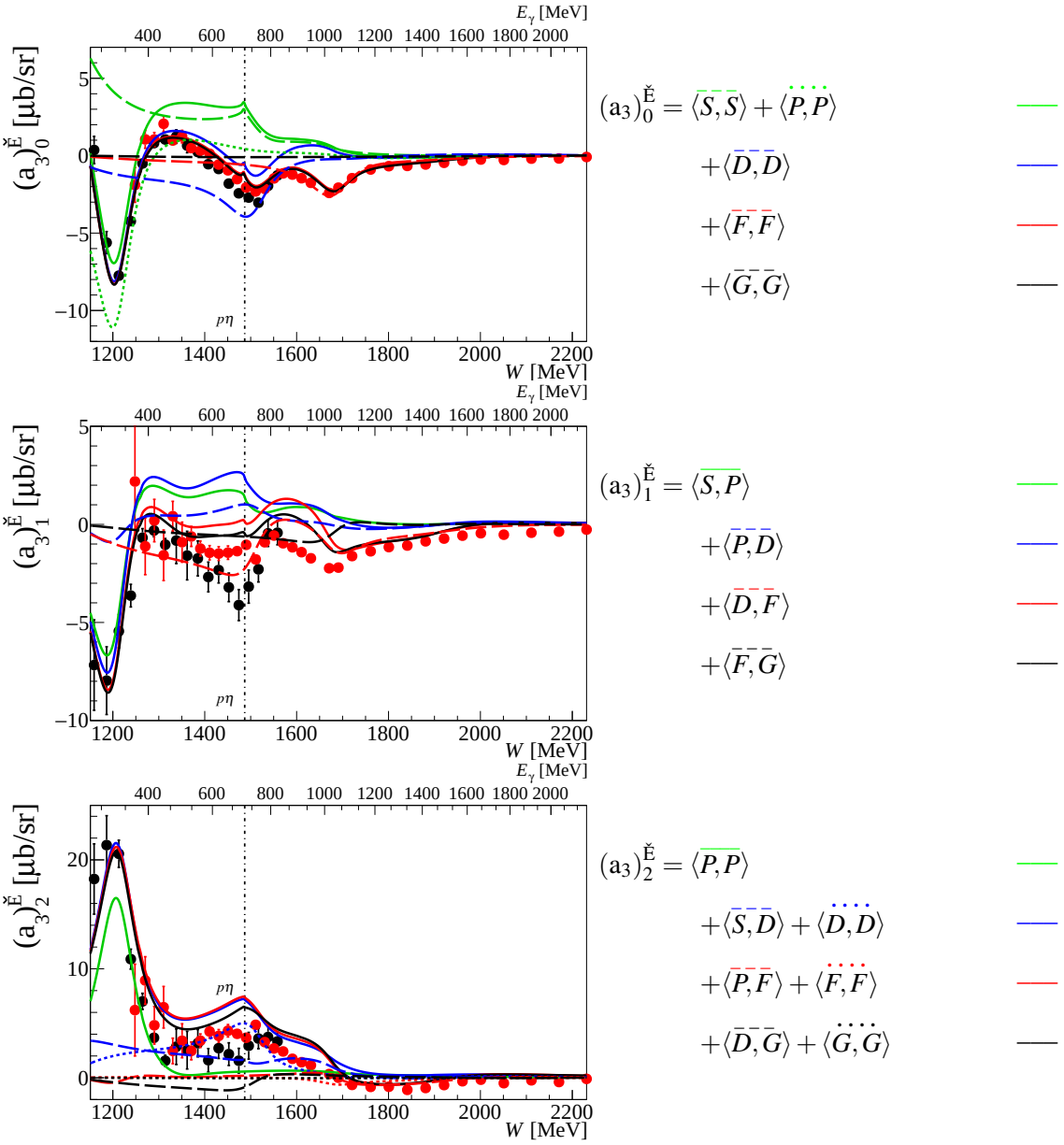

Fig. 9.23: Comparison of the fit coefficients $(a_3)^{\check{E}}_{0\cdots2}$ for $\vec{\gamma}\vec{p}\to n\pi^+$ as a function of the center of mass energy W. The resulting fit coefficients, indicated by the black points, are plotted on the left side together with the obtained once using the CLAS data in red [68]. They are compared to continuous curves which have been determined from the multipole solutions of the BnGa-2016 PWA solution [46]. The solution have been truncated at different L_{max}. Hereby, the green solid curve corresponds to $L_{max} = 1$, the blue solid curve to $L_{max} = 2$, the red solid curve to $L_{max} = 3$, and the black solid curve to $L_{max} = 4$. On the right panel, the contributing partial wave interference terms are given for the different L_{max} values. Thereby, $L_{max} = 1$ only contains the contribution of S-and P-waves, $L_{max} = 2$ additionally D-waves, $L_{max} = 3$ additionally F-waves, and $L_{max} = 4$ additionally G-waves. The individual interference terms are included as well and are indicated by their color and dashed or dotted curves. The dashed-dotted line marks the photoproduction threshold of the $p\eta$ channel.

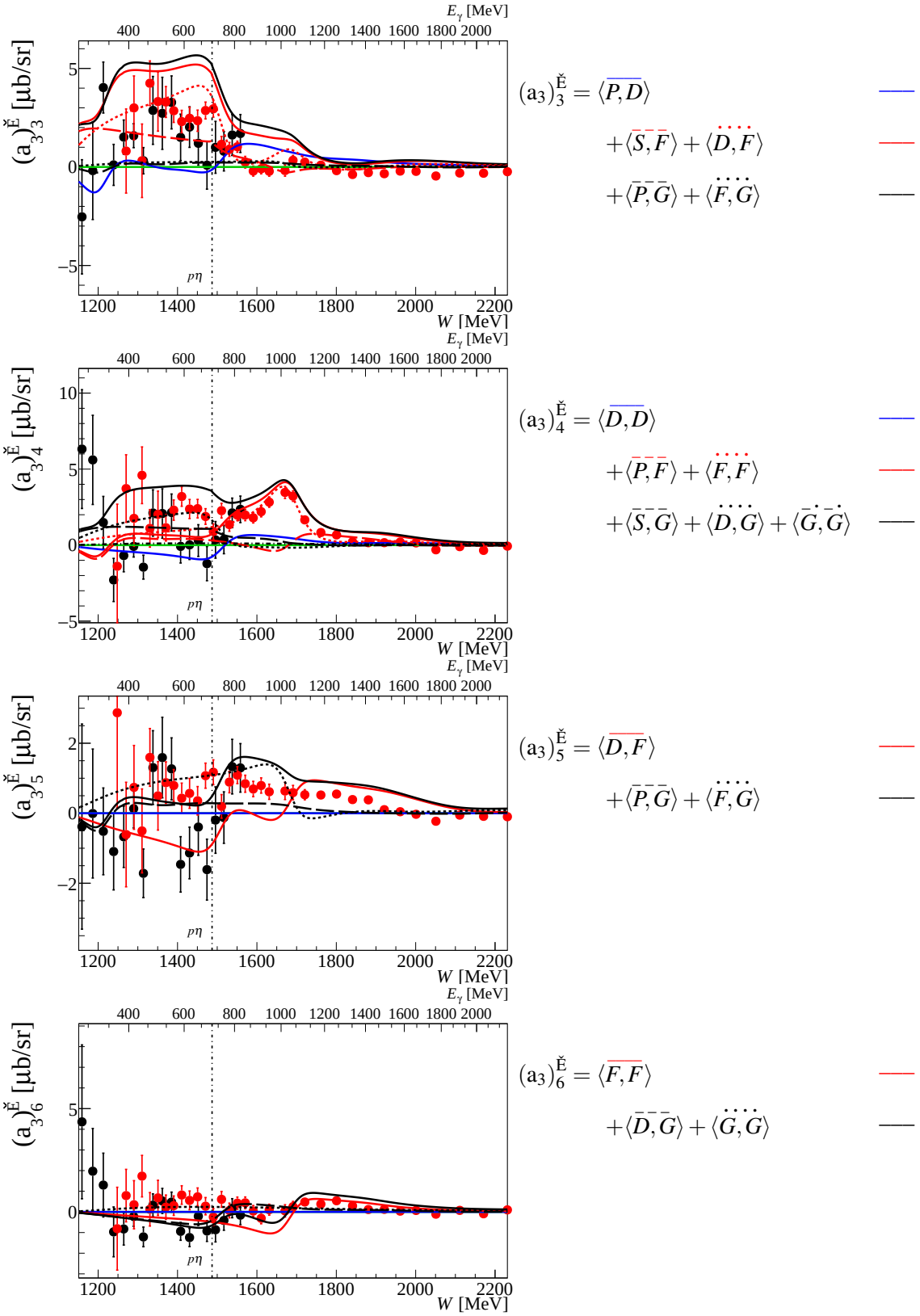

Fig. 9.24: Comparison of the fit coefficients $(a_3)^{\check{E}}_{3\ldots6}$ for $\vec{\gamma}\vec{p}\to n\pi^+$ as a function of the center of mass energy W. The remaining plots which correspond to Fig. 9.23. For further information, see caption of Fig. 9.23.

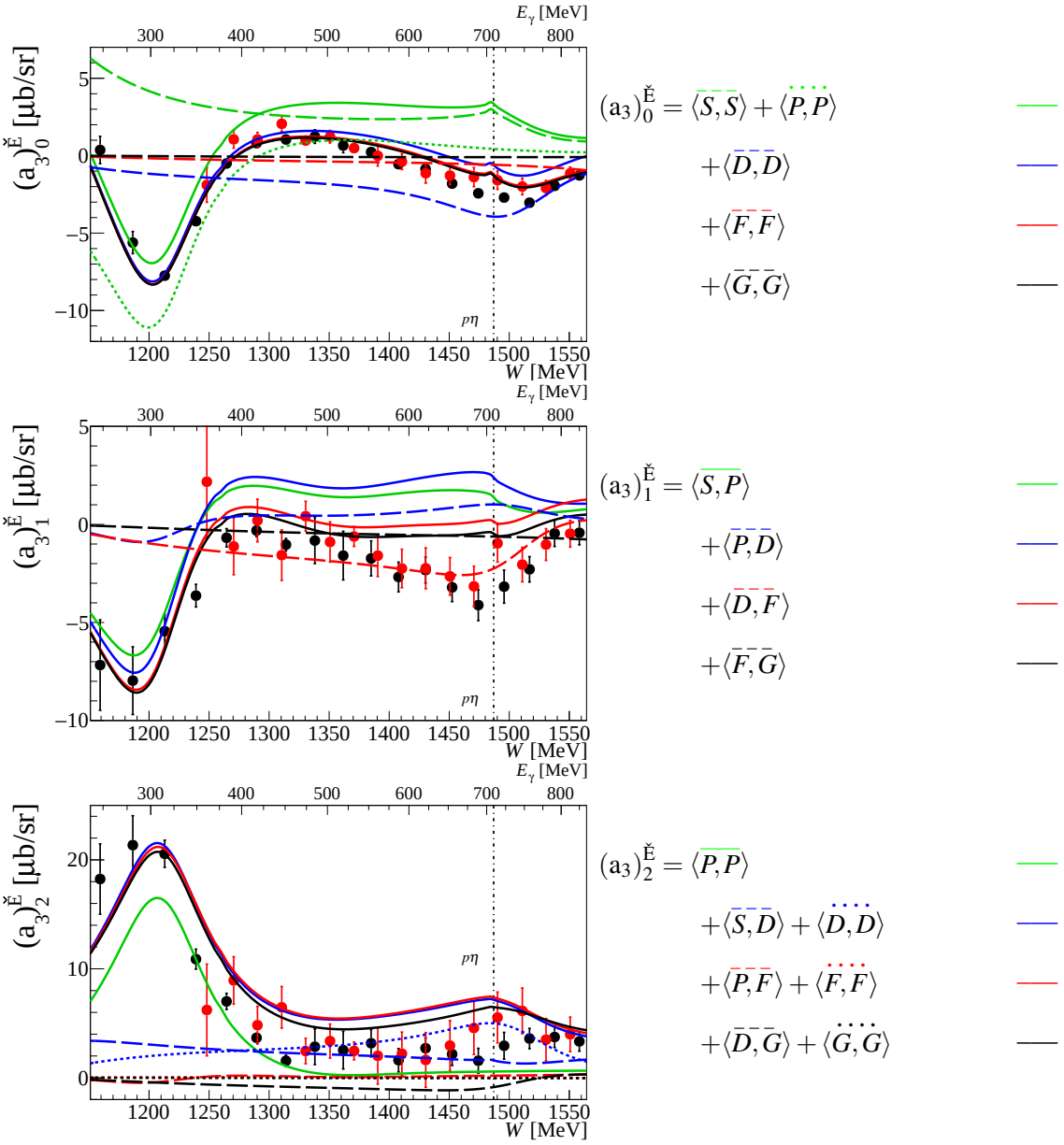

Fig. 9.25: Comparison of the matched fit coefficients $(a_3)_{0\cdots2}^{\check{E}}$ for $\vec{\gamma}\vec{p}\to n\pi^+$ as a function of the center of mass energy W. The resulting fit coefficients, indicated by the black points, are plotted on the left side together with the once with the matched CLAS data in red [68]. Hereby, matched means that all points above $\cos\theta_{\pi^+,\mathrm{CMS}} > 0.7$ are rejected from the fitting. By that, both experiment have the same acceptance in forward direction. The results are again compared to continuous curves which have been determined from the multipole solutions of the BnGa-2016 PWA solution [46]. The solution have been truncated at different L_{max}. Hereby, the green solid curve corresponds to $L_{max} = 1$, the blue solid curve to $L_{max} = 2$, the red solid curve to $L_{max} = 3$, and the black solid curve to $L_{max} = 4$. On the right panel, the contributing partial wave interference terms are given for the different L_{max} values. Thereby, $L_{max} = 1$ only contains the contribution of S-and P-waves, $L_{max} = 2$ additionally D-waves, $L_{max} = 3$ additionally F-waves, and $L_{max} = 4$ additionally G-waves. The individual interference terms are included as well and are indicated by their color and dashed or dotted curves. The dashed-dotted line marks the photoproduction threshold of the $p\eta$ channel.

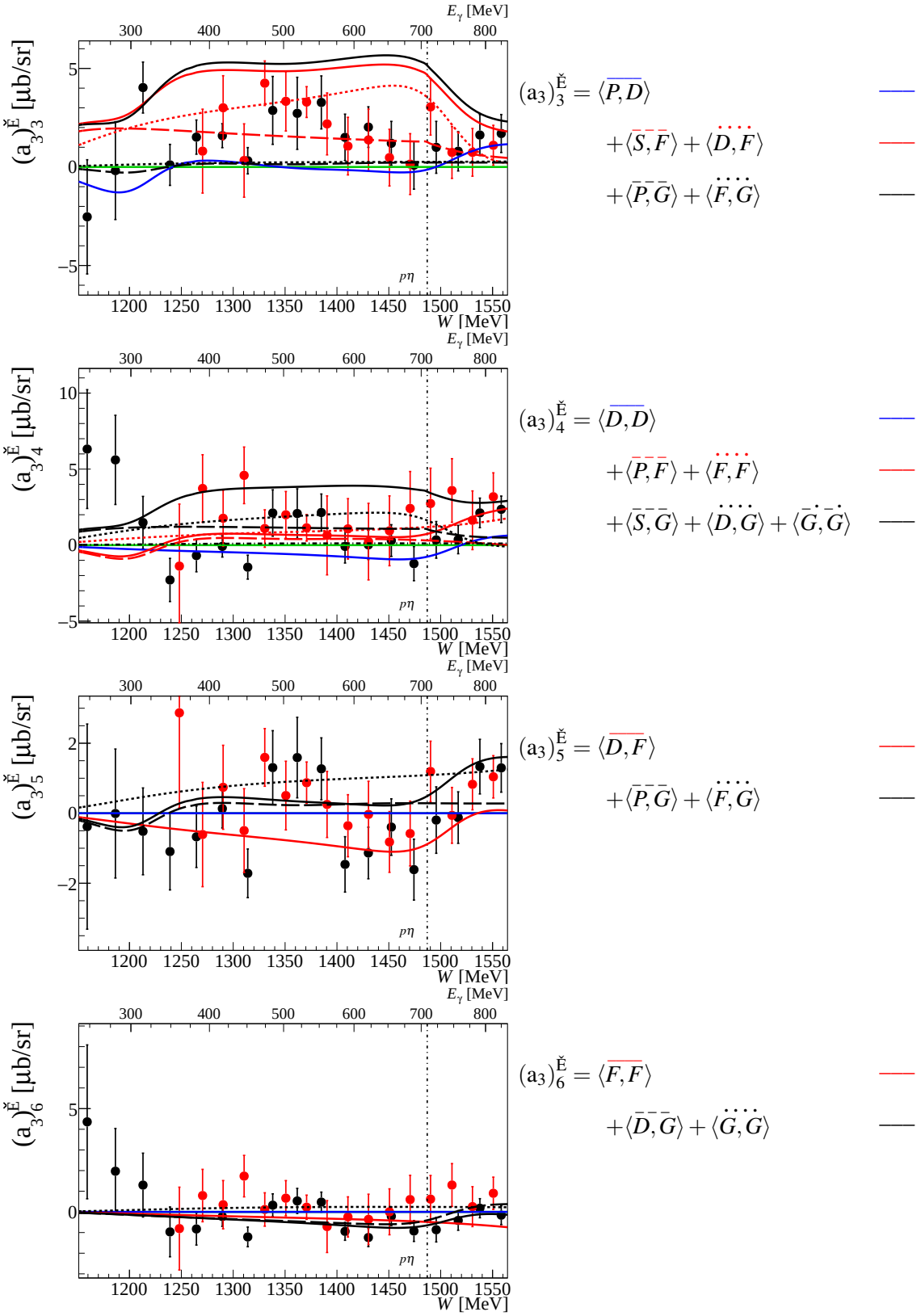

Fig. 9.26: Comparison of the matched fit coefficients $(a_3)^{\check{E}}_{3\ldots6}$ for $\vec{\gamma}\vec{p}\to n\pi^+$ as a function of the center of mass energy W. The remaining plots which correspond to Fig. 9.25. For further information, see caption of Fig. 9.25.

9.3 Comparison with Partial Wave Analysis (PWA) models

The results of the polarization observables are compared to four different PWA models, namely the BnGa, MAID, SAID, and JüBo models. For the comparison with PWAs, it is first important to know that a distinction between a prediction and a solution of the PWA model needs to be respected. A solution already fitted an existing data set in their PWA, whereas a prediction does not. Therefore, if available, the results are compared once with a prediction and once with a solution. The BnGa-2011-02 [72], JüBo-2013-01 [135], MAID-2007 [49] and SAID-CM12 [30] are all predictions for the double polarization observable G and E as they do not include the published CBELSA/TAPS and CLAS data. The latest solution of the BnGa-2016 [46] and JüBo-2017 [50] already fitted their PWAs to the G and E data of the CBELSA/TAPS and CLAS data besides other new data. For the observable E in the $n\pi^+$ channel, the CLAS data cover the same energy region as the new A2 data and thus BnGa-2016 and JüBo-2017 are PWA solutions. With only 23 points in the analyzed region of the new A2 data, the PWAs for the observable G in the $n\pi^+$ channel can be assumed to be a prediction. For the observable G in the $p\pi^0$ channel, the PWAs BnGa-2016 and JüBo-2017 are only solutions for $E_\gamma \geq 600\,\text{MeV}$.

9.3.1 Double Polarization Observable G for the reaction $\vec{\gamma}\vec{p} \to p\pi^0$

Fig. 9.27 and Fig. 9.28 show the comparison of the results, indicated by the black points, with the PWA predictions and solutions which have been mentioned in the introduction of this chapter.
In the first resonance region ($E_\gamma < 500\,\text{MeV}$), the absolute value of the double polarization observable G is quite small. However, the high precision of the new A2 data allows to discuss even small differences between the PWAs, especially in the number of zero-crossings.
In backward direction ($\cos\theta_{\pi^0,\text{CMS}} \leq -0.5$), the MAID-2007 PWA has always a positive sign and a zero-crossing afterwards towards negative values. Similar behavior is seen for the new BnGa-2016 PWA and the JüBo-2017 PWAs. The old JüBo-2013-01 PWA still shows a zero-crossing in backward-direction up to an energy of about 468 MeV whereas the old BnGa-2011-02 and the SAID-CM12 solution do not see any zero-crossings at all. In the first resonance region, a comparison with the data in this kinematic region clearly show that the solutions with a zero-crossing from positive to negative values are favored.
In forward direction ($\cos\theta_{\pi^0,\text{CMS}} \geq 0.7$), the SAID-CM12 and the old JüBo-2013-01 solution undergo another zero-crossing from negative values to positive values, whereas the MAID-2007 and both BnGa PWAs stay negative. The JüBo-2017 undergoes a zero-crossing in the forward direction up to an energy of 468 MeV and stays negative over the remaining energy region. A clear statement using the comparison with the data is not possible, as the forward direction is dominated by the 2 PED events and thus are affected by huge systematic uncertainties. Nevertheless, the inspection over the whole energy region below $E_\gamma < 500\,\text{MeV}$ can lead to a careful conclusion that the data more likely favor the solutions which do not undergo an additional zero-crossing in the forward direction.
Finally, the zero-crossings of G confirm the results of the L_{max}-fit procedure which concluded that

P-waves alone are not able to describe the data and that interference with D-waves and even higher waves are seen, e.g., with $N(1520)3/2^-(D_{13})$. The contribution of D-waves at low energies has been found in the expansion coefficient $(a_3)_3^{\check{G}}$ in the $\langle P,D\rangle$ interference term. This coefficient- and interference term are responsible for the zero-crossing from positive to negative values in the backward direction for the BnGa solution. Above 600 MeV the same coefficient is dominated with an opposite sign by the $\langle S,F\rangle$ term which corresponds to a zero-crossing in forward-direction. To achieve two zero-crossings, a relative high value for the higher expansion coefficients $(a_3)_{4\cdot6}^{\check{G}}$ compared to the lower ones is mandatory. These expansion coefficients are however close to zero and the same holds for the BnGa-2016 multipoles. Therefore, the BnGa solutions only undergo one zero-crossing.
In Fig. 9.29 and Fig. 9.30 the results are represented as a function of the mean value of the beam photon energy window E_γ for different $\cos\theta_{\pi^0,\mathrm{CMS}}$ bins. As the other representation of the results already showed, the biggest deviation between the data and the different PWAs is seen in the forward direction. One example is the 14th bin ($0.44 \leq \cos\theta_{\pi^0,\mathrm{CMS}} < 0.56$) where the new A2 data show a change in the sign which can not be described by either the BnGa and MAID PWA[6]. On the other hand, the old JüBo-2013-01 and the SAID-CM12 PWA undergo the zero-crossing but can not describe the data.
In the region of the $p\eta$ photoproduction threshold of about 708 MeV, the different PWA solutions, except for the MAID-2007 and the JüBo-2013-01 PWAs, show a hint of the $p\eta$-cusp. However, the statistics of the new A2 data is not precise enough to verify the cusp effect in this representation.

[6] As a reminder: In Sec. 9.1.1 it was shown that the new A2 data and the previous CBELSA/TAPS data disagree. Whereas the A2 data show a zero-crossing, the CBELSA/TAPS data do not.

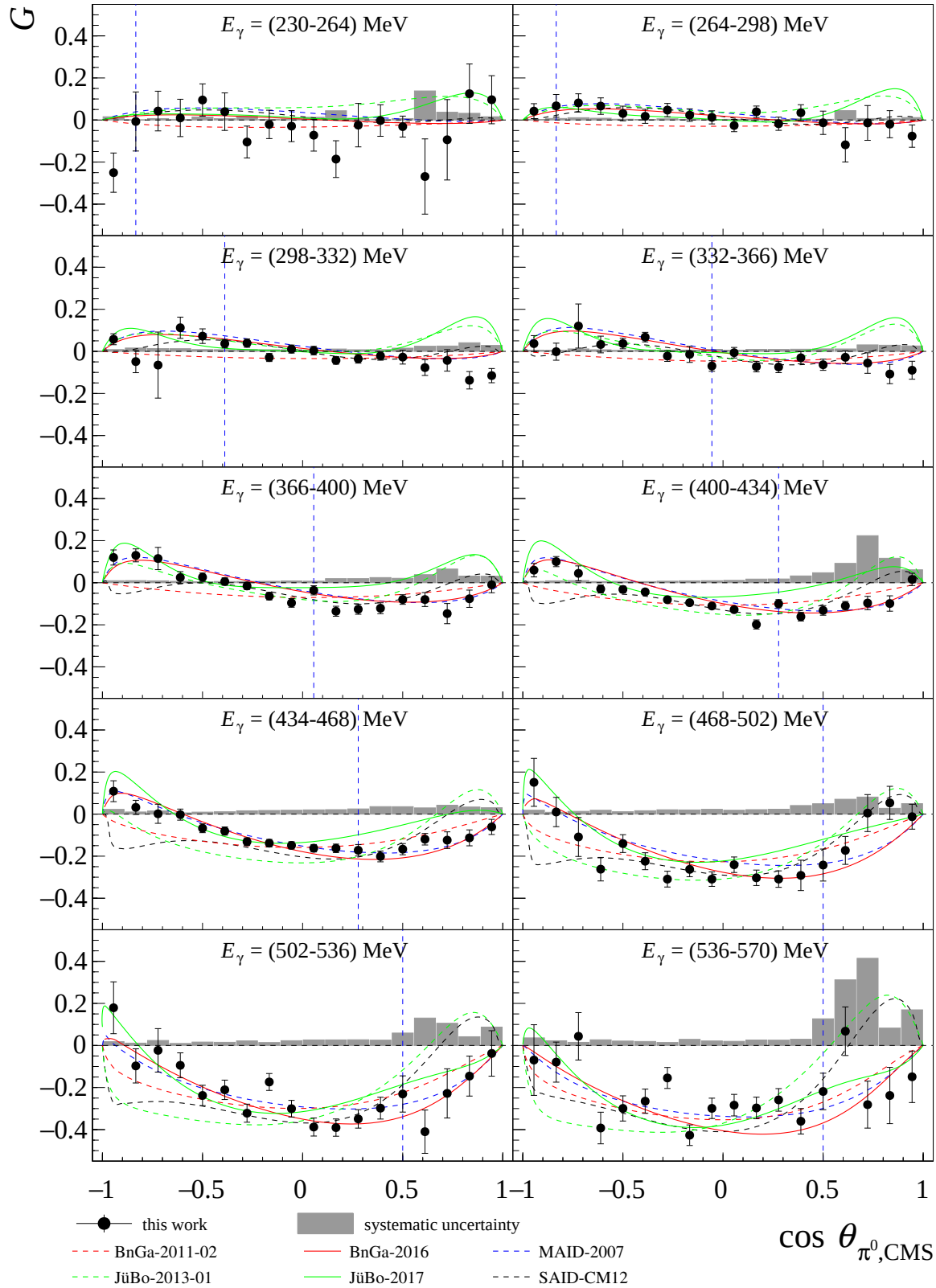

Fig. 9.27: Comparison of the results for the double polarization observable G with PWAs for $\vec{\gamma}\vec{p}\to p\pi^0$. The results of the double polarization observable G are shown as a function of $\cos\theta_{\pi^0,\mathrm{CMS}}$ for the beam photon energy from 230 MeV to 570 MeV. The black points represent the results of the new A2 data together with their statistical uncertainties. The blue dashed line indicates the position where the 2 PED events are added to the 3 PED events. The results are compared to the following PWAs: BnGa-2011-02 (red dashed line) [72], BnGa-2016 (red line) [46], MAID-2007 (blue dashed line) [49], JüBo-2013-01 (green dashed line) [135], JüBo-2017 (green line) [50] and SAID-CM12 (black dashed line) [30].

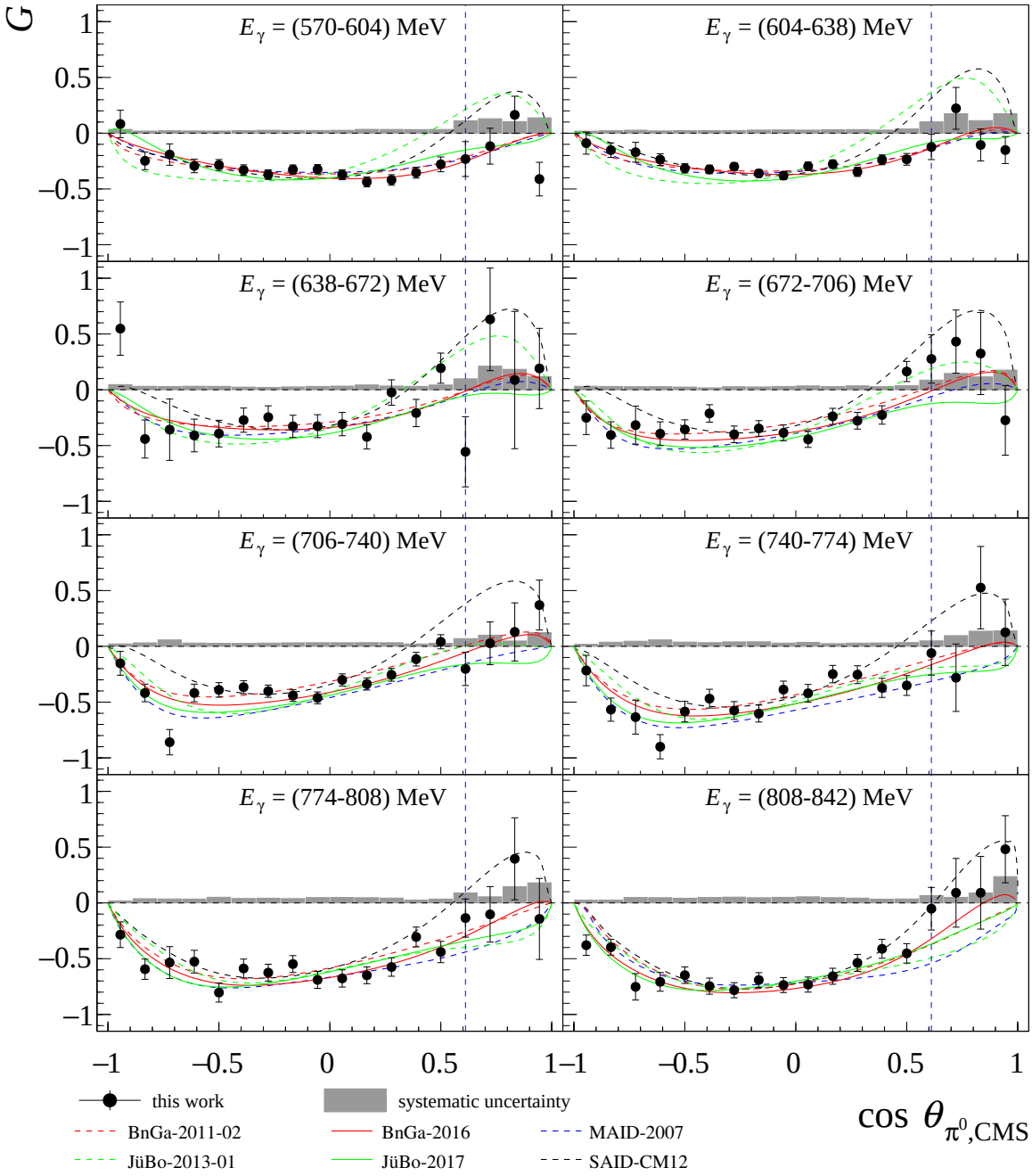

Fig. 9.28: Comparison of the results for the double polarization observable G with PWAs for $\vec{\gamma}\vec{p}\to p\pi^0$. The results of the double polarization observable G are shown as a function of $\cos\theta_{\pi^0,\mathrm{CMS}}$ for the beam photon energy from 570 MeV to 842 MeV. The black points represent the results of the new A2 data together with their statistical uncertainties. The blue dashed line indicates the position where the 2 PED events are added to the 3 PED events. The results are compared to the following PWAs: BnGa-2011-02 (red dashed line) [72], BnGa-2016 (red line) [46], MAID-2007 (blue dashed line) [49], JüBo-2013-01 (green dashed line) [135], JüBo-2017 (green line) [50] and SAID-CM12 (black dashed line) [30].

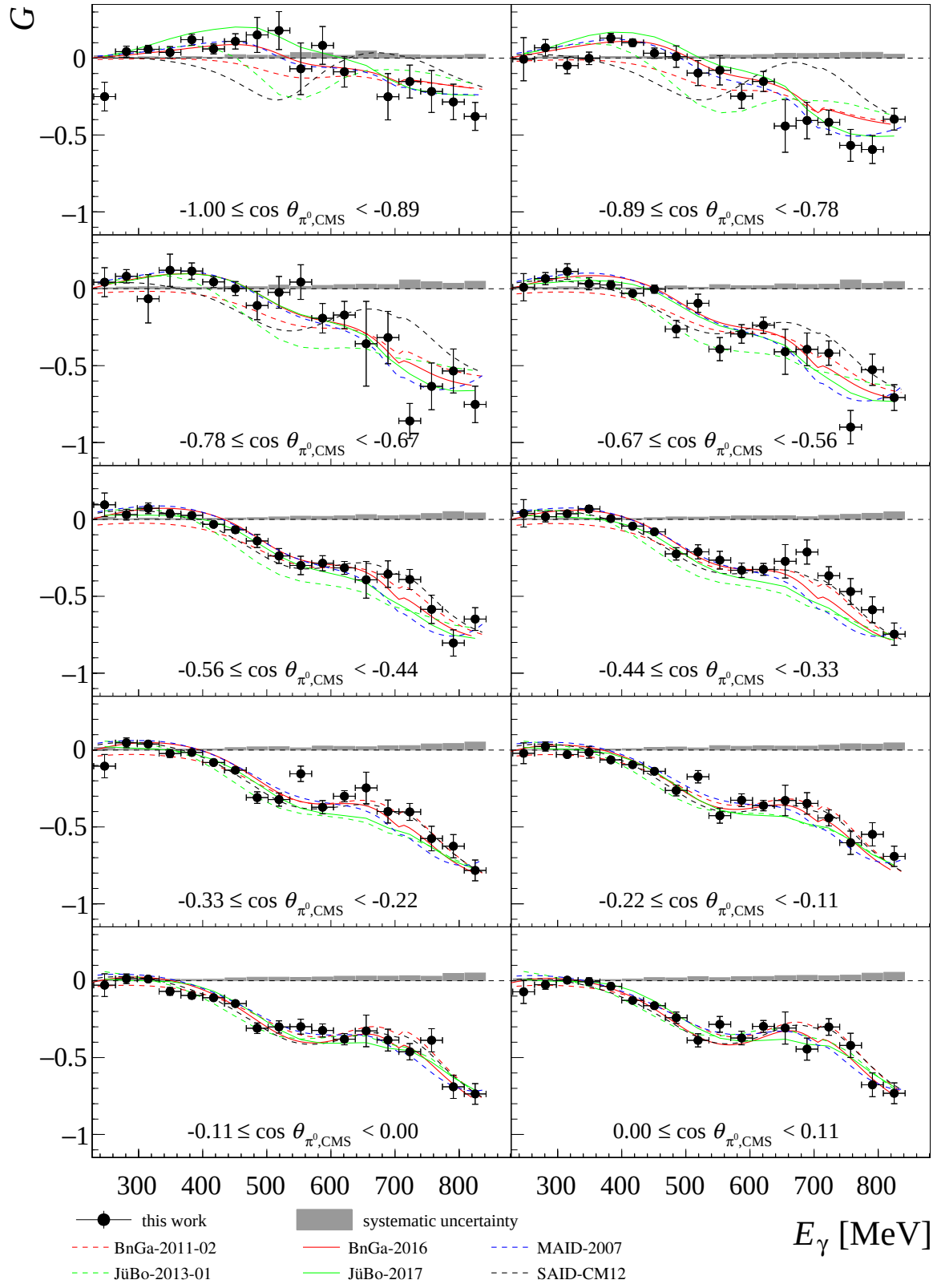

Fig. 9.29: Comparison of the results for the double polarization observable G with PWAs for $\vec{\gamma}\vec{p}\to p\pi^0$ as a function of the beam photon energy E_γ. The results of the double polarization observable G are shown as a function of the mean value of the beam photon energy bin E_γ for the kinematic range $-1.00 \leq \cos\theta_{\pi^0,\mathrm{CMS}} < 0.11$. The black points represent the results of the new A2 data together with their statistical uncertainties while the gray boxes shows the systematic uncertainties. The results are compared to the following PWAs: BnGa-2011-02 (red dashed line) [72], BnGa-2016 (red line) [46], MAID-2007 (blue dashed line) [49], JüBo-2013-01 (green dashed line) [135], JüBo-2017 (green line) [50] and SAID-CM12 (black dashed line) [30].

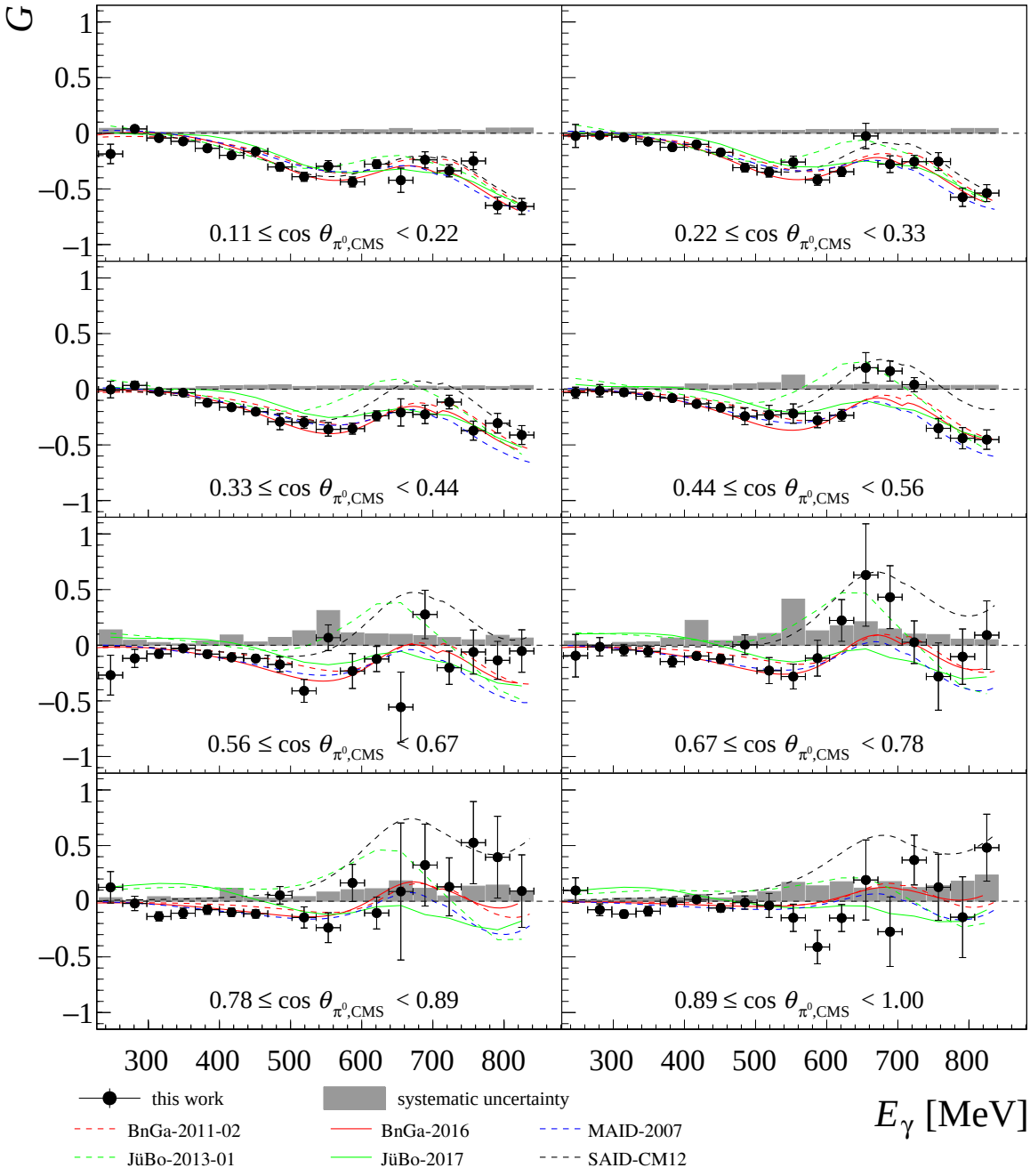

Fig. 9.30: Comparison of the results for the double polarization observable G with PWAs for $\vec{\gamma}\vec{p}\to p\pi^0$ as a function of the beam photon energy E_γ. The results of the double polarization observable G are shown as a function of the mean value of the beam photon energy bin E_γ for the kinematic range $0.11 \leq \cos\theta_{\pi^0,\mathrm{CMS}} < 1.00$. The black points represent the results of the new A2 data together with their statistical uncertainties while the gray boxes shows the systematic uncertainties. The results are compared to the following PWAs: BnGa-2011-02 (red dashed line) [72], BnGa-2016 (red line) [46], MAID-2007 (blue dashed line) [49], JüBo-2013-01 (green dashed line) [135], JüBo-2017 (green line) [50] and SAID-CM12 (black dashed line) [30]. Note the different y-axis range compared to Fig. 9.30.

To show the importance and the impact of the polarization observable overall, the multipole amplitudes of the BnGa, JüBo and SAID solutions were extracted and compared before and after the inclusion of new data for the single and double polarization observables E, G, H, T and P in the $p\pi^0$ channel[7] [39]. A comparison of the solutions is performed by plotting the combined variance of all three PWA multipole amplitudes up to $L = 4$ which is shown in Fig. 9.31. Hereby, the variance between two models is defined as:

$$\mathrm{var}(1,2) = \frac{1}{2}\sum_{i=1}^{16} \left(\mathscr{M}_1(i) - \mathscr{M}_2(i)\right)\left(\mathscr{M}_1^*(i) - \mathscr{M}_2^*(i)\right), \tag{9.4}$$

with $\mathscr{M}_1(i)$ and $\mathscr{M}_2(i)$ being the multipoles for the two compared PWA models 1 and 2.

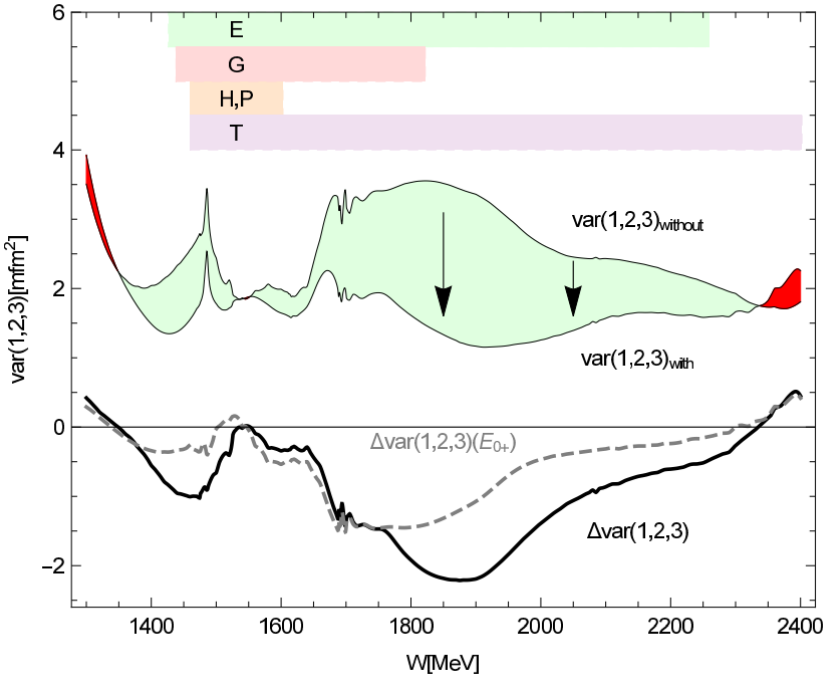

Fig. 9.31: The combined variance of the BnGa, JüBo and SAID PWA solutions. The combined variance of the BnGa, SAID and JuBo PWA solutions is presented for the multipole amplitudes up to L=4 for the $p\pi^0$ channel. The variances are once shown for the case without the new polarization observables and once with. The improvement is indicated by the green shaded area and by the black line as well. The contributon of the E_{0+} multipole to the improvement is displayed separately by the gray dashes line. Finally, the covered energy ranges of the polarization observables are shown at the top (figure taken from [39]).

It is clearly visible that the inclusion of the new polarization observable data (see colored bars in the top) significantly improves the differences between the PWAs and lead to a further convergence in the covered energy range. The author quote that especially the E_{0+} multipole helped to improve

[7] Note that the SAID-CM12 solution which has been used in this thesis, does not include the new data. Only JüBo-2017 and BnGa-2016 include these data.

the convergence of the different solutions. Its contribution is included as well in Fig. 9.31. Overall, large variances are still visible for the energy range below $W = 1500\,\text{MeV}$ where no new data were included. Note that the plot is only starting at $W = 1300\,\text{MeV}$. Thereby, the new A2 data for the double polarization observable G and the double polarization observable E [14] might help to further constrain the different PWAs even below $W = 1300\,\text{MeV}$. The author of the paper quote significant discrepancies, in particular in the low-mass region for the E_{0+} multipole [39]. Here, the background contribution show a much stronger contribution than the resonant contribution. The expansion coefficient $(\mathrm{a}_3)_1^{\check{\mathrm{E}}}$, which has been determined with the double polarization observable E using the new A2 data, is sensitive to an interference of S- and P-waves at low energies. It has been found that further improvements are needed in this interference [14], at least for the BnGa-2014 solution [39]. As the expansion coefficient $(\mathrm{a}_3)_2^{\check{\mathrm{G}}}$ within this analysis showed no significant necessity of an improvement of the P-waves at low energies, this might be a first hint that S-waves still need to be optimized in the $p\pi^0$ channel of the BnGa solution. A statement concerning the other solutions is up to now not possible as no $\mathrm{L}_{\mathrm{max}}$-fit procedure was performed with the other solution. Finally, the author of the paper claimed only small improvements in the imaginary part of the M_{1-} multipole but significant once in the real part. Here, especially the results of the new double polarization observable G might help as they show a strong sensitivity to the imaginary part of the M_{1-} multipole.

9.3.2 Double Polarization Observable G for the reaction $\vec{\gamma}\vec{p} \to n\pi^+$

Fig. 9.32 and Fig. 9.33 show the comparison of the results, indicated by the black points, with the PWA predictions and solutions which have been mentioned in the introduction of this chapter. In contrast to the $p\pi^0$ channel, all PWAs show similar behavior in the first resonance region. At low energies, the shape of G has a parabolic behavior which can be traced back to the dominance of P-waves, namely $N(1440)1/2^+(P_{11})$ and $\Delta(1232)3/2^+(P_{33})$. The zero-crossing in forward-direction is a confirmation of higher waves, e.g., D-waves including the $N(1520)3/2^-(D_{13})$ resonance. Another possible explanation can be that non-resonant contributions from the pion-pole and Kroll-Ruderman term and thus even higher waves are needed at low energies. This has especially been seen in the expansion coefficient $(\mathrm{a}_3)_3^{\check{\mathrm{G}}}$. At least, the BnGa solution needs the G-waves in terms of the $\langle P,G\rangle$ interference terms to describe the expansion coefficient. Asides from small differences in the forward direction, the JüBo-2017 solution presents a sudden changing behavior in backward direction in the beam photon energy range from 400 MeV to 502 MeV. However, only the energy bin from 400 MeV to 434 MeV owns good statistics in combination with low systematic uncertainties to rule out this behavior.

In the second resonance region, the zero-crossing in the forward direction moves from high forward angles towards backward angles and is completely negative starting at 672 MeV with a more defined structure compared to lower energies. This is as well visible in the expansion coefficient $(\mathrm{a}_3)_2^{\check{\mathrm{G}}}$ as the dominance of the $\langle P,P\rangle$ interference terms of the BnGa-2016 solution, which causes the strong positive parabolic shape, is close to zero at about 650 MeV.

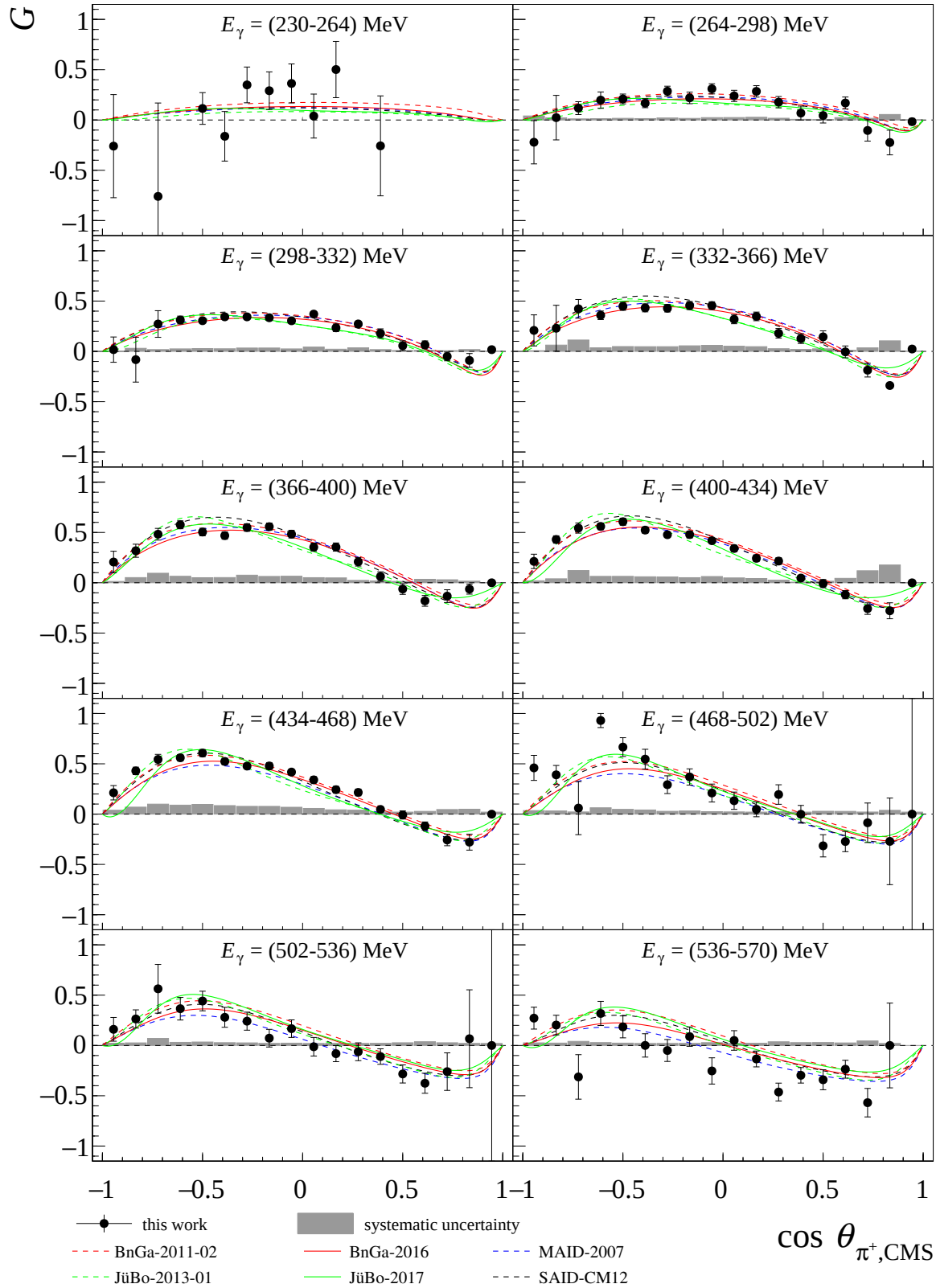

Fig. 9.32: Comparison of the results for the double polarization observable G with PWAs for $\vec{\gamma}\vec{p}\to n\pi^+$. The results of the double polarization observable G are shown as a function of $\cos\theta_{\pi^+,\mathrm{CMS}}$ for the beam photon energy from 230 MeV to 570 MeV. The black points represent the results of the new A2 data together with their statistical uncertainties while the gray boxes shows the systematic uncertainties. The results are compared to the following PWAs: BnGa-2011-02 (red dashed line) [72], BnGa-2016 (red line) [46], MAID-2007 (blue dashed line) [49], JüBo-2013-01 (green dashed line) [135], JüBo-2017 (green line) [50] and SAID-CM12 (black dashed line) [30].

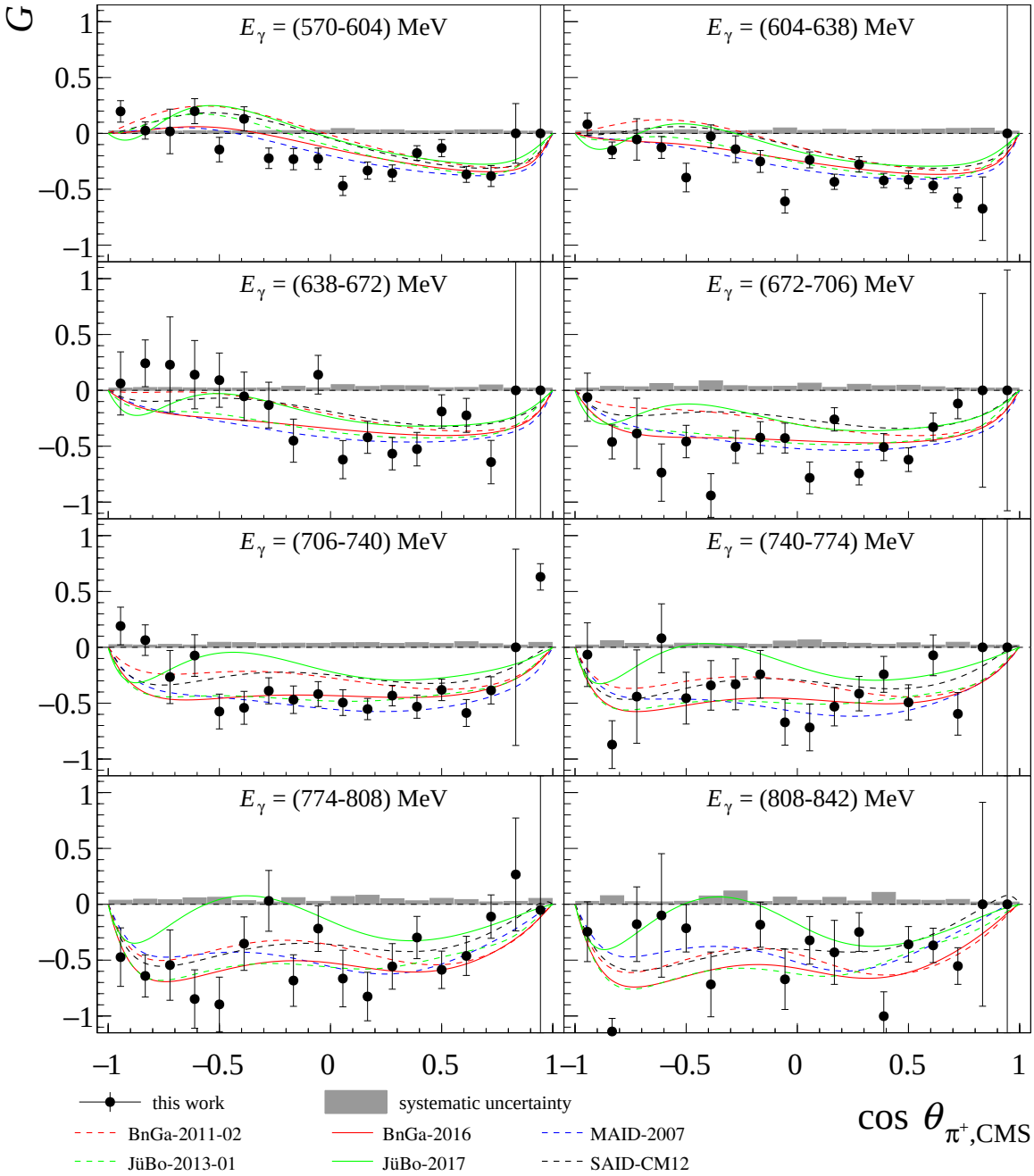

Fig. 9.33: Comparison of the results for the double polarization observable G with PWAs for $\vec{\gamma}\vec{p}\to n\pi^+$. The results of the double polarization observable G are shown as a function of $\cos\theta_{\pi^+,\mathrm{CMS}}$ for the beam photon energy from 570 MeV to 842 MeV.The black points represent the results of the new A2 data together with their statistical uncertainties while the gray boxes shows the systematic uncertainties. The results are compared to the following PWAs: BnGa-2011-02 (red dashed line) [72], BnGa-2016 (red line) [46], MAID-2007 (blue dashed line) [49], JüBo-2013-01 (green dashed line) [135], JüBo-2017 (green line) [50] and SAID-CM12 (black dashed line) [30].

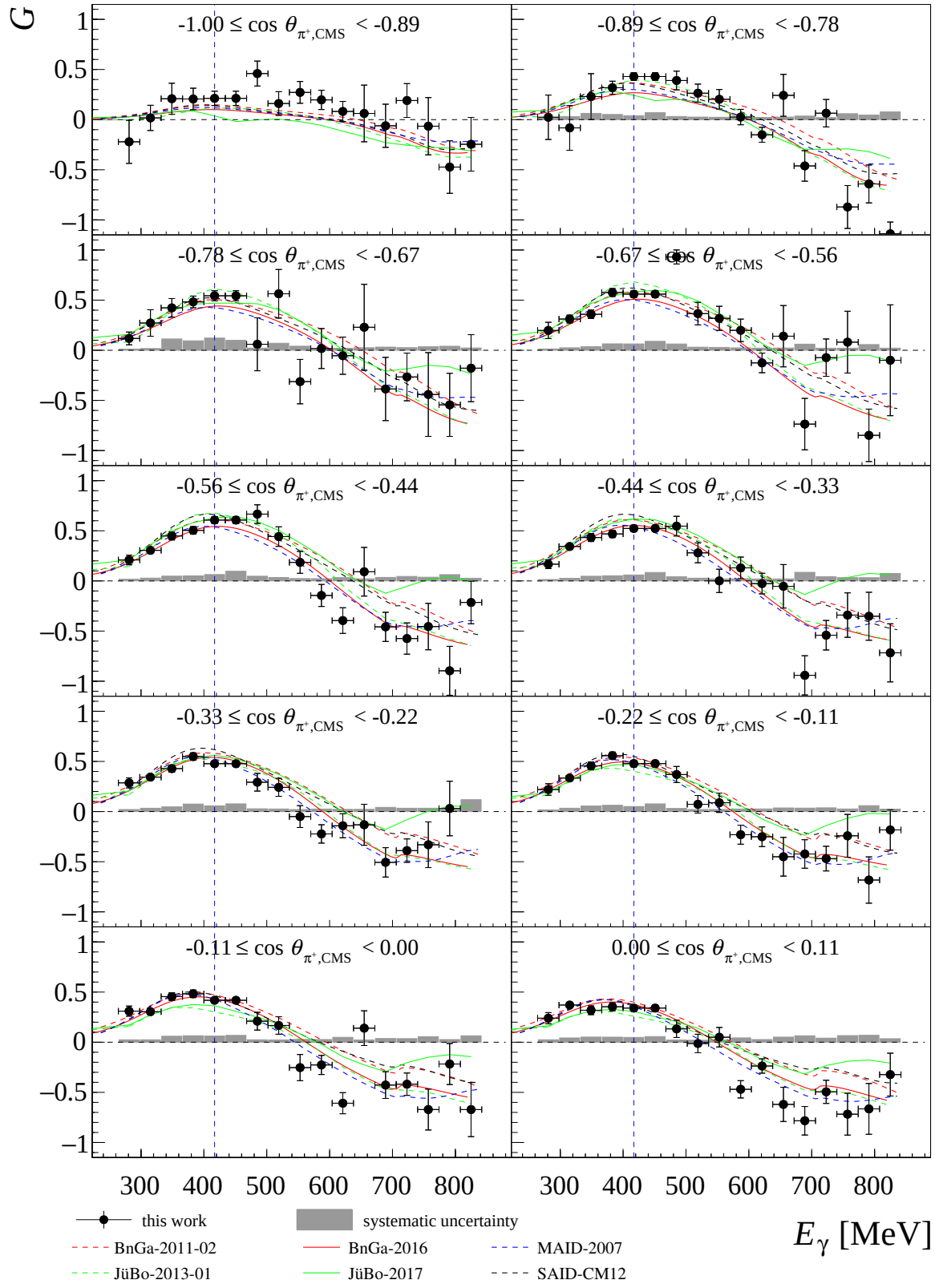

Fig. 9.34: Comparison of the results for the double polarization observable G with PWAs for $\vec{\gamma}\vec{p}\to n\pi^+$ as a function of the beam photon energy E_γ. The results of the double polarization observable G are shown as a function of the mean value of the beam photon energy bin E_γ for the kinematic range $-1.00 \leq \cos\theta_{\pi^+,\mathrm{CMS}} < 0.11$. The black points represent the results of the new A2 data together with their statistical uncertainties while the gray boxes shows the systematic uncertainties. The blue dashed line shows the energy range up to which the 1 PED events are included. The results are compared to the following PWAs: BnGa-2011-02 (red dashed line) [72], BnGa-2016 (red line) [46], MAID-2007 (blue dashed line) [49], JüBo-2013-01 (green dashed line) [135], JüBo-2017 (green line) [50] and SAID-CM12 (black dashed line) [30].

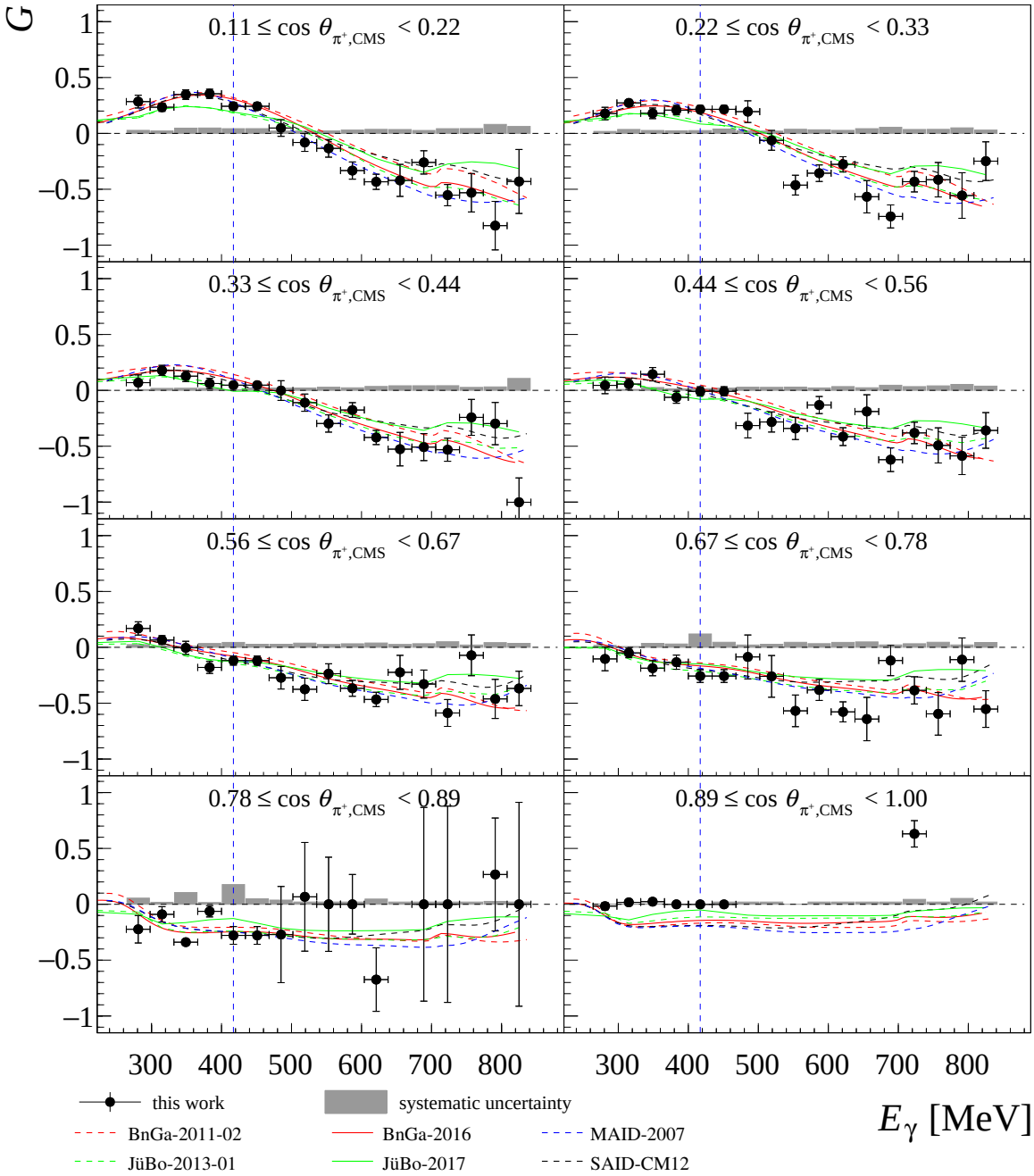

Fig. 9.35: Comparison of the results for the double polarization observable G with PWAs for $\vec{\gamma}\vec{p}\to n\pi^+$ as a function of the beam photon energy E_γ. The results of the double polarization observable G are shown as a function of the mean value of the beam photon energy bin E_γ for the kinematic range $0.11 \leq \cos\theta_{\pi^+,\mathrm{CMS}} < 1.00$. The black points represent the results of the new A2 data together with their statistical uncertainties while the gray boxes shows the systematic uncertainties. The blue dashed line shows the energy range up to which the 1 PED events are included. The results are compared to the following PWAs: BnGa-2011-02 (red dashed line) [72], BnGa-2016 (red line) [46], MAID-2007 (blue dashed line) [49], JüBo-2013-01 (green dashed line) [135], JüBo-2017 (green line) [50] and SAID-CM12 (black dashed line) [30].

Above 650 MeV, the negative sign is dominated by the interference of the $\langle S,D\rangle$ and $\langle D,D\rangle$ terms with additional structures caused by higher waves. Comparing the PWA in details, only the JüBo-2017 solution shows again a zero-crossing in backward direction with a strong angular dependence in the region of the $p\eta$ photoproduction threshold of about E_γ = 708 MeV. No other solution behaves like that and the data within their statistical precision can not confirm the JüBo-2017 solution.
In Fig. 9.34 and Fig. 9.35 the results are plotted as a function of the mean value of the beam photon energy window E_γ. In the region of the $p\eta$ photoproduction threshold, the different PWA solutions show a hint of the $p\eta$-cusp. However, the statistic of the new A2 data is not good enough to identify a clear cusp effect in this representation. Again, only the JüBo-2017 PWA can be ruled out in the energy region around the $p\eta$ photoproduction threshold region.

9.3.3 Double Polarization Observable *E* for the reaction $\vec{\gamma}\vec{p} \to n\pi^+$

Fig. 9.36 and Fig. 9.37 show the comparison of the results, indicated by the black points, with the PWA predictions and solutions which have been mentioned in the introduction of this chapter. Below roughly 434 MeV, all PWAs show a parabolic behavior with a negative amplitude which gets smaller with increasing energy. This can be assigned to the dominance of *P*-waves, namely the $\Delta(1232)3/2^+(P_{33})$ resonance. Nevertheless, small differences between the new JüBo-2017 and all other solutions are present in the backward direction, especially in the beam photon energy range from 366 MeV to 502 MeV. Such deviations were obtained in the same energy region for the double polarization observable *G* in both channels as well. However, the systematic uncertainties for the double polarization observable *E* in this kinematic region are too large to give any strong statement. Towards higher energies, the angular dependence gets more complex as higher waves contribute stronger. Here, the differences between the recent BnGa-2016 and the JüBo-2017 PWA, which both include the new *E* data of CLAS, and the older solutions SAID-CM12 and MAID-2007 get stronger. Whereas the MAID-2007 PWA shows deviations below E_γ of about 650 MeV, the SAID-CM12 solution presents differences starting at about 740 MeV.
Overall, all recent PWAs show a similar angular dependence which can be explained by the already existing data base for the observable *E* from the CLAS collaboration[8] [68] and the helicity dependent cross sections from the GDH/A2-collaboration [75]. Only small deviations in the backward direction and forward direction can be seen for the recent PWA solutions. Especially in these regions, the new A2 data can be used to further constrain the different PWAs.
Fig. 9.38 and Fig. 9.39 depicts the results as a function of the mean value of the beam photon energy window E_γ. Similar to the double polarization observable *G* in the $p\pi^0$ channel, a small cusp effect in the region of the $p\eta$ photoproduction threshold of about $E_\gamma = 708$ MeV is visible. In the 16th bin ($0.67 \leq \cos\theta_{\pi^+,\mathrm{CMS}} < 0.78$), the new A2 data and CLAS data both show a zero-crossing at about 350 MeV towards positive values and at about 470 MeV another zero-crossing back to negative values. This behavior is seen by all PWAs except by both BnGa PWAs.

[8] only included in BnGa-2016 and JüBo-2017

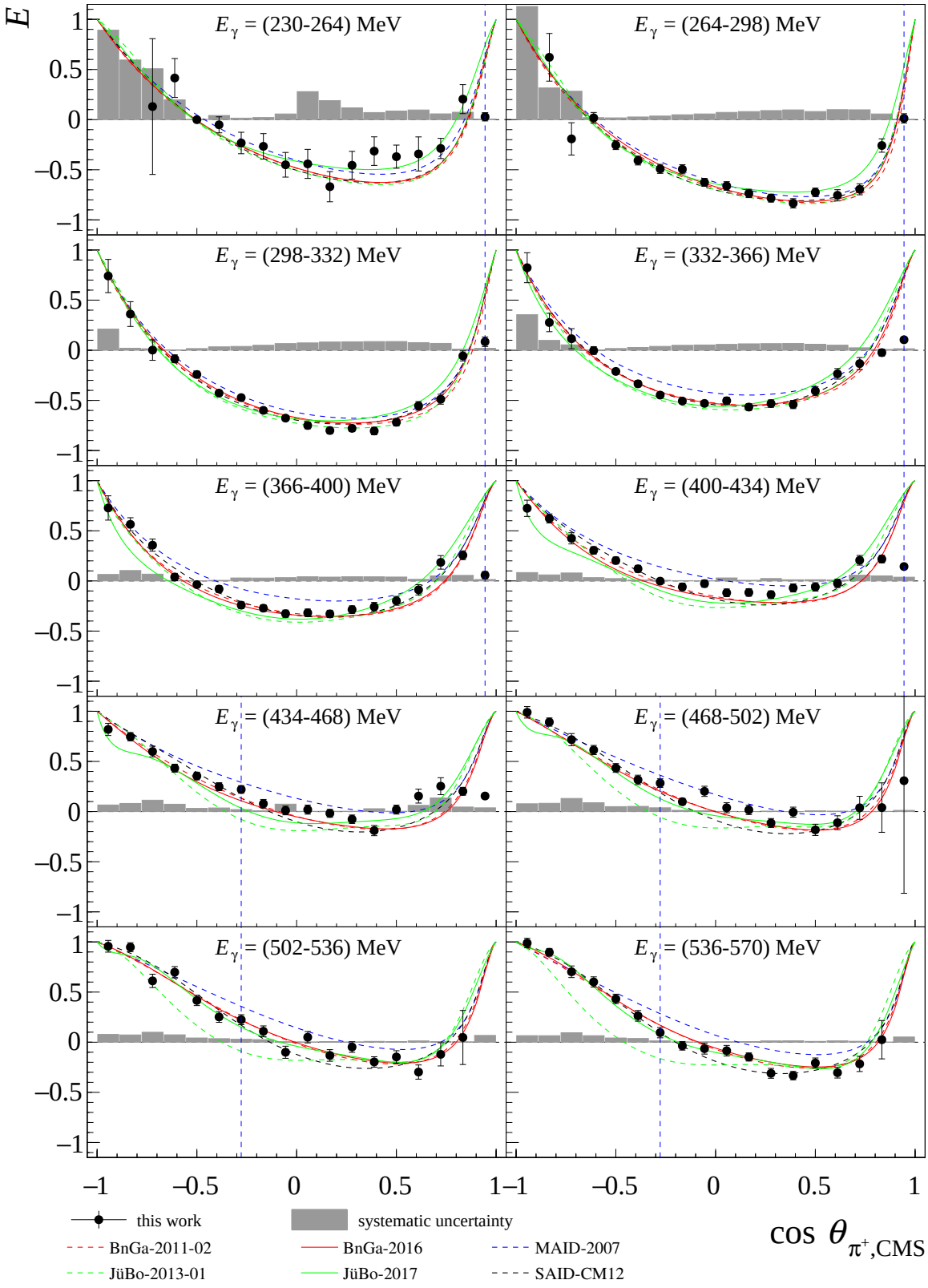

Fig. 9.36: Comparison of the results for the double polarization observable E with PWAs for $\vec{\gamma}\vec{p}\to n\pi^+$. The results of the double polarization observable E are shown as a function of $\cos\theta_{\pi^+,\mathrm{CMS}}$ for the beam photon energy from 230 MeV to 570 MeV. The black points represent the results of the new A2 data together with their statistical uncertainties. The blue dashed line indicates the position up to which point the 1 PED events are added to the 2 PED events. The results are compared to the following PWAs: BnGa-2011-02 (red dashed line) [72], BnGa-2016 (red line) [46], MAID-2007 (blue dashed line) [49], JüBo-2013-01 (green dashed line) [135], JüBo-2017 (green line) [50] and SAID-CM12 (black dashed line) [30].

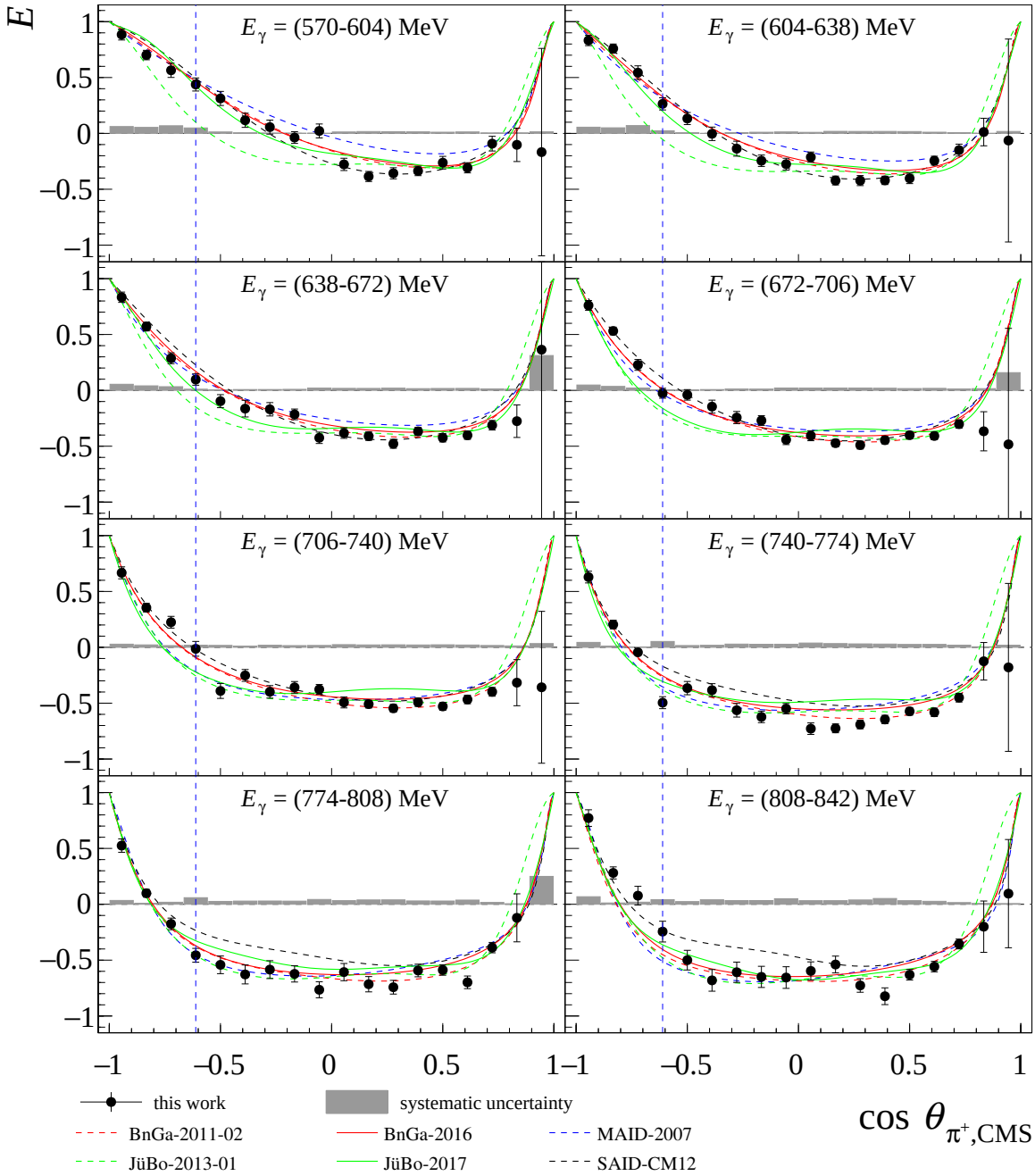

Fig. 9.37: Comparison of the results for the double polarization observable E with PWAs for $\vec{\gamma}\vec{p}\to n\pi^+$. The results of the double polarization observable E are shown as a function of $\cos\theta_{\pi^+,\mathrm{CMS}}$ for the beam photon energy from 570 MeV to 842 MeV. The black points represent the results of the new A2 data together with their statistical uncertainties. The blue dashed line indicates the position up to which point the 1 PED events are added to the 2 PED events. The results are compared to the following PWAs: BnGa-2011-02 (red dashed line) [72], BnGa-2016 (red line) [46], MAID-2007 (blue dashed line) [49], JüBo-2013-01 (green dashed line) [135], JüBo-2017 (green line) [50] and SAID-CM12 (black dashed line) [30].

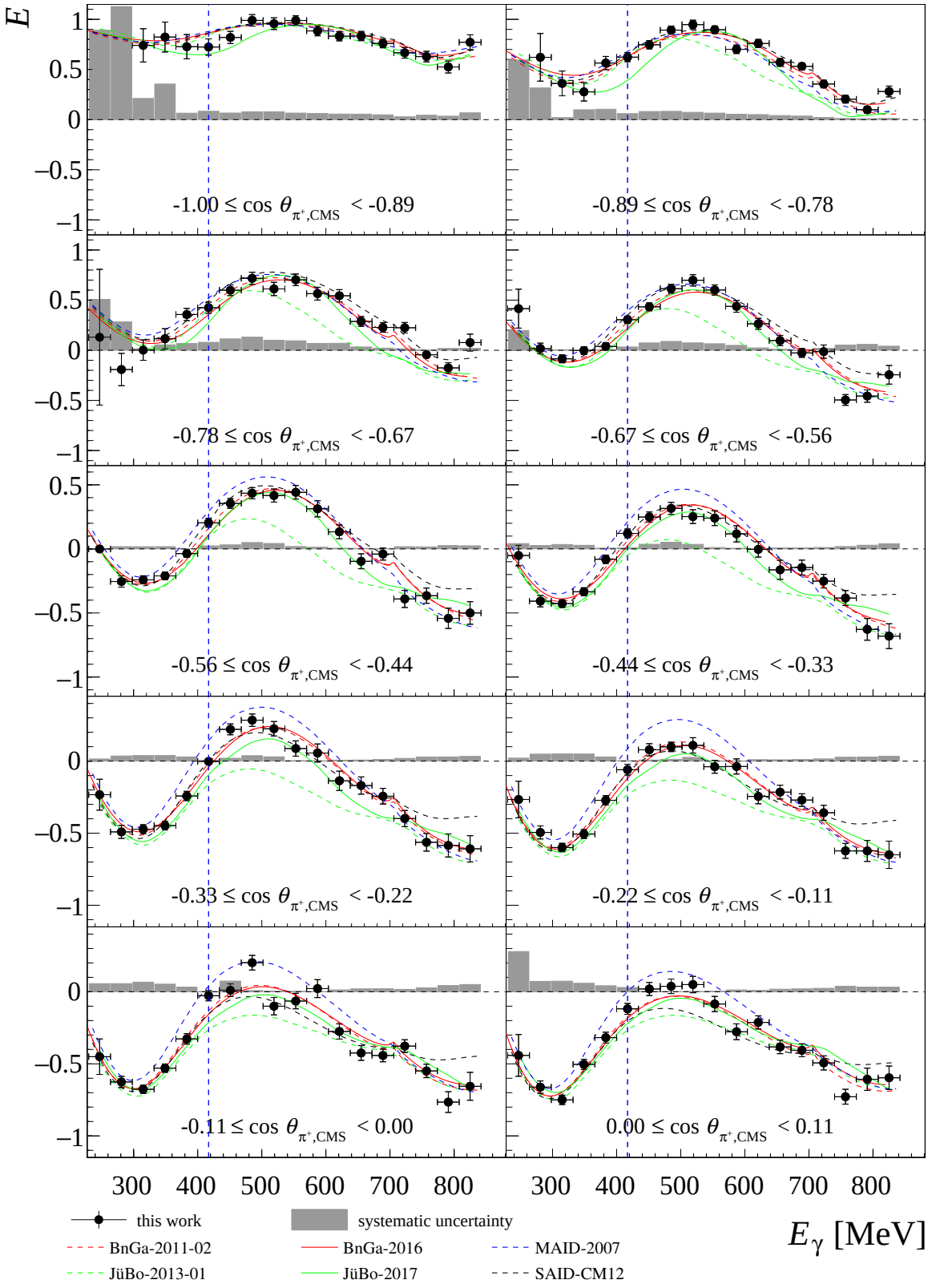

Fig. 9.38: Comparison of the results for the double polarization observable E with PWAs for $\vec{\gamma}\vec{p}\to n\pi^+$ as a function of the beam photon energy E_γ. The results of the double polarization observable E are shown as a function of the mean value of the beam photon energy bin E_γ for the kinematic range $-1.00 \leq \cos\theta_{\pi^+,\mathrm{CMS}} < 0.11$. The black points represent the results of the new A2 data together with their statistical uncertainties while the gray boxes shows the systematic uncertainties. The blue dashed line shows the energy range up to which the 1 PED events are included. The results are compared to the following PWAs: BnGa-2011-02 (red dashed line) [72], BnGa-2016 (red line) [46], MAID-2007 (blue dashed line) [49], JüBo-2013-01 (green dashed line) [135], JüBo-2017 (green line) [50] and SAID-CM12 (black dashed line) [30].

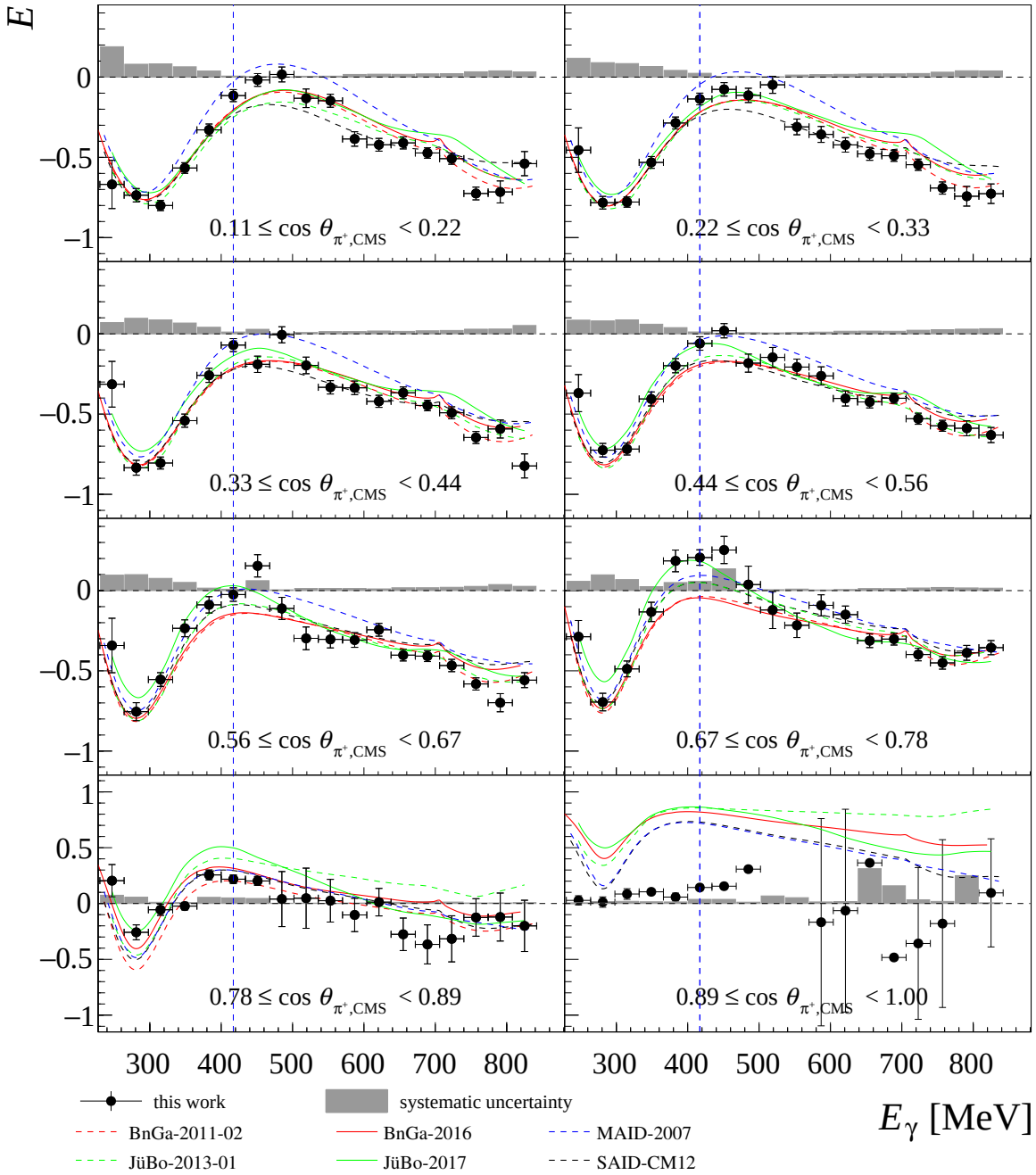

Fig. 9.39: Comparison of the results for the double polarization observable E with PWAs for $\vec{\gamma}\vec{p}\to n\pi^+$ as a function of the beam photon energy E_γ. The results of the double polarization observable E are shown as a function of the mean value of the beam photon energy bin E_γ for the kinematic range $0.11 \leq \cos\theta_{\pi^+,\mathrm{CMS}} < 1.00$. The black points represent the results of the new A2 data together with their statistical uncertainties while the gray boxes shows the systematic uncertainties. The blue dashed line shows the energy range up to which the 1 PED events are included. The results are compared to the following PWAs: BnGa-2011-02 (red dashed line) [72], BnGa-2016 (red line) [46], MAID-2007 (blue dashed line) [49], JüBo-2013-01 (green dashed line) [135], JüBo-2017 (green line) [50] and SAID-CM12 (black dashed line) [30].

In the future, a detailed study of the impact of new polarization observable data in the $n\pi^+$ final state, similar to the variance plots in Fig. 9.31 for the $p\pi^0$ final state, is important. The inclusion of the new CLAS data for the double polarization observable E and beam asymmetry Σ for the $n\pi^+$ final state together with the polarization observables of the $p\pi^0$ final state show evidence for a higher G-wave resonance state, namely the $\Delta(2200)7/2^-(G_{37})$, which is listed as a one-star resonance in the PDG. Significant improvements at lower energies were not reported [136]. Nevertheless, already the comparison of the new A2 results with the recent and older PWA solutions show the importance of the $n\pi^+$ final state and the necessity of a better data base. Even at low energies, differences are still present in the PWA solutions for the double polarization observable E and G. Especially, in the region of the $p\eta$ photoproduction threshold, significant differences and structures occur in the double polarization observable G.

9.4 The $E2/M1$ Ratio in the $\gamma N \to \Delta(1232)$ transition

In the $\Delta(1232)3/2^+(P_{33})$ resonance region, the precise data for the two double polarization observables in both channels can help to investigate the quadrupole deformation of the proton. Assuming a spherical form of the proton with only S-wave contributions, a quadrupole excitation of the $\Delta(1232)3/2^+(P_{33})$ is not possible. Consequently, the electric quadrupole photon multipole $E2$ is absent. The measurement of the ratio of the electric quadrupole $E2$ to the dominant magnetic dipole $M1$ photon multipole in the $\gamma N \to \Delta(1232)$ transition is sensitive to the non-spherical components which can be assigned mostly to D-wave contributions. Thus, several experimental efforts were performed in the past to optimize the data base of the polarization observables. These include the measurement of the beam asymmetry [37, 57, 137] or the helicity dependence of the total cross-section [20] coincidentally with the differential cross-section. Since the double polarization observable G is completely sensitive to the interference of multipoles, the new A2 data are perfectly suited to investigate the small contributing E_{1+} and M_{1-} multipole in the $\Delta(1232)3/2^+(P_{33})$ resonance region. These multipoles contribute to the electric quadrupole $E2$ and magnetic dipole $M1$, respectively, and thus can improve the $E2/M1$ ratio.

Chapter 10

Summary and Outlook

The measurement of polarization observables in meson photoproduction opens a window for a better understanding of the dynamics and interactions inside the nucleons. Within this thesis, the double polarization observables G and E have been determined in a beam photon energy range from 230 MeV to 842 MeV ($W = 1145\,\text{MeV} - 1569\,\text{MeV}$). They were recorded with the Crystal Ball experiment within the A2 collaboration. It is located at the electron accelerator MAMI in Mainz. Elliptically polarized photons, containing a linearly and a circularly polarized component at the same time, were produced via the interaction of a longitudinally polarized electron beam with a diamond radiator. The produced photons were incident on a longitudinally polarized butanol target, and the detection system detected the final state products.

About 3×10^7 events for the $p\pi^0$ channel and 4×10^7 for the $n\pi^+$ channel were selected. Thereby, background contamination of less than 2% for the $p\pi^0$ channel and less than 5% for the $n\pi^+$ channel was achieved. The extracted polarization observables demonstrate that the simultaneous determination of the double polarization observable E, using the circularly polarized component, and double polarization observable G, using the linearly polarized component, can be performed. From the experimental point of view, these results have a major impact for future experiments because now only the target polarization orientation needs to be switched between longitudinal and transverse to measure all polarization observables of the beam-target category.

The new high precision A2 data for the double polarization observable G in the $p\pi^0$ channel close the gap between the $\Delta(1232)3/2^+(P_{33})$ region and the already existing CBELSA/TAPS data. Both data sets are in good agreement with each other in the overlapping region. The comparison of the results with the recent PWA solutions indicates that further improvements need to be introduced in PWAs in the first resonance region where no high precision data were available up to now. For a better understanding of the contributing partial waves, the angular distributions were fit with a truncated expansion of associated Legendre polynomials, which is the called L_{max}-fit procedure. The procedure reveals some indication that the BnGa-2016 PWA solution might need some improvements

in the D-waves.
For the double polarization observable G in the $n\pi^+$ channel, this thesis presents a high precision measurement of this observable for the first time. Overall, in the first resonance region, a good agreement between the different PWA solutions is seen. The most significant discrepancies are obtained at energies in the region of the $p\eta$ photoproduction threshold. Here, the JüBo-2017 model deviates strongly from the obtained data and all other solutions. Finally, with the help of the L_{max}-fit, the $p\eta$ cusp can be seen in data.
For the double polarization observable E in the $n\pi^+$ channel, the ratio of 1.01 ± 0.07 between the results with a diamond and an amorphous radiator confirms that the measurement of the polarization observable E with elliptically polarized photons is feasible. Besides, the results for the double polarization observable E in the $n\pi^+$ channel were compared with the recently published data from the CLAS collaboration [68]. Although the detection of the final state is completely different for both experiments, the data sets agree very well with each other, resulting in a good understanding of the systematic effects within both data sets. The additional A2 data points below 350 MeV and overall in the backward direction might help to constrain the different PWA solutions further. With the help of the L_{max}-fit procedure, this data set together with the results of the CLAS collaboration strengthens the assumption that the BnGa-2016 multipole solution still needs improvement in the second resonance region, corresponding to a beam photon energy range from 500 MeV to 900 MeV ($W = 1350\text{ MeV} - 1600\text{ MeV}$).

The CLAS collaboration already has reported that an analysis of the G observable in the $p\pi^0$ and $n\pi^+$ channel is ongoing in the beam photon energy region from about 575 MeV to 2350 MeV [138]. In combination with the new high precision A2 data, the results of the double polarization observable G and E in the neutral and charged pion photoproduction off the proton might help to further constrain the resonances in the first and second resonance region. Especially the observable G with its feature to be only sensitive to the interference of different multipoles is perfectly suited for studying the $N(1440)1/2^+(P_{11})$ resonance. Also, with the sensitivity to the E_{1+} multipole, new input for the $E2/M1$ ratio determination, which describes the quadrupole deformation of the proton, is available.

Appendices

Appendix A

Additional information and plots

A.1 MWPC reconstruction tracks

An overview of all possibilities in the MWPC reconstruction and their percentage contribution in a typical run is shown in Tab. A.1.

Table A.1: Overview of the possible tracks and intersection which can be constructed by the MWPC reconstruction. I stands for the internal strip, W for the wire and E for the external strip. The track number is important for the analysis within the AcquRoot framework and should help later analyses to get access to it. Their percentage contribution in a typical run is shown in right column.

MWPC 1	MWPC 0	track number	%
IWE	IWE	63	56.5
IWE	IW	59	5.66
IWE	WE	62	10.11
IWE	IE	61	1.65
IW	IWE	31	6.99
WE	IWE	55	6.51
IE	IWE	47	2.68
IW	IW	27	2.00
EW	EW	54	2.67
IE	IE	45	1.35
IW	EW	30	2.16
EW	IW	51	1.29
IE	IW	43	0.52
IW	IE	29	0.29
IE	WE	46	0.61
WE	IE	53	0.26

A.2 Monte Carlo Simulation Studies

A.2.1 Internal Holding Magnetic Field

The simulated holding magnetic field of the butanol target has shown that the orientation of the magnetic field in data was always aligned against the z-direction of the incoming beam. This was proven by simulating protons and charged pions with a holding magnetic field in direction and against the z-direction of the beam. As the flight path of charged particles is deflected perpendicular to the z-axis, the generated azimuthal angle of the charged particles can be compared to the reconstructed ones. Depending on the orientation of the magnetic field, the particles are deflected to either higher or lower reconstructed azimuthal angles. For protons with the holding magnetic field against the z-direction, the deflection is in the order of 0.6° as can be seen in Fig. A.1.

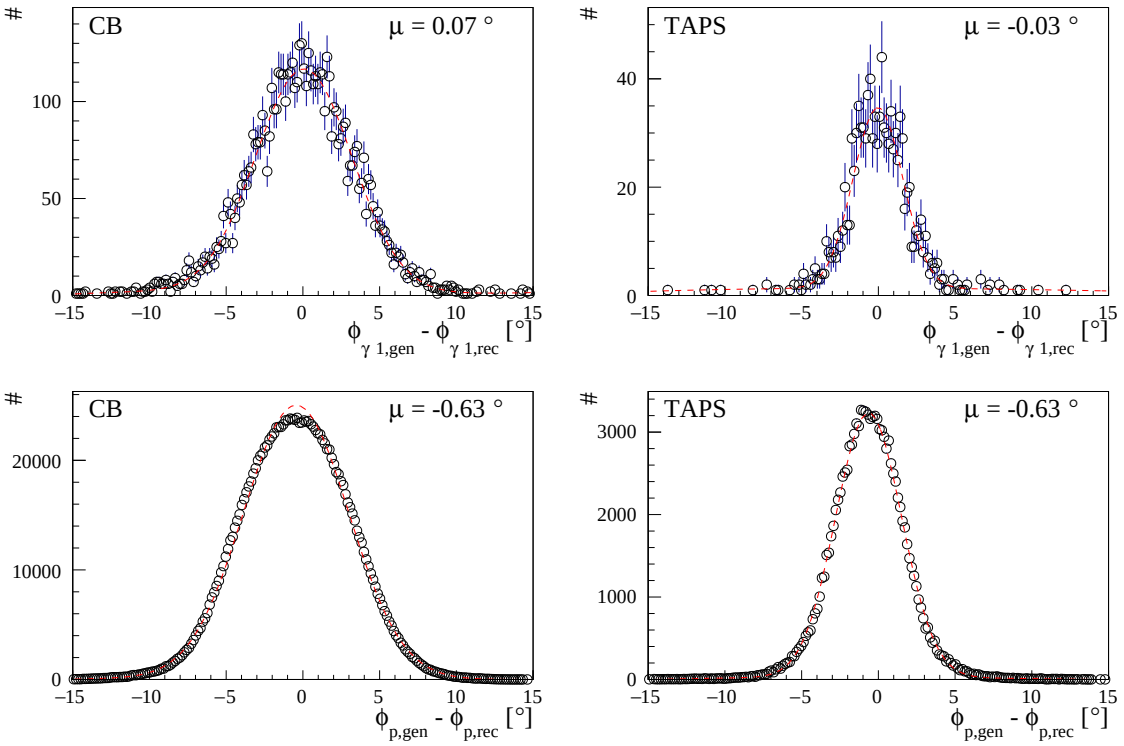

Fig. A.1: Impact of the internal holding magnetic field on the charged azimuthal angle. Shown are the differences between generated and reconstructed azimuthal angles of photons and protons in the CB and the TAPS for MC simulations with a holding magnet field of the butanol target in the z-direction. As expected, photons are not deflected by the magnetic field whereas protons are deflected by 0.63°.

The coplanarity of the reaction $\gamma p \rightarrow p\pi^0$ should therefore not be centered around 180° but rather at 179°. A magnetic field in the opposite direction would cause a coplanarity distribution centered around 181° as the protons are deflected exactly in the opposite direction. In Sec. 7.7.3, it was clearly shown that the data favor the magnetic field against the z-direction of the incoming beam. For the π^+ a higher deflection angle is expected due to its lower mass as can be seen in Fig A.2.

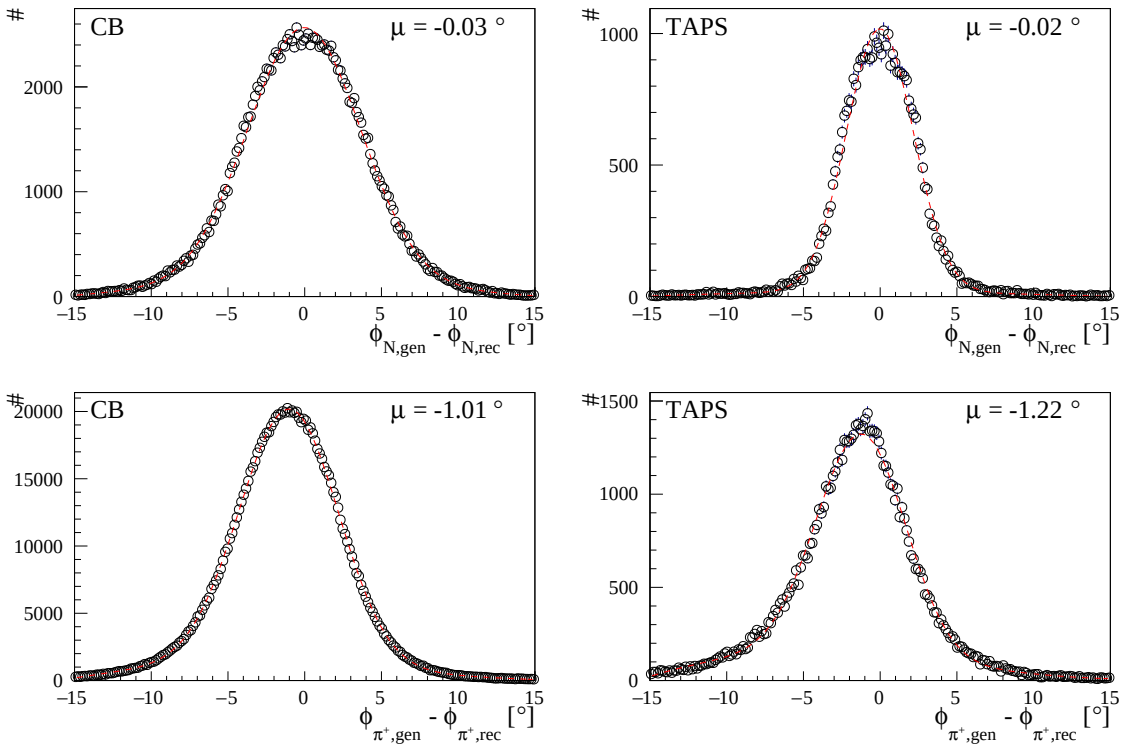

Fig. A.2: Impact of the internal holding magnetic field on the charged azimuthal angle. Shown are the differences between generated and reconstructed azimuthal angles of neutrons and π^+s in the CB and the TAPS for MC simulations with a holding magnet field of the butanol target in the z-direction. As expected, neutrons are not deflected by the magnetic field whereas π^+s are deflected by about 1°.

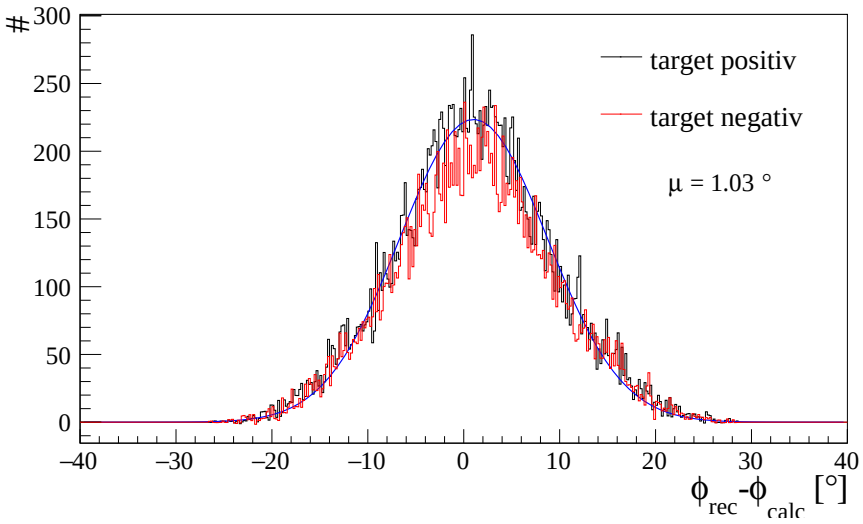

Fig. A.3: Impact of the internal holding magnetic field on the charged azimuthal angle in data. Shown are the differences between reconstructed and calculated azimuthal angle of the charged pions for both target orientations. As expected from simulations, π^+s are deflected by about 1°.

To test in detail which orientation of the magnetic field was selected, a comparison of the reconstructed and measured azimuthal angle of the pion was performed for both target polarization orientation (see Fig. A.3). As it turned out, both setting use the orientation of the magnetic field against the z-direction of the incoming beam. This can be explained by the fact that there are two possibilities to change the polarization direction of the butanol target, namely either the orientation of the magnetic field or the frequency of the irradiated microwaves has to be changed. Consequently, in data, the microwaves were changed rather than changing the orientation of the field.

A.2.2 Physics Classes

The GEANT package provides different physics classes to describe particle interactions. A list of these classes and their explanation is summarized in [97]. Moreover, the Basel group has studied in detail which physics class is the best to describe the reactions $\gamma p \to \pi^0$ and $\gamma p \to n\pi^+$ [97, 77]. As a result of their study, the physics class `QGSP_BERT_HP` was recommended because the neutron detection efficiency of this class matched the neutron detection efficiency in data the most.

A.3 Study of the different Target Positions

As mentioned in Sec. 8.1.2.3, the different beamtimes had different target center positions. Thus, to test the different target positions, a detailed study of the polar angular difference $\Delta\theta_p = \theta_{p,\text{calc}} - \theta_{p,\text{rec}}$ between the calculated and reconstructed proton polar angle in the reaction $\vec{\gamma}\vec{p} \to p\pi^0$ is used. The calculated proton polar angle is determined from the four momenta of the incoming beam photon, the target at rest and the photons in the final state. As the photons are reconstructed and calibrated under the assumption that the target cell is located at the center of the CB, a deviation of 0° in the polar angular difference indicate that the actual reaction is produced at a different z-position inside the target cell. Fig. A.4 shows for the beam photon energy range from 400 MeV to 434 MeV the different polar angular difference $\Delta\theta_p$ for the May 2015 beamtime in red and September 2015 in black. A similar comparison is performed for the September 2015 and May 2014 beamtime in Fig. A.5 whereas Fig. A.6 illustrates the comparison between May 2014 and November 2013. From the inspection of all Figs. it becomes clear that the September 2015 beamtime and the May 2015 beamtime behave similarly. On the other hand, a good agreement between May 2014 and November 2013 is obtained. A clear deviation between both of these groups is seen and thus the individual beamtimes were recorded with different target positions.

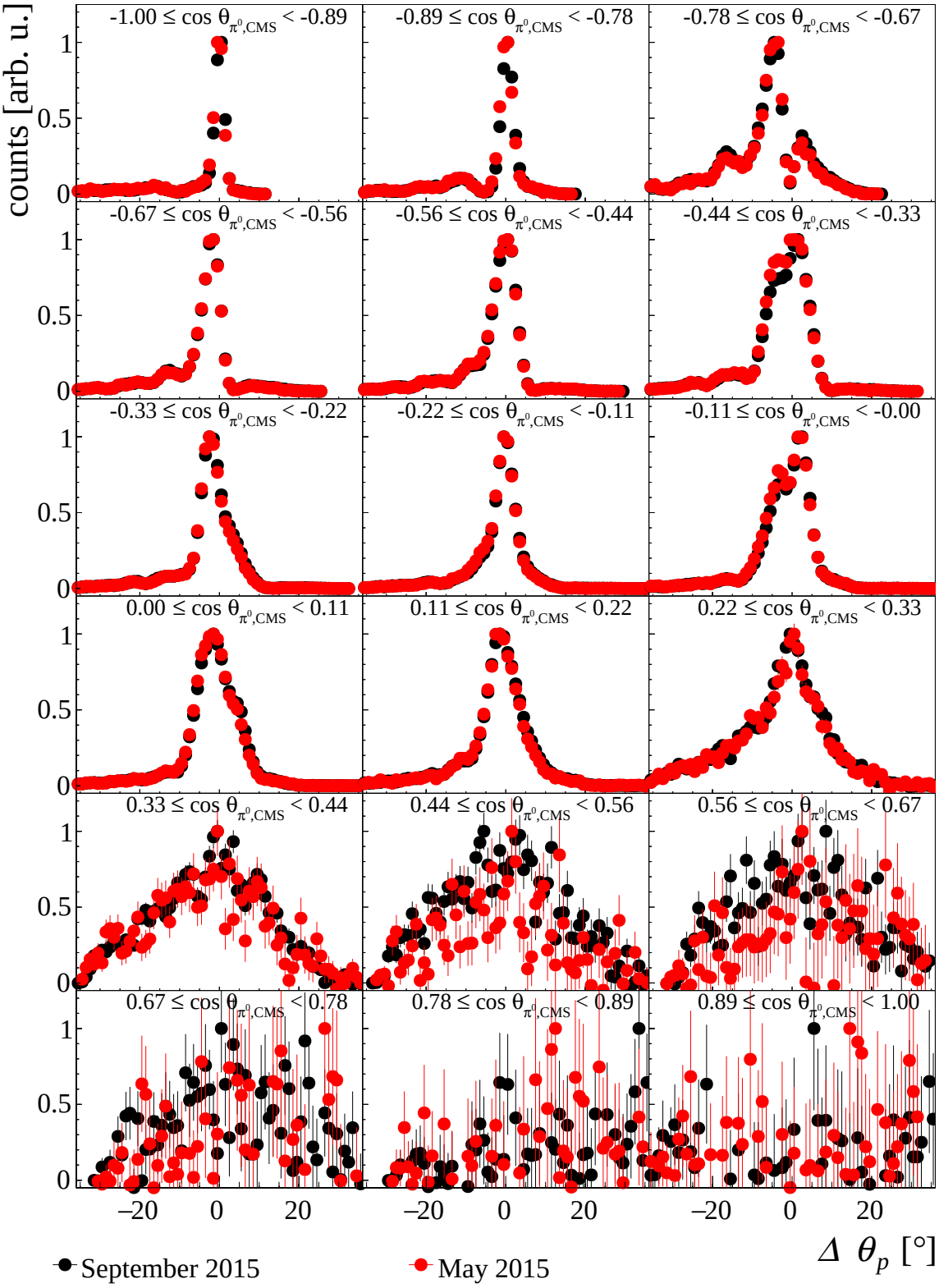

Fig. A.4: $\Delta\theta_p$ distribution forE_γ = (400-434) MeV for different beamtimes. Shown are the $\Delta\theta_p$ distributions as a function of $\cos\theta_{\pi^0,\mathrm{CMS}}$ for a given beam photon energy range. The butanol distributions are shown for the September 2015 beamtime in black and May 2015 in red.

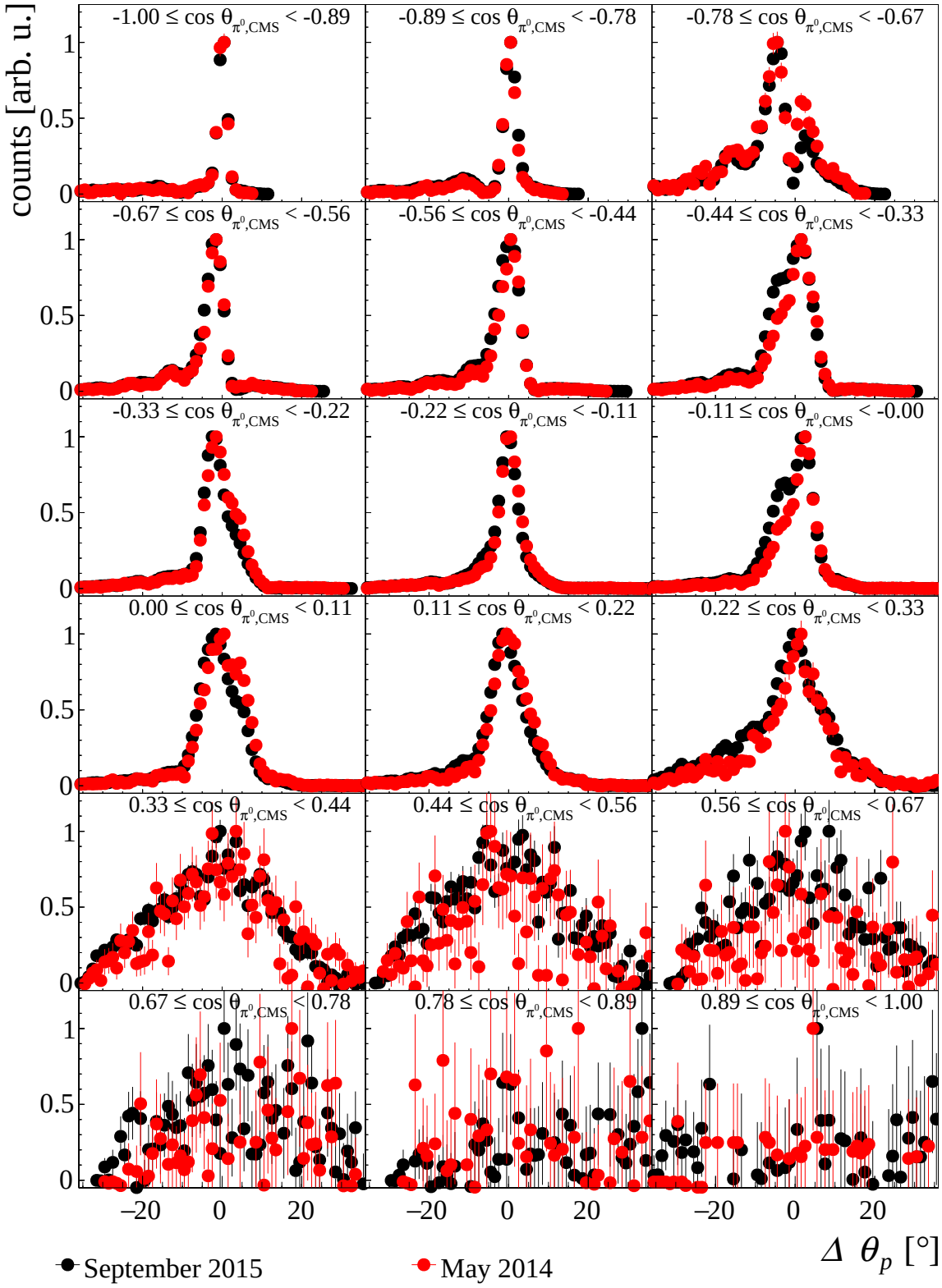

Fig. A.5: $\Delta\theta_p$ distribution forE_γ = (400-434) MeV for different beamtimes. Shown are the $\Delta\theta_p$ distributions as a function of cos $\theta_{\pi^0,\mathrm{CMS}}$ for a given beam photon energy range. The butanol distributions are shown for the September 2015 beamtime in black and May 2014 in red.

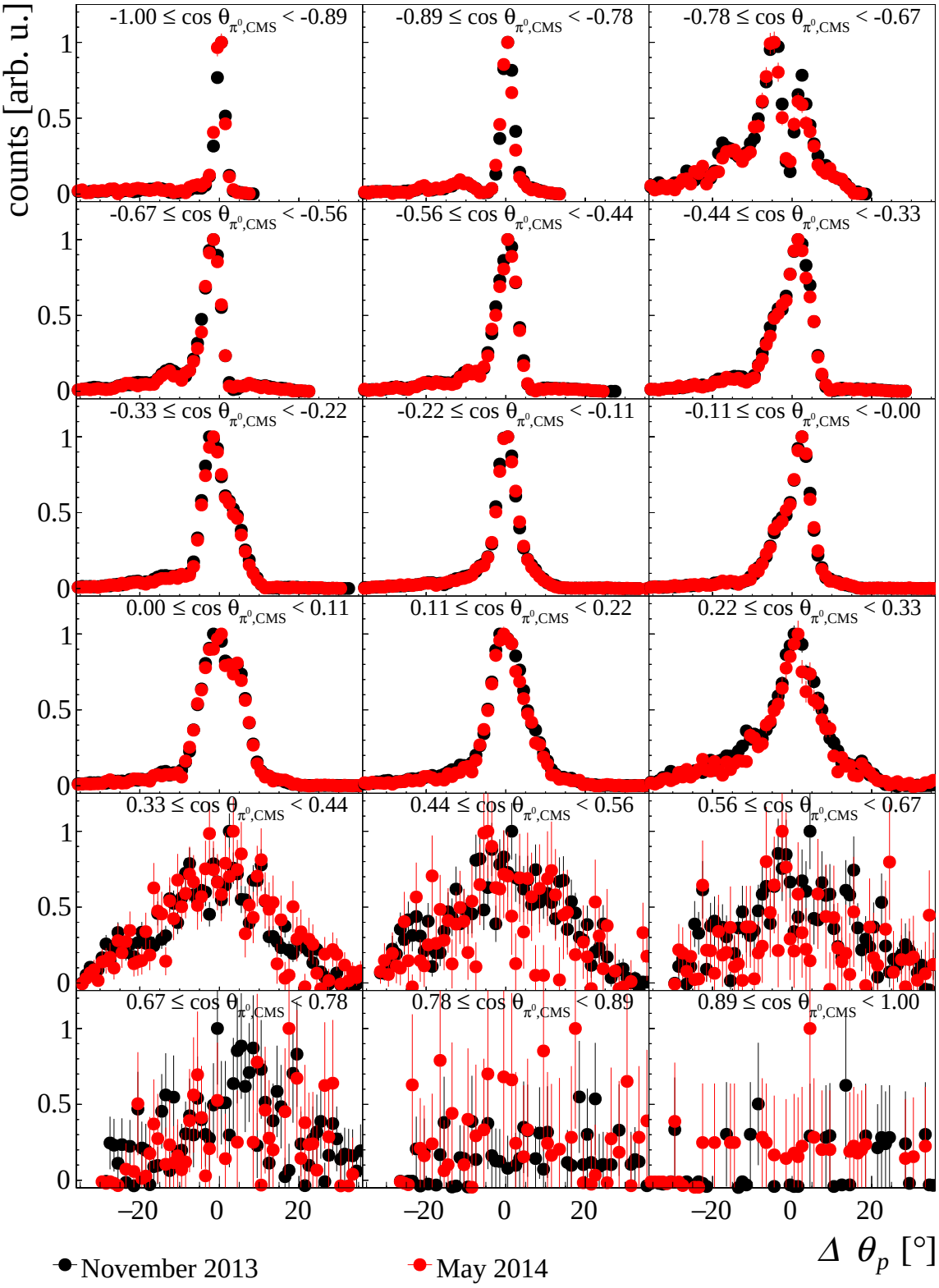

Fig. A.6: $\Delta\theta_p$ distribution forE_γ = (400-434) MeV for different beamtimes. Shown are the $\Delta\theta_p$ distributions as a function of $\cos\theta_{\pi^0,\mathrm{CMS}}$ for a given beam photon energy range. The butanol distributions are shown for the November 2013 beamtime in black and May 2014 in red.

A.4 Dilution Factor

In the following, the dilution factors d, which have been used to determine the double polarization observable G and E, are presented for all beamtimes and their corresponding coherent edge settings for both analyzed channels. Fig. A.7 and Fig. A.8 show the results of the $p\pi^0$ channel. Inspecting both Fig., it can be concluded that all dilution factors agree very good with each other within their systematic uncertainties. Differences in the dilution factor of the 2 PED events can be traced back to the problems discussed in Sec. 8.1.2.3. Similar results for the 2 PED events of the $n\pi^+$ channel are depicted in Fig. A.9 and A.10. Also here no huge deviation between the different dilution factors is visible.
The dilution factor of the 1 PED events are illustrated in Fig. A.11 and A.12. Note that the dilution factor is only shown for the 350 MeV and 450 MeV edge setting as these are the only data which were used to extract the double polarization observable G. The results are compared to the overall dilution factor of all beamtimes, indicated by the red points, which has been used for the extraction of the double polarization observable E. As the dilution factor is quite small, the systematic uncertainty is huge and thus the disagreement between the different dilution factors can be explained by that.

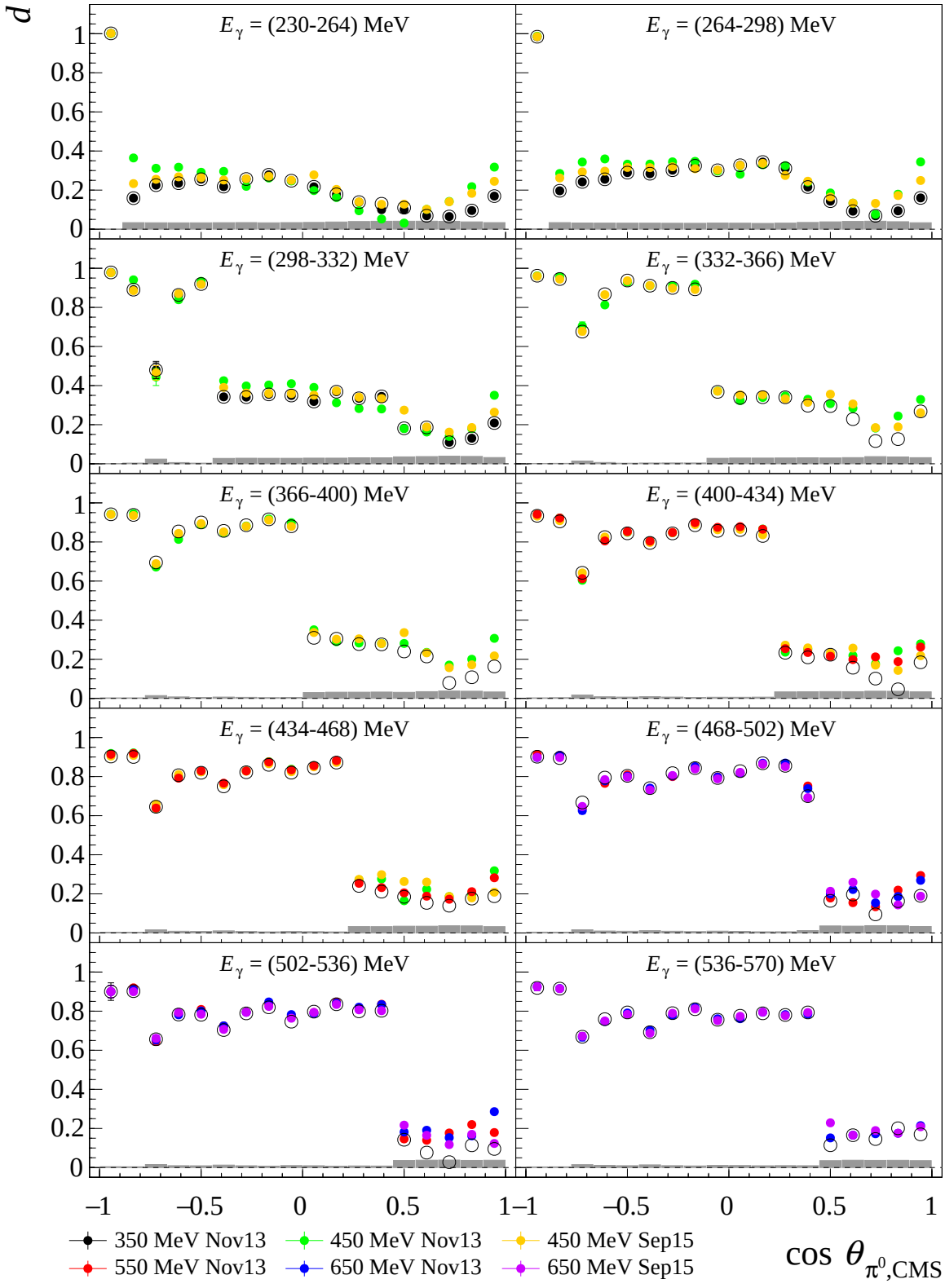

Fig. A.7: Comparison of the dilution factor for all beamtimes for the reaction $\vec{\gamma}\vec{p}\to p\pi^0$. Shown are the results of the dilution factor d as a function of $\cos\theta_{\pi^0,\mathrm{CMS}}$ for the beam photon energy from 230 MeV to 570 MeV for all beamtimes. The open circle shows the dilution factor d which has been determined with the 850 MeV edge setting of September 2015. Deviations from this dilution factor indicate the contribution of different trigger adjustments, reconstruction holes and target positions as has been discussed in Sec. 8.1.2.3. The systematic uncertainty coming from the dilution factor d is indicated by the gray boxes.

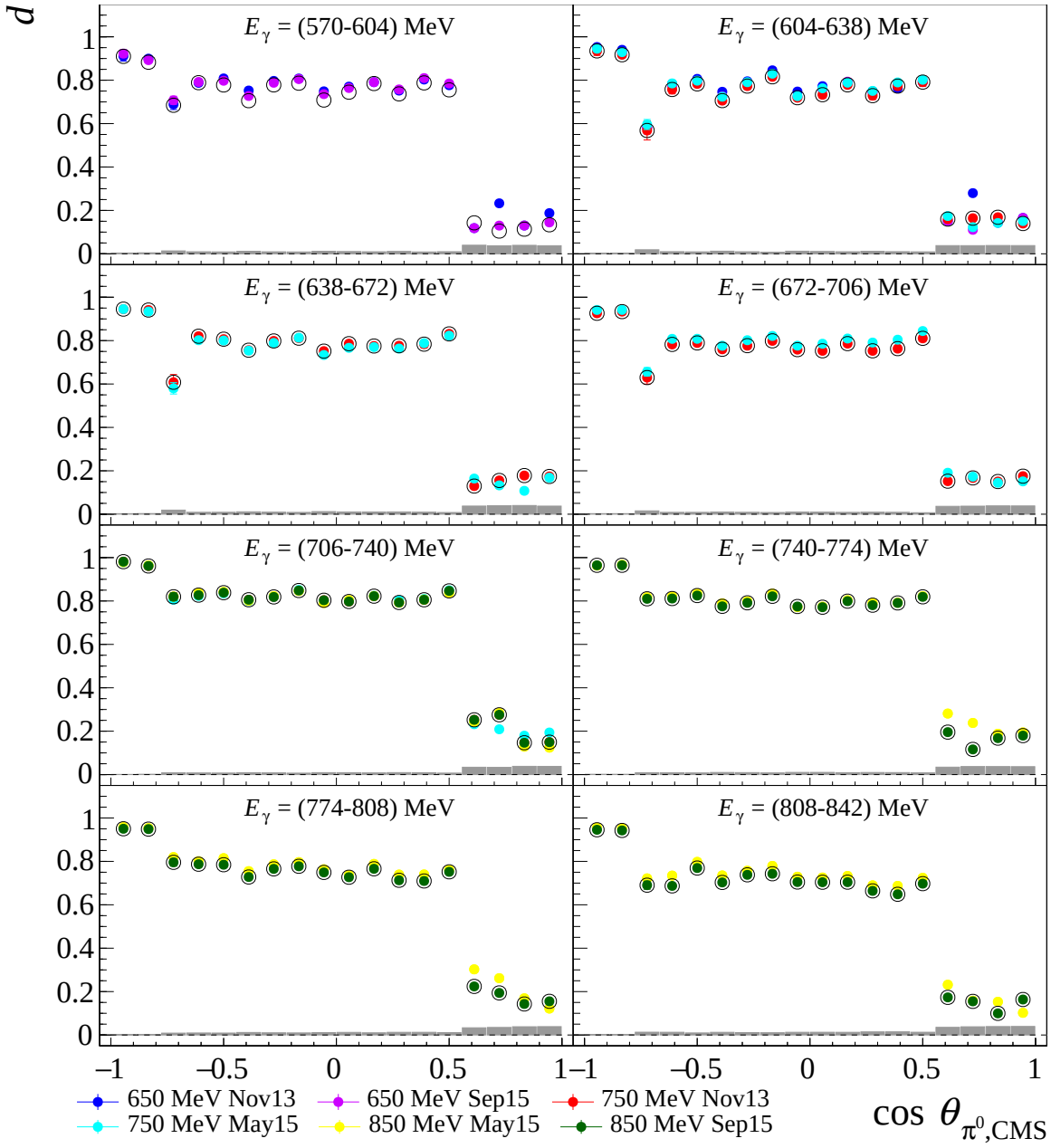

Fig. A.8: Comparison of the dilution factor for all beamtimes for the reaction $\vec{\gamma}\vec{p}\to p\pi^0$. Shown are the results of the dilution factor d as a function of $\cos\theta_{\pi^0,\mathrm{CMS}}$ for the beam photon energy from 570 MeV to 842 MeV for all beamtimes. The open circle shows the dilution factor d which has been determined with the 850 MeV edge setting of September 2015. Deviations from this dilution factor indicate the contribution of different trigger adjustments, reconstruction holes and target positions as has been discussed in Sec. 8.1.2.3. The systematic uncertainty coming from the dilution factor$d$ is indicated by the gray boxes.

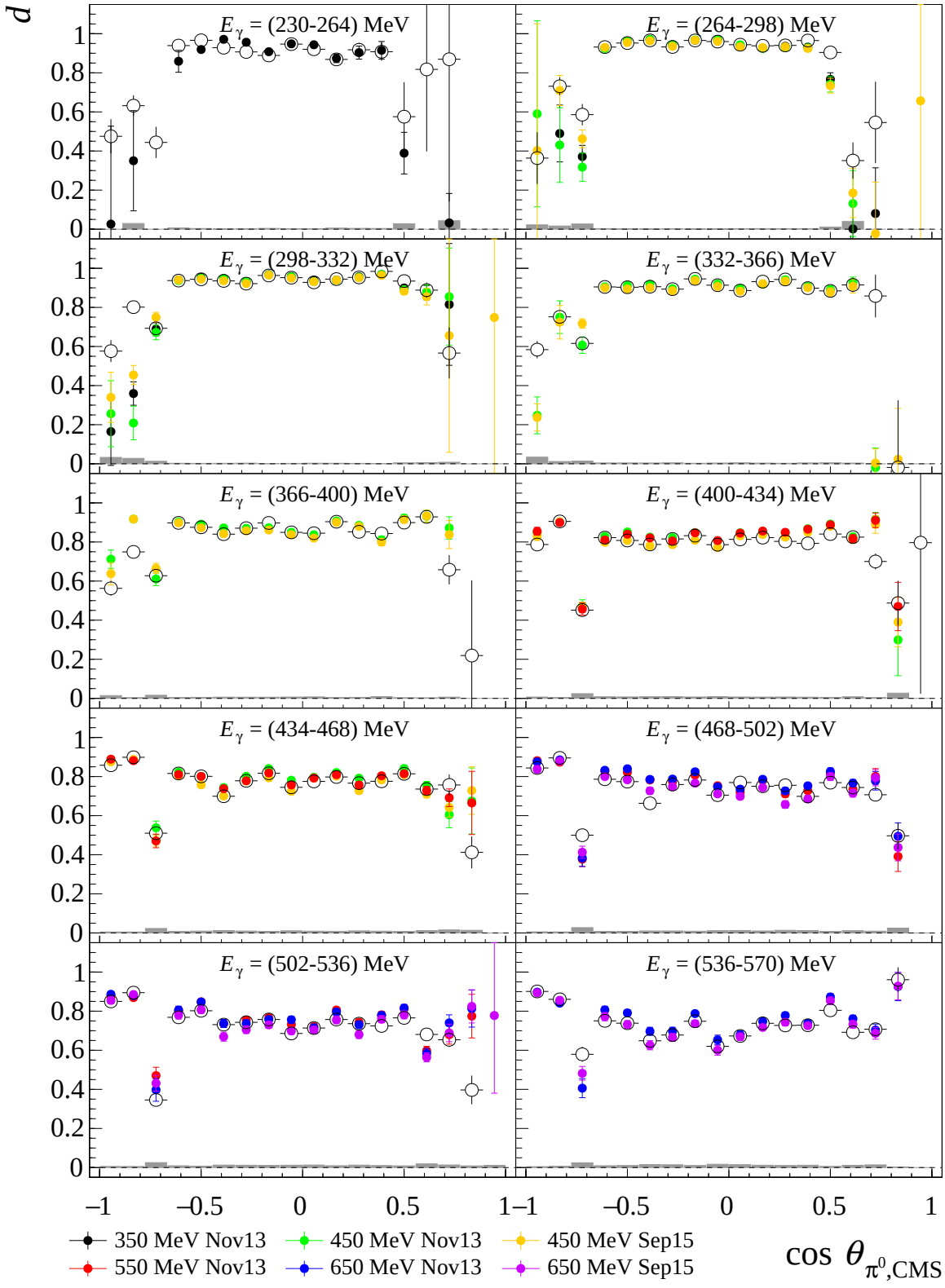

Fig. A.9: Comparison of the dilution factor of the 2 PED events for all beamtimes for the reaction $\vec{\gamma}\vec{p}\to n\pi^+$. Shown are the results of the dilution factor d of the 2 PED events as a function of $\cos\theta_{\pi^+,\mathrm{CMS}}$ for the beam photon energy from 230 MeV to 570 MeV for all beamtimes. The open circle shows the dilution factor d which has been determined with the 850 MeV edge setting of September 2015. Deviations from this dilution factor indicate the contribution of different trigger adjustments, reconstruction holes and target positions as has been discussed in Sec. 8.1.2.3. The systematic uncertainty coming from the dilution factor d is indicated by the gray boxes.

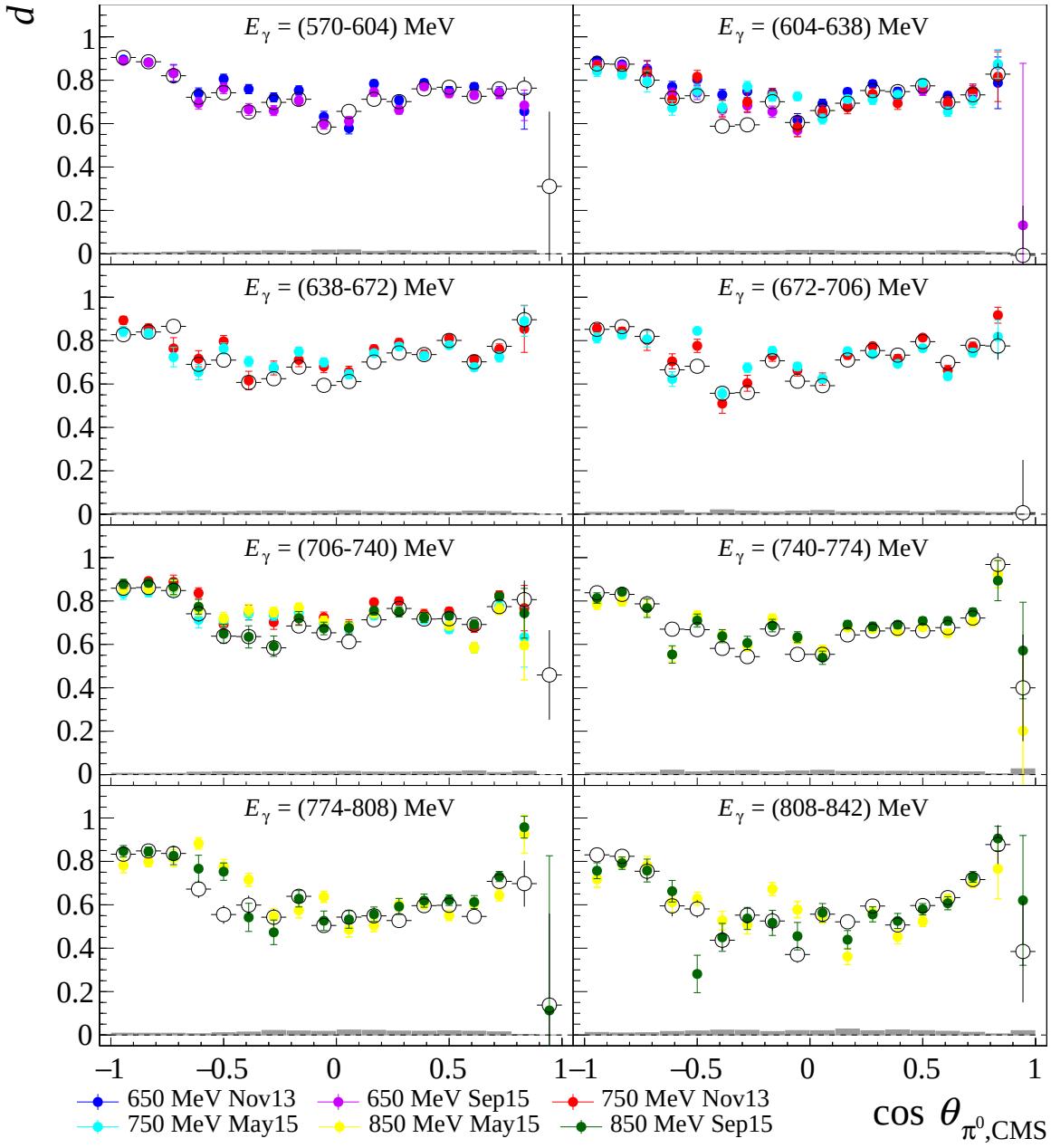

Fig. A.10: Comparison of the dilution factor of the 2 PED events for all beamtimes for the reaction $\vec{\gamma}\vec{p}\to n\pi^+$. Shown are the results of the dilution factor d of the 2 PED events as a function of $\cos\theta_{\pi^+,\mathrm{CMS}}$ for the beam photon energy from 570 MeV to 842 MeV for all beamtimes. The open circle shows the dilution factor d which has been determined with the 850 MeV edge setting of September 2015. Deviations from this dilution factor indicate the contribution of different trigger adjustments, reconstruction holes and target positions as has been discussed in Sec. 8.1.2.3. The systematic uncertainty coming from the dilution factor d is indicated by the gray boxes.

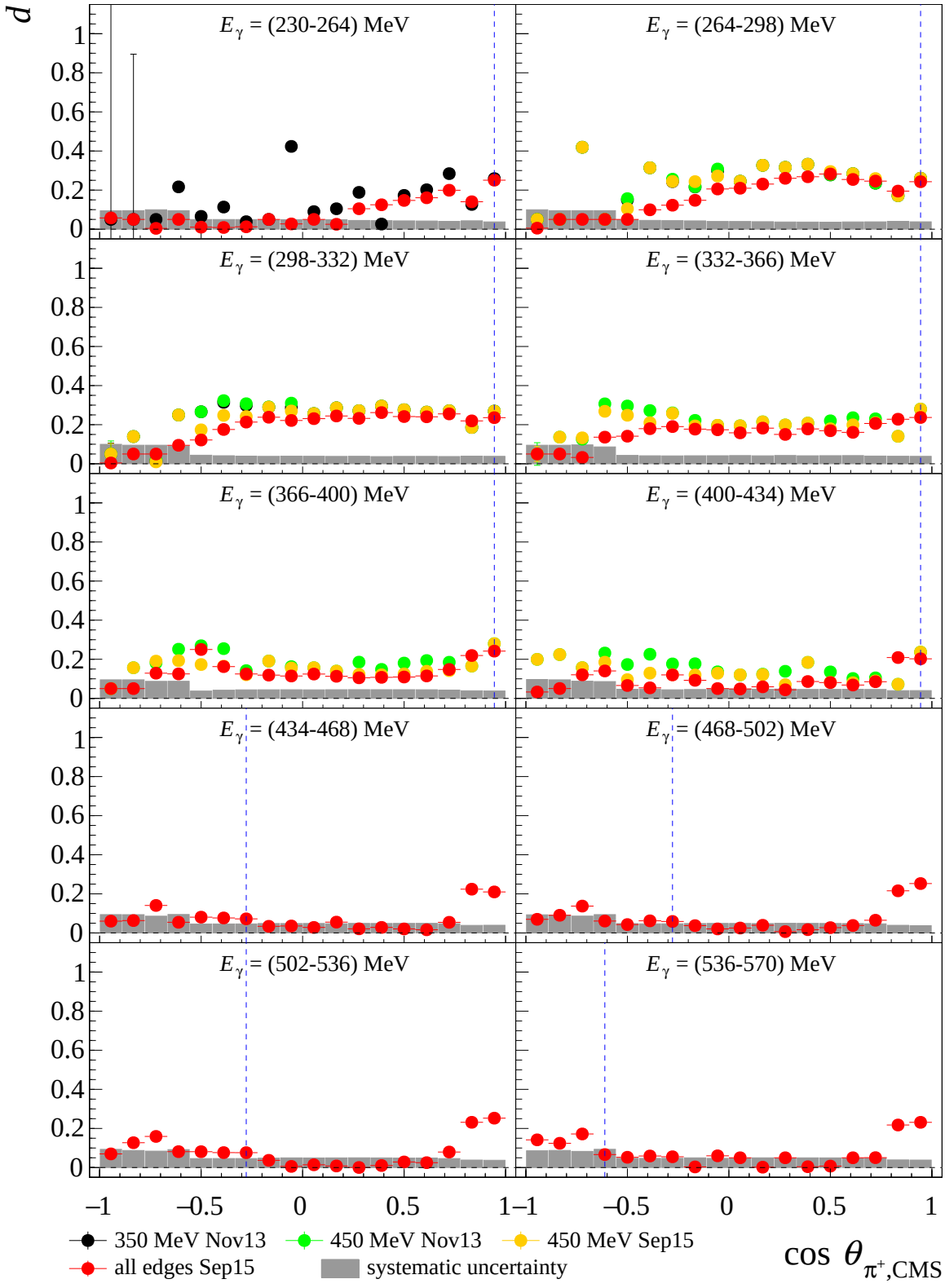

Fig. A.11: Comparison of the dilution factor of the 1 PED events for all beamtimes for the reaction $\vec{\gamma}\vec{p}\to n\pi^+$. Shown are the results of the dilution factor d of the 1 PED events as a function of $\cos\theta_{\pi^+,\mathrm{CMS}}$ for the beam photon energy from 230 MeV to 570 MeV for all beamtimes. The systematic uncertainty coming from the dilution factor d is indicated by the gray boxes. The blue vertical dashed line shows the position up to which point the 1 PED events are included in the extraction of the double polarization observable E.

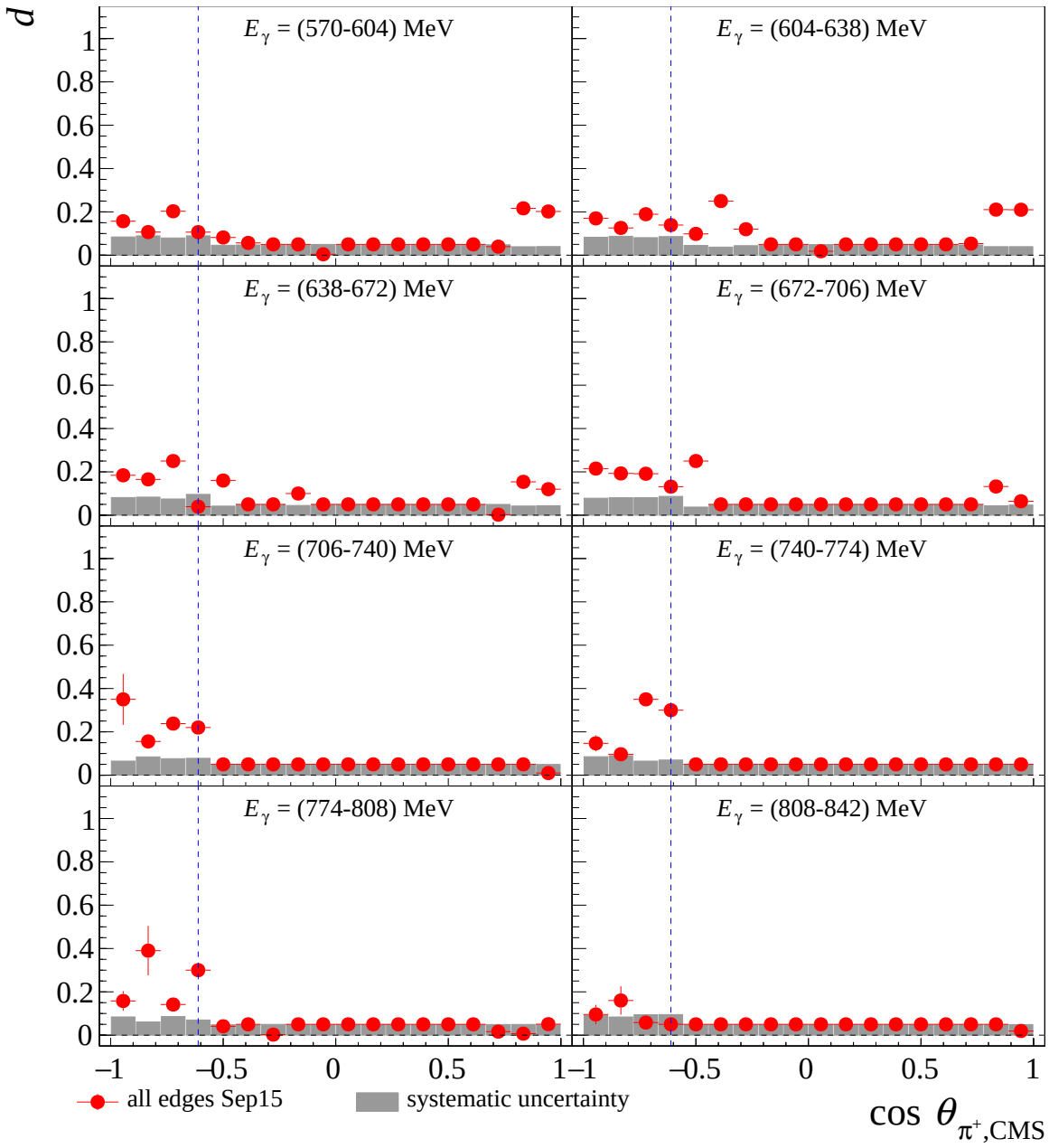

Fig. A.12: Comparison of the dilution factor of the 1 PED events for all beamtimes for the reaction $\vec{\gamma}\vec{p}\to n\pi^+$. Shown are the results of the dilution factor d of the 1 PED events as a function of $\cos\theta_{\pi^+,\mathrm{CMS}}$ for the beam photon energy from 570 MeV to 842 MeV for all beamtimes. The systematic uncertainty coming from the dilution factor d is indicated by the gray boxes. The blue vertical dashed line shows the position up to which point the 1 PED events are included in the extraction of the double polarization observable E.

A.5 Systematic Uncertainties of the Linearly Polarized Photons

Fig. A.13 shows the fitted coherent edge positions of the 450 MeV edge setting for the September 2015 beamtime. It is clearly visible that the edge was not completely stable at about 450 MeV edge. Similar behavior is seen on the right side for the 850 MeV edge of the May 2015 beamtime.

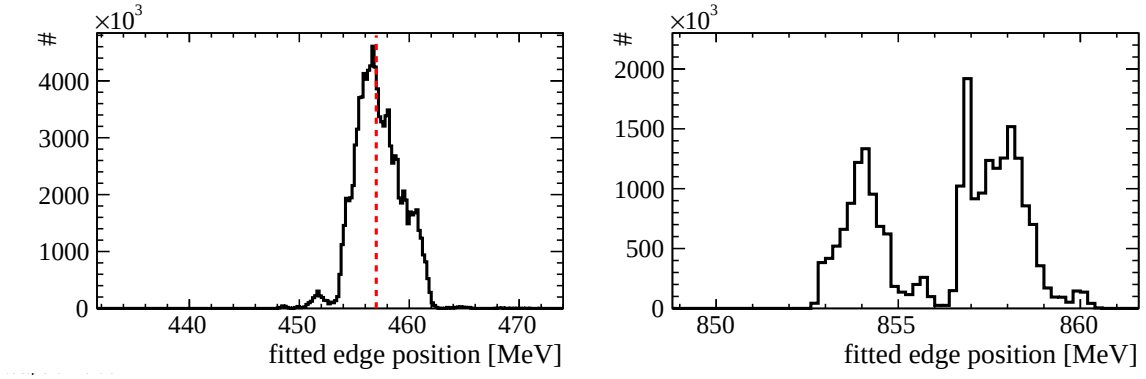

Fig. A.13: Fitted coherent edge positions of individual edge settings. Shown are the fitted coherent edge positions from the active coherent edge fitting for two edge settings. On the left side, the results are shown for the 450 MeV edge setting of the September 2015 beamtime whereas the left side shows the case for the 850 MeV edge setting of the Sep 15 beamtime. The red line on the left indicates the energy position where the data sets are split (see text).

To proof that the systematic uncertainties are well understood, the data of the 450 MeV edge setting is split into three data sets, namely:

all A data set which consists of all coherent edge positions of the 450 MeV edge setting.

low A data set which only takes the fitted coherent edge positions below 457 MeV.

high A data set which only takes the fitted coherent edges above 457 MeV.

For each set, the beam asymmetry Σ_B is determined with Eq. (8.37) for the same beam photon energy. As the asymmetry is determined for the same beam photon energy range, the only difference in the amplitude can be caused by a difference in the linear polarization degree. Thus, by determining the percentage deviation of the low/high data set to the all data set, the systematic uncertainties of the linear polarization degree can be studied. On the one hand, this test can show that different coherent edge positions produce the same results so that different coherent edge positions can be added up in the analysis. On the other hand, the test can prove that the active coherent edge fitting does not introduce any significant systematic uncertainties. Fig. A.14 shows as an example the result of both percentage deviations for the beam asymmetry Σ_B for the $n\pi^+$ channel for the beam photon energy E_γ from 400 MeV to 434 MeV [1]. On the left side, the percentage deviation to the low data set is shown whereas on the right for the high data set.

[1] The test was performed as well for other energy regions, other coherent edges and also for the $p\pi^0$ channel. All showed a similar result.

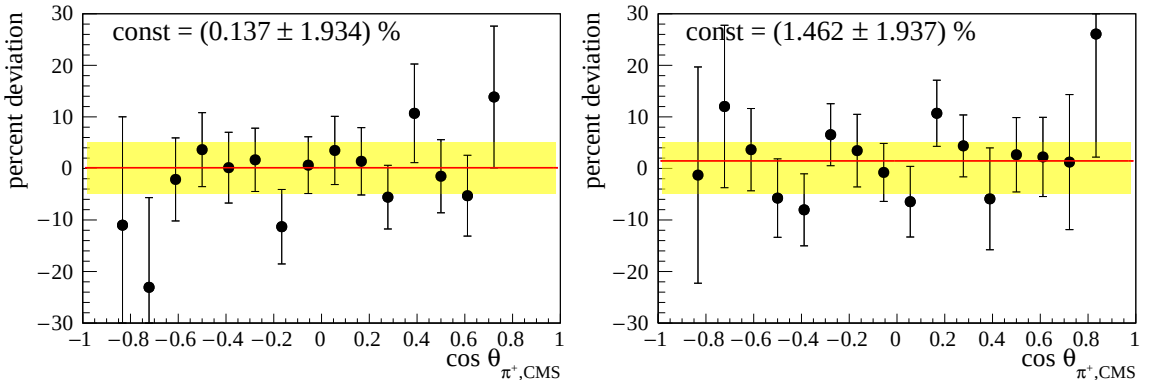

Fig. A.14: Percentage deviations between results with different coherent edges. Shown is on the left side the percentage deviation between the results of the beam asymmetry Σ_B of the low data set low to the all data set whereas on the right side for the high to the all data set. The red line indicates a linear fit to the percentage deviation and the yellow error band shows a 5% uncertainty band.

A linear fit was performed to the percent deviation which results in a percent deviation within its statistical uncertainties in the order of 3%. This is in perfect agreement with the assumed systematic uncertainties of about 5% which is indicated by the yellow narrow band. Note that the test was introduced and performed by C. Collicott of the A2 collaboration for a different data set as well and quoted similar results [139]. As has been discussed and shown in Sec. 8.2.1.1 the result can be again strengthen by Fig. A.15. Here, the effect of a manual shift of the coherent edge setting by $\pm$ 2 MeV is shown for an edge setting at 850 MeV. The resulting fractional error is here as well in the order of 3% which nicely agrees with the findings above and in Sec. 8.2.1.1.

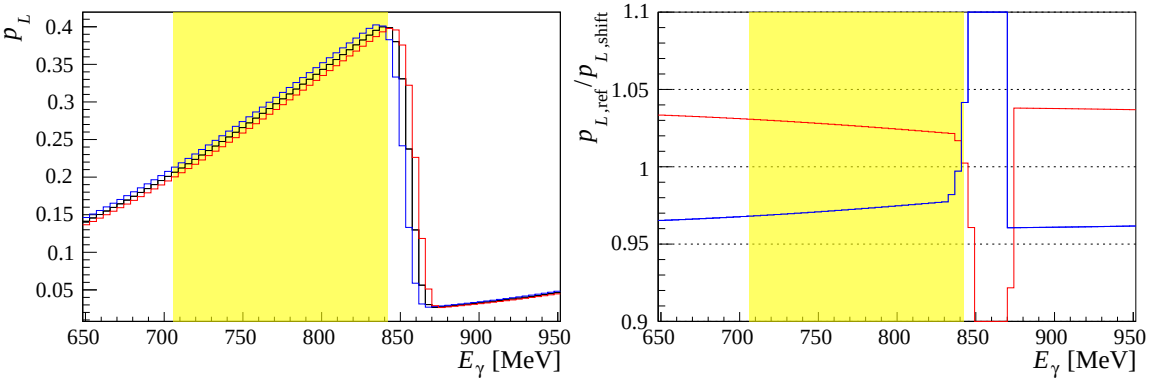

Fig. A.15: Systematic uncertainty test due to a shift of the coherent edge. The black line indicates the fitted coherent edge distribution for the edge position at 850 MeV. The red and blue line correspond to the distribution where the edge position were shifted by $\pm$ 2 MeV. On the right side, the fraction between the non-shifted polarization degrees and the shifted one is depicted. The yellow area depicts the energy range in which the polarization observables are extracted.

A.6 Studies on the Beam Polarization Offset Angle φ_0

To test the influence of the beam polarization offset angle φ_0 on the extracted polarization observable G (cf. Sec. 8.3.1.4), the determined offset angle was varied by $\pm 1^\circ$ and the observable were determined. Fig. A.16 presents the result for the three offset angles for the 850 MeV edge position of the May 2014 beamtime and for the 750 MeV of the May 2015 beamtime. For the May 2015 beamtime where both target polarization orientations are available, the results have a relative change in the order of about 2%. Only the χ^2/ndf got worse due to a not perfect $\sin 2\varphi_{\|}$ modulation anymore. The situation was different for the May 2014 beamtime. As G can not be determined by the amplitude of the $\sin 2\varphi_{\|}$ modulation, the relative changes between the three offset angle setting were significant. As expected, the shift of the beam polarization offset angle in either positive or negative direction resulted in a similar shift of the G results. Together with the already mentioned problems of the diamond crystal alignment, it has been decided to reject the May 2014 beamtime for the extraction of the double polarization observable G.

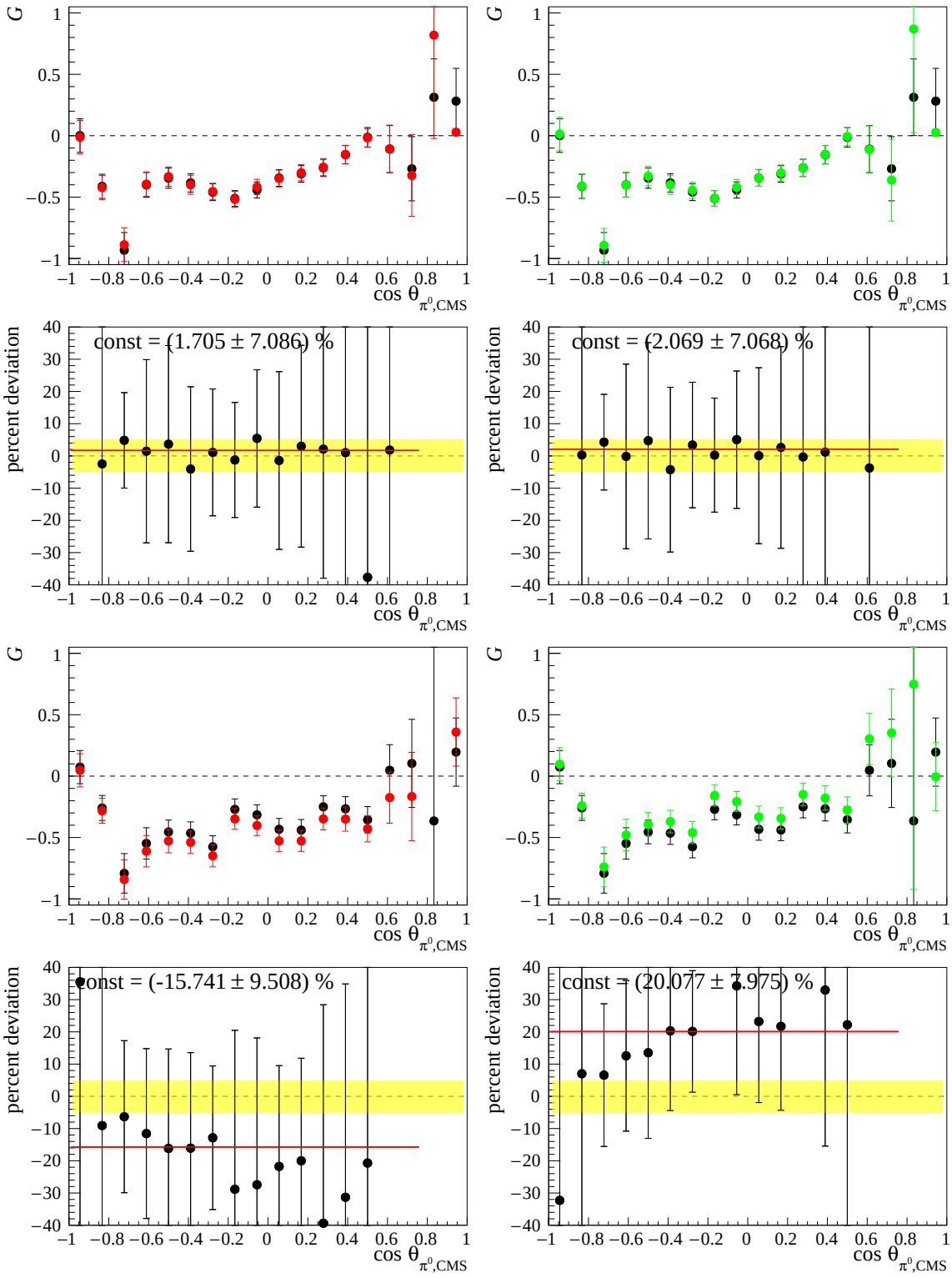

Fig. A.16: Systematic uncertainty test due to a shift of beam polarization offset angle. In the first and third row, the black points indicate the results for the double polarization observable G which have been determined with the extracted beam offset angle. The red and green points correspond to the results where the offset angle was shifted by $\pm$ 1°, respectively. In the second and fourth row, the fraction between the non-shifted offset angle and the shifted one is depicted. The yellow area depicts an uncertainty band of 5%. The first and third row corresponds to the results of the May 2015 beamtime for the coherent edge at 750 MeV and a beam photon energy $E_\gamma = (706 - 740)$ MeV while the second and fourth row to the May 2014 beamtime for the coherent edge at 750 MeV and a beam photon energy $E_\gamma = (774 - 808)$ MeV.

A.7 Results for the Beam Asymmetry Σ_B (Monte Carlo Simulations)

The results of the Monte Carlo studies for the beam asymmetry Σ_B are presented in Fig. A.17 and Fig. A.18. More details are presented within the Sec. 8.3.3.

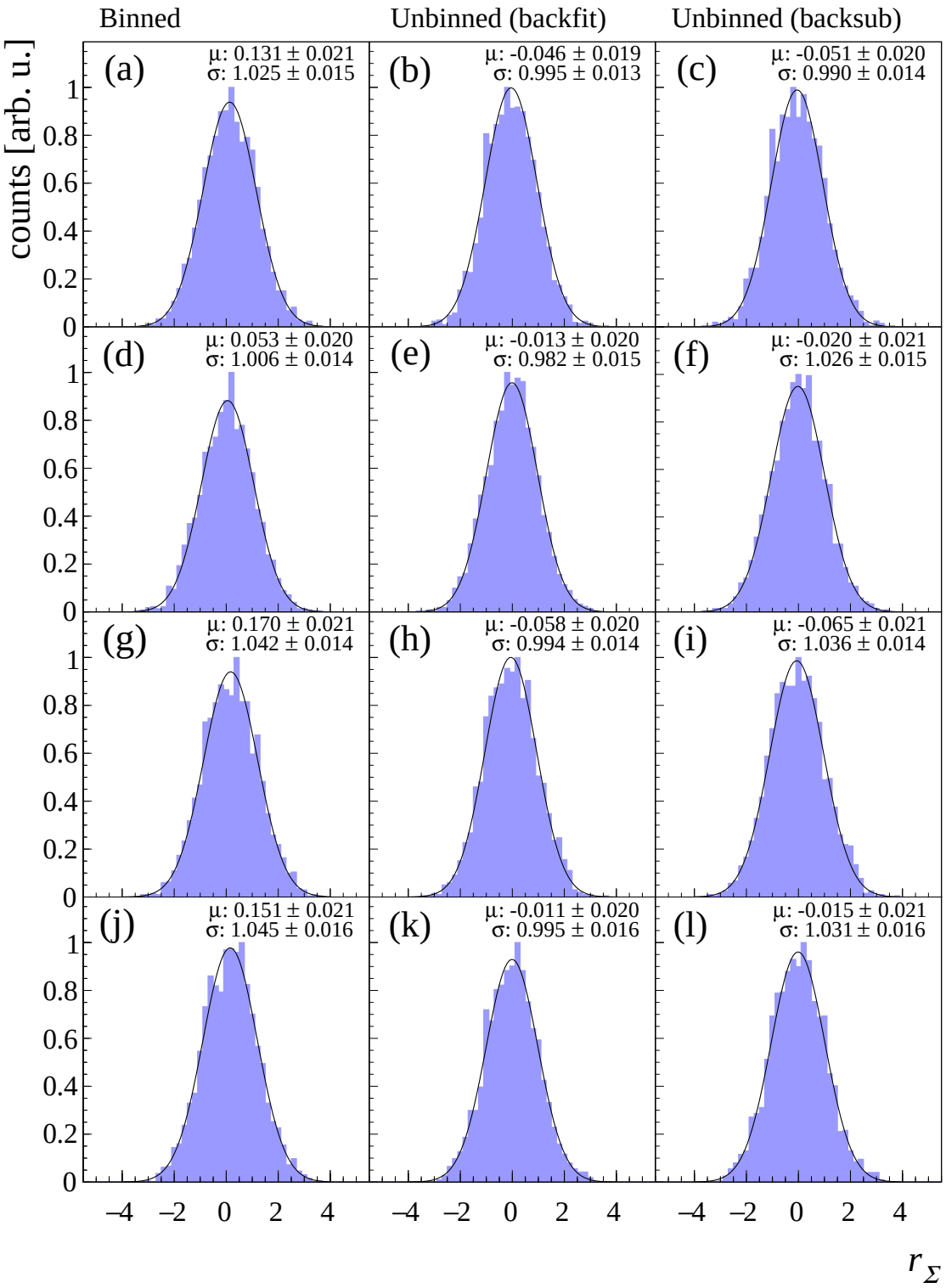

Fig. A.17: Normalized residuals for the results of the beam asymmetry Σ_B for the different Toy MC samples. Shown are the residuals for the different MC samples, defined in Tab. 8.4, and the different extraction methods. Hereby, the row number indicates the MC sample number and the column the three extraction methods. All distributions are in agreement with a normal distribution.

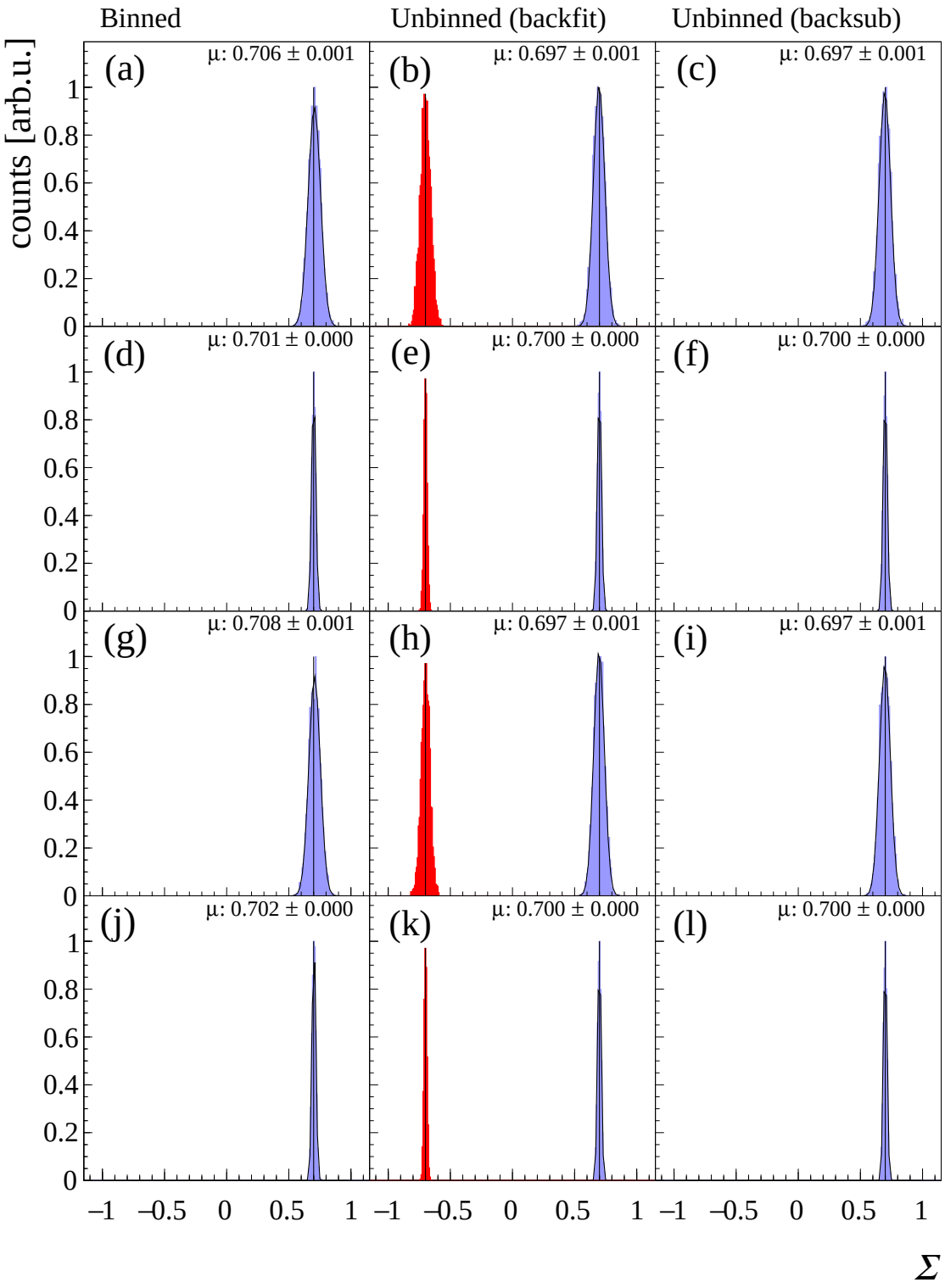

Fig. A.18: Results of the beam asymmetry Σ_B for the different Toy MC samples. Shown are the extracted polarization observable for the different MC samples, defined in Tab. 8.4, and the different extraction methods. Hereby, the row number indicates the MC sample number and the column the three extraction methods. The extracted polarization observables for the signal events (blue) are distributed around their input value of 0.7 and the extracted once for the background events (red) around their input value of -0.7.

A.8 Results for the Beam Asymmetry Σ_B

The results for the beam asymmetry Σ_B, using the likelihood function defined in Eq. (8.49), is shown in Fig. A.19 and Fig. A.20 for the reaction $\vec{\gamma}\vec{p} \to p\pi^0$ where in Fig. A.23 and A.24 for the reaction $\vec{\gamma}\vec{p} \to n\pi^+$. They are indicated by the black points together with their statistical uncertainties and have been determined in a beam photon energy range from 230 MeV to 842 MeV with a 34 MeV broad energy bin window and 18 angular bins. The gray box presents the systematic uncertainties. Note again that the presented results are an effective beam asymmetry since it not only contains reactions on unbound reactions but also unwanted reactions on bound protons:

$$\Sigma_B = d \cdot \Sigma_{\text{unbound}} + (1-d) \cdot \Sigma_{\text{bound}}. \tag{A.1}$$

However, as Σ_{bound} behaves similar to Σ_{unbound} except for additional smearing in energy and angle due to the additional Fermi motion, a qualitative comparison with other high-precision data is acceptable. Nevertheless, the comparison should be treated with caution, especially in kinematic regions where huge variations in the results with the energy or angle are obtained. Finally, please keep in mind that the dilution factor for the 2 PED events drops down to about 0.1 and thus the assumption $\Sigma_B \approx \Sigma_{\text{unbound}}$ is not valid anymore.

The results for the $\vec{\gamma}\vec{p} \to p\pi^0$ are compared to recent data for the beam asymmetry off unbound protons which are given by the A2 collaboration in red in Fig. A.19 [57], the A2 collaboration again in blue [55, 56], and the GRAAL collaboration in green [53, 66]. The CBELSA/TAPS data in Fig. A.20 are results on a butanol target and thus are also results for the effective beam asymmetry Σ_B [64, 45]. A final problem arises in the covered beam photon energy range for the individual energy bins and thus their deviations to each other. These vary quite significantly. Nevertheless, an overall good agreement between the new A2 data and all recently published data is given. To compensate the effect of the different energy binning, the results are as well compared as a function of the mean value of the beam energy window in Fig. A.21 and Fig. A.22. Thereby, the $\cos\theta_{\pi^0,\text{CMS}}$ bin of all published data was selected in such a way that the minimum distance to the corresponding bin of the new A2 data bin window is chosen. Note that a maximum deviation of 0.06 was accepted. In this representation, all data agree very good with each other. Major differences occur only in the region where the new data are dominated by the 2 PED events.

The results for the $\vec{\gamma}\vec{p} \to n\pi^+$ are compared to data from the A2 collaboration in red [67, 57], and the Graal collaboration in green [65, 66]. Although both data set were measured on a liquid hydrogen target and thus obtained the correct beam asymmetry on unbound protons, an overall very good agreement is given. A representation as a function of the mean value of the beam energy window is in this case not feasible as the previous data do not provide a sufficient angular coverage.

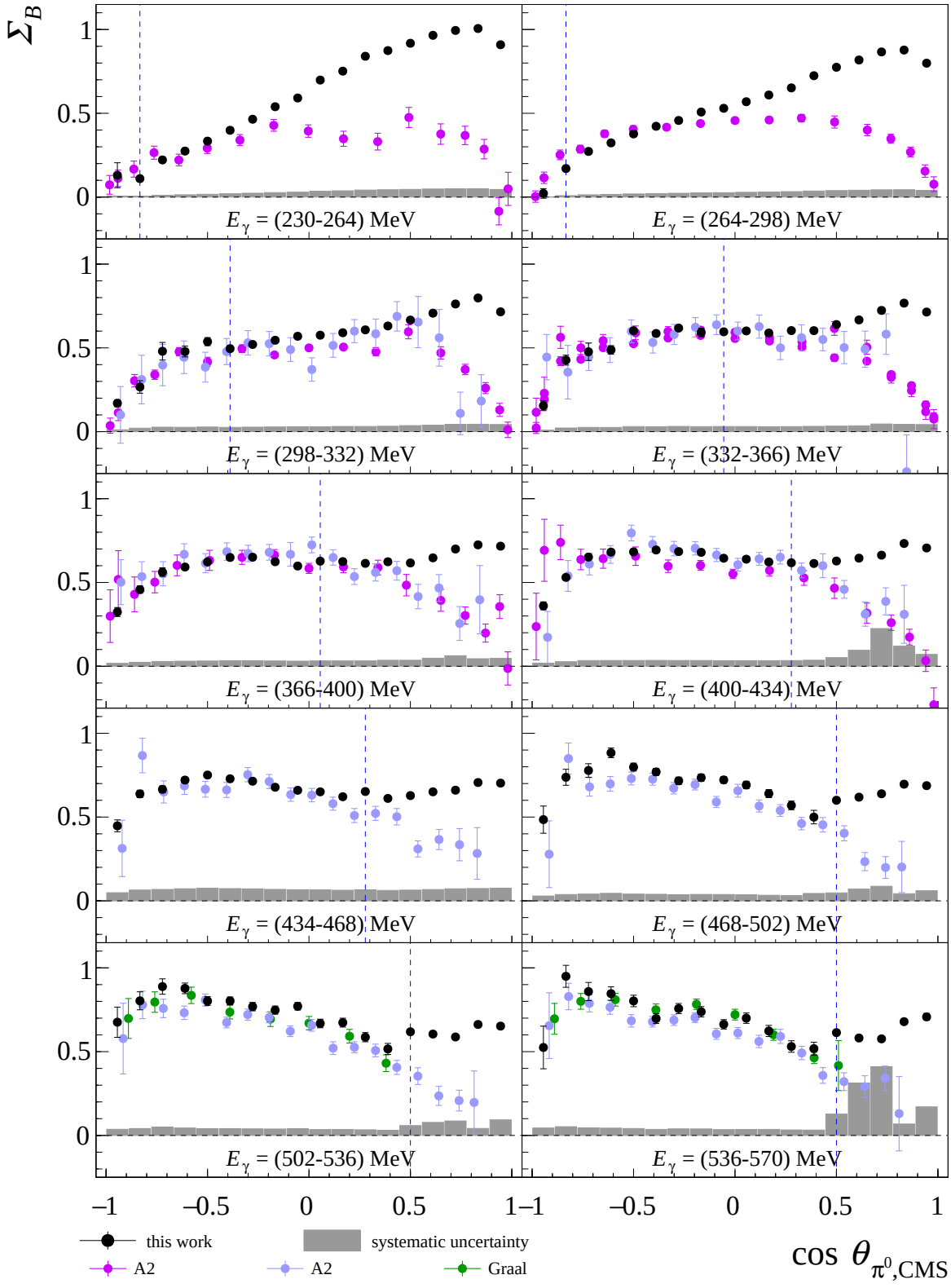

Fig. A.19: Comparison beam asymmetry Σ_B results with previous data for $\vec{\gamma}\vec{p}\to p\pi^0$. Shown are the results of the double polarization observable G as a function of $\cos\theta_{\pi^0,\mathrm{CMS}}$ for the beam photon energy from 230 MeV to 570 MeV. The black points represent the results of the new A2 data together with their statistical uncertainties whereas the gray boxes show the systematic uncertainties. The new A2 data are compared to the recent database which consists of the A2/GDH data [57] in violet, the A2 data in blue [55, 56], and the Graal data [53, 66] in green.

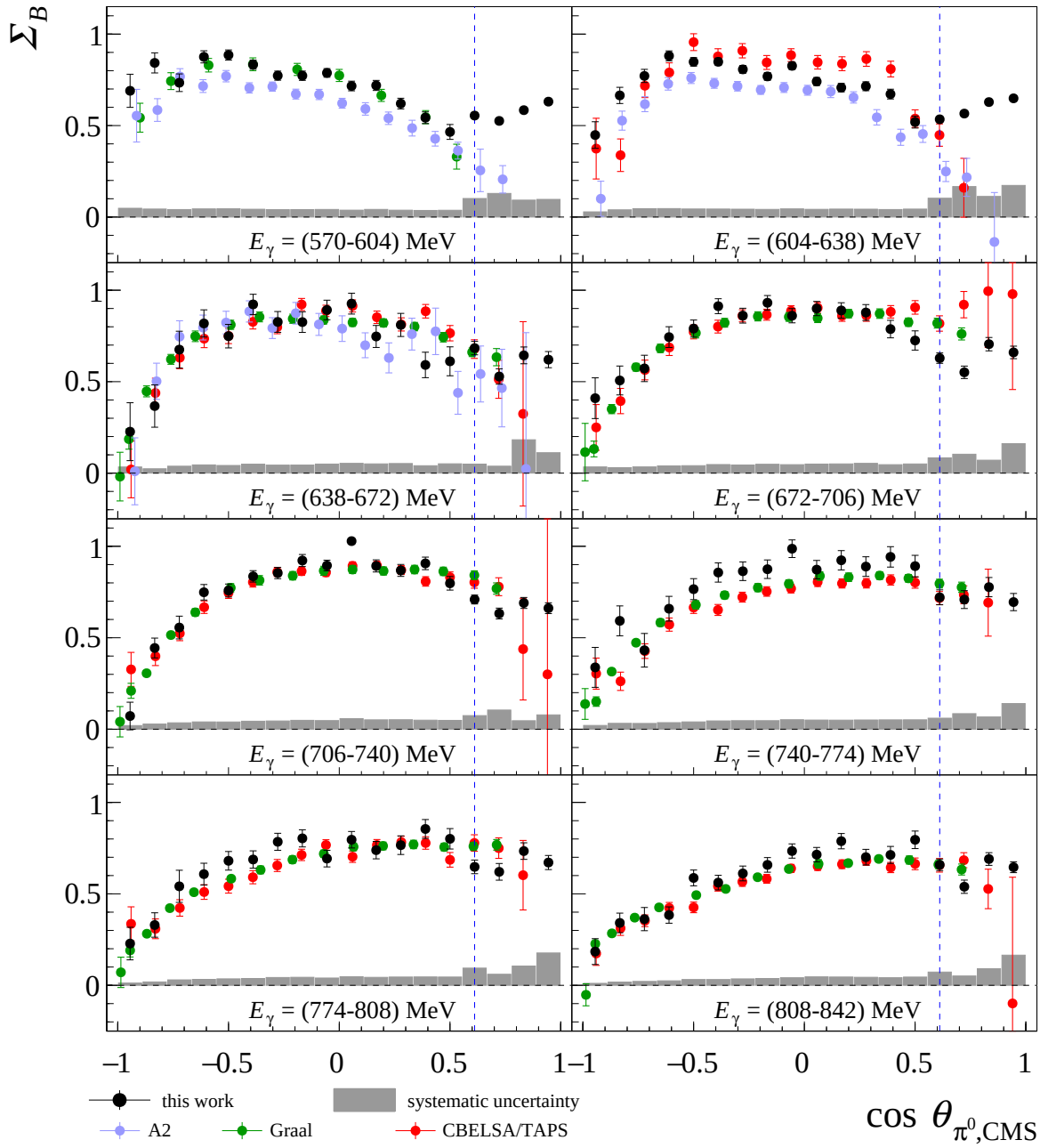

Fig. A.20: Comparison of the beam asymmetry Σ_B results with previous data for $\vec{\gamma}\vec{p}\to p\pi^0$. Shown are the results of the double polarization observable G as a function of $\cos\theta_{\pi^0,\mathrm{CMS}}$ for the beam photon energy from 570 MeV to 842 MeV. The black points represent the results of the new A2 data together with their statistical uncertainties whereas the gray boxes show the systematic uncertainties. The new A2 data are compared to the recent database which consists of the A2 data in blue [55, 56], the Graal data [53, 66] in green, and the CBELSA/TAPS data in red [64, 45].

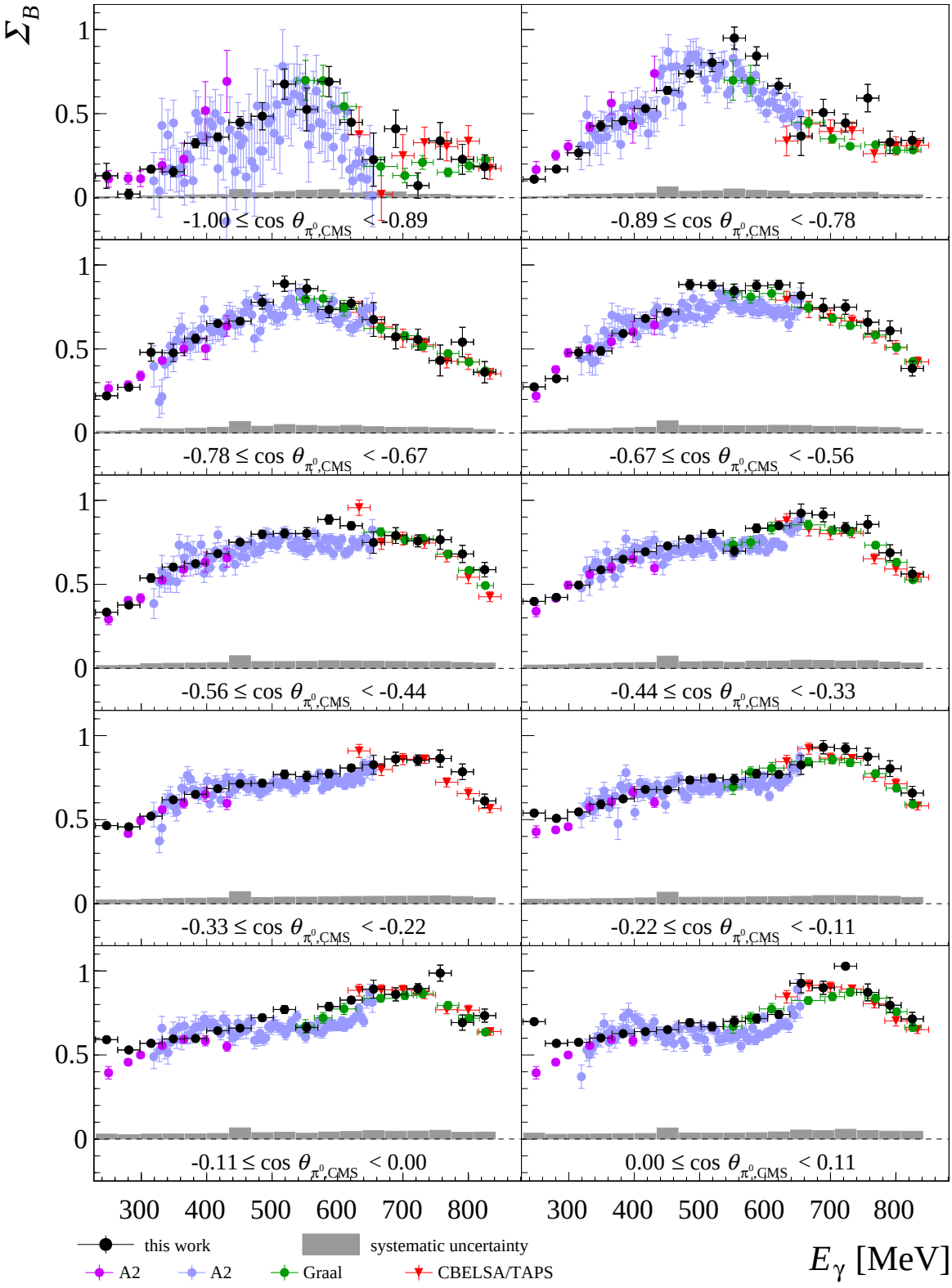

Fig. A.21: Comparison of the of the beam asymmetry Σ_B results with previous data for $\vec{\gamma}\vec{p}\to p\pi^0$ as a function of the beam photon energy E_γ. Shown are the results of the of the beam asymmetry Σ_B as a function of the mean value of the beam photon energy bin E_γ for the kinematic range $-1.00 \leq \cos\theta_{\pi^0,\mathrm{CMS}} < 0.11$. The black points represent the results of the new A2 data together with their statistical uncertainties whereas the gray boxes show the systematic uncertainties. The new A2 data are compared to the recent database which consists of the A2/GDH data in violet [57], the A2 data in blue [55, 56], the Graal data [53, 66] in green, and the CBELSA/TAPS data in red [64, 45].

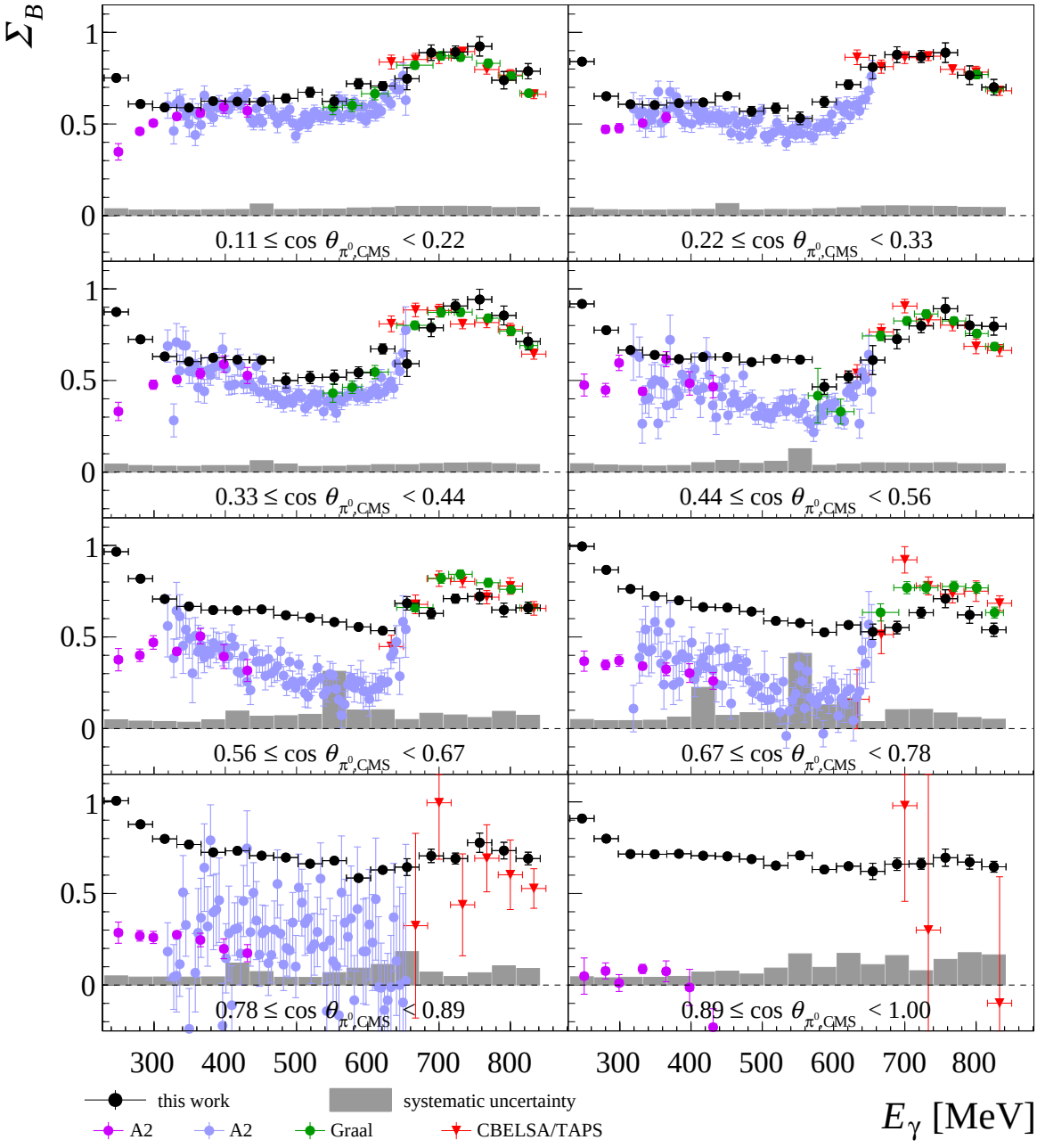

Fig. A.22: Comparison of the of the beam asymmetry Σ_B results with previous data for $\vec{\gamma}\vec{p}\to p\pi^0$ as a function of the beam photon energy E_γ. Shown are the results of the of the beam asymmetry Σ_B as a function of the mean value of the beam photon energy bin E_γ for the kinematic range $0.11 < \cos\theta_{\pi^0,\mathrm{CMS}} \leq 1.00$. The black points represent the results of the new A2 data together with their statistical uncertainties whereas the gray boxes show the systematic uncertainties. The new A2 data are compared to the recent database which consists of the A2/GDH data in violet [57], the A2 data in blue [55, 56], the Graal data [53, 66] in green, and the CBELSA/TAPS data in red [64, 45].

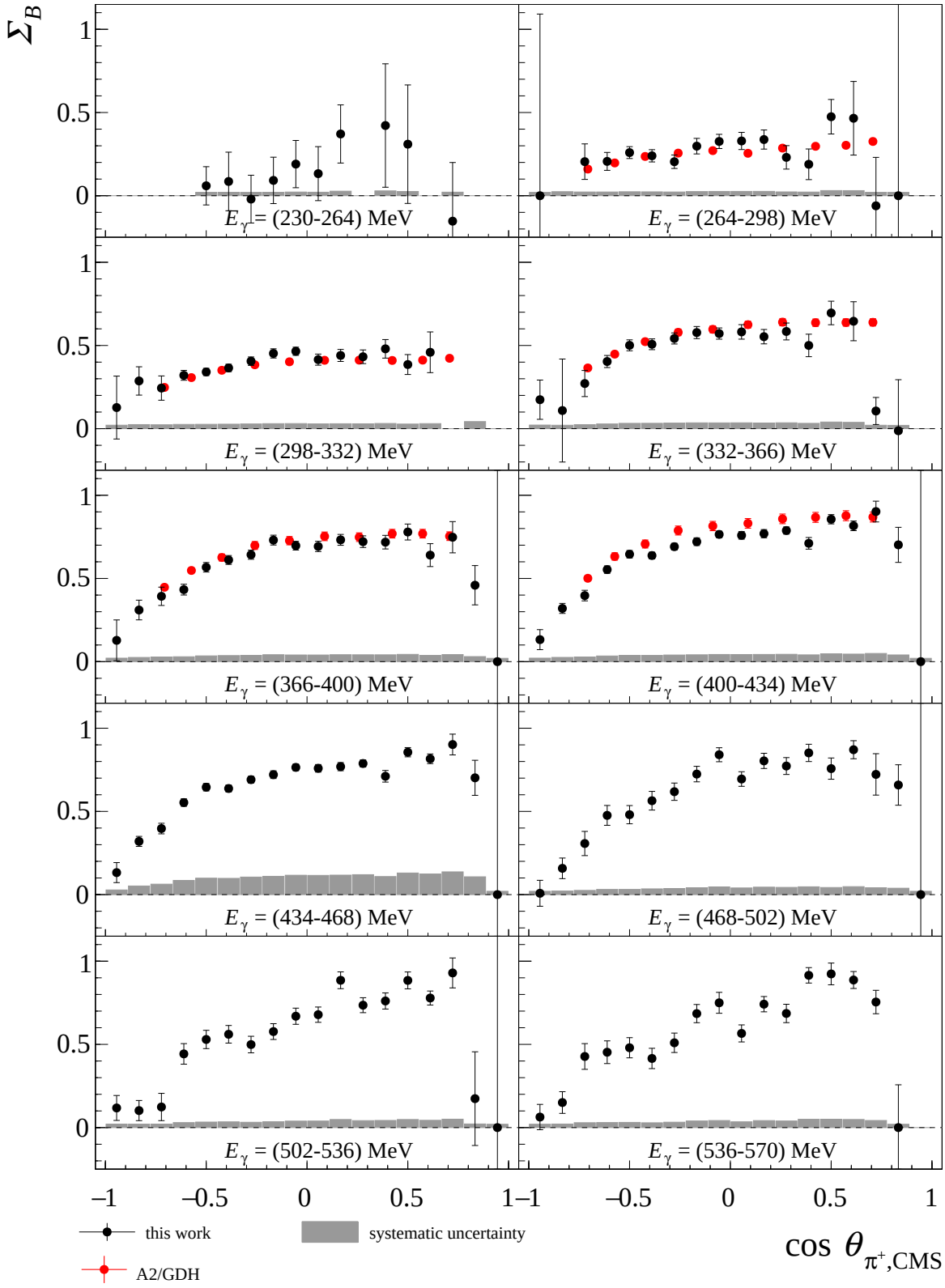

Fig. A.23: Comparison beam asymmetry Σ_B results with previous data for $\vec{\gamma}\vec{p}\to n\pi^+$. Shown are the results of the double polarization observable G as a function of $\cos\theta_{\pi^+,\mathrm{CMS}}$ for the beam photon energy from 230 MeV to 570 MeV. The black points represent the results of the new A2 data together with their statistical uncertainties whereas the gray boxes show the systematic uncertainties. The new A2 data are compared to the recent database which consists of data of the A2 collaboration in red [67, 57], and the Graal collaboration in green [65, 66].

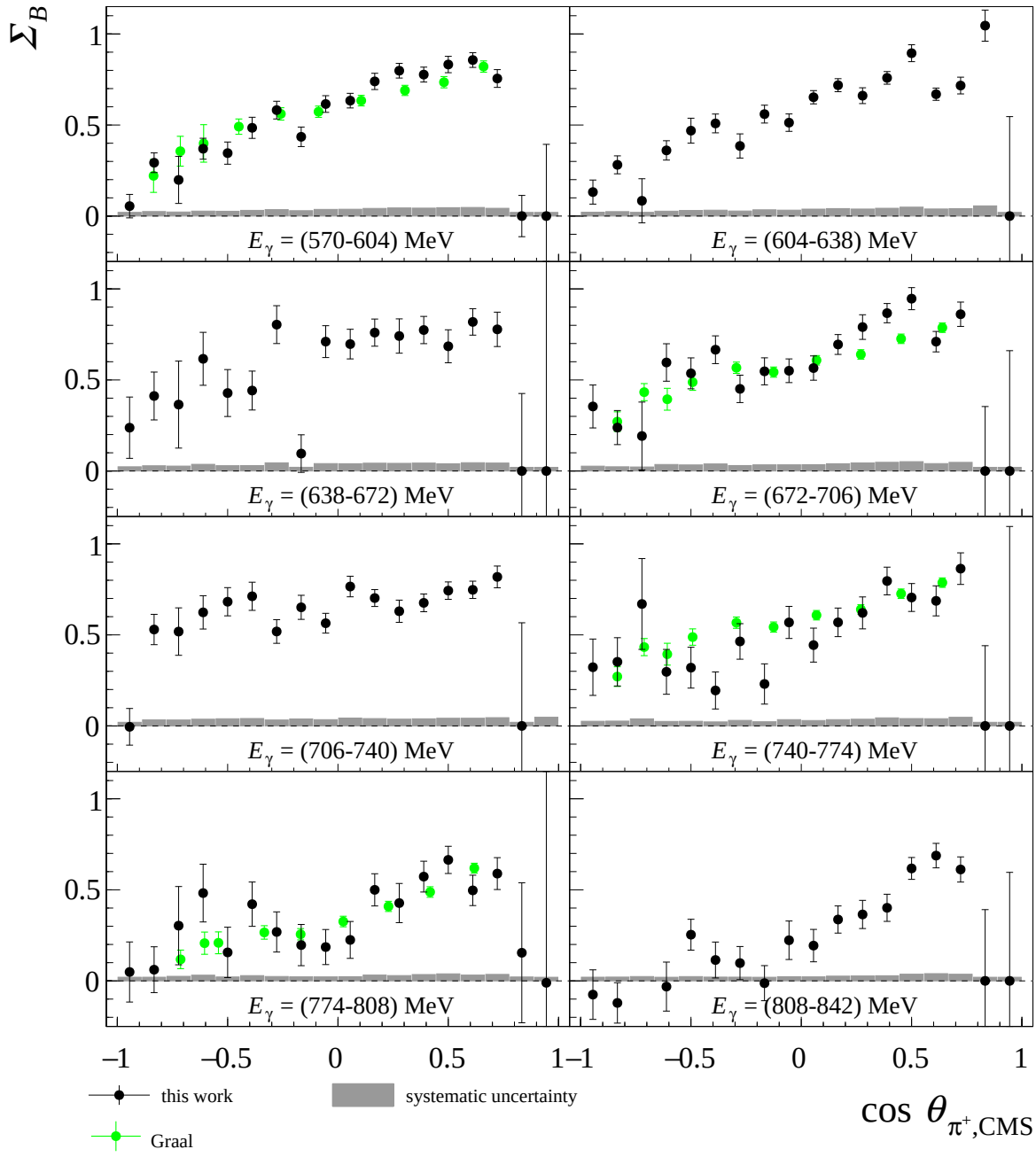

Fig. A.24: Comparison of the beam asymmetry Σ_B results with previous data for $\vec{\gamma}\vec{p}\to n\pi^+$. Shown are the results of the double polarization observable G as a function of $\cos\theta_{\pi^+,\mathrm{CMS}}$ for the beam photon energy from 570 MeV to 842 MeV. The black points represent the results of the new A2 data together with their statistical uncertainties whereas the gray boxes show the systematic uncertainties. The new A2 data are compared to the recent database which consists of data of the A2 collaboration in red [67, 57], and the Graal collaboration in green [65, 66].

A.9 Comparison of the Polarization Observable Results for different event patterns

For the $n\pi^+$ reactions, the double polarization observables G and E were extracted for the 1 PED and 2 PED events separately. Fig. A.25 presents the results for both event patterns and the combined results (cf. Sec. 8.3.5) for the double polarization observable G while Fig. A.26 and Fig. A.27 for the double polarization observable E.

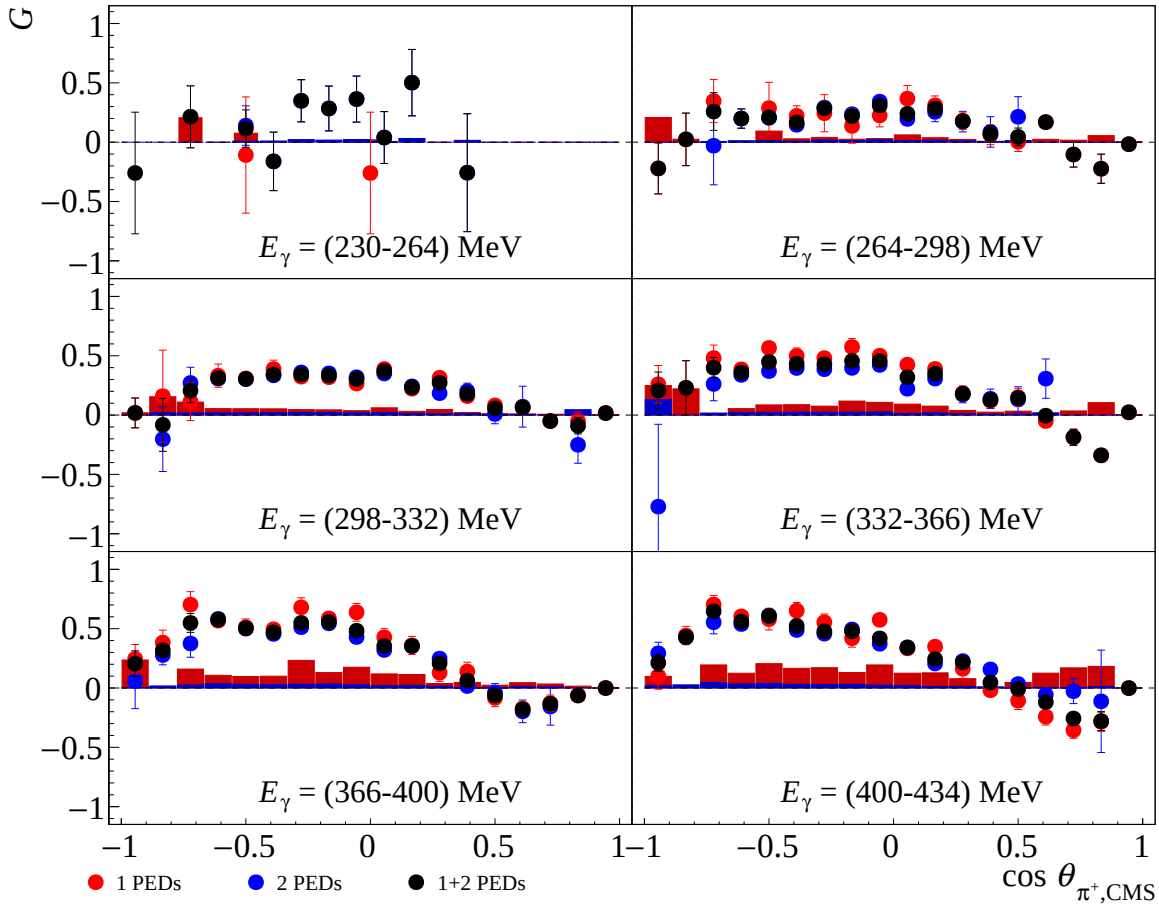

Fig. A.25: Comparison of the results of the different event patterns for the double polarization observable G for the reaction $\vec{\gamma}\vec{p}\to n\pi^+$. The results of the double polarization observable G are shown as a function of $\cos\theta_{\pi^+,\mathrm{CMS}}$ for the beam photon energy from 230 MeV to 434 MeV. They are plotted as dots together with their statistical uncertainties whereas the boxes represent the systematic uncertainties. Hereby, the red dots correspond to the 1 PED events, the blue dots to the 2 PED events, and the combination of both to the black dots.

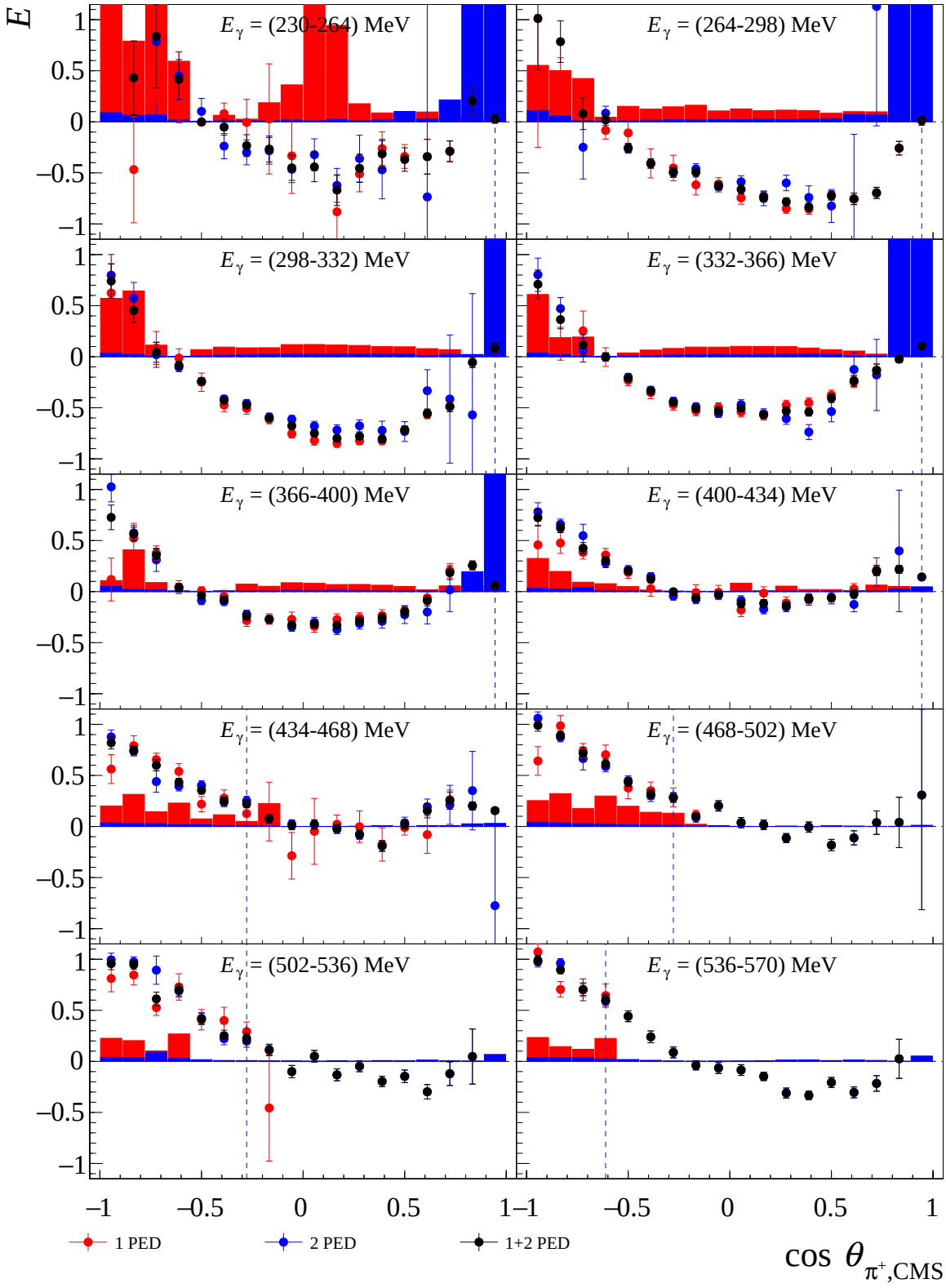

Fig. A.26: Comparison of the results of the different event patterns for the double polarization observable *E* for the reaction $\vec{\gamma}\vec{p}\to n\pi^+$. The results of the double polarization observable E are shown as a function of $\cos\theta_{\pi^+,\mathrm{CMS}}$ for the beam photon energy from 230 MeV to 570 MeV. They are plotted as dots together with their statistical uncertainties whereas the boxes represent the systematic uncertainties. Hereby, the red dots correspond to the 1 PED events, the blue dots to the 2 PED events, and the combination of both to the black dots. The blue dashed line indicates the position up to which point the 1 PED events are added to the 2 PED events

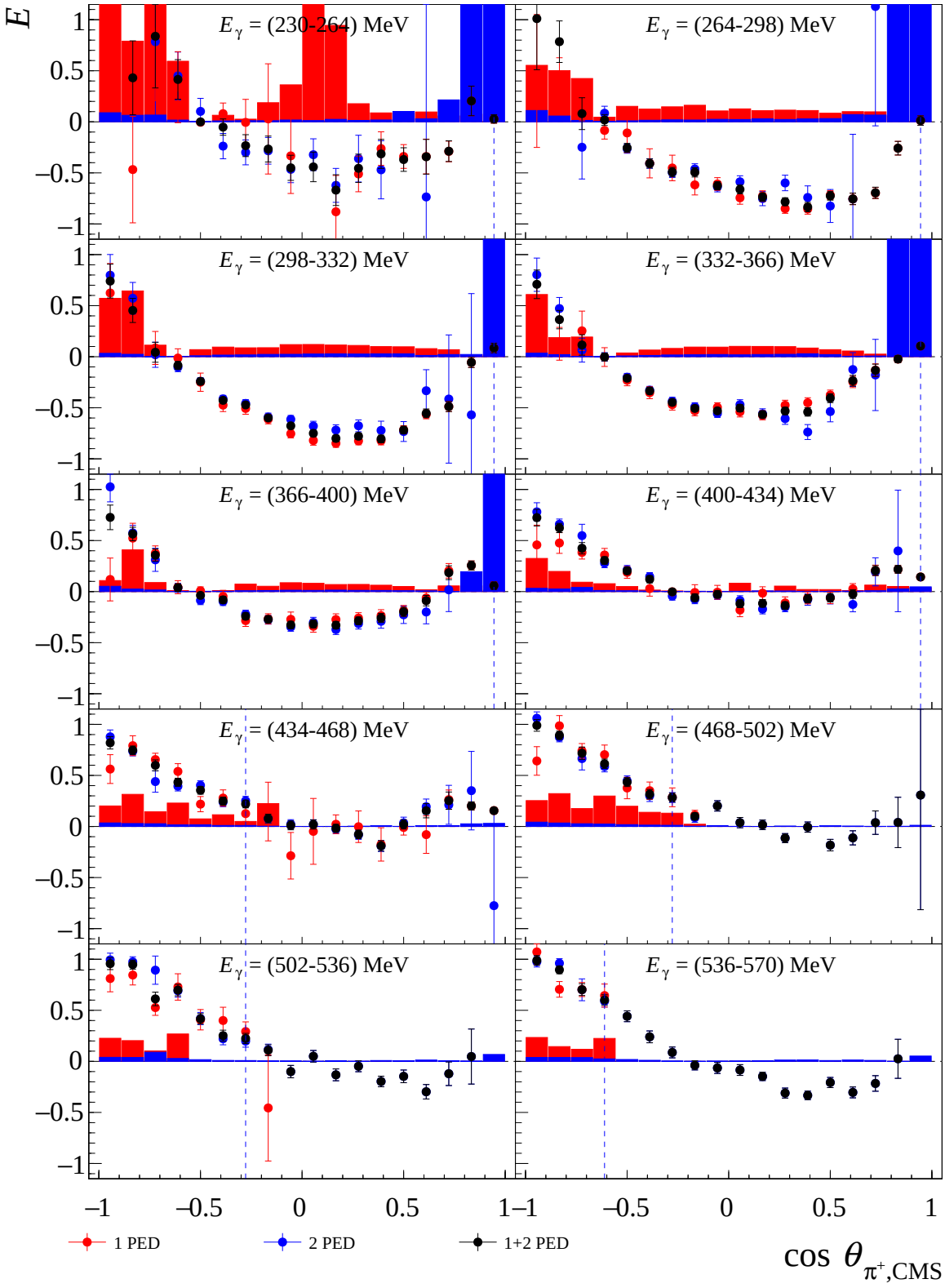

Fig. A.27: Comparison of the results of the different event patterns for the double polarization observable *E* for the reaction $\vec{\gamma}\vec{p}\to n\pi^+$. The results of the double polarization observable E are shown as a function of $\cos\theta_{\pi^+,\mathrm{CMS}}$ for the beam photon energy from 570 MeV to 842 MeV. They are plotted as dots together with their statistical uncertainties whereas the boxes represent the systematic uncertainties. Hereby, the red dots correspond to the 1 PED events, the blue dots to the 2 PED events, and the combination of both to the black dots. The blue dashed line indicates the position up to which point the 1 PED events are added to the 2 PED events.

A.10 Double Polarization Observable *E* for higher beam photon energies

In Sec. 9.2.2 it has been found that the extracted expansion coefficients which have been extracted with the CLAS data do not agree at all with the BnGa-2016 solution. Although the analysis of the A2 data was only optimized up to a beam photon energy of 842 MeV, the observable was nevertheless extracted for higher energies as well which is shown in Fig. A.28. Note that these results are very preliminary and thus will only give a rough comparison with the CLAS data at higher energies. These are shown in the Fig. A.29 up to Fig. A.31.

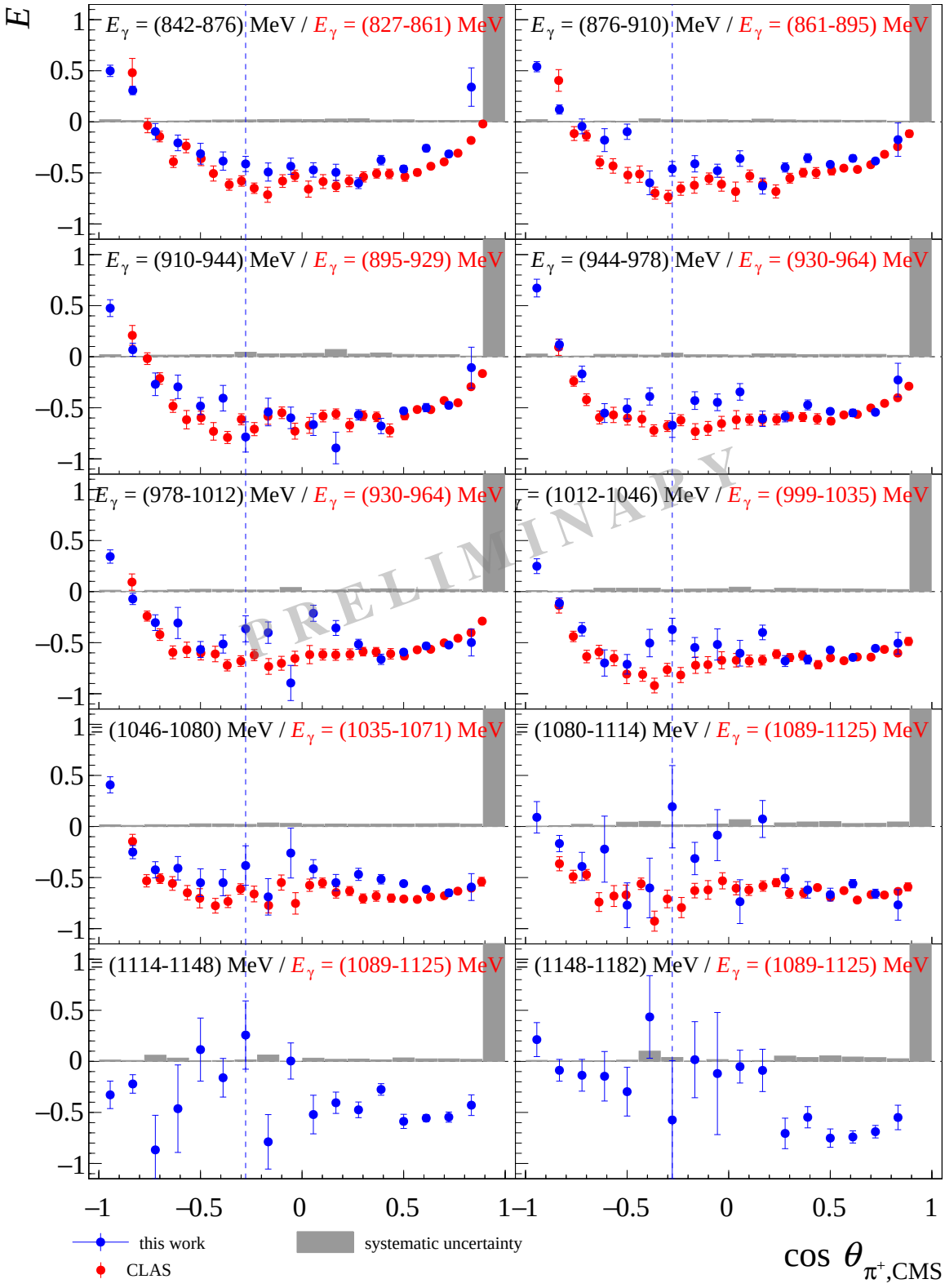

Fig. A.28: Comparison of the double polarization observable E results with previous data for $\vec{\gamma}\vec{p}\to n\pi^+$. Shown are the results of the double polarization observable E as a function of $\cos\theta_{\pi^+,\mathrm{CMS}}$ for the beam photon energy from 842 MeV to 1182 MeV. The blue points represent the results of the new A2 data together with their statistical uncertainties whereas the red points the CLAS data [68]. The blue dashed line indicates the position up to which point the 1 PED events are added to the 2 PED events whereas the gray boxes shows the systematic uncertainties.

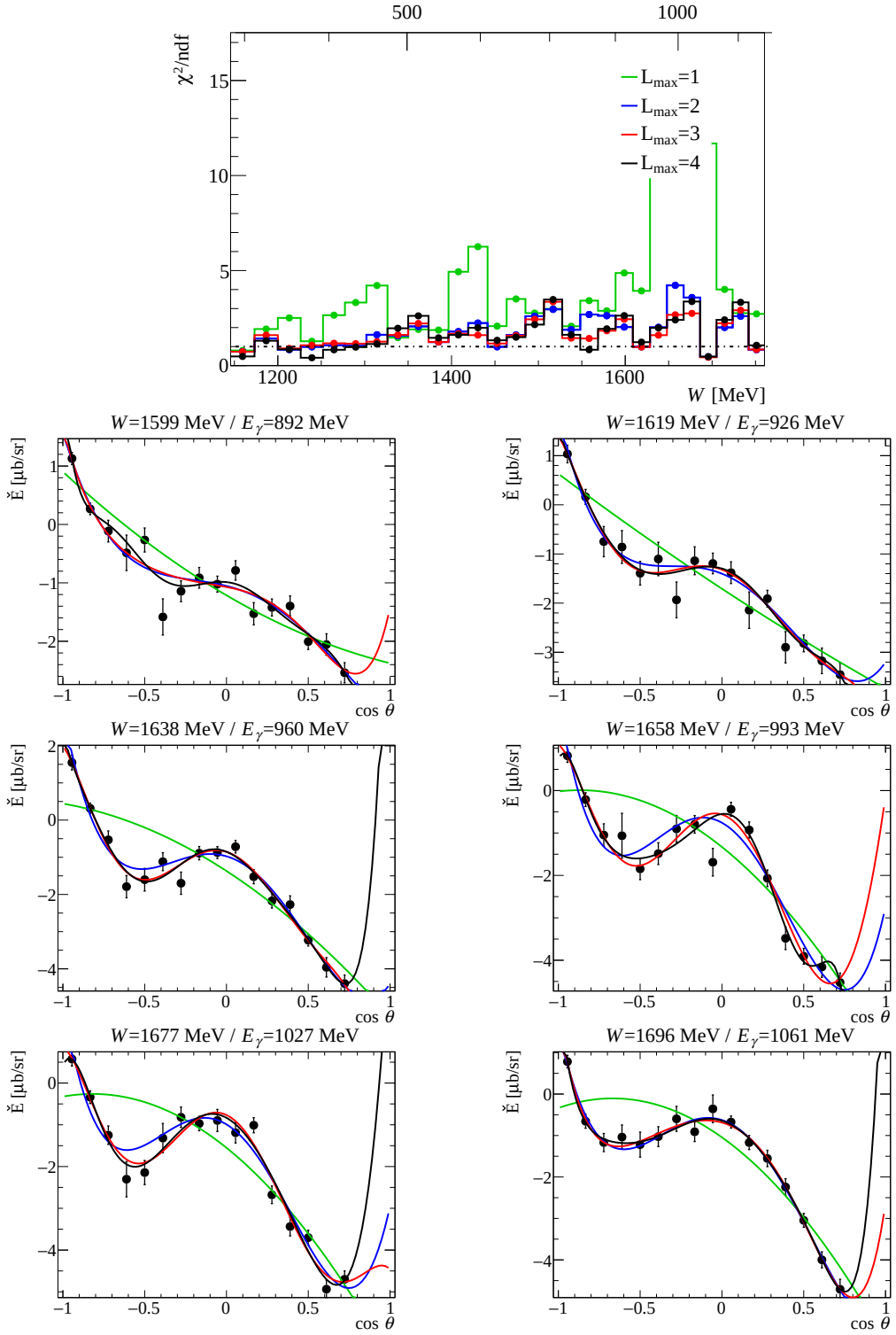

Fig. A.29: Associated Legendre polynomial fits to the profile function Ě for $\vec{\gamma}\vec{p}\to n\pi^+$ with higher energies. The profile function Ě as a function of the kinematic variable $\cos\theta_{\pi^+,\mathrm{CMS}}$ were fitted with associated Legendre polynomials which are described by Eq. (9.2). The fits have been truncated at different L_{max}. Hereby, the green line corresponds to $L_{max} = 1$, the blue line to $L_{max} = 2$, the red line to $L_{max} = 3$, and the black line to $L_{max} = 4$. As an illustration of the fits, six profile functions (black points) are presented in the second to fourth row together with the different truncated L_{max}-fits. The corresponding χ^2/ndf of all fits is depicted in the top row as a function of the center of mass energy W and the beam photon energy E_γ.

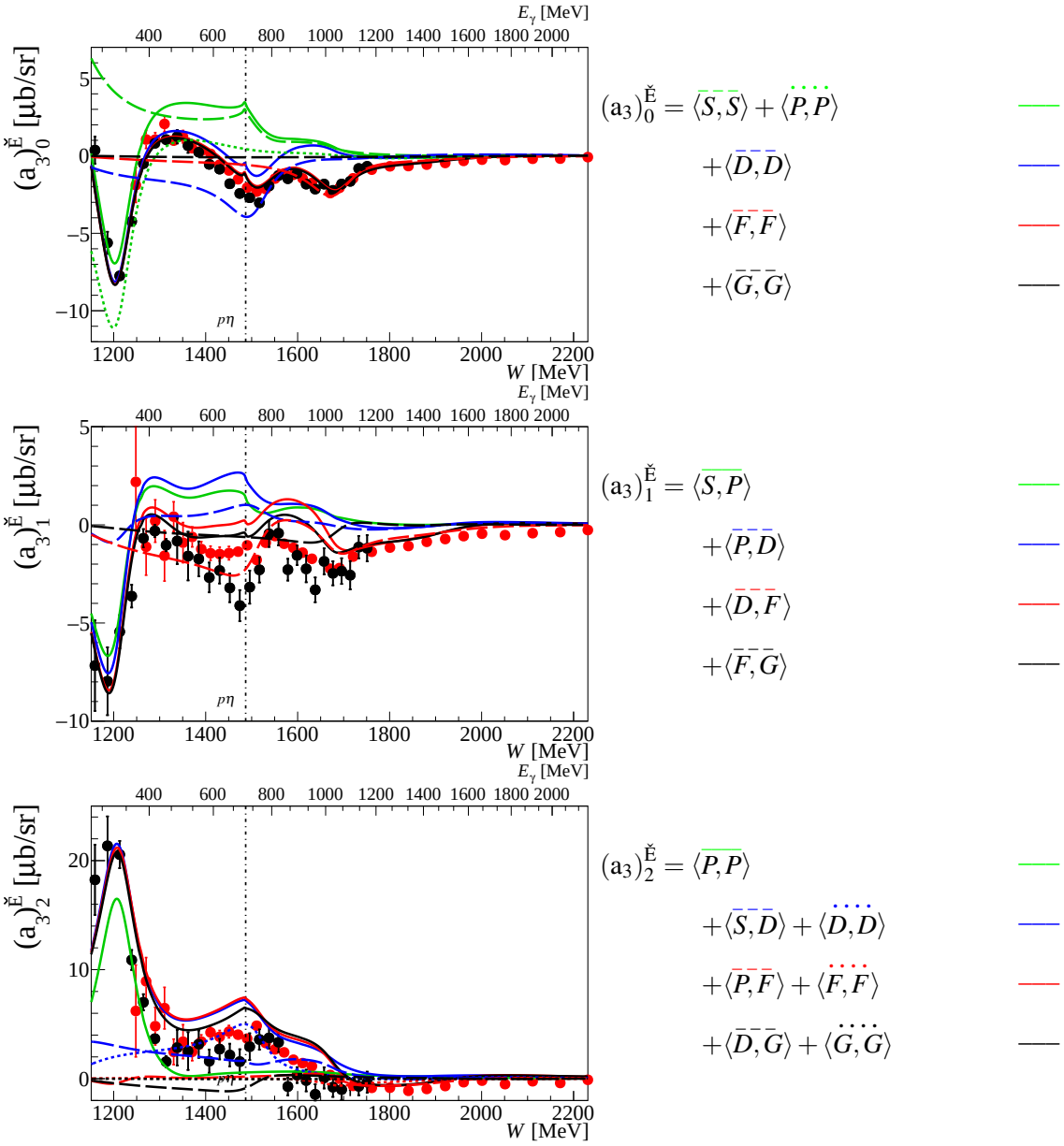

Fig. A.30: Comparison of the fit coefficients $(a_3)_{0\cdots2}^{\check{E}}$ for $\vec{\gamma}\vec{p}\to n\pi^+$ as a function of the higher center of mass energy W. The resulting fit coefficients, indicated by the black points, are plotted on the left side together with the obtained once using the CLAS data in red [68]. They are compared to continuous curves which have been determined from the multipole solutions of the BnGa2016 PWA solution [46]. The solution have been truncated at different L_{max}. Hereby, the green solid curve corresponds to $L_{max} = 1$, the blue solid curve to $L_{max} = 2$, the red solid curve to $L_{max} = 3$, and the black solid curve to $L_{max} = 4$. On the right panel, the contributing partial wave interference terms are given for the different L_{max} values. Thereby, $L_{max} = 1$ only contains the contribution of S-and P-waves, $L_{max} = 2$ additionally D-waves, $L_{max} = 3$ additionally F-waves, and $L_{max} = 4$ additionally G-waves. The individual interference terms are included as well and are indicated by their color and dashed or dotted curves. The dashed-dotted line marks the photoproduction threshold of the $p\eta$ channel.

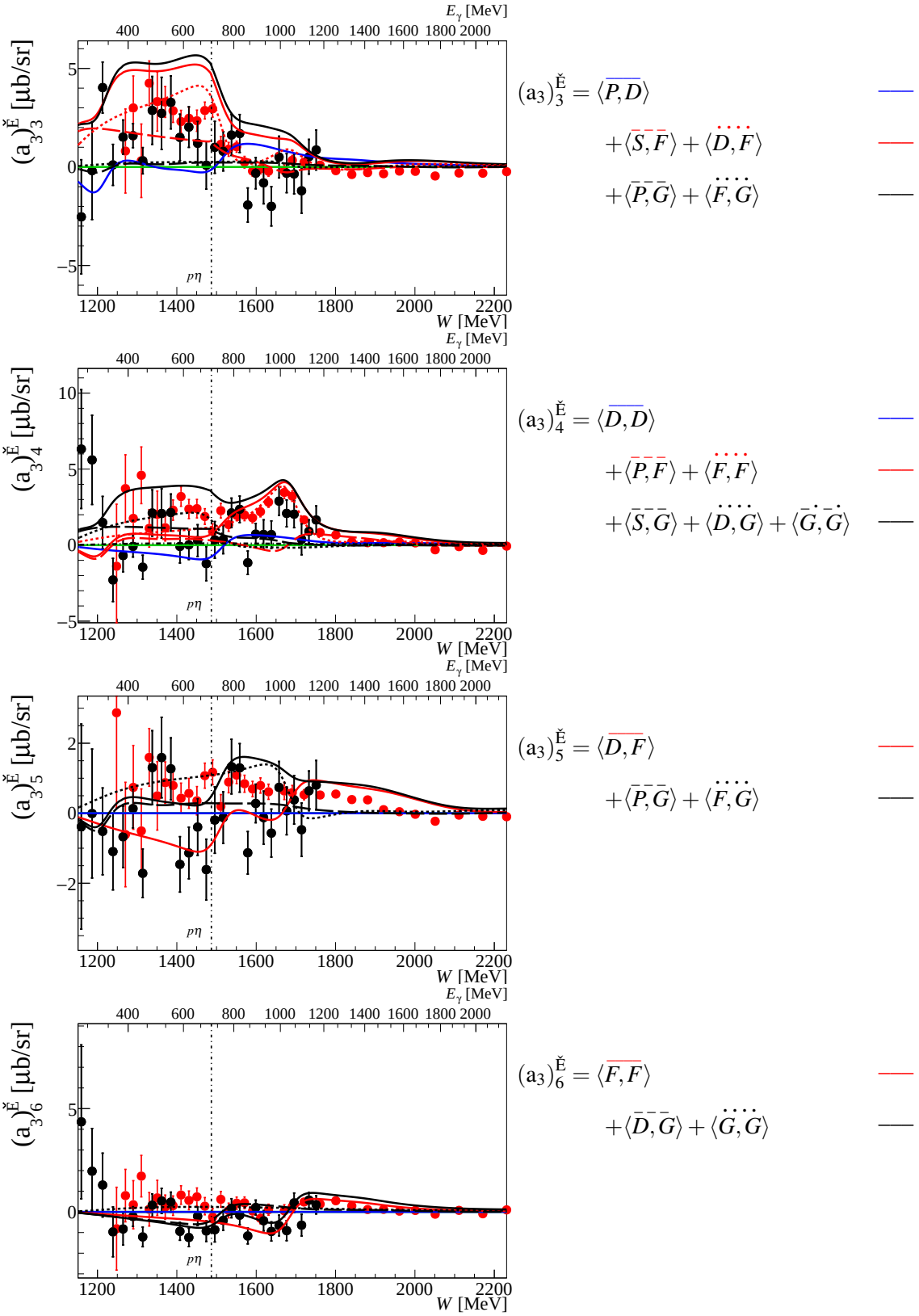

Fig. A.31: Comparison of the fit coefficients $(a_3)_{3\ldots6}^{\check{E}}$ for $\vec{\gamma}\vec{p}\to n\pi^+$ as a function of the higher center of mass energy W. The remaining plots which correspond to Fig. A.30. For further information, see caption of Fig. A.30.

Appendix B

Formulas

B.1 Novosibirsk Function

The Novosibirsk function has the form [140]:

$$f(x) = A \cdot \exp\left(0.5 \cdot \left(\ln^2(1+\Lambda\tau\cdot(x-\mu))/\tau^2+\tau^2\right)\right) \text{ with } \Lambda = \frac{\sinh(\tau\sqrt{\ln(4)})}{\sigma\tau\sqrt{(\ln(4)}}, \tag{B.1}$$

with A being the amplitude, μ the position of the peak, σ the peak widths, and τ the tail of the peak. The tail factor τ allows for an asymmetric shaped Gaussian distribution which is important to take the low energetic tail of the invariant and missing mass distributions of the selected data into account.

B.2 Chebyshev Polynomial used for Background Description

The Chebyshev Polynomial $f(x)$ up to the 4th order is given by:

$$f(x) = a\cdot x + b\cdot(2x^2-1) + c\cdot(4x^3-3x) + d\cdot(8x^4-8x^2+1) \tag{B.2}$$

with a, b, c and d being free parameters for the fitting procedure.

B.3 $\gamma p \to n\pi^+$

Due to the existing information of the initial state and the angular information of the π^+ in the final state, the two-body kinematic reaction $\gamma p \to n\pi^+$ is an over-determined reaction. Therefore, reaction kinematics can be used to build selection criteria on the data [141]. The initial state information is used to calculate the center of mass energy W, which is given by:

$$W^2 = m_n^2 + 2E_\gamma m_n \tag{B.3}$$

where m_n is the mass of the neutron and E_γ is the energy of the incoming beam photon. As a next step, quantities in the cms frame are defined.

$$p* = \frac{\sqrt{(W^2-(m_n+m_\pi)^2)\,(W^2-(m_n-m_\pi)^2)}}{2W}, \tag{B.4}$$

$$E_\pi^* = \frac{W^2-m_n^2+m_\pi^2}{2W}, \tag{B.5}$$

$$E_n^* = \frac{W^2-m_\pi^2+m_n^2}{2W}, \tag{B.6}$$

$$\beta_\pi^* = \frac{p^*}{E_\pi^*}. \tag{B.7}$$

$$\beta_n^* = \frac{p^*}{E_n^*}. \tag{B.8}$$

Thereby, E^* is the energy of the particles in the cms frame, p^* is the momentum, and β^* is the velocity as a multiple of the speed-of-light. With these quantities and β and γ in the lab frame, which are given by:

$$\beta = \frac{p}{E} = \frac{E_\gamma}{E_\gamma+m_n} \tag{B.9}$$

$$\gamma = \frac{E}{M} = \frac{E_\gamma+m_n}{W}, \tag{B.10}$$

the polar angle of the π^+ in the cms frame can be boosted to the lab frame:

$$\begin{aligned}\tan\Theta_\pi = \frac{p_\pi^T}{p_\pi^Z} &= \frac{p*\sin\Theta_\pi^*}{\gamma p^*\cos\Theta_\pi^*+\beta\gamma E_\pi^*} \\ &= \frac{\sin\Theta_\pi^*}{\gamma(\cos\Theta_\pi^*+\beta/\beta_\pi^*)}.\end{aligned} \tag{B.11}$$

Rewriting the Eq. (B.11) gives:

$$f(\Theta_\pi^*) =: \Theta_\pi - \mathrm{atan2}(\sin\Theta_\pi^*, \gamma(\cos\Theta_\pi^*+\beta/\beta_\pi^*) = 0, \tag{B.12}$$

which needs to be minimized numerically to obtain the value for the polar angle of the π^+ in the cms frame. One of the problem in this minimization is that the resulting values for the polar angle are discrete as the beam energy can only provide fixed energies with a width in the order of 2 MeV. A possible solution is to investigate the neutron polar angle if it has been detected. The correlation between the laboratory frame polar angle with the polar angle of the π^+ in the cms frame is given by:

$$\tan\Theta_n = \frac{\sin\Theta_\pi^*}{\gamma(-\cos\Theta_\pi^*+\beta/\beta_n^*)}. \tag{B.13}$$

Thus, the following functions need to be minimized as well:

$$g(\Theta_\pi^*) =: \Theta_N - \text{atan2}(\sin\Theta_\pi^*, \gamma(-\cos\Theta_\pi^* + \beta/\beta_n^*) = 0. \tag{B.14}$$

Taking into account the angular resolutions of both particles, the final combined function to be minimized is:

$$\chi^2 = \left(\frac{f(\Theta_\pi^*)}{\sigma_{\theta_\pi}}\right)^2 + \left(\frac{g(\Theta_\pi^*)}{\sigma_{\theta_N}}\right)^2 \tag{B.15}$$

After the global minimum was found [1], the polar angle of the neutron can be calculated based on the kinematics of the cms frame. Thus, the polar angle of the neutron in the cms frame is given by:

$$\Theta_n^* = \pi - \Theta_\pi^*. \tag{B.16}$$

Similar to Eq. (B.11), the polar angle of the neutron in the lab frame can be determined via:

$$\Theta_n = \text{atan2}(\sin\Theta_n^*, \gamma(\cos\Theta_n^* + \beta/\beta_n^*) \tag{B.17}$$

This kinematic calculation can be used to correlate the reconstructed polar angle of the neutron with the calculated one and thus select the events of interest.
In addition, the center of mass energies defined in Eq. (B.5) and Eq. (B.6) can be boosted back into the lab-frame and be compared with the measured energies. Thereby, the energies of the charged pion and neutron candidate in the lab-frame are given by:

$$E_\pi = \gamma \cdot (E_\pi^* + \beta p^* \cos\Theta_\pi^*) - m_\pi \tag{B.18}$$

$$E_n = \gamma \cdot (E_n^* + \beta p^* \cos\Theta_n^*) - m_n \tag{B.19}$$

where m_n and m_π are the rest masses of the neutron and the charged pion, respectively.

[1] For the events, where the neutron was detected, both minimization methods were performed and compared. Both were in perfect agreement.

List of figures

List of tables

Bibliography

[1] R. Frisch and O. Stern, "*Über die magnetische Ablenkung von Wasserstoffmolekülen und das magnetische Moment des Protons*", Zeitschrift für Physik **85** (1933) 4–16.

[2] R. W. McAllister and R. Hofstadter, "*Elastic Scattering of 188-Mev Electrons from the Proton and the Alpha Particle*", Phys. Rev. **102** (1956) 851.

[3] M. Thomson, *"Modern particle physics"*, Cambridge University Press, 2013.

[4] A. Bettini, *"Introduction to Elementary Particle Physics"*, Cambridge University Press, 2008.

[5] M. Gell-Mann and Y. Ne'eman, "*The Eightfold Way*", Nucl. Phys. **79** (1964) 477–478.

[6] R. Aaij et al., "*Observation of $J\psi p$ Resonances Consistent with Pentaquark States in $\Lambda_b^0 \to J/\psi K^- p$ Decays*", Phys. Rev. Lett **115** (2015) 072001.

[7] M. Tanabashi et al., "*The Review of Particle Physics*", Phys. Rev. D **98**.030001 (2018).

[8] H. L. Anderson et al., "*Total Cross Sections of Positive Pions in Hydrogen*", Phys. Rev. **85**.936 (1952).

[9] S. Capstick and W. Roberts, "*Quark models of baryon masses and decays*", Prog. Part. Nucl. Phys. S **45** (2000) 241–331.

[10] S. Capstick and W. Roberts, "*Missing Baryons*", Phys. Rev. D **49** (1994) 4570.

[11] U. Löring, B. Ch. Metsch, and H.R. Petry, "*The light baryon spectrum in a relativistic quark model with instanton-induced quark forces: The non-strange baryon spectrum and ground-states*", Eur. Phys. J. A **10** (2001) 395–446.

[12] M. Ronninger and B. Metsch, "*Effects of a spin-flavour dependent interaction on the baryon mass spectrum*", Eur. Phys. J. A **47** (2011) 162.

[13] K. Nakamura et al., "*The Review of Particle Physics*", J. Phys. G **37**.075021 (2010).

[14] F. Afzal, "*Measurement of the beam and helicity asymmetries in the reactions $\gamma p \to p\pi^0$ and $\gamma p \to p\eta$*", PhD thesis, University of Bonn, 2019.

[15] A. Thiel et al., "*Three-Body Nature of N^* and Δ^* Resonances from Sequential Decay Chains*", Phys. Rev. Lett **65** (2015) 091803.

[16] R. G. Edwards et al., "*Excited state baryon spectroscopy from lattice QCD*", Phys. Rev. D **84** (2011) 074508.

[17] O. Bartholomy et al., "*Neutral-Pion Photoproduction off Protons in the Energy Range 0.3 GeV < E_γ < 3 GeV*", Phys. Rev. Lett. **94** (2005) 012003.

[18] S. Schumann et al., "*Radiative π^0 photoproduction on protons in the $\Delta^+(1232)$ region*", Eur. Phys. J. A **43** (2010) 269.

[19] J. Ahrens et al., "*Helicity dependence of $\gamma p \to N\pi$ below 450 MeV and contribution to the Gerasimov-Drell-Hearn sum rule*", Phys. Rev. Lett. **84** (2000).

[20] J. Ahrens et al., "*Helicity dependence of the $\gamma p \to N\pi$ channels and multipole analysis in the Δ region*", Eur. Phys. J. A **21** (2004) 323–333.

[21] V. Crede et al., "*Photoproduction of η mesons off protons for 0.75 GeV < E_γ < 3 GeV*", Phys. Rev. Lett. **94** (2005) 012004.

[22] V. Crede et al., "*Photoproduction of η and eta$'$ mesons off protons*", Phys. Rev. C **80** (2009) 055202.

[23] E. F. McNicoll, S. Prakhov, and I. I. Strakovsky et al., "*Experimental study of the $\gamma p \to \eta p$ reaction with the Crystal Ball detector at the Mainz Microtron (MAMI-C)*", Phys. Rev. C **82** (2010) 035208.

[24] W. Struczinski et al., "*Study of photoproduction on hydrogen in a streamer chamber with tagged photons for 1.6 GeV < E_γ < 6.3 GeV*", Nucl. Phys. B **108** (1976) 45.

[25] A. Braghieri et al., "*Total cross-section measurement for the three double pion production channels on the proton*", Phys. Lett. B **363** (1995) 46.

[26] C. Wu et al., "*Photoproduction of ρ^0-mesons and Δ-baryons in the reaction $\gamma p \to p\pi^+\pi^-$ at energies up to $\sqrt{s}$ = 2.6 GeV*", Eur. Phys. J. A **23** (2005) 317.

[27] U. Thoma and M. Fuchs et al., "*N^* and Δ^* decays into $N\pi^0\pi^0$*", Phys. Lett. B **659** (2008) 87.

[28] V. Sokhoyan et al., "*High statistics study of the reaction $\gamma p \to p2\pi^0$*", Eur. Phys. J. A **51** (2015) 95.

[29] J. Ahrens et al., "*Helicity dependence of the reaction $\gamma p \to n\pi^+\pi^0$ in the second resonance region*", Phys. Rev. Lett. B **551** (2003) 49–55.

[30] R.L. Workman et al., "*Parameterization dependence of T-matrix poles and eigenphases from a fit to πN elastic scattering data*", Phys. Rev. C **86** (2012) 035202.

[31] A. Fix and H. Arenhoevel, "*Double pion photoproduction on nucleon and deuteron*", Eur. Phys. J. A **25** (2005) 115–135.

[32] M. Benmerrouche, N. C. Mukhopadhyay, and J. F. Zhang, "*Effective Lagrangian approach to the theory of photoproduction in the N^* (1535) region*", Phys. Rev. D **51** (1995) 3237–3266.

[33] E. M. Darwish and S.S. Al-Thoyaib, "*Incoherent pion photoproduction on the deuteron including polarization effects*", Annals of Physics **326** (2011) 604–625.

[34] B. Krusche and S. Schadmand, "*Study of Non-Strange Baryon Resonances with Meson Photoproduction*", Prog. Part. Nucl. Phys. **51** (2003) 399–485.

[35] Y. Wunderlich, "*The complete experiment problem of pseudoscalar meson photoproduction in a truncated partial wave analysis*", PhD thesis, University of Bonn, 2018.

[36] G. F. Chew et al., "*Relativistic Dispersion Relation Approach to Photomeson Production*", Phys. Rev. **106** (1957) 1345–1355.

[37] R. Leukel, "*Photoproduktion neutraler Pionen am Proton mit linear polarisierten Photonen im Bereich der Δ(1232)–Resonanz*", PhD thesis, University of Mainz, 2001.

[38] D. Drechsel and L. Tiator, "*Threshold pion photoproduction on nucleons*", J. Phys. G **18** (1992) 449–497.

[39] A. V. Anisovich, R. Beck, and M. Döring et al., "*The Impact of New Polarization Data from Bonn, Mainz and Jefferson Laboratory on $\gamma p \to \pi N$ Multipoles*", Eur. Phys. J. A **52** (2016) 284.

[40] K. Spieker, "*Determination of the polarization observables Σ and G in the reaction $\gamma p \to p\pi^0\pi^0$*", Master thesis, University of Bonn, 2013.

[41] W. Chiang and F. Tabakin, "*Completeness rules for spin observables in pseudoscalar meson photoproduction*", Phys. Rev. C **55** (1997) 2054–2066.

[42] I. S. Barker, A. Donnachie, and J. K. Storrow, "*Complete Experiments in Pseudoscalar Photoproduction*", Nucl. Phys. B **95** (1975) 347–356.

[43] Y. Wunderlich, F. Afzal, A. Thiel, and R. Beck, "*Determining the dominant partial wave contributions from angular distributions of single- and double-polarization observables in pseudoscalar meson photoproduction*", Eur. Phys. J. A **53** (2005) 86.

[44] M. Abramowitz and I. Stegun, *"Handbook of Mathematical Functions"*, Dover Publishing, 1972.

[45] A. Thiel, "*Bestimmung der Doppelpolarisationsobservablen G in π^0-Photoproduktion*", PhD thesis, University of Bonn, 2012.

[46] A. V. Anisovich et al., "*Proton-η' interactions at threshold*", Phys. Lett. B **785** (2018) 626–630.

[47] D. Rönchen, "*Baryon resonances in pion- and photon-induced hadronic reactions*", PhD thesis, University of Bonn, 2014.

[48] M. Döring, C. Hanhart, F. Huang, S. Krewald, and U.-G. Meißner, "*Analytic properties of the scattering amplitude and resonances parameters in a meson exchange model*", Nucl. Phys. A **829** (2009) 170–209.

[49] D. Drechsel, S. Kamalov, and L. Tiator, "*Unitary isobar model –MAID2007*", Eur. Phys. J. A **34** (2007) 69.

[50] D. Rönchen, M. Döring, and U.-G. Meißner, "*The impact of $K^+\Lambda$ photoproduction on the resonance spectrum*", Eur. Phys. J. A **54** (2018) 110.

[51] V. Crede et al., "*Photoproduction of neutral pions off protons*", Phys. Rev. C **84** (2011) 055203.

[52] P. Adlarson et al., "*Measurement of π^0 photoproduction on the proton at MAMI C*", Phys. Rev. C **92** (2015) 024617.

[53] O. Bartalini et al., "*Measurement of π^0 photoproduction on the proton from 550 to 1500 MeV at GRAAL*", Eur. Phys. J. A **26** (2005) 399–419.

[54] M. Dugger et al., "*Beam asymmetry Σ for π^+ and π^0 photoproduction on the proton for photon energies from 1.102 to 1.862 GeV*", Phys. Rev. C **89** (2014) 029901.

[55] S. Gardner, "*Polarisation Observables in Neutral Pion Photoproduction with MAMI*", PhD thesis, University of Glasgow, 2016.

[56] S. Gardner et al., "*Photon asymmetry measurements of $\vec{\gamma}\mathrm{p} \to \pi^0\mathrm{p}$ for E_γ=320−650 MeV*", Eur. Phys. J. A **52** (2016) 333.

[57] R. Beck et al., "*Determination of the E2/M1 ratio in the $\gamma N \to \Delta(1232)$ transition from a simultaneous measurement of $p(\vec{\gamma}, p)\pi^0$ and $p(\vec{\gamma}, \pi^+)n$*", Physical Rev. C **61** (2000).

[58] N. Sparks et al., "*Measurement of the beam asymmetry Σ in the forward direction for $\vec{\gamma}p \to p\pi^0$*", Phys. Rev. C **81** (2010) 065210.

[59] M. Sumihama et al., "*Backward-angle photoproduction of π^0 mesons on the proton at E_γ=1.5-2.4 GeV*", Phys. Lett. B **657** (2007) 32–37.

[60] J. Hartmann, "*Measurement of Double Polarization Observables in the Reactions $\gamma p \to p\pi^0$ and $\gamma p \to p\eta$ with the Crystal Barrel/TAPS Experiment at ELSA*", PhD thesis, University of Bonn, 2017.

[61] J. Hartmann et al., "*The polarization observables T, P, and H and their impact on $\gamma p \to p\pi^0$ multipoles*", Phys. Lett. B **748** (2015) 212–220.

[62] J. R. M. Annand et al., "*T and F asymmetries in π^0 photoproduction on the proton*", Phys. Rev. C **93** (2016) 055209.

[63] M. Gottschall et al., "*First Measurement of the Helicity Asymmetry for $\gamma p to p\pi^0$ in the Resonance Region*", Phys. Rev. Lett. **112** (2014) 012003.

[64] A. Thiel et al., "*Double-polarization observable G in neutral-pion photoproduction off the proton*", Eur. Phys. J. A **53** (2017) 8.

[65] J. Ajaka et al., "*Precise measurement of Σ beam asymmetry for positive pion photoproduction on the proton from 550 to 1100 MeV*", Physical Lett. B. **475** (2000) 372–377.

[66] O. Bartalini et al., "*Precise Measurement of Σ Beam Asymmetry for Positive Pion Photoproduction on the Proton from 800 to 1500 Mev*", Physical Lett. B **544** (2002) 113–120.

[67] J. Ahrens et al., "*Measurement of the G asymmetry for the $\gamma p \to N\pi$ channels in the $\Delta(1232)$ resonance region*", Eur. Phys. J. A **26** (2005) 135.

[68] S. Strauch et al., "*First Measurement of the Polarization Observable E in the $\vec{p}(\vec{\gamma}, \pi^+)n$ Reaction up to 2.25 GeV*", Phys. Lett. B **750** (2015) 53–58.

[69] A. Belayev et al., "*Investigation of the G and H parameters for the reaction $\gamma p \to n\pi^+$ in the region of the first πN resonance*", Sov. J. Nucl. Phys. **40** (1984) 83.

[70] P.J. Bussey et al., "*Measurement of the polarization parameters G and H in positive pion photoproduction*", Nucl. Phys. B **403-414** (1980) 83.

[71] W. J. Briscoe et al., *George Washington University Partial Wave Analysis*, URL: http://gwdac.phys.gwu.edu/ (visited on 08/22/2019).

[72] A. V. Anisovich et al., "*Properties of baryon resonances from a multichannel partial wave analysis*", Eur. Phys. J. A **48** (2012) 15.

[73] H. van Pee et al., "*Photoproduction of π^0 Mesons off Protons from the $\Delta(1232)$ Region to E_γ = 3 GeV*", Eur. Phys. J. A **31** (2007) 61–77.

[74] M. Dugger et al., "*π^0 photoproduction on the proton for photon energies from 0.675 to 2.875 GeV*", Phys. Rev. C **76** (2007) 025211.

[75] J. Ahrens et al., "*Measurement of the helicity dependence for the $n\pi^+$ channel in the second resonance region*", Phys. Rev. C **74** (2006) 045204.

[76] G. Blanpied et al., "*$N \to \Delta$ transition and proton polarizabilities from measurements of $p(\vec{\gamma}, \gamma)$, $p(\vec{\gamma}, \pi^0)$, and $p(\vec{\gamma}, \pi^+)$*", Phys. Rev. C **64** (2001) 25203.

[77] D. Werthmüller, "*Experimental study of nucleon resonance contributions to η-photoproduction on the neutron*", PhD thesis, University of Basel, 2014.

[78] M. Dehn et al., "*The MAMI C accelerator. The beauty of normal conducting multi-turn recirculators*", Eur. Phys. J. Special Topics **198** (2011) 19–47.

[79] K. Aulenbacher et al., "*The MAMI source of polarized electrons*", Nucl. Instr. Meth. A **391** (1997) 498–506.

[80] P. Martel, "*Measuring proton spin polarizabilities with polarized compton scattering*", PhD thesis, University of Massachusetts Amherst, 2013.

[81] H. Herminghaus, "*The Mainz microtron: Operation experience and upgrade progress*", *Proceedings of the 1988 Linear Accelerator Conference*, 1988.

[82] A. Jankowiak, "*The Mainz Microtron MAMI | Past and future*", Eur. Phys. J. A **28** (2006) 149–160.

[83] H. Herminghaus et al., "*The design of a cascaded 800 MeV normal conducting c.w. race track microtron*", Nucl. Instr. Meth. I **38** (1976) 1–12.

[84] B. Otte, "*Erste Messung der π^0-Photoproduction an transversal polariseirten Protonen nahe der Schwelle*", PhD thesis, University of Mainz, 2015.

[85] D. Howdle, "*Measurement of Polarisation Observables using Linearly Polarised Photons with the Crystal Ball at MAMI*", PhD thesis, University of Glasgow, 2012.

[86] J. C. McGeorge et al., "*Upgrade of the Glasgow photon tagging spectrometer for Mainz MAMI-C*", Eur. Phys. J. A **37** (2008) 129–137.

[87] J. Annand, *"The Glasgow/Mainz Bremsstrahlung Tagger Operations Manual"*, 2008.

[88] G. Reicherz, "*NMR Polarization Measurement*", *A2-meeting*, 2016.

[89] A. Abragam and M. Goldmann, "*Principles of Dynamic Nuclear Polarisation*", Reports on Progress in Physics **41** (1978) 395.

[90] A. Thomas, "*Polarised targets for 4π detectors at MAMI*", Eur. Phys. J. Special Topics **198** (2011) 171–180.

[91] H. London, G.R. Clarke, and Eric Mendoza, "*Osmotic Pressure of He^3 in Liquid He^4 with Proposals for a Refrigerator to Work below 1K*", Phys. Rev. **128** (1962) 1992–2005.

[92] N. Frömmgen, "*Aufbau und Test einer NMR-Apparatur zur Messung des Polarisationgrades hyperpolarisierter Targetnukleon*", Diploma thesis, University of Mainz, 2009.

[93] M. MacCormick et al., "*Total photoabsorption cross section for 4He from 200 to 800 MeV*", Phys. Rev. C **55(3)** (1997) 1033–1038.

[94] A. Mushkarenkov, "*Multi-wire proportional chamber*", *A2-meeting*, 2011.

[95] T.A. Rostomyanl, *"Cherenkov manual"*, Research Wiki, 2015.

[96] T. Rostomyan, "*THE CHERENKOV DETECTOR*", *A2-meeting*, 2013.

[97] M. Dieterle, "*Measurement of Polarization Observablesin π^0 and $\pi^0\pi^0$ Photoproduction from Protons and Neutrons at MAMI and ELSA*", PhD thesis, University of Basel, 2015.

[98] U. Timm, "*Coherent Bremsstrahlung of Electrons in Crystals*", Fortschritte der Physik **17** (1969) 765–808.

[99] H. Eberhardt, "*Bestimmung von Polarisationsobservablen in der π^0 und ω Photoproduktion am Proton mit dem CBELSA/TAPS-Experiment*", PhD thesis, University of Bonn, 2012.

[100] K. Livingston, "*The Stonehenge Tehnique. A new method for aligning coherent bremsstrahlung radiators*", Nucl. Instr. Meth. A **603** (2009) 205–213.

[101] K. Livingston, "*Bremsstrahlung*", A2-DAQ Wiki.

[102] P. Pauli, "*Investigation of the Absolute Normalisation of the Helicity Dependent Cross-Sections $\sigma^{1/2}$ and $\sigma^{3/2}$*", Master thesis, University of Bonn, 2016.

[103] K. Livingston, "*Polarization from Coherent Bremsstrahlung Enhancement*", CLAS NOTE 2011-020, 2011.

[104] R. Macrae, "*Polarisation Observables in π^0 Photoproduction at MAMI*", Master thesis, University of Glasgow, 2017.

[105] S. Costanza, "*Report in the Moeller analysis of the Jan/Feb 2014 beam time*", *A2-meeting*, 2014.

[106] V. Tioukine, K. Aulenbacher, and E. Riehn, "*A Mott polarimeter operating at MeV electron beam energies*", Review of Scientific Instruments **82** (2011) 033303.

[107] B. Otte, "*Aufbau und Test eines Møllerpolarimeters für das Crystal-Ball-Experiment an MAMI-C*", Diploma thesis, University of Mainz, 2008.

[108] G. Braun et al., "*TDC Chip and Readout Driver Developments for COMPASS and LHC-Experiments*", arXiv:hep-ex/9810048 (1998).

[109] E. Downie, "*Radiative π^0 photoproduction in the region of the $\Delta(1232)$ region*", PhD thesis, University of Glasgow, 2006.

[110] P. Drexler et al., "*The new read-out electronics for the BaF_2-calorimeter TAPS*", IEEE Transactions on Nuclear Science **50(4)** (2003) 969–973.

[111] P. Pedroni, "*Cherenkov Status report*", *A2-meeting*, 2014.

[112] D. Watts, "*PID-II status*", *A2-meeting*, 2014.

[113] J. R. M. Annand, *"Data Analysis within an AcquRoot Framework"*, 2008.

[114] R. Brun and F. Rademakers, "*ROOT - An Object Oriented Data Analysis Framework*", Nucl. Instr. Meth. A **389** (1997) 81–86.

[115] C. Collicott, "*Probing proton structure through single polarisation observables of compton scattering and π^0 photoproduction within the $\Delta(1232)$ region*", PhD thesis, University of Dalhouse, 2015.

[116] D. Glazier, *A Geant4 simulation for the CrystalBall@MAMI Setup"*, 2012.

[117] S. Agostinelli et al., "*Geant4 - a simulation toolkit*", Nucl. Instr. Meth. A **506** (2003) 250–303.

[118] J. Allison et al., "*Geant4 developments and application*", IEEE Trans. Nucl.Sci. **53** (2006) 270–278.

[119] M. Unverzagt, "*Bestimmung des Dalitz-Plot-Parameters α für den Zerfall $\eta \to 3\pi^0$ mit dem Crystal Ball am MAMI*", PhD thesis, University of Bonn, 2008.

[120] M. Lang, "*Aufbau des GDH-Experiments und Messung der Helizitätsabhängigkeit von $\vec{\gamma}\vec{p} \to p\pi^+\pi^-$ von der Schwelle bis 800 MeV with MAMI*", PhD thesis, University of Mainz, 2004.

[121] T.C. Awes et al., "*A simple method of shower localization and identification in laterally segmented calorimeters*", Nucl. Instr. Meth. A **311** (1992) 130–138.

[122] K. Molenaar, "*Performance of TAPS in the Tagged Photon Beam of MAMI*", Diploma thesis, University of Groningen, 1992.

[123] J. Wettig, "*Aufbau und Inbetriebnahme einer neuen HV-Versorgung für den Crystal Ball Detektor am MAMI*", Diploma thesis, University of Mainz, 2013.

[124] M. Martemianov et al., "*A new measurement of the neutron detection efficiency for the NaI Crystal Ball detector*", J. Instrum. **10** (2015).

[125] D. Watts, "*PID status*", *A2-meeting*, 2016.

[126] F. Zehr et al., "*Photoproduction of $\pi^0\pi^0$- and $\pi^0\pi^+$-pairs off the proton from threshold to the second resonance region*", Eur. Phys. J. A **48** (2012) 98.

[127] J. Ahrens et al., "*First measurement of the helicity dependence for the $\gamma p \to p\pi^+\pi^-$ reaction*", Eur. Phys. J. A **34** (2007) 11–21.

[128] E. Gutz, "*Measurement of beam asymmetries in the reaction $\gamma p \to p\pi^0\eta$ with the Crystal Barrel/TAPS experiment at ELSA*", Dissertation, University of Bonn, 2010.

[129] F. Afzal, "*Measurement of the double polarization observables E and G at the Crystal Ball experiment at MAMI*", *Hadrons 2016*, 2016.

[130] Wolfram Research Inc., "*Mathematica, Version 11.3*", Champaign, IL, 2018.

[131] A. Thomas, "*The Gerasimov-Drell-Hearn sum rule at MAMI*", Eur. Phys. J. A **28** (2006) 161–171.

[132] K. Livingston, private communication, 2019.

[133] P. E. Bosted, "*Experimental Tests of the GDH and other sum rules at SLAC*", GDH 2002, World Scientific (2003) 157–164.

[134] K. H. Althoff et al., "*Photoproduction of Neutral Pions at Backward Angles in the Resonance Region and the η-Cusp*", Z. Physik C, Particles and Fields **1** (1979) 327–336.

[135] D. Rönchen et al., "*Photocouplings at the Pole from Pion Photoproduction*", Eur. Phys. J. A **50** (2014) 101.

[136] A. V. Anisovich et al., "*Evidence for $\Delta(2200)7/2^-$ from photoproduction and consequence for chiral-symmetry restoration at high mass*", Phys. Lett. B **766** (2017) 357–361.

[137] R. Beck et al., "*Measurement of the E2/M1 Ratio in the $N \to \Delta$ Transition Using the Reaction $p(\vec{\gamma}, p)\pi^0$*", Physical Rev. Lett. **79** (1997) 606–609.

[138] S. Strauch, "*Non-strange baryons*", *NSTAR2019 – The 12th International Workshop on the Physics of Excited Nucleons*, 2019.

[139] C. Collicott, "*Systematics of photon polarisation*", Internal A2 note, 2017.

[140] M. Gottschall et al., "*Documentation of the TAPS Energy Calibration for the CB-ELSA/TAPS Experiment*", CB-ELSA/TAPS Note, 2009.

[141] J. Hartmann, "*Analysis of $\gamma p \to \pi^+ n$*", Internal Analysis Meeting, 2015.

Acknowledgements

First, I would like to thank my supervisor Prof. Dr. Reinhard Beck for giving me the great opportunity to be part of his research group and to write my dissertation in his group. I am grateful that I got to represent the group on various occasions and present my research results at international conferences. I considered these experiences extremely beneficial for myself and my thesis work.

I also want to express my gratitude to Prof. Dr. Michael Ostrick, Prof. Dr. Ulf-G. Meißner and Prof. Dr. Reinhard Klein for agreeing to be part of my thesis committee.

I want to thank all members of the A2 collaboration and the technical staff at MAMI in Mainz, Germany. Many people are involved in making an experiment of such scale work. There are, however, a few colleagues I want to thank specifically for their collaboration during this last six years: Dr. Farah Afzal, Edoardo Mornacchi , Federico Cividini, Dr. Susanna Costanza, Dr. Dominik Werthmüller, Dr. Natalie Walford, Michael Günther, Samuel Abt, Dr. Philippe Martel, Dr. Cristina Collicott, Maik Biroth, Jennifer Wettig, Sascha Wagner, Dr. Simon Gardner, Dr. Michaela Thiel, Dr. Lena Heijkenskjöld, and so many more. I also want to acknowledge the support from and the discussions I had with Prof. Dr. Paolo Pedroni, Dr. Ken Livingston, and Dr. Andreas Thomas regarding my data analysis.

Furthermore, I want to thank all members of the CBELSA/TAPS collaboration and the other research groups at the HISKP Bonn, Germany. I owe special thanks to Dr. Mikhail Mikhasenko, Nils Stausberg, Sebastian Ciupka, Eugenia Fix, Dr. Yannick Wunderlich, Jun.-Prof. Dr. Annika Thiel, and Dr. Farah Afzal. Thank you very much to everyone who made my time at the University of Bonn an unforgettable experience.

Last but not least, I want to thank my family and my girlfriend Rebecca. Words cannot express how thankful I am for your support and for being in my life. Thank you.